ISINN-29

Neutron Spectroscopy, Nuclear Structure, Related Topics

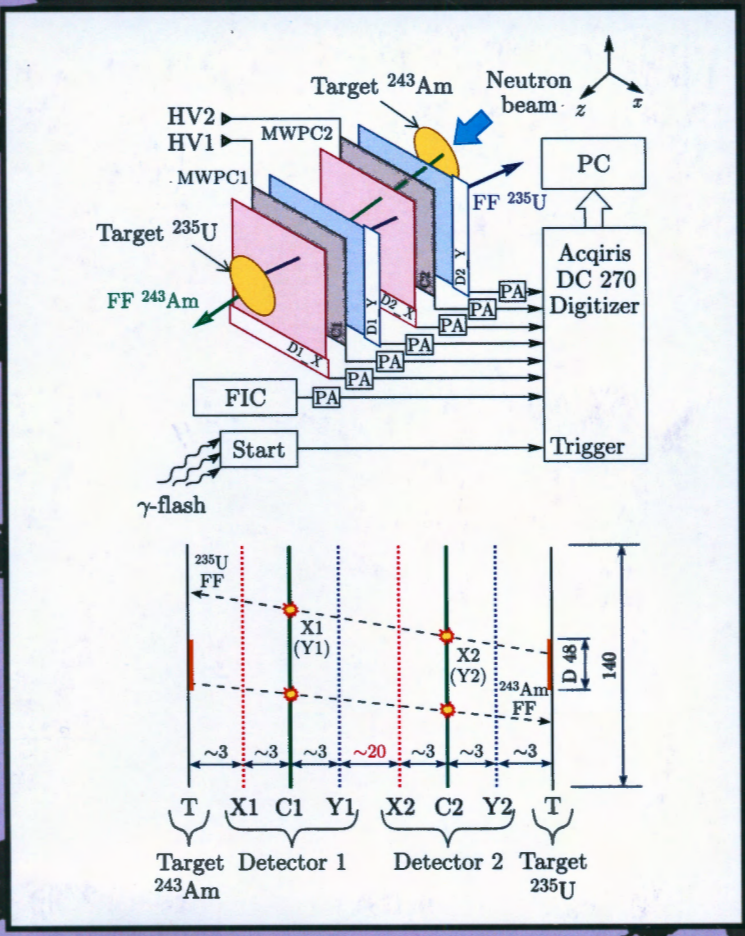

Joint Institute for Nuclear Research

FUNDAMENTAL INTERACTIONS & NEUTRONS, NUCLEAR STRUCTURE, ULTRACOLD NEUTRONS, RELATED TOPICS

XXIX International Seminar on Interaction of Neutrons with Nuclei

Dubna, Russia, May 29 – June 2, 2023

Proceedings of the Seminar

Dubna • 2023

УДК 539.125.5(042)
ББК 22.383.2я431+22.383.5я431+22.383.25я431
F97

Organized by

Frank Laboratory of Neutron Physics, JINR, Dubna
State Key Laboratory of Intense Pulsed Radiation Simulation and Effect, NINT, China
School of Nuclear Science and Technology, Lanzhou University, China

The contributions are reproduced directly from the originals presented by the Organizing Committee.

F97 **Fundamental** Interactions & Neutrons, Nuclear Structure, Ultracold Neutrons, Related Topics: Proceedings of the XXIX International Seminar on Interaction of Neutrons with Nuclei (Dubna, Russia, May 29 – June 2, 2023). — Dubna: JINR, 2023. — 320 p.

ISBN 978-5-9530-0604-0

This collection of papers reflects the present state of neutron-aided investigations of the properties of the nucleus, including fundamental symmetries, properties of the neutron itself, neutron-excited reactions, and the parameters of the nucleus that determine the reaction cross section, as well as the latest theoretical development of all these problems. The works on experimental investigations in the physics of fission by neutrons of various energies are presented in great detail. The present state of experiments on the physics of ultracold neutrons and facilities to obtain them is described at length. The status achieved by now of the latest (from the viewpoint of technique) experiments and environment studies is covered as well.

Фундаментальные взаимодействия и нейтроны, структура ядра, ультрахолодные нейтроны, связанные темы: Труды XXIX Международного семинара по взаимодействию нейтронов с ядрами (Дубна, Россия, 29 мая – 2 июня 2023 г.). — Дубна: ОИЯИ, 2023. — 320 с.

ISBN 978-5-9530-0604-0

В сборнике представлено современное состояние исследований свойств ядра с помощью нейтронов: фундаментальных симметрий и свойств самого нейтрона, возбуждаемых им реакций и параметров ядра, определяющих их сечения, а также последние теоретические разработки всех этих вопросов. Очень детально представлены работы по всем аспектам, связанным с экспериментальными исследованиями физики деления ядра нейтронами различных энергий. Достаточно полно описано современное состояние экспериментов по физике ультрахолодных нейтронов и установок для их получения, а также достигнутый к настоящему времени статус методически новейших экспериментов и результаты экологических исследований.

УДК 539.125.5(042)
ББК 22.383.2я431+22.383.5я431+22.383.25я431

ISBN 978-5-9530-0604-0

ORGANIZING COMMITTEE

Conference Chairs

Valery Shvetsov (JINR), Dongwei Hei (NINT), Ximeng Chen (LZU)

Directors of Local Organizing Committee

Walter Furman (JINR), Mengtong Qiu (NINT), Ze'en Yao (LZU)

Scientific Secretaries

Alexander Nezvanov (JINR), Liang Sheng (NINT), Zheng Wei (LZU)

Committee Members

Marina Frontasyeva (JINR), Yuri Kopatch (JINR), Egor Lychagin (JINR), Ludmila Mitsyna (JINR), Pavel Sedyshev (JINR), Inga Zinicovscaia (JINR), Liang Sheng (NINT), Wei Chen (NINT), Quanlin Shi (NINT), Xinjian Tan (NINT), Zhiming Li (NINT), Zhongming Wang (NINT), Tianjiao Liang (CSNS), Ruirui Fan (CSNS), Jian Gong (CAEN), Shilong Liu (CIAE), Xichao Ruan (CIAE), Zhiqiang Chen (IMP), Lei Yang (IMP), Guohui Zhang (PKU), Yigang Yang (THU), Liangzhi Cao (XJTU), Sheng Wang (XJTU), Wenbao Jia (NUAA), Bin Tang (ECUT), Ze'en Yao (LZU), Zheng Wei (LZU)

Secretariat

Elena Rusakovich (JINR), Tatiana Pikelner (JINR), Elena Kopach (JINR), Zheng Wei (LZU), Daqian Hei (LZU), Dapeng Xu (LZU), Changlin Lan (LZU), Junrun Wang (LZU), Xiaolong Lu (LZU), Dan Lin (LZU), Min Zhang (LZU), Jiatong Li (LZU), Xiufeng Weng (NINT), Keqing Gao (NINT), Jianxin Zhang (NINT), Xiao Liu (NINT), Bingjun Li (XJTU), Yihong Yan (XJTU)

CONTENTS

Nuclear Fission

Preface

The annual International Seminar on Interaction of Neutrons with Nuclei, ISINN-29, opened with a year delay on May 29, 2023, simultaneously in Dubna and Lanzhou (China). Like the two previous seminars, it was co-organized by the Frank Laboratory of Neutron Physics of JINR, the State Key Laboratory of Intense Pulsed Radiation Simulation and Effect of the Northwest Institute of Nuclear Technology (NINT, Xi'an, China), and the School of Nuclear Science and Technology of Lanzhou University. The Seminar was held in a hybrid format, bringing together in Dubna more than 90 participants from FLNP, FLNR, and VBLHEP JINR, NRC "Kurchatov Institute", PNPI (Gatchina), SINP MSU, INR RAS, INP (Novosibirsk), ITP (Chernogolovka), Moscow, Novosibirsk, Perm, Voronezh universities, scientific centers of Belarus, Egypt, Kazakhstan, Russia. Nearly 100 attendees representing universities and research centers in China gathered in Lanzhou, and a number of participants, including those from Argentina, Bulgaria, France, India, Romania, Serbia, Singapore, Turkey, USA, Uzbekistan, and Vietnam joined the Seminar via the Internet.

Opening the Seminar in Dubna, JINR Vice-Director L. Kostov reminded that the history of ISINN dates back to 1993, and if not for the force-majeure interruption last year, this Seminar would have become a jubilee one. During its thirty-year history, ISINN seminars have brought together specialists in various fields of neutron physics from many countries. Professor Hei Dongwei (NINT) and Academician Yan Chunhua (Lanzhou University) greeted the participants and wished them a successful and productive meeting.

Plenary and section reports of the Seminar covered its traditional topics: from the fundamental properties of the neutron to modern neutron sources, from promising experiments in the field of nuclear fission and nuclear reactions induced by fast neutrons to the physics of reactors and experimental methodology. As usual, investigations using nuclear and related analytical techniques in the environmental and material sciences were widely represented.

A total of 108 oral and 38 poster presentations were made. Due to the large volume of presented results and the large time difference between the Chinese participants and other representatives from Asian countries, it became necessary to organize parallel session meetings, as well as online and in-person poster sessions.

In these Proceedings, only the reports received from authors to the appointed dead-line are included. But, in general, the present Proceedings together with many report presentations available on the site http://isinn.jinr.ru/past-isinns/isinn-29/program.html provide a real idea of ISINN-29.

V. N. Shvetsov

Co-Chairman of ISINN-29

Advanced Neutron Sources and Perspective Experiments

Accelerator Based Neutron Source VITA for Measuring Nuclear Reaction Cross Sections and for Irradiating Advanced Materials

Bikchurina M., Bykov T., Kasatov D., Kolesnikov I., Koshkarev A., Osteinov G., Savinov S., Shchudlo I., Sokolova E., Sorokin I., Verkhovod G., Taskaev S.

Budker Institute of Nuclear Physics, ave. Lavrentiev 11, Novosibirsk, Russia

A compact accelerator-based neutron source has been proposed and created at the Budker Institute of Nuclear Physics in Novosibirsk, Russia. An original vacuum insulated tandem accelerator (VITA) is used to provide a dc proton/deuteron beam. The ion beam energy can be varied within a range of 0.3–2.3 MeV, keeping a high-energy stability of 0.1 %. The beam current can also be varied in a wide range (from 1 nA to 10 mA) with high current stability (0.4 %). VITA is used to generate a neutron flux via the $^{7}Li(p,n)^{7}Be$ or $^{7}Li(d,n)$ reactions, α-particles through $^{7}Li(p,\alpha)\alpha$ and $^{11}B(p,\alpha)\alpha\alpha$ reactions, 478 keV photons through $^{7}Li(p,p'\gamma)^{7}Li$ reaction, and positrons through $^{19}F(p,\alpha e^{+}e^{-})^{16}O$ reaction. The facility provides a neutron beam of almost any energy range: cold, thermal, epithermal, monoenergetic, and fast. The facility is used to study radiation blistering of metals during ion implantation, for the development of boron neutron capture therapy including use in clinics, for radiation testing of steel and boron carbide for ITER and fibers for CERN, for studying the composition of films by back-scattered protons, for in-depth investigation of the $^{11}B(p,\alpha)\alpha\alpha$ neutronless fusion reaction, for measuring nuclear reaction cross sections, *etc.* The report will describe the VITA, present and discuss the results obtained, and declare plans.

1. Introduction

The compact neutron source has been proposed and developed at the Budker Institute of Nuclear Physics and enables the generation of a stable neutron beam [1]. Neutrons are produced by the following reactions: $^{7}Li(p,n)^{7}Be$ or $^{7}Li(d,n)$. With different moderators, the neutron energy can vary in over a wide range of energies. The neutron source has applications in various fields, such as: boron neutron capture therapy, activation studies of materials, blistering studies of materials, fundamental studies issues of physics, and other applications.

2. Materials and Methods

Accelerator based neutron source VITA and a lithium target has been proposed and developed at the Budker Institute of Nuclear Physics in Novosibirsk, Russia [1]. The VITA is used to provide dc proton/deuteron beam with energy within a range of 0.3–2.3 MeV with current from 1 nA to 10 mA. The layout of the facility is shown in Figure 1.

The accelerator based neutron source VITA consists of vacuum-insulated tandem accelerator for obtaining a high-power DC proton beam, lithium target for generating neutrons and set of beam shaping assemblies. The lithium target is placed in the five possible positions.

The neutron source generates a stable monoenergetic proton or deuteron beam. Using different moderators the neutron energy can vary over a wide range of energies: cold (D_2O at cryogenic temperature), thermal (D_2O or plexiglass), epithermal (MgF_2 moderator), exclusively epithermal, over-epithermal, monoenergetic, fast. The facility is the source of two bright photon lines (478 keV, 511 keV), α-particles and positrons.

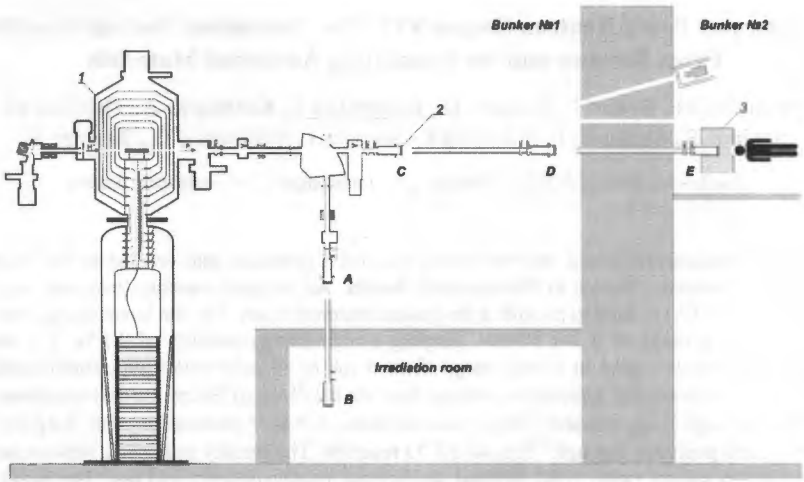

Figure 1. Layout of the experimental facility: 1 – vacuum-insulated tandem accelerator, 2 – lithium target, 3 – beam-shaping assembly. A, B, C, D, E – lithium target placement positions.

3. Study of metals radiation blistering during ion implantation

Using a CCD camera and a remote microscope, the in-situ observation dynamics of blister formation on copper and tantalum surfaces were carried out [2, 3].

It was found that the threshold of blister formation on copper surface depends on copper purity, in the purer copper it is greater. The maximum value of the threshold is 3 10^{19} cm^{-2}, the minimum one is 7 times less. The size of blisters on the copper surface depends on the purity copper, in cleaner copper the blisters are larger. The blister size varies from 40 ± 20 to 160 ± 50 μm. It has been found that after the blisters appear on the copper surface, further irradiation does not lead to surface modification.

Tantalum was found to be much more resistant to blister formation than copper. The threshold of blister formation in the form of bubbles or flakes on the tantalum surface exceeds 6.7 10^{20} cm^{-2}. At a fluence of 3.6 10^{20} cm^{-2} the surface modificates in the form of relief with a characteristic cell size of 1 μm.

An example image of the resulting blisters is shown in Figure 2. The blister was cut off with an electron beam to see its inner structure.

Figure 2. Electron microscope images of the blister of coarse-grained copper.

4. Development of the boron neutron capture therapy

Historically, VITA was proposed and created for the development of the boron neutron capture therapy (BNCT). Since 2008 year, when first neutrons were detected, there were made lots of investigations, dedicated to BNCT: trials on the different cell cultures, on laboratory mice and, nowadays, treatment of pets with natural tumors [4-16]. Photos of the trials are shown in Figure 3.

Figure 3. Photos of the BNCT trials on VITA. Upper left – Boron delivery drugs for BNCT, upper right – mice with an artificially injected tumor under the neutron generating target, bottom left – pet "Prometeus", bottom right – pet "Cappa".

The accelerator based neutron source VITA was installed in Xiamen, China. Nowadays preclinical human trials are conducted there [17]. Photo of the VITA for Xiamen (China) is shown in Figure 4.

Since the BNCT trials on the cell cultures, mice and animals were successful the Russian government resolution in 2021 year was to create an accelerated neutron source VITA for the Blokhin Oncology Research Center (Moscow, Russia). Nowadays it located in the BINP and in the stage of installing, by the end of 2024 it is planned to launch VITA at the Blokhin Oncology Research Center.

Figure 4. Accelerator based neutron source VITA in Xiamen, China.

5. Radiation testing of materials

VITA is actively used for radiation testing of perspective materials for ITER, CERN and other large facilities [18].

For ITER VITA has provided neutron activations study of sintered boron carbide ceramics (Viral). In the Figure 5 it can be seen the measured by the HPGe detector spectrum of γ-rays emitted by Viral after fast neutron irradiation.

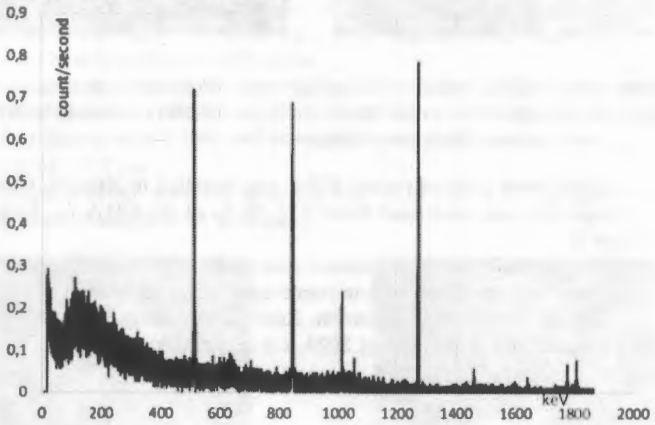

Figure 5. Measured spectrum of γ-rays emitted by sintered boron carbide ceramics (Virial) after fast neutron irradiation. On the vertical axis: the number of detector counts; on the horizontal axis: photon energy in keV.

For CERN on VITA was made a month experiment, in which fiber optics for experiments on the LHC in high-luminosity mode has been irradiated by fast neutrons, generated during $^{7}Li(d,n)^{8}Be$ reaction. Samples were irradiated to a fluence of $3 \cdot 10^{14}$ fast neutrons/cm^2 with real-time measurements of fiber optics transparency factor. After this experiment it was established that VITA can easily provide day-by-day generation of fast/epithermal neutrons up to 8-10 hours per day. In the Figure 6 is shown the dependence of optical fibers transparency versus fast neutron fluence up to a value of $3 \cdot 10^{14}$ neutrons/cm^2. There is a quite degradation of fiber optics, when neutrons are generating, without neutron generation optics is recovering, but not to the 100 %.

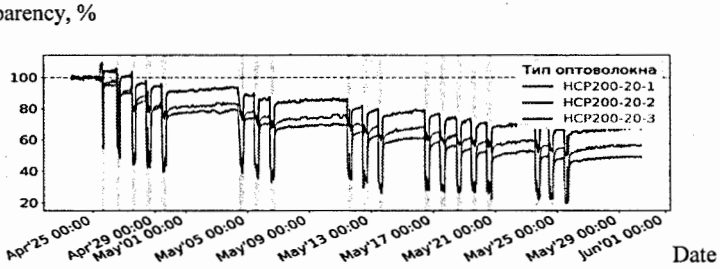

Figure.6. Dependence of optical fiber transparency versus fast neutron fluence.

Simultaneously with the fiber optics irradiation at VITA also irradiated:

– Semiconductor photomultiplier tubes and dc-dc converters for the ATLAS detector of the CERN Large Hadron Collider (Geneva, Switzerland);

– A diamond detector for the International Thermonuclear Experimental Reactor (ITER, Cadarache, France);

– Boron carbide plates for ITER;

– Neodymium magnets for the hybrid quadrupole lens of the high-power linac at the Institute of Theoretical and Experimental Physics (Moscow, Russia);

– Natural and synthetic diamonds for the Nikolaev Institute of Inorganic Chemistry (Novosibirsk, Russia) [19];

– Gas sensors based on titanium phthalocyanines for Novosibirsk State University (Russia).

6. Studying the composition of films by back-scattered protons

On VITA proton beam, collimated by a diaphragm, is actively used for studying of the different targets compositions, investigated by energy analysis of backscattered protons. The spectrum of backscattered protons measured with a semiconductor silicon detector (Si Charged Particle Radiation Detectors for Alpha Spectroscopy). Using obtained spectrum and simulations in the SIMNRA v.7.03 (Max Planck Institute for Plasma Physics, Germany) the depth distribution of elements on the sample is determined.

Example of this back-scattered protons analysis is provided in the Figure 7. The thickness of the main lithium layer is 30 μm, of the lithium oxide is 37 nm, of the carbon is 0.9 nm. The possibility to detect different elements defined by the element concentration, exposure time and cross-section of the interactions. Therefore, the 0.9 nm of carbon can be detected, due to resonance elastic scattering of the proton on the carbon.

The important conclusion that lithium target, produced in Budker INP, is covered by the thin films of lithium oxide and carbon, they perform a protective function, and these knowledge will be used in the delivery of lithium targets to the consumer.

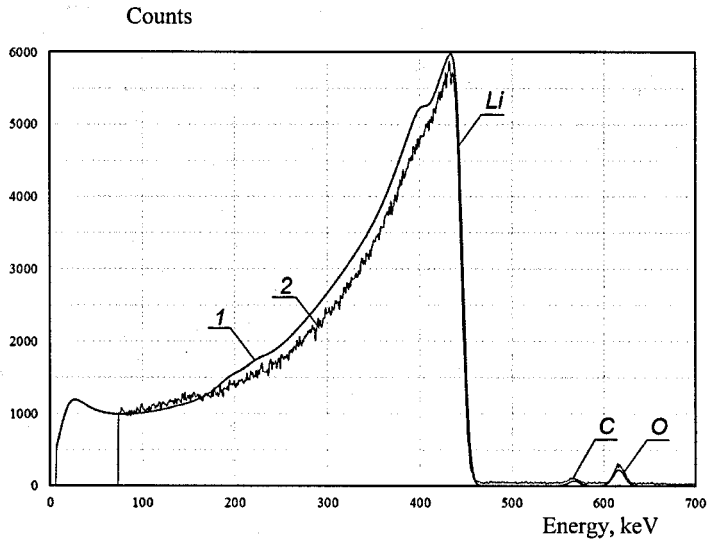

Figure 7. Spectrum of the back-scattered from the lithium target protons. 1 – SIMNRA simulation, 2 – experimental data, Li, C, O – lithium, carbon and oxygen peaks.

7. Measurements of the nuclear reaction cross sections

On VITA were measured cross-sections of the $^{7}Li(p,p'\gamma)^{7}Li$, $^{7}Li(p,\alpha)\alpha$ reactions, experimental results were included in the international databases (IBANDL, EXFOR) [20-22]. Measured spectrum are shown in Figures 8 and 9.

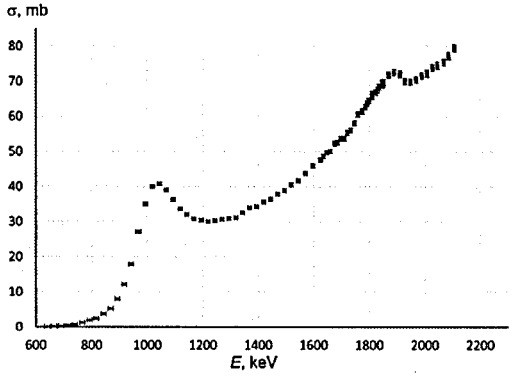

Figure 8. Cross-section of the $^{7}Li(p,p'\gamma)^{7}Li$ reaction in a range from 0.6 MeV to 2.15 MeV.

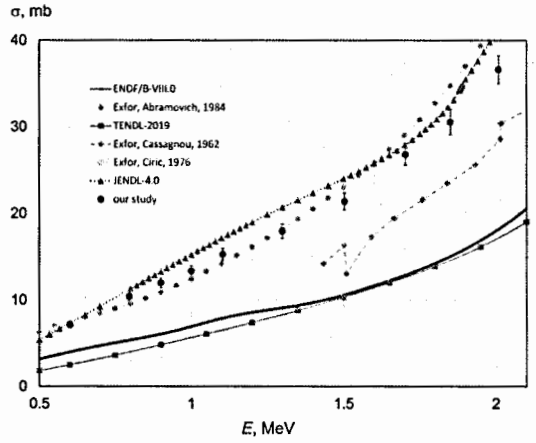

Figure 9. $^{7}Li(p,\alpha)^{4}He$ reaction cross section.

From the Figure 9 it can be seen, that our data are similar to the JENDL data and 2 times higher, than data from ENDF/B and TENDL.

Nowadays the data for $^{11}B(p,\alpha)\alpha\alpha$, $^{6}Li(d,)$ and $^{7}Li(d,)$ are obtained and processing. Detailed information is presented in the paper [23].

8. Conclusion

High flux neutron source based on a vacuum-insulated tandem accelerator (VITA) and a lithium target has been proposed and developed at the Budker Institute of Nuclear Physics in Novosibirsk, Russia. The compact neutron source enables the generation a stable neutron beam, two bright photon lines (478 keV, 511 keV), α-particles and positrons. In this paper the main studies conducted at VITA were summarized.

Funding

This research was funded by Russian Science Foundation, grant number 19-72-30005, https://rscf.ru/project/19-72-30005/.

References

1. S. Taskaev, E. Berendeev, M. Bikchurina, T. Bykov, D. Kasatov, I. Kolesnikov, A. Koshkarev, A. Makarov, G. Ostreinov, V. Porosev, S. Savinov, I. Shchudlo, E. Sokolova, I. Sorokin, T. Sycheva, G. Verkhovod. Neutron Source Based on Vacuum Insulated Tandem Accelerator and Lithium Target. Biology 10 (2021) 350.
2. A. Badrutdinov, T. Bykov, S. Gromilov, Y. Higashi, D. Kasatov, I. Kolesnikov, A. Koshkarev, A. Makarov, T. Miyazawa, I. Shchudlo, E. Sokolova, H. Sugawara, S. Taskaev. In Situ Observations of Blistering of a Metal Irradiated with 2-MeV Protons. Metals 2017, vol. 7, iss. 12, 558.

3. T. Bykov, N. Goloshevskii, S. Gromilov, D. Kasatov, Ia. Kolesnikov, A. Koshkarev, A. Makarov, A. Ruktuev, I. Shchudlo, E. Sokolova, S. Taskaev. In situ study of the blistering effect of copper with a thin lithium layer on the neutron yield in the $^{7}Li(p,n)^{7}Be$ reaction. Nuclear Inst. and Methods in Physics Research B 481 (2020) 62–81.
4. M. Dymova, S. Taskaev, V. Richter, E. Kuligina. Boron neutron capture therapy: current status and future perspectives. Cancer Communications, 2020; 40:406–421.
5. M. Dymova, M. Dmitrieva, E. Kuligina, V. Richter, S. Savinov, I. Shchudlo, T. Sycheva, I. Taskaeva, S. Taskaev. Method of measuring high-LET particles dose. Radiation Research 196 (2021) 192–196.
6. T. Bykov, D. Kasatov, A. Koshkarev, A. Makarov, V. Porosev, G. Savinov, I. Shchudlo, S. Taskaev, G. Verkhovod. Initial trials of a dose monitoring detector for boron neutron capture therapy. JINST 2021, vol. 16, P01024.
7. T. Popova, M. Dymova, L. Koroleva, O. Zakharova, V. Lisitskiy, V. Raskolupova, T. Sycheva, S. Taskaev, V. Silnikov, T. Godovikova. Homocystamide conjugates of human serum albumin as a platform to prepare bimodal multidrug delivery systems for boron-neutron capture therapy. Molecules 26 (2021) 6537.
8. M. Vorobyeva, M. Dymova, D. Novopashina, E. Kuligina, V. Timoshenko, Ia. Kolesnikov, S. Taskaev, V. Richter, A. Venyaminova. Tumor Cell-Specific 2'-Fluoro RNA Aptamer Conjugated with Closo-Dodecaborate as a Potential Agent for Boron Neutron Capture Therapy. International Journal of Molecular Sciences, 22 (2021) 7326.
9. V. Kanygin, A. Kichigin, A. Zaboronok, A. Kasatova, E. Petrova, A. Tsygankova, E. Zavjalov, B. Mathis and S. Taskaev. In vivo Accelerator-based Boron Neutron Capture Therapy for Spontaneous Tumors in Large Animals: Case Series. Biology 11 (2022) 138.
10. A. Zaboronok, P. Khaptakhanova, S. Uspenskii, R. Bekarevich, L. Mechetina, O. Volkova, B. Mathis, V. Kanygin, E. Ishikawa, A. Kasatova, D. Kasatov, I. Shchudlo, T. Sycheva, S. Taskaev, A. Matsumura. Polymer-Stabilized Elemental Boron Nanoparticles for Boron Neutron Capture Therapy: Initial Irradiation Experiments. Pharmaceutics 14 (2022) 761.
11. K. Aiyyzhy, E. Barmina, I. Zavestovskaya, A. Kasatova, D. Petrunya, O. Uvarov, V. Saraykin, M. Zhilnikova, V. Voronov, G. Shafeev, S. Taskaev, I. Zelepukin, S. Deyev. Laser ablation of Fe_2B target enriched in ^{10}B content for boron neutron capture therapy. Laser Physics Letters 19 (2022) 066002.
12. E. Byambatseren, A. Burdakov, T. Bykov, D. Kasatov, Ia. Kolesnikov, S. Savinov, T. Sycheva, S. Taskaev. Validation and optimization of the epithermal neutron flux detector using the $^{71}Ga(n,\gamma)^{72}Ga$ reaction. JINST 18 (2023) P02020.
13. D. Novopashina, M. Dymova, A. Davydova, M. Meschaninova, D. Malysheva, E. Kuligina, V. Richter, Ia. Kolesnikov, S. Taskaev, M. Vorobyeva. Aptamers for addressed boron delivery in BNCT: Effect of boron cluster attachment site on functional activity. International Journal of Molecular Sciences 24 (2023) 306.
14. I. Taskaeva, A. Kasatova, D. Surodin, N. Bgatova, S. Taskaev. Study of Lithium Biodistribution and Nephrotoxicity in Skin Melanoma Mice Model: The First Step towards Implementing of Lithium Neutron Capture Therapy. Life 13 (2023) 518.
15. V. Raskolupova, M. Wang, M. Dymova, G. Petrov, I. Shchudlo, S. Taskaev, T. Abramova, T. Godovikova, V. Silnikov, T. Popova. Design of the new closo-dodecarborate-containing gemcitabine analogue for the albumin-based theranostics composition. Molecules 28 (2023) 2672.

16. V. Kanygin, A. Zaboronok, A. Kichigin, E. Petrova, T. Guselnikova, A. Kozlov, D. Lukichev, B.J. Mathis, S. Taskaev. Gadolinium neutron capture therapy for cats and dogs with spontaneous tumors using Gd-DTPA. Veterinary Sciences 10 (2023) 274.
17. https://en.neuboron.com/news/296.html
18. A. Shoshin, A. Burdakov, M. Ivantsivskiy, R. Reichle, V. Udintsev, J. Guirao, S. Pak, A. Zvonkov, D. Kravtsov, N. Sorokina, Y. Sulyaev, A. Listopad, D. Gavrilenko, A. Taskaev, E. Shabunin, V. Seryomin, S. Shiyankov, E. Zaytcev, P. Seleznev, A. Semenov, S. Polosatkin, S. Taskaev, D. Kasatov, I. Shchudlo, M. Bikchurina, V. Modestov, A. Smirnov, A. Pozhilov, A. Lobachev, I. Loginov, O. Shagniev, I. Kirienko, I. Buslakov. Integration of ITER diagnostic ports at the Budker institute. Fusion Engineering and Design 178 (2022) 113114.
19. S.E. Dyusenova, D.D. Klyamer, A.S. Sukhikh, I.M. Shchudlo, S.Y. Taskaev, T.V. Basova, S.A. Gromilov. Influence of Magnetic Field on the Structure and Sensor Properties of Thin Titanyl Phthalocyanine Layers. Journal of Structural Chemistry, 2023, Vol. 64, No. 3, pp. 337–346.
20. S. Taskaev, T. Bykov, D. Kasatov, Ia. Kolesnikov, A. Koshkarev, A. Makarov, S. Savinov, I. Shchudlo, E. Sokolova, Measurement of the ^{7}Li(p,p'γ)^{7}Li reaction cross-section and 478 keV photon yield from a thick lithium target at proton energies from 0.65 MeV to 2.225 MeV. Nuclear Inst. and Methods in Physics Research, B 502 (2021) 85–94.
21. M. Bikchurina, T. Bykov, D. Kasatov, Ia. Kolesnikov, A. Makarov, I. Shchudlo, E. Sokolova, S. Taskaev. The measurement of the neutron yield of the ^{7}Li(p,n)^{7}Be reaction in lithium targets. Biology 10 (2021) 824.
22. S. Taskaev, M. Bikchurina, T. Bykov, D. Kasatov, Ia. Kolesnikov, A. Makarov, G. Ostreinov, S. Savinov, E. Sokolova. Cross-section measurement for the ^{7}Li(p,α)^{4}He reaction at proton energies 0.6–2 MeV. Nuclear Inst. and Methods in Physics Research B 525 (2022) 55–61.
23. M. Bikchurina, T. Bykov, D. Kasatov, I. Kolesnikov, A. Koshkarev, G. Ostreinov, S. Savinov, E. Sokolova, and S. Taskaev. Measurement of cross sections for nuclear reactions of interaction of protons and deuterons with lithium at ion energies 0.4–2.2 MeV. These proceedings.

Accelerator Version of the Intensive Lithium Antineutrino Source

V.I. Lyashuk §

Institute for Nuclear Research of the Russian Academy of Sciences, Moscow, Russia

The combination of decay parameters of the neutron-rich β⁻-decaying ^{8}Li isotope (short $T_{1/2}$ = 0.84 s) and its hard spectrum ($E_{\bar{\nu}}^{max}$ = 13 MeV and $<E_{\bar{\nu}}>$ = 6.5 MeV) of well-known distribution allow to consider ^{8}Li as a very perspective candidate for the artificial antineutrino source. The source can be produced at (n,γ)-activation of the starting ^{7}Li isotope. Creation of the ^{8}Li source can be realized in the tandem scheme of the proton accelerator with neutron producing heavy metal target inside the lithium blanket. The accelerator variant is optimized in efficiency of ^{8}Li generation and in dimension that is exclusively important for investigation of oscillation in problem of sterile neutrino search in case of $\Delta m^2 \sim 1$ eV^2 scale. The analysis of ^{8}Li creation in the lithium blanket-converter allowed to decrease it outer size down to ~ 70 cm strongly decreasing the escape of neutrons from the source construction.

1. Introduction. Advantage of the Lithium Antineutrino Spectrum Compare to Reactor Spectrum

Starting from the pioneer works of F. Reines and C. L. Cowan in 1953 up today the reactors continue to be the uneclipsed steady source of electron antineutrino for scientists as for flux as for cost of experiments [1]. But in spite of the apparent superiority on neutrino flux the nuclear reactors has a disadvantage: too-small hardness of $\bar{\nu}_e$-spectrum, which rapidly decreases and lies below 10 MeV [2]. The next serious problem of the reactor spectrum is the large errors. So, the authors of the work [3] concluded that the reactor $\bar{\nu}_e$-spectrum is known with averaged accuracy of less than ~ 4 % and the level of accuracy can be caused by data on ~(25–30)% of forbidden transfers at decay of the main fuel isotopes (^{235}U, ^{239}Pu, ^{238}U, ^{241}Pu). The composition strongly varies in time in operation period [4] and in case of reactor stops. The changing in composition leads to variation in $\bar{\nu}_e$-fluxes which are recalculated by means of correction factors for fuel isotopes. An additional unaccounted errors for $\bar{\nu}_e$-flux evaluation appear during reactor stops due to permanent presence of cooling pond for spent fuel. These errors can rise up to 1% compare to the operating reactor spectrum. It is usually considered that partial neutrino spectra $N_{\bar{\nu}}^i$ (where i is the fuel isotope) reach equilibrium conditions after 1 day from the reactor life time. But this evaluation must be corrected too as the summary spectrum increases from the beginning to the end of the reactor life time on the value (5–6)% in the region (1.8–3.0) MeV. [5]. The experimental detection of the bump in the reactor $\bar{\nu}_e$-spectrum added one more puzzle in interpretation of reactor $\bar{\nu}_e$-experiments [6].

For the purpose of the artificial neutrino source the ^{8}Li isotope is characterized by undoubted advantage in $\bar{\nu}_e$-spectrum over the reactor one. The $\bar{\nu}_e$-spectrum of neutron-rich ^{8}Li (β⁻-decay with $T_{1/2}$=0.84 s) is hard and well investigated: the maximal energy reaches ~13 MeV with average value 6.5 MeV [7], that exclusively important for detection rate owing

§ lyashuk@itep.ru

to the squared proportionality of the cross section to the neutrino energy $\sigma_\nu \sim E_\nu^2$ for the considered "reactor" energy range.

The natural lithium consists of ^{7}Li and ^{6}Li – two stable isotopes with 92.48% and 7.52% weight parts correspondingly. For creation of the intensive ^{8}Li electron antineutrino source at ^{7}Li(n,γ)^{8}Li-activation we need to exclude maximally the negative factor of strong neutron absorption at ^{6}Li(n,α)T process. The both cross sections follows to 1/v law (v is velocity) at $E_n \leq 1$ keV and at the thermal point E_n= 0.0253 eV the cross section relation $\sigma_{n,\alpha}(^6\text{Li})/\sigma_{n,\gamma}(^7\text{Li})$ is equal to (940 b / 0.045 b) according to TENDL-2019 and CENDL-3.2 neutron data libraries [8,9]. Clearly, that realization of the task is possible at high grade of ^{6}Li removal: the proposed (and considered in this work) purification on ^{7}Li is 99.99% [10, 11].

2. Antineutrino Source for the Scheme with Proton Accelerator. Compact Variant of the Source

Since the 70-th years of the XX-th century the possibility to apply the accelerator driven system on the base of spallation reaction for creation of the powerful neutron source began attract more and more attention and were realized and are constructing (ISIS, IN-06, JSNS/J-Park, KENS, LANSCE, SINQ, SNS, CSNS, ESS et al.). The large benefits of spallation neutron source (with targets usually made from tungsten, lead, tantalum, bismuth, uranium, mercury) is caused by the fact that as the proton energy is increasing the neutron yield Y_n (per proton) is increasing sharply: so, for heavy targets and proton energy E_p = 200–300 MeV the neutron yield is about $Y_n \approx$ (1.6–3.5), for E_p =500–600 MeV the yield increases up to $Y_n \approx 10$.

In accelerator driven systems for creation of intensive neutrino source by ^{7}Li(n,γ)^{8}Li activation we proposed to surround the target by lithium blanket-converter [12]. It was investigated the neutron yield and creation of ^{8}Li in the scheme of lithium blanket around the target (bombarded by proton of energy 50–300 MeV) manufactured from the lead, bismuth and tungsten (see Fig.1–2). The last has the high resistance to radiation damage under intensive proton beams and was considered as the main candidate for the target [13,14].

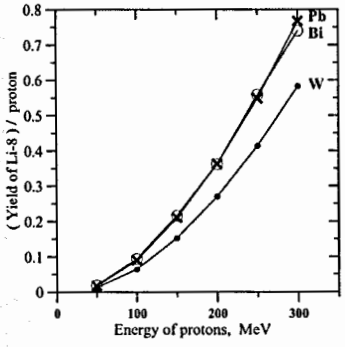

Fig. 1. Yield of ^{8}Li for lead, bismuth and tungsten target depending on the proton energy.

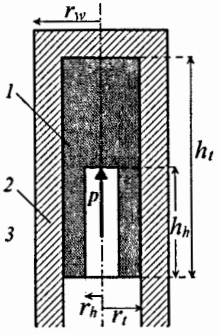

Dimension of the compact neutrino source (in Fig. 3–4):
r_w = 12 cm,
r_t = 7 cm,
r_h = 3 cm,
h_t = 30 cm,
h_h = 20 cm;
p – proton beam.

Fig. 2. Geometry of the tungsten neutron producing target. 1 – tungsten target; 2 – D_2O-cooler; 3 – lithium blanket-converter.

Such not high energies are considered with purpose to decrease the possible background in neutrino experiments and intensive π^0-meson production (generating the electron-photon showers) which occurs at higher energies. From the beginning of the accelerator variant of the $\overline{\nu}_e$-source investigation the blanket is considered in the cylindrical geometry (3.4 m in length, radial thickness – 1.7 m and central ^{174}W-target cooled by heavy water). For the blanket substance we used the heavy water solution of ^{7}LiOD with concentration 9.5% and 99.99% purification of ^{7}Li [13,14].

For the constructed now JUNO neutrino detector [15] it was demonstrated that the lithium blanket can be perspective $\overline{\nu}_e$-source for search of sterile neutrinos. The obtained results reveals that sensitivity to the mixing-angle may be extremely high: $\sin^2(2\theta) \leq 0.001$ for $\Delta m^2 \gtrsim 0.2$ eV^2 in the model (3+1) of three active plus one sterile neutrino [16].

The simulation of the possible sterile neutrino oscillation requested to take into account the distribution of ^{8}Li yield in the blanket (i. e., distribution of the $\overline{\nu}_e$-source) [17–19]. For this purpose the blanket was divided into cells: 10 equal steps in length and 10 equal layers in radius. The summary number of created cells was 105 ones including five nonstandard cells after the target. The obtained ^{8}Li yield in the cells confirmed the think to diminish the size of the neutrino source by separating of the central volume with more high yield (which ensure 68% of the total ^{8}Li yield in the volume with dimension – 136 cm in length and 97 cm in radius) from outer space (which would be source shield with function of neutron moderator and reflector). In order to prevent the neutron escape from the diminished size of lithium blanket the (above mentioned) outer space was filled by carbon and water (D_2O or H_2O).

The next steps in developing of more compact source for verification of the sterile neutrino models in short base line experiments (considering the cases of $\Delta m^2 \sim$ eV^2) [20–24]) are also dictated by possible errors caused by source dimension. In order to diminish the source size we base on the principle idea to increase strongly the rate of ^{7}Li(n,γ)^{8}Li reaction close to the target. Simultaneously it is need to ensure an effective neutron moderation near the target too. We propose an effective solution – to insert the thin ^{7}Li metal layer close to the tungsten target. Indeed, the nuclear concentration of ^{7}Li nuclei in the lithium metal (with purification 99.99% on ^{7}Li) is higher than it concentration in the outer heavy water solution of ^{7}LiOD in ~18 times. In analysis of the ^{8}Li yield distribution the source volume was divided into small cells similar to the works [17,18]. The layer shield of the source was optimized to decrease the neutron flux from the installation that allowed to strongly decrease the escape of neutrons down to ~0.2% per proton. The scheme of the proposed $\overline{\nu}_e$-source and it dimension is presented in the Fig.3a and Fig.3b.

The idea to insert the thin ^{7}Li layer for diminishing the size (and at the same time to ensure the high of ^{8}Li yield) was confirmed in the simulation at the proton energy E_p = 200 MeV. At the source length L= 70 cm the obtained ^{8}Li yield is k_p= 0.113 compare to: 1) k_p = 0.072 for the blanket with homogeneous heavy water LiOD-solution (i.e., without the lithium metal layer) and 2) k_p= 0.175 in the previous case [18,19] with L=136 cm. But 68% of created ^{8}Li nuclei are generated in the thin ^{7}Li metal layer, i.e., within the volume at the radius R = (22–27) cm. The Fig. 4 illustrates yield $Y_{^8Li}$ of ^{8}Li in the blanket cells and strong increase of the yield in the thin ^{7}Li metal layer compare the case of heavy water LiOD solution. The total mass of the ^{7}Li in the diminished lithium blanket (including LiOD solution plus metal layer) is 67.5 kg compare to 128.3 kg of the previous geometry [17–19].

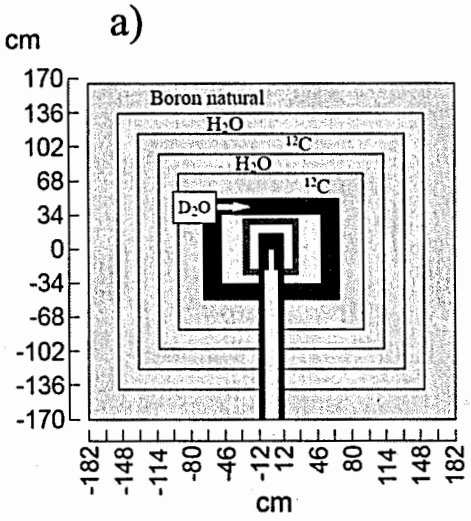

Fig.3a. Geometry of the lithium $\bar{\nu}_e$-source in the accelerator driven system. The all dimensions are given on the axes. Materials of zones around the central lithium volume with tungsten target (see Fig.3b) and channel of the proton accelerator are indicated.

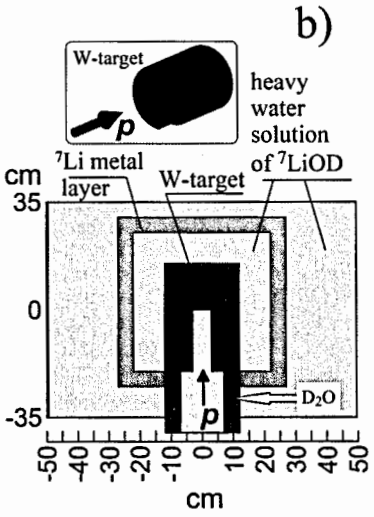

Fig. 3b. The magnified scheme of the central part of the lithium- $\bar{\nu}_e$-source (the tungsten target and lithium zones: ^{7}LiOD-solution, ^{7}Li-metal layer, ^{7}LiOD-solution). The all dimensions of zones around the central lithium volume with tungsten target and channel of the proton accelerator are given on the axes.

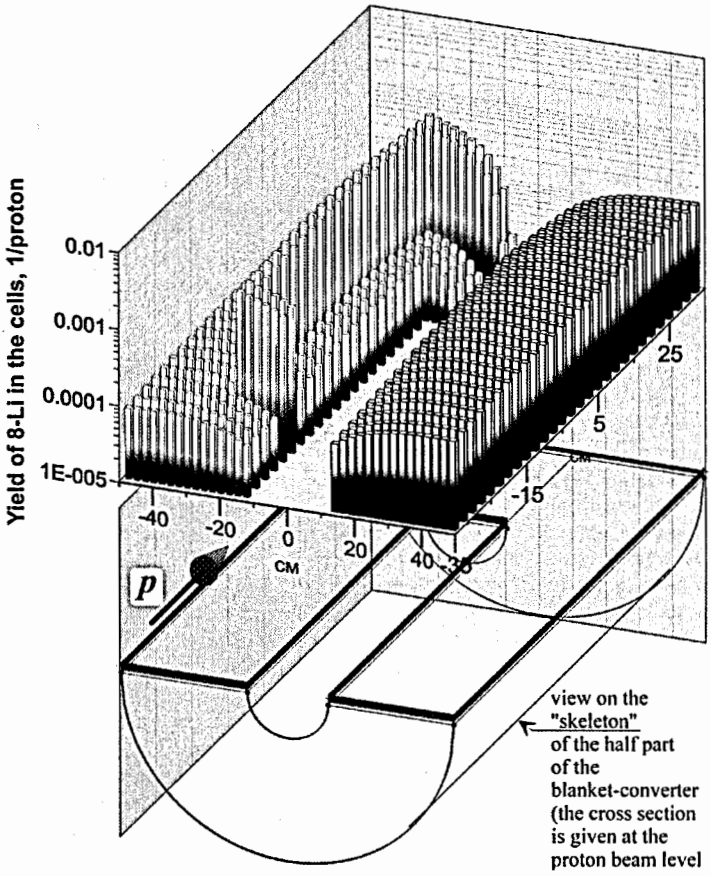

Fig. 4. Yield of ^{8}Li in the cells of the lithium blanket for accelerator scheme at the proton energy 200 MeV. The data are normalized per proton of the beam. The dimensions of the blanket are indicated. The left part of the distribution (at the X < 0) corresponds the yields in cells for discussed geometry of the blanket with the thin ^{7}Li metal layer (see Fig. 3b), in which the strong increase of ^{8}Li yield (compare the cells filled with ^{7}LiOD heavy water solution) is obtained. For comparison (of the strong effect from the lithium metal) the right part (at the X > 0) shows the ^{8}Li yield in the cells in case of the blanket (with the same dimensions) filled with ^{7}LiOD heavy water solution (i.e., without the lithium metal layer).

In the works [25,26] the authors proposed to construct the lithium $\overline{\nu}_e$-source (with the similar to [27] geometry and the same purity of ^{7}Li): the scheme was based on the proton accelerator (E_p = 60 MeV) and neutron generating ^{9}Be-target in the cylindrical lithium blanket-converter (with height 150 cm and diameter 200 cm) filled with metallic lithium. The

expected $N_{\overline{\nu}}$-flux from the converter [25,26] during 5 years (for 90% using of time and accelerator current I =10 mA) is evaluated as $1.29 \cdot 10^{23}$. For comparison the considered here compact $\overline{\nu}_e$-source (length L= 70 cm, diameter 99 cm; Fig. 4) with: ^{174}W-target , 200-MeV proton beam of the current in order smaller – 1 mA, a data-taking period of 5 yr and the same useful time of 90% will ensure the total $\overline{\nu}_e$-flux as 1.00×10^{23}. The requested highly enriched ^{7}Li mass can be decrease in 90 times: from 6.1 t (in [25,26] case) down to 67.5 kg.

3. Conclusion

It was considered two principal variants of intensive $\overline{\nu}_e$-source with hard spectrum ($E_{\overline{\nu}}^{max} \approx$ 13 MeV and average energy 6.5 MeV) produced by ^{8}Li at (n,γ)-activation of ^{7}Li isotope (with purity 99.99%): on the base of proton accelerator and neutron generating tungsten target.

The construction of the $\overline{\nu}_e$-source in tandem scheme of accelerator plus neutron producing target allows to work in the pure ^{8}Li -spectrum excluding the large spectrum errors arisen in case of the reactor neutrino source. The evident advantage of the accelerator variant is the possibility to ensure the strong decrease of the requested high purified ^{7}Li mass. The optimized scheme gives the possibility to minimize the mass of ^{7}Li (purification 99.99%) down to 67.5 kg. Realization of the accelerator variant allows to create the very compact $\overline{\nu}_e$-source with dimension reduced to 70 cm that is exclusively important for checking of short length of oscillation in sterile neutrino experiments.

The author sincerely thanks Yu.S. Lutostansky and M.D. Skorokhvatov for interest and helpful discussion.

REFERENCES

1. F. Reines F. and C.L. Cowan Jr., Phys. Rev. **92**, 830 (1953).
2. P. Huber, Phys. Rev. C **84,** 024617 (2011).
3. A.C. Hayes, J.L. Friar, G.T. Garvey, Gerard Jungman, and G. Jonkmans, Phys. Rev. Lett. **112**, 202501 (2014).
4. V.A. Korovkin, S.A. Kodanev, A.D. Yarichin, A. A. Borovoi, V.I. Kopeikin, L.A. Mikaelyan, V.D. Sidorenko, Soviet Atomic Energy **56**, 233 (1984).
5. V. I. Kopeikin, Phys. At. Nucl. **75**, 143 (2012).
6. A.C. Hayes, J.L. Friar, G.T. Garvey, D. Ibeling, G. Jungman, T. Kawano, R.W. Mills, Phys. Rev. D **92**, 033015 (2015).
7. V.G. Aleksankin, S.V. Rodichev, P.M. Rubtsov, P.A. Ruzansky. and F.E. Chukreev. *Beta and antineutrino radiation from radioactive nuclei* (Energoatomizdat, Moscow, 1989), ISBN 5-283-03727-4 (in Russian).
8. A.J. Koning, D. Rochman, J. Sublet, N. Dzysiuk, M. Fleming, S. van der Marck, Nucl. Data Sheets **155**, 1 (2019).
9. Zhigang Ge, Ruirui Xu, Haicheng Wu, Yue Zhang, Guochang Chen, Yongli Jin, Nengchuan Shu, Yongjing Chen, Xi Tao, Yuan Tian, Ping Liu, Jing Qian, Jimin Wang, Huanyu Zhang, Lile Liu, and Xiaolong Huang, EPJ Web of Conferences **239**, 09001 (2020).

10. Yu.S. Lyutostansky and V.I. Lyashuk, Reactor neutrons-antineutrino converter on the basis of lithium compounds and their solutions, Sov. Atom. Energ. **69**, 696 (1990).
11. Yu.S. Lyutostansky and V.I. Lyashuk, Nucl. Sci. Eng. **117**, 77 (1994).
12. Yu.S. Lutostansky, V.I. Lyashuk, Physics of Elementary Particles and Atomic Nucl., Lett. **2**, 60 (2005).
13. V.I. Lyashuk, Yu.S. Lutostansky, arXiv:1503.01280v2 [physics.ins-det].
14. V.I. Lyashuk, Yu.S. Lutostansky, Bull. Russ. Acad. Sci. Phys. **79**, 431 (2015).
15. T. Adam, F. An, G. An, Q. An, N. Anfimov, V. Antonelli, G. Baccolo, M. Baldoncini, E. Baussan, M. Bellato, L. Bezrukov, D. Bick, S. Blyth, S. Boarin, A. Brigatti, T. Brugiere, et al. (JUNO Collaboration), arXiv:1508.07166v2 [physics.ins-det].
16. V.I. Lyashuk and Yu. S. Lutostansky, Jetp Lett. **103**, 293 (2016).
17. V.I. Lyashuk, V.I., Results in Phys. **6**, 961 (2016).
18. V.I. Lyashuk, Particles and Nuclei, Letters **14**, 456 (2017).
19. V.I. Lyashuk, arXiv: 1609.02127 [physics.ins-det].
20. M. Maltoni, T. Schwetz, Phys. Rev. D **76**, 093005 (2007).
21. J. Kopp, M. Maltoni, T. Schwetz, Phys. Rev. Lett. **107**, 091801 (2011).
22. J.M. Conrad, C.M. Ignarra, G. Karagiorgi, M.H. Shaevitz, and J. Spitz, Advances in High Energy Physics **2013**, Article ID 163897, (2013).
23. M. Dentler, Á. Hernández-Cabezudo, J. Kopp, P. Machado, M. Maltoni, I. Martinez-Soler and T. Schwet, J. High Energ. Phys. **2018**, 10 (2018).
24. V.V. Khruschov, S.V. Fomichev, and S.V. Semenov, Phys. Atom. Nuclei **84**, 328 (2021).
25. A. Bungau, A. Adelmann, J.R. Alonso, W. Barletta, R. Barlow, L. Bartoszek, L. Calabretta, A. Calanna, D. Campo, J.M. Conrad, Z. Djurcic, Y. Kamyshkov, M.H. Shaevitz, I. Shimizu, T. Smidt, et. al., Phys. Rev. Lett. 109, 141802 (2012).
26. A. Bungau, R. Barlow, M. Shaevitz, J. Conrad, J. Spitz, arXiv:1205.5790v1 [physics.acc-ph].
27. Yu.S. Lutostansky and V.I. Lyashuk, *The concept of a powerful antineutrino source*, Bull. Russ. Acad. Sci. Phys. **75**, 468 (2011).

Modified Collimator for Neutron Therapy Applications: Enhancing Narrow Beam Detection of Fast Neutrons

Shehada A.M.

Chechen State Pedagogical University, Grozny, 364037, Russia
shihada@tpu.ru

In clinical practice, when working with a target that emits neutrons in 4π space, it is always required to concentrate them into a mono directional beam. This is necessary both to increase the particle flux density and to give it the desired shape and optimal cross-sectional area. In principle, the beam shape can be changed using a collimator, which makes it possible to significantly narrow it and achieve minimal neutron absorption in structural elements. In this paper, simulation works using MCNP5 code have been carried out to find the possibility and reality of applying narrow beam of 2 cm and less of fast neutrons in radiotherapy. Simulations were performed on the original design of the treatment 8.5×8.5 cm^2 collimator existed in the cyclotron laboratory of Tomsk Polytechnic University. The results showed that the neutron energy spectrum almost would not change in the fast region, but in opposite, there was about 11 % higher neutron flux when using the collimator with 2 cm aperture. The spatial distributions of fast neutrons were significantly narrower at 10 cm distance from the aperture compared to the original design 8.5×8.5 cm^2. The narrower and intense neutron beam would save the healthy tissues beside the tumor and also decrease the treatment time period which make the treatment procedures more comfortable. There is reason to hope that narrow beams will make neutron beam radiotherapy for the treatment of small and irregularly shaped tumors more accurate and safer for the patient.

1. INTRODUCTION

Neutrons are widely used in many fields. Therefore, there is a need for adapted sources of these particles. Until now, research has mainly focused on increasing the intensity of their output by improving the design and selection of component materials of the collimator.

T. Schönfeldt [1] adopted lead ^{208}Pb as a reflective filter for a neutron source. V. De Haan [2] showed that a moderator in a collimator with a fine graphite structure can increase the neutron flux by almost 10 times. E.B. Iverson [3] proposed a new design of the collimator assembly for obtaining more intense fluxes of slow neutrons.

The neutron flux can be increased by using special materials. Neutron scattering was studied, which depends on the geometry and composition of the moderator in the source of fission neutrons [4]. These studies require a large amount of calculations and the desired results have not yet been achieved. At the same time, the influence of the material composition and design on the spectrum of neutrons and gamma rays can be modeled using the Monte Carlo transport code of the MCNP type [5, 6].

Various designs of collimators have been studied to increase the flux density and improve the spectral properties of fast neutrons. Neutron therapy requires particles with energies in the range from 1 to 20 MeV, depending on the size of the area and the depth of the treated tissues. To do this, it is necessary to reduce the proportion of scattered and slow neutrons, and increase the proportion of fast ones [7, 8].

There are a number of publications in the scientific literature devoted to the influence of the geometry and materials of a collimator on the characteristics of fast neutrons produced in nuclear reactors or when light targets are bombarded with accelerated ions [9–11]. It is advisable to use it to limit the size of the irradiated medium. If the neutron source is too large, an undesirable penumbra appears on the irradiated object. The collimator will increase the flux density at a certain distance from the source, where it scatters neutrons and creates a collimated beam. The magnitude of the flux increment depends on the collimation field and the length of the collimator. On the other hand, if the neutron source is large across, the collimator may reduce the neutron flux rather than increase it. Most collimators can increase the flux density by 10–20% [9].

The main advantage of neutron therapy is that unlike gamma and electron therapy neutrons destroy damaged tissue irreversibly, i.e. there is no recurrence after neutron therapy. The negative aspects of neutron therapy are associated with affecting healthy tissues of the body.

The existing technology operates a wide horizontal beam, the direction of which we cannot control in fact. But by optimizing geometry and materials for collimator we will be able to focus the scattered neutrons to a narrow beam. A narrow beam allows introducing a safer method of irradiating tumors from different sides. Here the objective is to maximize the use of neutrons going out of the source and to focus them in such a way as to ensure a maximum therapeutic effect.

2. MEASUREMENTS AND METHOD

MCNP is a universal Monte Carlo code that can be used to transport neutrons, photons, electrons, or bound particles. Specific applications include many areas, such as radiation protection, dosimetry, radiography, medical physics, nuclear safety, detector design, design of accelerator targets, fission and fusion reactors, etc. The code handles an arbitrary 3D configuration of materials in geometric cells.

Important standard features that make MCNP easier to use include powerful source, criticality source, and surface source; both geometric and output plots; a rich collection of methods for reducing deviations; flexible calculation structure; and an extensive set of cross-section data as ENDF/B-VI for neutrons.

The collimator consists of several parts; non-removable parts; the iron (steel) collimator which is about 42 cm in length and removable polyethylene (PE) part 45 cm, as shown in Fig. 1.

Several scientific papers have been previously published dealing with optimization of the fast neutron collimator used in radiotherapy at Tomsk Polytechnic University. However, in one of these studies, a collimator ending in a nozzle with a diameter of 2 cm was used and compared with collimator' apertures of larger diameters. Nevertheless, it has not been studied if the neutron flux diverges after exiting the aperture when the end of the aperture is small (2 cm or less) compared to the case when the aperture is large (8.5×8.5 cm^2, for example). This issue is very important in radiation therapy, where the spatial distribution of the neutron beam should not be diverged, so if the beam is wide, it would expos healthy tissues to high doses. Also, the neutron flux becomes less intense in the target area (the tumor) for treatment, which increases the irradiation time required to reach the appropriate dose. In this work, the spectrum of fast neutrons and the spatial distribution of the end of a small aperture of 2 cm were studied, using simulations with the code MCNP5. The neutron spectrum used in the simulation has been accurately described in a previous work, and it is the spectrum resulting

from the collision of a beam of deuteron ions with an initial energy of 13.6 MeV on a 2 mm thick beryllium target. The spectrum and transverse spatial distribution of a neutron beam were simulated at a distance 10 cm from the end of the aperture. An additional small cylindrical collimator with a diameter of 2 cm was simulated for comparison and the shape and spectrum of the beam leaving the channel were studied.

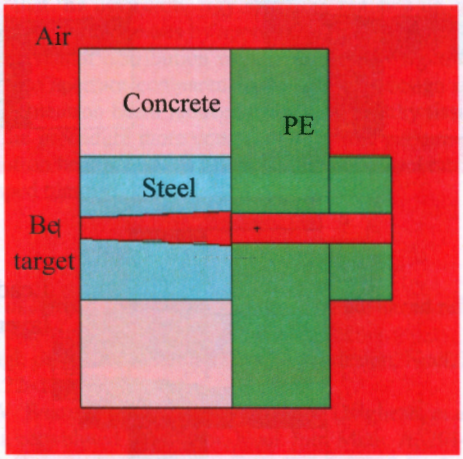

Fig.1. MCNP5 scheme of the original collimator 8.5×8.5 cm^2 deployed at the radiotherapy treatment room.

3. RESULTS AND DISCUSSION

The simulated work was carried out on the neutron collimator utilized in the radiotherapy room without any modifications (Fig.1). The results of the neutron spectrum as well as the spatial distribution were compared at a distance of 10 cm from the aperture. The simulation results were extracted for collimators with apertures diameter of 2 cm in different conditions, as shown in Figure 2. In Figure 2, an additional small collimator of polyethylene with an extension of 10 cm and a thickness of 20 cm with a cylindrical channel 2 cm in diameter was added, to investigate its effect on the spectrum of neutrons and their spatial distribution. In addition, in another step, an inner layer of lead metal (2-cm thickness) was added to the cylindrical channel of the additional part, to examine the change in the neutron spectrum and its spatial distribution, as well as the possibility of obtaining additional fast neutrons through the reaction (n, 2n).

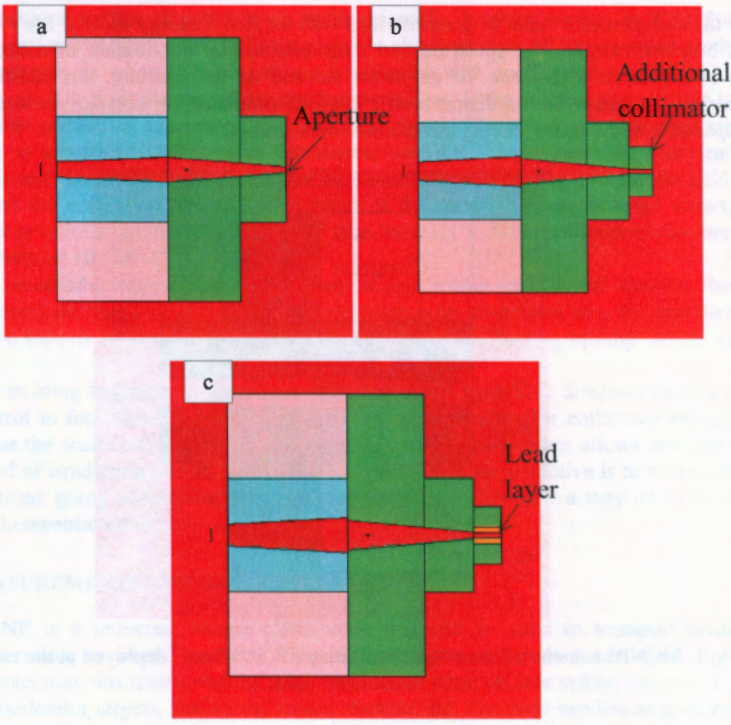

Fig.2. MCNP5 schemes of the simulated collimators; a) the collimator with 2 cm diameter of aperture, b) the collimator with 2 cm aperture and additional collimator 10 cm in length and 20 cm thickness, c) the case (b) plus an addition inner layer of lead metal.

It was found that the results of the MCNP simulation for the spectra of neutrons leaving the four different apertures of the four collimators. In general, the neutron spectra do not change in the energy range between 1 and 13 MeV. Moreover, the collimator with an aperture of 2 cm without any additional parts can increase the neutron flux by about 11 percent compared to the original collimator with an aperture of 8.5×8.5 cm^2. In addition, it can be noticed that the lower-energy (thermal) component is diluted by 3-folds when using the 2-cm aperture collimator. This result is crucial in reducing the flux of thermal neutrons in the case of radiation therapy, as it reduces the thermal neutron exposure of healthy tissues surrounding the tumor and decreasing the unnecessary radiation doses. Moreover, it is found that adding an additional small collimator of polyethylene reduces the fast neutron by about a half, but at the same time it decreases the thermal neutron flux several times. In fact, the reduction of the fast neutron flux is not considered a good feature in the field of fast neutron therapy, as it prolongs the period of radiation therapy. Furthermore, the thermal neutron flux can be reduced by a thin layer (filter) of cadmium or borated compounds. Adding lead layer did not improve the neutron spectrum and did not contribute to increasing the neutron flux. That is because of the fast neutrons have been collected by the conical collimator with an end

of 2 cm, and therefore there are no sufficient amounts of fast neutrons that can collide with the inner layer of lead and contribute to the increase of the neutron flux through the reaction (n, 2n).

4. CONCLUSION

The results show that the neutron energy spectrum remains nearly unchanged in the fast region, while the neutron flux increases by approximately 11% when using the collimator with a 2 cm aperture. The spatial distribution of fast neutrons is significantly narrower at a distance of 10 cm from the aperture compared to the original design of 8.5×8.5 cm^2. The narrower and more intense neutron beam reduces damage to healthy tissue and decreases the treatment time, making the procedure more comfortable for the patient. Narrow beams offer the potential to make neutron beam radiotherapy safer and more accurate for the treatment of small and irregularly shaped tumors.

REFERENCES

1. T. Schönfeldt, *et al.,* Broad spectrum moderators and advanced reflector filters using ^{208}Pb, Nucl. Instrum. Meth A, 2015, V.769, P.1–4.
2. V. de Haan, A high performance neutron moderator design, Nucl. Instrum. Meth A, 2015, V.794, P.122–126.
3. E.B. Iverson, D.V. Baxter, G. Muhrer, S. Ansell, R. Dalgliesh, et al., Neutron Beam Production with a convoluted Moderator, Nucl. Intr. Meth. A, 2014, V.762, P.31–41.
4. J.K. Zhao, J.L. Robertson, K.W. Herwig, F.X. Gallmeier, B.W. Riemer, Optimizing moderator dimensions for neutron scattering at the spallation neutron source, Rev. Sci. Instrum., 2013, V.84, № 12, P.125104.
5. A.X Da Silva, V.R Crispim, Moderator-collimator-shielding design for neutron radiography systems using ^{252}Cf, Applied Radiation and Isotopes, 2001, V.54, № 2, P.217–225.
6. N. Matsui, et al., Neutronics Analysis on the Beam Optics from Cylindrical Discharge Type Fusion Device, Fusion Sci. Technol., 2013, V. 64, № 3, P.692–696.
7. Франк-Каменецкий А.Д. Моделирование траекторий нейтронов при расчете реакторов методом Монте-Карло. Серия «Физика ядерных реакторов» № 9, Атомиздат, Москва, 1978, 96 стр.
8. J.G. Beckerley, Neutron physics - A Revision of I. Halpern's Notes on E. Fermi's Lectures in 1945, Technical Information Service, 1951, P.50–56.
9. Nuclear data for neutron therapy: status and future needs. TECDOC 992: IAEA, 1997, 129 P.
10. M. Catterall, Radiology now: fast neutrons-clinical requirements, Br. J. Radiol., 1976, V.49, № 579, P.203–205.
11. A.W. Keith, Neutrons from Deuteron Bombardment of Light Nuclei. PhD thesis, University of Wisconsin, Madison, 1972, 82 p.

of 2 cm, and therefore there are no sufficient amounts of fast neutrons that can collide with the inner layer of lead and contribute to the increase of the neutron flux through the reaction (n, 2n).

4. CONCLUSION

The results show that the neutron energy spectrum remains nearly unchanged in the fast region, while the neutron flux increases by approximately 11% when using the collimator with a 2 cm aperture. The spatial distribution of fast neutrons is significantly narrower at a distance of 10 cm from the aperture compared to the original design of 8.5×8.5 cm^2. The narrower and more intense neutron beam reduces damage to healthy tissue and decreases the treatment time, making the procedure more comfortable for the patient. Narrow beams offer the potential to make neutron beam radiotherapy safer and more accurate for the treatment of small and irregularly shaped tumors.

REFERENCES

1. T. Schönfeldt, *et al.,* Broad spectrum moderators and advanced reflector filters using ^{208}Pb, Nucl. Instrum. Meth A, 2015, V.769, P.1–4.
2. V. de Haan, A high performance neutron moderator design, Nucl. Instrum. Meth A, 2015, V.794, P.122–126.
3. E.B. Iverson, D.V. Baxter, G. Muhrer, S. Ansell, R. Dalgliesh, et al., Neutron Beam Production with a convoluted Moderator, Nucl. Intr. Meth. A, 2014, V.762, P.31–41.
4. J.K. Zhao, J.L. Robertson, K.W. Herwig, F.X. Gallmeier, B.W. Riemer, Optimizing moderator dimensions for neutron scattering at the spallation neutron source, Rev. Sci. Instrum., 2013, V.84, № 12, P.125104.
5. A.X Da Silva, V.R Crispim, Moderator-collimator-shielding design for neutron radiography systems using ^{252}Cf, Applied Radiation and Isotopes, 2001, V.54, № 2, P.217–225.
6. N. Matsui, et al., Neutronics Analysis on the Beam Optics from Cylindrical Discharge Type Fusion Device, Fusion Sci. Technol., 2013, V. 64, № 3, P.692–696.
7. Франк-Каменецкий А.Д. Моделирование траекторий нейтронов при расчете реакторов методом Монте-Карло. Серия «Физика ядерных реакторов» № 9, Атомиздат, Москва, 1978, 96 стр.
8. J.G. Beckerley, Neutron physics - A Revision of I. Halpern's Notes on E. Fermi's Lectures in 1945, Technical Information Service, 1951, P.50–56.
9. Nuclear data for neutron therapy: status and future needs. TECDOC 992: IAEA, 1997, 129 P.
10. M. Catterall, Radiology now: fast neutrons-clinical requirements, Br. J. Radiol., 1976, V.49, № 579, P.203–205.
11. A.W. Keith, Neutrons from Deuteron Bombardment of Light Nuclei. PhD thesis, University of Wisconsin, Madison, 1972, 82 p.

Nuclear Reactor Physics

Investigation of Gamma Dose Changes of High-Degree Occupation Hall of Tehran Research Reactor up to a Few Days after the LOCA Accident

Gholamzadeh Z.

Safety and Nuclear Research Reactor School, Nuclear Science and Technology Research Institute, Tehran, Iran

E-mail: Cadmium_109@yahoo.com

Loss Of Coolant Accident (LOCA) investigation of Tehran Research Reactor (TRR) exactly at the time when the reactor has been operating at its maximum power (5 MW) and the consequent impact of it on the reactor operators and other people in the vicinity of the reactor containment is a very important subject which should be carefully evaluated. The effects of the events have been there since the first nuclear reactor built in 1954. It should be noted that according to the documents, high dose rate (1–2 Sv/h) has been reported inside the rooms of the damaged Chernobyl nuclear power plant after the accident. Considering the different nuclear accidents and the regularity body concerns, the present work aimed to calculate the gamma dose rates in high-degree occupation portions from the TRR hall after LOCA accident. The main purpose of upgrading the technical documentation of the reactor is to ensure the safe operation of the reactor and to ensure the safety of the whole site in such accidents. In the present work, the dose rate received by the staff working in the TRR entrance room after the LOCA accident was investigated when the situation resulted in the complete baring of the nuclear core. MCNPX code was used to model the TRR containment with the most details.

Introduction

Safety is very important concern for operational nuclear power plants (NPP). Yearly different documents are prepared to cover the different types of safety issues in NPPs. One of these documents is the personnel internal and external exposure during the normal and accident situation of an NPP. It should be mentioned, according to the ALARA (As Low As Reasonably Achievable) principal and standard regulations the limit value for the average effective dose for radiation workers is 20 mSv/year or 10 μSv/h but at accident condition if the gamma dose rate of the workers exceeds than 1000 μSv/h the area should be evacuated [1–3]. Hence, regularity body of any NPP should perform annually-inspections to control and update the required safety documents. For the mentioned purpose some activities are being done in different NPPs which some of them are reviewed in the following.

Hoq et al. (2017) reported the 3 MW TRIGA Mark-II Research Reactor of Bangladesh Atomic Energy Commission (BAEC) has been under operation for about thirty years since its commissioning at 1986. For determining dose rate at different strategic points of the reactor facility, they measured neutron, beta and gamma radiation with reactor power level of 2.4 MW to estimate the rising level of radiation due to its operational activities. They reported high radiation dose is observed at the measurement position of the piercing beam port, which is caused by neutron leakage. Their study also deals with the gamma dose rate measurements at a fixed position of the reactor pool top surface for different reactor power levels under both Natural Convection Cooling Mode (NCCM) and Forced Convection

Cooling Mode (FCCM) and results showed the radiation dose rate is higher for NCCM in compared comparison with FCCM [4].

Abrefah et al. (2018) used two computer codes of ORIGEN-S; for computing changes in the isotopic concentrations during neutron irradiation and radioactive decay as well as to determine the source term; and MCNP6; which uses the source term estimated by ORIGEN-S code to calculate the dose rate for GHARR-1 research reactor. The 30 kW pool-type Ghana Research Reactor-1 (GHARR-1) is a commercial Miniature Neutron Source Reactor (MNSR) similar to the Canadian SLOWPOKE in design. Their obtained results showed that above the reactor core-floor level at 595 cm the measured dose rate is 4.27E+04 ± 0.0006 mGy/h [5].

Hence, the present work aimed to investigate the gamma dose rate of the high-occupation areas in Tehran Research Reactor (TRR) in Loss Of Coolant Accident (LOCA). The carried out calculations were performed with the imagination of that the LOCA is happened exactly at the operational time of the reactor at 5 MW.

Material and methods

To investigate the gamma dose rates in the mentioned areas of TRR, the site containment was modeled using MCNPX code. A square-lattice 33-assembly pool-type TRR core has been modeled using MCNPX 2.6.0 code, which is a Monte Carlo-based code with ability of 34-particle transport and modeling different geometries powerfully [6]. Light water is used as coolant for of the fuel assemblies in TRR. Graphite is used as the core reflector. A 3D TRR model was set up using MCNPX 2.6.0. SDEF capability has been used to introduce gamma source. TRR is an open pool, MTR type light water-moderated with a thermal power of 5 MW.

The reactor core is composed of two types of fuel assembly that are standard fuel elements and control fuel elements. The core consists of 28 standard fuel element (SFE) containing 19-fuel plates and 5 control fuel elements (CFE) containing 14 fuel plates according to the core specifications. The modeled reactor is a 5 MW reactor with 20% enriched MTR fuels and 500 m^3/h flow rate. The reactor core is composed of two types of fuel assembly that are standard fuel elements and control fuel elements. Two types of control rods are used in the TRR; which one made out of Ag-In-Cd alloy, and the other of stainless steel. Both have a set of two control plates as a fork type shape. The reactor fuel is U_3O_8-Al containing 20%-enriched uranium. Neutronic and thermal hydraulic characteristics of the fuel assemblies and control rods are summarized in Table 1 [7].

To define a gamma source as SDEF card in MCNPX code, the gamma source should be calculated using ORIGEN code, which is a widely used computer code for calculating the buildup, decay, and processing of radioactive materials. The code involves reactor models, cross sections, fission product yields, decay data and decay photon data [8].ORIGEN 2.1 is a versatile point-depletion and radioactive-decay computer code for use in simulating nuclear fuel cycles; it was developed at the Oak Ridge National Laboratory (ORNL) and distributed worldwide beginning in the early 1970s. It is used for existing reactors, including pressurized water reactors, boiling water reactors, liquid-metal fast breeder reactors, and Canada deuterium uranium reactors [9].

To calculate gamma dose rates two computational procedures were applied; one is simulation of gamma detectors to calculate a selected point dose rate, the second is the definition of mesh tally card in the MCNPX code input to calculate a dose rate distribution. Some Geiger Muller detectors (GM; LB 123 made by BETHOLD Company; the gamma detector sensitive volume dimension is 45 mm×170 mm (R×H).) were placed around the TRR

check in room to determine the gamma dose rates at different positions of the place. In addition, the dose rate distributions were calculated using the mesh tally capability of the MCNPX code. F4 tally with DE/DF card were used to apply flux to dose conversion factors for the gamma dose rate calculation. Figure 1 shows the modeled containment of TRR using MCNPX code.

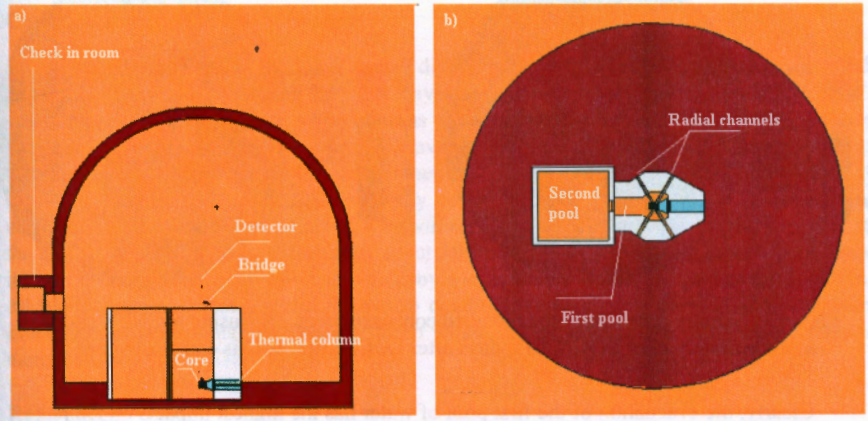

Figure 1: The modeled containment of TRR using MCNPX code, a) Axial view, b) Radial view.

Results and discussion

Figure 2 shows the average gamma dose rates at the height that is near the second floor just immediately and 7-days after LOCA, which was happened so that both first and second pools are bare (empty).

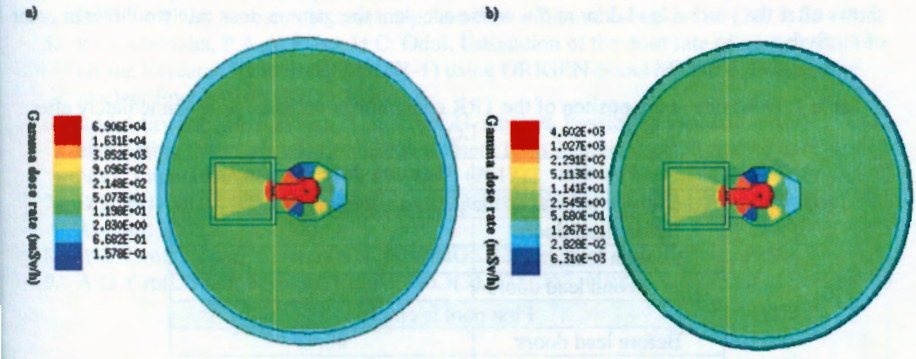

Figure 2: Gamma dose rate in the modeled containment of TRR using MCNPX code, a) immediately after LOCA, b) 7-days after LOCA; both of the pools are empty.

Fig.3 shows the average gamma dose rates at the height that is near the second floor exactly immediately and 7-days after LOCA, which was happened so that only first pool is bare (empty).

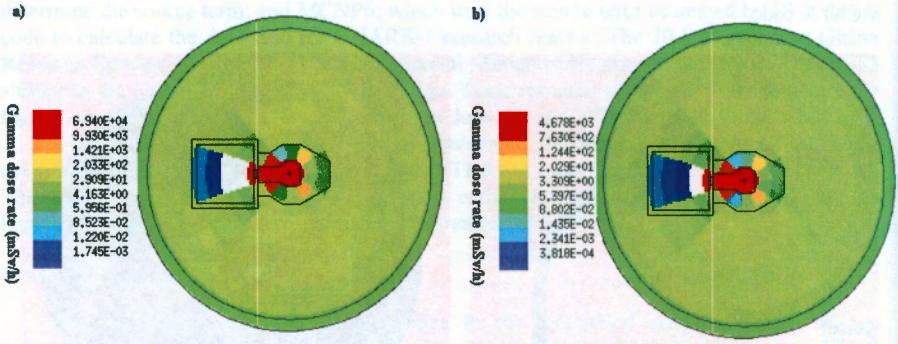

Figure 3: Gamma dose rate in the modeled containment of TRR using MCNPX code, a) immediately after LOCA, b) 7-days after LOCA; first pool is empty of water.

Clearly, the evacuation of the first pool of water has the highest impacts on the reactor hall dose rate because of the bared core high gamma emission rate. One of the important sections is the entrance door to the reactor hall as well as the check in room of the TRR reactor. Table 1 shows gamma dose rates at different position, which are very important regard to keeping the personnel exposure limitations. Obviously, the worse situation belongs to water evacuation accident of both pools. The second critical situation can be considered when the first pool and then the nuclear core are bare. In both situations the hall exit location experiences high gamma dose rates 55.09 and 38.21 mSv/h respectively. When both of the pools miss their water, the gamma dose rate between the lead doors of the TRR containment is about 41 μSv/h in the middle of the corridor between the two lead doors. The calculations shows after the second lead door at the worse accident the gamma dose rate would be in order of 4 μSv/h.

Table 1: Dose rate at the positon of the TRR containment entrance door immediately after LOCA

Position	Gamma dose rate (mSv/h)
Both of the pools are empty	
Before lead doors	55.09
Between lead doors	0.041
After second lead doors	0.004
First pool is empty	
Before lead doors	40.43
Between lead doors	0.00074
After second lead doors	< nSv/h

When the first pool is bare, after 7-days of LOCA the gamma dose rate exactly before the lead door would be 3.43 ± 0.17 mSv/h. The value is 3.2 ± 0.09 mSv/h when both of the pools are empty. Average gamma energy of the radioactive fuel assemblies is about 950 keV after LOCA and 763 keV at 7-days after LOCA, which the less average energy causes less gamma dose rates far from the bared core.

Conclusion

Investigation of gamma dose rate distribution inside the TRR containment after immediately LOCA and during the next days is very important in point of the operator's exposure views. The carried out calculations showed immediately after LOCA in condition that both the pools are empty a 50 mSv/h average gamma dose rate would be available in whole of the second floor of the containment. The value drops 10 times after 7-days of cooling. In addition, when the first pool only misses its water during the LOCA, the gamma dose rate of the second floor is about 4 mSv/h on average. Similarly after 7-days of cooling the average gamma dose rate decreases about 10 times. Clearly when the second pool keeps its water, some portion of gammas shield by the available water of the second pool. The calculations showed that even in the worse condition (immediately after LOCA and water evacuation of both pools) the check in room would not experience the gamma dose rates of more than 10 μSv/h.

References

1. Suwoto, H. Adrial, A. Hamzah, Zuhair, S. Bakhri, G.R. Sunaryo, Neutron dose rate analysis on HTGR-10 reactor using Monte Carlo code, IOP Conf. Series: Journal of Physics: Conf. Series 962 (2018) 012029.
2. Preliminary Safety Report Chapter 22 Radiological Protection, UK HPR1000 GDA project, 2017.
3. Generic Procedures for Response to a Nuclear or Radiological Emergency at Research Reactors, EPR-2011, IAEA.
4. M. Ajijul Hoq, M.A. Malek Soner, M.A. Salam, M.M. Haque, Salma Khanom, S.M. Fahad, Experimental study of radiation dose rate at different strategic points of the BAEC TRIGA Research Reactor, Applied Radiation and Isotopes 130 (2017) 29–33.
5. R.G. Abrefaha, P.A.A. Essel, H.C. Odoi, Estimation of the dose rate of nuclear fuel of Ghana Research Reactor-1(GHARR-1) using ORIGEN-S and MCNP 6, Progress in Nuclear Energy, 105 (2018) 309–317.
6. S.M. Mirvakili, M. Keyvani, S.S. Arshi, H. Khalafi, Possibility evaluation of eliminating the saturated control fuel element from Tehran research reactor core. J Nucl. Engin. and Des. Vol.248, 197–205, (2012).
7. D.B. Pelowitz, MCNPXTM user's manual. Los Alamos National Laboratory, Los Alamos. 2005.
8. A.G. Croff. A user's manual for the ORIGEN2 computer code, ORNL, 1980.
9. A.G. Croff. Nucl. Technol. Vol.62, No.3(3), 335–352, (1983).

The Use of Pb-208 as a Reflector of the NEPTUNE Reactor

A.A. Hassan, D.G. Chereshkov, T.S. Dikova

Joint Institute for Nuclear Research, Dubna, Russia
*e-mail: AKhassan@mephi.ru

In previously conducted researches [1–4], it was reasoned that it is possible to obtain a neutron generation lifetime of 30 ns by adding highly enriched uranium (90%). However, to limit the proliferation of nuclear weapons, the International Atomic Energy Agency recommends using uranium enriched by no more than 20% in research reactors. To this effect, in this work, the authors propose the use of Pb-208 as a neutron reflector as an alternative to Ni. Increasing the neutron generation lifetime required to make the reactor more stable and safer. For this to be realized, the neutron generation lifetime must increase from 8 to 30 ns.

Table 1, shows the names of the various core options and the distribution of uranium rods added to the reactor core. Table 2 illustrates the effect of changing the reflector material from Ni+Be to Pb-208 on neutron generation lifetime, multiplication factor, and effective fraction of delayed neutrons.

Table 1. Distribution of uranium rods in the considered variants of the calculations

Variantion	Location of uranium rods containing uranium in the reactor core	Number of uranium rods added to the reactor core
V1	Reactor core without any additives	0
V2	In the reactor core, the **first row** next to the neutron moderator was replaced with rods containing "UN - 10% enrichment"	50
V3	In the reactor core, the **first row** next to the neutron moderator was replaced with rods containing "UN - 20% enrichment"	50
V4	In the reactor core, the **first row** next to the neutron moderator was replaced with rods containing "UN50+NpN50 - 10% enrichment"	50
V5	In the reactor core, the **first row** next to the neutron moderator was replaced with rods containing "UN50+NpN50 - 20% enrichment"	50
V6	In the reactor core, the **second row** next to the neutron moderator was replaced with rods containing "UN - 10% enrichment"	48
V7	In the reactor core, the **second row** next to the neutron moderator was replaced with rods containing "UN - 20% enrichment"	48

Variantion	Location of uranium rods containing uranium in the reactor core	Number of uranium rods added to the reactor core
V8	In the reactor core, the **second row** next to the neutron moderator was replaced with rods containing "UN50+NpN50 - 10% enrichment"	48
V9	In the reactor core, the **second row** next to the neutron moderator was replaced with rods containing "UN50+NpN50 - 20% enrichment"	48
V10	In the reactor core, **part of rods** in the second and third rows next to the neutron moderator were replaced with rods containing "UN - 10% enrichment"	44
V11	In the reactor core, replaced **part of rods** in the second and third rows next to the neutron moderator with rods containing "UN - 20% enrichment"	44
V12	In the reactor core, **part of rods** in the second and third rows next to the neutron moderator were replaced with rods containing "UN50+NpN50 - 10% enrichment"	44
V13	In the reactor core, **part of rods** in the second and third rows next to the neutron moderator were replaced with rods containing "UN50+NpN50 - 20% enrichment"	44
V14	In the reactor core, **part of rods** in the second and third rows next to the neutron moderator were replaced with rods containing "UN - 5% enrichment"	44
V15	In the reactor core, the **second row** next to the neutron moderator was replaced with rods containing "UN60+NpN40 - 10% enrichment"	48
V16	In the reactor core, the **second row** next to the neutron moderator was replaced with rods containing "UN40+NpN60 - 20% enrichment"	48

Table 2. Neutron generation lifetime, effective multiplication coefficient, and effective fraction of delayed neutrons for variations V1-V16 using a Pb-208 reflector

Variantion	Neutron generation lifetime, ns	K-eff	β-eff, e-3
V1	10.7	1.016	1.3433
V2	821.4	1.003	1.4309
V3	943.9	1.010	1.4693
V4	263.3	1.007	1.3693
V5	415.5	1.012	1.3987
V6	58.8	0.989	1.3984
V7	68.6	0.996	1.4618
V8	27.2	1.001	1.3703
V9	37.2	1.005	1.4145

Variantion	Neutron generation lifetime, ns	K-eff	β-eff, e-3
V10	33.3	0.984	1.4186
V11	34.3	0.992	1.4657
V12	18.0	0.997	1.3722
V13	22.3	1.002	1.3897
V14	27.23	0.980	1.3709
V15	30.31	0.998	1.3693
V16	30.87	1.007	1.3783

CONCLUSION

The results proved that it is possible to increase the neutron lifetime in the Neptune reactor by adding low-enriched uranium to the reactor core with the need to change the neutron reflector from beryllium-nickel to lead-208 without the need for a slow neutron filter.

REFERENCES

1. Hassan, A.A. and E.P. Shabalin, *Fourth Generation Neutron Source in Dubna, "Solution of Pulse Power Fluctuation Problem"*. Physics of Atomic Nuclei, 2021. **84**(3): p. 227–236.
2. Shabalin, E.P., et al., *Reducing the Level of Power Vibrations in the NEPTUNE Pulsed Reactor.* Physics of Particles Nuclei Letters, 2021. **18**(3): p. 354–369.
3. Aksenov, V.L., M.V. Rzyanin, and E.P. Shabalin, JINR Research Reactors: a Look into the Future. ELEMENTARY PARTICLE AND ATOMIC NUCLEUS PHYSICS, 2021. **52**(6): p. 1349–1376 (In Russian).
4. Hassan, A., M. Bulavin, and V. Afanasyev, *Optimization of the cold moderator for the new pulsed reactor NEPTUN.* Nuclear Engineering Design, 2023. **404**: p. 112–192.

Neutronic Chain Reactions in Bismuth Salts

Solomon Lim

National University of Singapore High School of Mathematics and Science

The production of the industrially significant radionuclide polonium-210 from the neutron irradiation of bismuth metal and the subsequent beta decay of bismuth-210 is highly inefficient due to the small neutron capture cross section of bismuth-209. In this paper, we report a previously undescribed self-sustaining nuclear chain reaction involving self-propagating neutron multiplication in bismuth salts that allow for rapid and cost-effective production of polonium-210. The reaction proceeds in a cycle of three alternating elementary steps – the capture of neutrons by bismuth-209 and the subsequent formation of polonium-210, the emission of high-energy alpha particles by polonium-210, and the production of more neutrons from (α,n) and (n,2n) reactions on light element and bismuth-209 nuclei respectively. Furthermore, the high hydrogen density of the compound also confers it intrinsic neutron moderation properties, increasing the neutron capture cross section of bismuth-209 at thermal neutron energies. The chain reaction was proven to have successfully occurred by irradiating a sample of the bismuth salt with a 80 μCi neutron source and monitoring the activity levels of the reaction. It was found that the activity of the reaction increased exponentially after an initial stable period following a derived formula for polonium production trends for the reaction, thus validating the occurrence of the reaction. Furthermore, alpha spectroscopy confirmed that polonium-210 had been produced by characterising the 5.30 MeV alpha emission peak of the reaction in addition to using beta spectroscopy to identify the parent nuclide bismuth-210, further proving that the reaction was successful. Hence, this paper reports the successful initiation and characterisation of a novel nuclear chain reaction, and its potential applications offered by a method of rapidly producing large quantities of polonium-210.

Keywords: neutron irradiation, polonium-210, bismuth, chain reaction

1. Introduction

In 1931, neutrons were first produced by exposing beryllium to alpha particles from polonium-210 [1, 28, 29]. Since then, this method of neutron generation by irradiating light elements such as beryllium, lithium, and fluorine with an intense alpha source has been incorporated into radioisotopic neutron sources used in nuclear laboratories throughout the world. The mechanism by which the neutrons are produced proceeds via an (α, n) reaction which requires a source of high energy alpha radioactivity also makes it an ideal candidate for a wide range of applications, such as in neutron initiators in nuclear weapons [32], medical isotopes in radiotherapy [33], energy cells in radioisotopic thermoelectric generators [34], and ionising antistatic devices [35] (Fig. 1). All these applications mean that polonium-210 is an industrially significant radionuclide, and thus producing it in quantities that can accommodate global demand is of practical importance. However, polonium-210 can only be produced in microgram amounts in nuclear reactors via neutron irradiation of bismuth-209, which is slow due to the small neutron absorption cross section of the $^{209}Bi(n, \gamma)^{210}Bi$ reaction, measured to be 20.5 ± 1.1 millibarns [4, 5].

Upon closer inspection of the aforementioned nuclides, a cyclic relationship is found: polonium-210 emits alpha particles that produce neutrons on impact with light elements, and neutrons can be used to produce polonium-210. Thus, a chain reaction can be initiated in a mixture of atoms of bismuth-209 and light elements, using an initial neutron source to transmute the bismuth atoms into that of polonium, which would themselves emit high-energy alpha particles that impact the light elements, causing further neutron production. Furthermore, ^{209}Bi and ^{9}Be are also able to cause neutron multiplication via a (n, 2n) reaction with fast neutrons [6], increasing the neutron population of the system. To be suitable for sustaining neutron multiplication, the bismuth salt should contain a light element with high neutron yields from (α, n) reactions [7], e.g. ^{27}Al, ^{19}F, ^{10}B, ^{9}Be, as well as a high hydrogen content for neutron moderation, as the ^{209}Bi neutron capture cross section for ^{210}Po formation is greatly increased at thermal neutron velocities. Hence, bismuth beryllium acetate was used due to its high beryllium content, which is ideal for alpha-to-neutron conversion, as well as its intrinsic neutron multiplication and moderation properties.

Figure 1: Commercially available antistatic devices containing polonium-210.

The validity of this chain reaction was investigated by exposing a sample of bismuth beryllium acetate to the neutron emissions from a weak neutron source (80 μCi) and measuring the activity levels of the reaction mixture. It is expected that in the case of a non-proliferating reaction, the activity of the target will approach an equilibrium before decreasing, while the successful propagation of the chain reaction would result in a sigmoidal increase of polonium-210 produced in the reaction mixture due to the autocatalytic nature of the chain reaction [36, 37]. It was found that the pattern of increase in radioactivity of the irradiated bismuth beryllium acetate samples were characteristic of a self-sustaining chain reaction as described by a derived equation (proof and formulation in Appendix 1). Furthermore, alpha and beta spectrometry was also used to further confirm the propagation of neutron multiplication through the bismuth salt sample by characterising the alpha emission spectrum of polonium-210 and the beta spectrum of bismuth-210.

2. Materials and Methods

2.1. Bismuth salt selection and synthesis

Selection of the bismuth salt to be used to sustain the chain reaction was achieved by considering the various properties that the salt would need to possess in order to be able to allow the chain reaction to propagate. Firstly, upon considering the (α,n) reaction yields of the light elements from lithium to potassium [7] (Fig. 2), 3 elements were selected which have a

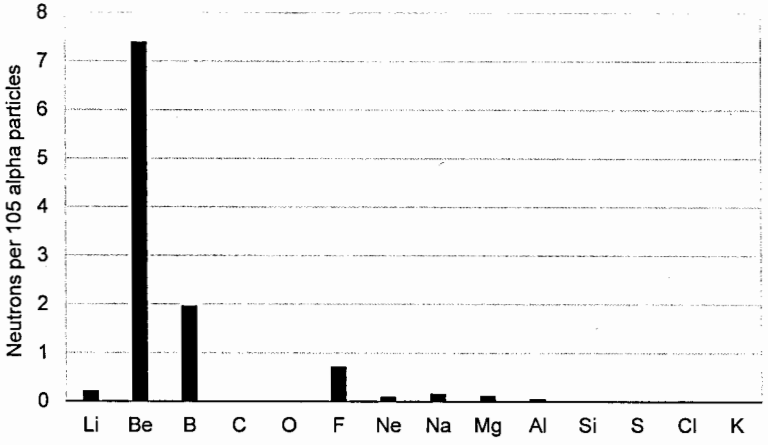

Figure 2: (α,n) yields of light elements at 5.41 MeV.

substantially higher yield than the rest – beryllium, boron, and fluorine. The use of boron would be unfavourable due to its high neutron absorption cross section of 749 barns [16, 38], which would have absorbed the neutrons much faster than bismuth atoms and thus cause the chain reaction to fail. Between beryllium and fluorine, beryllium was chosen due to its markedly higher (α,n) reaction yield [39].

Atoms of bismuth-209 and beryllium-9 are also able to undergo neutron multiplication reactions such as the (n,2n) reaction to sustain the thermal neutron population in the reaction mixture [6, 40, 41]. This also has the added advantage of lowering the average neutron energy, as the neutron multiplication cross section is much larger for neutrons with energies in the MeV range. This presents a non-competing reaction as the thermal neutrons are able to be captured by bismuth atoms due to the larger neutron capture cross section at lower energies, while fast neutrons are able to be multiplied by bismuth and beryllium atoms due to the larger neutron multiplication cross section at higher energies [15]. Moderation was accomplished by using a counterion with a high hydrogen density in order to saturate the salt with light atoms to slow the neutrons to thermal velocities. Furthermore, beryllium has also been shown to be an excellent neutron moderator for neutrons with higher energies, hence being an added component of moderation within the bismuth salt, serving dual properties of multiplication and moderation in addition to alpha-neutron conversion.

Acetate was used as a counterion in the bismuth salt due to its high hydrogen density for effective moderation, being composed of 5% hydrogen by mass. The hydroxide ion was considered as it has a higher hydrogen density of 15%, but the chemical instability of bismuth

beryllium hydroxide made it unsuitable for use in sustaining the chain reaction. Hence, **bismuth beryllium acetate** was chosen as the salt to sustain the chain reaction due to its ability to moderate and multiply neutrons while also possessing a high bismuth percentage and a high alpha-neutron conversion yield.

Bismuth beryllium acetate was prepared by precipitating the acetate salts of bismuth and beryllium respectively from a solution of hot peroxyacetic acid (Fig. 3) in order to minimise the formation of beryllium aerosols. The salt was obtained in good yield (89.3%) as an off-yellow powder. (Refer to Appendix 2 for detailed preparation procedure.)

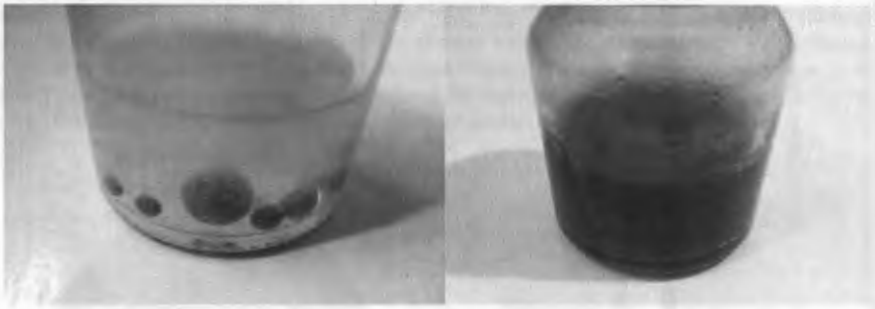

Figure 3: Dissolution of beryllium metal in peroxyacetic acid (left) and precipitation of bismuth beryllium acetate (right).

2.2. Materials

Radioactive americium-241 mast-mounted and plated sources were obtained from Radwell International MRO. The mast-mounted source was measured to have an activity of 60 μCi, and the two plated sources were measured to have an activity of 10 μCi each. Beryllium foil with a thickness of 0.3mm was purchased from CTPT Inc. Bismuth(III) oxide (>99.9% purity) was purchased from Inoxia Ltd. and used as received without further purification. Beryllium metal (granules) was purchased from Luciteria Inc. and used as received without further purification.

2.3. Neutron irradiation setup

Mast-mounted and plated americium-241 sources containing 60 μCi and 10 μCi of $^{241}AmO_2$ respectively plated onto gold foil on a steel base were used as sources of alpha particles for neutron generation, so as to ensure directed alpha particle emission. The neutron source was constructed by exposing a 0.3mm-thick layer of beryllium metal to the alpha radiation from the americium-241 source, allowing fast neutrons to be produced with a mean neutron energy of 4.2 MeV [8]. A 6 cm-thick layer of microcrystalline paraffin wax was used as a neutron moderator to reduce the fast neutrons to thermal energies of < 1 eV to increase the chances of neutron capture by the bismuth-209 atoms [9], and the thermal neutrons produced were used to irradiate a 10 g sample of bismuth beryllium acetate as shown in the irradiation setup diagram below (Fig. 4).

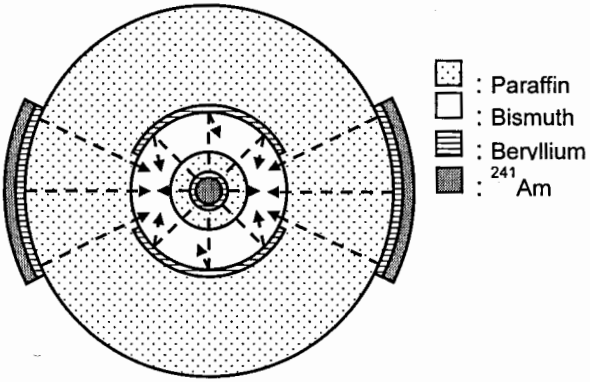

Figure 4: Neutron irradiation setup.

A central mast mounted neutron source with an activity of 60 microcuries is used to irradiate the surrounding bismuth salt radially, and two other plated neutron source with activities of 10 microcuries each irradiating the bismuth salt from outside. Two beryllium reflectors are also placed on the exposed sides of the bismuth salt in order to shield the excess neutron radiation and to increase neutron flux in the bismuth salt. This setup was adopted to maximise neutron capture in the bismuth salt due to the high neutron opacity of the salt itself which would have cause the outer layers to receive very little neutrons.

2.4. Radiation monitoring and analysis

The potentially harmful neutron, alpha, and beta radiation emitted by the reaction mixture were appropriately shielded as per the guidelines highlighted by the US Nuclear Regulatory Commission [10], the International Atomic Energy Agency [11], and the Singapore Radiation Protection Regulations [12]. The entire irradiation setup was housed in a 15 mm-thick polypropylene container containing a 40 mm-thick paraffin wax layer for radiation shielding.

To qualitatively demonstrate that the trend of the increase in radiation levels is characteristic of the proposed chain reaction, the live radiation levels were monitored with a Geiger-Müller counter and compared to the experimental patterns of growth with an expected rate of increase. The alpha radiation levels were taken as directly proportional to the amount of polonium-210 accumulated in the reaction mixture as the sole alpha-emitting radionuclide in the reaction scheme (excluding the initiator neutron source) is polonium-210. The rate of growth of polonium-210 is derived as the gradient of the polonium accumulation graph.

In order to confirm that polonium-210 has indeed been formed, two methods of characterisation were employed in this study – alpha and beta spectroscopy. Firstly, the most direct method of confirming the presence of polonium-210 was to detect its characteristic alpha peak at 5.30 MeV. This was accomplished via the proximity-count method, where the range of alpha particles in air was correlated to their energy by the equation shown below [42]:

$$R = \frac{0.543E - 0.168}{\rho},$$

where R is the range of the alpha particle, E is its energy, and ρ is the density of the medium. This thus presents a graph (Figure 5) that can be used to map their detected range to their energies, thus giving us the alpha spectrum of the reaction after correcting for the divergence of the radiation with the inverse square law.

Beta spectroscopy was used to identify the parent nuclide of polonium-210, which is bismuth-210 with a maximum beta energy of 1.16 MeV. The stopping power of the beta particles emitted can be calculated using the Bethe-Bloch formula, which correlates to the graph shown below (Figure 6) of the range of beta particles in paraffin wax. As beta particles

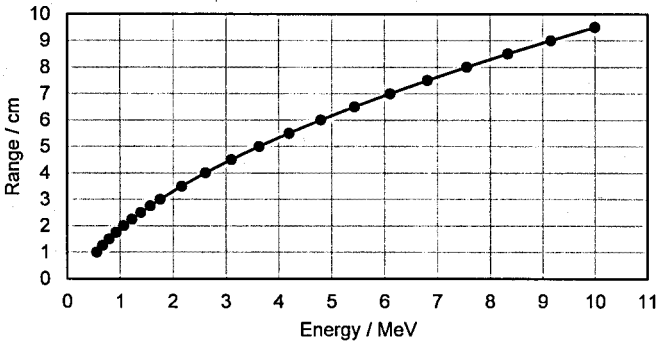

Figure 5: Range of α particles in air.

are emitted over a continuous spectrum unlike alpha particles, there wouldn't be any peak in the beta spectrum of bismuth-210, instead being identified with a drop-off point that correlates to its maximum beta energy at 1.16 MeV.

2.5. Mathematical modelling

In order to quantitatively verify that the chain reaction has indeed occurred, a mathematical model was devised to predict the chain reaction's growth as shown here. Due to the autocatalytic nature of the reaction, the growth of polonium-210 in the reaction mixture is predicted to possess a sigmoidal nature. Its growth mainly depends on 3 factors – the maximum amount of polonium-210 denoted by L, and two variables α and κ which correspond to neutron population growth and the decay ratio of polonium-210 from bismuth-210 respectively. It should also be noted that an upper limit to the amount of polonium is set by the term L in the chain reaction, as the formation of polonium-210 reaches a maximum before the neutron leakage and decay of initially formed polonium-210 causes the net amount of polonium-210 to be balanced by subsequent generations of the chain reaction which forms more polonium-210. (For detailed derivation and formulation, see Appendix 1.)

$$N_2 = L \cdot \frac{\alpha e^{\kappa t}}{1 + \alpha e^{\kappa t}} = \frac{L}{1 + \alpha e^{-\kappa t}},$$

$$L = N_{1(0)} \cdot \delta,$$

$$\alpha = \frac{\phi \sigma \rho A}{M \varepsilon},$$

$$\kappa = \frac{\lambda_1 n}{\lambda_2}.$$

Here N_2 is the number of ^{210}Po atoms at time t; $N_{1(0)}$ is the number of ^{209}Bi atoms present initially; δ is the propagation coefficient; ϕ is the neutron flux of the initial neutron source; σ is the neutron capture cross section of ^{209}Bi; ρ is the density of ^{209}Bi; A is Avogadro's number; M is the molar mass of ^{209}Bi; ε is the neutron multiplication factor; λ_1 is the decay constant of ^{210}Bi; λ_2 is the decay constant of ^{210}Po; n is the neutron conversion coefficient.

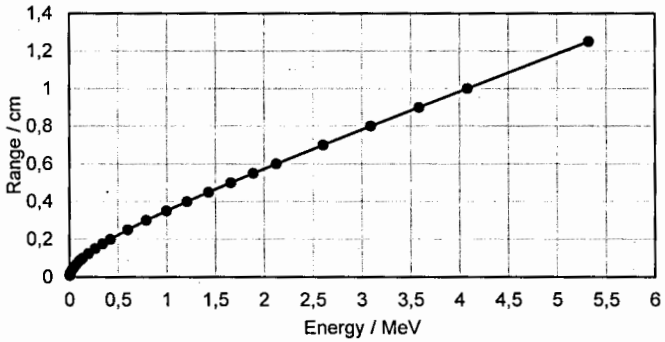

Figure 6: Range of β- particles in paraffin wax.

3. Results and Discussion

3.1. Alpha source characterisation

The alpha spectrum of the mast-mounted and plated americium-241 sources are shown below in Fig. 7 and 8 respectively. The alpha spectrum of the mast-mounted americium-241 source corresponds well to reference literature [17], possessing a characteristic peak at 5.48 MeV. This is indicative of high-purity and thin americium-241 foil being used in the mast-mounted source as a method of ensuring that uniform ionisation of the surrounding medium

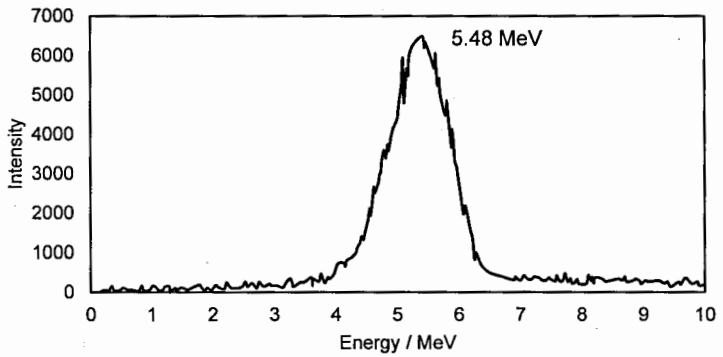

Figure 7: Alpha spectrum of mast-mounted americium-241 source.

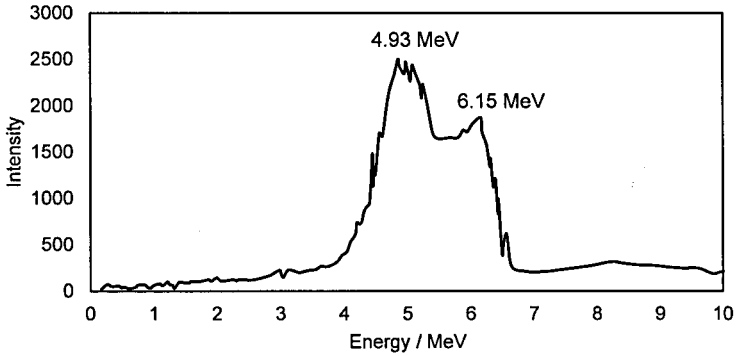

Figure 8: Alpha spectrum of plated americium-241 source.

can be achieved in a small area. Furthermore, the intensity of the alpha spectra obtained from the mast-mounted and plated sources also correspond to the relative activities of the sources (60 and 10 μCi respectively) after factoring in the solid angle of the sources from the detection point. However, the alpha spectrum of the plated americium-241 sources (Fig. 8) showed that peak-splitting was caused by the protective passivation layer on the americium-241 layer on the plates, which were initially designed to ensure that the americium-241would remain plated to the steel backing. This causes two peaks to be observed in the spectrum at 4.93 and 6.15 MeV respectively. 4.93 and 6.15 MeV respectively.

3.2. Neutron source characterisation

Utilising the elastic scattering of protons from paraffin wax under neutron irradiation, the fast neutron spectrum of the AmBe neutron source was characterised by mapping the proton recoil energy of the emitted radiation from the moderated neutron source to the corresponding neutron energy in the medium [19]. This yields the neutron spectrum of the emitted neutrons, which was compared to the ISO-8529 reference spectrum for AmBe sources. As shown in Fig. 9, the neutron spectrum of the AmBe source is in good agreement with the reference neutron spectrum [18], thus being suitable for use in initiating the chain reaction. Furthermore, the paraffin wax moderator also served as a neutron shield to prevent fast neutrons from the central mast-mounted neutron source from escaping the setup.

Accounting for the geometric layout of the irradiation setup [22], the thermal neutron flux in the bismuth salt was found to be $2.37 \cdot 10^2$ n cm^{-2} s^{-1}. The low neutron flux serves a dual purpose – firstly, it prevents excessive interference with the activity of the polonium-210 produced from the chain reaction so as to ensure that the accumulated polonium-210 can be accurately tracked and measured due to the small neutron capture cross section of bismuth-209 which would cause the amount of polonium-210 formed to be highly sensitive. Secondly, it also demonstrates that the chain reaction is able to be initiated even with weak radioisotopic neutron sources, such that high neutron fluxes are no longer required to produce polonium-210, as the chain reaction is able to propagate on its own through the reaction medium, causing the neutron population to increase in a self-sustaining manner. Once the neutron sources had been constructed and assembled with the irradiation setup, the chain reaction itself was initiated.

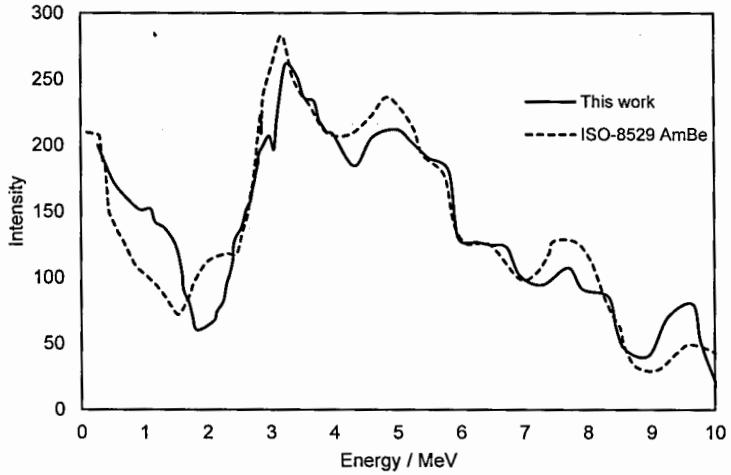

Figure 9: Neutron spectrum of AmBe source.

3.3.Chain reaction propagation

The characterisation of the chain reaction itself is shown in Fig. 10. As shown, the chain reaction does indeed proceed via a sigmoidal nature in the reaction mixture, starting with an initially low activity due to the small neutron capture cross section of bismuth-209 which results in relatively little polonium-210 being formed. This is analogous to the lag period in a conventional chemical autocatalytic reaction. After some time, the polonium concentration increases exponentially as the chain reaction propagates through the reaction mixture, that is the bismuth beryllium acetate, causing the thermal neutron population to increase exponentially. During this phase, as the atoms of bismuth-209 capture neutrons to form bismuth-210, this does not result in a direct emission of alpha particles but rather a decay according to a first-order mechanism to form polonium-210 which then emits alpha particles, hence causing the exponential phase to be longer than a direct neutron activation reaction due to the consumption and production of the bismuth-210 intermediate.

Furthermore, the decay product of polonium-210 which is lead-206 is also able to cause neutron multiplication via the (n,2n) reaction, further accelerating the reaction as more and more polonium atoms decay. Finally, the reaction slows down after about a week as the limit of polonium accumulation is reached. Not all the bismuth would be converted to polonium at the end of the reaction due to leakage of neutrons out of the reaction mixture coupled with the larger elastic scattering cross section of bismuth-209 compared to its small neutron capture cross section which means that some of the neutrons would simply scatter instead of being absorbed by bismuth-209 atoms [20]. This is represented in the reaction equation as the propagation coefficient, which is proportional to the limit of the amount of polonium-210 that can be extracted from the bismuth-209 feedstock material, which is similar to the conversion ratio in nuclear breeder reactors describing the rate of production of plutonium-239 while

accounting for its simultaneous consumption [21]. In a similar pattern, the limit of the amount of polonium-210 able to be produced will also never be equal to the amount of feedstock material due to the decay of the polonium-210 already produced as the chain reaction relies on the alpha particles produced from their decay to be propagated.

Hence, it can be seen from the measurements of the reaction that the chain reaction is indeed being propagated through the bismuth beryllium acetate medium, as evidenced by the rapid sigmoidal increase in activity of the reaction mixture which would otherwise not have occurred if neutron capture by bismuth-209 was the only process taking place.

The rate of growth of polonium-210 can also be derived from the gradient of the polonium accumulation curve, shown in Fig. 11 which shows that it reaches a maximum after 50 hours when the chain reaction is still propagating through the reaction mixture while not being impeded by the limits of the medium. In practical applications, this would be the point

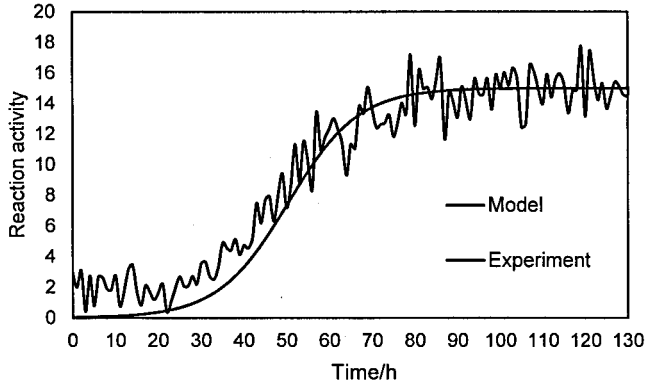

Figure 10: Theoretical vs experimental results.

at which it is the most economical to extract the polonium from the rest of the bismuth salt, as after this point a significant portion of the polonium would have decayed into lead-206 [45, 46]. Furthermore, the rate of growth of polonium-210 in the reaction mixture would also influence the neutron multiplication rate as lead-206 nuclei also possess a relatively large (n,2n) cross section at fast neutron energies. This would result in a positive feedback loop where the increased neutron population causes more nuclei of bismuth-209 to be converted to those of polonium-210, resulting in more lead-206 to be formed upon their decay and further increasing neutron multiplication rates by lead-206. However, this is not observed during normal neutron irradiation of bismuth-209 due to the balance by decreasing the amount of bismuth-209 available to multiply neutrons.

The rate of growth of polonium-210 is also constrained by several factors, most importantly the variable κ which is affected by the decay constants of polonium-210 and bismuth-210, as well as the neutron conversion coefficient. As the decay constants of both nuclides remain unchanged, the neutron conversion coefficient, i.e. the fraction of neutrons from a generation of the chain reaction that get captured by bismuth atoms from subsequent generations, would be the main influencing factor in determining how fast polonium-210 accumulates up to the limit L.

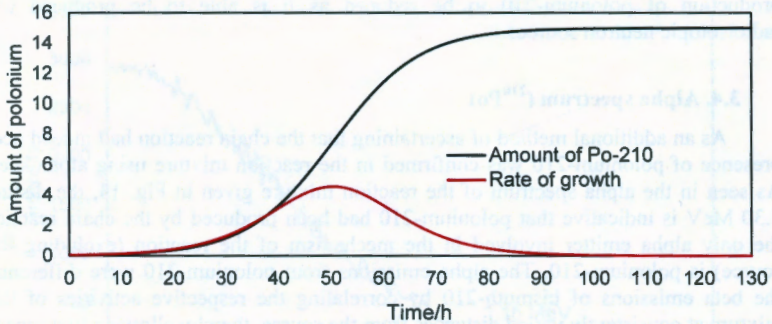

Figure 11: Rate of growth of polonium-210.

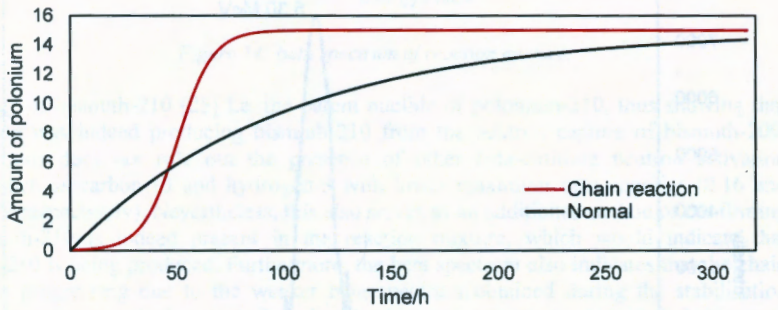

Figure 12: Growth of polonium-210 under chain reaction and normal conditions.

The polonium accumulation curve of the chain reaction was also compared to that of a normal irradiation scenario shown in Fig. 12, which shows that conventional irradiation methods allow for a greater initial rate of growth of polonium due to the larger number of bismuth atoms exposed to the neutron radiation closer to the neutron source without the interference of other atoms [43, 44], which is not the case in the chain reaction due to some neutrons being absorbed by auxiliary atoms, e.g. hydrogen and beryllium atoms. However, the chain reaction quickly surpasses it because of the rapid and exponential propagation of the polonium conversion reaction throughout the reaction medium due to the polonium-210 atoms formed in one generation acting as the "source" for the next, thus causing a cáscade reaction in the medium which is faster than the capture of individual neutrons by bismuth-209 atoms.

Furthermore, the production of polonium-210 is also influenced by the penetration of neutrons through the reaction medium, e.g. bismuth metal or salt, and thus the chain reaction would also produce polonium-210 at a faster rate as the neutrons produced in the chain reaction would be able to saturate the reaction mixture faster as compared to the mixture being irradiated by a point source [47, 48]. Hence, this chain reaction would allow for more polonium-210 to be produced at a faster rate after an initial lag period as compared to a normal irradiation route, which would allow dependence on high-flux nuclear reactors for the

production of polonium-210 to be reduced as it is able to be produced using weak radioisotopic neutron sources.

3.4. Alpha spectrum (^{210}Po)

As an additional method of ascertaining that the chain reaction had indeed occurred, the presence of polonium-210 was confirmed in the reaction mixture using alpha spectroscopy. As seen in the alpha spectrum of the reaction mixture given in Fig. 13, the distinct peak at 5.30 MeV is indicative that polonium-210 had been produced by the chain reaction [24], as the only alpha emitter involved in the mechanism of the reaction (excluding the initiator source) is polonium-210. The alpha emissions from polonium-210 were differentiated from the beta emissions of bismuth-210 by correlating the respective activities of the reaction mixture at consistently varied distances from the source, thereby allowing two separate graphs to be obtained.

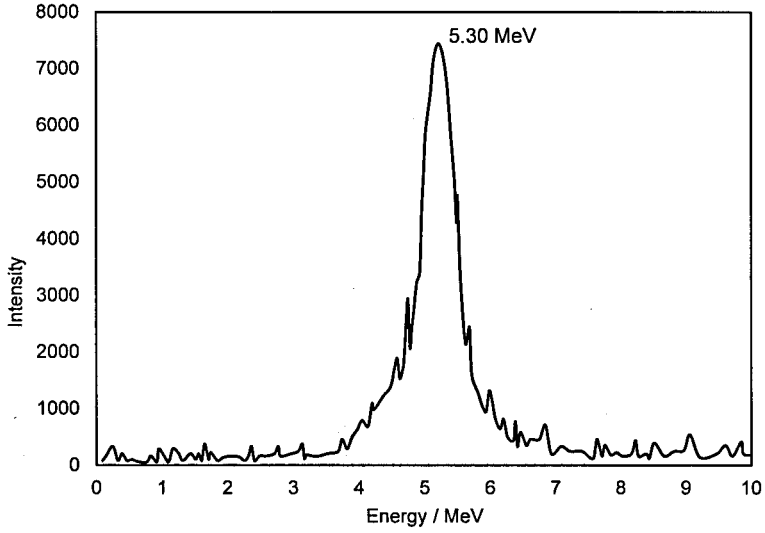

Figure 13: Alpha spectrum of reaction mixture.

Additionally, it was also seen that the alpha peak of the reaction mixture was considerably broader than expected due to the slowing down of alpha particles from scattering effects of the beryllium and hydrogen atoms [49, 50], which would have caused a large range of energies to be detected. Hence, purification of the polonium-210 produced from the reaction would aid in more accurate alpha spectroscopy measurements.

3.5. Beta spectrum (^{210}Bi)

The beta spectrum of the reaction mixture is also shown below. The beta spectrum graph in Fig. 14 shows a maximum energy of 1.16 MeV, which corresponds to the maximum

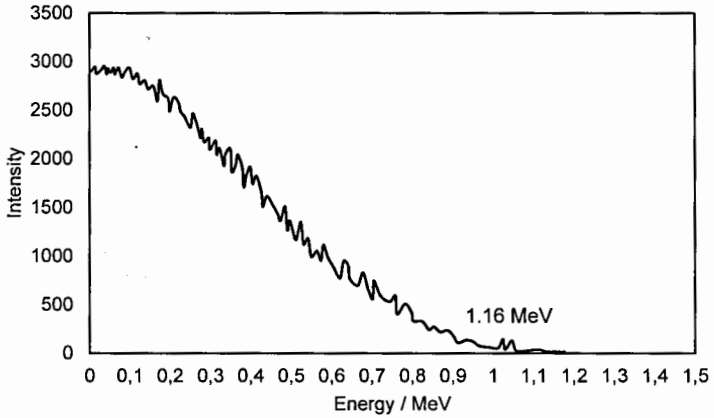

Figure 14: Beta spectrum of reaction mixture.

beta energy of bismuth-210 [25] i.e. the parent nuclide of polonium-210, thus showing that the reaction was indeed producing bismuth-210 from the neutron capture of bismuth-209. However, this does not rule out the presence of other beta-emitting neutron activation products such as carbon-13 and hydrogen-3 with lower maximum beta energies (0.16 and 0.018 MeV respectively). Nevertheless, this also serves as an additional method of confirming that bismuth-210 is indeed present in the reaction mixture, which would indicate that polonium-210 is being produced. Furthermore, the beta spectrum also indicates that the chain reaction is progressing due to the weaker beta spectrum obtained during the stabilisation period of the reaction, which was attributed to the decreasing amounts of bismuth-210 present due to its relatively short half-life compared to polonium-210, as well as a significant portion of the bismuth-210 having decayed to polonium-210.

4. Conclusions

Self-sustaining neutron multiplication has thus been proven to be achieved in a medium of bismuth beryllium acetate, producing the industrially and politically significant radionuclide polonium-210 in substantial quantities as a byproduct of the reaction. This chain reaction, which proceeds via a mechanism involving alternating (α, n) and alpha decay reactions, was confirmed and validated via the monitoring of the activity levels of the reaction mixture, as well as via characterisation of the alpha particle energies emitted from the mixture that were correlated to the alpha emission spectra of polonium-210 and the beta spectrum of the parent nuclide bismuth-210. The activity levels of the reaction mixture were shown to agree with a mathematical model of the chain reaction, notably demonstrating a sigmoidal alpha activity which was ascribed to the increasing quantities of polonium-210 produced.

This previously-unreported reaction also offers a relatively inexpensive and rapid method of producing polonium-210 in appreciable quantities, as highlighted by the alpha-emission characterisation of the reaction. Furthermore, purification of the polonium-210 produced is fairly straightforward and high-yielding, due to the crystalline nature of the

reagents involved that would allow for direct reduction of the salt, as opposed to conventional purification methods of polonium that require separation of the raw metal product from bismuth metal feedstock.

5. Future Work

Due to the strategic importance of the radionuclide polonium-210, e.g. in the nuclear weapon complex, political operations, satellite power generators, radiotherapy etc, this chain reaction would have many industrial applications. For example, the scalability of the reaction could be further researched in order to produce polonium-210 on an industrial level, which would alleviate the current scarcity of polonium as only 100 grams of it are produced annually [14]. This reaction could also be exploited to construct more efficient radioisotopic thermoelectric generators (RTGs) for use on board satellites [23], as the short half-life of polonium-210 ($T_{1/2}$ = 138 days) which hinders its incorporation into RTGs for long journeys would be resolved by the continuous generation of polonium from the bismuth salt feedstock, allowing the polonium to be replenished.

References

1. Becker, H., & Bothe, W. (1932). Die in Bor und Beryllium erregten ?-Strahlen. The European Physical Journal A, 76(7–8), 421–438. https://doi.org/10.1007/bf01336726
2. The Production of Neutrons by Bombardment of Beryllium with α -Particles on JSTOR. (n.d.). https://www.jstor.org/stable/97090
3. Richmond, J.L. (1954). Neutron, alpha, and special sources from polonium. https://doi.org/10.2172/934663
4. Reed, B.C. (2019). Rousing the dragon: Polonium production for neutron generators in the Manhattan Project. American Journal of Physics. https://doi.org/10.1119/1.5094138
5. Littler, D.J., & Lockett, E. (1953). The Pile Neutron Absorption Cross Sections of Bismuth. Proceedings of the Physical Society, 66(8), 700–704. https://doi.org/10.1088/0370-1298/66/8/303
6. Ádám, A., Hraskó, P., Pálla, G., & Quittner, P. (1963). The mechanism of the (n, 2n) reaction. Nuclear Physics. https://doi.org/10.1016/0029-5582(63)90112-3
7. Vlaskin, G.N., Khomyakov, Y.S., & Bulanenko, V.I. (2015). Neutron Yield of the Reaction (α,n) on Thick Targets Comprised of Light Elements. Atomic Energy, 117(5), 357–365. https://doi.org/10.1007/s10512-015-9933-5
8. Barbagallo, D., Bolduc, B., Hassett, B., Johnson, W.W., Koumba, K., Leeming, A., Mach, P., McCormack, J., McDonough, M.M., & Nyamwanda, J. (2020). Neutron Attenuation in Polyethylene Using an AmBe Source. Journal of Undergraduate Reports in Physics, 30(1), 100001. https://doi.org/10.1063/10.0002041
9. Waheed, A., Ali, N., Baloch, M.A., Qureshi, A.A., Munem, E.A., Rajput, M.A., Jamal, T., & Muhammad, W. (2017). Optimization of moderator assembly for neutron flux measurement: experimental and theoretical approaches. Nuclear Science and Techniques, 28(5). https://doi.org/10.1007/s41365-017-0213-z
10. U.S. Nuclear Regulatory Commission. (2011, July 5). Shielding Radiation: Alphas, Betas, Gammas, and Neutrons. https://www.nrc.gov/docs/ML1122/ML11229A721.pdf
11. *IAEA Publications*. (n.d.). https://www-pub.iaea.org/mtcd/publications/
12. *Radiation Protection (Ionising Radiation) Regulations 2023 - Singapore Statutes Online*. (2023, February 20). https://sso.agc.gov.sg/SL/RPA2007-S85-2023
13. Secondary Gamma Rays Excited by the Passage of Neutrons through Matter on JSTOR. (n.d.). https://www.jstor.org/stable/96255

14. Finn, P. (2008, February 18). Most Polonium Made Near the Volga River. The Moscow Times. https://www.themoscowtimes.com/archive/most-polonium-made-near-the-volga-river
15. Chart of the Nuclides 2014. (n.d.-b). https://wwwndc.jaea.go.jp/CN14/index.html
16. Collie, C.H., Meads, R., & Lockett, E. (1956). The Capture Cross Section of Neutrons by Boron. Proceedings of the Physical Society. https://doi.org/10.1088/0370-1298/69/6/305
17. Asaro, F., Reynolds, F.L., & Perlman, I. (1952). The Complex Alpha-Spectra of ^{241}Am and ^{242}Cm. Physical Review, 87(2), 277–285. https://doi.org/10.1103/physrev.87.277
18. Thomas, D., Bedogni, R., Méndez, R., Thompson, A.J., & Zimbal, A. (2018). REVISION OF ISO 8529—REFERENCE NEUTRON RADIATIONS. Radiation Protection Dosimetry, 180(1–4), 21–24. https://doi.org/10.1093/rpd/ncx176
19. Émission de protons de grande vitesse par la substances hydrogénées sous l'influence des rayons gamma très pénétrants. (+) Effet d'absorption de rayons gamma de très haute fréquence par projection de noyaux légers. (+) Projections d'atomes par rayo. - Herman H.J. Lynge & Søn A/S. (n.d.). https://www.lynge.com/en/physics/49447-emission-de-protons-de-grande-vitesse-par-la-substances-hydrogenees-sous-linfluence-des-rayons-gamma-tres-penetrants-effet-dabsorption-de-rayon
20. Mandeville, C.E., & Swann, C.P. (1951). The Scattering of Fast Neutrons by Bismuth and Lead. Physical Review, 84(2), 214–217. https://doi.org/10.1103/physrev.84.214
21. Nailatussaadah, Prastyo, P.A., Waris, A., Kurniadi, R., & Pramuditya, S. (2017). Preliminary Study of Plutonium Utilization in AP1000 Reactor. Journal of Physics. https://doi.org/10.1088/1742-6596/877/1/012003
22. J. Voigt. (2012). Neutron Sources. https://juser.fz-juelich.de/record/127645/files/02_Neutron_Sources.pdf
23. Hagis, W., & Dix, G.R. (1960). FINAL SAFETY ANALYSIS REPORT. SNAP III THERMOELECTRIC GENERATOR. https://doi.org/10.2172/4110813
24. Porres, M.L., Collado, G.M., Díaz, I., Rentería, M., & Cabrera, M.M. (2012). Determination of uranium and polonium in Sparus aurata by alpha spectrometry. Revista Mexicana De Fisica, 58(3), 224–227. http://scielo.unam.mx/pdf//rmf/v58n3/v58n3a11.pdf
25. I.E. Alekseev, & S.V. Bakhlanov. (2021). Precision Measurement of Bi-210 β Spectrum. arXiv. https://arxiv.org/pdf/2005.08481.pdf
26. Stewart, L. (1955). Neutron Spectrum and Absolute Yield of a Plutonium-Beryllium Source. Physical Review, 98(3), 740–743. https://doi.org/10.1103/physrev.98.740
27. Söderström, P.A., Matei, C., Capponi, L., Açıksöz, E., Balabanski, D.L., & Mitu, I.O. (2021). Characterization of a plutonium–beryllium neutron source. Applied Radiation and Isotopes, 167, 109441. https://doi.org/10.1016/j.apradiso.2020.109441
28. Breen, R., & Hertz. (1955). Gamma Radiation from Polonium Neutron Sources. Physical Review, 98(3), 599–604. https://doi.org/10.1103/physrev.98.599
29. Spinks, J.W.T., & Graham, G.A.R. (1950). PREPARATION AND CHARACTERISTICS OF A POLONIUM–BERYLLIUM NEUTRON SOURCE. Canadian Journal of Research, 28a(1), 60–66. https://doi.org/10.1139/cjr50a-005
30. Karraker, D.G., Ghiorso, A., & Templeton, D.H. (1951). Alpha-Decay Energies of Polonium Isotopes. Physical Review, 83(2), 390–393. https://doi.org/10.1103/physrev.83.390
31. Hamilton, T.F., & Smith, J.G. (1986). Improved alpha energy resolution for the determination of polonium isotopes by alpha-spectrometry. International Journal of Radiation Applications and Instrumentation. Part a. Applied Radiation and Isotopes, 37(7), 628–630. https://doi.org/10.1016/0883-2889(86)90084-5
32. Thomas, L. (2017). Polonium in the Playhouse: The Manhattan Project's Secret Chemistry Work in Dayton, Ohio. https://www.amazon.com/Polonium-Playhouse-Manhattan-Projects-Chemistry/dp/0814213383

33. Lajn, B. (2005). Polonium-210 alpha-radiotherapy of prostate cancer aimed on angiogenesis. https://inis.iaea.org/search/search.aspx?orig_q=RN:37060488
34. O'Brien, R.L., Ambrosi, R.M., Bannister, N., Howe, S.D., & Atkinson, H.V. (2008). Safe radioisotope thermoelectric generators and heat sources for space applications. Journal of Nuclear Materials, 377(3), 506–521. https://doi.org/10.1016/j.jnucmat.2008.04.009
35. Nuclespot Alpha Ionizer. (n.d.). Amstat Industries. https://amstat.com/esd-ionizer/nuclespot-alpha-ionizer/
36. Hanopolskyi, A.I., Smaliak, V.A., Novichkov, A.I., & Semenov, S. (2021). Autocatalysis: Kinetics, Mechanisms and Design. ChemSystemsChem, 3(1). https://doi.org/10.1002/syst.202000026
37. Mata-Perez, F., & Perez-Benito, J.F. (1987). The kinetic rate law for autocatalytic reactions. Journal of Chemical Education, 64(11), 925. https://doi.org/10.1021/ed064p925
38. Sutton, R., McDaniel, B.D., Anderson, E.E., & Lavatell, L.S. (1947). The Capture Cross Section of Boron for Neutrons of Energies from 0.01 ev to 1000 ev. Physical Review, 71(4), 272. https://doi.org/10.1103/physrev.71.272
39. Marion, J., Levin, J.S., & Cranberg, L. (1959). Elastic and Nonelastic Neutron Cross Sections for Beryllium. Physical Review, 114(6), 1584–1589. https://doi.org/10.1103/physrev.114.1584
40. Tsujimoto, K., Sasa, T., Nishihara, K., Oigawa, H., & Takano, H. (2004). Neutronics Design for Lead-Bismuth Cooled Accelerator-Driven System for Transmutation of Minor Actinide. Journal of Nuclear Science and Technology, 41(1), 21–36. https://doi.org/10.1080/18811248.2004.9715454
41. Chen, Y., Chen, G., Liu, R., Guo, H., Chen, W., Jiang, W., & Shen, J. (1991). Experiments of Neutron Multiplication in Beryllium. Fusion Technology, 19(3P2B), 1919–1924. https://doi.org/10.13182/fst91-a29622
42. Poston, J.W. (2003). Dosimetry. In Elsevier eBooks (pp. 603–650). https://doi.org/10.1016/b0-12-227410-5/00185-x
43. Obara, T., Miura, T., & Sekimoto, H. (2005). Fundamental study of polonium contamination by neutron irradiated lead–bismuth eutectic. Journal of Nuclear Materials, 343(1–3), 297–301. https://doi.org/10.1016/j.jnucmat.2004.08.035
44. Miura, T., Obara, T., & Sekimoto, H. (2004). Unfolding of polonium distribution in depth of irradiated lead–bismuth eutectic from α-particle pulse-height distribution. Applied Radiation and Isotopes. https://doi.org/10.1016/j.apradiso.2004.02.023
45. Miura, T., Obara, T., & Sekimoto, H. (2004a). Characteristics of Polonium Contamination From Neutron Irradiated Lead-Bismuth Eutectic. In 12th International Conference on Nuclear Engineering, Volume 1. https://doi.org/10.1115/icone12-49153
46. Bagnall, K.W. (1957). The chemistry of polonium. Quarterly Reviews, Chemical Society, 11(1), 30. https://doi.org/10.1039/qr9571100030
47. Reed, B.C. (2019b). Rousing the dragon: Polonium production for neutron generators in the Manhattan Project. American Journal of Physics. https://doi.org/10.1119/1.5094138
48. Artun, O. (2020). Production of Polonium-208, 209 and 210 for use in nuclear battery via particle accelerator. Applied Physics A. https://doi.org/10.1007/s00339-020-03557-8
49. Pommé, S. (2015). Typical uncertainties in alpha-particle spectrometry. Metrologia, 52(3), S146–S155. https://doi.org/10.1088/0026-1394/52/3/s146
50. Shi, R., Tuo, X., Yang, J., Cheng, Y., Zheng, H., Qibiao, W., & Deng, C. (2019). A peak shape model with high-energy tailing for high-resolution alpha-particle spectra. The European Physical Journal A, 55(8). https://doi.org/10.1140/epja/i2019-12827-x

Definition of Thermophysical Parameters of the IVG.1M Reactor Core with LEU Fuel

Irina V. Prozorova, Yekaterina A. Martynenko, Ruslan A. Irkimbekov, Yuri A. Popov, Artur S. Surayev, Vyachislav S. Gnyrya, Radmila R. Sabitova, Berik S. Medetbekov

Institute of Atomic Energy, National Nuclear Center of the Republic of Kazakhstan, Kurchatov, Kazakhstan

E-mail: Prozorova@nnc.kz

At present, as part of the international program aimed at reducing fuel enrichment in research reactors, the National Nuclear Center of the Republic of Kazakhstan has successfully completed the conversion project for the IVG.1M research reactor. The conversion of the reactor is necessary to contribute to the global efforts of reducing the use of highly enriched uranium fuel, which has the potential for nuclear weapons proliferation. During the conversion, the reactor core was equipped with water-cooled technological channels with innovative metallic fuel using fiber technology. During a series of power startups, the initial experimental data were obtained. The paper examines the thermophysical characteristics of the reactor core before and after the conversion by using both experimental data and computer simulation methods.

The objective of these studies was to investigate the thermophysical effects resulting from the conversion of the IVG.1M reactor to low enrichment fuel, and to determine the thermophysical operating conditions of the converted core.

Introduction

Most research reactors in the world were built in the middle of the 20th century using highly enriched uranium fuel (HEU), which contains up to 90% U-235. HEU fuel enables the development of compact cores with high neutron fluxes, offering versatility in various applications. However, its current usage is considered unsafe due to the potential for nuclear weapons proliferation. In 2010, the National Nuclear Center of the Republic of Kazakhstan initiated the conversion of the IVG.1M research reactor to low-enriched uranium fuel (LEU) as part of the international program aimed at reducing fuel enrichment in research reactors. [1].

The IVG1.M reactor was developed in the late 1980s as an adaptation of the IVG.1 gas-cooled reactor. It involved the incorporation of water-cooled technological channels (WCTC-HEU) and enhancements to the water supply system for reactor and channels cooling. The fuel rods in the WCTC-HEU were consisted of uranium-zirconium alloy with a uranium content ranging from 2% to 4% by weight, enriched to 90% for the U-235 isotope. The reactor successfully operated until 2020 [2].

The IVG.1M research reactor is a heterogeneous thermal nuclear reactor with a light water coolant and moderator, and a beryllium neutron reflector.

The reactor is cooled by a forced circulation system using a single-loop scheme without any heat exchange equipment. The cooling loop incorporates a drain tank with a volume of 1500 m3, which serves as a thermal accumulator. In accordance with its design, the water system includes the main cooling loop and the reactor's emergency cooling system.

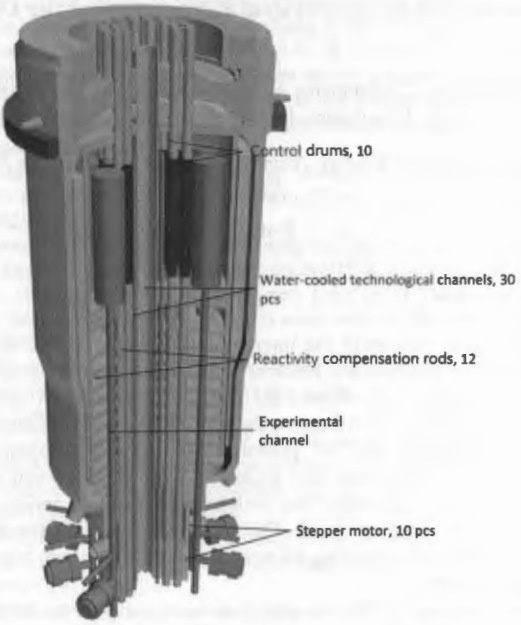

Figure 1. Scheme of the IVG.1M reactor.

When the reactor operates at a nominal power level of up to 10 MW, three 4MSK-10 pumps are utilized. The pumps are started before the power rises to the nominal level. During nominal operation, water is drawn from the drain tank and supplied to the distribution manifold by the three pumps. From there, the water follows four separate paths to provide cooling to the loop channel, a reactor head, a side reflector and the central channel with the core. Subsequently, the water is drained from the reactor through drain pipes and collected into the drain tank.

The reactor core is comprised of 30 WCTC with fuel assemblies (FA). WCTC are located in three rows: the first and second rows consist of 12 channels with 800 mm height, while the third row consists of 18 channels with FA height of 600 mm.

The designed thermal power of the IVG.1M research reactor, including the power of the fuel assemblies being tested in the reactor, is 60 MW. However, due to the incomplete implementation of the reactor cooling system modernization as outlined in the IVG.1M modernization project, the nominal power of the reactor is limited to 10 MW, which is achieved during the power startup phase.

During the conversion of the reactor from HEU to LEU, the aim was not only to preserve, but also improve the operational characteristics of the reactor core. Through computational and theoretical analysis, an optimal arrangement of the core was chosen without making changes to the design of the core elements, but only modifying the composition of the fuel assemblies. The LEU fuel elements are unique and consist of a composition of zirconium alloy E110 with uranium filaments distributed uniformly over the

cross section and a zirconium shell. The enrichment level of U-235 is 19.75%. Figure 2 shows the LEU fuel rod cross-section, and Figure 3 shows a general view of the set of rods.

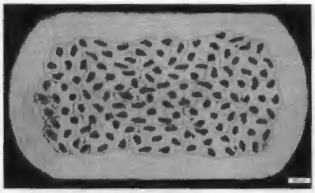

Figure 2. LEU fuel rod cross section.

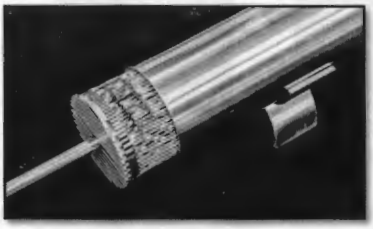

Figure 3. General view of the fuel assembly.

At the beginning of 2023, work on the conversion of the reactor core was completed in full, the reactor was put into operation, and a series of power start-ups were also carried out. The data obtained in a series of start-ups using modern computational methods make it possible to determine the thermophysical characteristics of the conversion core.

Research methodology

During a standard power start-up, thermotechnical parameters are measured and recorded, enabling the determination of the thermophysical characteristics of the IVG.1M reactor core with LEU fuel.

To calculate the power generated in each channel during the experiments, the water flow rates in each of the WCTC-LEU, along with the water temperature at the core inlet and the water temperature at the outlet of each channel, were taken into account.

The power released in one WCTC-LEU was determined using the following formula [3]:

$$N_i = [Q_i \cdot Cp \cdot (T_{out} - T_{in})]/1000000, \quad (1)$$

where N_i – power, allocated in the i-th channel, MW;

Q_i – water flow through the i-th channel, kg/s;

C_p – specific heat capacity of water at average temperature in the channel, J/(kg·°C);

T_{in} – reactor inlet water temperature, °C;

T_{out} – outlet water temperature WCTC-LEU, °C.

Since the registration data do not allow determining the temperature distribution of water and structural elements along the length of the fuel assemblies, computer simulation methods are used for this purpose. The calculation model used in the study is shown in Figure 4. The ANSYS Fluent software package was used for the calculation [4].

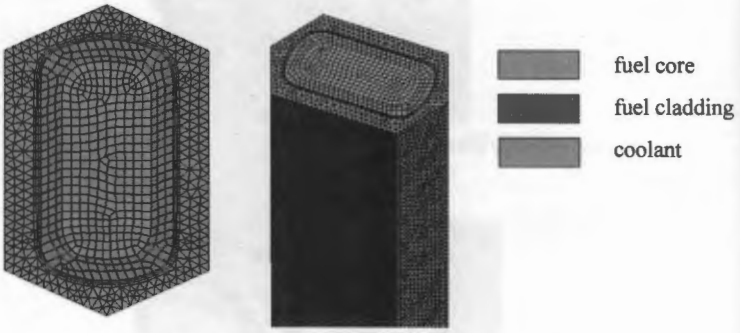

Figure 4. Calculation model.

During the thermophysical calculation, the following boundary conditions were set:

- a symmetry condition is imposed on the side faces of the model;
- for the coolant flow conditions, the flow velocity at the inlet (velocity inlet) and the flow exit (outflow) are used;
- the pressure in the cooling path is assumed to be 1 MPa;
- to account for the uneven energy release along the height of the fuel assembly, a text file with a profile was used to specify the energy release distribution.

The calculated thermophysical model was verified according to the results of experiments, the deviation between the calculated and experimental data is no more than 4°C. For the calculation, the properties of materials are taken from the reference literature [5, 6] and defined as a functional dependence on temperature. The energy release values used in the calculation were taken from the neutron-physical calculation.

During the reactor physical start-up in 2022, experiments were carried out to determine the energy release distribution in fuel assemblies of the 1st, 2nd and 3rd row of WCTC using physical mock-up [7].

Results

From October 2022 to February 2023, a series of nine power start-ups were conducted on the reactor with power ranging from 0.1 to 10 MW. The thermal engineering values obtained during the start-ups were used to determine the thermophysical characteristics of the reactor. The maximum nominal power level achieved during the power start-ups of the IVG.1M reactor was 10.22 MW.

The main parameters of the reactor cooling system obtained during the implementation of power start-ups are presented in table 1.

Table 1. Values of the main parameters of the reactor cooling system

Parameter name	Minimum value	Maximum value
Thermal power of stationary reactor modes, MW	0.01	10.22
Water consumption in the loop channel, kg/s	0.94	1.27
Water consumption through the lid, kg/s	4.7	6.9
Water consumption through the side reflector, kg/s	18.2	20.1
Total water consumption through WCTC kg/s	57.1	59.7
Water consumption at the drain from thermal screens, kg/s	0.55	0.62
Water pressure in the pressure manifold, MPa	1.07	1.12
Water pressure at the outlet from the reactor, MPa	0.91	0.97
Water temperature at the reactor inlet, °C	16.6	26.9
Water temperature under the reactor cover, °C	16.7	32.0
Water temperature at the outlet of the reactor, °C	19.6	68.4

The figure 5 illustrates a diagram of a typical power start-up, where two levels of stationary power of 6 and 10 MW were implemented. In addition, the diagram provides information regarding the water temperature at the core's inlet and outlet, as well as the total water flow through the WCTC-LEU.

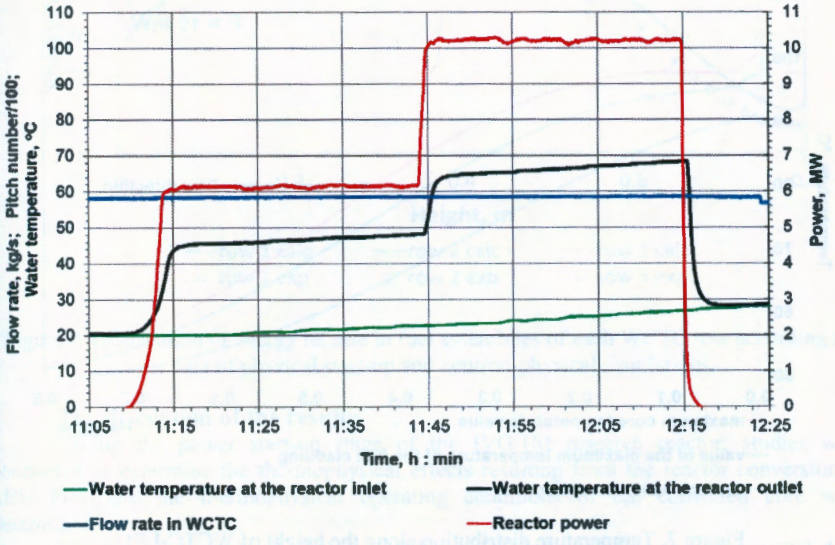

Figure 5. Reactor start-up diagram.

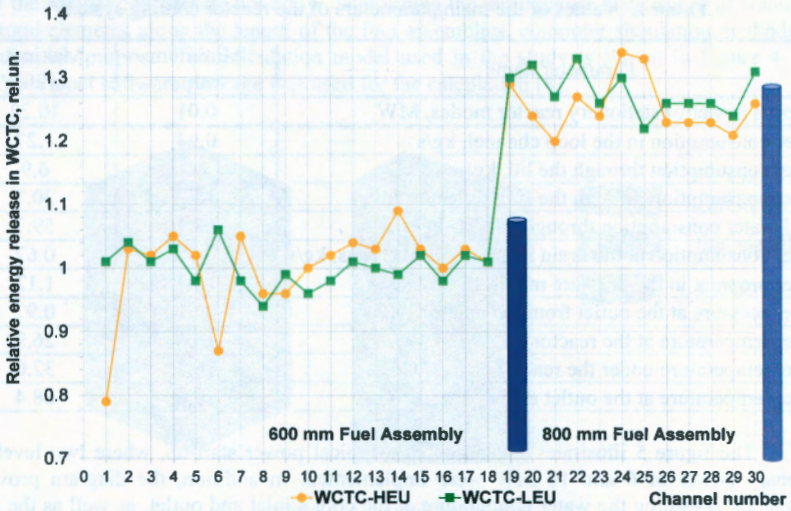

Figure 6. Distribution of relative energy release in the channels of the reactor core.

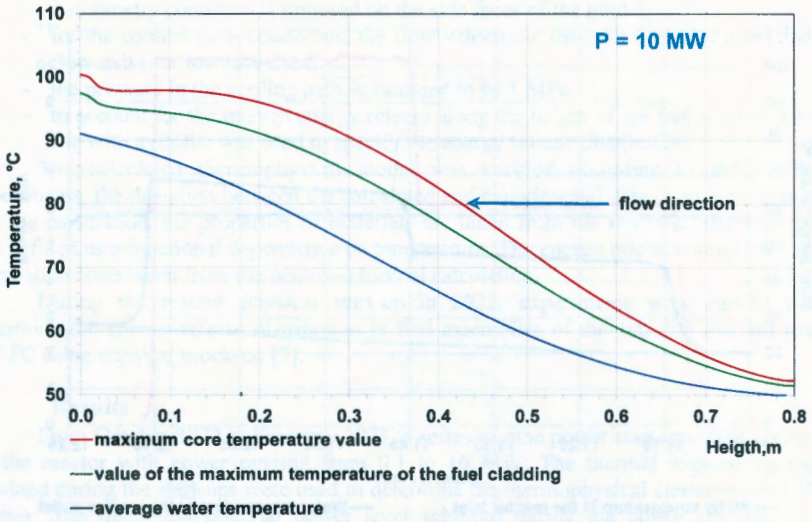

Figure 7. Temperature distribution along the height of WCTC-LEU.

Based on the average thermal power values of WCTC-LEU obtained during a series of start-ups, the relative energy release distribution in the channels was determined. The relative energy release was obtained by normalizing the power value of each WCTC-LEU to the

arithmetic mean power value of the channels located in the third row of the reactor core. Figure 6 shows a distribution diagram of the relative energy release in 30 WCTC. For comparison, the diagram also includes the relative energy release values obtained from the results of the reactor start-ups in 2017, when the core was equipped with WCTC-HEU.

Figure 7 shows the calculated temperature distribution along the fuel assembly height for the first row of WCTC, obtained through computer simulation at a reactor power of 10 MW. The water temperature at the inlet to the reactor is assumed to be 50°C, which corresponds to the maximum allowable temperature of the coolant at the inlet to the cooling path according to the passport data of WCTC-LEU.

Figure 8 presents the obtained distribution of energy release along the fuel assembly height in comparison with preliminary neutron-physical calculations performed using MCNP5 and a full-scale model of the IVG.1M reactor with LEU fuel [4].The energy release of the fuel assembly in the third WCTC row is lower compared to the other, due to its shorter length and further position from the reactor core center.

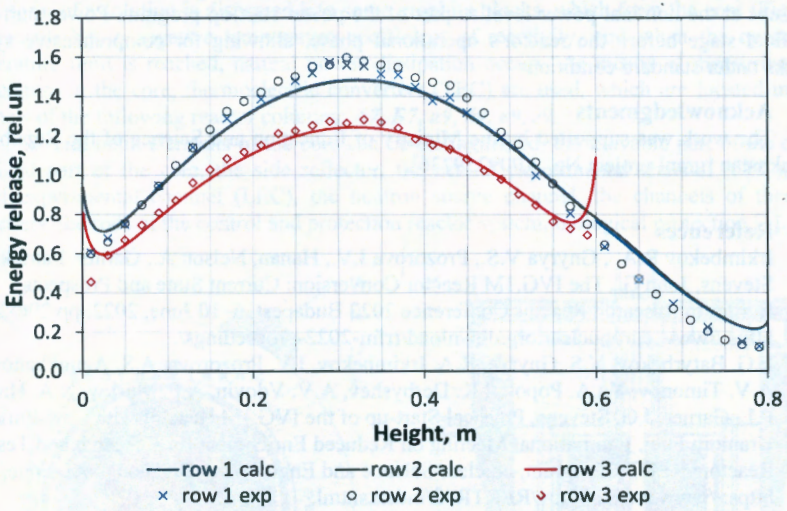

Figure 8. Distribution of energy release in fuel assemblies of each WCTC row according to the data of physical start-up and neutron-physical simulations.

The discussion of the results

During the power start-up stage of the IVG.1M research reactor, studies were conducted to determine the thermophysical effects resulting from the reactor conversion to LEU fuel, and the thermophysical operating conditions of the converted core were determined.

The thermophysical calculation model was verified according to experimental data, and the deviation between the calculated and experimental results was found to be within 4°C.

Based on the average values of the thermal power of WCTC-LEU obtained in a series of start-ups, the relative energy release distribution was determined. An analysis of the

distribution of the relative energy release in the channels of the reactor core shows that after the conversion, the energy release in the third row channels became more uniform.

Based on the analysis of the energy release distribution curves obtained from the physical start-up and the neutronic calculations, it can be concluded that the difference between the calculated and experimental data for LEU fuel lies within the measurement error, which indicates the reliability of the neutronic calculation model.

The analysis of the thermophysical parameters of the coolant recorded during the power start-ups, as well as the data obtained through calculation methods, has confirmed that the thermotechnical parameters of the WCTC-LEU during the start-ups corresponded to the values expected for the normal operation of the reactor.

Conclusion

Based on the results of the study, it can be concluded that the conversion of the IVG.1M reactor to LEU fuel successfully preserved the key functional characteristics of the reactor core. The operability of the LEU reactor core was confirmed through a series of reactor power start-ups at the nominal power level as part of the power start-up program. Power start-up is the final stage before the reactor's operational phase, allowing for comprehensive system checks under standard conditions

Acknowledgments

The work was supported by the Ministry of Education and Science of the Republic of Kazakhstan [grant project No. AP09259736].

References

1. Irkimbekov R.A. , Gnyrya V.S., Prozorova I.V., Hanan, Nelson A., Garner, Patrick L., Stevens, John G. The IVG.1M Reactor Conversion: Current State and Prospects. European Research Reactor Conference 2022 Budapest, 6–10 June, 2022, pp 296-299, https://www.euronuclear.org/download/rrfm-2022-proceedings/.
2. E.G. Batyrbekov, V.S. Gnyrya, R.A. Irkimbekov, I.V. Prozorova, A.S. Azimkhanov, A.V. Timonov, Yu.A. Popov, I.K. Derbyshev, A.V. Vdovin, A.P. Maslov N.A. Hanan, P.L. Garner, J.G. Stevens, Physical Start-up of the IVG.1M Reactor with Low-Enriched Uranium Fuel. International Meeting on Reduced Enrichment for Research and Test Reactors RERTR Program, Nuclear Science and Engineering Division at Argonne, https://www.rertr.anl.gov/RERTR42/index.shtml.
3. Mikheev M.A., Mikheeva I.M., "Fundamentals of heat transfer", M.: Energy, 1977.
4. ANSYS release 2021 R2. Documentation for ANSYS Workbench: ANSYS Inc. – 2021.
5. Rivkin S.L., Aleksandrov A.A. Thermodynamic properties of water and water vapor: a handbook. M: Energoatomizdat, 1984, 84 p.
6. Thermophysical Properties of Materials for Nuclear Engineering: A Tutorial and Collection of Data / International Atomic Energy Agency – Vienna, 2008.
7. R.R. Sabitova, I.V. Prozorova, R.A. Irkimbekov, Yu.A. Popov, S.V. Bedenko, A.A. Prozorov, A.K. Mukhamediyev (2022), Methods to Study Power Density Distribution in the IVG.1M Research Reactor after Conversion, Applied Radiation and Isotopes, Vol. 185, 2022, 110259, https://doi.org/10.1016/j.apradiso.2022.110259.
8. Irkimbekov R.A., Zhagiparova L.K., Kotov V.M., Vurim A.D., Gnyrya V.S. (2019) Neutronics Model of the IVG.1M Reactor: Development and Critical-State Verification. Atomic Energy – Vol. 127.– Issue 2.– P. 69–76., https://doi.org/10.1007/s10512-019-00587-1.

Thermal Model of the IGR Research Reactor

Surayev A.S., Vityuk V.A., Vityuk G.A., Irkimbekov R.A., Zhanbolatov O.M.

National Nuclear Center of the Republic of Kazakhstan, Kurchatov, Kazakhstan

E-mail: suraev@nnc.kz

1. Introduction

The pulsed graphite reactor (IGR) is one of the research nuclear reactors of the National Nuclear Center of the Republic of Kazakhstan. The active zone of the IGR is a graphite stack surrounded by protective housings. The stack consists of columns assembled from graphite blocks and graphite bushings. The cavities between the columns are filled with helium. Unlike most nuclear reactors, this one does not have fuel elements, and uranium fuel in the form of a solution is dispersed into some graphite blocks, which form the core (Fig. 1). The reactor has a negative temperature coefficient of reactivity, and when the operating temperature limit is reached, natural power dissipation occurs. As means of measuring the temperature in the core, thermoelectric converters (TEC) are used, which are located in the channels of the following reactor columns: ***А7, Б7, а9, б9, в9, г9***.

Several main elements of the core can be distinguished: the movable part of the core, the fixed part of the core, the side reflector, the central experimental channel (CEC), the lateral experimental channel (LEC), the neutron source channel, the channels of thermal converters, the rods of the control and protection reactor system, biological protection [1].

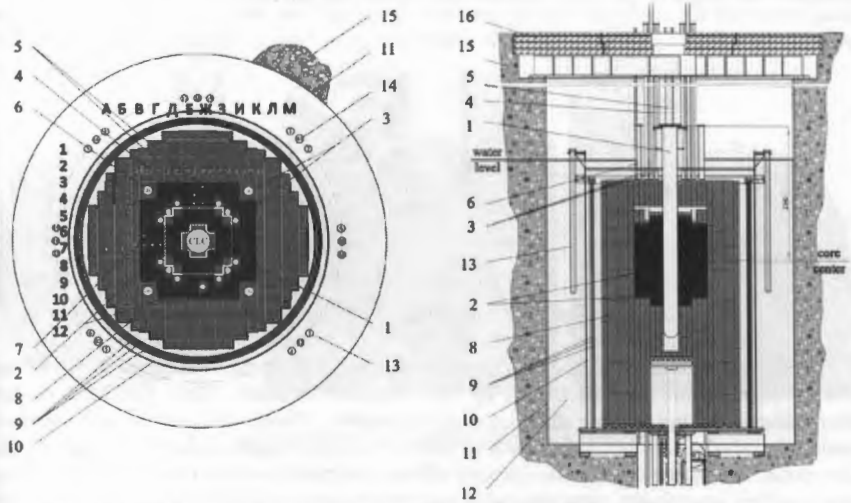

Fig.1. Vertical and horizontal section of the IGR reactor: 1– CEC; 2– active zone; 3– control rods channels; 4– channel for physical measurements; 5– TEC channels; 6– LEC; 7– neutron source channel; 8– reflector; 9– side screen (three shells); 10– casing; 11– water tank; 12– cooling water cavity; 13– ionization chambers; 14– neutron counter channel, 15– biological protection; 16– upper lid.

The IGR reactor is used to perform tests on fuel assemblies of designed reactor plants to justify their operating modes [2]. All reactor tests are accompanied by computational studies, including computer simulation of the thermal state of the reactor core and test object [3]. The simulation of the thermal state of the core of the IGR reactor is performed by the finite element method in the ANSYS software package [4]. This requires a qualitative model of the reactor core. With the growth of the computing power of personal computers and the development of computer simulation methods, a need arose to develop a new high-precision thermophysical model of the IGR reactor. At the same time, a number of requirements were presented for the new model. The new model should: 1) take into account all dimensional and material characteristics and physical properties of the core; 2) include a detailed core, taking into account the features and nuances of the design; 3) be formed programmatically, for example, using the VB.NET programming environment [5] directly from finite elements using the «bottom-up» method; 4) contain the optimal number of elements for describing the geometry, 5) provide the possibility of mutual data exchange with the neutron-physical model of the IGR reactor core.

2. The core design features

The IGR reactor core consists of 340 square columns. The columns are divided into several types depending on the blocks included in the column. The blocks differ in design. They have technological holes, protrusions, and grooves, which provide the possibility of their mutual engagement (Fig. 2.). For example, graphite blocks with a cross-section of ~ 98×98 mm impregnated with a solution of uranium are used to form the core columns, and unimpregnated graphite blocks with dimensions of ~ 197×197 mm^2 are used for the side reflector. The height of the blocks varies from 140 mm to 148 mm.

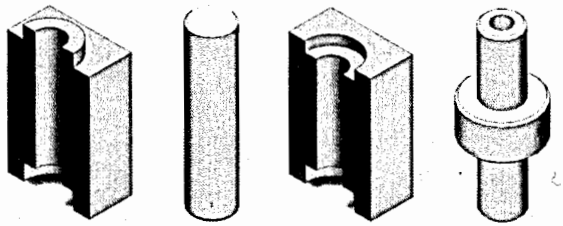

Fig. 2. External view of 3D models of graphite blocks and bushings.

Several fundamental mesh structures were developed for the most accurate description of each topology of graphite blocks by finite element methods. Mesh structures contain information about the location of nodes and their number. Based on this data, finite elements (mainly hexahedra) are generated, each of which consists of eight nodes (in rare cases, six). The mutual arrangement of nodes directly affects the quality of the elements of the future mesh, so their coordinates were calculated and optimized individually for each structure. For example, elemental grids of two types of graphite blocks are given, formed from one mesh structure (Fig. 3), consisting of 33 nodes and 24 hexahedral elements.

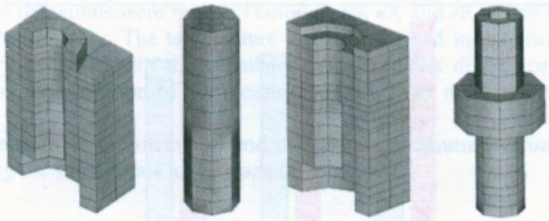

Fig. 3. Graphite details mesh.

The versatility of this structure makes it possible to model most of the core blocks by layer-by-layer construction of elements, as well as to form holes, grooves, and protrusions at different height levels without changing the number of nodes and the shape of the elements. The presence of a structured grid in graphite blocks greatly facilitates the generation of helium elements surrounding the columns and makes it possible to obtain a high-quality grid.

3. Results

The developed thermophysical model of the IGR reactor is an ordered and structured set of finite elements (Fig. 4), in which the important geometric parameters of graphite parts are preserved.

The model has 4 700 304 nodes, 4 614 328 elements, 8 427 element types, 3 materials, and 9 material types. Element types group the specified elements into individual graphite parts, it allows building of interface for transfer the temperature field from the thermophysical model to the neutron-physical one, and is important when computational studies of the core are performing.

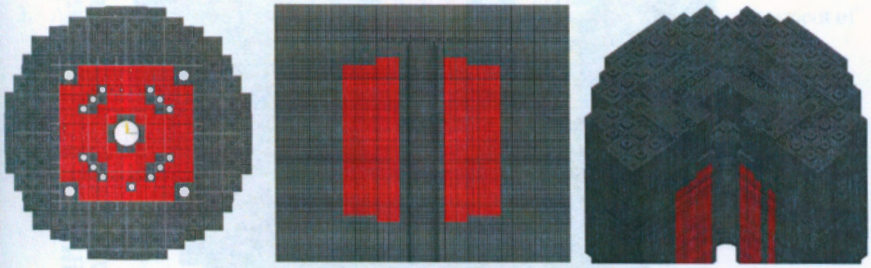
Fig. 4. Thermophysical model of the IGR reactor.

4. Validation

The model was validated by the core temperature measured by thermoelectric converters during the reactor start-up. A comparison of the measured temperature values with those calculated in the ANSYS program is presented in the form of a diagram in Figure 5.

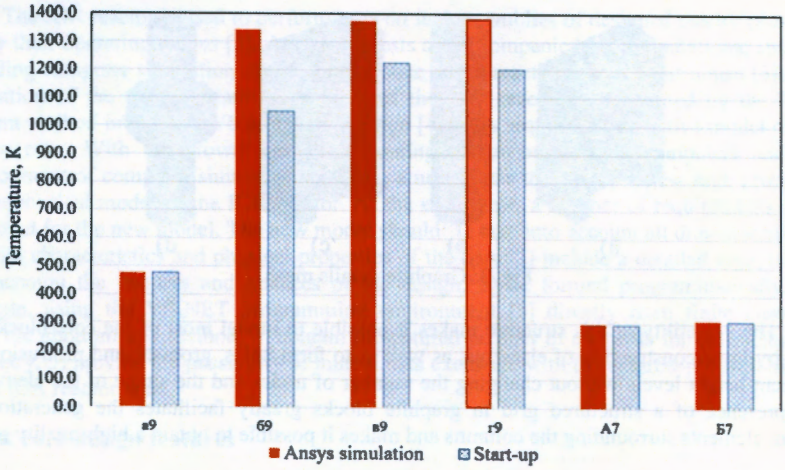

Fig. 5. Comparison of calculated and measured temperatures during start-up.

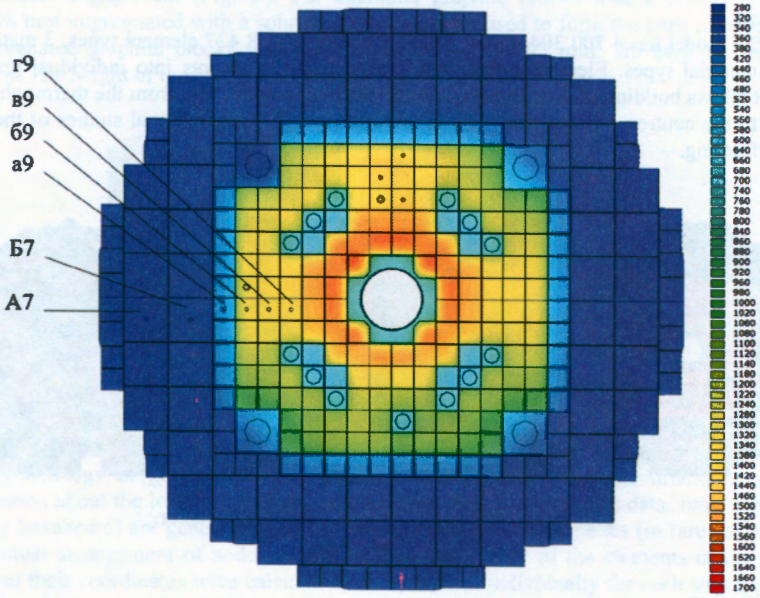

Fig. 6. Temperature distribution in the horizontal section of the core.

The largest deviations were found in columns ***б9, в9,*** and ***г9***, which amounted to 20%, 13%, and 11%, respectively. The temperature values measured in columns ***а9, А7,*** and ***Б7*** almost completely coincide with the calculated ones, and the difference does not exceed 1.0%. On average, the deviation of the measured values from the calculated ones does not exceed 7%.

The discrepancy in the measured and calculated temperature values in column ***г9*** is 12% after reaching the steady state at the stage of cooldown.

5. Conclusion

A full-scale three-dimensional model of the IGR reactor was built for carrying out thermophysical calculations, which makes it possible to take into account the uneven distribution of energy release associated with the asymmetry of the core. The model is built from structured and optimized finite elements associated with the neutron-physical model of the reactor. Implemented full interaction of models at the element level guarantees the transfer of data from one model to another in an explicit form. The model was created in the VB.NET programming environment for calculations in the ANSYS Mechanical APDL program [4].

The work was funded by the Science Committee of the Ministry of Science and Higher Education of the Republic of Kazakhstan (Grant No. AP09058353 «Design of tools to simulate dynamic neutron field of Nuclear Research Pulse Reactor»).

REFERENCES

1. Description of the IGR reactor: report (Deliverable 1.1 under Contract 0J-30461-0001A)/SSE IAE RSE NNC RK; A.D. Vurim, A.A. Kolodeshnikov, V.A. Gaidaichuk.– Kurchatov, 2011. – p. 40.
2. Erlan Batyrbekov, Vladimir Vityuk, Alexander Vurim, Galina Vityuk. Experimental opportunities and main results of the impulse graphite reactor use for research in safety area // Annals of Nuclear Energy. –2023. –Vol. 182. 109582. https://doi.org/10.1016/j.anucene.2022.109582.
3. A.S. Surayev, R.A. Irkimbekov, Z.B. Kozhabayev, V.A. Vityuk. Impact assessment of the IGR graphite block uneven impregnation with uranium on thermal strength properties // Recent Contributions to Physics. – 2022. – №. 3(82). – P.52-59. https://doi.org/10.26577/RCPh.2022.v82.i3.08.
4. Ansys Mechanical APDL. Thermal Analysis Guide, Ansys Inc., 2013.
5. Vick, Paul. 2004. The Visual Basic. Net Programming Language. Addison-Wesley Professional.

Intermediate and Fast Neutron Induced Reactions, Neutron Radiation Effects

Measurement of Cross Sections for Nuclear Reactions of Interaction of Protons and Deuterons with Lithium at Ion Energies 0.4–2.2 MeV

Bikchurina M., Bykov T., Kasatov D., Kolesnikov I., Koshkarev A., Ostreinov G., Savinov S., Sokolova E., and Taskaev S.

Budker Institute of Nuclear Physics, Novosibirsk, Russia
Novosibirsk State University, Novosibirsk, Russia

An accelerator based epithermal neutron source for the development of boron neutron capture therapy (BNCT), a promising method for the treatment of malignant tumors, and other various applications is proposed, created and is functioning at the Budker Institute of Nuclear Physics. The neutron source consists of a tandem accelerator of charged particles of an original design, a lithium neutron-generating target for generating neutrons as a result of the ^{7}Li(p,n)^{7}Be or ^{7}Li(d,n) reaction, and a beam shaping assembly for forming a therapeutic beam of epithermal neutrons. The facility is capable of producing α-particles through different reactions.

Knowledge of the cross sections of the reactions Li(p,), Li(d,) is important both for nuclear data evaluation, as well as within the framework of BNCT and other applications. In this work, the cross sections of the following nuclear reactions were determined with good accuracy for proton/deuteron energies E = 0.4–2.2 MeV: ^{7}Li(d,nα)^{4}He, ^{7}Li(d,α)^{5}He →α + n, ^{6}Li(d,α)^{4}He, ^{6}Li(d,p)^{7}Li, ^{6}Li(d,p)^{7}Li*, ^{7}Li(p,α)^{4}He. The measurements were made using a silicon-based semiconductor α-spectrometer by ion scattering spectroscopy. The energy distribution of alpha particles from a thick layer of boron carbide when irradiated with a proton beam with energies from 0.6 to 2.1 MeV was measured. The results show that it is possible to measure the cross sections of the nuclear reactions ^{11}B(p,α)^{8}Be and ^{11}B(p,α)αα using the thin boron layer. For the deposition of a thin layer of boron on a metal substrate it is proposed to carry out a magnetron sputtering method with preheating of the thermally insulated target by a low-current high-voltage discharge. Measurement of the reaction cross section is important for both boron-proton-capture therapy and for neutron-free thermonuclear energy on the ^{11}B(p,α)αα reaction.

1. Introduction

The prevalence of cancer and mortality rates are steadily increasing. Boron-neutron capture therapy (BNCT) is considered one of the promising approaches for treating malignant tumors [1,2]. BNCT is a form of binary radiotherapy, when the stable isotope boron-10 is accumulated in tumor cells using special pharmaceuticals and then irradiated with a stream of epithermal neutrons (0.5 eV– 10 keV). As a result of neutron capture by the atomic nucleus boron-10 (thermal neutron capture cross-section 3838 barns) the nuclear reaction ^{10}B(n,α)^{7}Li with energy release of 2.79 MeV occurs. This therapy has already been validly used in clinical trials to treat patients and has shown positive results.

Charged-particle accelerators are now used as neutron sources. The Budker Institute of Nuclear Physics SB RAS proposed and created [3] a VITA, which includes i) a tandem electrostatic accelerator of charged particles of original design (vacuum-insulated tandem accelerator) to produce a monoenergetic beam of protons or deuterons with energy from 0.3 to 2.3 MeV, current up to 10 mA, (ii) a thin lithium target to generate a powerful neutron flux in the ^{7}Li(p,n)^{7}Be and Li(d,n) reactions, (iii) beam forming systems to produce a beam of cold, thermal, epithermal or fast neutrons. The facility is equipped with gamma, alpha, and neutron spectrometers and dosimeters.

The interaction of a proton with lithium is also accompanied by the reaction $^{7}Li(p,\alpha)^{4}He$. This reaction is characterized by an energy yield of 14.347 MeV and is one of the thermonuclear reactions in stars. Existing data on the cross section of the reaction are very inconsistent; one of the goals of this work is to measure the cross section of the $^{7}Li(p,\alpha)^{4}He$ reaction.

As noted above, VITA can generate not only a beam of protons but also deuterons, so the second goal of this work is to study the interaction between lithium and deuterons, since this issue is poorly understood.

In addition to the $^{7}Li(p,\alpha)^{4}He$ reaction, the $^{11}B(p,\alpha)\alpha\alpha$ reaction is often considered for neutron-free fusion. In addition to the fundamental application, this reaction appears in the BNCT, which emphasizes the importance of studying the cross section of the interaction between boron-10 and proton. At the present time the cross sections of the interaction of natural boron with a proton are poorly studied, our goal was to study the nature of the interaction of boron with the proton beam.

2. Experimental facility

The study was carried out on an accelerator-based neutron source at the Budker Institute of Nuclear Physics in Novosibirsk, Russia [2]. A schematic of the experimental setup is shown in Figure 1. The vacuum-insulated tandem accelerator *1* produces a proton beam and directs it toward the lithium target *6*. The proton beam energy can be varied in the range of 0.6–2 MeV, maintaining a high energy stability of 0.1%. The beam current can also be varied in the range from 0.5 to 10 mA, ensuring its stability of 0.4%. At the VITA exit the proton beam has a transverse size of 10 mm, angular divergence up to ± 1.5 mrad, and a normalized emittance of 0.2 mm-mrad [4]. The proton beam current is measured and monitored with a non-contact NPCT current sensor (Bergoz Instrumentation, France) *2*.

In order to conduct research, the proton beam current on the target is reduced to less than 1.5 μA by placing a cooled collimator *2* in its path located 4 m from the target. The collimator is a 16 mm thick copper rectangular parallelepiped with sides 64 × 64 mm. A 1 mm diameter hole is drilled in the center of the aperture and a 10 mm countersink is made on both sides.

The position and size of the proton beam on the target is monitored by a Hikvision video camera *5*, which records the lithium luminescence under the action of protons [5]. The current of the proton beam falling on the lithium target is measured with a resistive voltage divider, using a target assembly *4* electrically isolated from the setup, like a deep Faraday cylinder.

The developed lithium target *6* is three-layered: a thin layer of pure lithium metal for neutron generation, a thin layer of material for proton absorption, and a thin copper substrate for efficient heat dissipation. The copper substrate is a 144 mm diameter copper disk with a thickness of 8 mm. On the proton beam side, an 84 mm diameter thin layer of lithium crystal density is thermal sprayed on the copper disk. A flat aluminum disk with a hole in the center for the supply of cooling water and two holes on the periphery for water drainage is clamped to the back side of the copper disk.

In scientific research, target assemblies with two or three spigots, angled 135°, 142.5°, or 168° to the beam axis, are used to observe or place diagnostic equipment.

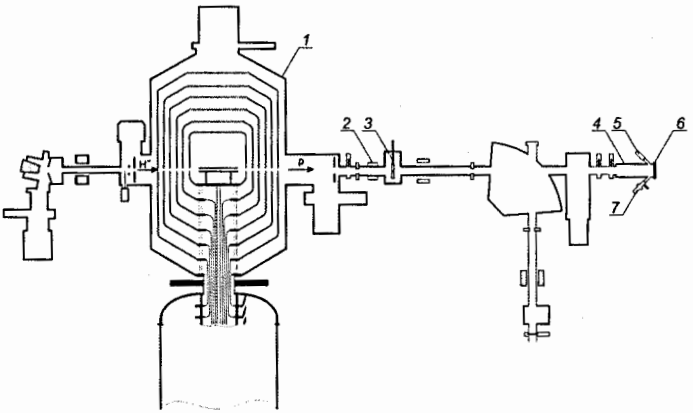

Figure 1 – Scheme of the experimental facility: *1* – vacuum insulated tandem accelerator, *2* – non-destructive DC current transformer, *3* – collimator, *4* – target assembly, *5* – video camera, *6* – lithium target, *7* – α-spectrometer.

The intensity and energy of α-particles are measured by an α-spectrometer *7* with a PDPA 1K silicon semiconductor detector (Institute of Physical and Technical Problems, Dubna, Russia). The area of the sensitive detector surface S = 20 mm^2, energy resolution – 13 keV, noise energy equivalent – 7 keV, capacity – 30 pF, input window thickness – 0.08 μm, standard natural background in the 3–8 MeV range – 0.15 imp/(cm^2·h).

3. Results and discussion

3.1. Measurement of cross section of ^{7}Li(p,α)^{4}He reaction

The ^{7}Li(p,α)^{4}He reaction is characterized by a high energy yield of 14.347 MeV and is one of the thermonuclear reactions involved in the stellar cycle of heavy element fusion in the universe [6]. This reaction also accompanies the generation of neutrons in the ^{7}Li(p,α)^{4}He reaction, which is used in a number of neutron sources [7] for boron-neutron capture therapy of malignant tumors [1,2,8]. Knowing the cross section of the ^{7}Li(p,α)^{4}He reaction is certainly important for evaluating nuclear data. However, the existing cross-section data sets in the literature are, unfortunately, contradictory in many cases [9–19]. Figure 2 shows cross section data for the ^{7}Li(p,α)^{4}He reaction and differential cross section data for this reaction.

To measure the cross section of the reaction ^{7}Li(p,α)^{4}He at a certain time *t* by a beam of protons with a current *i*, a lithium layer of thickness *l* is irradiated and α-spectrometer records α-particles escaping at a solid angle $\Omega_{lab} = S/R^2 = 7{,}511 \cdot 10^{-5}$, R = 516 mm, at an angle 168 ± 0,5° to the proton momentum. To measure the cross section, in addition to the library values, it is necessary to know the efficiency of the α-spectrometer, the thickness of the lithium layer, the nuclear density ^{7}Li in the lithium layer, the solid angle and the proton fluence.

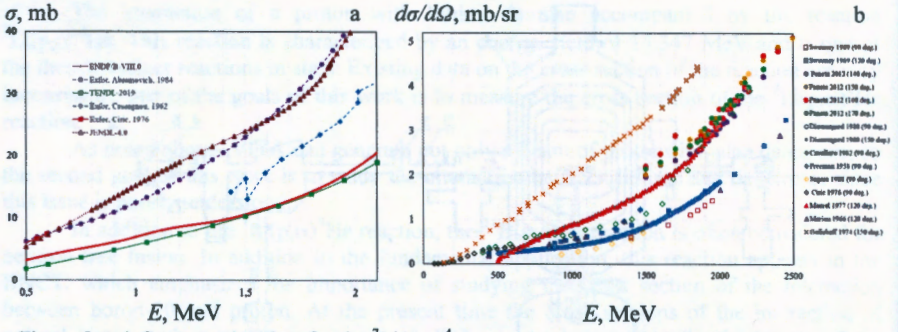

Figure 2 – a) Cross section data for the ^{7}Li(p,α)^{4}He reaction presented in the Java based nuclear information software JANIS v.3.0 [9]. b) Differential cross section of the ^{7}Li(p,α)^{4}He reaction.

The efficiency of the α-spectrometer was calibrated using two reference radiation sources based on the radionuclide plutonium-239 and a reference spectrometric α-source with the isotope ^{226}Ra and is equal to 100%. The nuclear density of ^{7}Li was calculated based on the lithium passport data and is $4.251 \cdot 10^{22}$cm^{-3} with an accuracy of 0.1 % [20–22]. Special attention was paid to the determination of the thickness of the lithium layer; for this purpose the most precise method was used – the method of comparing the yield of 478 keV γ-quanta from the examined lithium layer and from the thick layer irradiated with 1.85 MeV protons (Figure 3). We call the thick layer the lithium layer thicker than the proton path length in lithium to the reaction threshold energy ^{7}Li(p,p′γ)^{7}Li, equal to 478 keV [23]. The thickness is calculated using an expression of the proton energy loss rate in lithium as a function of its energy:

$$S = \frac{S_{low} \cdot S_{high}}{S_{low} + S_{high}} \text{ eV}/(10^{15}\text{at/cm}^2), \quad (1)$$

where $S_{low} = 1{,}6E^{0{,}45}$, $S_{high} = \frac{725{,}6}{E}\ln(1 + \frac{3013}{E} + 0{,}04578E)$, E in keV.
Thus, the thickness of lithium is $l = 0.422 \pm 0{,}013$ μm.

When measuring the cross section of the ^{7}Li(p,α)^{4}He reaction, the sensitive part of the α-spectrometer detector is placed at a distance of 516 mm from the lithium at an angle of $168 \pm 0.5°$ to the proton impulse. The characteristic spectrum recorded by the α-spectrometer is shown in Figure 3. The main signal (*1*, *2*, and *3* in Figure 4a) are protons backscattered on copper atomic nuclei, with *1* being single events, *2* being double events, and *3* being triple events. Against this background of single events, small peaks due to proton scattering on atomic nuclei of lithium, carbon, and oxygen (Li, C, and O in Figure 4b) stand out clearly. The lithium target was previously found to be covered by a thin layer of lithium oxide (10–50 nm) and a carbon film (0.5–2 nm). The back-scattered proton spectrum simulated by SIMNRA v.7.03 [24] with the above thickness of lithium, carbon and oxygen layers agrees well with that measured. Signal *4* is α-particle, signal *5* is events of simultaneous registration α-particle and back-scattered proton.

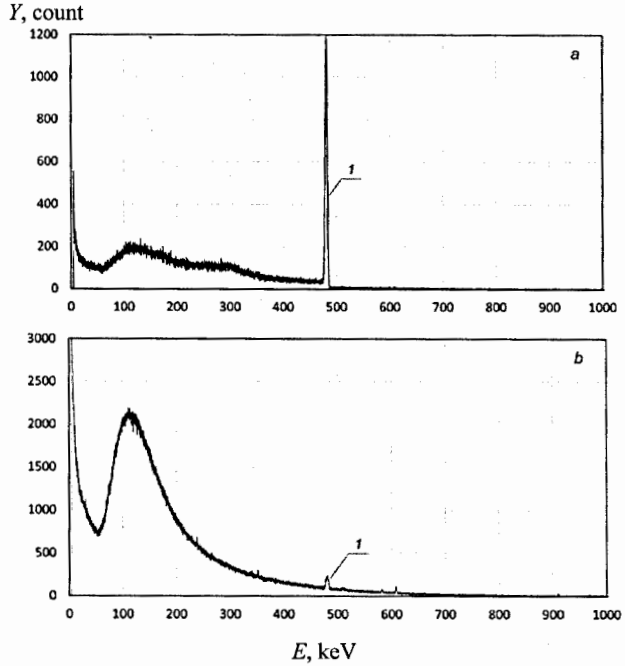

Figure 3 – Spectrum from HPGe γ-spectrometer: *a* – thick lithium layer, *b* – thin lithium layer.

The energy of α-particles depends on the energy of protons; let us determine this dependence. When a proton collides with a stationary lithium nucleus, a short-lived ($\tau \sim 10^{-18}$ s) compound nucleus is formed, which acquires momentum and, moving, decays into two α-particles. As the proton energy increases, the energy of the α-particle emitted at an angle 168° to the proton momentum decreases. Thus, if at the proton energy of 1 MeV the energy of the α-particle is 7.663 MeV, then at 2 MeV it is 7.523 MeV.

Maximums in the measured energy distributions of α-particles are obtained at energies lower than the calculated ones by 50–70 keV. Such a shift may be caused by ionization losses of the α-particle while passing through the lithium layer. According to the Bethe-Bloch formula [26], the ionization losses of the α-particle in lithium are ≈ 600 MeV/(g·cm^2), and the α-particle loses energy of ≈ 134 keV while passing a 0.422 μm thick lithium layer. Since α-particles are generated throughout the lithium thickness, on average they pass through 0.211 μm lithium and their average energy loss is 67 keV which agrees well with the measured energy shift. Consequently, the measured energy shift of the α-particle is due to its ionization losses as it passes through the lithium layer.

The measurements were made at 10 energy values. The cross section data obtained are presented in the tables in [29] and in Figure 5 and 6 in comparison with data from other authors and nuclear reaction databases. It can be seen that the values of the differential reaction cross section we obtained are in agreement with most of the Ciric [16] data measured at 90° and differ from the rest of the data. Our full cross section data are in good agreement

with the Abramovich data and the data in the JENDL 4.0 database [27]. It can be noted that our data on the cross section with good accuracy are exactly 2 times higher than the values presented in ENDF/B-VIII.0. We cannot explain such significant discrepancies in the data of different authors.

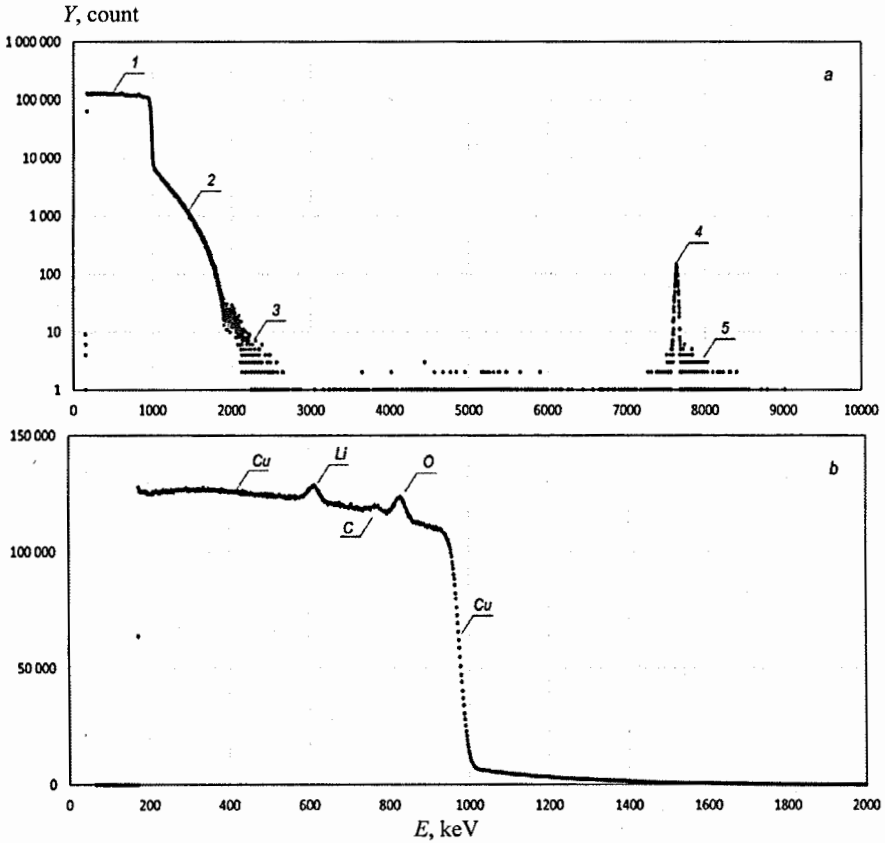

Figure 4 – Spectrum of charged particles recorded by α-spectrometer at proton energy 1 MeV: *1–3* – back-scattered protons from copper atoms (*1* – single events, *2* – double, *3* – triple), *4* – α-particles, *5* – simultaneous registration α-particle and proton. Cu, Li, C, and O – back-scattered protons from copper, lithium, carbon, and oxygen atoms.

The values of the $^{7}Li(p,\alpha)^{4}He$ reaction cross section we obtained were entered into the IBANDL (International Atomic Energy Agency Nuclear Data Library for Ion-Ray Analysis) and Exfor (experimental nuclear reaction data) databases [28].

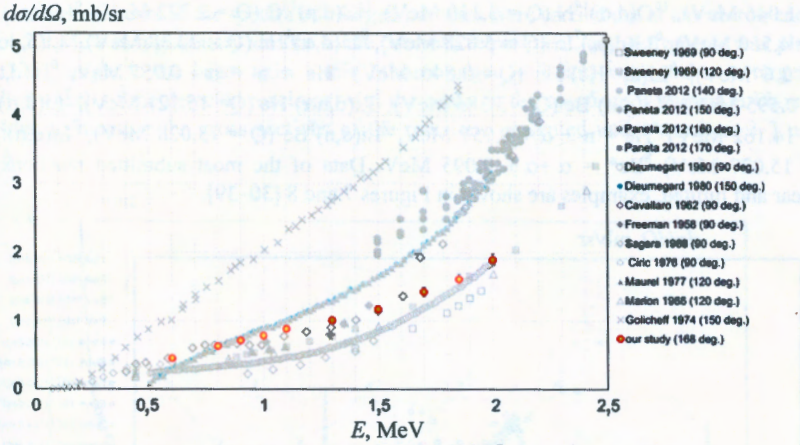

Figure 5 – Differential cross section of the $^{7}Li(p,\alpha)^{4}He$ reaction.

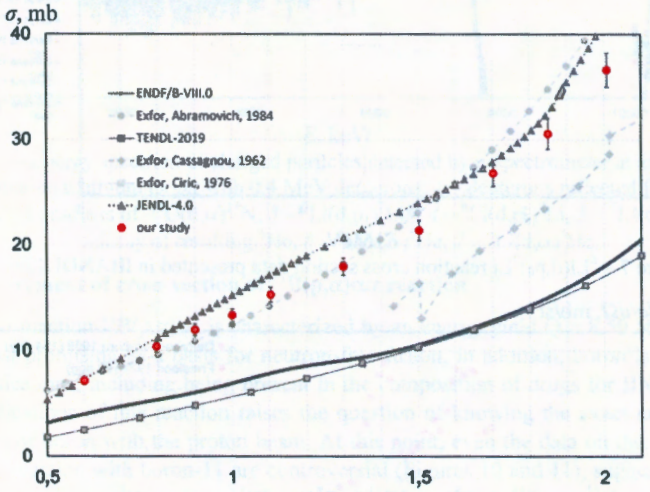

Figure 6 – Cross section of the $^{7}Li(p,\alpha)^{4}He$ reaction.

3.2. Measurement of cross section of $^{7}Li(d,)$, $^{6}Li(d,)$ reactions

VITA generates both proton and deuteron beams. The interaction of deuterons with lithium is used to generate fast neutrons in the non-threshold reaction $^{7}Li(d,n)^{8}Be$ (Q = 15.028 MeV), the reaction products are actively used in testing various materials, including the needs of CERN and ITER, as well as in cancer therapy with fast neutrons, fundamental research and other applications. In addition to this reaction, the lithium target enters into a number of other different interactions with the deuteron beam: $^{16}O(d,p)^{17}O$ (Q = 1.917 MeV), $^{16}O(d,p)^{17}O^{*}$

(Q= 1.046 MeV), $^{16}O(d,\alpha)^{14}N$ (Q = 3.110 MeV), $^{12}C(d,p)^{13}C$ (Q = 2.722 MeV), $^{6}Li(d,p_1)^{7}Li^*$ (Q = 4.550 MeV), $^{6}Li(d,p_0)^{7}Li$ (Q = 5.028 MeV), $^{6}Li(d,\alpha)^{4}He$ (Q = 22.38 MeV), $^{6}Li(d,p\alpha)^{3}H$ (Q= 2.6 MeV), $^{6}Li(d, ^{3}He)^{5}He$ (Q= 0.840 MeV) $^{5}He = n + \alpha + 0.957$ MeV, $^{6}Li(d,t)^{5}Li$ (Q= 0.595 MeV), $^{6}Li(d,n)^{7}Be$ (Q = 3.385 MeV), $^{7}Li(d,n\alpha)^{4}He$ (Q= 15.121 MeV), $^{7}Li(d,\alpha)^{5}He$ (Q= 14.162 MeV) $^{5}He = n + \alpha + 0.957$ MeV, $^{7}Li(d,n)^{8}Be$ (Q = 15.028 MeV), $^{7}Li(d,n)^{8}Be^*$ (Q= 15.027 MeV) $^{8}Be^* = \alpha + \alpha + 0.095$ MeV. Data of the most submitted reactions are unclear and limited, examples are shown in Figures 7 and 8 [30–39].

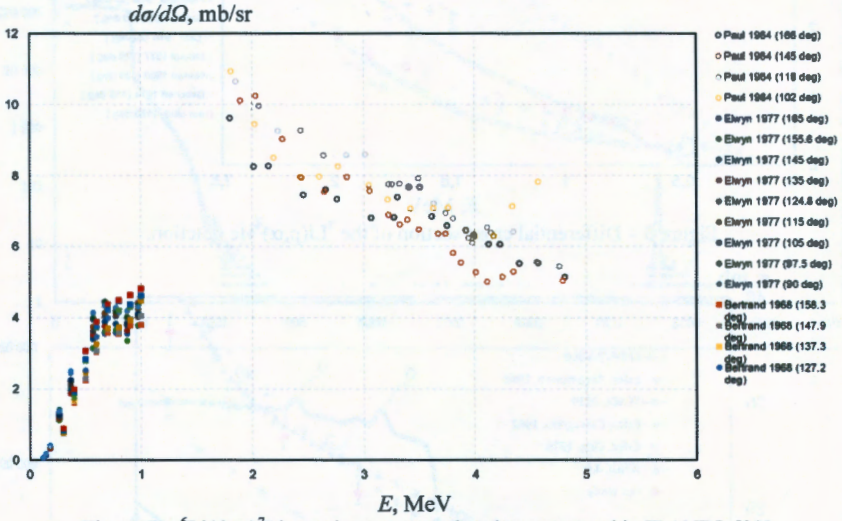

Figure 7 – $^{6}Li(d,p_0)^{7}Li$ reaction cross section data presented in IBANDL [28].

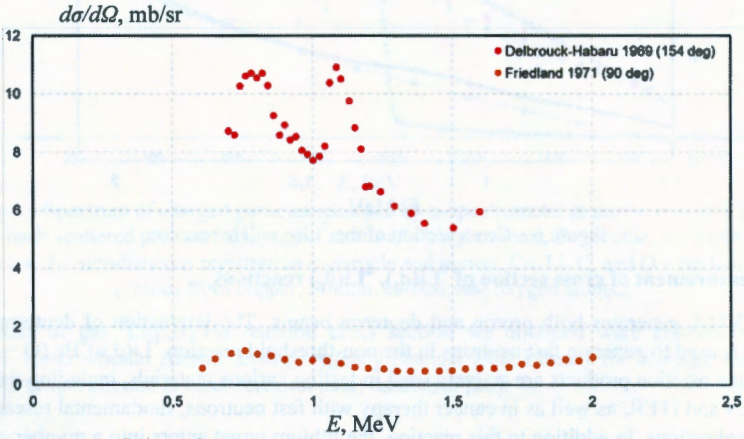

Figure 8 – $^{7}Li(d,\alpha)^{5}He$ reaction cross section data presented in IBANDL [28].

Measurements of the spectra of charged particles were carried out at a deuteron energy of 0.4-2.0 MeV in a geometry similar to the previous experiment, α-spectrometer was placed at a 135 ° angle to the beam axis, a thin lithium target (~ 2 μm) was used as a target. A detailed match of the detected reactions with the peaks in the spectrum is shown in Figure 9. We plan to measure the cross sections of the reactions presented under numbers 3-7 using VITA.

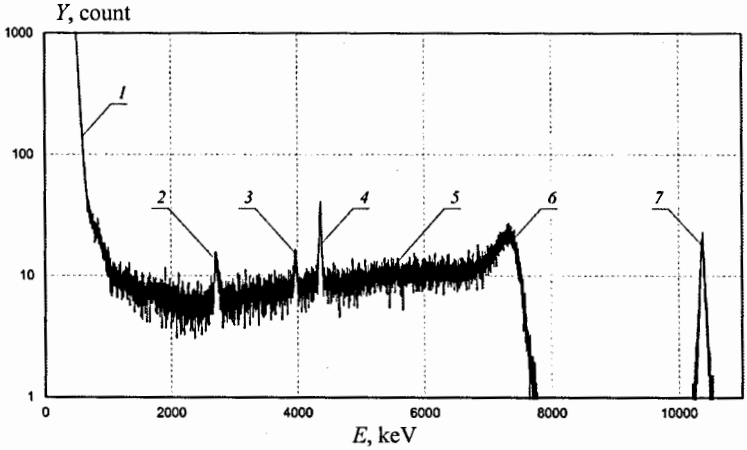

Figure 9 – Energy spectrum of charged particles detected by α-spectrometer at an angle 135° when irradiating a lithium target with 0.4 MeV deuterons: *1* – deuterons reflected from the target, *2* – reaction products of $^{16}O(d,\alpha)^{14}N$, *3* – $^{6}Li(d,p_1)^{7}Li^*$, *4* – $^{6}Li(d,p_0)^{7}Li$, *5* – $^{7}Li(d,n\alpha)^{4}He$ and decay of resulting ^{5}He, *6* – $^{7}Li(d,\alpha)^{5}He$, *7* – $^{6}Li(d,\alpha)^{4}He$.

3.3. Measurement of cross section of $^{11}B(p,\alpha)\alpha\alpha$ reaction

The reaction $^{11}B(p,\alpha)\alpha\alpha$ is characterized by an energy yield Q = 8.59 MeV and is one of the most promising as a basis for neutron-free fusion, in addition, boron is used in many other applications, including being present in the composition of drugs for BNCT, these and other applications of this reaction raises the question of knowing the exact cross section of interaction of boron with the proton beam. At this point, even the data on the progression of the proton reaction with boron-11 are controversial (Figures 10 and 11), suggesting that there are 4 possible routes: $^{11}B(p,\alpha)\alpha\alpha$, $^{11}B(p,\alpha_0)^{8}Be$, $^{11}B(p,\alpha_1)^{8}Be^*$, $^{11}B(p,\gamma)^{12}C$.

Measurements of charged particle spectra were carried out in a geometry similar to the previous experiment at proton energies of 0.4–2.15 MeV, α-spectrometer was placed at an angle of 135° to the beam axis, boron carbide (B_4C) was used as a target. The character of the proton energy dependence of the events is shown in Figure 12. One can see that as the energy increases, the right-hand peak corresponding to α_0 from the $^{11}B(p,\alpha_0)^{8}Be$ reaction increases with the proton energy, which coincides with the previously measured cross section of this boron-11-proton interaction route (Figure 10) [40–46]. One can also observe the complex character of the large peak, presumably formed by α_1 from the $^{11}B(p,\alpha_1)^{8}Be^*$ reaction, the decay of ^{8}Be and $^{8}Be^*$ into two α-particles, and the yield from the $^{11}B(p,\alpha)\alpha\alpha$ reaction. It is

still difficult to separate with certainty the contributions of the above reaction products on the spectrum. At this point, our team plans to further investigate the $^{11}B(p,\alpha)\alpha\alpha$ reaction on a thin boron carbide target and eventually obtain a cross section of this reaction.

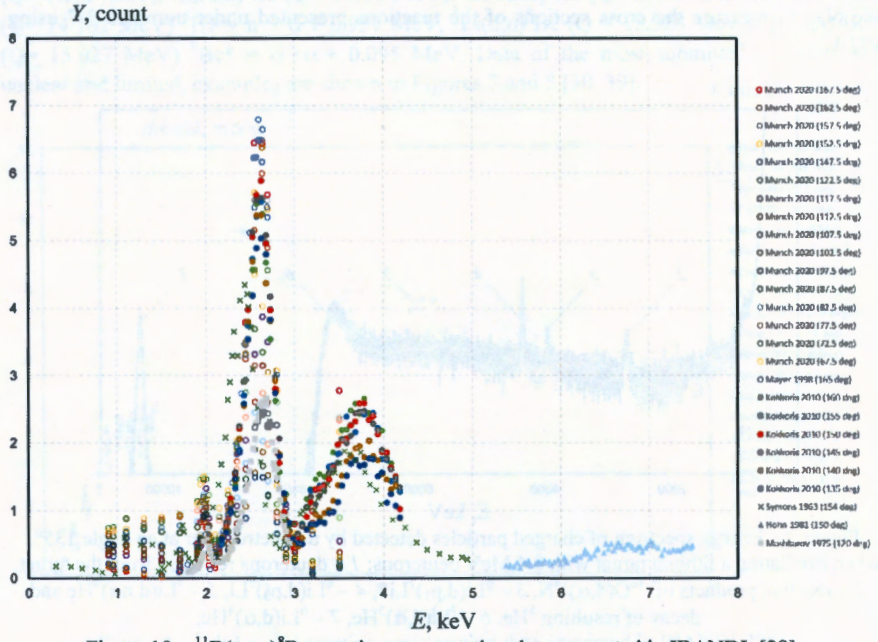

Figure 10 – $^{11}B(p,\alpha_0)^8Be$ reaction cross section data presented in IBANDL [28].

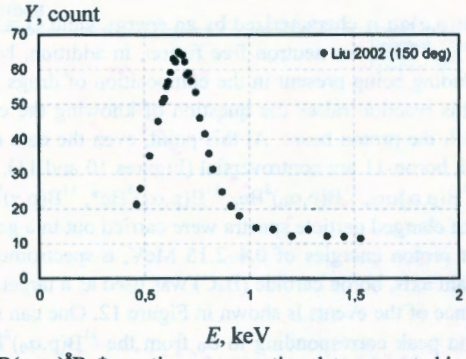

Figure 11 – $^{11}B(p,\alpha_1)^8Be^*$ reaction cross section data presented in IBANDL [28].

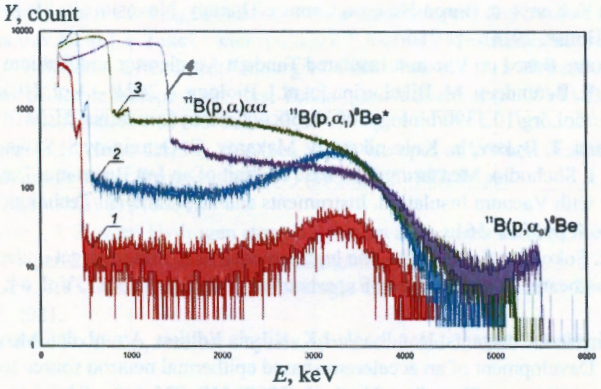

Figure 12 – Energy spectrum of charged particles detected by α-spectrometer at an angle 135° during the irradiation of boron carbide with protons with energy: *1* – 0.4 MeV, *2* – 0.5 MeV, *3* – 1.0 MeV, *4* – 2.0 MeV.

4. Conclusion

As a result of this study, the cross section of the $^{7}Li(p,\alpha)^{4}He$ reaction at proton energies from 0.6 MeV to 2 MeV was measured with high accuracy and precision. The high accuracy of the measurement was achieved by applying a new in situ method to measure the lithium thickness. The validity of this measurement is confirmed by agreement with the results of measurements made by five other independent methods: i) by measuring the mass of lithium deposited for sputtering, ii) by measuring the conductivity of water with which lithium was washed off the target copper substrate, iii) by the maximum shift in the energy distribution of α-particles, iv) by broadening the energy distribution of α-particles and v) by the energy distribution of back reflected protons on the lithium atomic nuclei.

The measured cross section of the $^{7}Li(p,\alpha)^{4}He$ nuclear reaction in the proton energy range of 0.6 MeV to 2 MeV was found to agree with the values given in the JENDL 4.0 nuclear reactions database and to be about 2 times greater than the values given in the ENDF/B VIII.0 and TENDL 2019 nuclear reactions databases.

The energy spectra of the reactions of lithium with deuterium $^{6}Li(d,p_1)^{7}Li^{*}$, $^{6}Li(d,p_0)^{7}Li$, $^{7}Li(d,n\alpha)^{4}He$, $^{7}Li(d,\alpha)^{5}He$, $^{6}Li(d,\alpha)^{4}He$ were measured and analyzed. An analysis of the character of the boron-11 reaction interaction with the proton was performed $^{11}B(p,\alpha)\alpha\alpha$.

Funding

This research was funded by Russian Science Foundation, grant number 19-72-30005, https://rscf.ru/project/19-72-30005.

References

1. W.A.G. Saurwein, A. Wittig, R. Moss, Y. Nakagawa (Eds.), Neutron Capture Therapy: Principles and Applications, Springer, 2012, https://doi.org/10.1007/ 978-3-642-31334-9.

2. S. Taskaev, V. Kanygin. Boron-Neutron Capture Therapy. Novosibirsk: SB RAS Publishing House, 2016. – p. 216.
3. Neutron Source Based on Vacuum Insulated Tandem Accelerator and Lithium Target / S. Taskaev, E. Berendeev, M. Bikchurina [et al.]. Biology. – 2021. – Vol. 10, nr 5. – P. 350. URL: https://doi.org/10.3390/biology10050350. – Дата публикации: 21.04.2021.
4. M. Bikchurina, T. Bykov, Ia. Kolesnikov, A. Makarov, G. Ostreinov, S. Savinov, S. Taskaev, I. Shchudlo. Measuring the Phase Portrait of an Ion Beam in a Tandem Accelerator with Vacuum Insulation. Instruments and Experimental Techniques, 2022, Vol. 65, No. 4, pp. 551–561.
5. Makarov, E. Sokolova, S. Taskaev. The luminescence of a lithium target under irradiation with a proton beam. Instruments and Experimental Techniques, 2021, Vol. 64, No. 1, pp. 24–27.
6. Tables of Physical Constants, Handbook. I.K. Kikoin Edition, AtomIzdat, Moscow (1976).
7. S. Taskaev, Development of an accelerator-based epithermal neutron source for boron neutron capture therapy, Phys. Part. Nucl. 50 (2019) 569–575, https://doi. org/10.1134/S1063779619050228.
8. IAEA-TECDOC-1223. Current Status of Neutron Capture Therapy. International Atomic Energy Agency, Vienna, 2001.
9. Java-based nuclear information software JANIS.
10. W. Sweeney, J. Marion, Gamma-ray ransitions involving isobaric-spin mixed states in Be^8, Phys. Rev. 182 (1969) 1007–1021, https://doi.org/10.1103/ PhysRev.182.1007.
11. V. Paneta, A. Kafkarkou, M. Kokkoris, A. Lagoyannis, Differential cross-section measurements for the $^7Li(p,p_0)^7Li$, $^7Li(p,p_1)^7Li$, $^7Li(p,\alpha_0)^4He$, $^{19}F(p,p_0)^{19}F$, $^{19}F(p,a_0)^{16}O$ and $^{19}F(p,\alpha_{1,2})^{16}O$ reactions, Nucl. Instrum. Methods Phys. Res. B. 288 (2012) 53–59, https://doi.org/10.12681/hnps.2492.
12. D. Dieumegard, B. Maurel, G. Amsel, Microanalysis of Flourine by nuclear reactions, Nucl. Instrum. Methods 168 (1-3) (1980) 93–103.
13. S. Cavallaro, R. Potenza, A. Rubbino, Li^7+p interaction and excited states of Be^8, Nucl. Phys. 36 (1962) 597–614, https://doi.org/10.1016/0029-5582%2862% 2990486-8.
14. J. Freeman, R. Hanna, J. Montague, The nuclear reaction $He^4(\alpha,p)Li^7$ and its inverse: II. The reaction $Li^7(p,\alpha)He^4$, Nucl. Phys. 5 (1958) 148–149, https://doi. org/10.1016/0029-5582(58)90013-0.
15. Sagara, K. Kamada, S. Yamaguchi, Depth profiling of lithium by use of the nuclear reaction $^7Li(p,\alpha)^4He$, Nucl. Instrum. Methods Phys. Res. B. 34 (1988) 465–469, https://doi.org/10.1016/0168-583X(88)90151-6.
16. D. Ciric, R. Popic, R. Zakula, B. Stepancic, M. Aleksic, J. Setrajcic, The interaction of ^7Li isotope with low energy proton and triton beams, Int. J. Sci. Res. 6 (1976) 115.
17. B. Maurel, D. Dieumegard, G. Amsel in Ion Beam Handbook (p. 133), ed. J. Mayer, E. Rimini, 1977, https://doi.org/10.1016/B978-0-12-480860-7.50011-3.
18. J. Marion, M. Wilson, The $^7Li(p,\gamma)^8Be^*$ reaction and single-particle levels in ^8Be, Nucl. Phys. 77 (1966) 129–148, https://doi.org/10.1016/0029-5582 (66) 90681-X.
19. Golicheff, M. Loeuillet, C.h. Engelmann, Determination des fonctions d'excitation des reactions $^{19}F(p,\alpha_0)^{16}O$ et $^7Li(p,\alpha_0)^4He$ entre 150 et 1800 keV: Application a la mesure des concentrations superficielles de lithium et de fluor, J. Radioanal. Chem. 22 (1–2) (1974) 113–129.

20. Method for in situ measuring the thickness of a lithium layer / D. Kasatov, Ia. Kolesnikov, A. Koshkarev [et al.]. – Текст : электронный // Journal of Instrumentation. – 2020. – Vol. 15. – P10006. – URL: https://doi.org/10.1088/1748-0221/15/10/P10006. – 12.10.2020.
21. Handbook of Stable Isotope Analytical Techniques. Volume II (2009) 1123–1321, doi:10.1016/B978-0-444-51115-7.00028-0.
22. Lieberman, G.J. Alexander, J.A. Sechzer, Stable isotopes of lithium: dissimilar biochemical and behavioral effects, Experientia 42 (9) (1986) 985–987, https:// doi.org/10.1007/BF01940701.
23. H. Andersen, J. Ziegler, Hydrogen stopping powers and ranges in all elements. Volume 3 of the stopping and ranges of ions in matter, Pergamon Press Inc., 1977.
24. SIMNRA v. 7.03 with SigmaCalc 2.0 for single user. License No. 1801-4848-WT- WA, Sept. 22, 2021.
25. Yu. Shirokov, N. Yudin, Nuclear Physics, Volumes 1 and 2, MIR Publishers, Moscow, 1982.
26. K.N. Mukhin. Experimental Nuclear Physics. - Moscow: Energoatomizdat, 1993.
27. JENDL – Japanese Evaluated Nuclear Data Library https://wwwndc.jaea.go.jp/jendl/jendl.html.
28. IBANDL – Ion Beam Analysis Nuclear Data Library https://www-nds.iaea.org/exfor/ibandl.htm.
29. S. Taskaev, M. Bikchurina, T. Bykov, D. Kasatov, Ia. Kolesnikov, A. Makarov, G. Ostreinov, S. Savinov, E. Sokolova. Cross-section measurement for the ^{7}Li(p, α)^{4}He reaction at proton energies 0.6–2 MeV. Nuclear Inst. and Methods in Physics Research B 525 (2022) 55–61.
30. J.M. Delbrouck-Habaru+(1969), Jour. Bull.Societe Royale des Sciences de Liege, Vol.38, p.240.
31. E. Friedland+(1971), Jour. Zeitschrift fuer Physik, Vol.243, Issue.2, p.126.
32. P. Paul+(1964), Jour. Nuclear Physics, Vol.53, Issue.3, p.465.
33. A.J. Elwyn+(1977), Jour. Physical Review, Part C, Nuclear Physics, Vol.16, p.1744.
34. F. Bertrand+(1968), Rept. Centre d`Etudes Nucleaires, Saclay Reports, No.3428.
35. B. Maurel,G.Amsel and D.Dieumegard, NIM, 191(1981), 349.
36. V. Foteinou et al., Nucl. Instr. and Meth. B 269, 2990 (2011).
37. F. Hirst+(1954), Jour. Philosophical Magazine, Vol.45, Issue.366, p.762.
38. G. Bruno+(1966), Jour. Journal de Physique, Vol.27, p.517.
39. G. Robaye+(1965), Jour. Bull.Societe Royale des Sciences de Liege, Vol.34, p.324.
40. M. Munch+(2020), European Physical Journal A: Hadrons and Nuclei, Vol.56, p.17.
41. M. Mayer et. al. Nucl. Instr. Meth. B143 (1998) 244.
42. M. Kokkoris+(2010), Jour. Nucl. Instrum. Methods in Physics Res., Sect.B, Vol.268, p.3539.
43. G.D. Symons and P.B.Treacy Nucl.Phys. v.46 (1963) 93.
44. K. Hohn+(1981), Jour. Jour. of Physics, Part G (Nucl.and Part.Phys.), Vol.7, p.803.
45. Ju.G. Mashkarov+(1975), Jour. Izv. Rossiiskoi Akademii Nauk, Ser.Fiz., Vol.39, p.1736.
46. J. Liu+(2002), Jour. Nucl. Instrum. Methods in Physics Res., Sect.B, Vol.190, p.107.

The Covariance Analysis of $^{nat}Sn(\alpha, x)^{122}Sb$ Nuclear Reaction Cross Sections

Mahesh Choudhary[1], Namrata Singh[1], Aman Sharma[1], A. Gandhi[1], Mahima Upadhyay[1], S. Dasgupta[2], J. Datta[2], and A. Kumar[1]

[1]*Department of Physics, Banaras Hindu University, Varanasi-221005, India*
[2]*Analytical Chemistry Division, Bhabha Atomic Research Centre, Variable Energy Cyclotron Centre, Kolkata-700064, India*

E-mail: maheshchoudhary921@gmail.com

Introduction

In nuclear medicine, a range of radioactive isotopes are employed for therapy and diagnosis. Several types of radioisotopes are produced by alpha-induced reactions with different types of targets. In this study, we have used ^{nat}Sn as a target material and alpha particle as a projectile. The radioisotopes $^{116, 117, 118, 119, 121, 123}Te$, $^{117, 120, 122, 124, 126}Sb$, ^{117}Sn and ^{111}In are produced from $^{nat}Sn(\alpha,x)$ nuclear reactions. In this work, we have obtained the production cross sections for $^{nat}Sn(\alpha,x)^{122}Sb$ nuclear reaction in the incident alpha energy range of about 24 – 40 MeV. This isotope has a broad spectrum of uses, ranging from medical imaging and cancer therapy to industrial radiography. The uncertainty propagation in the measured cross sections was calculated using covariance analysis by taking into account the micro-correlation between various variables such as particle number density, efficiency of the HPGe detector, decay constants and counts etc. [1–3]. The covariance analysis is a statistical technique employed in nuclear physics to quantify and manage uncertainties associated with experimental data, nuclear reaction models and nuclear data evaluations. It is particularly valuable in the study of nuclear reactions, where precise and reliable data are essential for numerous applications. The primary objective of covariance analysis in this context is to provide a comprehensive understanding of the uncertainties in nuclear reaction cross sections and other relevant parameters.

The comparison of measured cross sections for the $^{nat}Sn(\alpha,x)^{122}Sb$ nuclear reaction along with previous experimental results from EXFOR and theoretical calculations from the TALYS nuclear code is also presented. The theoretical prediction of the excitation function of nuclear reaction $^{nat}Sn(\alpha,x)^{122}Sb$ has been carried out using the TALYS nuclear reaction code. The TALYS is a Fortran-based nuclear reaction model code which is used to calculate different physical observables related to nuclear reactions. In the TALYS, six level density models were used to calculate the theoretical predictions [4–9]. The ldmodel-1, ldmodel-2, and ldmodel-3 are classified as phenomenological level density models, while ldmodel-4, ldmodel-5, and ldmodel-6 are classified as microscopic level density models. We have compared the results of the theoretical calculations with the experimental measurements of the nuclear reaction cross section.

Experiment Details

The experiment was performed at K-130 cyclotron, VECC, Kolkata, India for this study. The stacked foil activation technique followed by the offline gamma-ray spectrometry was used to measure the reaction cross sections for the $^{nat}Sn(\alpha,x)^{122}Sb$ nuclear reaction. We irradiated two stacks to determine the excitation function of $^{nat}Sn(\alpha,x)$ ^{122}Sb nuclear reaction

in the energy range from threshold energy for the nuclear reaction up to 40 MeV. The first stack consisted of five sets of foils arranged in ^{nat}Cu-^{nat}Sn-^{nat}Al order. We irradiated this stack with a 40 MeV alpha-particle beam for approximately 5 hours. The second stack consisted of three sets of foils arranged in ^{nat}Cu-^{nat}Sn-^{nat}Al order. We irradiated this stack with a 28 MeV alpha-particle beam for about 5 hours. Table 1 provides information about beam energy used for both stacks in the present experiment.

Table 1. The details of stacks used in this experiment

Stack	Beam Energy (MeV)	Beam Current (nA)	Irradiation Time (h)
1	40	~150	5
2	28	~150	5

In this experiment, ^{nat}Cu was used as a monitor to measure the intensity of the alpha-particle beam, ^{nat}Sn acted as the target foil for the nuclear reaction ^{nat}Sn(α,x)^{122}Sb, and ^{nat}Al acted as an energy degrader and catcher foil. The thickness of the ^{nat}Cu, ^{nat}Sn, and ^{nat}Al foils was 9 mg/cm², 11 mg/cm², and 6.75 mg/cm², respectively. The arrangement of foils is shown in Figure 1. The activity of the irradiated samples was measured by using the HPGe detector. In the previous articles [10-12], we discussed in detail the calibration of the HPGe detector's efficiency as well as the coincidence summing effect.

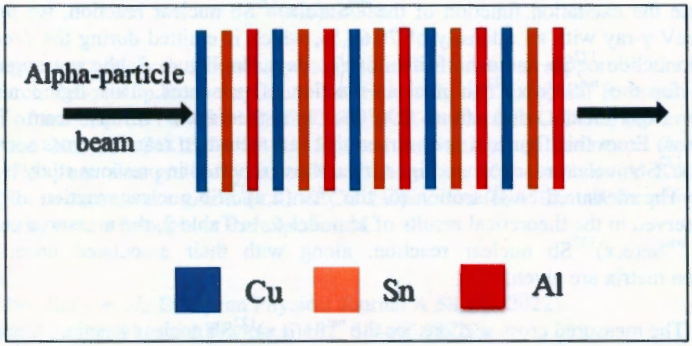

Figure 1. The foil arrangement used in the present experiment.

Data Analysis

The nuclear reaction cross-sections were calculated using the following standard activation formula

$$\sigma = \frac{C_\gamma \lambda}{\varepsilon_d \, I_\gamma N_t \Phi (1 - e^{-\lambda t_b}) e^{-\lambda t_c} (1 - e^{-\lambda t_m})} \quad (1)$$

In the above equation, σ is the nuclear reaction cross sections, C_γ is the peak area counts for the irradiated sample foils, λ is the decay constant for the nuclear reaction, N_t is the particle

density in the target material, ϕ is the incident particle flux per unit time (sec^{-1}), I_γ represents the gamma-ray intensity of the produced radioisotope, ε_d is the efficiency of the detector. In equation 1, the decay time, irradiation time and counting time for the monitor and sample foils are shown by t_c, t_b and t_m respectively.

Uncertainties in the measured cross-sections were determined by using covariance analysis. The covariance is a mathematical tool that can help to describe the detailed uncertainties with the cross-correlation between different measured quantities. The covariance matrix of cross-section I_σ can be written as

$$I_\sigma = H_x C_x H_x^T \tag{2}$$

Here, I_σ covariance matrix with order m x m, C_X covariance matrix of different attributes with order n x n. The H_X is sensitivity matrix which is given in the following equation

$$H_x^{ij} = \frac{\partial \sigma_i}{\partial x_j}, \ (i = 1,2,3,...m; j = 1,2,3,...n) \tag{3}$$

Results and Conclusions

In this section, the measured cross sections, correlation matrices and their uncertainties of nuclear reaction $^{nat}Sn(\alpha,x)^{122}Sb$ in the energy range 24 – 40 MeV are presented. To investigate the excitation function of the $^{nat}Sn(\alpha,x)^{122}Sb$ nuclear reaction, we measured the 564.24 keV γ-ray with an intensity of 70.68 %, which is emitted during the decay of ^{122}Sb. The radionuclide ^{122}Sb has a half-life of 2.72 days. In Figure 2, the measured excitation function for the $^{nat}Sn(\alpha,x)^{122}Sb$ nuclear reaction is presented. This figure also includes available experimental data from EXFOR and theoretical results from TALYS for comparison. From this figure, it is observed that our measured reaction cross sections for the $^{nat}Sn(\alpha,x)^{122}Sb$ nuclear reaction are higher than those reported in previous study by Rebeles et al. [13]. The measured cross section for the $^{nat}Sn(\alpha,x)^{122}Sb$ nuclear reaction aligns with the trend observed in the theoretical results of ldmodel-6. In Table 2, the measured cross sections for the $^{nat}Sn(\alpha,x)^{122}Sb$ nuclear reaction, along with their associated uncertainties and correlation matrix are given.

Table 2. The measured cross sections for the $^{nat}Sn(\alpha,x)^{122}Sb$ nuclear reaction, along with their associated uncertainties and correlation matrix

E_α (MeV)	Cross section (mb)	Correlation matrix					
25.07 ± 1.88	4.78 ± 0.29	1					
26.09 ± 0.90	2362 ± 0.33	0.023	1				
28.84 ± 1.73	17.84 ± 0.96	0.054	0.025	1			
32.29 ± 1.58	32.87 ± 1.76	0.055	0.056	0.061	1		
35.50 ± 1.33	39.99 ± 2.12	0.055	0.026	0.062	0.062	1	
38.52 ± 0.92	35.90 ± 1.90	0.055	0.026	0.062	0.062	0.062	1

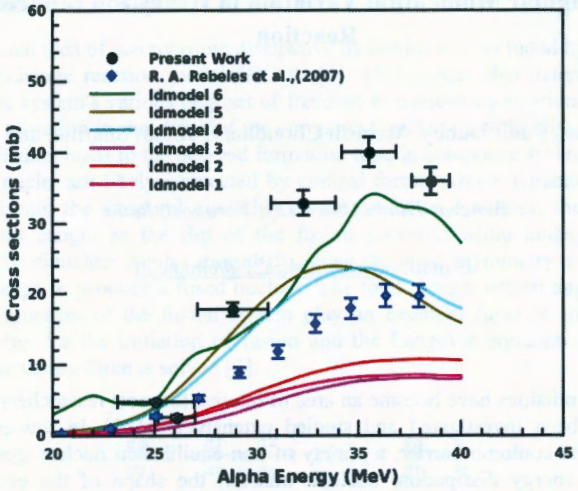

Figure 2. The measured cross sections for the $^{nat}Sn(\alpha,x)^{122}Sb$ nuclear reaction along with previous experimental results from EXFOR and theoretical calculations from the TALYS nuclear code.

Acknowledgement: Mahesh Choudhary is grateful for financial support in the form of Senior Research Fellowship from the Council of Scientific and Industrial Research (CSIR), Government of India, (File No 09/013(882)/2019-EMR-I) The IUAC-UGC, Government of India (Sanction No. IUAC/XIII.7/UFR-71353) and Institutions of Eminence (IoE) BHU [Grant No. 6031] are also gratefully acknowledged by one of the authors A. Kumar. We would also like to express our gratitude to VECC's Cyclotron (K-130) staff for providing us with high quality beams throughout the experiment.

References

1. M. Choudhary *et al.*, European Physical Journal A **58**, 95 (2022).
2. A. Gandhi *et al.*, Physical Review C **102**, 014603 (2020).
3. M. Choudhary *et al.*, Journal of Physics G: Nuclear and Particle Physics **50**, 015103 (2022).
4. A. Gilbert and A. G. W, Canadian Journal of Physics **43**(8), 1446–1496 (1965).
5. W. Dilg *et al.*, Nuclear Physics A **217**(2), 269–298 (1973).
6. A.V. Ignatyuk *et al.*,Physical Review C **47**(4), 1504 (1993).
7. S. Goriely *et al.*, Atomic Data and Nuclear Data Tables **77**(2), 311–381 (2001).
8. S. Goriely *et al.*, Physical Review C **78**(6), 064307 (2008).
9. S. Hilaire *et al.*, Physical Review C **86**(6), 064317 (2012).
10. A. Gandhi *et al.*, The European Physical Journal Plus **136**, 1 (2021).
11. A. Gandhi *et al.*, European Physical Journal A **57**, 1 (2021).
12. A. Gandhi *et al.*, Chinese Physics C **46**, 014002 (2022).
13. R.A. Rebeles *et al.*, Nuclear Instruments and Methods in Physics Research Section B **260**(2), 672–684 (2007).

Effect of Angular Momentum Variation in Heavy Ion Induced Fusion Reaction

Utkarsha Mishra*, Punit Dubey, Mahesh Choudhary, Aman Sharma, and Ajay Kumar

Banaras Hindu University, Varanasi, India

*E-mail: utkarshmishra22@bhu.ac.in

Introduction

Two-body collisions have become an area of interest for most researchers at the present time, they have been investigated and studied extensively [1–9]. In low-energy nuclear reactions above the coulomb barrier, a variety of non-equilibrium nuclear dynamics can be studied, such as energy dissipation, nucleon transfer, the shape of the evolution of the compound nucleus in a heavy ion fusion reaction, and so on. The completely fused compound nucleus releases evaporating neutrons, charged particles, and finally a cascade of γ-rays. In the light and medium mass systems, it is relatively straightforward to identify events associated with complete fusion by measuring the evaporation residues. Alternatively, the characteristic γ-rays emitted in the last step of this decay chain can be measured to identify a fusion event.

Research has improved several theoretical frameworks that are currently in use and that specifically take into account the dynamics of nucleus-nucleus interactions. Some of them include the statistical model (CASCADE) to calculate fusion cross-sections and the optical model for elastic scattering [10]. The user interface of many code developed in the Fortran programming dialect is complex; as a consequence, investigators must carefully prepare input files, that will include many lines. In other words, executing these codes would be extremely challenging for a non-expert user, who would therefore squander time.

In experimental nuclear reaction evaporation spectra of light particles from the compound nucleus help us to know about the reaction dynamics [1–3, 7]. Based on dynamical calculations of the trajectories in a multidimensional space, the geometrical shapes of the system from the initial approach of two separated spherical nuclei are described. Through the mononucleus regime, until either fusion or reseparation of two final fragments was observed, the early description of the heavy ion dynamics that lead to the diversion of a significant portion of the reaction cross section into deep-inelastic and quasi-fission channels was developed.

Plenty of investigations have been carried out regarding heavy-ion fusion reactions, and it has been demonstrated that these reactions depend on the entrance channel characteristics [4–9], including the mass asymmetry of the entrance channel, the excitation energy, the angular momentum, and the Z_PZ_T (charge product of the projectile and target), etc. To examine the nucleus at high spin or high temperature, fusion reactions are useful tools, and the dissipative evolution of compound nuclei is an active area of research in heavy ion induced fusion reactions. In such reactions, the colliding nuclei possess a certain amount of intrinsic angular momentum.

Dynamical Model Calculation

The original idea of macroscopic dissipative dynamics was included by H. Feldmeier in the particle exchange reaction model HICOL [3]. This model also determines the period required for the system's various degrees of freedom to achieve equilibrium. The analysis of the dynamical variation in the shape of the compound nucleus and the dissipation process in the entrance channel leads to the delayed formation time in composite systems. In this model, two spherical nuclei are likely connected by conical forms, which dynamically change in a series. To ascertain the temporal evolution of the collision dynamics, the target-projectile system becomes caught in the dip of the fusion potential while undergoing the fusion reaction, and the dinuclear combination drifts along the mass asymmetry coordinate through the mass exchange to produce a fused nucleus. The total charge, orbital angular momentum, and mass asymmetries of the fusion system play an essential function in determining the dynamical barrier for the initiation of fusion and the Langevin equation which includes a dissipative, fluctuating force is solved [7].

$$\frac{dp}{dt} = -\frac{dT}{dq} - \frac{dV}{dq} + X(t), \quad \frac{dq}{dt} = \frac{p}{M},$$

where V stands for the conservative potential, $T = \frac{p^2}{2M}$ signifies the collective kinetic energy, and M implies the mass tensor. $X(t)$ is the fluctuating force driven by the coupling of the collective degrees of freedom to the intrinsic degrees of freedom. By assuming the incompressible and irrotational flow of mass during the shape evolution in the collision, the mass tensor can be obtained from the profile function.

In the realm of super heavy mass, it has been extensively employed to examine fusion and fission events. The relevance of the neck behavior of the colliding system has been captured in code, which shows how appropriate processing of the mass parameter for the neck degree of freedom can reduce the theoretical overestimation of fusion probability in heavier colliding systems. The impact of the entrance channel mass asymmetry ($\alpha=(A_t - A_p)/(A_t + A_p)$) in the fusion kinetics of heavy ion-induced events has been a focus of various theoretical and experimental calculations [2–4] in the past.

Results and discussion

In this study, we have calculated the variation of compound nucleus formation time with the angular momentum as shown in Fig. 1 for the two different reactions that make the same compound nucleus. The dynamical model code HICOL is employed to calculate the formation time of a compound nucleus at different values of angular momentum.

In this realm, we have shown that when the angular momentum value is low, both reactions have nearly the same formation time, but when we increase the value of excitation energy, angular momentum value increases due to which a huge difference occurs in their formation time. Also, we observe that symmetric reactions result in a more dissipative evolution of the compound nucleus than an asymmetric system. From Fig. 1, it is clear that the compound nucleus ($^{107}In^*$) formed through $^{51}V + {}^{56}Fe \rightarrow {}^{107}In^*$ has a long formation time compared to the $^{32}S + {}^{75}As \rightarrow {}^{107}In^*$ which indicates the dissipation in the nuclear reaction during compound nucleus formation, because angular momentum may prevent the energy

from being transferred to other degrees of freedom and nuclei in collision experience more distortion at high angular momentum.

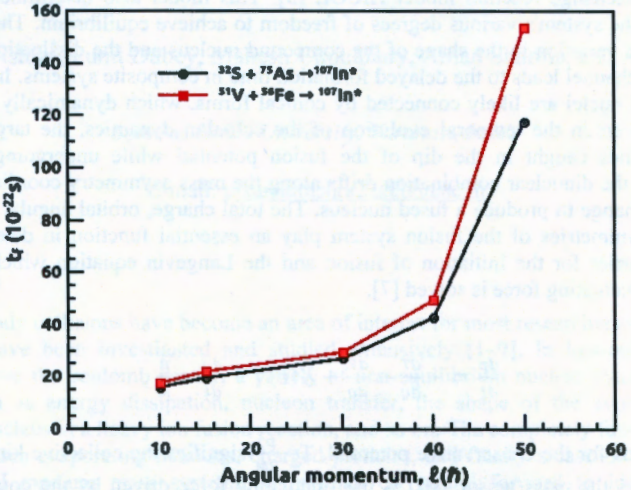

Fig.1. The influence of angular momentum on compound nuclear formation time.

The equations of motion are solved for a given angular momentum to determine the time development of various macroscopic variables. Fig. 2 depicts the relationship between σ (Neck Coordinates) and time for various angular momentum values. We observed that the time evolution of the neck coordinate exhibits varied behavior for the $^{51}V + ^{56}Fe$ reaction and quite distinct behavior for the $^{32}S + ^{75}As$ reaction. For the $^{51}V + ^{56}Fe$ system, the large value of neck coordinates (σ) indicates that the system has a more elongated shape for composite system than $^{32}S + ^{75}As$.

Summary

After a general discussion about angular momentum variation with the macroscopic variables of composite systems in heavy ion fusion dynamics, it was observed that angular momentum affects the evolution of the compound nucleus in symmetric as well as asymmetric systems. It means that both systems have the dissipative evolution of the compound nucleus, but the symmetric system takes more time to evolve than the asymmetric system. In this series, we have also observed that the neck coordinate is also influenced by the variation of angular momentum due to which symmetric systems have a more elongated shape than the asymmetric systems. The variation of angular momentum will be beneficial for the study of reaction dynamics.

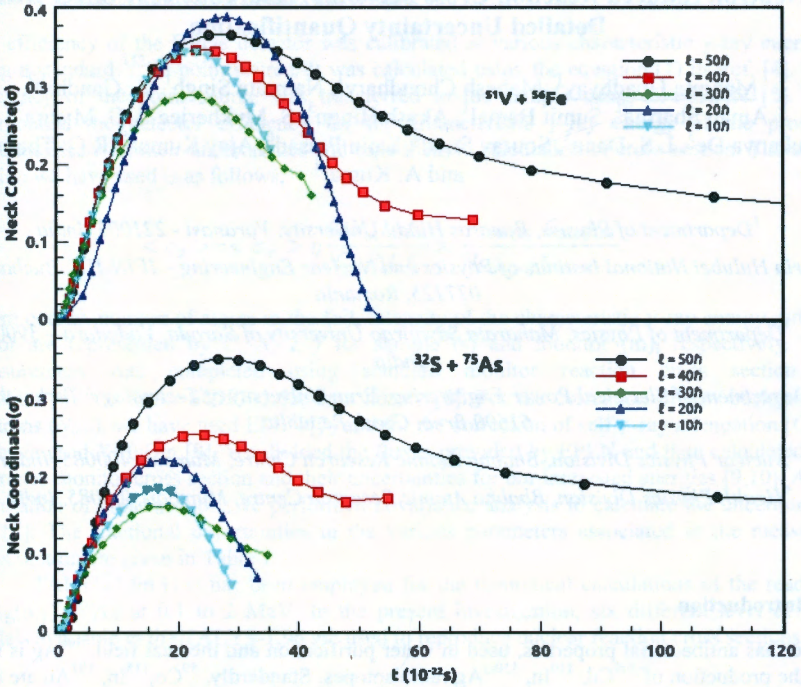

Fig.2. Neck coordinates as a function of time evolution of compound nucleus formation.

Acknowledgments

One of the authors (A. Kumar) would like to thank the IUAC-UGC, Government of India (Sanction No. IUAC/XIII.7/UFR-71535), the Institution of Eminence (IoE) BHU (Sanction No. 6031), for the financial support for this work.

References

1. Ajay Kumar *et al.*, Phys. Rev. C **68,** 034603 (2003).
2. Ajay Kumar *et al.*, Phys. Rev. C **70,** 044607 (2004).
3. N.K. Rai *et al.*, Phys. Rev. C **98,** 024626 (2018).
4. N.K. Rai *et al.*, J. Phys. G: Nucl. Part. Phys. **49,** 035103 (2022)
5. A. Kumar *et al.*, Nucl. Phys. A **798**, 1–15 (2008).
6. A. Kumar *et al.*, EPJ web conference. **86**, 00019 (2005).
7. J. Kaur *et al.*, Phys. Rev. C **70**, 017601 (2004).
8. N.K. Rai *et al.*, Phys. Rev. C **100**, 014614 (2019).
9. J. Kaur *et al.*, Phys. Rev. C **66,** 034601 (2002).
10. F. Puhlhofer *et al.*, Nucl. Phys. A **280**, 267 (1977).
11. H. Feldmeier *et al.*, Nucl. Phys. A **435**, 229 (1985).

Neutron Induced Reaction Cross Section Measurement for Silver with Detailed Uncertainty Quantification

Mahima Upadhyay[1], Mahesh Choudhary[1], Namrata Singh[1], A. Gandhi[1,2], Aman Sharma[1], Sumit Bamal[1], Akash Hingu[3], S. Mukherjee[3,4], G. Mishra[5], Sukanya De[5], L.S. Danu[5], Sourav Sood[6], Sajin Prasad[6], Ajay Kumar[5], R.G. Thomas[5], and A. Kumar[1]

[1]*Department of Physics, Banaras Hindu University, Varanasi - 221005, India*

[2]*Horia Hulubei National Institute of Physics and Nuclear Engineering – IFIN-HH, Bucharest, 077125, Romania*

[3]*Department of Physics, Maharaja Sayajirao University of Baroda, Vadodara – 390002, India*

[4]*Department of Electrical Power Engineering, Brno University of Technology, Technicka, 61600 Brno, Czech Republic*

[5]*Nuclear Physics Division, Bhabha Atomic Research Centre, Mumbai- 400085, India*

[6]*Health Physics Division, Bhabha Atomic Research Centre, Mumbai- 400085, India*

1. Introduction

Silver has antibacterial properties, used in water purification and medical field. ^{109}Ag is used for the production of ^{109}Cd, ^{110}In, ^{110m}Ag radioisotopes. Standardly, ^{59}Co,^{115}In, ^{197}Au are used as neutron flux monitors [1], but the product nuclide of ^{197}Au has a short half-life of 2.69 days. For long irradiations ^{197}Au is not preferred, whereas the product nuclide of ^{109}Ag has a half-life of 249.83 days and it can be preferred for long irradiations. ^{109}Ag can be used as flux monitor [2]. ^{110m}Ag is produced by the neutron capture reaction of ^{109}Ag which go through β-decay back to the valley of stability and make stable nuclei i.e., ^{110}Cd. ^{110}Cd is used for the production of ^{110}In, ^{113m}In radioisotopes which are well known for multipurpose imaging and scanning. Therefore, we need to execute cross section measurement of ^{109}Ag(n,γ)^{110m}Ag reaction.

2. Experimental Details

The experiment was carried out at the Folded Tandem Ion Accelerator (FOTIA) Facility, Bhabha Atomic Research Centre (BARC), Mumbai. For neutron production, ^{7}Li(p,n)^{7}Be reaction is used. The proton beam of energies 2.5, 3.0, 3.6 MeV with an energy spread of 0.02 MeV were bombarded on a 3 mg/cm^2 thick lithium target. The beam current was 30 nA. The silver (i.e. the activation sample) and natural indium foil (i.e. the monitor sample) were prepared in three different sets covered in aluminium foil. They were of area 10 x 10 mm^2. After irradiation of 24 hours, they were cooled and then counted using high-purity germanium (HPGe) detector. The nuclear decay data of characteristic γ–ray energy was acquired from NuDat 3.0 [3].

3. Data Analysis and Theoretical Framework

The efficiency of the HPGe detector was calibrated at various characteristic γ-ray energies using a standard ^{152}Eu point source. It was calculated using the equation (1) in Ref. [4]. The efficiency of the point source was transferred to the sample using EFFTRAN [5]. We interpolated the detector efficiency for the characteristic γ-ray energy of the product radionuclides with their uncertainties and used them in calculation of cross section. The cross section we have used is as follows,

$$< \sigma_s >=< \sigma_m > \eta \frac{C_s N_m I_m f_m}{C_m N_s I_s f_s} \times \frac{N_{low(s)}}{N_{low(m)}} \frac{C_{attn(s)}}{C_{attn(m)}}, \quad (1)$$

where counts, number of atoms in the foil, intensity of the characteristic γ-ray energy, timing factor are represented by *C, N, I, f* for sample (s) and monitor (m), respectively. The measurement was completed using standard monitor reaction cross section of ^{115}In(n,n'γ)^{115m}In from IRDFF-1.05, data library [6]. For the correction of low background neutrons (N_{low}), we have used EPEN [7] and for the correction of self γ-ray attenuation (C_{attn}) we have used XMuDat [8]. We divided the fluxes provided by EPEN and then calculated the reference monitor cross section and their uncertainties for our interested energies [9,10]. After calculation of cross section, we performed covariance analysis to calculate the uncertainties [11,12]. The fractional uncertainties in the various parameters associated in the measured cross section are given in Table 1.

TALYS-1.96 [13] has been employed for the theoretical calculations of the reaction ^{109}Ag(n,γ)^{110m}Ag at 0.1 to 2 MeV. In the present investigation, six different level density models available in the TALYS-1.96 are used to reproduce nuclear reaction cross sections.

Table 1. Fractional uncertainties in various parameters associated in the measured ^{109}Ag(n,γ)^{110m}Ag reaction cross section

Parameters	Fractional Uncertainty (%)		
	$<E_n>$ = 0.53 MeV	**$<E_n>$ = 1.05 MeV**	**$<E_n>$ = 1.66 MeV**
C_s	3.8069	4.3478	11.3961
C_m	2.8903	1.0086	0.7897
N_s	0.0681	0.0781	0.0887
N_m	0.1592	0.1215	0.1340
f_s	0.0158	0.0158	0.0159
f_m	0.0073	0.0087	0.0106
I_s	0.0941	0.0941	0.0941
I_m	0.2178	0.2178	0.2178
η	3.0469	3.0469	3.0469
σ_m	4.3700	3.0600	2.8100
Total Error (%)	7.16	6.21	12.15

4. Results and Discussions

The measured $^{109}Ag(n,\gamma)^{110m}Ag$ reaction cross sections at 0.53 ± 0.15, 1.05 ± 0.16, 1.66 ± 0.14 MeV neutron energies with their uncertainties, covariance, and correlation matrix are listed in Table 2. We plotted our experimental cross sections with the evaluated data from TENDL-2019, IRDFF-II, JENDL/AD, IRDF-2002G and data taken from EXFOR in Fig. 1. with theoretical results acquired from TALYS-1.96. The total uncertainty is 6-12% in the studied cross section. The evaluated data libraries are indicated as solid black for TENDL-2019 (dot-dash-dot-dash), IRDFF-II (dash-dash), JENDL/AD (dot-dot), IRDF-2002G (line). The different ldmodels are represented as ldmodel 1 (red), ldmodel 2 (green), ldmodel 3 (olive), ldmodel 4 (yellow), ldmodel 5 (light magneta) and ldmodel 6 (violet). The experimental data is in trend with the evaluated data libraries TENDL-2019, JENDL/AD except the data point at 0.53 MeV neutron energy. The computational results by using ldmodel-6 are best in agreement with the present experimental data.

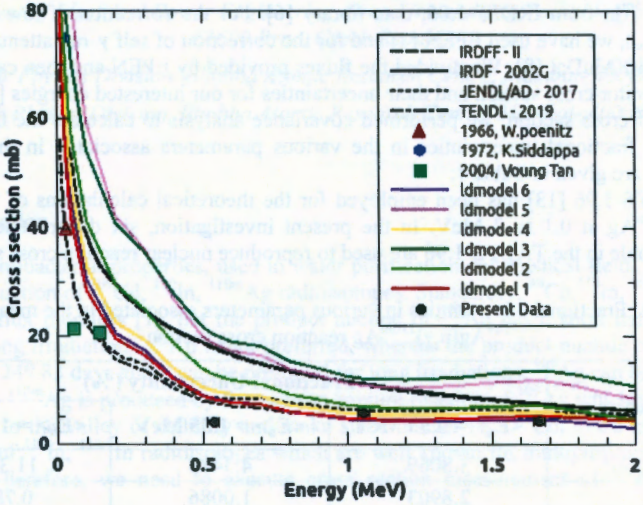

Fig.1. Cross sections measured in present work and its comparative studies.

Table 2. The $^{109}Ag(n,\gamma)^{110m}Ag$ cross sections measured in the present experiment with associated uncertainties and correlation coefficients

Energy (MeV)	Cross-section (mb)	Correlation Matrix		
0.53 ± 0.15	4.1063 ± 0.2941	1		
1.05 ± 0.16	5.7196 ± 0.3555	0.3018	1	
1.66 ± 0.14	4.2812 ± 0.5204	0.1387	0.1543	1

Acknowledgement

We would like to acknowledge FOTIA Facility staff, BARC for their cooperation in the experiment. One of the authors (A. Kumar) would like to thank Institutions of Eminence (IoE) BHU for the financial aid for this study.

References

1. R.B. Firestone *et al.,* Table of Isotop., 8th ed., (1995).
2. S. Nakamura *et al.*, J. Nucl. Sci. Tech. **40**, 119 (2003).
3. National nuclear data center, information extracted from the Nudat database, https://www.nndc.bnl.gov/nudat (2022).
4. M. Choudhary *et al.*, J. Phys. G: Nucl. Part. Phys. **50**, 015103 (2022).
5. T. Vidmar, Nucl. Inst. Methods in Phys. Res. Sect. A: Accel., Spectro., Detect. Assoc. Equip. **550**, 603 (2005).
6. E. Zsolnay, R. Capote, H. Nolthenius, and A. Trkov, International atomic energy agency technical report no, INDC (NDS)-0616 (2012).
7. R. Pachuau *et al.*, Nucl. Sci. and Engin. **187**, 70 (2017).
8. D. Millsap *et al.*, Appl. Radiat. Isotop. **97**, 21 (2015).
9. A. Gandhi *et al.,* Europ. Phys. J. Plus **136**, 819 (2021).
10. A. Gandhi *et al.*, Europ. Phys. J. A **57**, 1 (2021).
11. W. Mannhart, International Atomic Energy Agency Report No. INDC (NDS)-0588 (Rev.) (2013).
12. N. Otuka *et al.*, Radiat. Phys. Chem. **140**, 502 (2017).
13. A.J. Koning *et al.*, Internat. Conf. Nucl. Data for Sci. Tech. EDP Sciences, 211 (2007).

Properties of Compound States, Nuclear Structure, Fundamental Interactions

On the Significant Enhancement of the Stern–Gerlach Effect for Neutron, Diffracting in a Crystal at Bragg Angles Close to the Right One

V.V. Fedorov, V.V. Voronin, S.Yu. Semenikhin

NRC «Kurchatov Institute» – PNPI, Gatchina, Leningrad reg., Russia

A significant enhancement of any external force acting on a neutron during diffraction at Bragg angles close to $\pi/2$ is discussed for the case of Laue diffraction and detailed description of the effect is given. Such enhancement is due, on the one hand, to the smallness of the Darwin width compared to the Bragg angle, which leads to the well-known diffraction gain of about 10^5, and, on the other hand, to a significant slowing down of the neutron in the crystal at diffraction angles close to the right one, which can give an additional factor about 10^2 or more. Also discussed are the Kato trajectories for a diffracting neutron in a crystal and their "curvature" under the action of an external force. A simple derivation of Kato equations, describing these trajectories is given. As an example of such force we have considered the action on the neutron of a small gradient of the magnetic field. Taking into account the Bormann anomalous absorption effect, it is shown that the Stern–Gerlach effect will be clearly manifested for diffracting neutrons even in a weak magnetic field gradient. The effect amplification factor for a neutron in a crystal (at Bragg angle of 82°) can reach a value of 10^7 compared to a neutron in a "free" space (when the crystal is removed from the setup) in the same field gradient. Experimental results are demonstrated, they are in a good agreement with the theory.

1. In Laue diffraction of X-rays or particles by crystal there is a well-known and unusual amplification effect (see the review by Batterman and Cole [1], for example): small changes (within the Bragg width γ_B) in the angle between the wave vector **k**, of the incident radiation and the system of reflecting planes (i.e., the planes which are near the orientation satisfying the Bragg condition $\lambda = 2d \sin \theta_B$) alter the propagation directions of the rays (Bloch waves) in the crystal over a range θ_B which is much greater than the angle γ_B. The gain factor θ_B/γ_B can reach 10^5–10^6.

Such small deviation from the exact Bragg condition, which leads to significant change in direction of the diffracting ray in crystal, can be caused by a small elastic deformation [2] of the crystal or (for example, for neutrons) by the action of an external force (gravitational or magnetic, for example) [3]. Kato [2] has developed eikonal approach for Bloch waves to describe X-ray diffraction in distorted crystal. In two wave approximation he has got equations for two types of wave packets, propagating in crystal, analogous to those, describing the movement of relativistic "particles" under action of "Kato forces" of opposite direction, which curves the corresponding "Kato trajectories" of these two-wave packets (quasiparticles) in opposite directions. Later Zeilinger et al. [4] have interpreted this in a following way. The quasiparticles, corresponding to different kinds of Bloch waves have "effective masses" of opposite signs, and the enhancement of the external force, acting on neutrons (the large curvature of trajectories) is due to essential decreasing (by about 10^5–10^6 times) the quasiparticle effective masses[1)]. Authors [4] have measured the splitting of those neutron "trajectories" in the perfect crystal in magnetic field gradient. The effects for neutrons from both gravity and crystal deformation were discussed by Sumbaev [5] and measured [6].

Another important feature of Laue diffraction is the possibility of a significant slowing down of the neutron in the crystal by using Bragg angles close to $\pi/2$, since during diffraction the neutron moves on average along the crystallographic planes [7,8]. This velocity component determined by the Bragg angle can be significantly reduced at least by an order of magnitude, compared to the total neutron velocity. Thus, the residence time of the neutron in the crystal determined by namely this velocity component can be significantly increased. This was first noticed in [9] and proposed to be used to increase the effect of the electric dipole moment of a neutron on its diffraction in a non-centrosymmetric crystal. An experimental measurement of the time a neutron spends in crystal was carried out in [10,11].

A significant additional enhancement of the external effect on the diffracting neutron for Bragg angles θ_B close to the right angle was observed in the case of deformation of the crystal by a temperature gradient [12]. The new method to measure a neutron electric charge and the ratio of inertial to gravitational masses has been proposed [13] based on this magnification. The estimations have shown a feasibility to improve the accuracy of a neutron electric charge measurement by about two orders of magnitude in comparison with the current value, and to measure the ratio of inertial to gravitational masses m/m_G with the accuracy $\sim 10^{-6}$.

Here we give a simple derivation of the Kato equations for large Bragg angles using an explicit form of expressions for the neutron probability current density in a crystal (unlike Kato, who obtained his equations based on the dispersion surface equation for X-ray or particle in a crystal, using the normal direction of the energy flow in the crystal to the dispersion surface).

As an example of the mentioned amplification, we will consider the spatial splitting of an unpolarized neutron beam into two polarized beams (with opposite spin directions) during Laue diffraction at large Bragg angles in a crystal located in a small magnetic field gradient (analogous to the Stern–Gerlach effect). Note that, in contrast, the authors [4] observed the splitting of an unpolarized neutron beam into two also unpolarized beams.

2. Next, we will consider diffraction in a symmetrical Laue scheme (the crystal boundary is perpendicular to the reflecting planes, see Fig.1), in an ideal, non-absorbing, thick crystal at large diffraction angles (i.e. close to 90°).

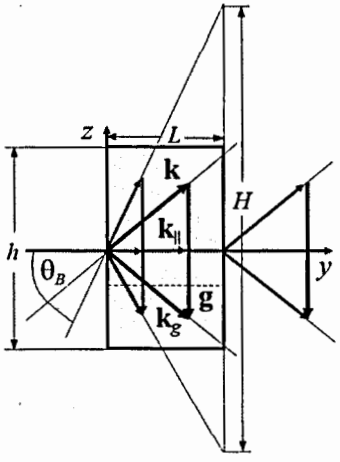

Fig.1. Symmetrical Laue diffraction scheme. L is a crystal thickness, h is its height, H is the length of the Bormann triangle base (shown for large Bragg angle, in this case $H > h$). $\mathbf{g}$ is a reciprocal lattice vector, characterizing the system of the reflecting planes. Vector $\mathbf{g}$ is perpendicular to them and its magnitude $g = 2\pi/d$, where d is interplanar distance, $\mathbf{k}$ is wave vector of the direct neutron wave in the crystal, $\mathbf{k}_g = \mathbf{k} + \mathbf{g}$ is that of the reflected wave. The equality $|\mathbf{k}_g| = |\mathbf{k}|$ is the exact Bragg condition, which is equivalent to the well-known expression $\lambda = 2d \sin\theta_B$.

What do these mean?

1. "Perfect" means that the mosaicity of a crystal much less, than the Bragg (Darwin) diffraction width.
2. "Non-absorbing" means that absorption length is more than the crystal thickness and much more than extinction length.
3. "Thick" means crystal thickness (~ 20 cm in our case) is much more than extinction length.
4. "Large diffraction angles" means $\theta_B = 78^\circ$–82°, $\tan\theta_B = 4.7$–7.1 (for example, $\tan 87^\circ = 19$).

The nuclear potential of the system of reflecting planes **g** responsible to diffraction has the form:

$$V_{\mathbf{g}}(\mathbf{r}) = V_0 + 2V_g \cos \mathbf{gr}, \tag{1}$$

where V_0 is the average nuclear potential of the crystal, $V_{\mathbf{g}}$ is the amplitude of the **g**-harmonic of the periodic crystal potential, which describes the reflecting planes. This potential can only transfer the momenta equal to 0 and $\pm\hbar\mathbf{g}$.

3. Let the neutron beam fall on the crystal at the Bragg angle (see Fig. 1). It is known from the theory of dynamic diffraction (see, for example [1,14]), that two types of Bloch waves $\psi^{(1)}$ and $\psi^{(2)}$ will be exited in the crystal in this case. They are symmetric and antisymmetric:

$$\psi^{(1)} = \frac{1}{\sqrt{2}}\left[e^{i\mathbf{k}^{(1)}\mathbf{r}} + e^{i\left(\mathbf{k}^{(1)}+\mathbf{g}\right)\mathbf{r}}\right] = \sqrt{2}\cos\left(\frac{\mathbf{gr}}{2}\right)e^{i\left[\left(\mathbf{k}^{(1)}+\frac{\mathbf{g}}{2}\right)\mathbf{r}\right]} \equiv \sqrt{2}\cos\left(\frac{\mathbf{gr}}{2}\right)e^{i\mathbf{k}_{\parallel}^{(1)}\mathbf{r}}, \tag{2}$$

$$\psi^{(2)} = \frac{1}{\sqrt{2}}\left[e^{i\mathbf{k}^{(2)}\mathbf{r}} - e^{i\left(\mathbf{k}^{(2)}+\mathbf{g}\right)\mathbf{r}}\right] = -i\sqrt{2}\sin\left(\frac{\mathbf{gr}}{2}\right)e^{i\left(\mathbf{k}^{(2)}+\frac{\mathbf{g}}{2}\right)\mathbf{r}} = -i\sqrt{2}\sin\left(\frac{\mathbf{gr}}{2}\right)e^{i\mathbf{k}_{\parallel}^{(2)}\mathbf{r}}. \tag{3}$$

The wave vectors $\mathbf{k}^{(1)}$ and $\mathbf{k}^{(2)}$ belong to two branches of the dispersion surface:

$$k^{(1,2)2} = K^2 + \Delta_g \mp \sqrt{\Delta_g^2 + \left|U_g\right|^2} \xrightarrow{\Delta_g << U_g} K^2 \mp \left|U_g\right| \tag{4}$$

Here k_0 is the wave vector of the incident neutron, and K is the same vector with the average refractive index of the crystal, taking into account:

$$K^2 \equiv n^2 k_0^2 = k_0^2 - U_0,\ U_{0,g} \equiv 2mV_{0,g}/\hbar^2. \tag{5}$$

The parameter

$$\Delta_g = \left(k_g^2 - k^2\right)/2 \equiv \left[\left(\mathbf{k}+\mathbf{g}\right)^2 - k^2\right]/2 = \left(2\mathbf{kg} - g^2\right)/2 \tag{6}$$

describes the deviation from the exact Bragg condition.

As a result, we see that in the case of $\Delta_g = 0$, neutrons in the states (1) and (2) will propagate in the crystal along the crystallographic planes with the slightly different wave vectors (see Fig. 2)

$$\mathbf{k}_{\parallel}^{(1,2)} = \mathbf{k}^{(1,2)} + \mathbf{g}/2, \tag{7}$$

because neutrons in state (1) are concentrated mainly on nuclear planes (at the maxima of the nuclear potential (1)), and in state (2) they are concentrated between them (at the minima of the nuclear potential).

Indeed,

$$|\psi^{(1)}|^2 = 2\cos^2(\mathbf{gr}/2) = 1+\cos(\mathbf{gr}), \tag{8}$$

$$|\psi^{(2)}|^2 = 2\sin^2(\mathbf{gr}/2) = 1-\cos(\mathbf{gr}). \tag{9}$$

Thus, neutrons in states (1) and (2) move in slightly different potentials and therefore have different kinetic energies (respectively, different values of wave vectors and velocities $v_{\parallel}^{(1)} < v_{\parallel}^{(2)}$), which reflects the presence of two branches of the dispersion surface of neutron in the crystal. The neutron velocities themselves are approximately equal

$$v_{\parallel}^{(1)} \approx v_{\parallel}^{(2)} \approx v_{\parallel} = \frac{\hbar k_{0\parallel}}{m} = v_0 \cos\theta_B \approx v_0\left(\frac{\pi}{2}-\theta_B\right) << v_0 \text{ at } \theta_B \approx \frac{\pi}{2}. \tag{10}$$

We pay attention that for Bragg angles, close to the right angle, the velocity component along the planes can be significantly less then the total neutron velocity.

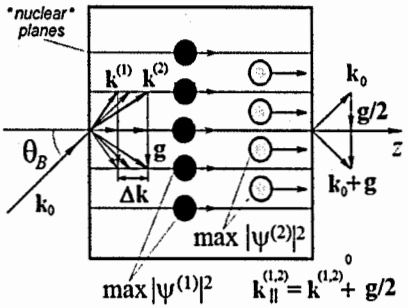

Fig. 2. Symmetrical Laue diffraction scheme. $|\mathbf{k}_g| = |\mathbf{k}|$ (the exact Bragg condition). Neutrons in symmetric (dark circles) and antisymmetric (light circles) states (1) and (2) propagate in the crystal along reflecting nuclear planes with slightly different wave vectors, concentrating on or between the planes.

The difference of wave vectors in a crystal for the exact Bragg condition $\mathbf{k}_0^2 = |\mathbf{k}_0+\mathbf{g}|^2$ is easily calculated, using the equation of the dispersion surface (4):

$$\mathbf{k}^{(2)2} - \mathbf{k}^{(1)2} = 2\mathbf{k}_0\Delta\mathbf{k} = 2k_0\Delta k\cos\theta = 2|U_g|, \tag{11}$$

and

$$\Delta k = \frac{|U_g|}{k_0\cos\theta} = \frac{2|V_g|}{\hbar v\cos\theta}. \tag{12}$$

Thus, the difference $|\Delta\mathbf{k}|$ contains the angle θ between $\mathbf{k}_0$ and $\Delta\mathbf{k}$. The vector $\Delta\mathbf{k}$ is normal to the crystal boundary, therefore in the case of symmetric Laue diffraction this angle coincides with the Bragg angle: $\theta = \theta_B$.

The interference of waves (1) and (2) in the crystal leads to periodic dependence of the intensities of diffracted beams (direct and reflected) on the thickness of the crystal or the Bragg angle (the so-called Pendellösung fringe). The phase difference that determines these intensity oscillations after passage through a crystal of thickness L is equal to:

$$\Delta\phi = \Delta kL = \frac{|U_g|L}{k_0\cos\theta_B} = \frac{2|V_g|}{\hbar}\frac{L}{v\cos\theta_B}. \tag{13}$$

The value $\xi_g \equiv 2\pi/\Delta k$ is the extinctio the time the neutron s n length. The value $L/v\cos\theta_B$ in the expression (13) is pends in crystal.

4. The different symmetry of the waves in the crystal leads to another, so called, Bormann effect. This is the effect of abnormal crystal transparency (or abnormal absorption) for waves passing through the crystal under the Bragg conditions. The effect is due to the fact that the wave (1) concentrated on the planes (atoms) is absorbed stronger than the wave (2) concentrated between them.

Neutron absorption in a crystal can be described by adding an imaginary part to the potential ($-iV'$), $V'(\mathbf{r}) <<< V(\mathbf{r})$ is real and positive. It also decomposes into harmonics. As a result, for exact Bragg condition, we will get

$$\mathbf{k}^{(1,2)2} = k_0^2 - U_0 + iU_0' \mp \left(U_g - iU_g'\right) = \mathbf{k}_0^2 - \left(U_0 \pm U_g\right) + i\left(U_0' \pm U_g'\right), \qquad (14)$$

where $U_{0,g}' \equiv 2mV_{0,g}'/\hbar^2$, $V_{0,g}'$ are corresponding harmonics of an imaginary part of the nuclear potential. So

$$\Delta k^{(1,2)} \equiv \left|\mathbf{k}^{(1,2)} - \mathbf{k}_0\right| = \frac{-\left(U_0 \pm U_g\right) + i\left(U_0' \pm U_g'\right)}{2k_0 \cos\theta_B}, \qquad (15)$$

and Bloch waves (1), (2) will damp with different absorption lengths, so that

$$\left|\psi^{(1,2)}\right|^2 = \left|\psi_0^{(1,2)}\right|^2 e^{-\frac{\left(U_0' \pm U_g'\right)L}{k_0 \cos\theta_B}} \equiv \left|\psi_0^{(1,2)}\right|^2 e^{-\frac{\mu_0\left(1 \pm \varepsilon_g\right)L}{\cos\theta_B}}. \qquad (16)$$

Here

$\varepsilon_g = \dfrac{V_g'}{V_0'}$, $\mu_0 \equiv \dfrac{1}{L_a} = \dfrac{U_0'}{k_0} = k_0 \dfrac{2mV_0'}{\hbar^2 k_0^2}$ is an average damping index, L_a is the corresponding absorption length. For example, for neutrons, moving in silicon (Si), $L_a \sim 40$ cm. For thermal and cold neutrons in a monoatomic crystal, due to the small size of the nucleus, all harmonics are practically the same, so ε_g can be close to 1. As follows from (16), at sufficiently large Bragg angles, a symmetric Bloch wave can be completely absorbed, while for an antisymmetric wave the crystal will be practically transparent.

5. In the general case $\left(\Delta_g \neq 0\right)$ the neutron wave functions in two wave approximation can be written as

$$\psi^{(1)}(\mathbf{r}) = \cos\gamma e^{i\mathbf{k}^{(1)}\mathbf{r}} + \sin\gamma e^{i\left(\mathbf{k}^{(1)}+\mathbf{g}\right)\mathbf{r}}, \qquad (17)$$

$$\psi^{(2)}(\mathbf{r}) = -\sin\gamma e^{i\mathbf{k}^{(2)}\mathbf{r}} + \cos\gamma e^{i\left(\mathbf{k}^{(2)}+\mathbf{g}\right)\mathbf{r}}. \qquad (18)$$

Here

$\tan 2\gamma = \dfrac{U_g}{\Delta_g} \equiv \dfrac{1}{w_g}$, $w_g = \dfrac{\Delta_g}{U_g} = \dfrac{\left(k_g^2 - k^2\right)}{2U_g} = \dfrac{\left(2\mathbf{kg} + g^2\right)}{2U_g}$ is the dimensionless parameter of the deviation from the exact Bragg condition, so we have

$$\sin^2\gamma = \frac{1}{2}\left[1 - \frac{w_g}{\sqrt{1+w_g^2}}\right], \quad \cos^2\gamma = \frac{1}{2}\left[1 + \frac{w_g}{\sqrt{1+w_g^2}}\right]. \qquad (19)$$

Averaging over fast oscillations with the period d the expression for the current density

$$\mathbf{j}^{(1,2)} = \frac{\hbar}{2mi}\left(\psi^{(1,2)*}\nabla\psi^{(1,2)} - \psi^{(1,2)}\nabla\psi^{(1,2)*}\right) = \frac{\hbar}{m}\mathrm{Im}\ \psi^{(1,2)*}\nabla\psi^{(1,2)}, \tag{20}$$

we get for two kinds of waves

$$\mathbf{j}^{(1)} = \frac{\hbar}{m}\left[\mathbf{k}^{(1)}\cos^2\gamma + \left(\mathbf{k}^{(1)}+\mathbf{g}\right)\sin^2\gamma\right] = \frac{\hbar}{m}\left[\left(\mathbf{k}^{(1)}+\frac{\mathbf{g}}{2}\right) - \frac{\mathbf{g}}{2}\frac{w_g}{\sqrt{1+w_g^2}}\right], \tag{21}$$

$$\mathbf{j}^{(2)} = \frac{\hbar}{m}\left[\mathbf{k}^{(2)}\sin^2\gamma + \left(\mathbf{k}^{(2)}+\mathbf{g}\right)\cos^2\gamma\right] = \frac{\hbar}{m}\left[\left(\mathbf{k}^{(2)}+\frac{\mathbf{g}}{2}\right) + \frac{\mathbf{g}}{2}\frac{w_g}{\sqrt{1+w_g^2}}\right]. \tag{22}$$

At the exact Bragg condition (w_g= 0) the neutron current densities $\mathbf{j}^{(1)}$ and $\mathbf{j}^{(2)}$ are parallel to the planes (z axis in Fig. 3) , so waves (1) and (2) will move along the planes in the crystal.

If $w_g \neq 0$, then the neutron currents (1) and (2) will diverge in opposite directions (Fig. 3).

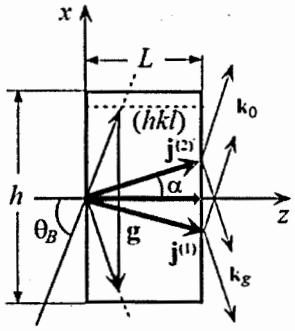

Fig. 3. The bold horizontal arrow gives the directions of the neutron current densities $\mathbf{j}^{(1)}$ and $\mathbf{j}^{(2)}$ for the exact Bragg condition w_g= 0. If $w_g \neq 0$, then the neutron currents $\mathbf{j}^{(1)}$ and $\mathbf{j}^{(2)}$ are deflected by an angle α in the opposite direction.

Kato trajectories are defined as the lines tangent to which coincide with the directions of the current density at each point. In the case of undeformed crystal and absence of the external forces, they are straight lines as shown in Fig. 3. If neutrons fall on the crystal with a small deviation from the Bragg angle, they diverge in opposite directions.

If the incident wave is a wave packet limited, for example, by an entrance slit, then the Kato trajectory will describe the movement of this packet in the crystal (this is correct, if the size of such two waves packet (slit width) is significantly larger than the extinction length).

If $w_g \neq 0$, then the neutron currents (1) and (2) will diverge, so that for a certain thickness of the crystal and finite width of the packets they cease to overlap and will reach the exit surface of the crystal in different points (Fig. 3.).

If deviation from the Bragg angle is small (within the Bragg width, that is w_g<<1), then $\mathbf{j}^{(1)}$ and $\mathbf{j}^{(2)}$ will have a simple form:

$$\mathbf{j}^{(1,2)} \approx \frac{\mathrm{h}}{m}\left[\mathbf{k}_{\parallel}^{(1,2)} \pm \frac{\mathbf{g}}{2}\frac{\Delta_g}{|U_g|}\right] \equiv \frac{\mathrm{h}}{m}\left[\mathbf{k}_{\parallel}^{(1,2)} \pm w_g\frac{\mathbf{g}}{2}\right]. \tag{23}$$

Note that $g/2k_{\mathrm{P}}^{(1,2)} \approx \tan\theta_B$, so the angles α of the slopes of the Kato trajectories for neutrons in states (1) and (2) are determined by $\tan\alpha = \mp w_g \tan\theta_{\mathrm{B}}$.

Also, it is important that in the symmetric Laue scheme waves $\psi^{(1)}$ and $\psi^{(2)}$ (see (17) and (18)) are excited in the crystal with the amplitudes, respectively, $\cos\gamma$ and $-\sin\gamma$ (see [14], for example). Therefore, for small deviations from the Bragg condition, i.e. for $w_g \ll 1$ the both states are excited in the crystal with almost the same probability 1/2, because

$$\cos^2\gamma = \frac{1}{2}\left(1+w_g\right) \approx \frac{1}{2}, \text{ and } \sin^2\gamma = \frac{1}{2}\left(1-w_g\right) \approx \frac{1}{2}.$$

However, at the same time, the directions of the currents (especially at Bragg angles θ_B close to 90°, when $k_\parallel \ll g/2$ and so $\tan\theta_B = g/2k_\parallel \gg 1$) can change very significantly, see (23). As we already have mentioned, the slopes of the Kato trajectories are determined by

$$\frac{dx}{dz} = \tan\alpha \approx \mp w_g \tan\theta_B, \tag{24}$$

from where follows

$$w_g \approx \frac{\tan\alpha}{\tan\theta_B} \equiv \frac{L\tan\alpha}{L\tan\theta_B}. \tag{25}$$

We see, that the deviation parameter has a simple meaning of the ratio of the coordinate $x = L\tan\alpha$ of the exit point of the Kato trajectory from the crystal to half the length of the base of the Bormann triangle (fan) $L\tan\theta_B$ (see Fig. 1, Fig. 3).

6. Thus, at diffraction angles close to 90°, even a small change in the parameter w_g will lead to a significant change in the direction of the neutron current. If an external force acts on the neutron, the parameter w_g will constantly change, so the trajectories will be curved, and for different types of Bloch waves they will diverge in opposite directions.

The change in the slope of the $x(z)$ curve, describing the Kato trajectory, will be determined by the expression

$$\frac{d^2x}{dz^2} = \mp\tan\theta_B \frac{dw_g}{dz} = \mp\frac{c_0}{v_\parallel}\frac{dw_g}{dt} \quad \left(c_0 \equiv \tan\theta_B\right). \tag{26}$$

Consider the action of a constant external force **F** on a neutron in a perfect undeformed crystal. Only the force component F_x along the vector **g** (x axis) leads to a change in the deviation parameter w_g. The force components parallel to the planes (along the y and z axes) do not change it. In this case the derivative of w_g is easily calculated

$$\frac{dw_g}{dt} = \frac{d}{dt}\frac{\left(2\mathbf{kg}+g^2\right)}{2U_g} = \frac{gdk_x}{U_g dt} = \frac{2m_n v_\perp}{\hbar^2 U_g}F_x = \frac{v_\perp}{V_g}F_x. \tag{27}$$

Here we used

$$v_\perp \equiv \frac{\hbar g}{2m_n}\left(v_\perp \approx v_{0x}, v_\parallel = v_{0z}, v_\parallel << v_\perp\right), \quad \frac{dk_x}{dt} \equiv \frac{m_n}{\hbar}\frac{dv_x}{dt} = \frac{F_x}{\hbar}.$$

Finally, the equation for Kato trajectories will be

$$\frac{d^2x}{dz^2} = \mp\frac{c_0}{v_\parallel}\frac{v_\perp}{V_g}F_x = \mp c_0^2\frac{F_x}{V_g} \equiv \mp c_0^2\frac{E_n}{V_g}\frac{F_\perp}{E_n}, \tag{28}$$

where $v_\perp / v_\parallel = c_0$, $F_x \equiv F_\perp$.

The classical Newton's equation for the neutron trajectory in the vacuum under the action of an external force $F_\perp$ directed perpendicular to its velocity is

$$m_n v^2 \frac{d^2x}{dz^2} = F_\perp, \quad \text{that is} \quad \frac{d^2x}{dz^2} = \frac{F_\perp}{2E_n}. \tag{29}$$

Thus, the equation for Kato trajectories can be rewritten as

$$\frac{d^2x}{dz^2} = \mp K_D \frac{F_\perp}{E_n}, \quad K_D = \frac{2c_0^2 E_n}{V_g} \equiv K_{0D} \tan^2 \theta_B. \tag{30}$$

Here $K_{0D} = 2E_n/V_g$ is the usual well known coefficient of the diffraction enhancement, $\tan^2 \theta_B$ describes an additional essential enhancement of the force action, it is associated with an increase of time the neutron spends in the crystal. We see that the effect of the force, due to diffraction in crystal, is increased many times compared to the "empty" space, and the total coefficient of such diffraction enhancement is K_D.

For example, for a system of planes (220) of a silicon crystal with an interplane distance d = 1.92 Å, which is often used in diffraction experiments with neutrons ($E_n = 5.5 \cdot 10^{-3}$ eV, $V_g = 5.2 \cdot 10^{-8}$ eV) the value of the total diffraction gain is:

$$K_{D(\mathrm{Si})}^{220} = 2.1 \cdot 10^5 \tan^2 \theta_B. \tag{31}$$

Already at the Bragg angle $\theta_B \sim 82^\circ$ ($c_0 = 7.1$) the value of K_D is $\sim 10^7$. For $\theta_B \sim 88^\circ$ ($c_0 \sim 30$) it will be $\sim 2 \cdot 10^8$, that is 3 orders more than the usual diffraction enhancement coefficient.

7. Experiment on observation of diffraction enhancement of the Stern–Gerlach effect for neutron was carried out [15,16] at the PF1B neutron beam of the ILL high flux reactor (Grenoble, France). Neutrons were deflected in a small gradient of the magnetic field. In an inhomogeneous magnetic field inside the crystal, forces of opposite direction will act on the neutrons with opposite spin projections (along and against the field) (as in the Stern–Gerlach experiment). Only the force components perpendicular to the planes along the vector **g** (x axis) lead to a change in the direction of the Kato trajectory:

$$F_\perp^{(\pm)} = \mp \mu_n \frac{\partial B}{\partial x} \approx \mp 6 \cdot 10^{-12} \left[\frac{\mathrm{eV}}{\mathrm{G}}\right] \frac{\partial B}{\partial x}\left[\frac{\mathrm{G}}{\mathrm{cm}}\right] \equiv \mp F_w. \tag{32}$$

In our case $\partial B / \partial x \approx 3$ G/cm, so $F_w \sim 2 \cdot 10^{-11}$eV/cm.

The schematic diagram of the experiment is shown in Fig. 4. Two identical crystals are placed in an inhomogeneous magnetic field (Fig. 5). More detailed description see [15,16].

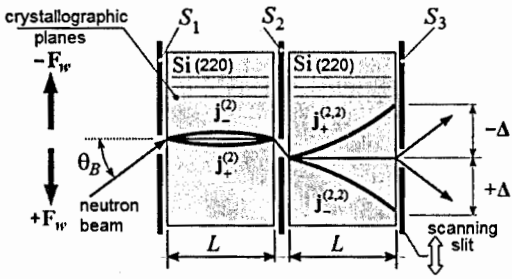

Fig. 4. A double crystal scheme of Laue diffraction with direct neutron beam collimation. $\pm\mathbf{F}_w$ are forces acting on different components (along and against the direction of the magnetic field gradient) of the neutron spin. S_1, S_2 are collimating slits, S_3 is scanning slit, $\pm\Delta$ are displacements of the scanning slit for neutron registration. Kato trajectories for different spin projections are shown in both silicon (Si) crystals.

Nonpolarized neutron beam with a monochromaticity of $\Delta\lambda/\lambda \sim 10^{-2}$ after the monochromator (neutron wave length can be tuned within a range of λ = (3.5–3.9) Å) is impinging the entry face of the probing silicon crystal having dimensions of 130×130×218 mm^3. In the experiment the (220) diffraction planes with an interplane spacing of d = 1.92Å were used. The maximum variation of lattice spacing over the entire crystal volume is in the order of $\Delta d/d \sim 10^{-7}$. To obtain a two-crystal geometry, the Si crystal has a cut in the middle with a depth of 72 mm and a width of 1.6 mm, see Fig. 6.

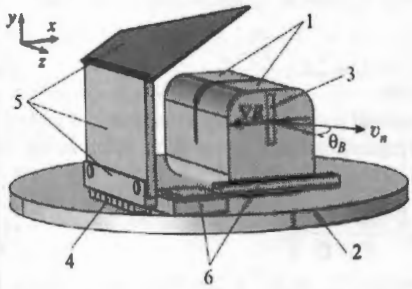

Fig. 5. The design of a magnetic system for creating a magnetic field gradient in a crystal. 1 – silicon crystal, 2 – rotation stage (also part of field guide), 3 – neutron beam exit area, 4 – permanent magnets, 5 – magnetic field guide, 6 – piezo motor for exit slit S_3.

Fig. 6. Silicon probing crystal.

Note, that in our case (large crystal thickness and Bragg angle, i.e. $L_{\text{eff}} = L \tan\theta_B >> L_a$, in both crystals only antisymmetric weakly absorbed waves (2) for both spins "survive". The corresponding Kato trajectories will deviate in different directions (see Fig. 4).

The slits S_1 and S_2 (at x = 0) separate in the first crystal the trajectories of neutrons, which bent in a certain way under the action of forces (set the initial slopes for 2 spin projections). In the absence of forces, these would be trajectories with zero inclination (parallel to the planes, i.e. the z axis) of neutrons falling on the crystal exactly at the Bragg angle.

The presence of an external force will bend these trajectories, so only neutrons falling on the first crystal with fixed (opposite for opposite spins) parameters of deviation can pass through the second slit.

Thus, these slits determine the initial angles of inclination of the trajectories $\pm\alpha_0$. They can be found from the trajectory equations (30) with the boundary condition $x(0) = x(L) = 0$. As a result, in the first crystal these trajectories corresponding to neutrons with opposite polarizations will be described by the curves

$$x^{\pm}(z) = \pm\frac{c_0^2 F_w}{2V_g}(L-z)z. \tag{33}$$

In the second crystal, these trajectories will start at opposite angles of inclination, so that the forces will continue to bend them in the same direction ($z' = z - L$):

$$x^{\pm}(z') = \pm\frac{c_0^2 F_w}{2V_g}(L+z')z'. \tag{34}$$

As a result, on the exit face of the second crystal, the trajectories of neutrons with different polarizations will shift to

$$x^{\pm}(2L) = \pm\frac{c_0^2 F_w}{V_g} L^2, \tag{35}$$

so, in such a scheme with direct collimation of the beam, the effect of two crystals (of thickness L) doubles (the effect for one crystal in the case of doubling its thickness is quadrupled). The distance between the trajectories at the exit face of the second crystal (splitting) will be equal to

$$\Delta_{2L} = \frac{2c_0^2 F_w}{V_g} L^2 \equiv \frac{4c_0^2 E_n}{V_g} \frac{F_w}{2E_n} L^2 = 2K_D \frac{F_w}{2E_n} L^2. \tag{36}$$

Note that the sensitivity of this experiment to external force acting on a neutron in a crystal is determined by the magnitude of the force F_w required to shift the neutron beam at the exit from the second crystal by the width of the third slit δ_{S3}:

$$F_\delta = \frac{V_g}{2c_0^2 E_n} \frac{2E_n}{L^2} \delta_{S3} = \frac{1}{K_D} \frac{2E_n}{L^2} \delta_{S3}. \tag{37}$$

Here K_D is the diffraction gain coefficient, the value $(2E_n\,\delta_{S3})/L^2$ is the force perpendicular to the direction of motion of the neutron and necessary for its displacement by δ_{S3} in vacuum. We noted already that $K_{D(\mathrm{Si})}^{220} = 2\cdot 10^5 \tan^2\theta_B$, which can reach $\sim 10^7$ for Bragg angle of 82°.

Measurements [15,16] were carried out for Bragg angles θ_B from 78° to 82°. The minimum sizes of collimating slits (δ_{S1}= 17 mm, δ_{S2} = 15 mm, δ_{S3} = 18 mm) were selected to obtain sufficient statistical accuracy during a limited time of the experiment.

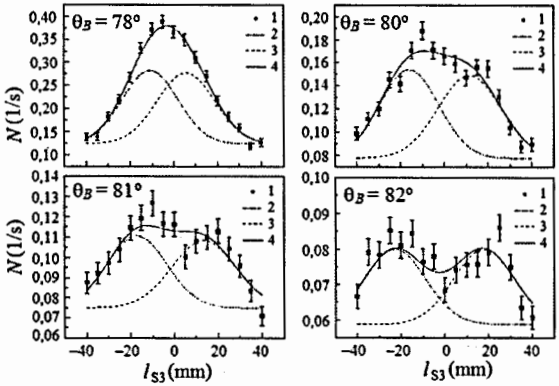

Fig. 7. Intensity distributions at the exit of the probing crystal for a maximum field gradient in the vicinity of the neutron beam for different angles θ_B = (78–82)° (l_{S3} is the position of the scanning slit S_3).

At a maximum angle of 82°, the splitting value is $\Delta_{\mathrm{exp}} = (4.1 \pm 0.1)$ cm. Using the data from Fig. 7, and expr. (36) we can extract the value of the field gradient (open circles in Fig. 8):

$$\nabla B \equiv \frac{\partial B}{\partial x} = \frac{E_n}{\mu_n K_{D(\mathrm{Si})}^{220} L^2} \Delta_{\mathrm{exp}}. \tag{38}$$

The average value of the magnetic field gradient over the neutron beam in the experiment turned out to be $\nabla B_{\mathrm{av}} = (3.12 \pm 0.09)$ G/cm, which is consistent with estimates based on

magnetometer readings at three points on each side (entrance and exit) of the crystal, which gave the value (3.0 ± 0.3) G/cm, see [17].

The calculation of the spatial splitting of a neutron beam with a wavelength λ = 3.8 Å, $E_n \approx 5.5$ meV (which corresponds to $\theta_B = 82°$), in free space when passing the same distance (21.8 cm) in the same magnetic field gradient through the same 3-slit collimator, but without a crystal (removed from the installation) gives $3.9 \cdot 10^{-7}$ cm. To split by 4.1 cm, the beam must travel ~ 900 m!

Thus, the experimentally measured coefficient of diffraction enhancement is equal $K^{220}_{D(\mathrm{Si})\mathrm{exp}} \approx 2.1 \cdot 10^5 \tan^2\theta_B \approx 1.05 \cdot 10^7$, at $\theta_B = 82°$, which is in good agreement with the theory.

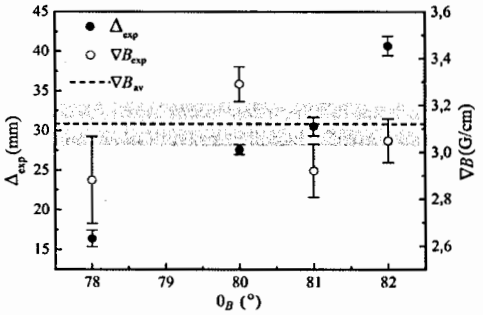

Fig. 8. The dependences of the distance Δ_{exp} between the intensity maxima for two spin projections (Fig. 7) and the field gradient on the Bragg angle. Dotted line is the average value of the magnetic field gradient.

8. Based on the count rates in this experiment [15,16], it is possible to estimate its sensitivity (the error in measuring the external force) achieved per day:

$$\sigma(F_{\mathrm{ext}}) \approx 2 \cdot 10^{-12} \frac{\mathrm{eV}}{\mathrm{cm} \cdot \mathrm{day}} = 2 \cdot 10^{-3} m g_E \frac{1}{\mathrm{day}}, \tag{39}$$

where g_E is the acceleration of gravity near the Earth's surface. The use of cold neutron sources, such as the planned for PIK reactor with a spectral neutron flux density of ~ $5 \cdot 10^8$ n/Å·cm^2·c, makes it possible to use slits ~ 0.1 mm in size and Bragg angles up to 88° , while the neutron count rate from one exit slit can reach 50 n/s, which results in an improvement in sensitivity by about 12 000 times. An additional increase in sensitivity by an order of magnitude, for example, can be obtained by using a multi-slit (100 slits) version of the installation. Thus, in principle, sensitivity can reach the level:

$$\sigma(F_{\mathrm{ext}}) \approx 1.7 \cdot 10^{-17} \frac{\mathrm{eV}}{\mathrm{cm} \cdot \mathrm{day}} = 1.7 \cdot 10^{-8} m g_E \frac{1}{\mathrm{day}}. \tag{40}$$

The attraction force of a neutron by the Sun in the Earth's orbit is

$$F_{GS} = G \frac{m_G M_S}{R_O^2} = 6 \cdot 10^{-13} \mathrm{eV/cm} \approx 6 \cdot 10^{-4} m g_E, \tag{41}$$

where m_G and M_S are the gravitational masses of the neutron and Sun, R_O is the radius of the Earth's orbit around the Sun (m is the inertial mass of neutron).

So, there is a good possible application of such installation to measuring the ratio of the inertial and gravitational masses of the neutron. With the sensitivity (40) for 100 days of measurements, one can obtain an error in measuring the ratio m/m_G, better than the current value [17], approximately by two orders of magnitude, more detailed see [18].

Footnote

[1] The fact itself that an electron in a crystal has effective masses of opposite signs near the boundaries of Brillouin zones, where its dispersion curve has gaps, is well known, see, for example the textbook by G.S. Zhdanov "Solid state physics". Moscow University Press, 1962 (in Russian).

References

1. Batterman B.W., Cole H. Dynamical diffraction of X-ray by perfect crystals. Rev. Mod. Phys., 1964, **36**, 681–717.
2. Kato N. Pendellösung fringe in distorted crystals.
   I. Fermat's principle for Bloch waves. J. Phys. Soc. Jap., 1964, **18**, 1785–1791;
   II. Application to two beam cases. J. Phys. Soc. Jap., 1964, **19**, 67–77;
   III. Application to homogeneously bend crystals. J. Phys. Soc. Jap., 1964, **19**, 971–985.
3. Werner S.A. Gravitational and magnetic field effects on the dynamical diffraction of neutrons. Phys. Rev., 1980, **B 21**, 1774–1789.
4. Zeilinger A., Shull C.G., Horne M.A., Finkelstein K.D. Effective mass of neutrons diffracting in crystals. Phys. Rev. Lett., 1986, **57**, 3089–3092.
5. Sumbaev O.I. Interference effects due to gravity a magnetic field gradient or Earth's rotation in neutron diffraction by an elastically bent single crystal. Preprint LIYaF-676, Leningrad, 1981, 13p.
6. Alekseev V.L., Lapin E.G., Leushkin E.K., Rumyantsev V.L., Sumbaev O.I., Fedorov V.V. Gravitational effect in neutron diffraction by a curved quartz single crystal. Sov. Phys. JETP, 1988, **67** (8), 1727–1733,
7. Fedorov V.V., Smirnov A.I. Properties of electromagnetic radiation emitted by an electron diffracted in a single crystal. Sov. Phys. JETP, 1974, **39**, No.2, 271–274.
8. Shull C.G., Zeilinger A., Squires G.L., Horne M.A., Atwood D.K., Arthur J. Anomalous flight time of neutrons through diffracting crystals. Phys. Rev. Lett., 1980, **44**, 1715–1718.
9. Fedorov V.V., Voronin V.V., Lapin E.G. On the search for neutron EDM using Laue diffraction by a crystal without a centre of symmetry. Preprint LNPI-644. Leningrad,1990, 36 p; J. Phys.,1992, **G 18**, 1133–1148.
10. Voronin V.V., Lapin E.G., Semenikhin S.Yu., Fedorov V.V. Direct measurement of the delay time for a neutron in a crystal in the case of the Laue diffraction. JETP Lett., 2000, **71**, 76–79.
11. Fedorov V.V., Lapin E.G., Semenikhin S.Yu., Voronin V.V. First observation of new effects at the set-up for searching for a neutron electric dipole moment by a crystal-diffraction method. Appl. Phys., 2002, **A 74**, Suppl. 1, 298–301.
12. Fedorov V.V., Kuznetsov I.A., Lapin E.G., Semenikhin S.Yu., Voronin V.V. Neutron Laue diffraction in a weakly deformed crystal at the Bragg angles close to $\pi/2$. JETP Lett., 2007, **85**, No.1, 82–85.
13. Fedorov V.V., Kuznetsov I.A., Lapin E.G., Semenikhin S.Yu., Voronin V.V. Diffraction enhancement and new way to measure neutron electric charge and the ratio of inertial to gravitational mass. Nucl. Instr. Meth., 2008, **A593**, 505–509.
14. P.B. Hirsch, A. Howie, R.B. Nicholson, D.W. Pashley, M.J. Whelan (Eds.), Electron Microscopy of Thin Crystals, Plenum, New York, 1965.
15. Voronin V.V., Semenikhin S.Yu., Shapiro D.D., Braginets Yu.P., Fedorov V.V., Nesvizhevsky V.V., Jentschel M., Ioffe A., Berdnikov Ya.A. Diffraction enhancement of the Stern–Gerlach effect for a neutron in a crystal. JETP Lett., 2019, **110**, No. 9, 581–584.
16. Voronin V.V., Semenikhin S.Yu., Shapiro D.D., Braginets Yu.P., Fedorov V.V., Nesvizhevsky V.V., Jentschel M., Ioffe A., Berdnikov. Ya.A. 7-order enhancement of the Stern-Gerlach effect of neutrons diffracting in a crystal. Phys. Lett, 2020, **B 809**, 135739.
17. Schmiedmayer J. The equivalence of the gravitational and inertial mass of the neutron. Nucl. Instr. Meth., 1989, **A 284**, 59–62.
18. Voronin V.V., Kuznetsov I.A., Lapin E.G., Semenikhin S.Yu., Fedorov V.V. Diffraction enhancement effect and new possibilities of measuring the electric charge of the neutron and its inertial-to-gravitational mass ratio. Phys. Atom. Nucl., 2009, **72**, No. 3, 470–476.

Theoretical Works of G.C. Wick in Neutron Physics in the 30-ies

Christopher R. Gould[1], Eduard I. Sharapov[2]

[1]*Physics Department, North Carolina State University, Raleigh, NC 27708, USA*
E-mail: chris_gould@ncsu.edu

[2]*Joint Institute for Nuclear Research, 141980 Dubna, Moscow Region, Russia*
E-mail: sharapov@nf.jinr.ru

The name of the Italian theorist Gian-Carlo Wick is well known in the *particle* physics. Nevertheless, in the middle of 30-ies, working in the Enrico Fermi group in Rome, he published several important works in another field – in the *neutron* physics. These works are little known by the present young physicists. Our report will deal only with results on the thermal neutrons albedo problem and his basic theory of the inelastic thermal neutrons scattering by condensed matter. This theory became the first such theory in this field. The history of these works, their physical essence and the relevance to the neutron physics will be discussed.

1. Introduction

The name of the Italian theorist Gian-Carlo Wick is well known in the *particle physics*. Meanwhile in the years from 1932 to 1937, when he was working in the Physics Institute of the University "La Sapienza" in Rome, he published, in Italian and German languages, several important works in the *neutron physics*. Eighty year later, in his reminiscent paper "Physics and physicists in the Thirties" [1] he wrote (citation from the page 567): "When, in the fall of 1932 I was offered an assistantship by Fermi, I became Fermi's pupil and I worked in almost daily contact with him for about five years, and I have learned more from him then from anyone else". And further, on the page 575, G.C. Wick added that his own works there were inspired "in a particular way by the experimental work in Rome that I could watch every day with my own eyes. As an example, the evaluation of the results of work with slow neutrons required the solution of diffusion problems; I found an extremely simple technique to solve some these problems."

At the very beginning, just after arrival to Rome in 1933, Wick solved the suggested to him by E. Fermi problem of the magnetic moment of the hydrogen *molecule* [2] in the Otto Stern experiments, which was important for the determination of then unknown value of the *proton* magnetic moment. Simultaneously he participated [3], [4] in the physical interpretation of the new phenomenon discovered in 1933 by Emilio Segre and Edoardo Amaldi in the atomic physics – the displacement of high spectral lines of alkali atoms in the atmosphere of a foreign gas (details on the Enrico Fermi explanation of this effect and the role of G.C. Wick in it, are discussed by us in [5]). With publication in 1934 of the E. Fermi theory of beta-decay, G.C. Wick showed that this theory well describes not only the emission of electrons but also the emission of positrons just discovered by Frederic Joliot and Irene Curie; even more, in [6] he theoretically predicted the phenomenon of K-electron capture in radioactive nuclei, which was experimentally demonstrated only in 1937 in Berkeley, USA, by Luis W. Alvarez. As to the Rome, the physicists of the Fermi group, including G.C. Wick, switched to the neutron

physics studies which gave the fateful results to the group itself and to the pure and applied nuclear science everywhere. Namely, by spring of 1934, the artificial radioactivity induced by *fast* neutrons, which were produced by a nuclear reaction, was discovered, and then, by autumn of 1934, the effect of multiple amplification of the radioactivity, when it induced by the *thermal* neutrons, was discovered. The details of these events and the paramount role of Enrico Fermi in this discovery have been recently described by F. Guerrra, M. Leone and N. Robotti in [24].

This report will deal only with Wick's results on thermal neutron scattering, in particular on the neutron albedo problem, and with his basic theory of the inelastic thermal neutrons scattering in condensed matter, that became the first such theory in this field. The history of these works, their physical essence and the relevance to the neutron physics will be discussed.

2. Thermal neutrons albedo problem

'Albedo' is Latin word meaning 'whiteness'. It was introduced into optics by Johhann Heinrich Lambert in his 1760 work "Photometria" [7]. In simple words, it means the diffused light reflection coefficient of the surface of a medium. Numerically, for example, for the plane-parallel beam, this is the ratio of the flux reflected in all directions by the unit area of the surface to the incident *flux density* (the flux per unit area of the beam). We will see in this section that for thermal neutrons the situation with albedo is more involved.

On the problem of albedo G.C. Wick and E. Fermi were working both, though separately, using different approaches. As for a media, both use an infinite half-space of a hydrogenous material. Wick applied to neutrons the Boltzmann transport equation of radiation, known to be valid for the 3D geometry, while E. Fermi invented his own intuitive 'one dimensional model' of neutron diffusion. G.C Wick published the result first [8]. E. Fermi published several months later [9] and made a comparison of their results. G.C. Wick resumed to work on the albedo problem later and published in 1943 [10] a more elaborated results with extended discussion.

G.C. Wick's approach was to use the Boltzmann integro-differential equation for probability density function $f(\boldsymbol{r},\boldsymbol{v};t)$ (here and later symbols in bold are vectors) to describe the thermal neutron distribution in a hydrogen media during diffusion. However, he greatly simplified mathematics by using a specific physical model of diffusion, assuming, following E Fermi, that the thermal neutron scattering during neutron collisions with the nuclei is the spherically symmetric. Moreover, he also assumed that all neutrons have the same constant speed corresponding to the thermal energy of about 30 meV. Physically this is valid on average because neutrons are in thermal equilibrium with hydrogen molecules, they diffusion can be taken as a stationary process, therefore the transport equation can be taken as not dependent on time. The x-axis was chosen as the symmetry axis and the x coordinate was the only spatial variable instead of $\boldsymbol{r}$. The only angular variable was the angle θ, actually the cosine $u = cos\theta$, between the direction of the neutron velocity v (with the value normalized to $v = 1$) and the positive direction of the x-axis. With these assumptions, his Boltzmann transport equation had the form:

$$u\frac{df(x,u)}{dx} + f(x.u) - \frac{N}{2(N+1)}\int_{-1}^{+1} f(x,u)du = 0. \qquad (1)$$

When neutrons fall on a paraffin medium, occupying half-space from the boundary surface $x = 0$ to $x \rightarrow \infty$, some of them come back through the boundary surface x=0 after

collisions with nuclei in the paraffin, which means that they are reflected. Others are captured instead. The probability density at the boundary is represented by $f(0,u)$ with the positive u-values for ingoing and the negative – for outgoing cases. In general, the quantity $f(x,u)d\tau du$ has the physical meaning of the number of neutrons in the volume $d\tau$ having 'velocities' values from u to $u+du$. The N is a *physical characteristics* of the medium, namely the ratio of the thermal neutron cross sections for scattering and capture by the Hydrogen nuclei, $N = \sigma_s/\sigma_c$. The physical meaning of N is the number of the neutron mean free paths between collisions.

Besides the albedo problem, G.C. Wick also calculated the angular distribution of thermal neutrons inside and outside of paraffin, as well as the radioactivity induced by neutrons in the paraffin media. For these problems the equation (1) contained the additional term – the source of fast neutrons inside paraffin, which we omit. G.C. Wick solved his integro-differential equation by expressing the *integral in Eq. (1)* as the weighted *sum* of several terms: $\sum_i^{2n} p_i f(x_i, x_i)$, where the weights p_i and the optimal discrete coordinates x_i should be calculated following the Gauss's formula for the numerical quadratures and mathematical procedures developed by GC Wick. It this way the problem is converted to the solution of the system of several linear differential equations. The desired accuracy of such approximation depends on the number of terms in the sum. Three terms were enough for the albedo problem.

G.C. Wick initially pointed out [7] and later argued in details that two kinds of albedo should be considered for describing the diffusion of thermal neutrons. First one, albedo β, called the *current albedo*, was introduced in the accordance with a classical definition as the ratio of the number of reflected neutrons to the number of the incident neutrons. In terms of the probability density function, the albedo β, is then the ratio of neutron currents:

$$\beta = -\int_{-1}^{0} uf(0,u)du / \int_{0}^{1} uf(0,u)du. \qquad (2)$$

The result of the β calculation depends on the initial function $f(0,u)$ at the boundary surface for $0<u<1$, that is, on the angular distribution of the incident neutrons. For the *isotropic* flux density, G.C. Wick obtained the 'strong' estimate $\beta=1 - 4/(\sqrt{(3N)})$ to be compared with the E. Fermi result $\beta=1 - 2/(\sqrt{(N)})$. However, the neutron angular distribution measurements were not made yet in the 30-ies, no comparison of these expression with the experiment have been made.

The second definition, albedo β_m, was introduced by E. Amaldi and E. Fermi [12]. It was deduced from neutron densities measured by with the 1/v activation detectors and a thin absorber inside the paraffin cube, which was cut in two parts. Wick calls it the *measurable albedo* (the index 'm' in the β_m), which he defines in his theory as:

$$\beta_m = \int_{-1}^{0} f(0,u)du / \int_{0}^{1} f(0,u)du. \qquad (3)$$

His theoretical approximation reported in [10] is $\beta_m=1 - 2/(\sqrt{(N+1)+1})$. The Fermi-Amaldi experimental values were $\beta_m=0.82$ and $N=125$. Using this formula and the modern values 50 barn for the scattering and 0.33 barn for the capture cross sections, one obtains $\beta_m=0.85$.

The main Wick's achievement in his 'albedo series' papers is the development of an alternative mathematical method of the solution of the transport integro-differential equation. Subrahmanyan Chandrasekhar, the Nobel prize winner, gave the credit to Wick for the new method and started to use it for solving various problems of the radiative transfer in the theory

of stellar atmospheres [11]. The next merit of papers [8],[10] as well as [9] was that they served for development and clarification of the physical understanding of the results obtained by the Fermi group in the experiments on slow neutron diffusion in the paraffin and water. Finally, they were well important for defending the Fermi group position in the discussions on the controversy [12],[13],[14],[15] which have arisen on the albedo problem.

There was the criticism given by authors [14] of the albedo interpretation, and correspondingly, of experimental results in the Rome. E. Fermi, E. Amaldi and G.C. Wick refuted it in the publication [13].

3. Wick's theory of neutron inelastic scattering by crystalline media

To the year 1937, all members of the Fermi group, but E. Amaldi and G.C. Wick, left Rome and Wick himself has got the offer from Bruno Rossi and Gilberto Bernardini to collaborate on the analysis of their cosmic-rays experiments, which he accepted. Nevertheless in 1937 he developed, on his own, the basic principles of the theory of inelastic slow neutrons scattering in the condensed media, and published them in papers [16], [17], [18]. In short, the Wick's initional point of view consisted in suggestion that in crystalline media slow neutrons scatter differently that is usually accepted, e.g., for the scattering in gases, because thermal neutrons should exchange energy and momentum with *phonons*, which are the quanta of crystal lattice vibrations. For such a case, the equations for the conservation of energy and the wave vectors are different than for the scattering by free nuclei. Wick had starting the discussion with the case of the crystal lattice at zero temperature – for the 'cold' crystal. For such a case the slow neutron inelastic scattering in crystals may only *excite* (nothing to absorb!) the acoustic phonons of the frequency ν and the wavelength λ, and the two conservation equations can be written, as the first one,

$$\boldsymbol{p_1 - p = hs},$$

here **p** and $\mathbf{p_1}$ are vectors of neutron momenta before (p) /after (p_1) scattering, **s**- phonon wave vector with the value $s = 1/\lambda$), and the second one

$$\frac{p_1^2}{2m} + h\nu = \boldsymbol{p}^2/2m.$$

It follows from these equations that, for inelastic scattering with the phonons creation (neutrons lose energy), the initial neutron momentum should satisfy the condition

$$p > m\nu\lambda + h/2\lambda.$$

Because this condition is usually happens for many crystals in thermal energy region, G.C. Wick wrote about it in more details using the known concept of Brillouin zones and the Debye model for crystals. As to an another inelastic process – the scattering by neutron absorbing the acoustic phonons of crystals – G.C. Wick makes a short comment that this is expected to decrease with the decreasing of the crystal temperature and, at practically attainable temperatures, the crystal becomes transparent for neutrons with the wavelength $\lambda_n > 2d$ (here d is the crystal lattice constant).

Finally Wick calculates the total cross section of slow neutrons inelastic scattering in crystals, basically in the frame of the theory developed by E. Fermi for the neutron scattering by protons bound in molecules, but applying this time the specific of the wave functions in

crystals. The final result is given as the cross section containing an integral over the 'eigen-frequencies' of the crystal vibrations (equation (14) in [18]). For the "cold crystal", $\lambda_n < 2d$ and $p \gtrsim h/2d$ Wick estimates the partial inelastic cross section with the neutron energy lost (photons emitted) between ε and $\varepsilon + d\varepsilon$ as:

$$d\sigma = \frac{\sigma_0 6d}{MhV^3}\,\varepsilon d\varepsilon,$$

where the σ_0 is the neutron interaction cross section with free nuclei, M is their mass and $V = vd$ is a particular velocity of phonons. Also, G.C. Wick deduced an 'approximate' expression for inelastic neutron scattering cross section with the neutron energy gain (absorption of phonons) for the case of the crystal at low temperature and $\lambda_n < 2d$, as:

$$\sigma = \sigma_0 \frac{3h^3}{16\pi M p^2 V d^3} T^3 \theta^{-3}.$$

It should be note, that Wick distinguishes two possible parts of neutron scattering cross section: *coherent* (the interfering part) and *incoherent* (noninterfering part).
The expressions above are for fully incoherent cross sections.

We would like to conclude this Section by quotation from E. Amaldi's fundamental review [19] of the history of nuclear and neutron physics in 30ies: the Wick's papers "paved the way for a very important and presently widely used technique for measuring the dispersion relations of the phonons in crystals and providing direct information on the dynamics of solid state substances".

4. Further developments in neutron spectroscopy of condensed matter

The first theorist after Wick, who steps on the way of the theory of neutron solid state physics, was Isaak Pomeranchuk in Russia [20]. He examined, in more details than Wick, the influence of low temperature upon scattering of slow neutrons by crystals. Soon, following their ideas, many theoreticians started to develop new approaches to the description of slow neutrons inelastic scattering in the condensed matter. The full enough reference list of their works up to the 50-ies can be found in [21]. However, the really new epoch in this field started with publication by George Placzek and Leon Van Hove of their papers [21],[22] on the crystal dynamics, the dispersion relations and correlation functions, in which it was shown how they can be studied theoretically and experimentally using slow neutrons. Also, about that time the intense neutron beams became available at the nuclear research reactors and began to be used as a very powerful neutron sources for neutron spectroscopy of the condensed matter. Though, for the pioneering contributions to the developing of neutron scattering techniques for studies of condensed matter, Bertram N. Brockhouse [23] and Clifford G. Shull obtained Nobel Prize in 1994 only.

5. Acknowledgment

Authors are thankful to Professors F. Guerra, N. Robotti and A. Guttman for the discussions which helped to start and to shape this report.

REFERENCES

1. Wick G.C. 1988. Physics and Physicists in the Thirties. In: Quarks, Leptons, and their Constituents. The Subnuclear Series 22:565–577, edit by Antonio Zichichi. Plenum Press, New York and London.
2. Wick, G.C. 1933. Sul momento magnetico di una molecola d'idrogeno. Il Nuovo Cimento 10(3):118–127.
3. Segre, E. Wick, G.C. 1933. Serie degli alcalini in campo electrico. *Il Nuovo Cimento* (1924-1942). 10(5):211–220.
4. Wick, G.C. 1933. Su un problema del calcolo della probabilita. Atti Acad. Lincei Rendiconti. 19: 27–33.
5. Gould, Christopher R, and Sharapov Eduard I. 2022. Fermi's favorite figure – the history of the pseudopotential concept in atomic and neutron physics. Eur. Phys. J. H. 47(10):1–8.
6. Wick, G.C. 1934. Sugli elementi radioactivivi di F. Joliot e I. Curie. Atti Acad. Lincei Rendiconti. 19:319–324.
7. Lambert, J.H.1760. Photometria, sive De mensura et gradibus luminous, celerum et umbrae. Deutsch hrsg. Von E. Anding. Volume v.1, 1892.
8. Wick, G.C. 1936. Sulla diffusion dei neutron lenti. Atti Acad. Lincei Rendiconti. 23:774–782.
9. Fermi E. 1936. Sul moto dei neutroni nelle sostanze idrogenate. Ricerca Scientifica 7(2):13–53.
10. Wick, G.C. 1943. Uber ebene Diffusionsprobleme. Zeitschrift fur Physik. 121:702–718.
11. Chandrasekhar, S. 1944. On the radiative equilibrium of a stellar atmosphere.II. Astrophysical Journal 100:75–86.
12. Amaldi, E. Fermi, E. 1936. On the absorption and the diffusion of slow neutrons. Phys. Rev. 50:899–928.
13. Fermi, E. Amaldi E. and Wick, G.C. 1938. On the albedo of slow neutrons. Phys. Rev. 53:493–494.
14. Halpern, O. Lueneburg, R Cark, O. 1938. Multiple scattering of neutrons I. Theory of the albedo of a plane Boundary. Phys. Rev. 53:173–183.
15. Ageno, Mario. 1946. Sull'albedo dei neutroni lenti. Il Nuovo Cimento (1943–1954) 3(1):3
16. Wick, G.C. 1936. Sulla diffusion dei neutroni. Ricerca Scientifica 7(1):134, 7(1):220.
17. Wick, G.C. 1936. Sulla diffusion dei neutroni nei cristalli. Ricerca Scientifica 7(2) 8:400.
18. Wick, G.C. 1937. Uber die Streung der neutronen on atomgittern. Physikalische Zeitschrift 38: 403–406.
19. Amaldi, Edoardo. 1984. From the discovery of the neutron to the discovery of nuclear fission. Physics Reports 111(3–4):3–331.
20. Pomeranchuk, I. 1938. On the scattering of slow neutrons in a crystal lattice. Soviet Journal JETP 8:894–906.
21. Placzek, G. Van Hove, L. 1954. Crystal dynamics and inelastic Scattering of neutrons. Phys. Rev. 93:1207–1214.
22. Van Hove, Leon. 1954. Correlations in Space and Time and Born Approximation Scattering in Systems of Interacting Particles. Phys. Rev. 95(1):249–262.
23. Brockhouse, Bertram N. 1995. Slow Neutron Spectroscopy and the Grand Atlas of the Physical World. Rev. Mod. Phys. 67:735–751 (Nobel Prize Lecture).
24. Guerra, Francesco Leone, Mateo and Robotti, Nadia 2006. Neutron induced artificial radioactivity: neutrons and neutron sources. Physics in Perspective 8:255–281.

ELECTRON MASS AS THE BASIC PARAMETER OF THE STANDARD MODEL

S.I. Sukhoruchkin

Petersburg Nuclear Physics Institute of NRC "Kurchatov Institute", 188300 Gatchina

1. Introduction

Nuclear physics and neutron resonance spectroscopy are based on the Standard Model (SM) as a theory of all interactions. The high accuracy in determining the neutron resonance energy (achieved by the time-of-flight method), as well as high accuracy in the mass measurements allowed us to consider together the empirical correlations in neutron resonances, nuclear data and particle masses.

Symmetry motivated and electron-based approach to development of the Standard Model [1] allowed us to determine three relations in SM parameters. All of them contain the electron mass m_e, and (1) and (2) - the parameter $\delta = 16m_e$=8.176 MeV=$m_\omega/96$=$m_\omega/6\cdot 16$ [1], introduced in [2] as close to 8.165 MeV, the doubled pion mass splitting value (4.5936(5) MeV [3]).

$$m_\tau = 2m_\mu + 2m_\omega \approx 2\cdot 13\cdot 16m_e - 2m_e + 2\cdot 96\cdot 16m_e = 2m_{K^*} \qquad (1)$$

$$m_n = 115\cdot 16m_e - m_e - \delta m_N/8 \qquad m_p = 115\cdot 16m_e - m_e - 9(\delta m_N/8). \qquad (2)$$

$$\alpha/2\pi = 115.9\cdot 10^{-5} = \varepsilon'' : \varepsilon' = \varepsilon' : 2m_e = m_e : M_q = m_\mu : M_Z = M_q : 3M_{H^0}. \qquad (3)$$

Here m_τ, m_μ and m_e are the lepton masses, m_ω and m_{K^*} are the meson masses, $\delta m_N = m_n - m_p$ – the nucleon mass splitting, $\alpha/2\pi$ – QED radiative correction to the magnetic moment of the electron [4], applied in [2] to the electron mass, ε''=1.34 eV and ε'=1.2 keV the parameters of superfine and fine structures in the positions of neutron resonances [2,5], M_q is the constituent quark mass [6,7], M_Z – Z boson mass, M_{H^0} is the scalar boson mass. In this work, we consider the lepton mass relations $m_\tau = 2m_\mu + 2m_\omega$ (1) and show the distinguishing character of each of its components [1].

2. Symmetry motivated empirical relations

The muon mass m_μ was discussed in literature [8-10] as a distinguishing parameter of the Standard Model.

In Table 1 numbers of fermions in the central field (top, N^{ferm}) are compared with numbers N in a representation $N\cdot\delta$ of the masses m_μ, f_π, $m_{\pi^\pm}$ and ΔM_Δ (the first line Table 1). Ratios m_e/M_q, m_μ/M_Z, $f_\pi/(2/3)m_t$, $\Delta M_\Delta/M_{H^0}$ are given in the third line of Table 2. Boxed are the hole configuration in $1p$ shell ($1s^4_{1/2}$, $1p^8_{3/2}$, $1p_{1/2}$) and valence configuration over the shells $1s^4_{1/2}$, $1p^8_{3/2}$, $1p^4_{1/2}$ (N=13 and 17 in the columns 3 and 5 in Table 1). Masses of leptons and $L = 207 = 9\cdot 23 = 13\cdot 16 - 1$ correspond to a hole configuration consisting of 13 mass/energy intervals (parameters δ).

It was mentioned in a number of works (see [5]) that the ratio 1:13 often appears when analysing neutron resonance spacings.

The exact coincidence of the mass of the third lepton m_τ with twice the sum of the mass of the second lepton m_μ and the vector omega meson mass m_ω (see (1) and

Table 1: Comparison of the number of fermions in the central field (top line, N^{ferm}) with numbers N in a representation $N \cdot \delta$ of masses m_μ, f_π, $m_{\pi^\pm}$, ΔM_Δ. Ratios m_e/M_q, m_μ/M_Z, $f_\pi/(2/3)m_t$, $\Delta M_\Delta/M_{H^0}$ are given in the third line.

N^{ferm}	16	16·13-1=L	16·16	16·17+1	16·18
N(δ)	N = 1	13	16	17	18
Part.	δ	m_μ	f_π	$m_{\pi^\pm}$	ΔM_Δ
Value	in MeV	106.0	130.7(1)	139.57039(18)	147
Ratio.	m_e/M_q	m_μ/M_Z	$f_\pi/M_{H'}$		$\Delta M_\Delta/M_{H^0}$
Value	$\alpha/2\pi$	$115.87 \cdot 10^{-5}$	$114 \cdot 10^{-5}$		$117 \cdot 10^{-5}$
Comm.		hole in $1p$	filled shells	valence	
ECQM			$M^\omega{}_q = 3f_\pi$		$M_q = 3\Delta M_\Delta$

Table 2, 3rd column, 1776.86(12) MeV and 1776.62(24) MeV) was found in [11]. This is a manifestation of discreteness with the parameter $\delta = 16m_e$ in particle masses and nuclear excitations.

The equation (1) is a new [1,11] exact relation between three well-known parameters: masses of two leptons and the mass of the ω meson, which acts as two constituent quarks. Both lepton masses have been measured accurately, but their values have not been determined theoretically, not predicted: the origin of mass is still unresolved problem. Nevertheless, such an exact integer relation 1:2 should be taken into account in the future theoretical models.

It was noticed that the sum of the muon mass and the mass of omega meson is close to $m_{K^*}(892)^\pm$=891.66 MeV: 106 MeV+782 MeV=888 MeV, and $2 \cdot 96 \cdot 16m_e$ is close to $2m_{K^*}$=2×891.66 MeV [1]. In Fig. 1, where the particle masses are compared with the pion parameters, the proximity of the ratio m_τ/m_{K^*}=1776.9 MeV/891.7 MeV=1.99 to 2 is seen.

Table 2: Particle masses (in MeV) of different generations (families) [1,11].

Particle	Lepton	Mass	Quark Q=2/3	Mass	Quark Q=-1/3	Mass
1 fam.	e	0.511	u-quark	2.16(49)	d	4.67(48)
	m_e		$(3m_e)$	(1.53) [6]	$9m_e$	4.60
2 fam.	μ	105.658	c	1270(20)	s	93(11)
			$9m_\pi$	1256		
3 fam.	τ	1776.86(12)	t	172900	b	4180(30)
$2m_\mu+4M_q^\omega=2m_\mu+2m_\omega$		1776.62(24)			$9M_q =$	3959
$2m_\mu+192\delta$		1781.108				
$2m_{K^*}$		1783.52(150)				

Correlations have been observed between the integer numbers of the pion masses (k=8, 10 and 12) and the masses of the constituent quarks M_q and M_q^ω [1]. The relations within

the ECQM should be considered from the symmetry motivated point of view, including the 3:1 ratio between m_e and the value of $M_{H^0}(\alpha/2\pi)^2$ in addition to $M_q = m_e(\alpha/2\pi)^{-1}$.

The formation of constituent quarks masses described by symmetry motivated relations within ECQM can be continued on the basis of new results on the properties of particles containing heavy quarks.

This unexpected coincidence of the mass of the third lepton m_τ with twice the sum of the mass of the second lepton m_μ and the vector omega meson mass m_ω (see (1), 1776.86(12) MeV and 1776.62(24) MeV), and appearence of the masses of precisely these particles may be also connected with the closeness of the strange quark mass m_s to the muon mass: 93±10 MeV and 106 MeV, see Table 2. This means that the constituent strange quark mass K* is close to the sum of masses of omega meson and strange quark. Taking into account that the mass of omega meson is exactly $96{\cdot}16m_e$ (from the exact equality of two parts equation (1)), it follows that the mass of τ lepton differs very little from the integer number of the electron mass.

The masses of fundamental fields $M_Z = m_\mu(\alpha/2\pi)^{-1}$ and $M_{H^0}=m_e/3(\alpha/2\pi)^{-2}$, and the main parameter of the NRCQM [6,7] $M_q = m_e(\alpha/2\pi)^{-1}$ are interconnected with symmetry motivated relations and QED correction to the electron mass (Table 1), which can be investigated by neutron resonance spectroscopy [1].

The above discussed symmetry motivated relations in particle mass spectrum are shown in Fig. 1.

The relations between the masses of nucleons and the electron (CODATA relations (2)) are now very accurately determined. The ratio of the neutron and electron masses m_n/m_e=1838.6836605(11) means that the shift $\delta m_n = 161.6491(6)$ keV from integer number of electron masses $115{\times}16m_e$ - m_e is exactly 1/8 of the nucleon mass splitting $\delta m_N = m_n - m_p$=1293.3322 keV, or $\delta m_N : \delta m_n = 8.00086(3) = 8{\times}1.000(1)$.

The relation (3) is considered in [5].

A number of authors [12-19] drew attention to the distinguishing character of nuclear excitations close to δm_N, m_e and $2m_e$.

The parameter $\delta = 16m_e$ can be considered as a general discreteness parameter [1], which allows us to represent particle masses and NRCQM parameters in integers: $m_\mu = 13\delta$ - m_e, $m_\pi = 17\delta + m_e$, $f_\pi = 16\delta$ [20], $\Delta M_\Delta = 18\delta$, $m_\tau = 2m_\mu+2m_\omega \approx 2{\cdot}13\delta+2{\cdot}2{\cdot}48\delta$ and $M_q=3\Delta M_\Delta = 3\times18\delta$, $M_q^\omega = 3f_\pi = 3{\times}16\delta$ (integers n=13, 16, 17, 18, 54=3×18, 3×16=48 and the corresponding parameters are given in the Table 1). Integers n=13, 16, 17 and 18 are of great importance in the symmetry motivated approach to the Standard Model development. The distinguishing character of the n=13 and n=17 is shown in the Table 2 where the hole and valence configurations the most close to the filled shell are boxed.

There are two exact empirical relations with the parameter f_π=130.7±0.1 ± 0.36 MeV [20]. The first, between the vector omega meson mass m_ω=782.66 MeV and f_π=130.7 MeV, equal to 5.988 (the value $m_\omega/2$=391.33 MeV, is an estimate of the mass of constituent quark M_q^ω). The second, $M_q^\omega/16 \cdot 3$=8.153 MeV, is close to 8.176 MeV=$16m_e = \delta$.

The shift $\delta m_n = 161.6491(6)$ keV = 17×1.2 keV = $17\varepsilon'$ coincides with the parameter of the tensor forces $\Delta^{TF} = 161$ keV found in nuclei where one-pion excange dynamics dominates (^{18}F, ^{55}Co, ^{124}Sb...), and with the radiative correction $\alpha/2\pi$ to the pion mass: 139.57 MeV×115.9 $\cdot 10^{-5} \approx$161 keV. Similar fine structure interval [2] in CODATA relations, namely, 170 keV = 511 keV/3 = $m_e/3$ connected with a shift in the mass of each of constituent quarks that form nucleons, is observed in many near-magic nuclei.

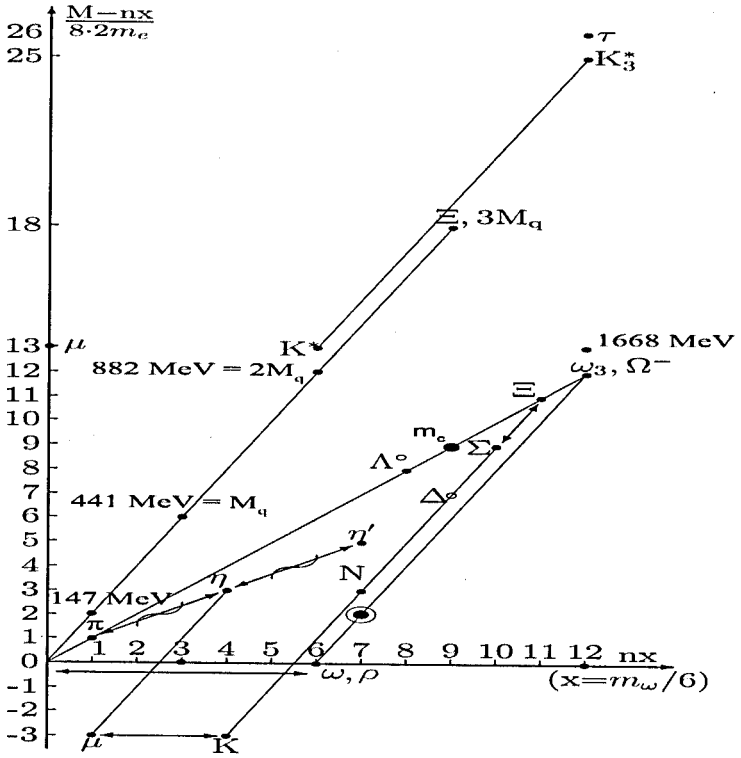

Figure 1: Evolution of baryon mass from $3M_q$ to M_N in a two-dimensional presentation: the values in the horizontal direction are given in units of $16 \cdot 16m_e = f_\pi$=130.7 MeV, the remainders M_i-n$(16 \cdot 16m_e)$ are plotted along vertical axis in $16m_e$. Nucleon mass in a nuclear medium (circled point) is close to $\Delta M_\Delta + 6f_\pi$. Different slopes correspond to 3 pion parameters: $f_\pi = 16\delta$, $m_{\pi^\pm} = 17\delta$ and $\Delta M_\Delta = 18\delta$. The mass of τ lepton (marked as τ) is $2m_\mu + 2m_\omega$=1776.86(12) MeV (n=26 at the left axis).

Table 3: Representation [1,12] of particle masses (3 top sections) and nuclear data (bottom) by the expression $n \cdot 16 m_e (\alpha/2\pi)^X M$ with QED correction to the mass $\alpha/2\pi$, where X is the degree and M is the factor. Boxed values m_μ, M_Z, M_{H°, $\delta^\circ, \delta, \delta', \delta''$ and $\Delta M_\Delta = m_s$, $m_e/3$ are considered in [1,12]. Double boxed are the constituent quark masses. Intervals in nuclear binding energies (X=0) and fine structure in nuclear states are considered elsewhere.

X	M	n = 1	n = 13	n = 16	n = 17	n = 18
-1	3/2			m_t=173.2		
GeV	1	$\boxed{16M_q=\delta^\circ}$	$\boxed{M_Z=91.2}$	M'_H=115		$\boxed{M_{H^\circ}=125}$
0	1	$16m_e=2m_d-2m_e$	$\boxed{m_\mu=106}$	f_π=130.7	m_π, Λ_{QCD}	$\boxed{\Delta M_\Delta=147}$
MeV	1	ΔE_B	106	130	140	147
	2	Fig. 3	212	262		296
	3	NRCQM		$\boxed{\boxed{M_q^\omega=391}}$		$\boxed{\boxed{M_q=441}}$
	4	Radial excit.			$(b\tilde{b})$=563.0	$(c\tilde{c})$=589.1
	6			m_ω=782		$2M_q$=882
	9				m_c=1270(20)	
	10	$m_\Lambda = 19m_\pi$			1390-1407	
	12	$m_\Omega = 12m_\pi$			1671-1688	
	60	Fig.7 [11]				8848
	64	$\eta_b(1S), \Upsilon(1S)$				9399-9460
1	1	$\boxed{16m_e=\delta=8\varepsilon_o}$			$k\delta$-m_n-m_e=161.651	$\boxed{170 = m_e/3}$
keV	8,8 · 4	CODATA, Fig.1[12]	3936	δm_N=1293.3		
1	1	$\boxed{9.5=\delta'=8\varepsilon'}$	123	152	Δ^{TF}=161	170 (Sn)
keV	2		247 (^{91}Zr)		322 (^{33}S)	340 (^{100}Mo)
2	1,4	$\boxed{11=\delta''=8\varepsilon''}$	143 (As)		749 (Br, Sb)	Neutron
eV	4,8		570 (Sb)		1500 (Sb, Pd)	reson.

3. Global analysis of particle masses

To check independently relations (1) and (2), we used a global analysis of the particle mass spectrum, similar to the analysis of the positions of neutron resonances [5,21]. In Fig. 2, ΔM distribution of all differences between particle masses, leptons and hadrons contains maxima in the region of 0-1000 MeV (top): at 3 MeV (not shown, corresponding to zero, since the averaging interval ΔM_{ij} is 5 MeV), 16 MeV (corresponding to stable intervals with the double value of the common period 8.176 MeV=δ=16m_e, introduced in [2] and observed in the CODATA relations), and 49 MeV$\approx 6\delta$. An unexpectedly large number of maxima in the distributions in Fig. 2 coincide with constituent quark masses and the τ-lepton mass: M_q^ω=391 MeV, M_q=445 MeV, $2M_q^\omega$=781 MeV, $4M_q^\omega$=1563 MeV, $m_\tau \approx 1774$ MeV.

The sequence of maxima at 3504 MeV, 3962 MeV, 4427 MeV (Fig. 2, bottom) corresponds to integer number of k = 8, 9, 10 of the constituent quark mass M_q.

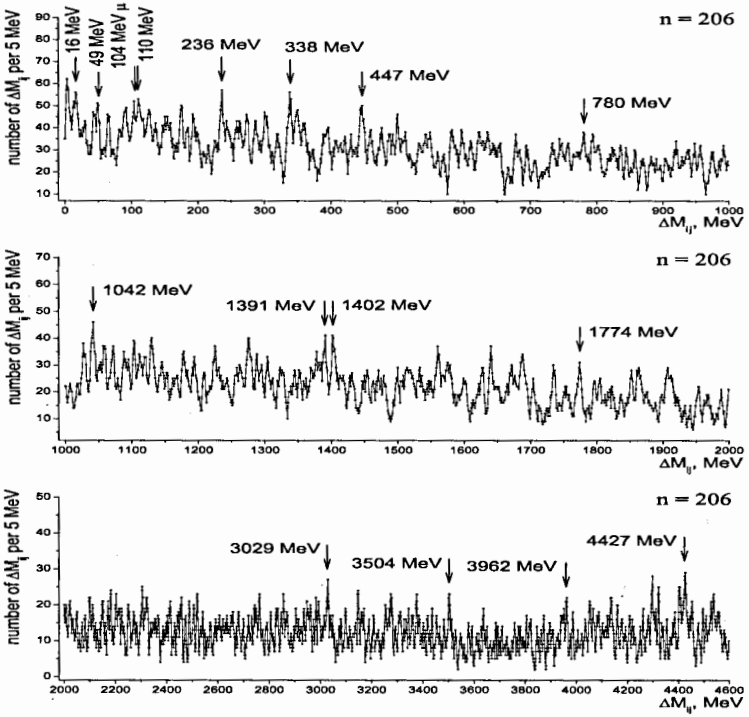

Figure 2: ΔM distribution of all differences between particle masses from PDG-2021 (averaging 5 MeV) the region 0–4600 MeV. Maxima at 16 MeV= 2δ, 49 MeV=6δ, 338 MeV$\approx m_\omega - M_q$, 447 MeV$\approx M_q$, 780 MeV=m_ω, 1042 MeV=$8f_\pi$, 1931-1402 MeV=$10m_\pi$ and 1774 MeV$\approx m_\tau$. Intervals 3504 MeV$\approx 8M_q = \delta°/2$, 3962 MeV$\approx 9M_q$ and 4427 MeV$\approx 10M_q$ are considered in [1].

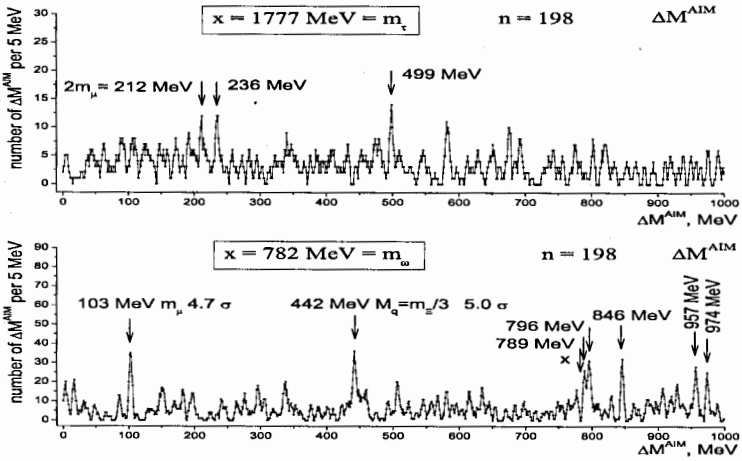

Figure 3: ΔM^{AIM} distribution of particle masses from PDG-2020 for the energy region 0-1000 MeV adjacent to fixed intervals x [1]. *Top:* $x = m_\tau$=1777 MeV, maximum at 212 MeV=$2m_\mu$. *Bottom:* $x = m_\omega$=782 MeV with the maximum at 103 MeV=m_μ and 442 MeV=M_q.

To check the systematic character of the observed grouping of the energy intervals the correlation Adjacent Interval Method (AIM) program was used [22-24]. In this method, not all intervals were analyzed, but only those adjacent to previously selected states. The selection of states (to analyze the intervals between them or between them and other states of the spectrum) was made taking into account their participation in the formation of maxima in the total distribution of intervals (which corresponded to their distinguishing character). Fixing the intervals x in the full spectrum of states (which formed a maximum at this value x), the distribution of intervals from the ends of x intervals to all other states of the spectrum was analyzed. Such accompanying intervals were denoted as ΔM^{AIM}.

In Fig. 3, top, the distribution of intervals adjacent to 1777 MeV=m_τ=x is shown, and the maximum at 212 MeV=$2m_\mu$=m_τ-$2m_\omega$ in the response function of the AIM program is seen. This means that the value 1777 MeV is the sum of $2m_\mu$=212 MeV and $2m_\omega$=1564 MeV=2·782 MeV (see also Fig. 1). The distinguishing character of intervals 103 MeV and 442 MeV can be seen in Fig. 3, bottom.

From the integer ralations between the positions of maxima at 16 MeV and 49 MeV (Fig. 2, top, ratio 3.06), at 780 MeV and 49 MeV (Fig. 2, top, ratio 15.92), 442 MeV and 49 MeV (Fig. 3, bottom, ratio 9.02) we see that there is a common period of about 16 MeV$\approx 2\delta$ in the energies forming these maxima.

The parameter δ being determined from the positions of two first maxima in Fig. 2, top, and their ratio 1:3, is (16 MeV+49 MeV=65 MeV)/2(1+3=4)=8.125 MeV. From positions of maxima at 780 MeV and 442 MeV ($\approx$441 MeV, the mass of the constituent quark) and ratios 16 and 9 (780 MeV+442 MeV=1222 MeV)/(9+16=25)=48.88 MeV=6δ, it is 8.147 MeV. These obtained values practically coincide with δ=8.176 MeV=$16m_e$ [2].

5. Conclusions

Considering the particle masses of three generations (families), new important accurate relation was found between the masses of leptons and hadrons: $m_\tau = 2m_\mu + 2m_\omega$ (1). The muon mass m_μ contained in this expession manifests the distinguishing character of the symmetry motivated dynamics of the lepton ratio L=m_μ/m_e=13×16-1. The lepton mass relation is indirectly confirmed in neutron resonance spasing distributions by appearing the ratio 1:13 (see [5]). From the integer ralations between the positions of maxima in distribution of all differences between particle masses, discreteness with the parameter $\delta = 16m_e$ was confirmed. A possible extension of the Standard Model was considered in [25-27]. All this confirms the role of the electron mass as the main parameter of the Standard Model.

References

1. S.I. Sukhoruchkin, Nucl. Part. Phys. Proc. **318-323** (2022) 142.
2. S.I. Sukhoruchkin, *Stat. Prop. Nuclei*, Pl. Press, 1972, p. 215.
3. R.L. Workman *et al.*. PDG 2022. Progr. Theor. Exp. Phys., **2022** (2022) 083C01.
4. V. Belokurov, D. Shirkov, *Theory Part. Interact.* AIP, 1991.
5. S.I. Sukhoruchkin *et al.*, Grouping in neutron resonances. These proceedings.
6. C. Itoh *et al.*, Phys. Rev. D **40** (1989) 3660.
7. L.A. Glozman, Nucl. Phys. A **629** (1998) 121c.
8. R. Feynman, *QED: The strange theory of light and matter*, 1986. Princ. Univ. Press.
9. Y. Nambu, Nucl. Phys. A (1998) **629** 3c.
10. S.F. King, CERN Courier (2020) **60** No 1. p. 23.
11. S.I. Sukhoruchkin, Nucl. Part. Phys. Proc. **312-317** (2021) 185.
12. S.I. Sukhoruchkin, Z.N. Soroko, D.S. Sukhoruchkin, M.S. Sukhoruchkina, Proc. ISINN-28 (Dubna, 2021), JINR E3-2021-48. p. 234.
13. O.I. Sumbayev, Doklady Ac. Nauk USSR **316** (1991) 1116.
14. O.I. Sumbayev, A. Smirnov., L. Kondurova, JETF **61** (1971) 1276.
15. S.L. Sakharov, Bull. Rus. Acad. Sci. Phys. **64** (2000) 743; Izv. AN USSR Ser. Fiz. **64** (2000) 930.
16. S.I. Sukhoruchkin *et al.*, Proc. ISINN-28 (Dubna, 2021), JINR E3-2021-48. p. 247.
17. S.I. Sukhoruchkin, Z.N. Soroko, M.S. Sukhoruchkina, Proc. ISINN-28 (Dubna, 2021), JINR E3-2021-48. p. 259.
18. S.I. Sukhoruchkin *et al.*, Proc. ISINN-27 (Dubna, 2019), JINR E3-2020-10. p. 40.
19. S.I. Sukhoruchkin, M.S. Sukhoruchkina, Proc. ISINN-27 (Dubna, 2019), JINR E3-2020-10. p. 54.
20. M. Suzuki, Phys. Rev. D. **54** (1996) 319.
21. S.I. Sukhoruchkin, Proc. Conf. Nucl. Data for Reactors, Paris, 1966. V. 1. p. 159. IAEA Vienna. 1967.
22. S.I. Sukhoruchkin, Proc. L Winter School of PNPI. S.-Petersburg, 2017, pp. 45–119.
23. S.I. Sukhoruchkin, Proc. LI Winter School of PNPI. SPb, 2018, pp. 43–139.
24. S.I. Sukhoruchkin, *et al.*, Proc. ISINN-10 (Dubna, 2002). JINR E3-2003-10. p. 308.
25. S.I. Sukhoruchkin, PoS (ICHEP2016) 1198.
26. S.I. Sukhoruchkin, Program and Theses 40th Meeting on Nucl. Spectr. Struct. At. Nucl., Leningrad, 1990, Nauka, p. 147.
27. S.I. Sukhoruchkin, *Symm. Meth. Phys.*. Dubna, 1993. JINR E2-94-347, p. 528.

GROUPING OF NEUTRON RESONANCE POSITIONS

S.I. Sukhoruchkin, Z.N. Soroko, M.S. Sukhoruchkina

Petersburg Nuclear Physics Institute of NRC "Kurchatov Institute", 188300 Gatchina

1. Introduction

Neutron resonance spectroscopy is a part of nuclear physics based on the Standard Model (SM) as a theory of all interactions. Measurements of neutron cross-sections of heavy nuclei and their analysis at the Institute of Atomic Energy (IAE) and Institute of Theoretical and Experimental Physics (ITEP), carried out in 1950s and later, found out deviations from the statistical model, manifested in unexpected coincidences of neutron resonance positions in different nuclei. In 1950s, I.V. Kurchatov as a director of IAE, have sent to ITEP a communication about this observation of the proximity of neutron resonance positions in compound nuclei: ^{236}U (0.2738 eV), ^{240}Pu (0.296 eV), ^{242}Pu (0.264 eV) and ^{242}Am (0.3051 eV). This simalteneous consideration of the same effect of grouping of the resonance positions at ≈0.3 eV in different nuclei became the starting point for global analysis of nuclear data [1,2].

Two groupings were considered in neutron resonance positions in the energy region of $E_o \leq 50$ eV. The first one, about 0.3 eV, and the second grouping about 5.5 eV. The effect of coincidence of neutron resonance positions in ^{236}U, ^{240}Pu, ^{242}Pu and ^{242}Am at $E_n \approx 0.3$ eV was reported at the First Geneve Conference on the Peaceful Use of Atomic Energy (1955) [3]. The grouping about 5.5 eV was reported in Paris in 1966 year [4].

Spacing in neutron resonance positions is the energy difference (after recoil correction) between the nuclei highly excited states (E_i - E_j, where i≠j). The use of spacing distributions along with distributions of neutron resonance positions (which in turn represent the difference between nuclear excitation energy and neutron separation energy) to study nonstatistical effects is preferable due to the larger number of spacings. In addition, in neutron resonance spectroscopy it is possible to select neutron resonances by reduced neutron width, reflecting the nucleon structure: large neutron widths correspond to a large component of the single-particle wave function.

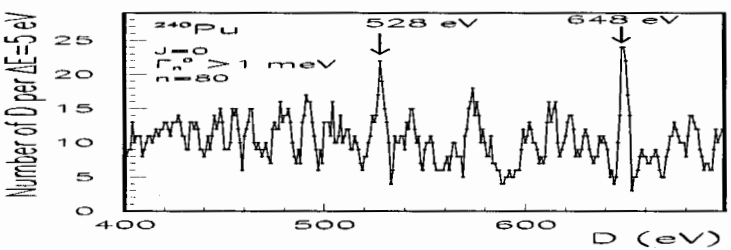

Figure 1: D distribution in 0^+ resonances of ^{240}Pu.

The systematic character of the proximity of resonance positions and spacings in the compound nuclei ^{240,242}Pu and ^{242,244}Am is difficult to check using spacing distributions due to the very small interval considered ($\approx$0.3 eV). However, the resonance at $E_n \approx 0.3$ eV in ^{240}Pu can be considered as a part of 0^+ levels spectrum of spacing distribution of this nucleus, where stable intervals of 500-600 eV are observed, see Fig. 1.

The second grouping 5.5 eV in neutron resonance positions was found in 1950s in compound nuclei ^{233}U (5.980 eV), ^{235}U (5.157 eV), ^{237}U (5.45 eV), ^{239}U (6.67 eV). This grouping was preserved in 1966 [4] and later, in the sum distribution of resonance positions of all nuclei, see Fig. 2.

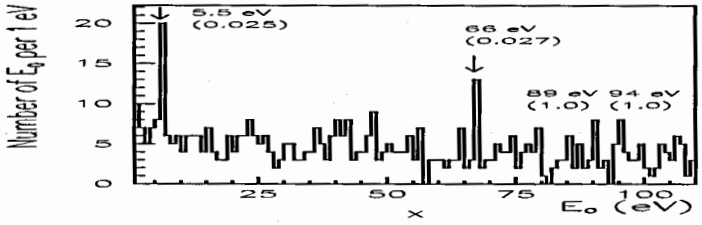

Figure 2: Distribution of neutron resonance positions known in 1966 year. Selection of one strongest resonance (max Γ_n^o) in the interval 10 eV (random probability is given in parentheses).

2. Superfine structure of neutron resonance positions

The maximum at 5.5 eV=4ε'' (where ε''=1.34 eV is the parameter of the superfine structure introduced in [1]) is a stable interval in compound nucleus ^{238}Np spectrum [5]. In Np positions of the doublet of resonances at 1.32 eV and 1.48 eV are close to the maximum (at 1.1 eV) in the spacing distribution (Fig. 7, top, in [5]), while in the distributions for more strong resonances maxima are observed at 4.1 eV=3ε'', 5.6 eV=4ε'' and 16.4 eV=12ε'', as well as at 54.8 eV=5δ''=40ε'' and 87.8 eV, close to 88 eV=8δ''=64ε'' (where δ''=11 eV=2·5.5 eV) (Fig. 7 in [5]).

Many authors, starting from W.W. Havens [6], have paid attention to nonstatistical effects in spacing distributions of different nuclei. Coincidence of positions of neutron resonances in light nuclei was reported in JINR, Dubna, 12-14 June 1964, at the Meeting of Interaction of Neutrons with Nuclei in the energy region 1 eV – 100 keV [7]: "Relationship between the fine structure in nuclear masses and the effect of coincidence of neutron levels of light nuclei". K. Ideno and M. Ohkubo have found stable interval 143 eV in ^{76}As equal to 13×8ε'' [8]. In neighbor heavy compound nuclei ^{233}Th and ^{236}U integer number 13 of the period 5.5 eV was also noticed. A recent analysis of the ^{236}U compound nucleus [9] demonstrate the presence of a stable interval that is multiple of 5.5 eV. For example, in Fig. 6 in [9] in adjacent interval distribution for J=4 ^{236}U resonances for x=44.2 eV an exact ratio 13:4 = 143.4 eV(=5.5 eV×13 × 2) : 44.2èV(=5.5 eV×4 × 2) is marked.

Thorium isotopes have 90 protons, corresponding to the filled $f_{7/2}$ subshell. It was noted long ago that the spacing distribution of its L=0 resonances is clearly nonstatistical. On the histogram with the averaging parameter 5 eV in Fig. 3 (top), the equidistancy of

the maxima at k=1, 2, 3, 5 of the estimated period 11 eV corresponds (as k=288/11=26) to the strongest maximum at D=288 eV (marked with an arrow). Fixing all such intervals (x=288 eV) in the spectrum of all s-wave resonances, we obtain maximum at a doubled value of 576 eV. Such an interval corresponds to the distance between strong neutron resonances (maximum at 573 eV in Fig. 3, bottom, with the selection of resonances with a reduced neutron widths greater than 1 meV, deviation from the random level $\approx 3\sigma$). A small maximum at 42 eV on the same distribution (Fig. 3, bottom) corresponds to a 1:13 ratio between strong resonances (between states with a relatively large single-particle component in the wave function).

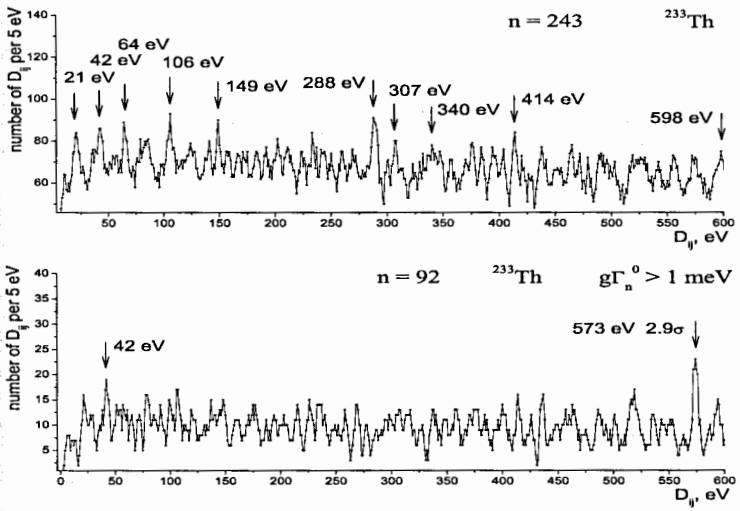

Figure 3: *Top:* Spacing distribution of all L=0 neutron resonances in ^{233}Th. *Bottom:* Spacing distribution of all L=0 strong neutron resonances in ^{233}Th (from [9]).

3. Fine structure of nuclear excitations and binding energies

It was noticed [10] that in ^{141}Ce, the positions of the two strongest resonances (Γ_n^o marked with asterisk in Table 1) are in the ratio 9:4=2.25 (2.253, in fact). The same ratio (2.237) exists between the energies of low-lying excitations ^{143}Ce (Table 1, bottom). The triplet of these closely spaced levels (the next E^* is at 633 keV) is the result of the residual interaction between three valence neutrons. One could notice a 1:2 ratio of the values E'_n in ^{141}Ce to E^*in ^{143}Ce (ratio 0.505). E'_n of strong s-resonances in some other N=83 nuclei are related to these E'_n. For example, E'_n in ^{142}Pr is close to that of ^{141}Ce (marked as $8\varepsilon'$=8×1.188 keV), while E'_n in ^{140}La is close to ε' (see Table 1). In the near-magic ^{145}Sm (N=83), the position of the p-wave resonance with the largest Γ_n^1 is close to ε', while the stable spacing of its s-wave and p-wave resonances (n=143, D=3689 eV and n=62, D=2485 eV, see Fig. 5) are close to $3\varepsilon'$=3564 eV and $2\varepsilon'$=2376 eV. Stable intervals D=595 eV=$\varepsilon'/2$ and D=294 eV=$\varepsilon'/4$ were found in resonances ^{134}Cs and ^{128}I.

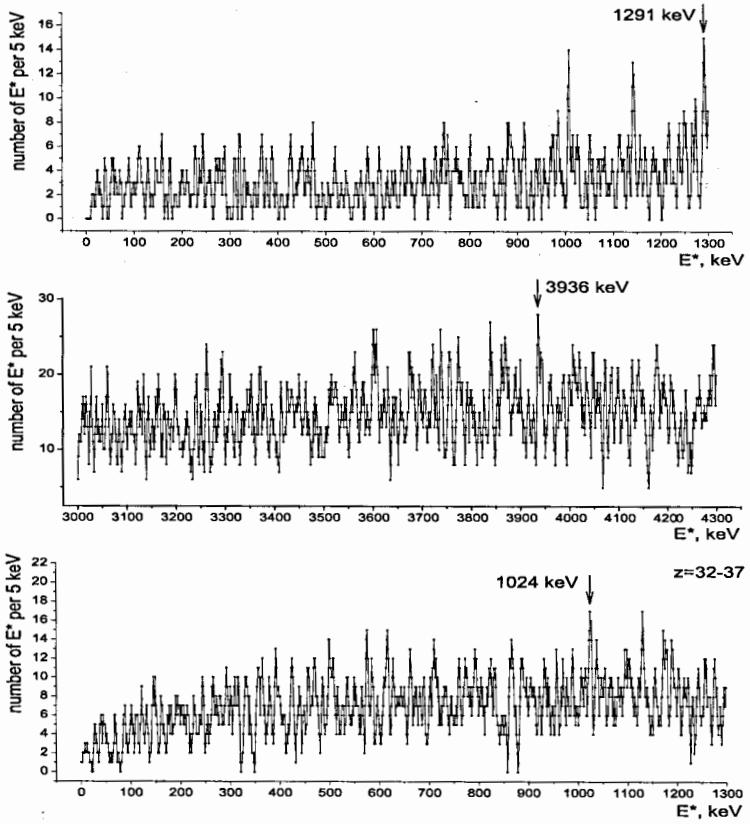

Figure 4: *Top and cetner*: E^*-distribution in nuclei with Z=4-29 for E^*<1300 keV and 3000-4300 keV [9]. Arrows mark δm_N and $4\times8\times13\delta'$=3936 keV (see also Table 2). The equidistant maxima at E^*=1008 keV=$2\times17\delta'+4\times18\delta'$, 1142 keV=$5\times17\delta' + 2\times18\delta'$ and 1291 keV=$8\times17\delta'$ are explained in [9]. *Bottom:* The E^*-distribution in all nuclei with Z=32-35. The maximum at 1024 keV=$6\times18\delta'$ is close to ε_o=1022 keV=$2m_e$.

The interest in the number 13 in expressions for intervals of fine and superfine structures is associated with the lepton ratio L=207=13×16-1, which contains this number. The importance of this number 13 can be demonstrated by the new expressin for the mass of τ lepton [11]:

$$m_\tau = 2m_\mu + 2m_\omega \approx 2\cdot13\cdot16m_e - 2m_e + 2\cdot96\cdot16m_e = 2m_{K^*}. \qquad (1)$$

Table 1: (from [5]) Comparison of positions and spacings in light and near-magic nuclei with integer values of the fine structure parameter $\varepsilon' = \delta'/8 = 1.188\,\mathrm{keV}$. *Top:* Positions E'_n (keV) of strong neutron resonances in light and magic nuclei and periodicity in the spacing distributions in resonances ^{61}Ni (top right). *Center:* Values E_n (keV) in nuclei with N=83=82+1, maxima in spacing distributions ^{141}Ce. *Bottom left:* The positions of strong neutron resonances in isotopes with Z=35-39 are compared with the integer of the period ε'=1.188 keV=9.505 keV/8, found in the positions of strong resonances in Z=57-59, N=83 nuclei (center). *Bottom right:* Excitation energies E^* (keV) of ^{143}Ce. Boxed are values ε'=1.188 keV=9.505 keV/8, δ', $2\delta'$ and $(9/4)\delta'$ discussed in the text.

Nucl.	Ca-Ni	^{61}Ni	^{61}Ni	^{61}Ni	^{61}Ni	^{61}Ni
l_n	l_n=0	D(keV)				
E_n	18.8	4.8	9.3	14.1	19.0	24.7
$k(\varepsilon')$	16	4	8	12	16	20
$k\times\varepsilon'$	19.0	4.8	9.6	14.4	19.0	24.7
Nucl.	^{141}Ce	^{141}Ce	^{142}Pr	^{141}Ce	^{141}Ce	^{141}Ce
J_i^π	$1/2^+$	$1/2^+$	$(5/2^-)$			
Γ_n^o,meV	660*	3060*	160	D	D	D
E_n	9.573	21.570	9.598	21.7	43.1	86.2
E^*,E'_n	9.505	21.418	9.530			
$k(8\varepsilon')$	1	9/4	1	9/4	9/2	9
$k\times8\varepsilon'$	9.504	21.384	9.504	21.4	42.5	85
Nucl.	^{140}La	^{80}Br	^{82}Br	^{86}Rb	^{143}Ce	$J_o^\pi=3/2^-$
J_i^π	3^+	l_n=0	l_n=0	l_n=0	$7/2^-$	$5/2^-$
Γ_n^o,meV	54	72.0	120	159	E^*	E^*
E_n	1.179	1.201	1.209	2.398		
E^*,E'_n	1.170	1.186	1.194	2.370	18.9	42.3
$k(8\varepsilon')$	1/8	1/8	1/8	2/8	2	9/2
$k\times8\varepsilon'$	1.188	1.188	1.188	2.376	19.0	42.77

It was found that the clustering of strong resonances in ^{82}Br has a small (0.03) occasional probability of grouping [10]. It is shown in Table 1 that E'_n of the strongest resonances in ^{80}Br, ^{82}Br and ^{86}Rb are close to ε' and $2\varepsilon'$. In ^{182}Ta, E'_n of the two strongest s-resonances are ε' and $\varepsilon'/2$ [5].

In Fig. 4, E^*-distributions in nuclei with Z=4-29 for E^*<1300 keV and 3000-4300 keV are given. Arrows mark 1291 keV, close to 1293.3 keV=δm_N and 3936 keV=4×8×13δ', where δ'=9.5 keV=8×1.188 keV=8ε'. The maximum at 3936 keV confirms the distinguishing character of the 13th energy interval in nuclear excitations, see Table 2.

Table 2: Excitations (in keV) of light nuclei from ^{33}S to ^{39}Ca at 3936 keV=32×13δ'. Boxed are stable excitations close or multiple to this excitation.

$2J^\pi$	^{33}S	^{38}Cl	^{39}K	^{37}Ar	^{38}Ar	^{39}Ca	$D_{ij}(^{18}F)$	$D_{ij}(^{20}F)$
3^+	0.0	E^*_{exp}	E^*_{exp}	E^*_{exp}	E^*_{exp}	E^*_{exp}	493 keV	490 keV
5^+	1967	1982	2523	1410	2167	2469		984 keV=
3^+	3935	3938	3939	3937	3937	3936	3936/8	3936 keV/4

In Fig. 5, we show that in the D-distributions of neutron resonances in ^{145}Sm for orbital momenta L=0 and L=1 the maxima are located exactly at $3\varepsilon'$ and $2\varepsilon'$.

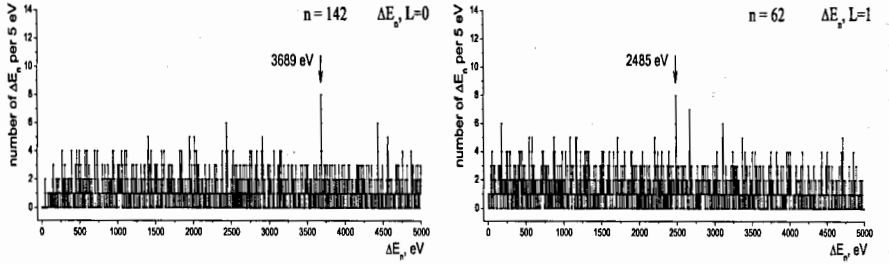

Figure 5: Spacing distributions of neutron resonances in ^{145}Sm (for orbital momenta L=0 and L=1 with maxima at $3\varepsilon'$ and $2\varepsilon'$ (3689 eV/2485 eV=1.48≈3/2, ε'=1.226 keV).

In high energy excitations of nuclei around N=82, many authors (M. Ohkubo, K. Ideno, F. Belyaev [12] and others [13,14]) observed fine structure effects in the spacing distributions of neutron resonances. From the exact ratio 9:4 between the strong resonances in ^{141}Ce (N=82) and the excitation spectra of this and neighboring nuclei, the common period ε'=1.188 keV was derived. The recently observed stable intervals $2\varepsilon'$ and $3\varepsilon'$ (Fig. 5) confirmed the relation $\varepsilon'=\varepsilon_o(\alpha/2\pi)^{-1} = 2M_q(\alpha/2\pi)^{-2}$ with QED correction to the electrom mass. This means that the CODATA relations [11,15] confirm all earlier observed "strange unexpected" empirical correlations.

Similar nonstatistical effects were found in the nuclear binding energies [9]. In nuclei around N=82, differing by ΔZ=2, ΔN=4 (or ^{6}He cluster), Values ΔE_B turn to be multiple (k=10) of the parameter $9m_e$=4.6 MeV (see Fig. 6, left). This parameter $9m_e$ is close to the value of d-quark mass (4.67(48) MeV) [15]. Grouping at 147 MeV (equal to 18δ [15]) in nuclei differing by 4^4He-clusters is shown in Fig. 6, right. The discreteness in binding energies was found in many nuclei. For example, the stable interval ΔE_B=106 MeV, close to the mass of muon, corresponds to 13 intervals of the common period δ=16m$_e$.

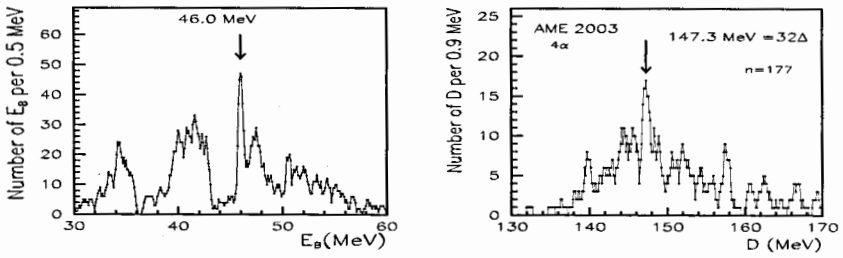

Figure 6: Grouping of ΔE_B at 46.0 MeV in nuclei differing by ^{6}He-cluster (*left*) and differing by 4^4He-clusters (*right*).

3. Discreteness with the parameter $\varepsilon_o = 2m_e$ in nuclear data

Recent data confirm the important role of common relations (with parameter $\alpha/2\pi$) between small stable intervals of the superfine structure (1.34 eV), intervals of the fine structure (1.2 keV), parameters m_e, M_q and scalar boson mass 125 GeV [1,11]. Fine and superfine structures with the parameters $\varepsilon' = 1.2$ keV and $\varepsilon'' = 1.34$ eV observed in neutron resonance spectra together with the stable nuclear excitations $2m_e = 1022$ keV and parameters $2M_q = 882$ MeV and $M_{H^\circ} = 125$ GeV form a sequence of ratios:

$$\alpha/2\pi = 115.9 \cdot 10^{-5} = \varepsilon'' : \varepsilon' = \varepsilon' : 2m_e = m_e : M_q = m_\mu : M_Z = M_q : 3M_{H^\circ}. \quad (2)$$

Table 3: (from [5]) Comparison of the parameter $\alpha/2\pi$=115.96·10^{-5} with the anomalous magnetic moment of the electron $\Delta\mu_e/\mu_e$ (top line) and with the ratios between the mass/energy values introduced in [1,13,14] (lines No 4-6) and other parameters mentioned in literature.

No.	Parameter	Components or the ratio	Value $\times 10^5$
	$\Delta\mu_e/\mu_e$	$=\alpha/2\pi$-0.328 α^2/π^2	115.965
	$2\delta m_\pi - 2m_e$	(81652(10) keV)/($16m_e$=δ)	132(12)
1	$\delta m_\mu/m_\mu$	$(23\times 9m_e\text{-}m_\mu)/m_\mu$	112.1
2	m_μ/M_Z	m_μ/M_Z=91182(2) MeV	115.87(1)
3	$\delta m_n/m_\pi$	$(k\times m_e\text{-}m_n)/m_\pi$=161.649 keV/$m_\pi$	115.86
4	$\varepsilon''/\varepsilon'$	1.35(2) eV/1.16(1) keV	116(3)
5	$\varepsilon'/\varepsilon_o$	1.16(1) keV/ε_o=1022 keV	114(1)
6	$(\varepsilon_o/6)/\Delta M_\Delta$		116.02
7	$(\Delta M_\Delta = M_q/3)/M_{H^\circ}$	147 MeV/125 GeV	118
8	δ/δ°	$\delta^\circ = 16M_Z/(L=207)$=7.048 GeV	116.0

It was noted [1] that the radiative correction to the electron mass is similar to the correction to its magnetic moment. This allowed to connect the value m_e with the masses of fundamental scalar and constituent quark [11]. The relation (2) is a continuation (in the high energy region) of the established in 1970s empirical relations (with the same parameter close to $\alpha/2\pi$) between superfine and fine structures in resonance spectra.

Discreteness in particle masses and nuclear data are considered in [11,13-14].

In Table 1 in [15], numbers of fermions in the central field (top, N^{ferm}) are compared with numbers N in a representation $N \cdot \delta$ of the masses m_μ, f_π, $m_{\pi^\pm}$, ΔM_Δ.

Discreteness in E_B, fine structure in E^* at δm_N=1293 keV and 3936 keV (Fig. 4) correspond to N=13 and N=17 in Table 1 in [15].

5. General remarks and conclusions

The discreteness in neutron resonance parameters is the main element of the "data-driven science" approach initiated by I.V. Kurchatov in 1950s, who drew attention to the unexpected coincidence of nuclear resonance positions in different elements. It turned out that this effect was obtained not only in heavy fissile nuclei, but also in other regions of the nuclear chart and depends on the nucleon structure, the stabilizing shell effect, and the influence of vacuum. The global symmetry motivated approach to the method of analyzing nuclear data and particle masses allowed us to confirm the role of the electron mass as the main parameter of the Standard Model as a theory of all interactions.

References

1. S.I. Sukhoruchkin, Deviations from the statistical description of neutron level spacing distributions and stabilizing effects of nuclear shells in positions of nuclear exciting states. *Stat. Prop. Nuclei*, Pl. Press, 1972, p. 215.
2. S.I. Sukhoruchkin, Z.N. Soroko, M.S. Sukhoruchkina, Nonstatistical effects in resonances of heavy nuclei. Proc. ISINN-28 (Dubna, 2021), JINR E3-2021-48. p. 259.
3. Y.B. Adamchuk *et al*, Measurements of fission cross sections and total cross sections of some isotopes of heavy elements on monochromatic neutrons, carried out using a mechanical selector. Proc. Int. Conf. on Peaceful Uses of Atomic Energy, P/645, **Vol. 4**, p. 223. N.-Y., 1956; **Vol. 4**, p. 259. AN USSR, Moscow, 1958.
4. S.I. Sukhoruchkin, Parameters of neutron strength function structure of medium weight and heavy nuclei. Proc. Conf. Nucl. Data for Reactors, Paris, 1966. **Vol. 1**, p. 159. IAEA, 1967.
5. S.I. Sukhoruchkin, Z.N. Soroko, M.S. Sukhoruchkina, Fundamental aspects of neutron spectroscopy. Proc. ISINN-28 (Dubna, 2021), JINR E3-2021-48. p. 247.
6. W.W. Havens Jr., Neutron resonance phenomena. *Progr. Fast Neutron Phys.*. Univ. Chicago Press, 1963, p. 215.
7. S.I. Sukhoruchkin, Relationship between the fine structure in nuclear masses and the effect of coincidence of neutron levels of light nuclei. Proc. Meet. Interact. Neutrons with Nuclei , Dubna, 1964. Preprint JINR 1845 (1964), p. 35, p. 39.
8. K. Ideno, M. Ohkubo, Non random distributions in neutron resonance levels. J. Phys. Soc. Jpn. **30** (1971) 620.
9. S.I. Sukhoruchkin *et al.*, Neutron Resonances in the Global Constituent Quark Model. Proc. ISINN-28 (Dubna, 2021), JINR E3-2021-48. p. 234.
10. M. Ohkubo, Yu. Kawarasaki, M. Mizumoto, Neutron resonance parameters of bromine-79 and bromine-81. J. Nucl. Sci. Techn. **18(10)** (1981) 745; JAERI-M-93-012, 1993.
11. S.I. Sukhoruchkin, Electron-based Constituent Quark Model. Nucl. Part. Phys. Proc. **318-323** (2022) 142.
12. F. Belyaev, S. Borovlev, Nonstatistical Effects in the Distribution of Distances between Neutron Levels. Yad. Fiz. (1978) **27** 289; Sov. J. Nucl. Phys. (1978) **27** 157.
13. S.I. Sukhoruchkin, Discreteness in the Standard Model parameters. Proc. L Winter School of PNPI. p. 45. S.-Petersburg, 2017.
14. S.I. Sukhoruchkin, Analysis of the particle mass spectrum in PDG-2016. Proc. LI Winter School of PNPI. p. 43. S.-Petersburg. 2018.
15. S.I. Sukhoruchkin, Electron mass as the basic parameter of the Standard Model. These Proceedings.

Nuclear and Related Analytical Techniques in Environmental and Material Science

Application of the Tagged Neutron Method for Elemental Analysis of Sinter

V.Yu. Alexakhin[1,2], E.I. Andreev[1], A.I. Lichkunova[1], I.K. Komarov[1], E.A. Razinkov[1], Yu.N. Rogov[1,2], M.G. Sapozhnikov[1,2], I.E. Chirikov-Zorin[1,2]

[1]*Diamant LLC – Dubna, Russia*
[2]*JINR – Dubna, Russia*

The results of the application of the conveyor analyzer AGP-K based on tagged neutron method at a metallurgical company are discussed. The method of tagged neutrons makes it possible to determine the mass concentrations of the sinter elements in real time without taking probes. The large penetrating power of fast neutrons allows obtaining information of large layer of sinter, up to 300 mm. A comparison of the obtained data with the values of chemical analysis is given.

1. Introduction

For many smelters, it is important to provide elemental content of the raw materials constant with time. For example, for the smelting of iron and steel, it is important that the basicity, the ratio CaO/SiO_2, of the sinter be as stable as possible over time. However, at present, the elemental composition of the sinter is controlled by sampling and subsequent chemical analysis of the samples. This is a labor-intensive process that takes a long time, requiring at least several hours. The AGP-K conveyor analyzer allows obtaining data on the elemental composition of material on the conveyor every 40-60 seconds.

The analyzer used tagged neutron method (TNM) [1-4] which allows non-destructive elemental analysis of materials remotely. The principal scheme of the TNM is shown in Fig.1.

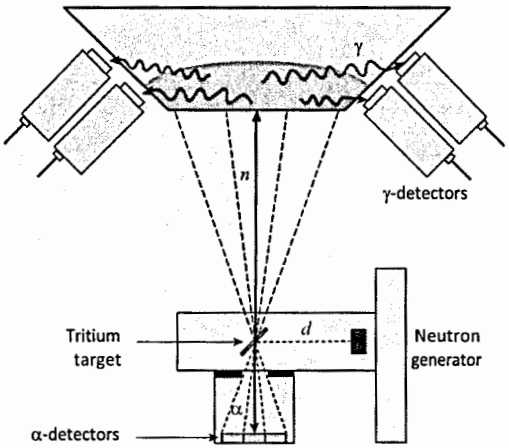

Fig.1. Principal scheme of tagged neutron method.

The object to be analyzed is irradiated with a beam of fast neutrons with an energy of 14.1 MeV produced by the reaction $d + {}^3H \rightarrow {}^4He + n$. In this reaction, neutrons and α-particles travel in opposite directions. Therefore, by detecting the α-particle, the direction of the neutron momentum can be determined. This procedure is called neutron tagging. A fast neutron with an energy of 14.1 MeV interacts with the nuclei of the material under study in inelastic scattering reactions (n, n'γ). The excited nuclei emit γ-quanta. Since each chemical element has its own characteristic γ-spectrum, it is possible to perform elemental analysis of the object.

Main advantage of the TNM other standard technique of neutron activation analysis, like PGNAA (Prompt Gamma Neutron Activation Analysis), is a drastic suppression (on factor 200) of the background events. That is due to selection of γ-quanta only from the investigated object. For that only γ-quanta, which come to the detector within narrow time window (on the order of 100 ns), which starts from the arriving of α-particle in the α-detector, are used for the analysis. The TNM is the only neutron method which provides time information about arriving of γ-quanta.

2. Description of the apparatus

The AGP-K analyzer consists from the neutron module, electronic cabinet and computer of the operator. The neutron module is installed under the conveyor belt (see, Fig.2). The neutron source is portable neutron generator ING-27 produced by VNIIA named Dukhov (Moscow). It provides constant flux of 14 MeV neutrons with intensity 5×10^7 s^{-1}. Gamma quanta from inelastic scattering reactions are detected by a system of BGO scintillation detectors. The data are transmitted to the electronic cabinet and processed by the operator's computer.

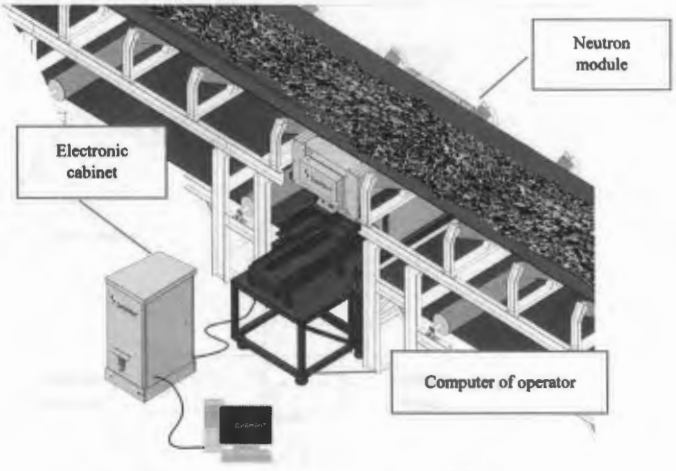

Fig.2. General scheme of the analyzer AGP-K.

Elemental analysis is performed for all ore material on a conveyor belt from 40 up to 300 mm thick. The mass concentrations of Al, Ca, C, Fe, Mg, O, and Si are measured at the same time and converted to the corresponding mass oxides ratios.

3. Results

In Fig.3 the measured behavior of basicity of sinter during two hours is shown.

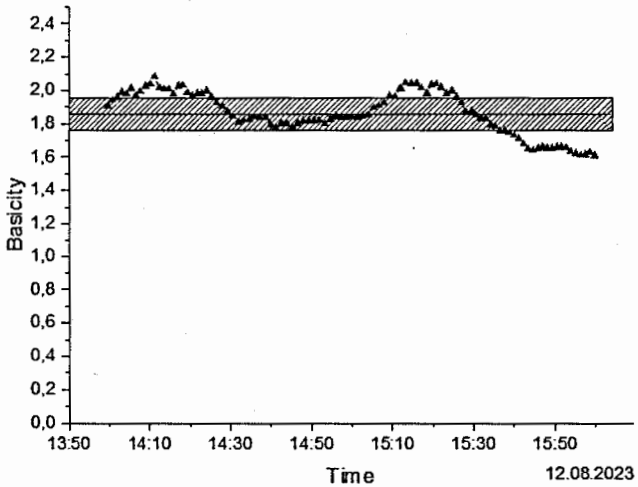

Fig.3. Measurements of sinter during two hours. The time between neighboring points is 40 s.

The operator must keep the basicity values within the shaded area. However, our measurements show that the rapid oscillations of basicity are taking place. The operative information about these changes of basicity signals the operator to take some actions to correct the basicity. It allows operator to decrease the fluctuations of the basicity which is important for the steel production. Decrease of sinter basicity RMS by 0.01 leads to coke saving by 0.13–0.19% and increase of steel production by 0.22–0.33%. Exploitation of the analyzer during first year resulted to decreasing the RMS of basicity by 0.04.

In Fig.4 a comparison between results of chemical analysis and data of AGP-K analyzer is shown.

One could see a general satisfactory agreement between chemical analysis and AGP-K data, however, there are some periods of disagreement. To solve these problems a special recalibration procedure is created. This procedure permanently performs for comparison with chemical analysis data and automatically changes the calibration parameters in case of significant disagreement.

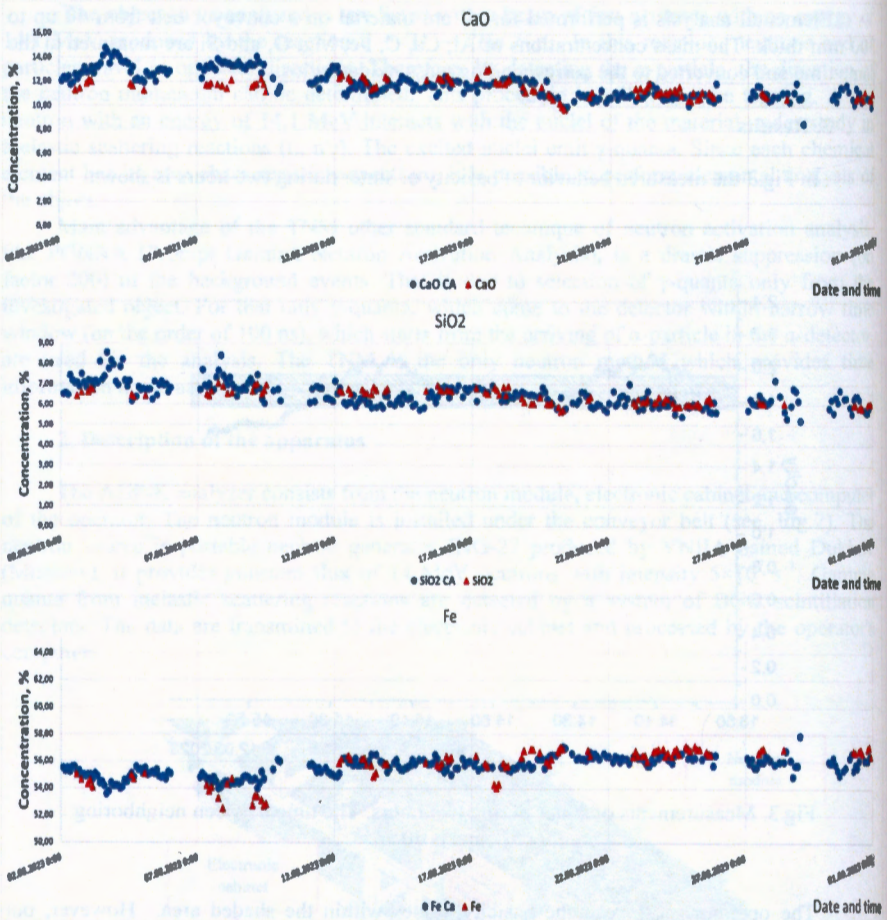

Fig.4. Measurements of mass concentration of CaO, SiO_2 and Fe over a month period. Blue circles are data of chemical analysis, orange ones correspond to results of AGP-K analyzer. Each data point corresponds to two hours of measurements.

One could see a general satisfactory agreement between chemical analysis and AGP-K data, however, there are some periods of disagreement. To solve these problems a special recalibration procedure is created. This procedure permanently performs for comparison with chemical analysis data and automatically changes the calibration parameters in case of significant disagreement.

4. Conclusion

The AGP-K analyzer based on tagged neutron method is successfully worked in harsh conditions of metallurgical companies. It provides data on the elemental composition of sinter on the conveyor every 40–60 seconds. That allows performing a complete automation of sorting processes and quality control of material on conveyor. On-line analyzer AGP-K could be used as a sensor of elemental composition of the substance on the conveyor, providing basic information for systems of total digitalization of production.

References

1. V. Valkovic, 14 MeV Neutrons: Physics and Applications // ISBN-13: 978-1482238006.
2. V.Yu. Alexakhin et al., Detection of Diamonds in Kimberlite by the Tagged Neutron Method. Nuclear Instruments and Methods A785 (2015) 9.
3. V.Yu. Alexakhin, E.A. Razinkov, Yu.N. Rogov, A.B. Sadovsky, M.G. Sapozhnikov, I.D. Dashkov, D.N. Grozdanov, Yu.N. Kopach, V.R. Skoy, N.A. Fedorov, Determination of carbon concentration in soil using the tagged neutron method, Phys.Part.Nucl.Lett., 2022, v.19, p.717-723
4. V.Yu. Alexakhin, A.I.Akhunova, E.A. Razinkov, Yu.N. Rogov, M.G. Sapozhnikov, I.E.Chirikov-Zorin, Use of the Tagged Neutrons Method for the Analysis of Material on a Conveyor, Physics of Atomic Nuclei, 2022, Vol. 85, No. 11, pp. 1866–1871.

Characterization of Nano-Sized Titanium Dioxide

Gunel Imanova[1], Anar Aliyev[1], Zaur Mansimov[1], Matlab Mirzayev[1,2], Salimkhan Aliyev[1]

[1]*Institute of Radiation Problems, Ministry of Science and Education of the Republic of Azerbaijan, Baku AZ-1143, B. Vahabzade 9, Azerbaijan*

[2]*Joint Institute for Nuclear Research, Dubna, Russia*

Titanium dioxide pigments are finely divided white powders which are chemically inert or unreactive, in contrast to all commonly used materials for paper filling or coating systems, and are used to increase opacity. Titanium dioxide is classified based on its crystalline arrangement as either anatase or rutile. The high light reflectivity, low light absorption and small particle size make this pigment ideal for obtaining high opacity. In their finely divided form, these pigments are very intensely white. With this characteristic, even at low concentration levels, titanium dioxide pigments are a major contributor to the optical performance of brightness and opacity of paper. If only brightness is needed, calcium carbonate is a more cost-effective pigment.

Titanium dioxide finds universal application as a whitening and brightening agent, and is extensively used in the paint, textile, rubber, plastic, paper, cosmetic, leather, ceramic, and food industry. In less purified grades, it is the basic natural pigment used in white house paint. There are two crystalline modifications of titanium dioxide: rutile and anatase. Only the anatase variety finds its use as a color additive for foodstuffs. The principal uses of this natural white pigment are in sub-coating of confectionery panned goods and in drinks. As with the other food grade pigments it must be dispersed to give full coloring power. It disperses quite easily in liquids. It remains suspended only in viscous liquids and semi-solid materials. Titanium dioxide is also used along with sugar syrup for usage in the sub-coating of tabletted products. This color additive has a permanent place in the list of food additives.

Titanium dioxide is a catalyst for the sunlight energized oxidation of organic polymers, and the semiconductor mechanisms involved are reasonably well understood. At its surface, titanium dioxide transforms the energy of ultraviolet light into chemical energy. This chemical energy reacts with oxygen and water to generate two free radicals, hydroxyl and peroxyl:

$$h\nu[TiO_2] + O_2 + H_2O \rightarrow OH^{\bullet} + HO_2^{\bullet}$$

The free radicals can, in turn, react with and destroy almost any organic molecule:

$$OH^{\bullet} + HO_2^{\bullet} + \text{—}CH_2\text{—} \rightarrow CO_2 + H_2O$$

As a result, paint films pigmented with unprotected titanium dioxide are said to chalk, that is, turn into dust by prolonged outdoor exposure. For anatase pigment, the effect is severe enough to all but preclude its outdoor use. Paint films pigmented with conventional rutile are less prone to degradation, but the chalking problems of titanium dioxide pigments were all but resolved by chemistry developed by Iler and subsequent extensions. This chemistry made it possible to encapsulate certain inorganic particulates in shells of silica glass. Today, silica

encapsulated rutile pigments perform exceedingly well in even the most demanding outdoor applications.

Two other advantages of TiO_2 are its chemical stability and the fact that it can be manufactured in an optimum crystal size of ca. 0.2 μm. As a consequence of their high degree of light scattering and low absorption of visible light, titanium dioxide pigments are the whitest and brightest of all the commercial white pigments. There are three naturally occurring crystallographic forms of titanium dioxide: anatase, brookite and rutile. Rutile is the most common and stable form. Its structure, shown in Figure 1, is based on a slightly distorted hexagonal close-packing of oxygen atoms with the titanium atoms occupying half of the octahedral interstices. Anatase and brookite are both based on cubic packing of the oxygen atoms, but the coordination of the titanium is again octahedral.

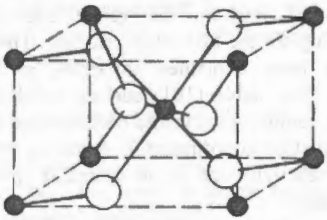

Figure 1. Unit cell of rutile. Black circles: titanium atoms; open circles: oxygen atoms.

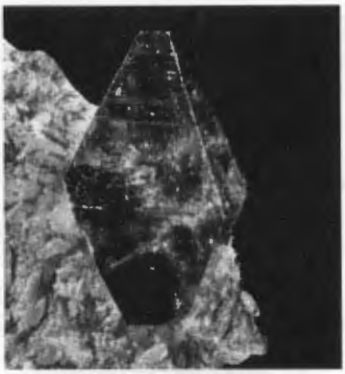

Figure 2. Photograph of a crystal of anatase.

Only anatase and rutile are manufactured on a large scale. Anatase was the first to become commercially available, but rutile is now the more important. The small pigmentary crystals of both forms are strong absorbers of UV light: this leads to photo-catalysed degradation of organic molecules unless the TiO_2 surface is protected. The particularly high photoactivity of anatase renders it unsuitable for exterior finishes because of the rapid degradation of the protective film. The pigmentary rutile crystals are generally coated with alumina and/or silica and treated with organic compounds.

Titanium dioxide (TiO_2) is a multifunctional material of interest for a broad range of applications ranging from (photo)catalysis to energy storage. The low toxicity and the abundance of titanium have favored the emergence of Ti-based compounds. Over the years, several approaches have been developed to modify/improve the properties of TiO_2. These included reducing the particle size to the nanoscale, controlling their morphology, and doping with heteroatoms to tune the electronic structure and structural features.

Anatase, a natural mineral, is one of the polymorph of TiO_2. The name "anatase" is derived from the Greek word "ana," which means "elongated" and refers to the mineral crystal's shape (Figure 2). Using Wulff construction and calculated surface energies, the equilibrium shape of a TiO_2 anatase crystal has been predicted to consist of a truncated octahedron, which agrees with experimental observations. The crystal exposes only two types of surfaces with 96% of (101) and 4% of (001) surface. Calculations of surface energies indicate 0.44 J/m^2 and 0.90 J/m^2 for (101) and (001) surface, respectively, highlighting the highest stability for the (101)-type surface. The difference of stability of the two types of surfaces has been explained in terms of the density and nature of undercoordinated Ti species. The stable (101) surface exhibits 50% titanium in a sixfold coordination mode and 50% titanium in a fivefold coordination mode, whereas the metastable (001) surface contains only fivefold coordinated Ti featuring enhanced interfacial properties. Such a difference in surface reactivity has led to extensive researches on the preparation of TiO_2 crystals with specific facets.

The role of anions during solution-based synthesis of inorganic compounds is multiple. Depending on their complexing ability toward cations, anions can drive the nucleation/crystallization toward a specific crystal structure. They can also adsorb onto surfaces thus orienting, in a particular direction, the growth of particles.

Determination of the Efficiency of Neutron Detectors in an Experiment of Inelastic Neutron Scattering on ^{12}C

Ionkin V.K.[1], and TANGRA collaboration

[1]*Faculty of Physics, Lomonosov Moscow State University (MSU), Moscow, Russia*

TANGRA

Project "TANGRA" (TAgged Neutrons & Gamma-RAys) [1] at JINR-FLNP (Dubna) is aimed at studying nuclear reactions caused by fast neutrons. As part of the TANGRA collaboration, an experiment is being conducted to study the reaction of inelastic neutron scattering on a carbon nucleus $^{12}C(n, n')^{12}C^*$ using the method of labeled neutrons. The 14.1 MeV neutrons are produced in fusion reaction

$$d + t \rightarrow \alpha + n + 17.59\ \text{MeV}$$

in VNIIA portable neutron generator ING-27 (Fig.1)[2]. The built-in ING-27 neutron tube 256-pixel a-detector allows to "tag" and count neutrons, because the both reaction products are emitted nearly collinear in opposite directions.

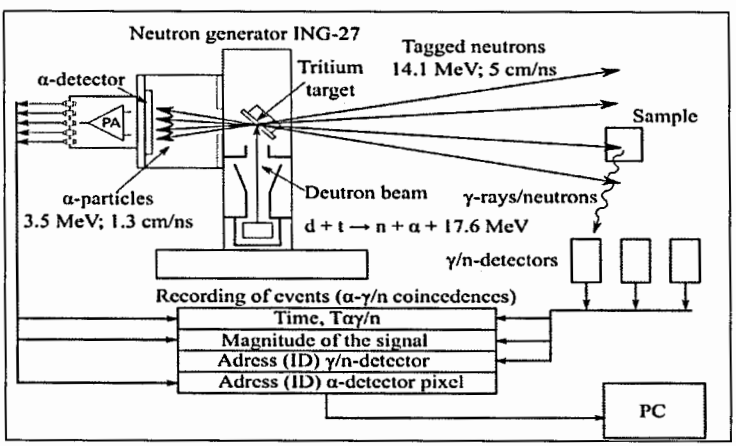

Fig.1. Schematic diagram of the experiment using of method of labeled neutrons.

Experimental installation

The installation is a neutron generator with a carbon ^{12}C screen located in front of it, surrounded by detectors at different angles with the increments of 15° (Fig.2). The angles 90, 180 and 270 are omitted due to the expected high neutron absorption in the target. 0 is omitted

due to a direct neutron beam, which will spoil the statistics with a large number of high-energy events.

Plastic scintillation detectors

Plastic scintillation detectors are used in this experiment. Neutron falling into a plastic scintillator EJ-200 [3], knocks out the hydrogen in its composition, which, flying, increases the ionization of the medium and secondary gamma radiation. Secondary photons formed in the scintillator under the action of incident neutrons. They are registered in the PMT ETL 9821KFLB FEU [4].

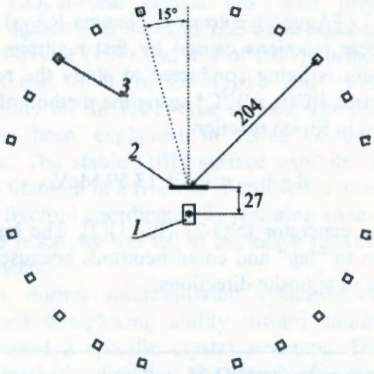

Fig.2. Scheme of the experimental installation. 1– ING-27 neutron generator, 2– carbon target, 3– n-detectors included in an array of 20 plastic scintillation detectors. All dimensions are given in cm.

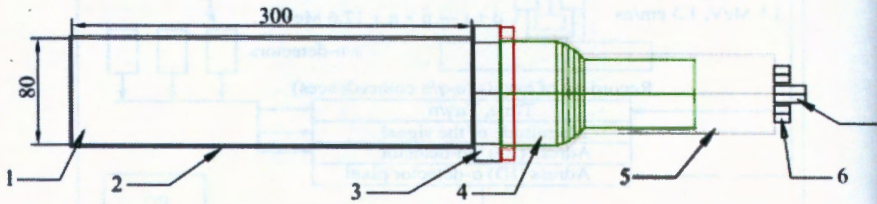

Fig.3. Detector based on a plastic scintillator. 1– plastic scintillator, 2– reflective winding, 3– aluminum holder, 4– PMT ETL9821KFLB, 5– magnetic shield, 6– BNC connectors (x2), 7– SHV connector. All dimensions are given in mm.

Method of determination efficiency

An important part of data analysis is to determine the efficiency of the detectors used in the experiment. This is important both for determining the sensitivity limits of measuring instruments and for estimating the total neutron flux for each detector. Efficiency estimates

can be made using different methods, in particular, for a similar experiment, V. Valkovich's group used the following equations [5–6]:

$$(E_{thr}) = \frac{N_H\sigma_H}{N_H\sigma_H+N_C\sigma_C}(1 - e^{-d(N_H\sigma_H+N_C\sigma_C)})\left(1 - \frac{E_{thr}}{E_{neutron}}\right),$$

where N_H is a density of hydrogen atoms, N_C is a density of carbon atoms, σ_H and σ_C – total cross sections for scattering of neutrons having energy E_n, on H and C, d= 8cm. Thus, determination of efficiency of detectors requires energy calibration and determination of threshold energy of plastic detectors, used in experiment.

Energy calibration

Energy calibration begins with the processing of time-of-flight spectra. Red vertical lines indicate the kinematically predicted positions of peaks from incoming neutrons. After approximation by Gauss scattering, 1.5 sigma region is highlighted with black lines on both sides to isolate neutrons from desired regions.

Next step is a determination of incoming neutrons energy on amplitude spectra. The amplitude spectra consist of events belonging to the regions of neutron peaks of the previous step. The neutron energy is reduced in accordance with the cannel of edge of these spectra (the vertical line in Fig.4).

After this calibration line is constructed in order to determine the threshold energy (Fig.6).

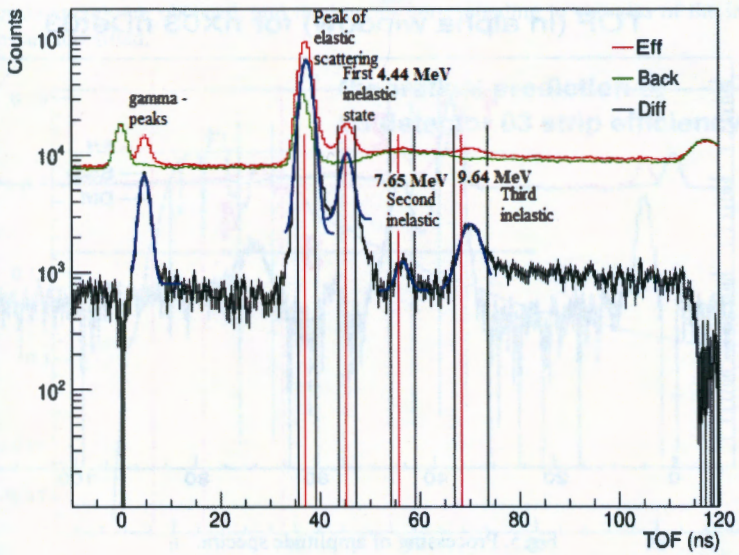

Fig.4. Processing of time-of-flight spectra.

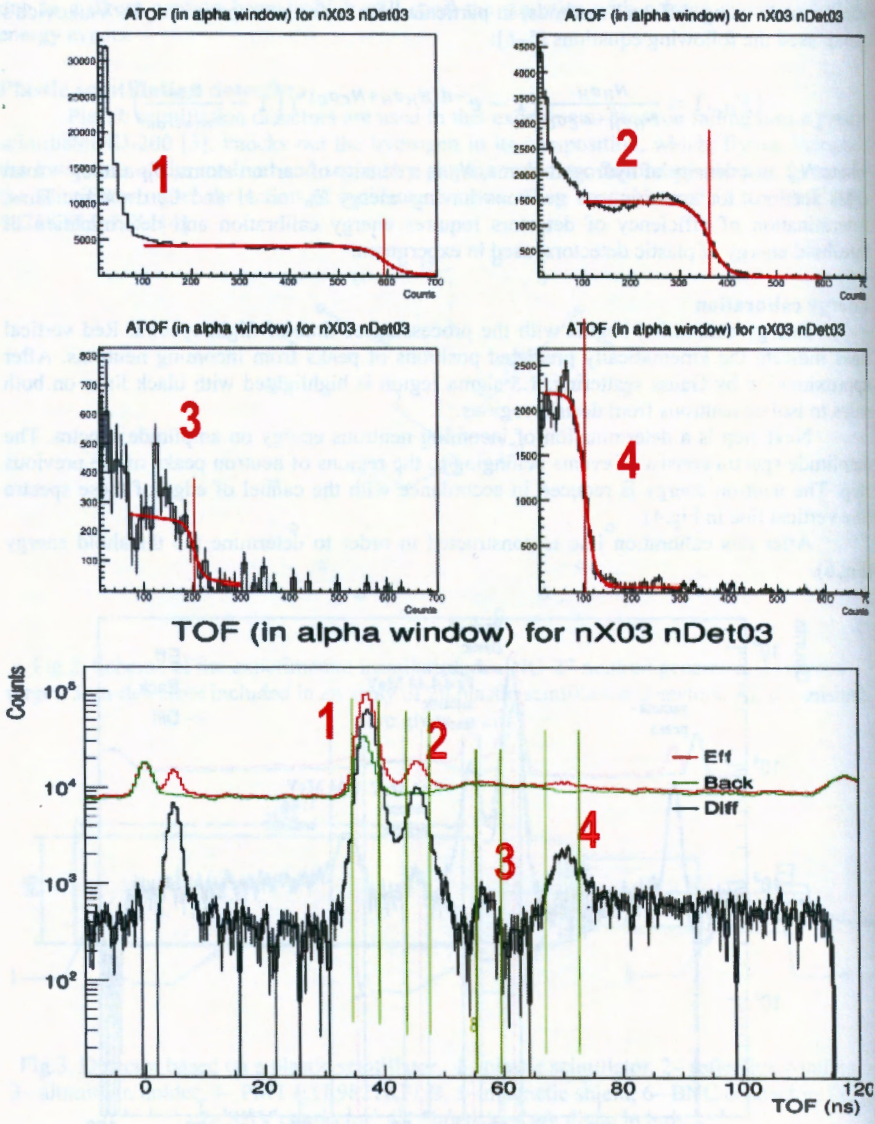

Fig.5. Processing of amplitude spectra.

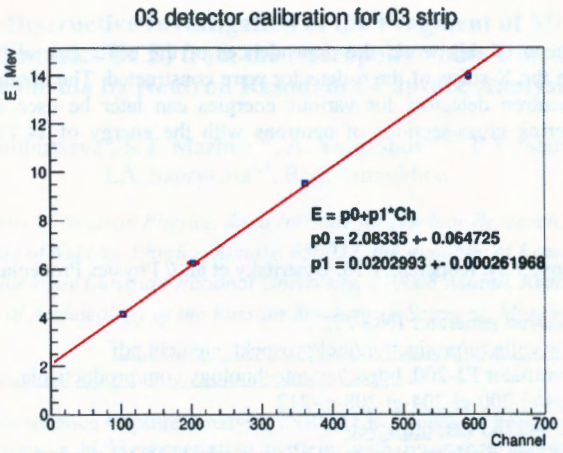

Fig.6. Calibration line for 3rd detector/3rd strip alpha detector.

Determine efficiency

Finally, using values of the threshold energy, dependence of the detector efficiency on the neutron energy are obtained, and the regions corresponding to energies of the incoming neutrons are identified.

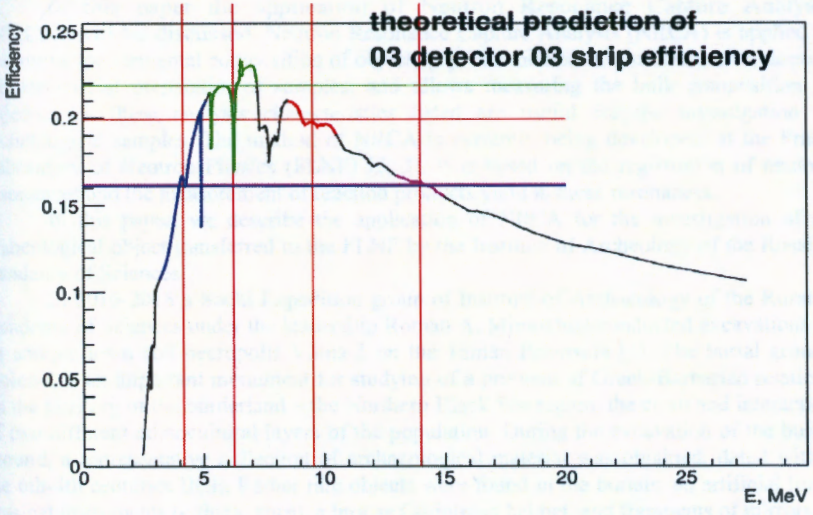

Fig.7. Dependence of the detector efficiency on the neutron energy.

Conclusion

In the course of this work, the dependences of the efficiency of detectors in their combination with the X-strips of the α-detector were constructed. The obtained values of the efficiencies of neutron detectors for various energies can later be used to determine the differential scattering cross-sections of neutrons with the energy of 14.1 MeV on carbon nuclei.

References

1. I.N. Ruskov, Y.N. Kopatch, V.M. Bystritsky et al. // Physics Procedia 2015. 64. P. 163.
2. VNIIA Neutron generator ING-27, http://www.vniia.ru/production/incl/prospekt_element.pdf
3. Plastic scintillator EJ-200, https://eljentechnology.com/products/plastic-scintillators/ej-200-ej-204-ej-208-ej-212
4. PMT ETL 9821KFLB, https://et-enterprises.com/products/photomultipliers/product/p9821b-Series
5. Knoll, G.F. 1979. Radiation detection and Measurement. John Wiley Sons, Hoboken, New Jersey, USA.
6. Mubarakmand S. and Anwar M. 1971. Neutron detection efficiency of an organic scintillator. Nuclear Instruments and Methods 93: 515–518.
7. A. Koning // IAEA NDS Document Series IAEA(NDS)-235, 2020.

Non-Destructive Investigation of the Fragment of Mirror (6th–4th Centuries BCE) from the Necropolis Volna 1 on the Taman Peninsula by Neutron Resonance Capture Analysis

N.V. Simbirtseva[1], S.T. Mazhen[1,2], A. Yergashov[1,2,3], P.V. Sedyshev[1], I.A. Saprykina[1,4], R.A. Mimokhod[4]

[1]*Frank Laboratory of Neutron Physics, Joint Institute for Nuclear Research, Dubna, Russia*
[2]*Institute of Nuclear Physics, Almaty, 050032, the Republic of Kazakhstan*
[3]*L.N. Gumilyov Eurasian National University, 010008 Astana, Kazakhstan*
[4]*Institute of Archaeology of the Russian Academy of Sciences, Moscow, Russia*

Neutron Resonance Capture Analysis (NRCA) is known as non-destructive method. The use of neutrons, a highly penetrating particle, with resonance energy, allows one to investigate archeological objects without damaging. NRCA is based on the registration of neutron resonances in radiative capture and the measurement of the yield of reaction products in these resonances. We have applied the method for the analysis of several archeological objects from the necropolis Volna 1. In this paper, we concentrate on a study of fragments of mirrors.

1. INTRODUCTION

In this paper the application of Neutron Resonance Capture Analysis (NRCA) will be discussed. Neutron Resonance Capture Analysis (NRCA) is applied to determine the elemental composition of objects [1]. The method is non-destructive, doesn't require special preparation of samples, and allows measuring the bulk composition of objects. All these analysis characteristics listed are useful for the investigation of archeological samples. The method of NRCA is currently being developed at the Frank Laboratory of Neutron Physics (FLNP) [2, 3]. It is based on the registration of neutron resonances and the measurement of reaction products yield in these resonances.

In this paper, we describe the application of NRCA for the investigation of an archeological object transferred to the FLNP by the Institute of Archeology of the Russian Academy of Sciences.

In 2016-2018 a Sochi Expedition group of Institute of Archaeology of the Russian Academy of Sciences under the leadership Roman A. Mimokhod conducted excavations of an antique town soil necropolis Volna 1 on the Taman Peninsula [4]. The burial ground Volna-1 is an important monument for studying of a problem of Greek-Barbarian relations on the territory of the borderland – the Northern Black Sea region, the clash and interaction of two different ethnocultural layers of the population. During the excavation of the burial ground, a representative collection of archaeological material was obtained, dated within the 6th-4th centuries BCE. Rather rare objects were found in the burials: an artificial limb, musical instruments (cithara, harp), a bronze Corinthian helmet, and fragments of mirrors.

The mirror has high vertical ledges, presumably belong to the Borysthenitic type of mirrors (Fig.1). The handle is lost, the remains of the fastening are preserved on the mirror. The metal of the mirror is degraded to a large extent, it is not possible to restore the height

of the side and the design of the fastening. Analysis of the elemental composition by the XRF method is difficult. In this regard, data on the elemental composition obtained by the NRCA method are of great importance.

Fig. 1. The fragment of mirror (6th-4th centuries BCE).

2. EXPERIMENT

The sample was irradiated with neutrons at the resonance neutron source IREN to obtain time-of-flight spectra of (n,γ) reactions. The main part of the IREN facility is the linear electron accelerator LUE-200 with a non-multiplying neutronproducing target of W(90%)+Ni+Fe-alloy. The detailed description and parameters of the facility can be found in [5-7].

The measurements were carried out at a 58.6-m flight path of IREN beamline 3. To obtain time-of-flight spectra the sample was placed inside the large liquid scintillation detector. The START signal is generated by the synchronizer of the IREN facility, the STOP signals come from the detector. The measurements of the investigated sample lasted about 37 h. The resonance energies were determined by the following formula:

$$E = \frac{5227L^2}{t^2}, \quad (1)$$

where t – time of flight in microseconds, L – flight path in meters, E – kinetic energy of aneutron in eV. The resonances of copper and tin were identified on the time-of-flight spectrum (Fig.2) based on the values of resonance energies in [8, 9].

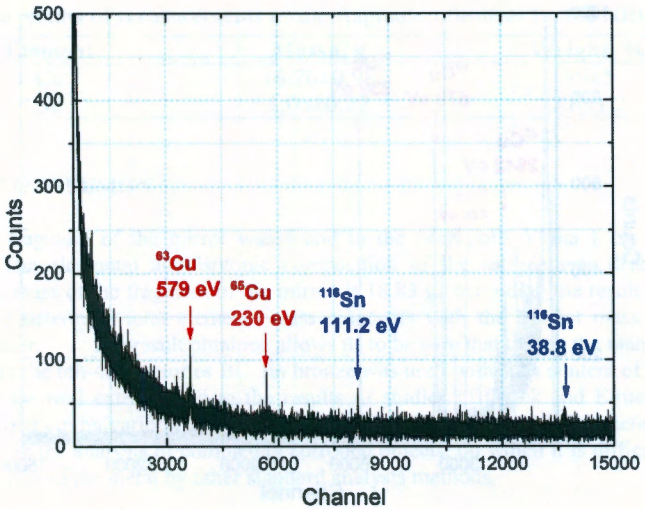

Fig. 2. The part of reactions time-of-flight spectrum (n,γ) obtained in measurements on the fragment of mirror. The time channel width is 50 ns.

The measurements with standard samples of identified elements were made in addition to the measurement with the investigated sample. Parts of time-of-flight spectra of (n,γ) reactions on the material of standard copper and tin samples are shown in Figure 3, 4.

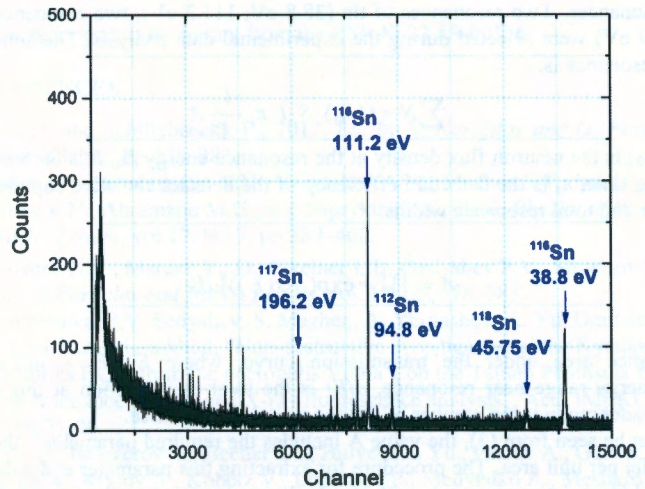

Fig. 3. The part of reactions time-of-flight spectrum (n,γ) of tin standard sample. The time channel width is 50 ns.

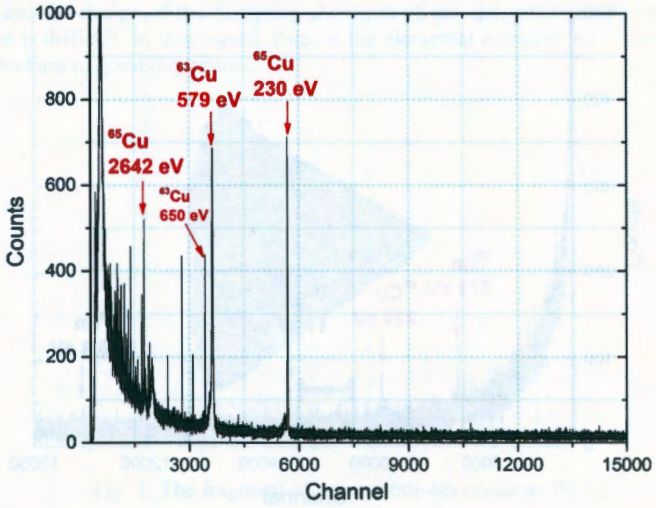

Fig. 4. The part of reactions time-of-flight spectrum (n,γ) of copper standard sample. The time channel width is 50 ns.

3. DATA ANALYSIS AND RESULTS

The number of element nuclei in the sample was determined by using the number of counts in resonances. Two resonances of tin (38.8 eV, 111.2 eV), two resonances of copper (230 eV, 579 eV) were selected during the experimental data analysis. The sum of detector counts in a resonance is:

$$\sum N = f(E_0) \cdot S \cdot t \cdot \varepsilon_\gamma \cdot \frac{\Gamma_\gamma}{\Gamma} A \qquad (2)$$

Where, $f(E_0)$ is the neutron flux density at the resonance energy E_0, S is the sample area, t is measuring time, ε_γ is the detection efficiency of the detector radiative capture, $\Gamma\gamma$, Γ are the radiative and total resonance widths.

$$A = \int_{E_1}^{E_2} [1 - \exp(n\sigma(E))] dE \qquad (3)$$

is a resonance area under the transmission curve, where E_1, E_2 – initial and final values of energy range near resonance, $\sigma(E)$ is the total cross section at this energy with Doppler broadening, n is the number of isotope nuclei per unit area.

As can be seen from (3), the value A includes the required parameter – the number of isotope nuclei per unit area. The procedure for extracting this parameter and a description of the use of additional measurements with standard samples are described in [2]. The analysis results are presented in Table 1.

Table 1. The results of measurements of the fragment of mirror by the NRCA method

Element	Massa, g	Weight, %
Cu	16.76±0.98	89±5
Sn	1.06±0.22	5.6±1.2

4. CONCLUSION

The fragment of the mirror was found in the necropolis Volna 1 on the Taman Peninsula. The elemental and isotopic composition of the sample was determined by NRCA. The mass of the fragment of the mirror is 18.83 g. According the result of analysis the value of determine total elements mass coincides with the artifact mass within the margin of error. The result obtained allows us to be sure that during the manufacture of this mirror in the 6th-4th centuries BC. tin bronze was used with a tin content of up to 10%. These data are well extrapolated to the results of studies of Greek and Etruscan bronze mirrors, carried out by various methods of analysis. In this case, the NRCA method showed good results in the analysis of completely corroded objects, on which it is difficult to study the composition of the metal by other standard analysis methods.

Acknowledgements. The authors express their gratitude to the staff of the IREN facility and A.P. Sumbaev, the head of the facility development, to V.V. Kobets, the head of sector No.5 of the Scientific and Experimental Injection and Ring Division of the Nuclotron (Veksler and Baldin Laboratory of High Energy Physics), for the supporting with uninterrupted operation of the facility in the process of measurements. We are also grateful to D. Borisov, a laboratory assistant of the Neutron-Nuclear Interactions Research sector, for useful discussion.

The study was supported by a grant from the RSF № 23-18-00196.

REFERENCES

1. Postma H. and Schillebeeckx P., 2017, *Ed. by N. Kardjilov and G. Festa* Springer, Cham., pp.235–283.
2. Sedyshev P.V., Simbirtseva N.V., Yergashov A.M., Mazhen S.T., Mareev Yu.D., Shvetsov V.N., Abramzon M.G., and Saprykina I.A., 2020, *Physics of Particles andNuclei Letters*, vol.**17**, No.3, pp.389–400.
3. Bazhazhina N.V., Mareev Yu.D., Pikelner L.B., Sedyshev P.V., Shvetsov V.N., 2015, *Physics of Particles and Nuclei Letters*, vol. **12**, pp. 578–583.
4. N. Simbirtseva, P.V. Sedyshev, S. Mazhen, A. Yergashov, A. Yu. Dmitriev, I. A. Saprykina, R.A. Mimokhod, "Non-destructive investigation of the Kyathos (6th-4th centuries BCE) from the necropolis Volna 1 on the Taman Peninsula by neutron resonance capture and X-ray fluorescence analysis", Acta IMEKO, 2022, 11(3), 20.
5. Belikov O., Belozerov A., Becher Yu., Bulycheva Yu., Fateev A., Galt A., Kayukov A., Krylov A., Kobetz V., Logachev P., Medvedko A., Meshkov I., Minashkin V., Pavlov V., Petrov V., Pyataev V., Rogov A., Sedyshev P., Shabratov V., Shvec V., Shvetsov V., Skrypnik A., Sumbaev A., Ufimtsev V., and Zamrij V., 2010, *Journal of Physics: Conf.* Ser. **205**, 012053.

6. Sumbaev A., Kobets V., Shvetsov V., Dikansky N., and Logatchov P., 2020, *https://iopscienchttps://doi.org/10.1088/1748-0221/15/11/T11006*
7. Maletsky H.,.Pikelner L.B.,.Rodionov K.G., Salamatin I.M., and Sharapov E.I., 1972, *Communication of JINR13-6609* Dubna, JINR, 1–15 (in Russian).
8. Sukhoruchkin S.I., Soroko Z.N., and Deriglazov V.V., 1998, *Low Energy NeutronPhysics. Landolt Bornstein. V.* **I/16B**, Berlin: Springer Verlag.
9. Mughabghab S.F., 1984, Neutron Gross Sections, Neutron Resonance Parameters andThermal Gross Sections. *Academic Press*, New York.

Using Rutherford Backscattering Spectroscopy to Investigate ErF_3 Doped CaF_2 Samples

P.L. Tuan[1,2,*], M. Kulik[3], M. Stef[4], T.V. Phuc[5,6], N.T.B. My[1,7], N.N. Anh[8,9], T.Y. Zelenyak[1], G. Buse[4], A. Racu[4], A. Doroshkevich[1], L.H. Khiem[5,6], V.D. Cong[1,5]

[1]*Frank Laboratory of Neutron Physics, Joint Institute for Nuclear Research, Dubna, 141980, Russia;*
[2]*Hanoi Irradiation Center, Vietnam Atomic Energy Institute, Hanoi, 129000, Viet Nam;*
[3]*Institute of Physics, Maria Curie-Skłodowska University, Pl. Marii Curie-Skłodowskiej 1, 20-031 Lublin, Poland;*
[4]*Faculty of Physics, West University of Timisoara, 300223 Timisoara, Romania;*
[5]*Institute of Physics, Vietnam Academy of Science and Technology, 10 Dao Tan, Ba Dinh, Hanoi, 118500, Viet Nam;*
[6]*Graduate University for Science and Technology, Vietnam Academy of Science and Technology, 18 Hoang Quoc Viet, Cau Giay, Hanoi, 122100, Viet Nam;*
[7]*Institute for Nuclear Science and Technology, Vietnam Atomic Energy Institute, Hanoi, 122100, Viet Nam;*
[8]*Faculty of Fundamental Science, PHENIKAA University, Yen Nghia, Ha Dong, Hanoi 12116, Viet Nam;*
[9]*PHENIKAA Research and Technology Institute (PRATI), A&A Green Phoenix Group JSC, No.167 Hoang Ngan, Trung Hoa, Cau Giay, Hanoi 11313, Viet Nam.*

Rutherford backscattering spectroscopy (RBS), a nuclear method, was used to study ErF_3 doped CaF_2 samples at varied concentrations. The acquired results allow us to determine the linked changes in the element concentrations of the samples as Er^{3+} ions are doped. Furthermore, we construct the model using the SIMNRA computer code to simulate the RBS spectra of all the studied samples with varying incidence angles. We may use the model to determine the depth profile of elements obtained directly from the RBS experiment spectra because the simulated spectra correspond well with the experimental spectra.

Keywords: RBS; SIMNRA; depth profile; calcium fluoride;

**Corresponding author:* phanluongtuan@gmail.com

1. Introduction

Rutherford backscattering spectroscopy (RBS) is based on the principles of elastic scattering, which were first discovered by Ernest Rutherford in the early 20th century. Rutherford conducted his famous gold foil experiment, in which he bombarded a thin gold foil with alpha particles and observed their scattering patterns [1]. This experiment led to the discovery of the atomic nucleus and provided the foundation for RBS. Over the years, RBS has undergone continuous refinement and improvement. The advent of accelerator technology with the availability of high-energy ion beams and sophisticated detectors, such as silicon surface barrier detectors [2] and position-sensitive detectors, enabled more accurate and precise measurements of the backscattered particles [3]. These advancements facilitated the analysis of thinner films and provided a deeper understanding of surface layers and interfaces. In addition to technological advancements, the development of computer algorithms and

modeling techniques has played a vital role in the progress of RBS. Theoretical models and simulations have been developed to interpret the experimental data, allowing researchers to extract detailed information about the sample, such as elemental depth profiles and film thicknesses [4,5]. Today, RBS has become a powerful analytical technique in materials science, semiconductor industry, and nuclear physics research. It is a non-destructive method used to investigate the composition and structure of thin films and surfaces [6].

In this study, we investigate ErF_3 doped CaF_2 samples using the RBS method. To accomplish this, the samples were produced with varying concentrations of ErF_3. The RBS examines were conducted with varying incident angles to investigate the depth profile of elements in the samples. SIMNRA computer code was used to build the model, which was used to determine the concentration and depth distribution of elements in the samples.

2. Rutherford backscattering spectroscopy (RBS)

RBS is based on the elastic scattering of high-energy ions (usually helium or hydrogen) from the nuclei in a sample. RBS is unique in that it allows quantification without the use of reference standards. The RBS can determine elemental composition, atomic concentration, depth distribution of elements in samples. A detailed explanation of the basic concepts behind the RBS approach was provided in [1] and the following is a brief introduction. Fig. 1 shows the backscattering process schematic.

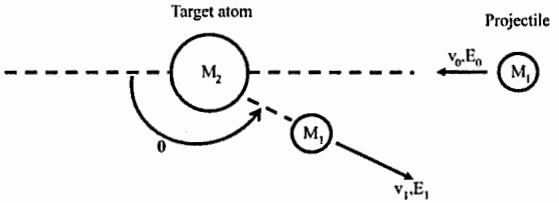

Fig. 1: Graphic illustrating an elastic collision between a projectile with mass M_1, velocity v_0, and energy E_0 and a resting target mass M_2.

A stationary particle of mass M_2 collides elastically with an incoming ion of mass M_1 traveling at v_0 and with kinetic energy E_0. Following collision, the incident ion moves with a velocity of v_1 and kinetic energy of E_1 at a scattering angle of θ with regard to the incident direction. The kinematic factor K, which depends on the mass of the incident ion M_1, mass of the scattered particle M_2, and the scattering angle θ, is the ratio of the kinetic energy after a collision to the kinetic energy before a collision.

$$K = \frac{E_1}{E_0} = \frac{M_1.v_1^2}{M_2.v_0^2} = \left(\frac{M_1.cos\theta + \left(M_2^2 - M_1^2.sin^2\theta\right)^{1/2}}{M_1+M_2}\right)^2 \quad (1)$$

If E_0, M_1, and θ are known, one may use this method to calculate M_2 by measuring the energy E_1 following a collision. The RBS method gives an option for determining the atomic mass of elements in samples with kinematic factor K. The differential scattering cross section $\frac{d\delta}{d\Omega}$ with the solid angle of detection Ω gives the likelihood that a collision will produce a detected particle. Rutherford's formula yields the cross section for differential scattering:

$$\frac{d\sigma}{d\Omega} = \left(\frac{Z_1 Z_2 e^2}{2E}\right)^2 \cdot \frac{\left\{cos\theta + \left[1 - \left({}^{M_1}/_{M_2} sin\theta\right)^2\right]^{1/2}\right\}^2}{sin^4\theta\left[1 - \left({}^{M_1}/_{M_2} sin\theta\right)^2\right]^{1/2}} \quad (2)$$

Only when $M_1 << M_2$ does this formula hold true for values in the laboratory frame of reference. This equation makes $\frac{d\delta}{d\Omega}$ proportional to Z_2^2. Heavy atoms scatter light atoms far more effectively than light atoms do for any given projectile. So, compared to light elements, RBS is considerably more sensitive to them. A typical surface-barrier detector system in RBS has a solid angle Ω that is rather small and could be referred to as a differential solid angle $d\Omega$. The average differential scattering cross section, often known as the scattering cross section σ, is then conveniently introduced:

$$\sigma = \left(\frac{1}{\Omega}\right) \cdot \int_{\Omega} \left(\frac{d\sigma}{d\Omega}\right) d\Omega \quad (3)$$

With very small detector angle Ω, $\sigma \rightarrow \frac{d\delta}{d\Omega}$

In the experimental setup, a uniform beam is incident on a uniform target at normal incidence. The target is bigger than the region covered by the beam. The total number of detected particles, denoted as A, can be expressed as:

$$A = \sigma\Omega \cdot Q \cdot Nt \quad (4)$$

This equation demonstrates that the number of atoms per unit area in the target (elements composition), Nt, may be calculated when σ and Ω are known and the number of incident and detected particles are tallied. The additional energy loss that occurs as the beam enters and exits the target can be used to estimate the depth of a specific type of nucleus. The depth of penetration of the beam depends on its initial energy.

3. Experiments

The preparation of ErF_3 doped CaF_2 samples with different concentration was conducted at West University of Timisoara, Romania utilizing the vertical Bridgman method [7]. The RBS measurements were carried out at the Frank Laboratory of Neutron Physics (FLNP), Joint Institute for Nuclear Research (JINR), Dubna, Russia. The operating pressure in the scattering chamber was less than 10^{-4} Pa. The samples were put on the holders which is possible to change the incident angle continuously without breaking vacuum. To investigate the depth profile of elements in the samples, the various incident angles at 30^0 and 0^0 were applied. The diameter of α-beam with energy 2 MeV, which was generated by EG5 Van de Graff accelerator, is 1 mm. The silicon planar detector with 15 ÷ 25 keV energy resolution was placed at the scattering angle of 170^0 away from the beam incident direction. The solid angle of the particle detector was 0.002 sr. More details connected with the RBS experimental setup were reported in [4,5] The calculated spectra have been derived with the help of the SIMNRA computer code [8].

4. Results and discussions

The spectra from RBS experiments are presented in Fig. 2 for the samples with different concentration of ErF_3 doped CaF_2.

We have identified three kinematic borders in the spectra, which are located close to channels 800, 600, and 400. The energy of He^+ ions backscattering on Er atoms at the surface

layer of the samples is indicated by the kinematic border around channel number 800. The Er concentration in the samples is correlated with the height of the Er signal in the region between channels 600 and 800. The energy of He^+ ions backscattering on Ca and F nuclei in the samples is shown by the other kinematic limits close to channels 600 and 400.

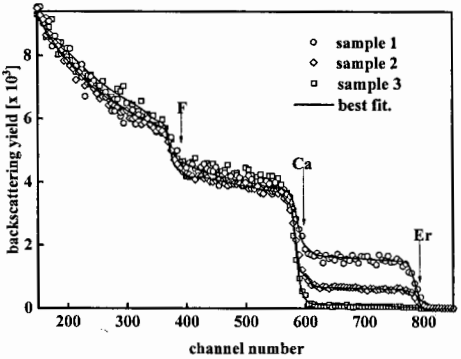

Fig. 2: RBS spectra collected from ErF_3 doped CaF_2 samples.

The depth profile of the samples under investigation is studied using the SIMNRA computer code. The computer code can simulate the RBS spectrum of a sample model that the user has defined. The program includes all experimental details, such as detector resolution, energy per channel, incidence angle, and scattering angle. Users must provide SIMNRA with identical replicas of the detector and ion beam specifications used in the investigations. The sample structure information is also known as the sample model. In particular, the model allows for the examination of the sample's depth profile by allowing for the division of the model into numerous layers. A four-layer model was used in this investigation. The element concentrations of Ca, F, and Er are among the model parameters for each layer. These model parameters are adjusted until the simulated and observed RBS spectra agree. In Table 1, the thickness and elemental makeup of the models are displayed.

Table 1: Depth profiles of all elements are contained in the CaF_2:ErF_3 samples

The models	Layers	Thickness (10^{15} atoms/cm^2)	atomic concentration (%)		
			F	Ca	Er
Sample 1	1	4000	66.50	31.50	2.00
	2	5000	66.30	31.70	2.00
	3	4000	66.29	31.71	2.00
	4	6000	66.30	31.70	2.00
Sample 2	1	4000	65.50	33.82	0.68
	2	6000	65.00	34.30	0.70
	3	3000	65.02	34.28	0.70
	4	5000	64.99	34.31	0.70
Sample 3	1	6000	61.93	38.00	0.07
	2	5000	62.00	37.93	0.07
	3	6000	62.03	37.90	0.07
	4	7000	62.01	37.92	0.07

5. Conclusion

RBS is a non-destructive method that can provide in-depth knowledge on the distribution and composition of elements in a material. This investigation's goal is to assess the RBS-mediated incorporation of ErF_3 into CaF_2 samples. The results of this study can help improve our understanding of the atomic-scale interactions between ErF_3 and CaF_2 while also shedding light on doped samples. The model was successfully built using the SIMNRA computer code, and it offers detailed data on the distribution and elemental composition of the samples.

Acknowledgments

The authors wish to acknowledge the technical staff of the EG-5 group, FLNP, JINR for the RBS measurements. The study was performed in the scope of RO-JINR Project No. 366/2021 item 84, and Vietnam-the International Center of Physics at the Institute of Physics Grant ICP.2022.04.

References

1. W.K. Chu, J.W. Mayer, and M.A. Nicolet, Backscattering Spectroscopy, Academic Press, New York, 1978.
2. Kim HS, Park SH, Ha JH, Cho SY, Kim YK. Characteristics of Silicon Surface Barrier Radiation Detectors for Alpha Particle Detection. JKPS 2008; 52:1754-1758. https://doi.org/10.3938/jkps.52.1754.
3. Grupen, C., & Shwartz, B. (2008). Particle Detectors (2nd ed., Cambridge Monographs on Particle Physics, Nuclear Physics and Cosmology). Cambridge: Cambridge University Press. doi:10.1017/CBO9780511534966
4. T.V. Phuc, M. Kulik, D. Kołodyńska, L.H. Khiem, P.L. Tuan, J. Zuk, M. Turek, Investigations of chemical and atomic composition of native oxide layers covering SI GaAs implanted with Xe ions, Surface and Coating Technology 387 (2020). doi.org/10.1016/j.surfcoat.2020.125871.
5. P.L. Tuan, M. Kulik, J. Nowicka-Scheibe, J. Zuk, P. Horodek, L.H. Khiem, T.V. Phuc, Nguyen Ngoc Anh, M. Turek, Investigations of chemical and atomic composition of native oxide layers covering SI GaAs implanted with Xe ions, Surface Coating. Technol. 394 (2020), doi.org/10.1016/j.surfcoat.2020.125871
6. Nastasi, M., Mayer, J.W., & Wang, Y. (2014). Ion Beam Analysis: Fundamentals and Applications (1st ed.). CRC Press. doi.org/10.1201/b17310
7. I. Nicoara, M. Stef, Growth and Characterization of Doped CaF2 Crystals, Modern Aspects of Bulk Crystal and Thin Film Preparation, InTechOpen (2012). DOI: 10.5772/28943.
8. M. Mayer, SIMNRA User's Guide, Max-Planck-Institut fur Plasmaphysik, Garching, Germany.

Development of a Methodology for Analyzing Organic Carbon and $\delta^{13}C$ in Soil and Sediment Samples through EA-IRMS

Tran Quang Thien*, Le Xuan Thang, Nguyen Thi Huong Lan, Phan Son Hai, Tran Tuan Anh , Nguyen Minh Dao, Nguyen Huu Nghia, Phan Quang Trung, Vo Thi Mong Tham

Dalat Nuclear Research Institute, Lamdong, Vietnam

** E-mail: tranquangthien@outlook.com*

This study presents a method for analyzing carbon content and carbon isotope ratio ($\delta^{13}C$) of soil and sediment samples. Quality control (QC) samples were used to evaluate analytical precision and accuracy. The standard deviations and biases of $\delta^{13}C$ (‰) and carbon content were calculated for each QC sample. The results showed that the measurements for B2153 Low Organic Content Soil IRMS Standard and IVA Peat Soil had the largest and smallest standard deviation values for $\delta^{13}C$ (‰), respectively. The bias of $\delta^{13}C$ (‰) also varied significantly among the samples, with the measurements for B2151 exhibiting the highest bias and those for IAEA-CH3 exhibiting the smallest. Regarding carbon content, the standard deviation values for the samples ranged from 0.07% to 0.20%. The B2151 High Organic Content Sediment IRMS Standard sample showed the smallest bias, while the largest bias belonged to sample IVA Peat Soil. In addition, the process of removing carbonates from soil and sediment samples using a 0.5M HCl solution was shown to be stable and dependable. The $\delta^{13}C$ of total organic carbon (TOC) values of the analyzed samples ranged from -28.56 ± 0.01 to -23.35 ± 0.11 (‰). Sample soil mix had the highest concentration of TOC, resulting in a depleted $\delta^{13}C$ value that was much lower than the remaining samples. Lastly, a strong correlation between the $\delta^{13}C$ of Total C values in the sediment samples and TOC/Total C ratio was observed.

Keywords: *$\delta^{13}C$, organic carbon, carbonate removal*

1. Introduction

Soil and sediment are important components of the Earth's ecosystem, and understanding their composition is crucial for many environmental and agricultural applications. One important aspect of soil and sediment analysis is the determination of the organic carbon content, which is used to evaluate the quality and fertility of soils, and to assess carbon sequestration potential. Organic carbon (OC) is a key component of the carbon cycle as it represents a large pool of carbon in the Earth's system. OC can function as a sink or source of carbon depending on the environmental conditions, and its fate can have significant implications for the global carbon cycle [1–2]. OC and $\delta^{13}C$ analysis are powerful tools for

understanding the origin and fate of carbon in soil and sedimentary environments. One widely used method for analyzing carbon content and isotopic composition is elemental analysis-isotope ratio mass spectrometry (EA-IRMS) [3–4].

EA-IRMS allows for simultaneous determination of carbon content and isotopic composition in the samples. The $\delta^{13}C$ value, the ratio of ^{13}C to ^{12}C expressed as a deviation from the Vienna Pee Dee Belemnite (VPDB) standard, is commonly used to evaluate the isotopic composition of OC in the samples [5]. The ratio of stable isotopes $\delta^{13}C$ is commonly used as a proxy for the source of organic matter, the degree of degradation, and the environmental conditions during sediment formation. A higher $\delta^{13}C$ ratio indicates a higher contribution of terrestrial plant material or anoxic conditions, while a lower ratio indicates a higher contribution of marine organic matter or oxide conditions [6–7].

Carbonate minerals, however, can interfere with the accurate measurement of organic carbon content, particularly when using isotopic analysis techniques such as EA-IRMS. Carbonates contain carbon that can be easily converted into CO_2 during analysis, leading to erroneous results for the organic carbon content and isotope ratios. Therefore, it is necessary to treat the sediment samples with acid to remove the carbonates and retain only the organic carbon for analysis.

To address this issue, researchers have developed methods to remove carbonates from soil and sediment samples prior to analysis. These methods typically involve the use of strong acids, such as hydrochloric acid (HCl) or acetic acid (CH_3COOH), to dissolve the carbonates while leaving the organic matter intact [8].

This study aims to contribute to this effort by developing a procedure for carbonate removal from soil and sediment samples using HCl. The procedure will be optimized to ensure efficient removal of carbonates while minimizing damage to the organic matter and will be validated using a range of soil and sediment samples from different environments. The effectiveness of the procedure will be assessed by comparing the results obtained before and after carbonate removal, and by evaluating the accuracy and precision of the organic carbon content and isotope ratios obtained using EA-IRMS.

2. Material and methods

2.1. Sample description

Determining the carbon content and isotopic ratios in soil and sediment samples is an important task for geologists and environmental scientists. The EA-IRMS method is a well-established technique that allows for the accurate measurement of both the amount of total organic carbon (TOC) and the isotope ratio $\delta^{13}C$ in various soil and sediment samples. We first established a standardized method for analyzing the samples by using standard reference material (SRM) samples. To ensure the accuracy and precision of the analysis, a set of carbon content and carbon isotope ratio standards are used for quality control (QC). Afterwards, we evaluated several sediment samples that contained varying levels of TOC and TIC (total inorganic carbon) and used the established method to determine the TOC and $\delta^{13}C$ isotope ratio. The information on samples was shown in Table 1.

Table 1. Information of samples

Type	Sample	Matrix	$\delta^{13}C_{VPDB}$, (‰)	C (%)
SRM	IVA Ure	Ure	-36.54±0.06	-
	IAEA-603	Calcite	+2.46±0.01	-
	IVA Sulphanilamide	Sulphanilamide	-	41.81±0.21
QC	IVA Peat Soil	Soil	-	15.95±0.03
	IAEA-CH-3	Cellulose	-24.72±0.04	-
	Elemental Microanalysis B2151	High Organic Content Sediment IRMS Standard	-28.85±0.10	7.45±0.14
	Elemental Microanalysis B2153	Low Organic Content Soil IRMS Standard	-22.88±0.40	1.86±0.14
Sample	LS	Lake Sediment		
	MS	Marine Sediment		
	NIST 2709 mix with $CaCO_3$	Soil		
	Soil mix with $CaCO_3$	Soil		

2.2. Carbonate removal

The carbon content of a sedimentary sample was analyzed in this study. The sample consisted of both organic and inorganic carbon, and to determine the $\delta^{13}C_{TOC}$, a weak acid solution (dilute HCl) was used to remove the carbonate component.

To remove the carbonate, a portion of the air-dried sample (0.5g) was placed in a round-bottom centrifuge tube and a weak acid solution (0.5M HCl) was added. The tube was gently shaken to ensure the acid covered the entire sample and then placed in an ultrasonic bath for 60 minutes to break up any remaining carbonate particles. The tube was then centrifuged to separate the remaining sample residue from the liquid, and the process was repeated twice to ensure complete removal of the carbonate.

The remaining sample residue was washed six times with deionized water to remove any remaining acid or carbonate particles. The liquid was then pipetted out, and the sample was dried in an oven at 60°C. Finally, the sample was ground to a fine powder (100 to 200 μm) using an agate mortar before being analyzed with the EA-IRMS.

To conduct this study, the sample was treated twice more with HCl solution using the same procedure used to remove carbonate. The aim was to assess how effective the carbonate removal process was, as well as to see how using HCl solution affected the TOC content and $\delta^{13}C$ value of the sample being analyzed.

2.3. Analysis

To analyze stable isotope ratios of carbon in sediment samples, the system EA-IRMS (model: Flash IRMS), made by Thermo Scientific in Germany, was used.

To begin the analysis, each sample is weighed at 0.5 – 3 mg and placed into a small tin capsule 8 mm × 5 mm (height × diameter). The sample is then loaded into the MAS 200R autosampler and fed into the EA's combustion chamber.

In the combustion chamber, the sample is ignited with O_2 gas in a quartz tube at 1020°C. The resulting product is a mixture of gases, which includes CO_2 and H_2O. These gases are transported by a high-purity helium gas (99.999% purity) at a rate of 110 mL/min to

the reduction chamber. Then, residual O_2 is removed. The H_2O component formed during the combustion process is removed and retained by the water trap column, which contains magnesium perchlorate. The only gases that remain is CO_2, which continue to be transported into the gas chromatographic column.

In the gas chromatographic column, N2 is separated from CO2, and the content of C in the sample is determined by the Thermal Conductivity Detector (TCD). Finally, the He carrier CO_2 into the IRMS to determine the $\delta^{13}C$ in the sample.

The results of stable isotope ratios and uncertainties were calculated using The Kragten spreadsheet approach based on the SRM sample provided in Table 1. The QC samples were analyzed together to verify the process [5]. For the analysis of the concentration of C, a calibration curve was constructed from the Sulphanilamide sample with varying masses.

3. Results and Discussion

Table 2 presents the standard deviations of analytical values and bias for $\delta^{13}C$ (‰) and carbon content in the QC samples. The largest standard deviation value for $\delta^{13}C$ (‰) is associated with the B2153 sample (0.12 ‰), while the smallest is linked to IAEA-CH3 (0.03‰). This indicates that the measurements for B2153 are more variable compared to those of IAEA-CH3. The bias of $\delta^{13}C$ (‰) also varies significantly among the samples. The measurements for B2151 exhibit the highest bias (0.87%), while those for IAEA-CH3 exhibit the smallest bias (0.04%).

Table 2. Results analysis of QC samples

QC	n	$\delta^{13}C_{VPDB}$ (‰)			C (%)		
		Certificate	Analysis	Bias (%)	Certificate	Analysis	Bias (%)
IVA Peat Soil	3	-	-	-	15.95±0.03	15.20±0.20	-4.70
IAEA-CH-3	4	-24.72±0.04	-24.71±0.03	0.04	-	-	-
B2151	3	-28.85±0.10	-29.10±0.09	0.87	7.45±0.14	7.32±0.07	1.74
B2153	2	-22.88±0.40	-22.82±0.12	-0.26	1.86±0.14	1.94±0.08	4.30

Regarding carbon content, the standard deviation values for the samples range from 0.07% for sample B2151 to 0.20% for sample IVA Peat Soil. Thus, the measurements for IVA Peat Soil show greater variability compared to those for B2151. The B2151 QC sample shows the smallest bias (1.74%), indicating that the measurements for this sample are closer to the true value, while the largest bias (-4.70%) belongs to sample IVA Peat Soil. This indicates that the measurements for IAV Peat Soil are further from the true value than those for other samples.

The process of removing carbonates from soil and sediment samples using a 0.5M HCl solution has been shown to be stable and dependable. This is supported by the results of a Carbonate re-removal analysis of the treated samples in Table 3, which showed that dilute HCl solution did not affect the $\delta^{13}C$ or TOC values in the analyzed samples. When comparing the results of the Carbonate re-removal samples with the results of the Carbonate removal samples, there were small fluctuations in the values within the analytical error.

Table 3. Results analysis of samples

Sample	None Carbonate removal		Carbonate removal		Carbonate re-removal	
	$\delta^{13}C_{VPDB}$ (‰)	Total C (%)	$\delta^{13}C_{VPDB}$ (‰)	TOC (%)	$\delta^{13}C_{VPDB}$ (‰)	TOC (%)
LS	-23.02±0.02	1.44±0.01	-23.35±0.11	1.29±0.01	-23.79±0.17	1.26±0.01
MS	-18.54±0.15	0.72±0.01	-23.86±0.15	0.47±0.02	-23.66±0.14	0.51±0.01
NIST 2709 mix	-15.34±0.16	2.12±0.16	-25.58±0.13	1.01±0.04	-25.56±0.10	0.90±0.10
Soil mix	-17.04±0.01	8.10±0.03	-28.56±0.01	5.18±0.08	-28.55±0.10	4.99±0.22

The $\delta^{13}C$ of TOC values of the analyzed samples ranged from -28.56 ± 0.01 to -23.35 ± 0.11 (‰). Sample Soil mix had the highest concentration of TOC (5.18 ± 0.08 %) and accounted for the majority of Total C (about 64% of Total C), resulting in a depleted $\delta^{13}C$ value that was much lower value than the remaining samples. For sample LS, the TOC content occupied a substantial portion of the sample (1.29 ± 0.01 % of TOC in 1.44 ± 0.01 % of Total C), resulting in no difference between the $\delta^{13}C$ of TOC and $\delta^{13}C$ of Total C.

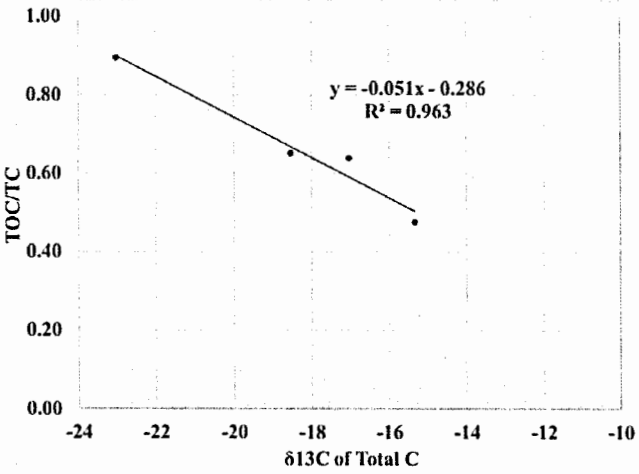

Figure 1. Relationship between $\delta^{13}C$ of Total C and TOC/Total C ratio.

The $\delta^{13}C$ of Total C values in the sediment samples strongly correlated between the ratio of TOC/TC and $\delta^{13}C$ of TOC in the sample. The linear regression equation in Figure 1 shows that when the ratio of TOC/TC in the sample is small, indicating a larger TIC content, the mutual influence of the mixture of TOC and TIC in the sample will lead to a higher $\delta^{13}C$ of Total C value than samples with a large TOC/TC ratio (which are samples containing mainly organic carbon). The strong correlation with $R^2 = 0.963$ can be used as a reference to predict the TIC present in the sample and choose a suitable method to remove carbonate in the sample.

4. Conclusion

The results of this study indicate that the use of a 0.5M HCl solution to remove carbonates from soil and sediment samples is a stable and dependable method for preparing samples for $\delta^{13}C$ and TOC analysis. The Carbonate re-removal analysis showed that the dilute HCl solution did not affect the analytical values of the samples, indicating that the method is reliable. The $\delta^{13}C$ values for the analyzed samples ranged from -28.56 ± 0.01 to -23.35 ± 0.11 (‰), with the sample with the highest TOC content showing the lowest $\delta^{13}C$ value. The standard deviation and bias values varied among the QC samples, indicating differences in measurement variability and accuracy among the samples. Overall, the results of this study provide important insights into the preparation and analysis of soil and sediment samples for $\delta^{13}C$ and TOC measurements and contribute to the development of more accurate and reliable methods for studying carbon cycling in terrestrial ecosystems.

References

1. Jackson, E.L., English, N.B., Irving, A.D., Symonds, A.M., Dwane, G., Nevin, O.T., & Maher, D.T. (2019). A multifaceted approach for determining sediment provenance to coastal shipping channels. Journal of Marine Science and Engineering, 7(12), 434. https://doi.org/10.3390/jmse7120434
2. Schwarzbauer, J., Dsikowitzky, L., Heim, S., & Littke, R. (2005). Determination of 13C/12C-ratios of anthropogenic organic contaminants in river water samples by GC-IRMS. International Journal of Environmental Analytical Chemistry, 85(6), 349–364. https://doi.org/10.1080/03067310500060944
3. Mabit, L., Gibbs, M., Mbaye, M., Meusburger, K., Toloza, A., Resch, C., Klik, A., Swales, A., & Alewell, C. (2018). Novel application of CSSI techniques to investigate on-site sediment origins across arable fields. Geoderma, 316, 19–26. https://doi.org/10.1016/j.geoderma.2017.11.012
4. Graham, M.C., Eaves, M.A., Farmer, J.G., Dobson, J., & Fallick, A.E. (2001). A study of carbon and nitrogen stable isotope and elemental ratios as potential indicators of source and fate of organic matter in sediments of the Forth Estuary, Scotland. Estuarine, Coastal and Shelf Science, 52, 375–380. https://doi.org/10.1006/ecss.2000.0726
5. Dunn, P.J.H., & Carter, J.F. (2018). Good Practice Guide for Isotope Ratio Mass Spectrometry Second Edition 2018. FIRMS Network. ISBN: 978-0-948926-33-4.
6. Nguyen, T.H.H., Vu, H., Ha, L.A., Giap, T.V., & Vuong, N.V. (2018). A procedure of determining carbon-13 composition in soil organic carbon on an Isotope Ratio Mass-Spectrometer. Nuclear Science and Technology, 8(1), 23–28. https://doi.org/10.26583/nst.2018.8.1.03
7. Komada, T., Anderson, M.R., & Dorfmeier, C.L. (2008). Carbonate removal from coastal sediments for the determination of organic carbon and its isotopic signatures, δ13C and Δ14C: Comparison of fumigation and direct acidification by hydrochloric acid. Limnology and Oceanography: Methods, 6, 254–261. https://doi.org/10.4319/lom.2008.6.254
8. Fernandes, M., & Krull, E. (2008). How does acid treatment to remove carbonates affect the isotopic and elemental composition of soils and sediments? Environmental Chemistry, 5, 33–39. https://doi.org/10.1071/EN07080

Neutron Induced Reactions, Calculations

Evaluation of a Mistaken Asymmetry in the Projected Experimental Search of Spatial Anisotropy of Gammas from ^{109}Ag(n, γ) Reaction at Neutron Energies near 32-eV p-Wave Resonance

Kuznetsov V.L.[1,2], Mitsyna L.V.[1], Rebrova N.V.[1], Sedyshev P.V.[1]

[1]*Frank Laboratory of Neutron Physics, JINR, Dubna*
[2]*Laboratory of Neutron Research, INR RAS, Troitsk*

Investigations of the spatial parity violation in nuclear reactions, which were started in 60-th years of the last century, are of current importance up to now. In the compound-nuclear reaction, a weak interaction appears as small states mixing which results in anisotropy of the reaction-products emission. According to theoretical estimation, there is a dynamic magnification factor for the mixing of the states of opposite parities, and for middleweight and heavy nuclei it has to be ~10^3.

An experiment is prepared for a detection of the anisotropy of γ-quanta emission at the radiative decay of ^{110}Ag nucleus after capture of neutrons with energies in the region of 30.6-eV s-wave and 32.7-eV p-wave resonances of ^{109}Ag isotope. As these two closely spaced states just have opposite parities, the dynamic magnification factor is a promoting cause for experimental detection of the sought γ -emission anisotropy effect. The experiment is planned to run by the time-of-flight method at 10-m flight-path of the IREN facility.

A multiple scattering of neutrons before capture in the target always distorts the shape of neutron-capture resonances measured with the time-of-flight technique, and there are difficulties for a choice of the sample thickness in order to minimize an undesirable distortion of the desired anisotropy effect. A compromise must be found, as the unambiguity of the required effect demands a thin target, while a thick target is preferable for a high statistical accuracy. It might be as well to provide an absolute advantage of neutron capture without their scattering in the target and, at the same time, the statistics must be high enough. Moreover, the investigated p-wave neutron resonance of ^{109}Ag is located on a slope of its strong s-resonance which complicates a background removal.

As the experiment preparation, Monte-Carlo simulations have been made to determine a contribution of multiple scattering of neutrons before their capture in natural-silver plates (51.8% of ^{109}Ag and 48.2% of ^{107}Ag) of several thicknesses (0.05, 0.1, 0.15, 0.25, 0.35, 0.5 and 0.65 cm) and the same 10×10 cm^2 cross size. Capture and scattering cross sections of ^{109}Ag and ^{107}Ag isotopes were taken from the tables of ENDF/B data-library, where Doppler broadening was already taken into account.

In Fig.1 there are calculations of total capture of neutrons by natural silver of these different thicknesses (close points) as well as cross sections for neutrons captured without scattering in the targets (open circles), for neutrons captured after multiple (crosses) and after single (open squares) scattering. In these calculations, an equal statistics of 10^7 events was taken for all points of incident-neutrons energies.

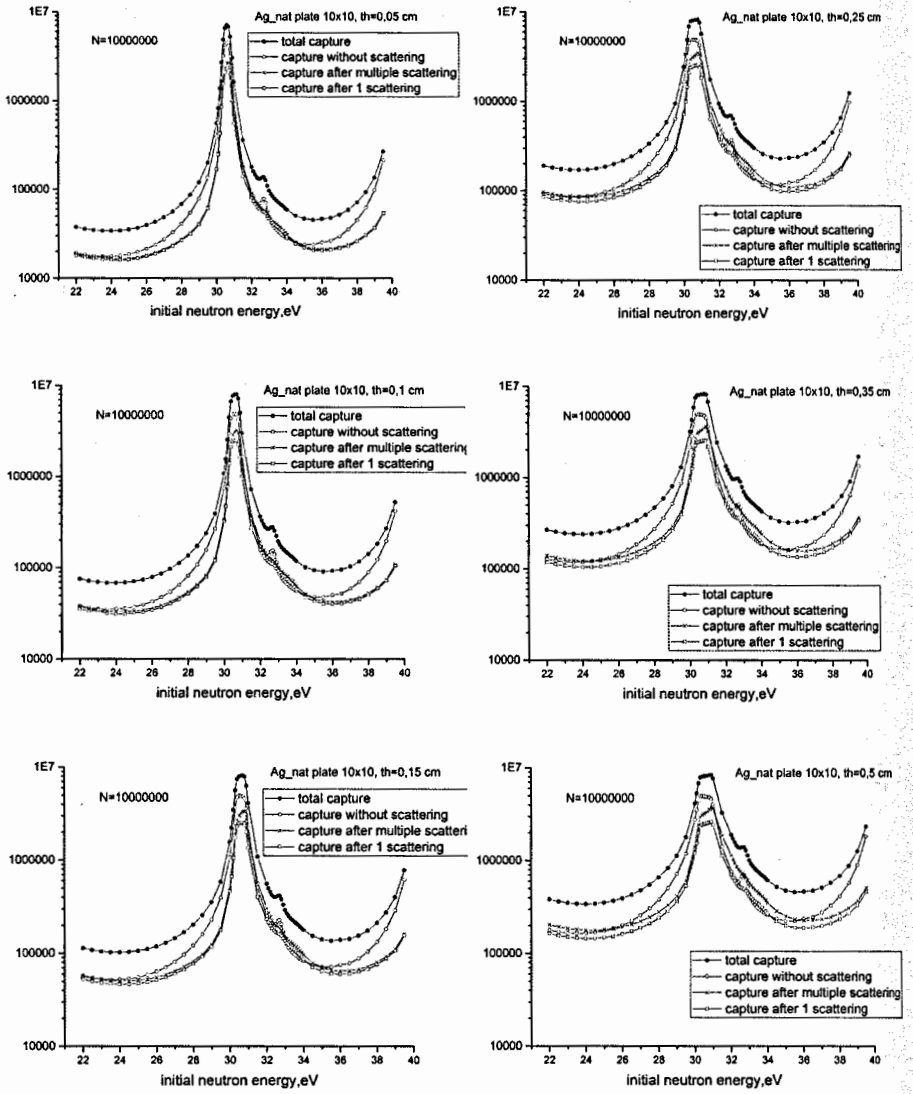

Fig.1. Calculations of capture of neutrons by the natural-silver targets which are 10×10 cm^2 plates with thicknesses 0.05, 0.1, 0.15, 0.25, 0.35, and 0.5 cm.

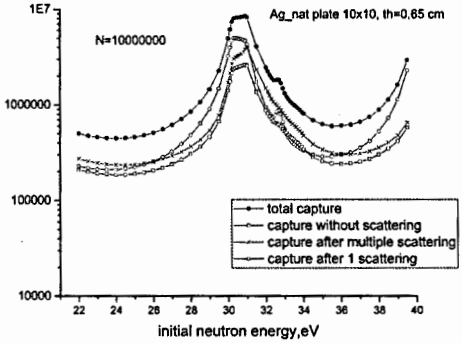

Fig.1. Calculations of capture of neutrons by 10×10 cm^2 natural-silver plate with thickness 0.65 cm.

The calculations with taking into account a multiple scattering of neutrons before their capture show a noticeable asymmetry of the neutron-capture peaks. The peaks are gently sloping from the side of incident-neutron energies bigger than maxima energies. At the incident-neutron energies more than 30.6-eV s-wave resonance maximum, captured neutrons are growing in number, as a decrease in energy of neutron after scattering approaches its reduced energy to the maximum of capture cross-section. This effect brings an additional difficulty in correct determination of experimental background.

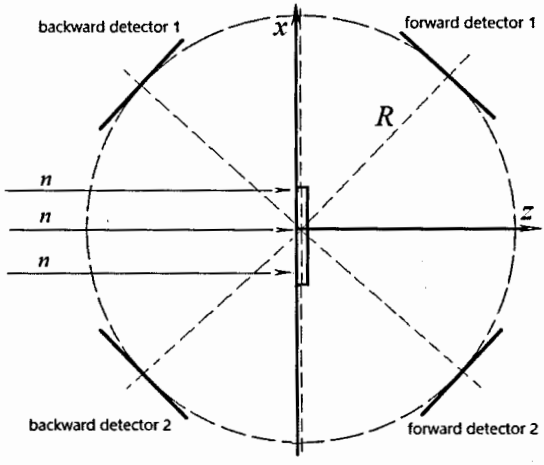

Fig.2. The X-Z plane view for Monte-Carlo calculations of record of emitted γ-quanta.

In order to estimate a value the distorting kinematic asymmetry of γ-quanta emission at incident-neutron energies near 32.7-eV p-wave resonance of ^{109}Ag, the Monte-Carlo calculations of this kinematic effect were made in real geometry under condition of emission isotropy of γ-quanta, which were recorded by 4 detectors placed at R=15 cm distance from the center of the target at the angles 45°, 135°, 225° and 315°. In Fig.2 the X-Z vertical view for Monte-Carlo calculations is presented. The sizes of the entry windows of all detectors were

the same – 6.5 cm in width and 7.6 cm in height (Y axis-size), the targets were 10×10 cm^2 plates with different thicknesses (Z axis-size). In this case calculations were made for 10^9 incoming neutrons with given incident-neutron energy.

Fig. 3 shows the asymmetry effect $\varepsilon(E)$ calculated for γ-quanta emitted from the natural-silver target with thickness of 0.35 cm under condition of quanta-yield isotropy. The upper pictures of Fig.3 represent the $\varepsilon(E)$-effect calculated when neutrons are captured without scattering in the target in wide investigated incident-neutron energy interval and specifically near investigated p-wave resonance, correspondingly. In the lower pictures there is the kinematic effect at total neutron capture with taking into account multiple scattering.

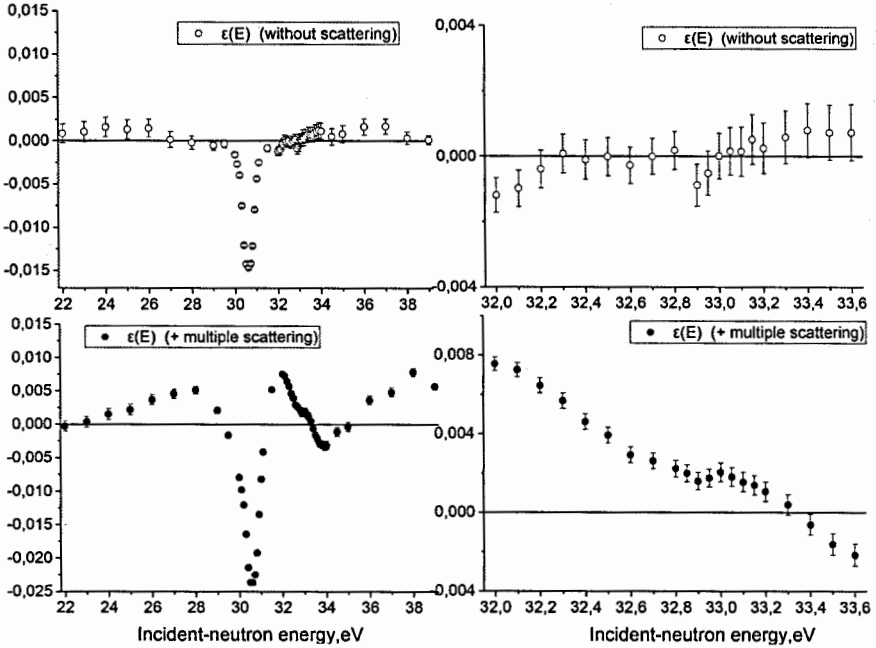

Fig.3. An asymmetry effect $\varepsilon(E)$ calculated under condition of γ-quanta isotropic emission from ^{109}Ag(n,γ)-reaction in the natural-silver 10×10 cm^2 target with thickness of 0.35 cm. In upper pictures: $\varepsilon(E)$ effect without taking into account multiple scattering of neutrons before capture; in lower pictures: $\varepsilon(E)$ effect of γ-quanta emission at total neutron capture. From the left: $\varepsilon(E)$ effect calculated in wide neutron-energy interval; from the right: $\varepsilon(E)$ near investigated p-wave resonance.

The anisotropy effect can be calculated as

$$\varepsilon(E) = \frac{N_{1f}(E) + N_{2f}(E) - N_{1b}(E) - N_{2b}(E)}{N_{1f}(E) + N_{2f}(E) + N_{1b}(E) + N_{2b}(E)}.$$

Here $N_{1f}(E)$ and $N_{2f}(E)$ are numbers of γ-quanta recorded by forward detectors, which are placed at angles 45° and 315° relative to the incident-neutron direction, $N_{1b}(E)$ and $N_{2b}(E)$ are numbers of gammas recorded by backward detectors at angles 135° and 225°, correspondingly. An increase in the target thickness leads to enlargement of neutron capture, so number N of detected gammas rises. The mean-square error decreases $\sim 1/\sqrt{N}$. Taking into account statistical errors of counts, an absolute uncertainty $\Delta\varepsilon(E)$ of foregoing ratio is determined by formulae

$$\Delta\varepsilon(E) = \varepsilon(E)\sqrt{\frac{1}{N_{1f}(E)+N_{2f}(E)+N_{1b}(E)+N_{2b}(E)} + \frac{N_{1f}(E)+N_{2f}(E)+N_{1b}(E)+N_{2b}(E)}{\left(N_{1f}(E)+N_{2f}(E)-N_{1b}(E)-N_{2b}(E)\right)^2}}.$$

As the upper picture of Fig.3 (from the left) shows, there is an evident asymmetry of gammas under conditions of γ-quanta isotropic emission, even if neutrons are captured without scattering in the target. This effect is explained by a preponderance of a neutron capture cross-section over scattering at the incident-neutron energies near 30.6-eV s-resonance of ^{109}Ag. As there is an inverse relation between neutron run in the target and the total cross-section at corresponding neutron energy, so at incident-neutron energies near strong s-resonance, when the total cross-section is inherently capture one, a marked difference appears in solid angles to forward and backward detectors.

The kinematic asymmetry effects were also calculated at the incident-neutron energies near investigated p-wave resonance of ^{109}Ag for 10×10 cm^2 plate-targets with thicknesses (th) of 0.05, 0.1, 0.15, 0.25, 0.5, and 0.65 cm. These calculations are shown in Fig.4a and Fig.4b.

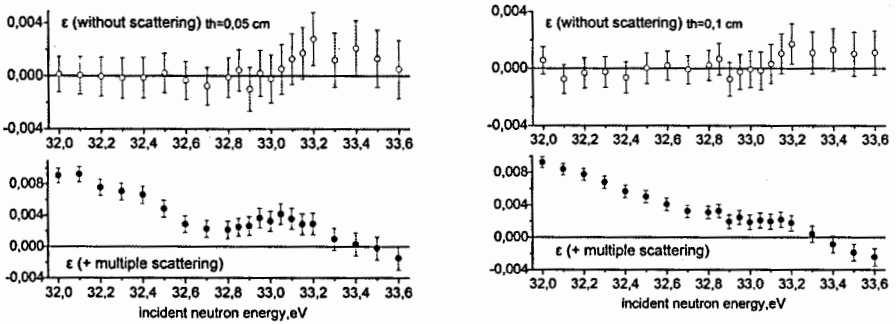

Fig.4a. The kinematic-asymmetry effects $\varepsilon(E)$ calculated under condition of γ-quanta isotropic emission in ^{109}Ag(n,γ)-reaction at the incident-neutron energies near investigated p-wave resonance. The natural-silver targets are 10×10 cm^2 plates of 0.05 cm (from the left) and 0.1 cm (from the right) thicknesses. In upper pictures: $\varepsilon(E)$ effect without taking into account multiple scattering of neutrons before capture; in lower pictures: $\varepsilon(E)$ effect at total neutron capture in the target.

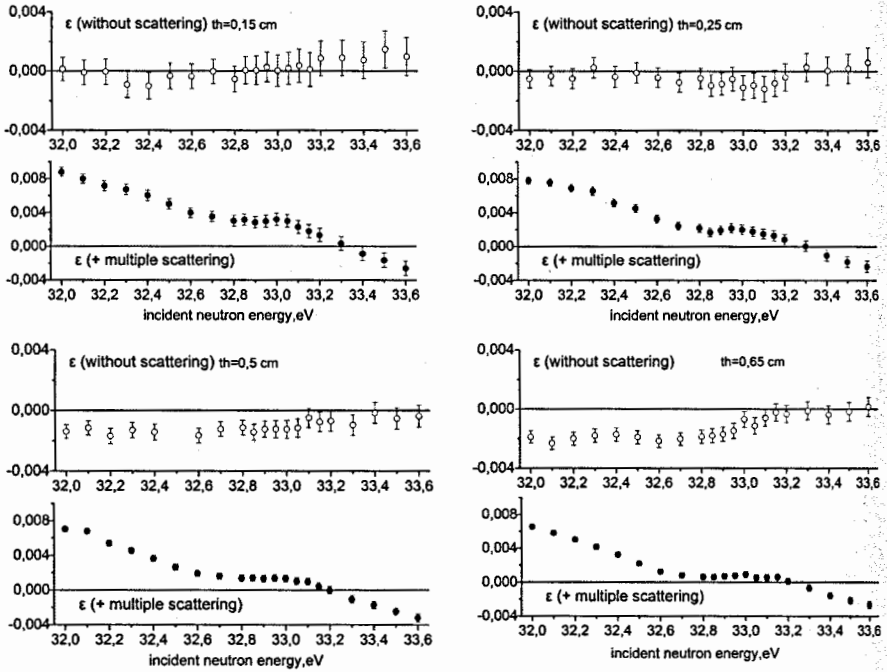

Fig.4b. The kinematic-asymmetry effects $\varepsilon(E)$ calculated under condition of γ-quanta isotropic emission in ^{109}Ag(n,γ)-reaction at the incident-neutron energies near investigated p-wave resonance. The natural-silver targets are 10×10 cm^2 plates of different thicknesses (th= 0.15, 0.25, 0.5, and 0.65 cm). In upper pictures: $\varepsilon(E)$ effect without taking into account multiple scattering of neutrons before capture; in lower pictures: $\varepsilon(E)$ effect at total neutron capture in the target.

Thus, Monte-Carlo calculations showed that under condition of isotropic γ-emission from ^{109}Ag(n,γ) reaction, the asymmetry-effect of gamma-quanta recording near 32.7eV-resonance is about 1%. For a correct analyze of the experimental anisotropy in order to obtain the statistically significant value of spatial asymmetry (or to evaluate it reliably), it is important to establish and take into account the asymmetries which distort counts of the detectors and inevitably contributed to the sought spatial anisotropy.

Observation of Structural Gamma Quanta in Neutron Radiative Decay

Khafizov R.U.[a], Kolesnikov I.A.[a], Nikolenko M.V.[a], Tarnovitsky S.A.[a], Tolokonnikov S.V.[a], Torokhov V.D.[a], Trifonov G.M.[a], Solovei V.A.[a], Kolkhidashvili M.R.[a], Konorov I.V.[b]

[a]*NRC «Kurchatov Institute», Russia*
[b]*Technical University of Munich, Munich, Germany*

khafizov_ru@nrcki.ru

The purpose of the study of neutron radiative decay is to further advance the atomic project for which the «Kurchatov Institute» was established. In the last experiment when we first detected radiative decay events, the value of its main characteristic, decay branching ratio (BR) significantly exceeded the one calculated according to the Standard Model of Electroweak Interaction. In this experiment we were the first to measure the branching ratio (B.R.) of radiative neutron decay B.R. = $(3.2\pm1.6)10^{-3}$ (where C.L.= 99.7% and gamma quanta energy threshold is equal to 35 Kev). On the other hand, theoretical calculations of this value according to the Standard Model give 1.5 times lower value. Thus, in our experiment we recorded additional gamma quanta which are structural gamma quanta emitted by the quarks that a neutron consists of.

Introduction

The study of neutron radiative decay is essential for the further development of the atomic project as it creates a new basis for advancing the controlled nuclear fusion. In our recent experiment to measure the relative intensity B.R. of neutron radiative decay we discovered extra gamma quanta produced during neutron decay with the bremsstrahlung gamma quanta emitted from the regular beta decay products. These extra gamma quanta are structural gamma quanta; they carry information about the quark structure of the neutron and are formed during the u and d quarks transition.

Below (see Fig. 1) follow the Feynman diagrams describing neutron decay. The first diagram describes the usual beta decay of the neutron, which produces three particles: a beta electron, a proton, and an antineutrino. This diagram describes the main mode of neutron decay. In the experiment we recorded the number of such decays by the number of double coincidences of the electron and the proton N_D. However, in any decay with the formation of charged particles there is a so-called radiative decay mode, in which, in addition to the regular decay products, an additional particle, a gamma-quantum, is recorded. This additional radiative gamma quantum is a bremsstrahlung gamma quantum emitted from a charged particle which is flying in the bremsstrahlung electric field of another charged particle. In case of neutron beta decay, bremsstrahlung gamma quanta can be emitted from proton (second diagram in Fig. 1) and beta electron (third diagram in Fig. 1). However, there is still a possibility of gamma emission, which occurs when the structure itself of the elementary particle changes. In the case of neutron decay this process is shown in the fourth diagram in Fig. 1, when gamma-quantum is emitted from the very top of the decay at the transition of u and d quarks included in the structure of neutron and proton. In the experiment, we recorded the number of radiative decay events of the neutron by triple coincidences of electron, proton,

and gamma-quantum N_T.

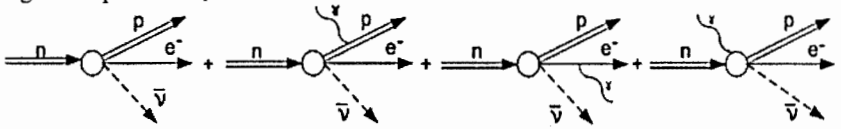

Fig.1. The diagrams describing ordinary beta decay and neutron decay with gamma-quantum emission.

The main characteristic of elementary particle decay is its relative intensity, branching ratio (BR):

$$BR = I(\text{radiative decay}) / I(\text{ordinary decay}) = N(e,p,\gamma) / N(e,p)/k = N_T / N_D/k,$$

where the numbers of triple N_T and double N_D coincidences should be taken directly from the experimental spectra of triple and double coincidences, so that a determination BR indeed reduces to measuring the spectrum of e-p double coincidences and the spectrum of e-p-γ triple coincidences. Without performing an analysis of these spectra, it is impossible to evaluate the branching ratio BR. An additional coefficient k is the so-called geometric factor. It takes into account the geometry of the experimental facility used. The geometric factor k is determined by means of a Monte Carlo simulation of the experiment using the package of CERN programs GEANT IV.

Until recently, the rare radiative mode of neutron decay was not discovered and was considered only theoretically [1–4]. Our first attempt at detecting events of radiative neutron decay was undertaken at the Institut Laue–Langevine (ILL) in employing an intense cold-neutron beam [5]. The experiment that our group performed in 2005 at the FRMII reactor of the Technische Universität München became the first experiment that resulted in observing this process [6]. We were the first to identify events of radiative neutron decay by means of triple coincidences in which an emitted gamma-quantum was recorded as a third particle in addition to the electron and recoil proton. Thus, we were able to measure the branching ratio for the radiative mode of neutron decay. The result was $BR = (3.2\pm1.6)\cdot10^{-3}$ at a coincidence level of C.L.=99.7%, the gamma energy being in excess of 35 keV. In the experiments performed earlier at ILL [6] our group was able to measure only the upper limit on this branching ratio. A year later, a group of experimentalists from the National Institute of Standards and Technology (NIST) published in Nature the results of their experiment devoted to studying radiative neutron decay [7]. Their result was $BR = (3.13\pm0.34)\cdot10^{-3}$ at C.L. = 68%, the gamma energy there ranging between 15 and 340 keV. However, there were no triple coincidences in this experiment but only the spectra of double coincidences of electron - gamma-quantum and electron - ion. Obviously, without registering exactly the triple coincidence of electron, gamma-quantum, and proton, it is impossible to talk about registering the events of neutron radiative decay. Such double coincidences occur during the well-studied process of ordinary ionization of the residual gas by electrons in the chamber, as a result of which a glow appears. For example, in nature such a phenomenon is observed as the polar lights at the edge of the atmosphere. The authors of this [7] and later work [8] recorded this radiation of gamma quanta in the hard and invisible area of the spectrum, they had created the ideal conditions for this. There, as will be shown below, was a strong magnetic field, and highly rarefied residual air in the chamber, and ionizing particles (beta-electrons). In addition, the authors of this work recorded ions instead of protons, because due to the strong magnetic

field they were not able to distinguish protons and the large ionic background occurring in the experimental facility. Thus, the BR value given by the authors of [7] is the ratio of the intensity of gamma emission during the ionization of rarefied air molecules to the total number of ionization acts by beta-electrons.

Experimental facility

The layout of the proposed experimental facility is shown in Fig. 2. Passing along a rather long neutron guide equipped with a collimating system formed by LiF diaphragms, an intense beam of cold neutrons enters a vacuum chamber (1) through the last LiF diaphragms (9) positioned immediately in front of the decay zone being studied. The decay zone is viewed by detectors of three types simultaneously. These are a proton detector (3) formed by microchannel plates (MCP), an electron detector (13) formed by photomultiplier tubes 7 cm in diameter covered with a scintillator plastic 3 mm thick, and six gamma detectors (11). These six detectors surround the electron detector (see the lower panel in Fig. 2) at an angle of 35° and are formed by photomultiplier tubes covered with a sensitive CsI layer. The layer thickness is 4 mm. It is chosen in such a way that the gamma-quantum detection efficiency is equal to unity. Six gamma detectors (11) surround the electron detector (13) (see the lower panel in Fig. 2) are arranged at an angle of 35° and are protected by a cup (12) made of 6-mm lead. In principle, coincidences between the electron detector and any of the six gamma detectors can completely suppress the background of bremsstrahlung, which arises only in that section where electrons are detected. From Fig. 2, it can be seen that, in this case, part of the data is lost. However, the neutron-beam intensity of 10^{12} n/c/cm^2 in our chamber is quite sufficient in order to compensate for this loss and to retain an acceptable data-accumulation rate. Recoil protons produced in the decay zone travel through the space surrounded by a cylindrical time-of-flight electrode (7) toward the proton detector (3). After that, they are focused on this detector by means of spherical focusing electrodes (2). The focusing electrostatic field is generated between high-voltage spherical (2) and cylindrical (7) electrodes and grids (6 and 5), on one hand, and the underground proton-detector grid (4), on the other hand. It is noteworthy that recoil protons fly isotropically out of the decay vertex. An additional grid (10) is positioned on the opposite side of the decay zone in order to avoid the loss of protons that go toward the electron detector.

A signal from an electron detected in the scintillator plastic of the electron detector (13) serves a start signal that opens all time windows for all detectors. A pulse from one of the gamma detectors (11) is recorded simultaneously with this signal, but only in the case where a signal from the proton detector (3) is generated within a reasonably short time interval will this electron– gamma-quantum coincidence be recorded by an electronic system for data acquisition and data processing as an event of radiative neutron decay. Along with these triple coincidences, our electronic system records ordinary electron–proton coincidences. It should be noted that, in the case of radiative decay, the emitted gamma-quantum is detected in our facility by the gamma detectors (11), which are placed around the electron detector (13), earlier than the electron is detected by the electron detector (13). In other words, the electron should be delayed with respect to the emitted gamma-quantum in the time spectrum of triple coincidences but by an extremely small amount, e.g., a nanosecond. It is precisely this fact that will enable us to identify the peak associated with radiative gamma quanta in the spectrum of triple coincidences. In addition to triple coincidences, our setup also collects double coincidences corresponding to ordinary neutron decay. Here, it is worth noting that a very high quality of the system of diaphragms from LiF ceramics is necessary to obtain an

acceptable low level of the background in gamma quanta from an intense cold-neutron beam while passing this beam through the whole facility from the entrance window to the thick LiF ceramic target absorbing it. The entrance window and the absorbing target are the main sources of gamma background in the facility, therefore the neutron guide must be long enough and its axis must coincide with the beam axis as precisely as possible. In our case, the entrance window for the beam was at a distance of 7 meters from the area viewed by the detectors, and the absorbing target was 3 meters. In the next section we will use the time spectra of double and triple coincidences to obtain the experimental value of the main characteristic of the radiative neutron decay (BR).

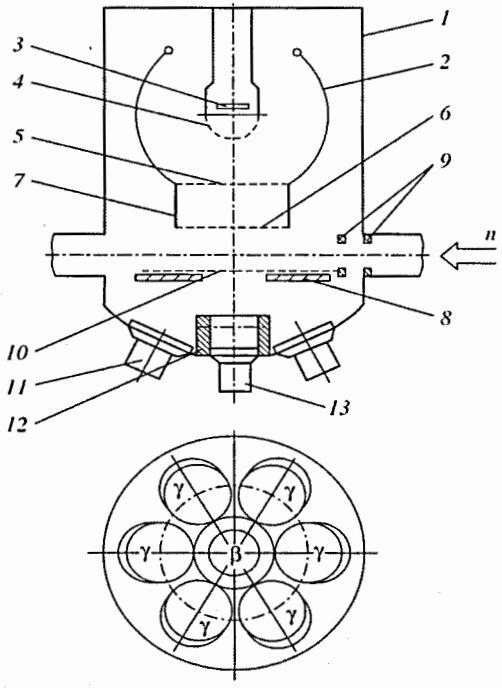

Fig.2. Layout of the experimental facility: (1) vacuum chamber, (2) high-voltage (18 to 20 kV) spherical electrodes for focusing recoil protons, (3) proton detector, (4) grid of the proton detector (underground), (5, 6) grids of the time-of-flight electrodes, (7) time-of-flight electrode (at a voltage of 18 to 20 kV), (8) plastic collimator (5 mm thick and 70 mm in diameter) for beta electrons, (9) LiF diaphragms, (10) grid for rotating recoil protons in the backward direction (at a voltage of 22 to 26 kV), (11) six photomultiplier tubes for CsI(Tl) gamma detectors, (12) lead cup, and (13) photomultiplier tube equipped with a plastic scintillator for detecting electrons.

Timing spectra of double and triple coincidences

Here we will analyze the spectra of double coincidences between beta-electron and proton, and also the spectra of triple coincidences between beta-electron, proton and gamma-

quantum. We will compare our results with the results obtained by two other groups from NIST.

Fig.3 demonstrates the summary statistics on double e-p coincidences (coincidences of a light beta-electron moving at a speed comparable to the speed of light and a delayed heavy proton, whose speed is much lower and is determined by the potential of the accelerating electrostatic field). Therefore, Fig.3 clearly shows two major peaks: one peak with a maximum in channels 99-100, which is the response to electron registration by the electronic registration and recording system [5, 6] of the experimental facility. The position of this peak determines the arrival time of the signal from the electron detector, which consists of PMTs and is coated with scintillation plastic. This peak is not physics-related in its nature. Instead, it is a response to the registration of the electron. As soon as the electronic system registers an electron, it opens a time window of one hundred channels forward and backward in time. Thus, the 100th channel is the master channel, and each channel corresponds to 25 nanoseconds, so the spectra can view all events in 2.5 μs before and after the arrival of the electron. The next peak visible on Fig. 3 has a maximum in channel 120, it is physics-related in its nature and is a proton peak, i.e. the peak of e-p coincidences of beta-electron with delayed proton. Its position determines the time of proton registration by the electronic system, and the distance between these two peaks determines the proton delay time.

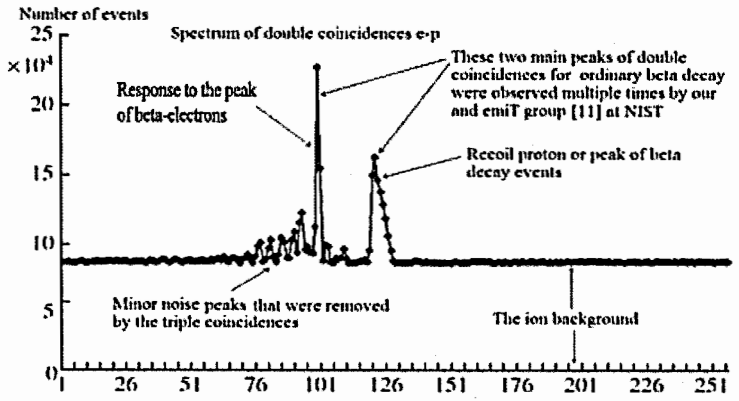

Fig.3. Timing spectrum for e-p coincidences. Each channel corresponds to 25 ns. The peak at channels 99-100 corresponds to electron registration by the electronic system. The coincidences between the decay electrons and delayed protons (e-p coincidences) are contained in the wide peak centered at channel 120.

An analogous situation was first noted in [9], then it was observed during the experiment on the measurement of the correlation coefficients by the group at ILL [5,10] and emiT group at NIST [11], and it was also mentioned at [12]. We would especially like to emphasize the correspondence of our spectrum of double coincidences with an analogous spectrum from the result obtained by the emiT group from NIST [11]. In Fig. 4 we present their spectrum and diagram for the registration of the beta electron and the recoil proton. A comparison of our results with the results of the emiT group shows their unquestionable similarity. Moreover, the position of the second proton peak in Fig. 4 (emiT group), like in

Fig.3 (our result), corresponds well to the simple estimate obtained by dividing the length of a proton trajectory by its average speed.

Here we will also note the presence of a significant homogenous ionic background in Fig.3 and Fig.4. However, in both cases this background allows to easily distinguish the neutron decay peak, and, thus, we can easily determine the number of N_D double coincidence events, i.e. the number of registered neutron beta decays. Note the most important point in the methodology of the experiment: this large ionic background cannot be distinguished from the small number of neutron decay protons (i.e. from beta decay events) in the presence of strong magnetic fields, and thus N_D cannot be determined.

Following Avogadro's law, even in the case of a very deep vacuum under pressure of $10^{-6} - 10^{-8}$ mbar air molecule concentration remains very high. In fact, it is sufficient for beta-electrons produced in neutron decay to create a significantly high ionic background in the chamber, exceeding the number of decay protons by many orders of magnitude. These ions create a homogeneous background in the absence of strong magnetic fields, throughout the whole spectrum of double coincidences. It should also be noted that the concentration of ions in the chamber does not fall in proportion to the pressure, but much more gradually, as the cubic root of the pressure. Here one must note that the probability of ion creation along the trajectory of beta-electron is in inverse proportion to the average distance between neighboring ions, i.e. is proportional not to the molecule concentration but to the cubic root of this value. This fact means that the ionic background remains significant even when the pressure is reduced by a factor of 100, which is observed when comparing our results with those of the emiT group. The emiT group's vacuum was two orders of magnitude greater, but the ionic background dropped only 4-6 times compared to ours. This estimate is confirmed when one compares the spectra on Fig. 3 and Fig. 4. Our spectrum, presented on Fig.3, has a 1:1 ratio of the value of e-p coincidences peak and the value of the background. The emiT group (Fig.4) spectrum has a ratio of 4:1 – 5:1, i.e. only 4-5 times our number, that is equal to the cubic root of 100.

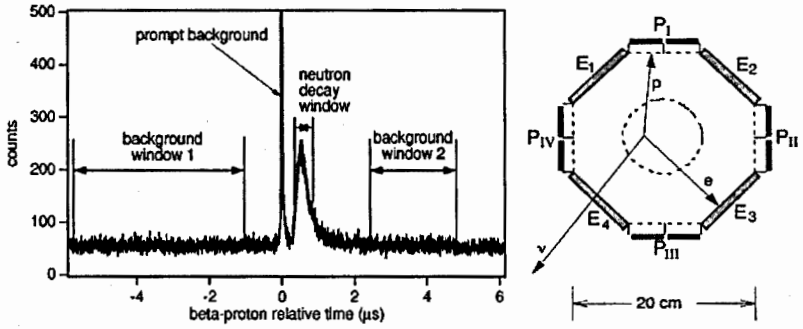

Fig.4. On the left: spectrum of double electron-proton coincidences obtained by emiT Group [11] with two peaks and a significant ion background value comparable to the neutron decay peak; on the right: emiT group scheme for registering beta electron and recoil proton.

Fig.3 shows that the total number of events in e-p coincidences peak in our experiment equals $N_D=3.75\cdot10^5$. This value significantly exceeds the value we obtained in our previous

experiment conducted in ILL. At that time, due to the low statistics volume we could not identify the B.R. itself and instead defined only the upper B.R. limit [5]. So, in both cases Fig. 3 and Fig. 4 show not one but two peaks above the homogeneous ionic background.

The remaining peaks on Fig.2 are small, with just seven peaks distinct from the statistical fluctuations. These occurred because of the noise in the electric circuits of the FRMII neutron guide hall. There are no other physics-related reasons for their occurrence. The fact is that our experiment was the first at the newly opened FRMII reactor, and the neutron guide hall was still undergoing intensive commissioning work. These peaks were appearing during the working days and disappearing over the weekends. Such behavior was observed as we collected statistics.

Now we will compare our results and the results obtained by the emiT group with the third result, that is the spectrum of double coincidences obtained by another NIST group [12]. Unfortunately, the authors did not publish the spectrum of double coincidences in their original article [7], but published it much later [12]. Fig 5 displays the spectrum on the left and the diagram of NIST experimental facility on the right. Fig. 5 clearly shows one single and a very wide peak with a long tail, which has nothing in common with either our peak or the emiT group peak.

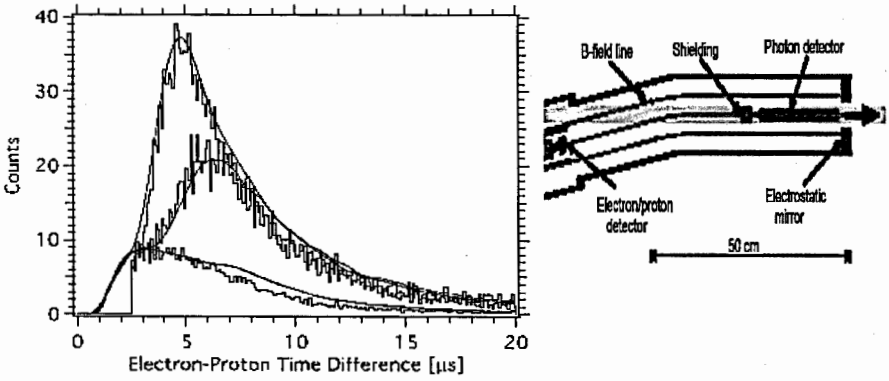

Fig.5. On the right: the facility diagram. On the left: spectrum of double coincidences published in [12]. The lower curve corresponds to 0 volts, the middle curve corresponds to 300 volts and the highest curve corresponds to 500 volts in an electrostatic mirror. The location of the peak and its width differ from our and the emiT's results by one and two orders of magnitude. The location and the width of the peak also deviate by one and two orders of magnitude from the elementary estimates of the proton decay delay times.

The significant deviation obtained is explained by the fact that the peak in the NIST experiment consists not of protons but rather of ions. The density of gas molecules inside the experimental chamber is proportional to pressure and according to the Avogadro's Law is at the order of 10^7 mol/cm^3 even at the pressure of 10^{-8}–10^{-9} mbar. This is a very significant number, quite sufficient for creation of the large ionic background in the presence of ionizing radiation created in the chamber by beta-electrons of neutron decay. The energy of beta-electrons significantly exceeds the energy of ionization. Besides, as mentioned above, the probability of ionization is inverse proportional not to volume taken up by one molecule but to the average distance between molecules. It is precisely due to this reason that the ionic

background falls much more gradually, proportionally to the cubic root of the pressure and not proportionally to the pressure. We observed a similar behavior of the ion background many times during our experiment; roughly speaking, if the pressure in the chamber dropped by an order of magnitude, the background decreased by only a factor of two or more. As mentioned above, comparing our results with those of the emiT group gives a drop in the ionic background of only 4–5 times, not two orders of magnitude. In the emiT group experiment the conditions were the same as in the second NIST group experiment, therefore the ionic background should be the same too. The light ions, together with the beta decay protons, should have a delay time comparable to 1 μs. The pulses from these particles are simply not visible in the spectrum due to the second NIST group's use of combined electron-proton detector in order to register both electrons and protons with ions. Figure 6 shows a huge pulse from an electron, which simply "blinds" the detector for the time the small pulse from the proton and light ions arrives. The maximum of the ion peak in this group experiment, according to the delay times estimations (delay time is proportional to square root of ion mass), falls exactly to the 4–6 μs on the air ions consisting of nitrogen and oxygen.

Fig.6 presents the pulse forms from the electron, ion, and gamma-quantum published by the second experimental group from NIST [7]. Firstly we should note the exceptionally long and flat front from the gamma pulse of 15 μs, which arises because of the extremely slow detectors on avalanche diodes. The authors used them because they used strong magnetic fields of several tesla, in which fast PECs do not work. As was pointed out above, a strong pulse from an electron makes weak pulses from ions and protons invisible during the first microseconds after its arrival. Namely this fact explains the dead zone around zero of the diagram in Fig. 5 which is where the pulses from the decay protons should come.

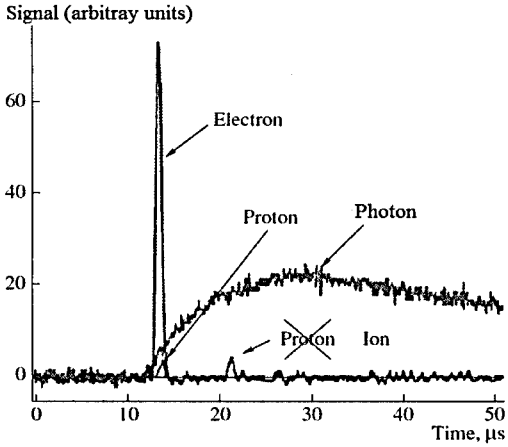

Fig.6. The signal from the proton has to be delayed by less than one microsecond, which is why it is located at the base of the strong electron signal and so cannot be registered by the combined electron-proton detector. The pulses that are delayed by longer than 1 microsecond are pulses not from protons, as it was indicated in ref. [7], but rather from ions, formed in the viewed decay zone. A pulse from a photon has a front of about 15 μs.

Let us now proceed to analysing of our triple coincidences spectra presented on Fig.7. As it was mentioned above, both double coincidences spectra obtained by our (Fig.3) and the emiT (Fig.4) groups present two main peaks located on the horizontal ionic background. As for the spectrum of triple coincidences, we should observe not two but three peaks: one radiative peak and two peaks similar to the ones in the double coincidence diagram. Let us review this similarity in more detail: the peaks on the spectrum of double coincidences are as if transferred to the spectrum of triple coincidences.

We have two channels carrying background noise with some average signal frequency f_1 and f_2. Then the probabilities for the signal hitting the time window of value T are equal for both channels $p_1=f_1T$ and $p_2=f_2T$, respectively. If we now apply the electronic coincidence scheme, then the probability of random coincidence p_c of signals on the first and second channel in the coincidence scheme with the same value of time window T is equal to product of two independent events probabilities $p_c= p_1p_2 = f_1Tf_2T$ and frequency of coincidence respectively is equal to $f_c=f_1f_2T$. Suppose now on the first channel there is not a homogeneous horizontal background of pulses with mean frequency f_1, but some input spectrum with its peaks S_{in} – then after the coincidence scheme an output spectrum proportional to the input $S_{out}= S_{in}f_2T$ with a ratio f_2T appears, note that the higher the homogeneous background on the second channel f_2, the more frequent the coincidence and the higher this ratio. Thus, all the peaks in the input spectrum also appear in the output spectrum from the coincidence scheme.

However, simply multiplying the input spectrum by a number changes the height of the peak only, but both its width and its position remain unchanged. The real electronic coincidence circuit with the detector unit also makes hardware changes to the shape of the spectrum itself. Let us review these changes in more detail on our triple coincidence spectrum, shown in Figure 7. The figure shows three peaks: the leftmost peak of triple coincidences located in channel 103, which consists of the supposed number of neutron radiative decay events we measure; two peaks from the input spectrum of double coincidences. These are the response peaks to the registration peak of electrons and delayed protons, respectively, but both response peaks on the spectrum of triple coincidences are significantly wider and located closer to each other than in the original spectrum of double coincidences (Fig.3). These two wide peaks in channels 106 and 120 converge so that there is a rather high jumper between them. In addition, there is a small parasitic electron peak, the nature of which is related to the electronic circuitry of the registration of gamma-quantum pulses.

Such distortions of the output spectrum are controlled by a standard procedure, introducing a response function for gamma channel $R_\gamma(t,t')$ [6] , which is also necessary for calculating the number of triple coincidences N_T in radiative peak:

$$S_{out}(t) = \int S_{in}(t')R_\gamma(t,t')dt'.$$

This functional multiplication instead of simple multiplication of the input spectrum by a number takes into account all the distortions of the real spectrum. Namely, the response function method is able to consider both the change of the peak width and the convergence of two response peaks located around channels 106 and 120. In a particular case, if we use the local response function with zero width as a δ-function with some coefficient, it becomes a simple multiplication of the input spectrum by the number mentioned above. If we use the non-local response function then its width will lead to an increase in the widths of the response peaks, roughly speaking, by the width of the response function, and its tails will lead to a convergence of the peaks in the output spectrum compared to the original spectrum. This

is exactly the picture we observe when comparing our double and triple coincidence spectra in Fig.3 and Fig.7. Thus, using the method of nonlocal response function we can distinguish the peak of radiative gammas on inhomogeneous double-humped background.

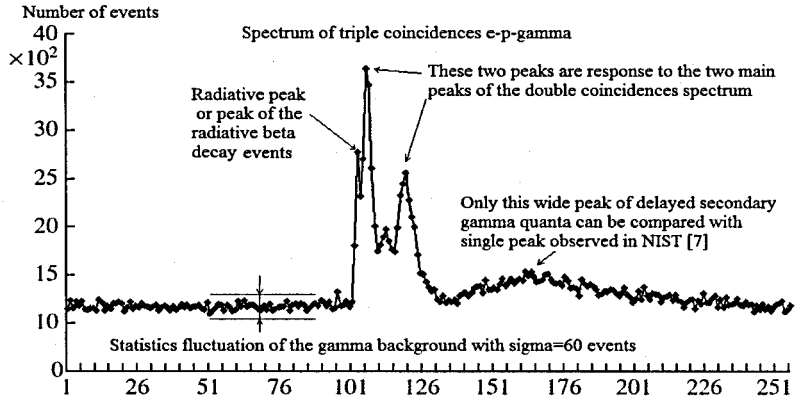

Fig.7. Timing spectrum for triple e-p-γ coincidences. Each channel corresponds to 25 ns. In this spectrum, three main peaks in channels 103, 106 and 120 can be distinguished. The leftmost peak in 103 channel among these three main peaks is connected with the peak of radiative decay events.

As for the wide peak in channel 165, it has a physical nature, has nothing in common with the peak of radiative decay and is well distinguished from it delaying at a considerable distance of 1 μs from it. This peak is created by the radioactive gamma quanta and emitted during ionization of rare atmosphere within our experimental chamber. The molecular of this medium is ionized by registered beta-electrons. This event is well studied and does not have anything in common with the new event of radiative neutron decay but happens due to the ionization of highly rarefied air by charged particles. It is this phenomenon that was observed by the second NIST group, who published a single peak shown in Fig.8 (see [7]). Let us note that the spectrum published by these authors is not a spectrum of triple coincidences; otherwise, as mentioned above, it would have had additional response peaks from the spectrum of double coincidences of the electron with the recoil proton, or, as in their case, with the ions. In fact, this experiment used everything needed to investigate the phenomenon known as polar lights. Firstly, it is the residual rarefied air, whose density just corresponds to the density of air at heights of 150–200 km, where natural polar lights occur; secondly, it is the presence of ionizing radiation in the form of beta electrons, flying from an intense beam of cold neutrons; and thirdly, it is the presence of magnetic fields. Thus, the authors of this experiment measured the relative intensity as the ratio of gamma-quanta produced by the ionization of air molecules to the total number of ions flying out of the same viewed decay zone under the influence of the electrostatic field. This ratio is also proportional to the fine structure constant $\alpha = 1/137$ and thus has the same order of magnitude as the BR in the case of neutron radiative decay.

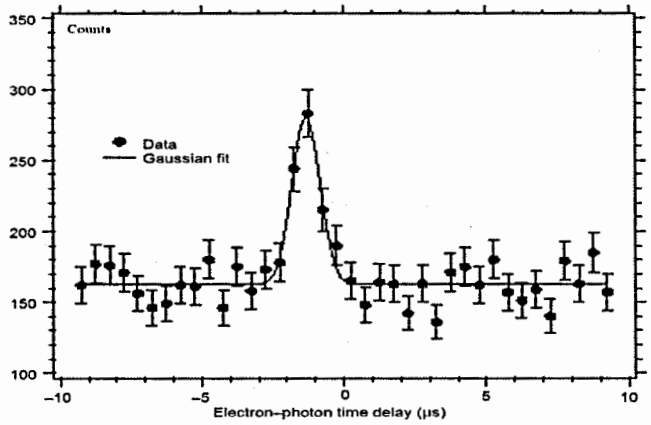

Fig.8. The single peak of "electron-photon" coincidences, shifted to the left of 0 – the time of electron registration – by 1 μs, published in [7, 8]. On the spectrum of triple coincidences (see Fig. 7) in our experiment a similar wide peak is located after the electron registration and there are no wide peaks before the beta-electron registration.

After analyzing triple coincidences spectra with the help of the non-local response function $R_\gamma(t,t')$ we finalize the number of radiative neutron decays N_T=360 with a statistics fluctuation of 60 events. B.R. can be expressed as a ratio of N_T to N_D as BR = N_T / N_D/k, where coefficient k=0.3 is the geometrical factor that we can calculate by using geometry of the facility as well as anisotropic emission of radiative gamma-quanta during neutron decay [4]. With the number of observed double e-p coincidences $N_D = 3.75 \cdot 10^5$ and triple e-p-γ coincidences N_T = 360, one can deduce the value for the main characteristics of neutron decay, branching ratio B.R.= $(3.2 \pm 1.6) \cdot 10^{-3}$ (99.7 % C.L.) with the threshold gamma energy ω=35 keV. In this case we chose C.L.= 99.7%, which corresponds to an error of 3σ, and the resulting error was 50% of the mean B.R. If, however, we choose the standard confidence limit C.L.= 68% with an error of 1σ, the error is only 15% of the mean value. On the other hand, this experimental mean of B.R. = 3.2 is 1.5 times higher than that calculated by the standard model of electroweak interaction. This means that approximately one-third of the gamma quanta we recorded are structural.

Conclusion

The main result of our experiment is the identification of neutron radiative decay events. The location and the width of the radiative peak correspond both to the estimates and the detailed Monte Carlo simulation of the experiment. We measured the relative intensity of rare neutron decay mode, B.R.= $(3.2 \pm 0.53) \cdot 10^{-3}$ (with C.L.=68% and gamma quanta energy over 35 keV). It means that the average experimental B.R. value exceeds the theoretical one calculated within the standard electroweak model by 1.5 times. At the same time, the deviation of the theoretical and experimental relative intensities exceeds the standard error of 1σ. This fact means that the experiment detected additional structural gamma quanta, which are now emitted by the quark structure of the neutron during the transition of d quark to u

quark. As follows from the comparison of experimental and theoretical values of the relative intensity of radiative gammas emitted during neutron decay, every third registered radiative gamma-quantum is a structural one.

In order to confirm and more accurately determine the intensity of structural gamma quanta emission, it is necessary to conduct a new experiment with a larger volume of collected statistics and with a lower threshold of energies of registered gamma quanta. We prepared such experiment several years ago, however, due to the lack of a PIK research neutron reactor, we cannot conduct it on an intense beam of cold neutrons.

The comparison of our results with emiT group's results on the spectra for regular neutron decay shows a complete coincidence. Both we and the emiT group obtained identical double-coincidence spectra with two peaks on the horizontal ionic background. We are very pleased to state this fact. Unfortunately, we cannot say same for another NIST group which claims to measure the relative intensity of neutron radiative decay.

Not only do they not register triple coincidences, without which it is impossible to talk about the measurement of B.R., but they also cannot register neutron radiative decay events at all. Instead, the authors of the experiment study the emission of gamma quanta by residual air molecules in the chamber when they are ionized by beta electrons from neutron decay. This process is well studied and has nothing to do with neutron radiative decay. In nature, this effect of ionization of rarefied air by electrons is observed in the form of polar lights. At the same time, as can be seen from our triple coincidence spectrum in Fig. 7, this peak of delayed gamma quanta is located after electron registration with a considerable delay of the order of 1μs and is well distinguished from the peak of neutron radiative decay. This result is in a sharp contradiction with the result of NIST group which published their only peak of double electron-gamma coincidence also for 1 microsecond, however not after, but before electron registration (see Fig.8). That is in a sharp contradiction with results of elementary evaluations, this peak simply could not appear, if it is located at such a large distance before the electron registration. We consider the location of the peak of the double electron-gamma coincidences as suggested by the authors of the contribution to Nature [7] as a sheer misrepresentation, and we understand how it happened [13]. We strongly recommend that the NIST researches withdraw their contribution to Nature and submit a new one where the only peak of the double electron-gamma coincidences is located where they actually observe it in the same 1 microsecond - not before but after the electron registration.

We express our sincere gratitude to NRC «Kurchatov Institute» Honorary President Academician E.P. Velikhov for his support, without which we would not have been able to conduct our experiments on neutron radiative decay, neither in France at ILL, nor in Germany at TUM. We would like to thank Academician S.S. Gerstein and Professor P. Depomier of Montreal University for their interest and discussions of our work.

References

1. Gaponov Yu.V., Khafizov R.U. Phys. Lett. B 379 (1996) 7–12.
2. Radiative neutron beta-decay and experimental neutron anomaly problem. By Yu.V. Gaponov, R.U. Khafizov. Weak and electromagnetic interactions in nuclei (WEIN '95): proceedings. Edited by H. Ejiri, T. Kishimoto, T. Sato. River Edge, NJ, World Scientific, 1995. 745p.
3. R.U. Khafizov, N. Severijns. About the possibility of conducting an experiment on radiative neutron beta decay. Proceedings of VIII International Seminar on Interaction of Neutrons with Nuclei (ISINN-8) Dubna, May 17–20, 2000 (E3-2000-192), 185–195.
4. Khafizov R.U. Physics of Particles and Nuclei, Letters 108 (2001) 45–53.

5. M. Beck, J. Byrne, R.U. Khafizov, et al., JETP Letters 76, 2002, p. 332.
6. R.U. Khafizov, N. Severijns, O. Zimmer et al. JETP Letters 83 (2006), p. 5.
7. J.S. Nico, et al. Nature, v. 444 (2006)1059–1062.
8. M.J. Bales, R. Alarcon, C.D. Bass, et al., Phys. Rev. Lett. 116 (2016), 242501.
9. B.G. Yerozolimsky, Yu.A. Mostovoi, V.P. Fedunin, et al., Yad. Fiz. 28, 98 (1978) [Sov. J. Nucl. Phys. 28, 48 (1978)].
10. I.A. Kuznetsov, A.P. Serebrov, I.V. Stepanenko, et al., Phys. Rev. Lett., 75 (1995) 794.
11. L.J. Lising, S.R. Hwang, J.M. Adams, et al., Phys. Rev. C. v.6, 2000, p. 055501.
12. R.L. Cooper, T. E. Chupp, M. S. Dewey, et al, Phys. Rev. C 81, 2010, p. 035503.
13. N. Severijns. Nature, v. 444 (2006) 1014–1015.

Angular Distribution in Fast Neutrons Induced Reactions on ^{64}Zn Isotope

C. Oprea[1], A.I. Oprea[2]

[1]*County Center for Education, 11 Mihai Eminescu str., 410019, Oradea, Bihor County, Romania*

[2]*Frank Laboratory of Neutron Physics, Joint Institute for Nuclear Research, 141980 Dubna, 6 Joliot Curie str., Moscow Region, Russian Federation*

Cross sections, angular distributions, forward-backward asymmetry effect and alpha spectra in fast neutrons induced processes on ^{64}Zn nucleus were investigated. Theoretical evaluations were realized using own authors codes and dedicated software for the investigation of the structure of atomic nuclei and nuclear reactions mechanisms. Contributions to the cross sections, angular correlations and alpha spectra of nuclear reactions mechanisms (direct, compound and pre-equilibrium ones) were obtained. Cross sections and angular distributions theoretical evaluations are in good agreement with existing experimental data from literature and those obtained in FLNP. Further, from the comparison of theoretical and experimental data, parameters of Woods-Saxon potential (volume, surface and spin-orbit each with real and imaginary part) were extracted.

For neutrons energy of few MeV's, experimental forward-backward effect was observed. For this incident energy of neutrons only compound mechanism is acting and therefore the measured asymmetry cannot be explained by the presence of direct processes. The possible explanations of measured forward-backward effect are also analyzed.

INTRODUCTION

Interaction of fast neutrons with light, medium and heavy nuclei are traditionally investigated for a long time at FLNP JINR, Dubna [1,2]. Fast neutrons processes are important for fundamental and applicative researches. For fundamental investigations, neutrons reactions allow to obtain new data on structure of atomic nuclei and nuclear reaction mechanisms. Neutrons represent an efficient tool for applicative studies necessary for fission and fusion projects, Accelerated Driven Systems researches (ADS), material sciences, reprocessing of nuclear waste, neutrons activation analysis and other [3,4].

Chemical element Zinc (Z = 30) has five natural isotopes. Their atomic mass A and natural occurrence (abundance) are (^{A}X(abundance[%])): ^{64}Zn(48.6%), ^{66}Zn(27.7%), ^{67}Zn(4%), ^{68}Zn(18.5%) and ^{70}Zn(0.6%) respectively [5,6].

Nuclear reaction, $^{64}Zn(n,\alpha)^{61}Ni$, with incident neutrons from 0.5 up to 25 MeV was investigated. Cross sections, angular distributions and alpha spectra were evaluated using dedicated software, authors programs and computer simulations. Theoretical evaluations were compared with experimental data obtained mainly at FLNP JINR, Dubna and in collaboration with Institute of Heavy Ions Physics from Pekin, China.

ELEMENTS OF THEORY

Authors has investigated previously the $^{64}Zn(n,\alpha)^{61}Ni$ fast neutrons reactions and were established that compound nucleus mechanism is dominant [7,8]. In this case, cross sections and angular distributions can be obtained in the frame of statistical model of nuclear reactions and Hauser-Feshbach approach, according to relations [9]:

$$\sigma_{n\alpha} = \left(\pi\lambda_n^2 T_n T_\alpha W_{n\alpha}\right)\cdot\left(\sum_c T_c\right)^{-1}, \quad (1)$$

where T are the transmission coefficients; $W_{n\alpha}$ is the width fluctuation correction factor (WFC); c represents the open channels (sum is over all possible open channels)

Differential cross section (angular distribution) as function of solid angle (Ω) is:

$$d\sigma/d\Omega = \pi\lambda^2(2I+1)T_I\sum_J\left(A_J\left(l,j\,|\,l',j'\,|\,\theta\right)\right)\cdot\left(1+\sum_{p,q}T_p\left(E_q'\right)/T_{I'}\left(E'\right)\right)^{-1}, \quad (2)$$

$$A_J\left(l,j\,|\,l',j'\,|\,\theta\right) = \sum_{m,m'}\left|\left(l,j;0m\,|\,l,j;Jm\right)\right|^2\left|\left(l',j';m'm-m'\,|\,l',j';Jm\right)\right|^2\left|Y_{l'm'}(\theta,\varphi)\right|^2, \quad (3)$$

where the sums are over quantum numbers (obeying conservation laws); Ω is the solid angle; θ is the polar angle; ϕ is the azimuth angle (is not appears in (2), (3) due to parity conservation).

Transmission coefficient represents the probability of a micro-particle to pass a potential barrier and therefore its value is lower than 1 and greater or equal with zero. There are many methods to evaluate transmission coefficients but the authors have chosen the quantum-mechanical approach based on reflection factor [7,10].

Width fluctuation correction factor indicates the correlation between incident and emergent channels. For neutrons reactions with energy around 0.5 MeV WFC factor is approximately 1 demonstrating no correlations between incident and emergent channels. By increasing the incident neutrons energy this factor is slowly decreasing and at 10–15 MeV WFC is about 0.7. From three methods of WFC factor evaluations, all with long and complicated calculations, the authors have chosen the approach from [11].

In order to take into account direct and pre-equilibrium processes in the evaluation of cross sections, angular distributions, yields and other observables, Talys code was used. Talys is a freeware soft, working under Linux, dedicated to structure of atomic nuclei and nuclear reactions mechanisms evaluations. In this code are implemented all nuclear reaction mechanisms and a large database including energy, spin and parity of the levels, parameters of optical potentials and levels density for more than 3000 natural and synthesized nuclei [12].

In the calculations direct mechanism was described by Distorted Wave Born Approximation (DWBA) [12,13] and pre-equilibrium one by two-components exciton model [12,14]. Interaction in incident and emergent channels is described by Woods-Saxon optical potential, with volume, surface and spin-orbit components, each with real and imaginary part. For charged particles it is necessary to include also Coulomb potential [12].

RESULTS AND DISCUSSIONS

Cross section of $^{64}Zn(n,\alpha)^{61}Ni$ reaction (Q = 3.86 MeV – nuclear reaction heat) with neutrons with energies starting from 0.5 up to 25 MeV was calculated. Theoretical results are shown in Figs. 1a and 1b. In Fig. 1a, contribution of nuclear reaction mechanisms was obtained. Main contribution to the cross section is given by compound processes (curve 2). After 8 MeV multistep compound pre-equilibrium mechanism is enabled (curve 3), and around 18 MeV "pure" compound and pre-equilibrium compound are overlapped. Contribution of direct processes (curve 4) to the cross section can be neglected. Cross section of (n,α) reaction is given by curve 1 and is the sum of 1–3.

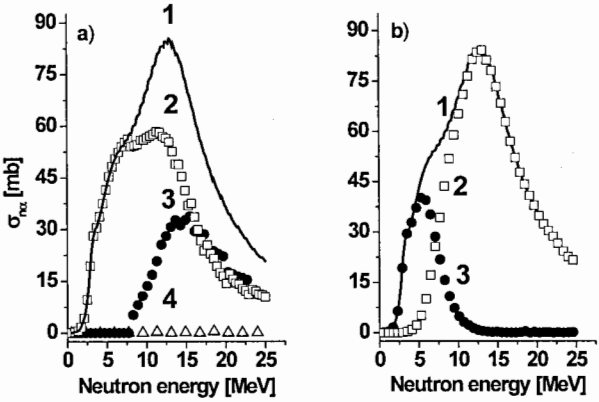

Fig. 1. Cross section evaluation of $^{64}Zn(n,\alpha)^{61}Ni$. a) Nuclear reaction mechanisms: 4 – direct; 3 – pre-equilibrium compound; 2 – compound; 1 – total (4+3+2). b) Contribution of residual nucleus states: 3 – discrete; 2 – continuum; 1– total (3+2).

In Fig. 1b the same cross section is separated in contribution of discrete and continuum states of residual nucleus ^{61}Ni. Cross section of discrete states is important up to 10 MeV and is much higher than in the other (n,α) processes investigated by authors. Continuum states (curve 2) are acting in whole neutrons energy interval but they become dominant after 12–13 MeV. Curves 1 in Figs. 1a and 1b are the same and both are the sum of extracted components.

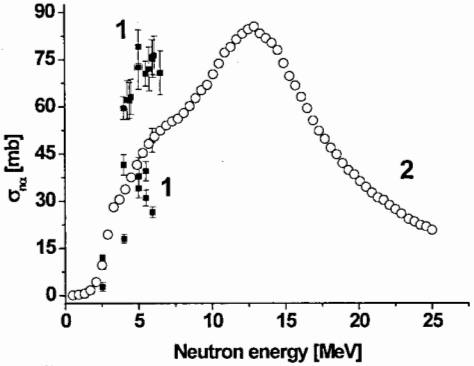

Fig. 2. $^{64}Zn(n,\alpha)^{61}Ni$ cross section. Theory and experiment. 1 – Experimental data. 2 – Theoretical evaluation.

Comparison between theoretical and experimental cross section data are represented in Fig. 2. Experimental data were obtained mainly in international collaboration of FLNP JINR, Dubna with Chinese research institutes [16,17]. Two groups of data can be observed and can be described theoretically but with two different sets of input parameters. The authors have

chosen an "average" set between both groups of measurements. Curve 2 in Fig. 2 is the same with curves 1 in Figs. 1a and 1b.

Angular distributions in a large neutrons energy interval were evaluated and compared with experimental data. In Fig. 3a theoretical and experimental differential cross section for E_n = 4 MeV are shown. In Fig. 3b alpha spectrum obtained in $^{64}Zn(n,\alpha)^{61}Ni$ at 4 MeV neutrons incident energy is represented.

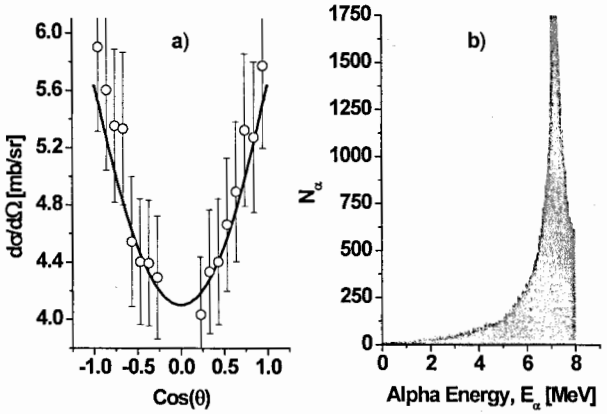

Fig. 3. Angular distribution and alpha spectra in $^{64}Zn(n,\alpha)^{61}Ni$ for $E_n = 4$ MeV. a) Differential cross section. b) Modeled alpha spectrum.

Differential cross section from Fig. 1.a was considered as weighted sum of Legendre Polynomials:

$$\frac{d\sigma}{d\Omega} = \sum_{k=0,even} a_k P_k(Cos(\theta)). \tag{4}$$

Experimental data, taken from [16], are well described but with large errors. Like in the case of cross section, from Fig. 2, measurements are affected by the presence of other open channels with participation of alpha particles. At this energy, angular distribution is given only by compound processes.

Alpha spectra from Fig. 1.b were obtained using angular correlation which is calculated by norming differential cross section to cross section. Angular distribution of polar angle θ, was modeled by Direct Monte Method, according to the relation:

$$\frac{2\pi}{\sigma_{n\alpha}} \int_0^{\theta_c} W(\theta)\sin(\theta)d\theta = r \Rightarrow \theta_c, r \in [0,1), \theta \in [0,\pi). \tag{5}$$

In the simulations, target is considered with finite dimensions and it was taken into account energy loss of alpha particles in the target. Modeled alpha spectrum from Fig. 3b was obtained on a target with 263 μg/cm^2 thickness and 4 MeV neutrons energy.

Simulation of alpha spectra for different energy is of interest in the analysis of possible asymmetry effects in $^{64}Zn(n,\alpha)^{61}Ni$ reaction. Authors from [16,17] revealed some forward-

backward effects (FB) in (n,α) processes on other medium and heavy nuclei. Considering description of measurements from [16,17], FB effect has the following expression:

$$A_{FB} = A_{FW} / A_{BW} = \int_{0}^{\pi/2} W(\theta)\sin(\theta)d\theta \Big/ \int_{\pi/2}^{\pi} W(\theta)\sin(\theta)d\theta, \quad (6)$$

where A_{FB} is the number of forward events (azimuth and polar angle, $\phi \in [0,2\pi]$, $\theta \in [0,\pi/2]$); A_{BW} is the number of backward events ($\phi \in [0,2\pi]$, $\theta \in [\pi/2,\pi]$)

Taking into account procedure of generation of the events according with relations (4–6), modeled FB effect for 10^6 events, 263 μg/cm^2 thickness and 4 MeV neutrons energy, is:

$$A_{FB}^{SIM} = 1.001 \pm 0.0017. \quad (7)$$

Result from (7) is expected because angular distribution is given only by compound mechanism. There is no direct component, the mechanism responsible for asymmetries in differential cross section. Analysis of experimental data, at 4 MeV-energy [16], revealed the existence of an experimental FB effect of 1–2% affected by large error.

$$A_{FB}^{EXP} = 1.017 \pm 0.09. \quad (8)$$

Theoretical evaluations from the present work were obtained considering 30 levels of residual nuclei for elastic and inelastic scattering and 10 levels for reaction channels. In the calculations all nuclear reactions mechanisms possible open channels were enabled.

Table 1. Parameters of Woods-Saxon potential by components: volume, surface and spin-orbit with real and imaginary part

Channel	Volume WS – Real			Volume WS – Imaginary		
	V [MeV]	r_V [fm]	a_V [fm^{-1}]	W [MeV]	r_W [fm]	a_W [fm^{-1}]
n	52.69	1.203	0.668	0.19	1.279	0.668
α	169.37	1.184	0.676	25.70	1.340	0.500
	Spin – orbit – Real			Spin – orbit - Imaginary		
	V_{SO} [MeV]	r_{VSO} [fm]	a_{VSO} [fm^{-1}]	W_{SO} [MeV]	r_{WSO} [fm]	a_{WSO} [fm^{-1}]
n	5.08	1.024	0.590	0.01	1.024	0.590
α	0	0	0	0	0	0

Parameters of Woods-Saxon potential [12], for incident and emergent channels, obtained from analysis of cross section data are shown in Table 1.

CONCLUSIONS

Cross sections, angular distributions, alpha spectra and FB effect, for ^{64}Zn(n,α)^{61}Ni nuclear reaction induced by fast neutrons with energies from 0.5 up to 25 MeV were investigated. Using dedicated software and codes written by authors, cross sections, angular distributions were calculated and compared with experimental data from literature. The good agreement between experimental and theoretical cross sections and angular distributions data

suggested the modeling of FB effect, applying Direct Monte-Carlo method. In the computer modeling, at 4 MeV neutrons energy, FB effect was not obtained, in comparison with existing experimental data. At 4 MeV incident energy only compound mechanism is acting and therefore no FB effect can be revealed. For full incident energy interval, contribution to the cross sections of nuclear reaction mechanisms and of discrete and continuum states of residual nuclei were extracted. Analyzing theoretical and experimental cross section data, parameters of nuclear potentials for incident and emergent channels was also obtained.

In the future it is necessary to extend and continue the analysis of angular distributions for energy higher than 4 MeV. In the same time, new cross section (n,α) measurements in a large energy interval are of interest in order to improve cross sections experimental data and computer modeling.

REFERENCES

1. I.M. Frank, *Fifteen Anniversary of the Discovery of the Neutron*, Sov. Phys. Usp., vol. 25, p. 279 (1982).
2. L.B. Pikelner, Yu.P. Popov, E.I. Sharapov, Intensive Nuclear Spectroscopy with Neutrons in *Fifteen Anniversary of the Discovery of the Neutron*, USSR Academy of Science, Nuclear Physics Department, Nauka Publishing House, Moscow p. 80 (1983) (in Russian).
3. T. Kooyman, L. Buiron, G. Rimpault, *Annals of Nuclear Energy*, vol. 112, pp. 748 (2018).
4. Y.M. Gledenov, M.V. Sedysheva, P.V. Sedyshev, A. Oprea, Z. Chen, Y. Chen, J. Yuan, G. Zhang, G. Tang, G. Khuukhenkhuu, P.J. Szalanski, *Nucl.Sci.Techn.*, Suppl. 2, p. 342 (2002).
5. J. Meija, T.B. Coplen, M. Berglund, W.A. Brand, P. De Bievre, M. Groning, N.E. Holden, J. Irrgeher, R.D. Loss, T. Walczyk, T. Prohaska, *Atomic Weights of Elements* (IUPAC Technical Reports) , *Pure Appl. Chem.*, 2016, Vol. 88 no. 3, p. 265 (2013).
6. G. Audi, H.A. Wapstra, Nucl. Phys. A, Vol. 595, p. 409 (1995).
7. A.I. Oprea, C. Oprea, C. Pirvutoiu, D. Vladoiu, Rom Rep in Phys, vol. 63, no. 1, p. 107 (2011).
8. Y. Gledenov, M. Sedysheva, P. Sedyshev, A. Oprea, Z. Chen, Y. Chen, J. Yuan, G. Zhang, G. Tang, G. Khuukhenkhuu, P. Szalanski, Journal of Nuclear Science and Technology, Suppl.2B, p. 342–345 (2002).
9. W. Hauser, H. Feshbach, 1952, *Phys. Rev.*, vol. 87, 2, p. 366 (1952).
10. A. Foderaro, The Neutron Interaction Theory, The MIT Press, Cambridge, Massachusetts and London, England (1971).
11. P.A. Moldauer, Rev. Mod. Phys., 1964, vol. 36, p. 1079 (1964).
12. A.J. Koning, S. Hilaire, M.C. Duijvestijn, .TALYS-1.0., *Proceedings of the International Conference on Nuclear Data for Science and Technology*, April 22-27,2007, Nice, France, editors O. Bersillon, F. Gunsing, E. Bauge, R. Jacqmin, S. Leray, EDP Sciences, p. 211 (2008).
13. G.R. Satchler, *Direct Nuclear Reactions*, Oxford University Press, New York (1983).
14. A.J. Koning, M.C. Duijvestijn, *Nucl. Phys.* A, vol. 744, p. 15 (2004).
15. C. Oprea, A.I. Oprea, Bulletin of the Russian Academy of Sciences: Physics, Allerton Press Inc. and Springer Nature Switzerland AG, 85, 12, 1471 (2021).
16. G. Zhang, J. Zhang, R. Cao, L. Guo, J. Chen, Yu.M. Gledenov, M.V. Sedysheva, P.J. Szalanski, Nuclear Science and Engineering 160, p. 123 (2008).
17. J. Yuan, Z. Chen, G. Tang, G. Zhang, J. Chen, Z. Shi, Yu. M. Gledenov, M. Sedysheva, G. Khuukheenkhuu, Nuclear Science and Engineering, 144, p. 108 (2003).
18. J.F. Ziegler, SRIM & TRIM Software – http://www.srim.org – accessed at 15.05.2023.

Forward-Backward Asymmetry Effect in Slow Neutrons Capture by Silver Nucleus

P.V. Sedyshev[1], A.I. Oprea[1], C. Oprea[2], V.L. Kuznetsov[1,3]

[1]*Frank Laboratory of Neutron Physics (FLNP), Joint Institute for Nuclear Research (JINR), 141980 Dubna, 6 Joliot Curie str., Moscow Region, Russian Federation*

[2]*County Center for Education, 11 Mihai Eminescu str., 410019, Oradea, Bihor County, Romania*

[3]*Laboratory of Neutron Research, INR RAS, Troitsk*

Forward-backward asymmetry effect in the capture process of slow neutrons on Silver nucleus was investigated. Cross sections, angular distributions, and forward-backward effect were obtained in the frame of the mixing states of compound nucleus with the same spin and opposite parities formalism. Simulated gamma spectra, taking into account different type of target and gamma loss, were also evaluated. Using modeled gamma spectra, the influence of target properties (composition, target thickness) on the investigated effect were analyzed. Forward-backward effect together with other asymmetry and parity breaking effects allow to extract new information on neutrons and gamma reduced partial widths and matrix element of weak non-leptonic interaction.

INTRODUCTION

Asymmetry and spatial parity and time breaking effects, in slow neutrons induced processes traditionally were investigated for a long time in FLNP JINR Dubna [1,2]. Furthermore, first experimentally proof of the existence of spatial parity violation effect in slow neutrons capture reaction by Cadmium nuclei was realized in 1964 also at FLNP [3]. In the beginning, the search of symmetry breaking effects was oriented on the capture of slow and resonance neutrons by heavy nuclei. With the improvements of experimental technique and theoretical progresses, the investigations were extended to light and medium nuclei and to other nuclear reactions like (n,p), (n,α), neutrons induced fission etc. [4,5].

Symmetry breaking effects were revealed experimentally by mean of asymmetry coefficients which can be obtained using angular correlations. Parity non-conservation in nuclear reaction phenomena were explained by the existence of non-leptonic weak interaction between nucleons in nuclear systems "incident particle + target" [6]. In consequence, dealing with weak interaction, symmetry breaking effects have very low values of order of 10^{-9}–10^{-7}.

In the case of slow neutrons induced reaction, nuclear process is going with formation of an intermediate compound nucleus in the presence of resonances. Theoretically it was demonstrated that compound nucleus resonances enable amplification mechanisms (kinematic, dynamic, structural) of asymmetry and parity breaking effects increasing the corresponding coefficients up to 10^{-1} [7,8].

The search of asymmetry and parity breaking effects in nuclear reaction is of great importance because allow to extract the matrix element of weak interaction and demonstrates the universality of weak forces [9].

In the present work, in the frame of so-called resonance-resonance approach and two-level approximations, forward-backward asymmetry effect, obtained in capture process of slow and resonant neutrons by ^{109}Ag nuclei was analyzed.

ELEMENTS OF THEORY

Relation of definition of forward–backward asymmetry coefficient (effect) is:

$$\alpha_{FB} = \frac{W(\theta = 0) - W(\theta = \pi)}{W(\theta = 0) + W(\theta = \pi)}, \tag{1}$$

where W is the angular correlation; θ is the polar angle

Angular correlation in the case of capture process of un-polarized neutrons by nuclei has the expression:

$$W(\theta) = 1 + \alpha(\vec{n}_n \cdot \vec{n}_\gamma) + \beta(\vec{n}_n \cdot \vec{n}_\gamma)^2 = 1 + \alpha\cos(\theta) + \beta\cos^2(\theta), \tag{2}$$

where α, β are coefficients; $\vec{n}_n, \vec{n}_\gamma$ are the unit vectors of direction of incident neutrons and emitted gamma quanta respectively.

Geometry of the experiment and for the evaluations is represented in Fig. 1.

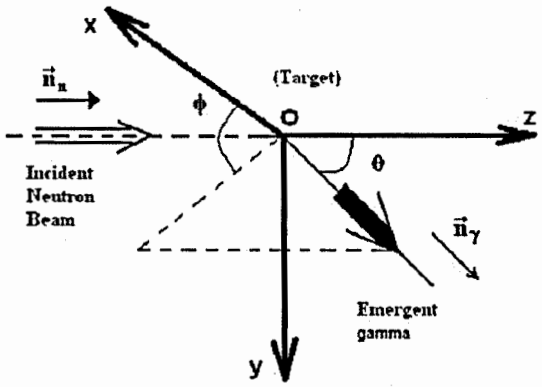

Fig. 1. Geometry of capture experiment for the calculations.

Angular correlation is proportional to differential cross section according to the following relations:

$$W(\Omega) \sim \frac{d\sigma}{d\Omega} = |f|^2 = \sum_i |f_i|^2 + \sum_{i \neq j} \mathrm{Re}\, f_i^* f_j, \tag{3}$$

where $d\sigma/d\Omega$ is differential cross section; Ω is solid angle; f_i are amplitudes of (n,γ) reaction.

In the case of slow neutrons capture process, with formation of compound nucleus, described by resonance, reaction amplitude f are described in the formalism of the mixed states of compound nucleus with the same spin and opposite parities [7,8]. According to this formalism, asymmetry and parity breaking effects can be evidenced in the vicinity of pair of

resonances with the same spin and opposite parities. Considering a number of isolated, well defined resonances of compound nucleus, reaction amplitudes can be written for each state [2,7,8]. Furthermore, compound nucleus resonances are enhancing the asymmetry and parity violation effects through amplification mechanisms mentioned above [2,7,8].

In (n,γ) process for incident neutrons with orbital momentum l_n = 0,1 compound nucleus resonance (S and P resonance respectively) are formed. Then, reaction amplitudes have the form:

$$f_1 = -\frac{1}{2k} C(I, I_z, a, a_n; J_S, J_{Sz}) C(I', I_z', a_\gamma, a_{\gamma z}; J_S, J_{Sz}) \cdot \frac{T_S^n T_S^{\gamma *}}{(E - E_S) + i\frac{\Gamma_S}{2}} Exp(-i\varphi_0), \quad (4)$$

$$f_2 = -\frac{2\pi}{k} \sum_{\substack{j_n, j_{nz}, \nu_n \\ j_p, j_{pz}, \nu_p}} C(I, I_z, j_n, j_{nz}; J_P, J_{Pz}) C(1, \nu_n, a_n, a_{nz}; j_n, j_{nz}) \cdot C(I', I_z', j_\gamma, j_{\gamma z}; J_P, J_{Pz}),$$

$$C(L, \nu_\gamma, a_\gamma a_{\gamma z}; j_\gamma, j_z) \frac{T_P^n(j_n) T_P^*(j_\gamma)}{(E - E_P) + i\frac{\Gamma_P}{2}} \cdot Y_{1\nu_n}^*(\vec{n_n}) Y_{1\nu_{\gamma p}}(\vec{n_\gamma}) Exp(-i\varphi_1), \quad (5)$$

where C are the Clebsch-Gordan coefficients depending on quantum numbers; $J, J', J_z, J_z', I, I_z, I', I_z'$ are the spins of compound (S and P), target, residual nuclei respectively with their projections (z); $a_n, a_{bz}, a_\gamma, a_{\gamma z}$ are the spins of neutrons and gamma quanta and their projections; L is total orbital momentum; $T_{S,P}^{n,\gamma}$ are the reduced amplitudes in S and P states respectively for neutrons and gamma quanta; ϕ_1, ϕ_2 are phases in S and P states respectively.

Amplitudes f_1, f_2 describe the following nuclear process: capture of neutrons with orbital momentum l_n = 0, 1 (s and p neutrons) and formation of S and P resonance of compound nucleus respectively, followed by emission of gamma quanta. These amplitudes are describing strong nuclear interaction which is parity conserving and they are not including weak non-leptonic interaction.

Applying relations (1–3) in the case of (n,γ) reaction induced by slow, resonance unpolarized neutrons, with formation of a compound nucleus described by a pair of S and P resonances (expressions (3), (4)), differential cross section, angular correlation and forward-backward effect (coefficient) are obtained. In terms of amplitudes f_1, f_2 forward-backward effect is:

$$\alpha_{FB} = \frac{2\,\mathrm{Re}\, f_1 f_2^*}{|f_1|^2 + |f_2|^2}. \quad (6)$$

The relation (6) suggests that forward-backward effect, in the frame of resonant-resonant formalism [2,7,8] can be interpreted as result of interference in compound nucleus of resonances with the same spin and opposite parities.

RESULTS AND DISCUSSIONS

Capture process of slow and resonant neutrons by ^{109}Ag nucleus was investigated, Compound nucleus, ^{110}Ag is characterized by a pair of S and P resonances with the following

energies, spins and parities ($E_{S,P}, J^{\pm}_{S,P}$): $E_S = 30.6(\text{eV}); J_S = 1^+$ and $E_P = 32.7(\text{eV}); J_S = 1^-$ [10]. Silver is a heavy nucleus, and for neutrons with energies of tens of eV's compound nucleus has a large number of resonances. In order to evidence forward-backward asymmetry effect, as first step, it is enough to consider only the mentioned resonances because they have the same spin and opposite parities, the condition necessary to observe asymmetry and parity violation effects.

First, expression of differential cross section was obtained (7), after that, angular distribution and finally, the forward-backward effect according to relations (1–6).

$$\frac{d\sigma}{d\Omega}(E_n,\theta) = \frac{g\lambda_n^2}{4}\left[\frac{\Gamma_n^S\Gamma_\gamma^S}{S[E_n]} + \frac{\Gamma_n^P\Gamma_\gamma^P}{P[E_n]}\right] + \frac{3\lambda_n^2}{80\sqrt{7}}\left[\frac{\Gamma_n^P\Gamma_\gamma^P}{P[E_n]}\left(4X_nY_n + \sqrt{2}Y_n^2\right)Y_n^2 P_2(\cos\theta)\right] + \\ + \frac{3\lambda_n^2}{10} cfb1(E_n)\left[\left(\frac{Y_n}{\sqrt{2}} - X_n\right)\left(\frac{X_\gamma}{\sqrt{3}} - Y\gamma\right)\right], \tag{7}$$

where the functions are:

$$cfb1(E_n) = \frac{\left(2\Gamma_n^S\Gamma_\gamma^S\Gamma_n^P\Gamma_\gamma^P\right)^{1/2}}{P[E_n]S[E_n]}\left\{\left[(E_n - E_S)(E_n - E_P) + \frac{\Gamma_S\Gamma_P}{4}\right]\cos\phi - \left[(E_n - E_S)\frac{\Gamma_P}{2} - (E_n - E_P)\frac{\Gamma_S}{2}\right]\sin\phi\right\}, \tag{7.1}$$

$$S[E_n] = (E_n - E_S)^2 + \frac{\Gamma_S^2}{4}; P[E_n] = (E_n - E_P)^2 + \frac{\Gamma_P^2}{4}; \Gamma_{S,P} = \Gamma_n^{S,P} + \Gamma_\gamma^{S,P} + \Gamma_p^{S,P} + \Gamma_\alpha^{S,P} + \ldots \tag{7.2}$$

Forward-backward asymmetry effect is:

$$\alpha_{FB}(E_n) = \frac{\left(\frac{Y_n}{\sqrt{2}} - X_n\right)\left(\frac{X_\gamma}{\sqrt{3}} + Y_\gamma\right) cfb1(E_n)}{cf2(E_n) + cf3(E_n)\left(4X_nY_n + Y_n^2\right)Y_\gamma^2} \tag{8}$$

with functions:

$$cfb1(E_n) = \frac{\left(2\Gamma_n^S\Gamma_\gamma^S\Gamma_n^P\Gamma_\gamma^P\right)^{1/2}}{P[E_n]S[E_n]}\left\{\left[(E_n - E_S)(E_n - E_P) + \frac{\Gamma_S\Gamma_P}{4}\right]\cos\phi - \left[(E_n - E_S)\frac{\Gamma_P}{2} - (E_n - E_P)\frac{\Gamma_S}{2}\right]\sin\phi\right\}, \tag{8.1}$$

$$cf2(E_n) = \frac{\Gamma_n^S\Gamma_\gamma^S}{S[E_n]} + \frac{\Gamma_n^P\Gamma_\gamma^P}{P[E_n]}; cf3(E_n) = \frac{1}{5\sqrt{7}}\cdot\frac{\Gamma_n^P\Gamma_\gamma^P}{P[E_n]}, \tag{8.2}$$

partial reduced widths and properties:

$$X_n = \pm\sqrt{\frac{\Gamma_n^S\left(\frac{1}{2}\right)}{\Gamma_n^S}}; Y_n = \pm\sqrt{\frac{\Gamma_n^P\left(\frac{3}{2}\right)}{\Gamma_n^P}}; X_\gamma = \pm\sqrt{\frac{\Gamma_\gamma^S(l_\gamma)}{\Gamma_\gamma^S}}; Y_n = \pm\sqrt{\frac{\Gamma_\gamma^P(l_\gamma)}{\Gamma_\gamma^P}}, \tag{8.3}$$

$$X_n^2 + Y_n^2 = 1; X_\gamma^2 + Y_\gamma^2 = 1$$

and phases:

$$\varphi = \varphi_{neutron} = ArcTan\left(\frac{R}{\lambda_n}\right). \tag{8.4}$$

Using expressions (7–8) angular correlation was obtained. For the simulation of forward-backward asymmetry coefficient, angular distribution of polar angle θ was evaluated by Direct Monte-Carlo method. Expression of generated polar angle is:

$$\theta = \pm ArcCos\left[\frac{-2+\beta}{2(\alpha+\beta)}\left(1 \pm \sqrt{\frac{(-2+\beta)^2}{4(\alpha+\beta)^2} \pm \frac{2+\alpha-4r}{\alpha+\beta}}\right)\right], \tag{9}$$

where α, β are coefficients from relation (2).

Because spatial parity is conserving, azimuth angle has an uniform distribution and is generated with the formulae:

$$\varphi = 2 \cdot \pi \cdot r', \tag{10}$$

here r, $r' \in [0,1]$ are random numbers.

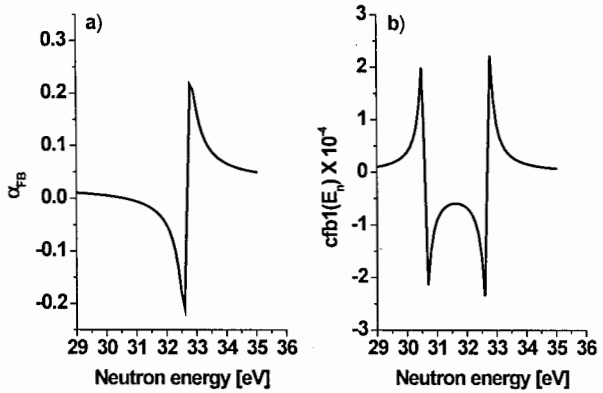

Fig. 1. a) Forward-backward neutrons energy dependence. b) Neutrons energy dependence of $cfb1(E_n)$ function (8.1).

In Fig. 1.a forward-backward effect is represented in the two levels approximation. The shape of the dependence is that prescribed by theory. In previous work of the authors analogue shape dependences were obtained in the analysis of $^{35}Cl(n,p)^{35}S$ reaction with slow and resonance neutrons [4,11]. Maximum value of forward-backward effect is around 0.2 between S and P resonances and is decreasing fast, moving away from resonances.

In Fig. 1.b neutrons energy dependence of $cfb1(E_n)$ is represented, This function, $cfb1(E_n)$, has the largest influence in the shape and quantitative dependence of forward-backward asymmetry coefficient. Resonance positions can be well observed in the figure.

Forward-backward effect was further computer modeled considering a finite target and attenuation of gamma quanta in the target. Attenuation law of gamma quanta is:

$$N = N_0 \cdot Exp(-\mu \cdot x), \tag{11}$$

where μ is attenuation coefficient; x is the distance covered by gamma quanta.

Applying relations (9–10) for the generation of polar and azimuth angles respectively, considering relations (1–8), a target of 2 cm thickness, $\mu = 0.4$ cm^{-1} attenuation coefficient for

silver and incident neutrons energy up to 40 eV, simulated forward-backward effect is:

$$\alpha_{BN}^{SIM} \cong 0.1. \tag{12}$$

The result (12) was obtained for 10^5 events, and about 35% of generated gammas of which are lost in the target. Due to the thickness of the target the effect is decreasing by approximately 2 times. Similar results have been obtained by authors in the analysis of asymmetry and spatial parity violating effects on (n,p) reaction with slow and resonance neutrons on ^{35}Cl and ^{14}N nuclei [4,11].

CONCLUSIONS

Capture process of slow and resonant neutrons by ^{109}Ag nucleus was investigated. Cross, section, differential cross section, angular correlations and forward-backward effect were evaluated in the frame of resonant-resonant formalism and two-level approximation. Forward-backward effect was also simulated, using theoretical results of angular correlation, expression of forward-backward effect and Direct Monte-Carlo method for generation of polar and azimuth angles respectively. Forward-backward energy evaluated dependence is in concordance with similar investigations of authors. For silver, modeled forward-backward effect is exactly half of theoretical effect for point-like target and about two times smaller for target with finite dimensions.

The results obtained in this work can be considered preliminary. It is necessary to investigate the influence of other resonance of ^{109}Ag because this nucleus has a lot of resonances close one to another. The formalism of the calculation of angular distribution must be improved by an averaging method for a large number of close resonances.

It is necessary in the future to investigate theoretically and experimentally other asymmetry and parity breaking effects on slow and resonant neutrons capture process by silver isotopes.

REFERENCES

1. E.I. Sharapov, J.D. Bowman, S.I. Penttila, G.E. Mitchell, Physics of Elementary Particles and Atomic Nuclei, vol. 32, 7, p. 241 (2000).
2. V.E. Bunakov, Physics of Elementary Particles and Atomic Nuclei, vol. 26, 2, p. 285 (1995).
3. Yu.G. Abov, P.A. Krupchitsky, Yu.A. Oratovsky, Phys. Lett., Vol. 12, 1, p. 25 (1964).
4. Yu.M. Gledenov., R. Machrafi, A.I. Oprea, V.I. Salatski, P.V. Sedyshev, P.I. Szalanski, V.A. Vesna, I.S. Okunev, Nucl. Phys. A, vol. 654, p. 943c (1999).
5. V.R. Alfimenkov, A.N. Chernikov, L. Lason,Yu.D. Mareev, V.V. Novitski, L.B. Pikelner, V.R. Skoy, M.I. Tsulaya, A.M. Gagarski, I.S. Guseva, S.E Golosovskaya, I.A. Krasnoschokova, A.M. Morozov, G.A. Petrov, V.I. Petrova, A.K. Petukhov, Yu.S. Pleva, V.E. Sokolov, G.V. Val'ski, S.M. Soloviev, Nucl. Phys. A, vol. 645, p. 31 (1999).
6. N. Tanner, Phys. Rev., vol. 107, p. 1203 (1957).
7. V.V. Flambaum, G.F. Gribakin, Prog. Part. Nucl. Phys., vol. 35, p. 423 (1995).
8. V.E. Bunakov, L.B. Pikelner, Progr. Part. Nucl. Phys., Vol. 39, p. 337 (1997).
9. R.P. Feynmann, M Gell-Mann, Phys. Rev., vol. 109, p.193 (1957).
10. S.F. Mughabghab, Atlas of Neutron Resonances: Resonance Properties and Thermal Cross Sections, vol. 2, Amsterdam-Oxford-Cambridge, Elsevier Science (2018).
11. A.I. Oprea, C. Oprea, Yu.M. Gledenov, P.V. Sedyshev, C. Pirvutoiu, D. Vladoiu, *Romanian Reports in Physics*, vol. 63, no. 2, p. 357 (2011).

Computer Simulation PFN Transport in Neutron Detector

Olga Sidorova[1,2] and Shakir Zeynalov[1]

[1]*Joint Institute for Nuclear Research, Dubna, Moscow region, Russia*
[2]*Dubna State University, Dubna, Moscow region, Russia*

e-mail: sidorova@jinr.ru

This work reports results of prompt fission neutron (PFN) emission process simulation of IREN source of resonance neutron induced fission of U-235 using special computer code, developed by authors. The fast neutron detector consisted of 32 liquid scintillation neutron detectors manufactured by SIONICS (Netherland) company. Beam of resonance neutrons produced by IREN facility of Joint Institute for Nuclear Research (JINR) irradiated double Frisch gridded ionization chamber (DFGIC) with uranium target located on the common cathode. PFNs produced in target will be detected by multi-module set of 32 liquid scintillator filled neutron detection modules. In the planned experiments beam of resonance neutrons from the IREN source would irradiate the uranium target of DFGIC, producing fission fragments and PFN. The fast neutron detectors are able to detect PFN and separate the PFN from the background gamma radiation using pulse shape analysis method. For each fission event the following information should be recorded: time stamp of event, fission fragments (FFs) emission angles in respect to the selected coordinate system, FFs pulse heights, and the PFN pulse shape information. The multi-modular structure of PFN detector has the advantage due to higher neutron registration efficiency from the one hand, and the drawback due to the cross-talks between adjacent modules. That effect can produce systematic uncertainty to the multiplicity of the final results. In this work the effect of cross-talks was evaluated using numerical simulation of PFN transport and were taken into account in the final results.

Introduction

Investigation of PFN properties is important in studies of nuclear fission process, due to PFN are carry information on excitation energies of fissile nuclei [1]. For detailed study mass and kinetic energy (MKE) distributions of fission fragments and PFN emission in reactions $^{235}U(n_{res},f)$, $^{237}Np(n_{res},f)$, and $^{239}Pu(n_{res},f)$ induced by resonance neutrons, and in spontaneous fission of $^{252}Cf(sf)$, the neutron detector was manufactured and located in the resonance neutron beam line (flight path length ~9.2m) of IBR30. For detailed study MKE distributions of fission fragments and process of PFN emission in fission of ^{235}U, ^{237}Np and ^{239}Pu nuclei, induced by resonance neutrons and in spontaneous fission of ^{252}Cf, neutron detector (ND) was developed and located at beam line of IREN source in JINR (flight path length ~9.2 m). ND consist of two shoulders contained 16 neutron detecting modules each. The modules are aluminum cylinders with diameter of 80 mm and the height 50 mm filled with scintillating liquid BC501. The modules have transparent for light window to which PMT was glued. The modules were located on the four circles made as cross sections of virtual sphere with radius of 0.5 m: 12 modules were located at two sections with diameters of

30 cm and the rest 20 at two sections with diameter D=450 mm (Figs.1,2). The full angle, covered by the PFN modules was 5.12% of 4π.

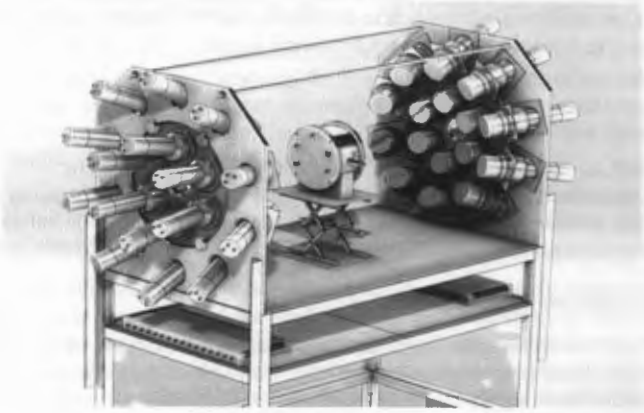

Fig. 1. Photo of neutron detector along with ionisation chamber.

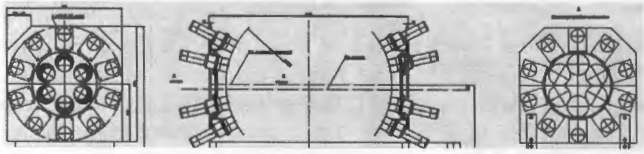

Fig. 2. Schematical view of neutron detector.

The target was made of 1 μm thin organic film with vacuum evaporated gold of ~50 μг /см^{2}and ^{235}U (of 0.99999 purity) with 70 μг /см^{2}onto one of its surfaces. The target diameter was 70 mm, and it was mounted on the center of common cathode hole. When the neutron captured by U nucleus, the fission fragments are detected in two separate ionization chambers composing the double ionization chamber filled with P10 gas mixture flowing (20 ml/min) through the chamber, working under normal conditions. The chamber able to measure polar and azimuth angles of fission fragments. Special software was developed for data analysis and data acquisition of fission fragments induced signals.

PFN detecting module

PFN detecting module was made of aluminum cylinder having diameter 80 mm and height 50 mm. Module was filled with BC-501scintillation liquid. The PMT tube was glued to transparent side of the cylinder and was used to amplify the signals (light sparks), generated when PFN collided with molecules of BC-501. PFN caused pulses were amplified by PMT and analyzed in data acquisition software to separate PFN from gamma radiation using pulse shape analysis. The PMT pulse was accepted by data acquisition software if its kinetic energy exceeds the 0.15 MeV level. To track the trajectory of the PFN from the origin point inside

the neutron detector to the point, where neutron was captured, or leave the detector volume, a special software code was developed, using Monte Karlo method [3,4]. The following original conditions were assumed: PFN was emitted from the random point of the target, it had randomly selected launching angle in respect to the target plane. The kinetic energy value was distributed according to Maxwell low, as in the following formula:

$$F(E_0) = \frac{2\pi}{\sqrt{(\pi kT)^3}} \cdot \sqrt{E_0} \cdot e^{\frac{E_0}{kT}},$$

where $kT = 1.0MeV, k$ – is Boltsman constant, and T– is the target temperature.

Trajectory parameters and kinetic energy value were traced from the emission point to the point, where the neutron leave the system or was captured in scintillator volume or its kinetic energy value decrease to the level below $10^{-5}MeV$.

PFN interactions inside the scintillator volume

Liquid BC-501 has the chemical formula CH_2O. Assuming two types of reactions with scintillator molecule: elastic scattering or capture of PFN by one of the atoms of scintillator, the following identifiers were used:

$\sigma_C^{elastic}(E), \sigma_H^{elastic}(E), \sigma_O^{elastic}(E), \sigma_{CH_2O}^{elastic}(E)$– the elastic scattering reaction cross-section of PFN with kinetic energy value E with the atoms: C, H, O, and with molecule CH_2O respectively.

$\sigma_C^{capture}(E)\sigma_H^{capture}(E), \sigma_O^{capture}(E), \sigma_{CH_2O}^{capture}(E)$– the capture reaction cross-section of PFN with kinetic energy value E with atomsC, H, O and molecule CH_2O respectively.

$\sigma_C^{total}(E), \sigma_H^{total}(E), \sigma_O^{total}(E), \sigma_{CH_2O}^{total}(E)$–the total cross-section of interaction of PFN with kinetic energy value E with the atoms C, H, O, or molecule CH_2O respectively.

Let X- is the X free path thin of PFN with kinetic energy value E inside the scintillation liquid. Assuming simulated X has exponential distribution with the following probability density:

$$p(X = x) = \lambda \cdot e^{-\lambda x},$$

where

$$\lambda = N \cdot \sigma_{CH_2O}^{total}(E),$$

$$\sigma_{CH_2O}^{total}(E) = \sigma_C^{total}(E) + 2 \cdot \sigma_H^{total}(E) + \sigma_O^{total}(E),$$

N– is the number of molecules in 1 см^3 of scintillator volume. Scintillation liquid formula is CH_2O, its density is$\rho = 0{,}815\ {}^{g}/_{cm^3}$. Neglecting binding energy, we find atomic weigh of CH_2O is 30,02109 as

$$N = \frac{6{,}0221408 \cdot 10^{23} \cdot 10^3 \cdot 815}{30{,}022109} = 163{,}4866 \cdot 10^{20}\text{molecules}.$$

Probability of reaction between PFN and atom of scintillator $\rho_C^{total}(E), \rho_H^{total}(E)$ и $\rho_O^{total}(E)$ are proportional to corresponding cross-sections, taking into account the multiplicity of atoms in the molecules of the scintillator as

$$\rho_C^{total}(E)/\rho_H^{total}(E)/\rho_O^{total}(E) = \sigma_C^{total}(E)/2 \cdot \sigma_H^{total}(E)/\sigma_O^{total}(E).$$

Probability of type of interactions between neutron and selected atom of molecule of scintillator is proportional to respective cross-sections:

$$\rho_{atom}^{capture}(E)/\rho_{atom}^{elasic}(E) = \sigma_{atom}^{capture}(E)/\sigma_{atom}^{elastic}(E), atom = C, H, O.$$

Interaction between PFN and atom leads to kinetic energy loss of the particle. Full energy obtained by material of scintillator module from the moving neutron was calculated as sum of energy release in elastic collisions of neutrons with hydrogen atoms and in the neutron capture by the atom of scintillator. The module generates a signal when the energy transferred to the material of scintillator was higher than the threshold value:

$$E_{modul} > 0.15\ Mev.$$

Results of simulation

The goal of this work was to estimate the share of multiple scatterings (2,3,4,5) of the given particle at the atoms of the medium. Multiple scattering of the neutrons inside the neutron detector could imitate false multiplicity. In this connection it was necessary to estimate the share of such multiple scattering using computer simulation of the transport of neutrons inside the detector volume. We have developed computer code, generated 20 scenarios of PFN emission causing signals in a given detector. Results obtained in simulation process presented in Table with the following identifiers:

R – serial number of the scenario;

N_R^i - the number of neutrons detected in scenario R in I modules;

$N_R^{\geq 5}$- the number of neutrons detected in scenario R in 5 or more modules;

N_R^{real}–the real number of neutrons, registered by system in scenario R:

$$N_R^{real} = \sum_{i=1}^{\infty} N_R^i;$$

$N_R^{visible}$ –the number of sparks, registered by ND in scenario R:

$$N_R^{visible} = \sum_{i=1}^{\infty} N_R^i \cdot i;$$

ε_R - is the systematic relative error in measurement of number of neutrons in scenario R

$$\varepsilon_R = \frac{N_R^{visible} - N_R^{real}}{N_R^{visible}}.$$

As $N_R^{\geq 5} = 0$ for all R, so

$$N_R^{real} = \sum_{i=1}^{4} N_R^i;$$

$$N_R^{visible} = \sum_{i=1}^{4} N_R^i \cdot i.$$

Table. Results of simulation neutron transport in ND

R	N_R^1	N_R^2	N_R^3	N_R^4	$N_R^{\geq 5}$	N_R^{real}	$N_R^{visible}$	ε_R
1	19169	1055	25	0	0	20249	21354	0.052
2	19281	1108	25	0	0	20414	21572	0.054
3	19290	1071	34	0	0	20395	21534	0.053
4	19032	1058	29	1	0	20120	21239	0.053
5	19102	1120	33	0	0	20255	21441	0.055
6	19288	1069	31	0	0	20388	21519	0.053
7	19087	1114	27	0	0	20228	21396	0.055
8	19215	1102	23	0	0	20340	21488	0.053
9	19092	1149	28	0	0	20269	21474	0.056
10	19161	1089	32	0	0	20282	21435	0.054
11	19396	1081	19	0	0	20496	21615	0.052
12	19180	1140	29	1	0	20350	21551	0.056
13	19106	1104	16	1	0	20227	21366	0.053
14	19152	1072	33	1	0	20258	21399	0.053
15	19173	1105	31	0	0	20309	21476	0.054
16	19256	1078	20	0	0	20354	21472	0.052
17	19171	1145	22	0	0	20338	21527	0.055
18	19049	1125	31	2	0	20207	21400	0.056
19	18938	1110	26	0	0	20074	21236	0.055
20	19096	1110	28	0	0	20234	21400	0.054

Conclusion

In this investigation of PFN registration using detector, consisting of 32 BC501 liquid filled scintillator modules was done. Detectors have the ability to separate neutrons from prompt gamma radiation using pulse shape analysis. Computer simulation of neutron transport inside the detector body was done along with estimation of systematic errors caused by multiple scattering of neutrons. Statistical accuracy of simulation was estimated to be less than 5%:

$$N_R^{real} \approx 0{,}95 \cdot N_R^{visible}.$$

References

1. H. Nifenecker, M. Ribrag, J. Frehaut, J. Gauriau, *Prompt neutron yields of the fission fragments of ^{252}Cf as a function of the charge of the fragments* // Nuclear Physics 1969. V. 131. No. 2. P. 261-266.
2. F.-J. Hambsch, H.-H. Knitter, C. Budtz-Jorgensen, and J.P. Theobald, Fission mode fluctuation in the resonances of $^{235}U(n,f)$, Nuclear Physics A -1989. -Vol. 491. –P. 56 – 90.
3. Allen Downey. *Physical Modeling in MATLAB* // Needham: Green Tea Press, 2009, 166 p.
4. I.M. Sobol. *Monte Carlo Method* (Popular Lectures in Mathematics) // University of Chicago Press, 1975, pp. 47-51.

Neutron Detection & Methodical Aspects

New Time Pick-Off Algorithm for Time-Of-Flight Measurements with PIN Diodes

Kamanin D.V.[1], Pyatkov Yu.V.[1,2], Zhuchko V.E.[1], Goryainova Z.I.[1,*], Falomkina O.V.[3], Pyt'ev Yu.P.[3], Korsten R.[4], Kuznetsova E.A.[1], Naumov P.Yu.[2], Solodov A.N.[1], Strekalovsky O.V.[1,5], Zhukova A.O.[1]

[1]*Joint Institute for Nuclear Research, Dubna, Russia;*
[2]*National Nuclear Research University "MEPHI", Moscow, Russia;*
[3]*Lomonosov Moscow State University, Physics Faculty, Computer Methods in Physics Division, Moscow, Russia;*
[4]*University of Stellenbosch, South Africa;*
[5]*Dubna State University, Dubna, Russia*

**E-mail:* zoyag2021@gmail.com

New off-line time pick-off algorithm for time-of-flight measurements of heavy ions with PIN diodes is presented. The digital image of the detector signal obtained in experiment is processed in order to find a real signal start when a particle hits the detector. By this way, so-called plasma delay between the time stamp and a real signal start is taken into account automatically. The algorithm was tested using the data obtained on the ion beams. The algorithm allows to obtain unbiased estimates of the heavy ion velocities and masses in a wide range of these parameters.

INTRODUCTION

To correctly measure heavy ion's time-of-flight (TOF) with PIN diodes, it is necessary to account for the so-called plasma delay effect (PDE) which is due to generation of plasma in a heavy ion track in the PIN diode.

The processes in the ion track at the initial stage of its evolution manifest themselves in such a way that signal from PIN diode could be described as a slowly growing function. This initial part of the signal at least partially lies inside a "noise track". Later the leading edge of the signal becomes almost linear. It is possible to account for PDE by using the method developed in Ref. [1], but this procedure may not correctly work for small masses and energies. We developed an alternative approach aimed at finding an actual start of the signal. It is done by approximating signal's initial part by parabolic curve which vertex coincides with the mean value of the noise track and serves as the "true" signal's start. The first realization of this idea was "Parab" algorithm [2] in which parabolic function was used for interpolation of the signal's noisy region. To increase a robustness of the algorithm against a choice of the region for parabola interpolation, Parab was followed by "Parablin" time pick-off algorithm [3]. Within this algorithm the parabolic function was seamlessly sewed with a linear function which approximated points of the rising edge of the signal lying above the noisy region. Parablin's main drawback was the need to manually choose points for linear function approximation. To further increase robustness of the time pick-off procedure, we propose "Paraspline" algorithm in which the initial part of the signal is described by parabola, seamlessly sewed with a spline that automatically approximates points above the noisy region, without user interference.

PARASPLINE ALGORITHM DESCRIPTION

Let us select the data area $(x_1,...,x_n, y_1,...,y_n)$, $n \le N$, consisting of points lying to the right of point (x_0, y_0) (Fig 1), which is the border to the right of the "reliable points" of the signal: to the left of this point all points of the signal belongs to the interval $[y_b-3\sigma, y_b+3\sigma]$, where y_b is the mean value of the noise, σ is the noise standard deviation, so it is impossible to reliably distinguish noise from signal. The size n of the area $(x_1,...,x_n, y_1,...,y_n)$ is chosen large enough, $n \ge 200$.

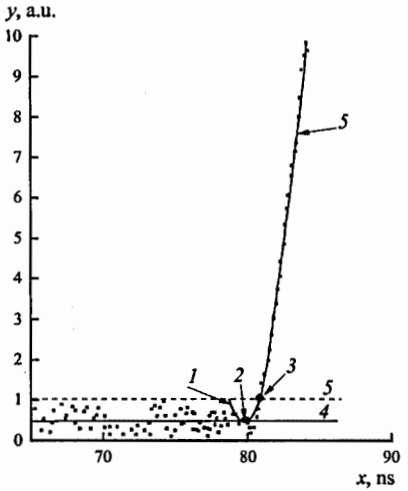

Fig. 1. Waveform from the PIN diode stored with a step 0.2 ns. *1* – parabolic approximation of the initial part of the signal; 2 – the parabola vertex x_p accepted as a time stamp; 3 – sewing point (x_0, y_0); 4 – line corresponded to the mean value of the base-line y_b; *5* – line corresponded to $y_b+3\sigma$; *6* – spline approximation of the quasilinear part of the signal.

We define the smoothing spline $s(\cdot)$ [4] of order q as a solution of the following minimum problem:

$$\min\left\{p\int_a^b (s^{(q)}(x))^2 dx + \sum_{j=1}^{n}(s(x_j) - y_j)^2\right\}, \qquad (1)$$

Parameter vector of $s(\cdot)$ is varied to rich a minimum of the functional (1) . The smoothness of $s(\cdot)$ increases with increasing order of the spline q and increasing smoothing factor p. Factor p must be known before the minimization of (1). The main idea of the paraspline algorithm is as follows.

1. Fix the value of the smoothing factor p. With this fixed value of the smoothing parameter, we find the smoothing spline $S_p(\cdot)$ of order $q = 2$, which minimize the functional (1) and is the best approximation for signal $(x_1,...,x_n, y_1,...,y_n)$ (that is, a cubic spline on intervals (x_i,x_{i+1}), $i = 1,...,n-1$, $n \ge 2$).
2. The parabola with a vertex on the mean of the signal's baseline (point (2) in Fig. 1) is defined by the following equation:

$$y = ax^2 + bx + \frac{b^2}{4a} + y_b \tag{2}$$

It is necessary to sew the smoothing spline $S_p(\cdot)$ smoothly (equality of values and derivatives) on its left border x_0 (the sewing point) with the parabola defined by the formula (2). After the smoothing spline $S_p(\cdot)$ is found, we have two equations for finding the parameters a and b of the parabola:

$$\begin{gathered} Ax_s^2 + bx_s + \frac{b^2}{4a} + y_b = S_p(x_s) = g \\ 2ax_s + b = S_P'(x_s) = h \end{gathered} \tag{3}$$

Hence, we find that

$$\begin{gathered} a = \frac{h^2}{4(g - y_b)} \\ b = h - \frac{2x_s h^2}{4(g - y_b)} \end{gathered} \tag{4}$$

As the point of the time stamp, we take the point with the abscissa $x_p = -b/2a$ (i.e., abscissa of the parabola vertex).

Thus, for each value of the smoothing factor p (for example, using the grid $[p_1,\ldots,p_n]$ in increments of 0.1 or 0.01, depending on the software) we find the smoothing spline $S_p(\cdot)$ of order $q = 2$ and the binding point x_p of the parabola, as well as the parameters of the parabola. The value of the smoothing parameter is determined based on article [4] as follows. The smoothing spline $S_p(\cdot)$ can be presented in the form of two terms: the first term is the "smooth" term $\sigma_p(x_i)$, $i = 1,\ldots,n$, estimating the dependence of the signal of interest on time, and the second is the differences $\mu_p(x_i) = y_i - \sigma_p(x_i)$, $i = 1,\ldots,n$, representing the noise dependence on time.

If the smoothing spline (i.e., the smoothing factor p) is selected correctly, then the smooth term should not contain "visible" traces of noise, and the difference should not have "regular" components from the signal. If the smoothing spline σ_p with the "correctly selected" smoothing factor is re-applied to the difference $\mu_p(x_i) = y_i - \sigma_p(x_i)$, $i = 1,\ldots,n$, we get the spline $v_p(x)$, identically equal to zero.

Therefore, to find the "correct" value of the smoothing factor, for each value of the smoothing factor p in some grid $[p_1,\ldots,p_n]$, we calculate the spline $v_p(x)$ and its norm $\|v_p(x)\|^2$. The value of the smoothing factor, at which the norm is minimal, will be considered optimal. Thus, we also find the binding point x_p of the parabola corresponding to this value of the smoothing factor.

EXPERIMENTAL VERIFICATION OF THE PARASPLINE ALGORITHM

A successful time pick-off algorithm should provide both an unbiased time stamp and good time resolution. In order to test the first characteristic, the following series of experiments was performed. Using time-of-flight spectrometer LIS (Fig. 2) with two flight paths, the velocity V of each heavy ion was measured twice, namely estimate V_1 was obtained on the flight path L_1 using two microchannel plates-based detectors St_1 and St_2, and estimate V_2 was obtained on the flight path L_2 with a help of the detector St_2 and PIN diode. Timing

detectors St_1 and St_2 are free from the plasma delay effect that is why the value V_1 can be considered "true" velocity. If the plasma delay is taken into account correctly, thanks to Paraspline algorithm, the mean difference $\langle V_1 - V_2 \rangle$ should be close to zero within a change of V_1 when the ion passes through a thin foil 4 in St_2 (Fig. 2). The spectrometer was placed at the beam of heavy ions knocked out from the target foils by the 160 MeV Xe beam of the accelerator IC-100 in FLNR (JINR).

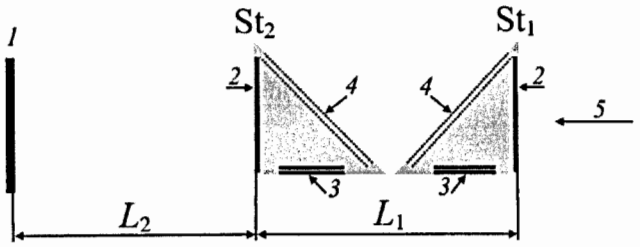

Fig. 2. Layout of LIS spectrometer. St_1, St_2 – microchannel plates-based timing detectors (are shown in gray); *1* – ^{252}Cf source; *2* – emitter-foil; *3* – microchannel plate; *4* – electrostatic mirror; *5* – ion beam; L_1 – 14.2 cm; L_2 – 14.1 cm.

The results of a comparison between V_1 and V_2 for the ions of Cu and Zr are presented in Fig. 3. The difference between the velocities does not exceed 0.4%.

Due to the kinematics of the rare ternary decays in our experiments, the energy of one of the decay products to be detected does not exceed several MeV. To ensure the correct unbiased mass reconstruction especially for the low-energy heavy ions we measured the masses of several different ions in the wide range of energies, using LIS spectrometer (Fig. 2). The values V_2 were used for mass reconstruction, while pulse height defect in the PIN diode was taken into account according the procedure presented in Ref. [5]. The results are shown in Fig. 4.

As can be inferred from Fig. 4, the mass reconstruction procedure involving Paraspline time pick-off algorithm provides quite satisfactory mass spectrometry of heavy ions in the wide range of masses and energies.

Experimental estimate of the time resolution for heavy ions when Paraspline time pick-off algorithm is used are also of interest. It a special methodic task which could be solved accurately only by using the mono energetic ion beams that are inaccessible.

Two main components contribute to a variance of the time stamp for heavy ions. The first one is due to the uncertainly of estimate of the plasma delay, especially for the detector signals in the wide range of amplitudes. The results presented above demonstrate that Paraspline time pick-off algorithm provides unbiased time stamp within the errors of the measurements. The influence of the second factor namely electronic noise we estimated in a following way. By definition, each detector signal could be presented as a sum of its mean shape and a random implementation of noise process. We collected a library of the noise samples $\xi_i(t)$. In fact, each sample is a record of some part of the noise track before the start of detector signal (Fig. 1). Thus, all such samples are statistically independent and represent actual spectrometer noise. The shape of the real detector's signal after strong smoothing could be considered as its mean shape $F(t)$. Then the series of the "quasi-experimental" signals $\phi_i(t)$ can be generated according to the formula:

$$\phi_i(t) = F(t) + \xi_i(t), i = 1 \div 100 \quad (5)$$

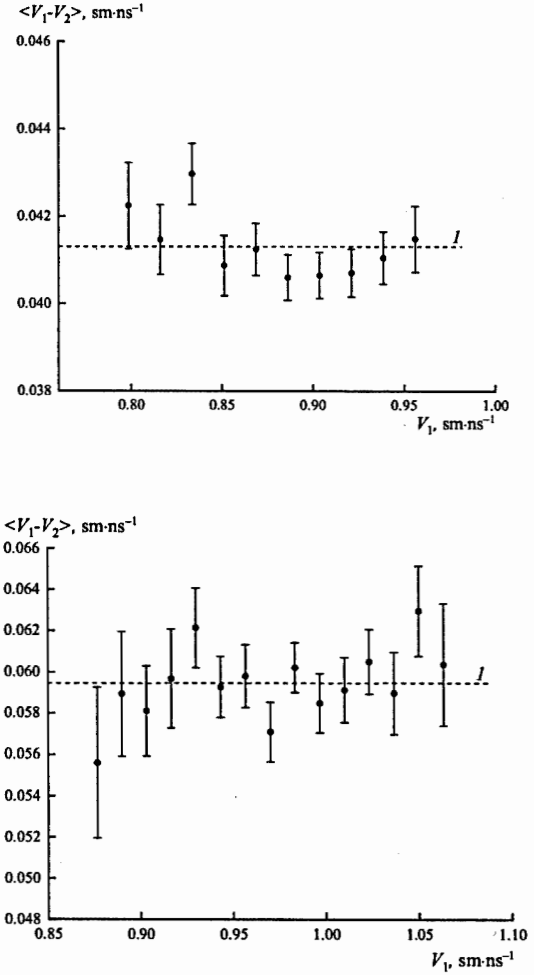

Fig. 3. Mean difference $<V_2 - V_1>$ as a function of V_1 for the a) Cu ions, b) Zr ions. The horizontal dashed line *1* – calculated mean value $<V_2 - V_1>$.

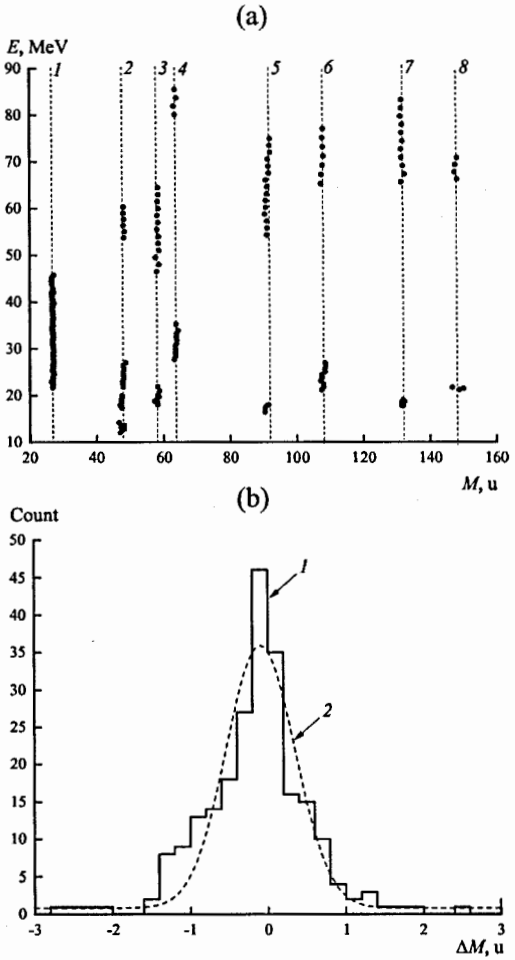

Fig. 4. a) Mass-energy distribution for all ions studied in the experiment. (Uncertainties of M are within point's size). The vertical dashed lines corresponded to the ions of Al, Ti, Ni, Cu, Zr, Au respectively are marked by numbers 1÷8. The experimental mass values for the Au ions are shifted in the figure to the left by 50 u. b) Spectrum of ΔM of measured masses for all ions from the known ones. *1* – Experimental spectrum; *2* – Gaussian fit with standard deviation 0.37 u.

For each signal $\phi_i(t)$ a time stamp τ_i is found using Paraspline algorithm. For all the series of quasi-experimental signals the probability distribution $P(\tau)$ is calculated. The $P(\tau)$ function looks like a Gaussian with the FWHM $\approx$ 200 ps for the signal with an amplitude typical for fission fragments. For the signal with a six times smaller amplitude, the FWHM is about 400 ps. This tendency of time resolution becoming better with increasing steepness of

the signal's leading edge is typical for all known time pick-off algorithms. The obtained values of FWHM are better than that (600 ps) mentioned in Ref. [6] at comparable conditions, but in our case, it is only partial contribution to the full-time resolution.

CONCLUSIONS

Correctness of the new Paraspline time pick-off algorithm was tested in experiment at the accelerator. Heavy ions knocked out from the Al, Ti, Ni, Cu, Zr, Au foils by the 160 MeV ^{132}Xe beam were used. The ion energies lie within the range (12÷87) MeV. It is shown that the algorithm allows obtaining unbiased estimates of the heavy ion velocities and masses of the detected ions. Algorithm provides good noise induced time resolution (200÷400) ps, inversely proportional to the signal amplitude.

REFERENCES

1. Neidel H.O. et al. // Nucl. Instrum. Meth. 1980. V. 178. p. 137.
2. Pyatkov Yu.V., Kamanin D.V., von Oertzen W. et al. // Eur. Phys. J. A. 2010. V. 45. No. 1. p. 29.
3. Pyatkov, Yu.V., Kamanin, D.V., Strekalovsky, A.O. et al. // Bull. Russ. Acad. Sci.: Phys, 2018, V. 82, No. 6, pp. 804–807.
4. Pyt'ev Y. P., Falomkina O. V., Shishkin S. A. // Pattern Recognition and Image Analysis: Advances in Mathematical Theory and Applications. 2019. V. 29, No. 4. pp. 577–591.
5. Pyatkov Yu.V., Kamanin D.V. et al. // Bull. Russ. Acad. Sci.: Phys, 2020, V. 84, No. 4, pp. 604-608 (in Russian).
6. Y.S. Kim et al., //NIMA. Volume 329, Issue 3, 1 June 1993, pp. 403-417.

Neutron Spin-Filter with Spin-Exchange Interaction of ^{3}He Nuclei and the Atoms of a Saturated Ferromagnetic

V.R. Skoy

Frank Laboratory of Neutron Physics, Joint Institute for Nuclear Research, 141980 Dubna, Russia

The model of a spin - exchange interaction between the nuclear magnetic moment of ^{3}He and the magnetic moments of electrons in a ferromagnetic is proposed. If a ferromagnetic is saturated an interaction leads to a gradual rising of ^{3}He nuclear polarization inside a volume surrounded by this ferromagnetic. The conditions for a practical implementation of a neutron spin filter with the polarized ^{3}He nuclei are considered, as well as the variants of its design.

1. Polarization of ^{3}He Nuclei by the Alkali Metal Atoms

The physical origin of polarization of the noble gases with spin $I = 1/2$ is the hyperfine interaction $\alpha(\vec{I} \cdot \vec{S})$ between the nuclear and unpaired atomic magnetic moments. Magnetic moment of an unpaired electron with $S = 1/2$ may belong to a noble gas itself, or to the other atoms, which collide with noble gas ones. We shall consider collisions of ^{3}He and alkali metal atoms with a single unpaired electron on the outer atomic shell.

We shall assume that the colliding atoms form an insulated system with conservation of the total angular momentum (TAM), and their orbital momentum is zero. That means TAM is equal to the total spin of the system. Since the nuclear and electron spins are equal to 1/2, then TAM = 0 for a mutual state $(+I, -S)$. That means a flip from $(+I, -S)$ to $(-I, +S)$ with the same TAM is possible. When the atoms collide in state $(+I, +S)$ with TAM = +1, a flip to a state $(-I, -S)$ with TAM = –1 isn't possible. Thus, when the alkali atoms are polarized (have certain projection of S), the flips of the ^{3}He nuclear spins going in the same direction and nuclear polarization gradually increases.

In practice a vapor of alkali metals (Rb, K, etc.) is optically pumped by a circularly polarized laser with the wavelength 795 nm. The light absorption produces a population of a certain magnetic sublevel in alkali atom [1]. Both ^{3}He and Rb atoms are confined in a sealed glass cell. The number density of Rb atoms in vapor $n_{Rb} \sim 10^{15}$ cm^{-3} is provided by the heating of a cell up to 150–180°C. A cell is stored in a homogeneous magnetic field of an order of 30–100 Gauss and collinear to a direction of a laser beam.

After collision of ^{3}He and Rb with a mutual spins flip, Rb atom absorbs a quantum of laser light, returns to its initial state and ready to next collision. A probability of a mutual spins flip is about 0.1.

Thus, a nuclear polarization requires two mandatory conditions. First, the atomic unpaired electrons must be aligned in a certain direction. Second, a mutual flip of ^{3}He and atomic spins should occur during their collisions.

2. Polarization of ^{3}He Nuclei by the Ferromagnetic Atoms

We have considered collisions in a cell volume. We may also imagine another system when the inner cell walls are made of a saturated ferromagnetic. Ferromagnetic in a saturated state represents almost a single domain where all magnetic moments (and spins) of the

unpaired electrons have a given direction. Now, let us assume a possibility of mutual spins flip when ^{3}He collides with ferromagnetic atoms in a wall. After collision ferromagnetic atom quickly returns to its equilibrium state owing an exchange interaction, which is an origin of ferromagnetism itself.

The assumption about a mutual spins flip is a hypothesis. We may imagine such flip by the next way. In the rest frame of an atomic electron magnetic moment of ^{3}He which moving toward generates variable magnetic $B(t)$ with Fourier frequency spectrum $b(\omega)$. At the moment of collision both nuclear μ_I and electronic μ_S magnetic moments are in the common magnetic field B_z of a ferromagnetic wall. A common field generates Zeeman spitting $\hbar\omega_I = \mu_I B_z$ and $\hbar\omega_S = \mu_S B_z$, respectively. Since an electron normally stands in a state with minimal energy it should take energy $\hbar\omega_S$ for a flip. Particularly it may take a fraction $\hbar(\omega_S - \omega_I)$ from field $B(t)$ and missing part $\hbar\omega_I$ directly from nuclear spin and makes it to flip. In general the flips are possible with the frequencies ω_I and $\omega_S + \omega_I$ as well. At last, the energy for a spins flip is scooped from a kinetic energy of moving ^{3}He atom. This means requirement: $\mu_S B_z << kT$. At normal temperature it takes place even for the strong ferromagnetics with $B_z \sim 2$–3 T.

One should stress that the above described mechanism takes place in direct collisions of ^{3}He with ferromagnetic atoms on a wall surface. The Hamiltonian of interaction for this case is

$$H = \mu_I B_z + \alpha(\vec{I} \cdot \vec{S}). \tag{1}$$

In case of no direct collisions (interlayer of any sort) the second term in (1) is absent and polarization of ^{3}He is just thermal equilibrium

$$p_I = \tanh(\mu_I B_z / kT) << 1. \tag{2}$$

The time dependence of nuclear polarization in case (1) can be obtained from a model of fluctuated magnetic fields which are generated by the moving electron spins in the locations of nuclear spins I [2]:

$$\frac{dI_z(t)}{dt} = -\Gamma_\alpha [I_z(t) - S_z]. \tag{3}$$

Here an index denotes the components along B_z. The solution of (3) with equilibrium (not dependent on time S_z) and $I_z(0) = 0$ is

$$\begin{aligned} I_z(t) &= S_z\left(1 - e^{-\Gamma_\alpha t}\right), \\ \Gamma_\alpha &= 1/T_{IS} = n_S v \sigma_3 / d. \end{aligned} \tag{4}$$

Here T_{IS} is typical relaxation time of nuclear polarization due to hyperfine interaction, which depends on frequency components $b(\omega_S \pm \omega_I)$ and $b(\omega_I)$ of a fluctuated magnetic field, n_S – number of ferromagnetic atoms per cm^2, v – average speed of ^{3}He atoms, σ_3 – cross section of ^{3}He atom collision with spin flip, and d – distance between cell walls.

If one consider the other interactions which affect nuclear polarization with the characteristic rate constant Γ, then the solution (4) will be

$$I_z(t) = S_z \cdot \frac{\Gamma_\alpha}{\Gamma_\alpha + \Gamma}\left[1 - e^{-(\Gamma_\alpha + \Gamma)t}\right]. \quad (5)$$

For a saturated ferromagnetic (electron polarization is 1), a nuclear polarization of ^{3}He may be expressed as

$$p_3(t) = \frac{\Gamma_\alpha}{\Gamma_\alpha + \Gamma}\left[1 - e^{-(\Gamma_\alpha + \Gamma)t}\right]. \quad (6)$$

If one take for iron (4 unpaired electrons) $n_S = 4\times1.2\times10^{15}$ cm^{-2} and $d = 5$ cm, then will obtain $\Gamma_\alpha \approx 10^{15}\cdot(v\sigma_3)$ c^{-1}. Now if we assume $v\sigma_3$ is of order as for Rb - ^{3}He collisions, we shall get $\Gamma_\alpha \sim 1/20$ hours.

Cross section σ_3 is the crucial quantity for a practical application of above mechanism. However it is hard to judge about it definitely from a general point of view. System Rb - ^{3}He with collision of just two individual atoms is relatively simple. The quality picture assumes that for a mutual spins flip ^{3}He nucleus and Rb electron should get quite closer. In a case of ferromagnetic wall a picture gets much complicated because of interaction between the atoms inside it. An individual ferromagnetic atom of an iron group has the unpaired electrons on a 3d-shell with outer 4s- coupled shell. The outer shell prevents ^{3}He nucleus gets near to 3d-electrons. However in a macroscopic sample exchange interaction provides overlapping of orbitals with forming of zone structure in ferromagnetic. The electrons of s-shell spread among the big number of atoms and form a paramagnetic gas, which give not significant contribution to the magnetic properties of a ferromagnetic. The electrons of d-shell still hold their place in every atom. Thus it's probably that ^{3}He nuclei may interact with 3d-electrons quite effectively due to spreading of s-shells in a ferromagnetic sample. In the rare-earth ferromagnetic one can expect interaction of ^{3}He nuclei with f-shell electrons as well [3].

3. Relaxation of Nuclear Polarization

The most obvious reason for a decay of nuclear polarization p_I is a gradient of a magnetic field of any behavior $dB(x)/dx$ transverse to a direction of p_I. Transverse magnetic field makes a spin to presses around it. If a field magnitude is different in the points of some region, the precession frequencies are different too, which cause a destruction of a uniform alignment (polarization) of the spins along a region.

The gradients may arise because of the outer irregular fields, paramagnetic admixtures in a volume (oxygen) or in a surface. A specific case is a rough wall surface. Magnetic field near it sharp ledges may be very inhomogeneous and destroy polarization of ^{3}He. Moreover, it's hard to clean up a rough surface from oxide and oil layers after mechanical processing. Besides, a ferromagnetic must be saturated, otherwise the domains with different direction of magnetization may cause a particular loss of polarization.

As result the minimal technical demands for practical application should be:

1. ^{3}He must be free from any paramagnetic admixtures (getter).
2. Low roughness of a ferromagnetic surface (polishing, rolling).

3. High purity of the all inner surfaces. Absence of oxide, oil layers, and hydrogen as much as possible (chemical and us- clearing, pumping out with heating).
4. Magnetic saturation of ferromagnetic wall.

4. Designs of Spin Filter

A) Side wall is a permanent magnet with magnetization along the axis.
B) Inner surface of a cell is a soft magnetic material - thin ferromagnetic layer, which may have practically rectangular hysteresis loop. That may provide high residual magnetization. Outside is a permanent magnet like in A) to keep inner layer in a highly saturated state.

A B C

C) Inner surface of a cell is covered by a hard magnetic material (thin permanent magnet).

Acknowledgment

Author expresses gratitude to V.L. Aksenov for his attention, valuable remarks and useful discussion about the subject of presented work.

References

1. T.G. Walker, W. Happer, Rev. Mod. Phys., Vol. 69, No. 2, 629, 1997.
2. А. Абрагам, Ядерный магнетизм, ИИЛ, Москва 1963. (A. Abragam, Nuclear Magnetism, Oxford Press, 1961).
3. V.L. Aksenov, T.V. Tropin, Lectures on Theory of Condensed State, Physical Department of Moscow State University, Moscow, 2020, (in Russian).

The Development of the Setup for the Study of *P*-Even Correlations in *p*-Wave Resonances

A.Yergashov[1,2], C. Hramko[1], Yu.N. Kopatch[1], V.L. Kuznetsov[1], L.V. Mitsyna[1], N.V. Rebrova[1], P.V. Sedyshev[1]

[1]*Frank Laboratory of Neutron Physics, Joint Institute for Nuclear Research, Dubna, Russia*
[2]*Institute of Nuclear Physics, Almaty, Republic of Kazakhstan*

Studying the properties of p-wave neutron resonances in the low-energy region is much more difficult than s-wave ones, because of the centrifugal barrier, which significantly reduces the probability of neutron capture with $l \geq 1$. Meanwhile, p-wave resonances have specific properties that are not inherent in s-resonances. These properties include the two-component nature of the neutron widths Γ_p^n upon excitation of compound states with spins $J = I \pm 1/2$. In the representation of the total momentum of the neutron, $j = l + s$, $j = 1/2$ or $3/2$, and $\Gamma_p^n = \Gamma_{p\,1/2}^n + \Gamma_{p\,3/2}^n$. Accordingly, to represent the channel spin $S = I + s$ ($S = I \pm 1/2$) we have $\Gamma_p^n = \Gamma_{p\,I+1/2}^n + \Gamma_{p\,I-1/2}^n$. Experimental data on the Γ_p^n components are very poor.

In recent years, in connection with the discovery of parity non-conservation effects in p-wave resonances, an additional incentive to study the structure of Γ_p^n has appeared, since the theoretical interpretation of these effects requires knowing the quantities $x = (\Gamma_{p1/2}^n/\Gamma_{p\,3/2}^n)^{1/2}$. It should be noted that experiments to determine the values of x for these resonances present significant difficulties due to the smallness of the neutron widths $\Gamma_p^n \leq 10^{-6}$ eV, which makes it practically impossible to observe resonance scattering and complicates measurements with γ-quanta. The scheme of the experiment for a study of the angular distribution of γ-quanta of the direct transition after capture by the ^{81}Br nucleus of neutrons with energies close to the energy of the p-wave resonance of this nucleus with $E_p = 0.88$ eV is shown in Figure 1. The studies were carried out with unpolarized neutrons and were aimed at obtaining information about the parameters of this resonance, first of all, about the value of x. In Figures 2 and 3 the TOF spectrum and its part with the KBr resonance of interest were presented.

The measurements were carried out on the 4th channel of the IREN facility, on 11 m base. The characteristics of the IREN resonant neutron source are given in Table 1.

Table 1. IREN parameters

Maximum current (A)	3
Repetition frequency (Hz)	50
Duration of the electronic pulse (ns)	100
Electron energy (MeV)	70
Beam power (kW)	0.5

The results of measuring thermal Φ(th) and resonance Φ(res) neutron flux on the 4th channel of the IREN experimental hall, using gold foils by two methods, are presented below.

1. Monitor pair method with and without cadmium –

$$\Phi(\text{th}) = 8.66\times10^3 \text{ n/cm}^2 \text{ s}; \quad \Phi(\text{res}) = 4.75\times10^3 \text{ n/cm}^2 \text{ s};$$

2. Golden Screen Method – $\Phi(\text{th}) = 1.48\times10^4$ n/cm^2 s.

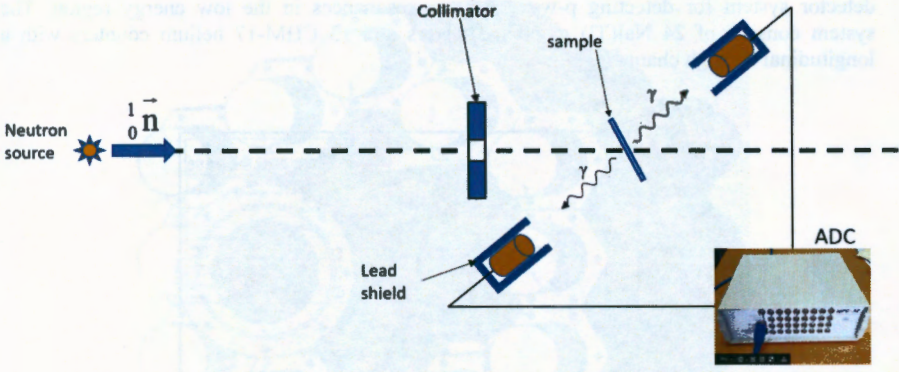

Figure 1. Scheme of the experiment.

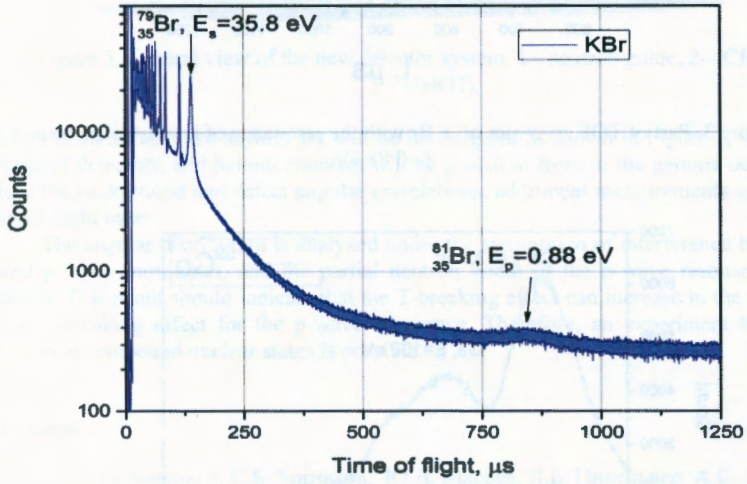

Figure 2. TOF spectrum of KBr.

In addition to the measurements with KBr, measurements were also made with the following samples: Ag, Co, Sn. Figure 4 shows a fragment of the TOF spectrum of ^{59}Co measured with the BGO detector. The scattered neutron from the sample, hitting BGO and interacting with it, gives rise to a resonance on Ge with the energy of 102 eV, it adjusts to a ^{59}Co resonance with an energy of 132 eV.

In order to protect the gamma detector from scattered neutrons, which, having interacted with the detector substance, can give an additional background, it was decided to put helium counters in front of the gamma detectors. Figure 5 shows the design of a new

detector system for detecting p-wave neutron resonances in the low energy region. The system consists of 24 NaI(Tl) gamma detectors and 13 CHM-17 helium counters with a longitudinal through channel.

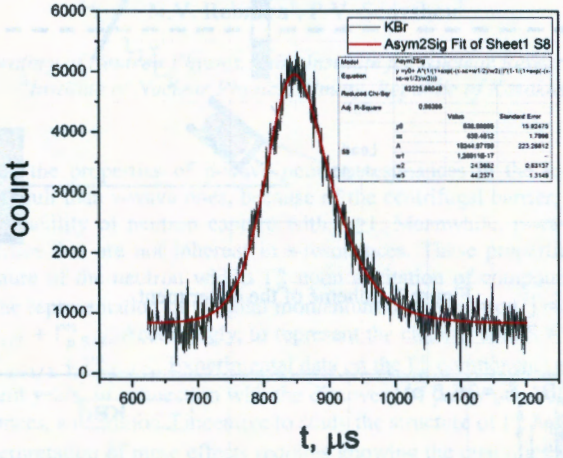

Figure 3. Part of TOF spectrum of KBr with the resonance of interest with the energy E=0.88 eV.

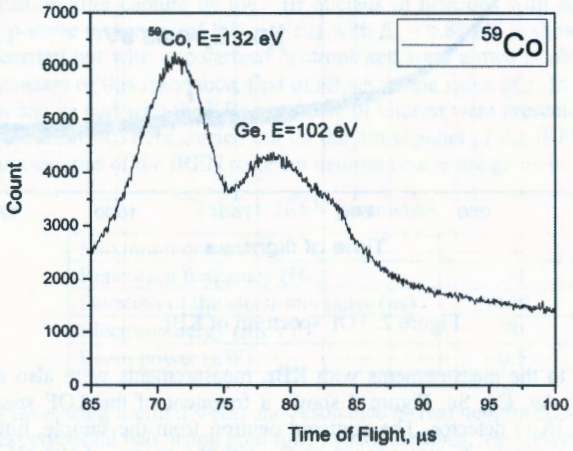

Figure 4. Part of TOF spectrum of ^{59}Co.

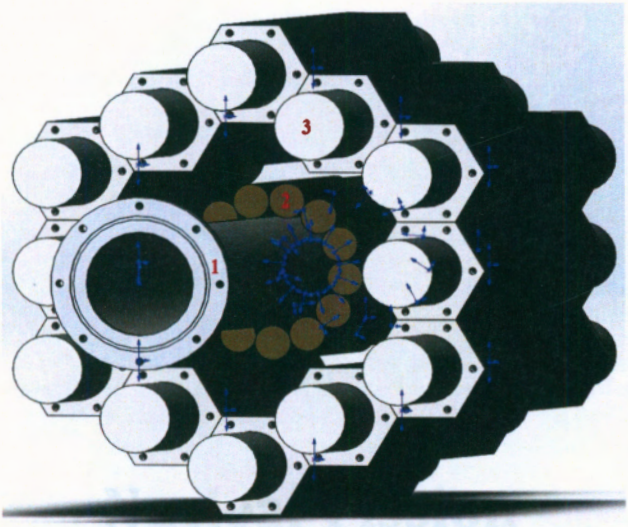

Figure 5. General view of the new detector system. 1 - neutron guide, 2 – CHM-17, 3 – NaI(Tl).

Forward-backward asymmetry will be investigated as shown in Figure 1, with a large number of detectors, and helium counters will be placed in front of the gamma detectors. To reduce the background and detect angular correlations, additional measurements are made on a larger flight base.

The angular distribution is analyzed under the assumption of interference between the s- and p-wave amplitudes, and the partial neutron width of the p-wave resonance will be obtained. This result should indicate that the T-breaking effect can increase in the same order as the P-breaking effect for the p-wave resonance. Therefore, an experiment to study T-violation in compound nuclear states is possible.

References

1. В.П. Алфименков, С.Б. Борзаков, Ю.Д. Мареев, Л.Б. Пикельнер, А.С. Хрыкин, Э.И. Шарапов. Корреляции в угловом распределении гамма квантов при захвате нейтронов в области р-резонанса, Краткие сообщения ОИЯИ №10, стр. 19–25, 1985.
2. T. Okudaira, et al., Angular Distribution of γ-rays from Neutron-Induced Compound States of ^{140}La, arXiv:1710.03065v4 [nucl-ex] 12 Feb 2018.
3. Mughabghab S.F. Neutron Gross Sections, Neutron Resonance Parameters and Thermal Gross Sections, Academic Press, New York (1984).
4. В.Р. Ской, Э.И. Шарапов. Р-четные угловые корреляции в резонансах (n,γ)-реакциях, Физика элементарных частиц и атомного ядра, 1991, том 22, вып.6, стр. 1400–1432.

Nuclear Fission

Study of Neutron Multiplicity in $^{232}Th(n,f)$ Reaction Using TALYS-1.96

Punit Dubey and Ajay Kumar

Banaras Hindu University, Varanasi, India

E-mail: ajaytyagi@bhu.ac.in

Introduction

The nuclear scientific community views ^{232}Th as an option for fuel in the future nuclear energy program. The fissile element utilized in contemporary commercial reactors is uranium-235 (^{235}U), which constitutes a mere 0.72% of natural uranium. The ^{238}U isotope, which constitutes 99.27% of natural uranium, cannot undergo fission within existing thermal reactors. To optimize the utilization of available resources, two primary fuel cycles are suggested for prospective implementation: the $^{238}U/^{239}Pu$ and $^{232}Th/^{233}U$ fuel cycles. In the context of the $^{238}U/^{239}Pu$ cycle, the fissile material is identified as ^{239}Pu, which is derived from ^{238}U by the process of neutron capture followed by two successive beta decays. In the $^{232}Th/^{233}U$ cycle, the fissile material is ^{233}U, which undergoes transmutation from ^{232}Th through the processes of neutron capture and two subsequent beta decays. The $^{232}Th/^{233}U$ cycle presents appealing characteristics, including the greater natural abundance of thorium compared to uranium, the generation of a lower quantity of waste, and a reduced presence of transuranic isotopes in the waste. The generation of the fissile nucleus ^{233}U in the thorium-uranium fuel cycle occurs through the process of the $^{232}Th(n,\gamma)^{233}Th$ reaction, which is then followed by two consecutive β-decays. The cross-section of the $^{232}Th(n, 2n)^{231}Th$ reaction exhibits a sharp increase beyond a threshold energy of 6.648 MeV. The provided diagram illustrates the schematic representation of the Thorium-Uranium (Th–U) fuel cycle.

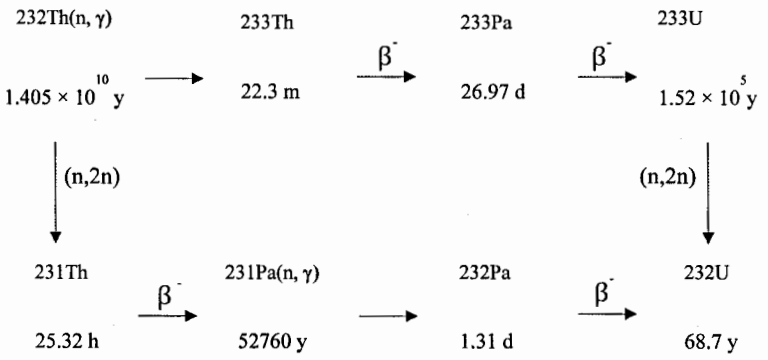

Th-U Cycle

Several experimental studies have been undertaken to ascertain the cross-section [1–4]; yet there is a scarcity of investigations [5–7] that have been carried out to compute the overall neutron multiplicity above an energy threshold of 10 MeV. Several scholars have conducted

theoretical and experimental investigations on detecting neutron multiplicities in fusion-fission dynamics generated by heavy ions [8–14]. However, works [5–7] are scarce, focusing on reactions induced by particles and neutrons.

In this study, we have performed calculations to determine the neutron multiplicity for the ^{232}Th(n,f) reaction at various incident energies. These calculations were conducted using the TALYS 1.96 [15].

Result and Discussion

In this work, we have compared the experimental data of average neutron multiplicity at different incident energies from EXFOR with the evaluated data from ENDF/B-VI, JENDL-4.0, and the calculated data from TALYS-1.96, as shown in Fig. 1. The experimental data are in good agreement with the evaluated data from both the ENDF/B-VI and JENDL-4.0 libraries and at high incident energy (14.7 MeV), the TALYS 1.96 data are also in agreement with the experimental data.

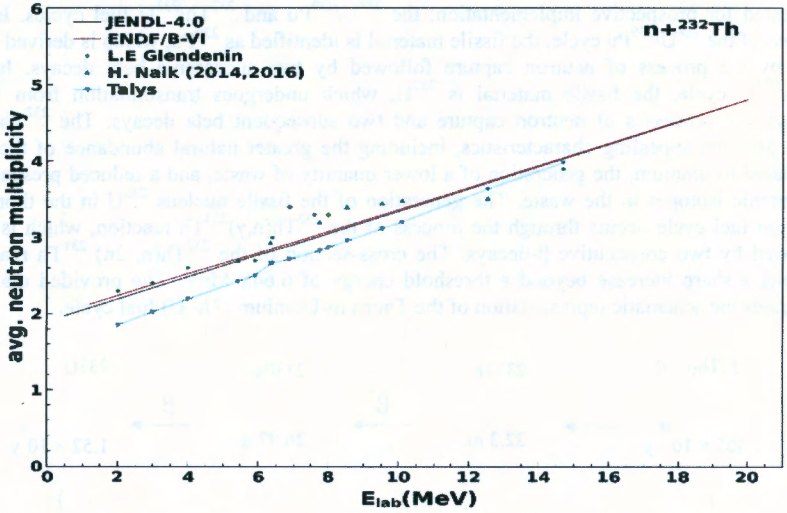

Fig.1: Comparison of experimental and evaluated data w.r.t. TALYS calculated data for ^{232}Th(n,f) reaction.

As shown in Fig. 2, we have also calculated the prompt neutron multiplicity at 14.7 MeV as a function of mass (A) and charge (Z). This figure reveals that neutron multiplicity is highly dependent on both Z and A fission fragments, as evidenced by the peaks at $_{54}$Xe^{141,142,143,144} and $_{56}$Ba^{146,147,148,149}. Therefore, it is evident from the graph that neutron multiplicity varies with respect to Z and A.

The theoretical framework being suggested facilitates the computation of some measurable neutron characteristics, specifically the neutron emission function ν(A), which represents the total number of released neutrons as a function of the initial fragment mass and the total neutron emission number ñ. The aforementioned functions of neutrons play a crucial role in the field of neutron physics and find extensive applications in various contexts

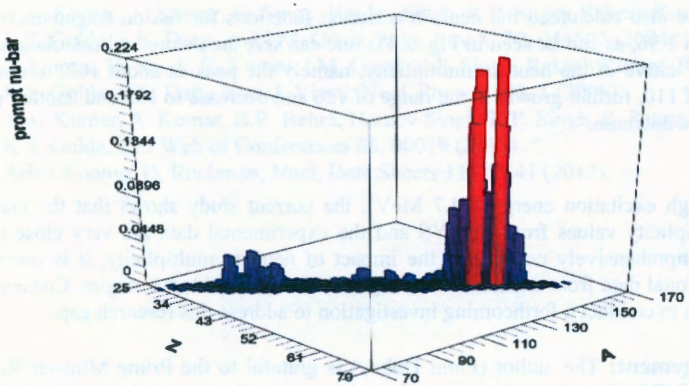

Fig.2: Prompt neutron multiplicity as a function of mass (A) and charge (Z) using TALYS 1.96 for ^{232}Th (n,f) reaction at 14.7 MeV.

involving neutron fluxes. The most significant factors influencing ν(A) and ñ include the isotopic makeup of the initial nucleus and its excitation energy or temperature T. The calculation of the ν (A) function is derived from the probabilistic determination of the realisation (yield) of a two-fragment cluster, which consists of a pre-neutron emission fragment with mass A and an equilibrium number of neutrons ñ.

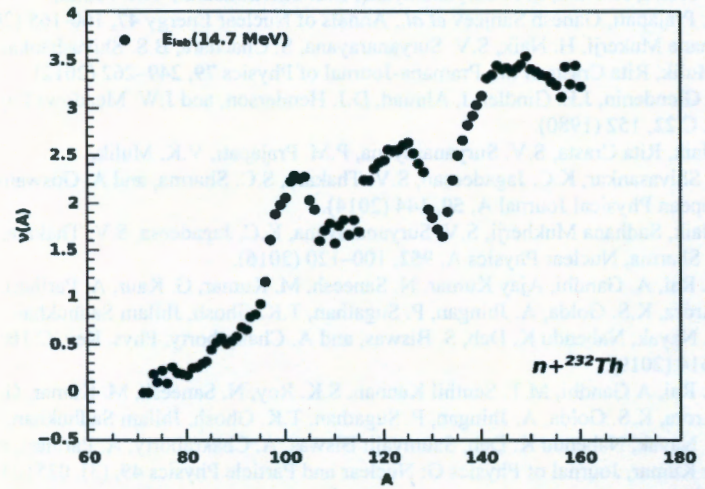

Fig.3: The fission neutron yield is given as a function of the fission fragment mass (A) ^{232}Th (n,f) calculated using TALYS-1.96 code at 14.7 MeV.

We have also calculated the neutron emission functions for fission fragments of ^{233}Th using TALYS 1.96, as can be seen in Fig. 3. As one can see, the theoretical calculations show a "saw-tooth"-curve of the neutron multiplicity, namely the peak at about 102, minimum in the vicinity of 110, further growth in the range of 126 and decrease to 133 and another peak at 150 and then a decrease.

Conclusion

At a high excitation energy (14.7 MeV), the current study shows that the computed neutron multiplicity values from TALYS and the experimental data are very close to each other. To comprehensively understand the impact of neutron multiplicity, it is essential to acquire additional data from experiments at higher values of incident energies. Consequently, we have plans to conduct a forthcoming investigation to address this research gap.

Acknowledgement: The author (Punit Dubey) is grateful to the Prime Minister Research Fellowship (PMRF ID - 0101841) for the financial support for this work. One of the authors (A. Kumar) would like to thank the Institutions of Eminence (IoE) BHU [Grant No. 6031] and IUAC-UGC, Government of India (Sanction No. IUAC/XIII.7/UFR-71353).

References

1. Yonghao Chen, Yiwei Yang, Zhizhou Ren, Wei Jiang, Ruirui Fan, Han Yi, Rong Liu *et al.,* Physical Letters B **839**, 137832 (2023).
2. Yu.M. Gledenov, Zengqi Cui, Jie Liu, Haoyu Jiang, Yiwei Hu, Haofan Bai, Jinxiang Chen *et al.,* Eur. Phys. J. A **58**, 86 (2022).
3. Rita Crasta, H. Naik, S.V. Suryanarayana, B.S. Shivashankar, V.K. Mulik, P.M. Prajapati, Ganesh Sanjeev *et al.,* Annals of Nuclear Energy **47**, 160-165 (2012).
4. Sadhana Mukerji, H. Naik, S.V. Suryanarayana, S. Chachara, B.S. Shivashankar, V. Mulik, Rita Crasta *et al.,* Pramana-Journal of Physics **79**, 249–262 (2012).
5. L.E. Glendenin, J.E. Gindler, I. Ahmad, D.J. Henderson, and J.W. Meadows Phys. Rev. C **22**, 152 (1980).
6. H. Naik, Rita Crasta, S.V. Suryanarayana, P.M. Prajapati, V.K. Mulik, B.S. Shivasankar, K.C. Jagadeesan, S.V. Thakare, S.C. Sharma, and A. Goswami, The European Physical Journal A, **50**, 144 (2014).
7. H. Naik, Sadhana Mukherji, S.V. Suryanarayana, K.C. Jagadeesa, S.V. Thakare, S.C. Sharma, Nuclear Physics A, **952**, 100–120 (2016).
8. N.K. Rai, A. Gandhi, Ajay Kumar, N. Saneesh, M. Kumar, G. Kaur, A. Parihari, D. Arora, K.S. Golda, A. Jhingan, P. Sugathan, T.K. Ghosh, Jhilam Sadhukhan, B.K. Nayak, Nabendu K. Deb, S. Biswas, and A. Chakraborty, Phys. Rev. C **100**, (1), 014614 (2019).
9. N.K. Rai, A Gandhi, M.T. Senthil Kannan, S.K. Roy, N. Saneesh, M. Kumar, G. Kaur, D. Arora, K.S. Golda, A. Jhingan, P. Sugathan, T.K. Ghosh, Jhilam Sadhukhan, B.K. Nayak, Nabendu K. Deb, Saumyajit Biswas, A. Chakraborty, A. Parihari, and Ajay Kumar, Journal of Physics G: Nuclear and Particle Physics **49**, (3), 035103 (2022).
10. N.K. Rai, Vivek Mishra, and Ajay Kumar, Phys. Rev. C **98**, 024626 (2018).
11. A. Kumar, A. Kumar, G. Singh, B.K Yogi, R. Kumar, S.K. Datta, M.B. Chatterjee, and I.M. Govil, Phys. Rev. C **68**, 034603 (2003).

12. Ajay Kumar, A. Kumar, G. Singh, Hardev Singh, R.P. Singh, Rakesh Kumar, K.S. Golda, S.K. Datta, and I.M. Govil, Phys. Rev. C 70, 044607 (2004).
13. A. Kumar, H. Singh, R. Kumar, I.M. Govil, R.P. Singh, Rakesh Kumar, B.K. Yogi, K.S. Golda, S.K. Datta, and G. Viesti, Nucl. Phys.A **798**, 1 (2008).
14. Ajay Kumar, A. Kumar, B.R. Behra, Hardev Singh, R.P. Singh, R. Kumar and K.S. Golda, EPJ Web of Conferences **86**, 00019 (2015).
15. Arjan Koning, D. Rochman, Nucl. Data Sheets **113**, 2841 (2012).

Measurement of Fission Cross Section and Angular Distributions of Fission Fragments from Neutron-Induced Fission of ^{243}Am in the Energy Range 1–500 MeV

A.M. Gagarski[1], A.S. Vorobyev[1], O.A. Shcherbakov[1], L.A. Vaishnene[1], A.L. Barabanov[2,3], T.E. Kuz'mina[4]

[1] *NRC "Kurchatov Institute", B.P. Konstantinov Petersburg Nuclear Physics Institute, 188300, Gatchina, Leningrad district, Russia*
[2] *NRC "Kurchatov Institute", 123182, Moscow, Russia*
[3] *National Research Nuclear University "MEPhI", 115409, Moscow, Russia*
[4] *V.G. Khlopin Radium Institute, 194021, St.-Petersburg, Russia*

Fission cross sections and angular distributions of fission fragments from the neutron-induced fission of ^{243}Am have been measured in the energy range 1–500 MeV at the neutron time-of-flight spectrometer based on the neutron complex GNEIS at the 1GeV proton synchrocyclotron of the NRC "Kurchatov Institute" - PNPI (Gatchina). The description of the experimental set-up consisted of two MWPC counters with targets of ^{243}Am and ^{235}U is given, as well as the some principal details of experimental data processing.

The fission cross section of ^{243}Am was obtained by ratio method using ^{235}U as a standard. The anisotropy of fission fragments $W(0^{\circ})/W(90^{\circ})$ was deduced from the experimental data on angular distributions of ^{243}Am. The anisotropy data are of particular interest because in the investigated energy range 1–500 MeV other experimental data are practically absent, despite the ever-growing interest in this field, stimulated by the creation of new nuclear technologies. This work is a part of the program dedicated to investigations of neutron-induced fission at intermediate energies.

Introduction

The data on nuclear fission in intermediate energy range 1–200 MeV are of prime importance for the advanced nuclear technologies such as Accelerator-Driven Systems (for nuclear power generation and nuclear transmutation). The information about angular distribution of fission fragment is also very important to verify parameters of theoretical models used for adequate fission process description in neutron energy range above 20 MeV. The systematic study of angular distributions of fission fragments is limited to that these experimental data are very scarce in neutron energy range above 20 MeV and are practically absent for neutron energy range above 100 MeV. Data on the angular distributions of fission fragments are important for accurate measurements of fission cross-sections, since they should be taken into account as an efficiency correction for detectors other than 4π. There is no such data for ^{243}Am, unless two data points of Fursov et al. [1] at the energy 2.5 MeV.

One of the main problems in the reprocessing of spent nuclear fuel produced in modern nuclear reactors are Am and Cm isotopes due to their high activity and long half-life. Am is the most dangerous due to its high yield and high activity. ^{243}Am contributes also to the formation of ^{239}Pu. The share of ^{243}Am among other minor Am actinides is ~15% in spent fuel

from thermal reactors. Today, the transmutation of nuclear waste in fast neutron reactors seems to be one of the promising ways to reduce the radiotoxicity of spent nuclear fuel.

The practical implementation of plans for both the creation of a closed fuel cycle based on fast nuclear reactors and the disposal of radioactive waste is impossible without reliable and accurate nuclear data. For example, the required accuracy of the fission cross section of ^{243}Am(n,f) is 7% when designing the sodium-cooled fast reactor (SFR) and 2% for designing the accelerator-driven minor actinide burner reactor (ADMAB) [2]

The data available on the fission cross section of ^{243}Am are mainly limited to the neutron energies below 20 MeV [1, 3–11]. These data were obtained using both monoenergetic neutron beams and time-of-flight technique with "white" neutron spectrum at the pulsed accelerators (neutron sources) including nuclear explosion. The available experimental data reveals a significant scatter, which reaches 30% in the neutron energy range of 2–10 MeV (Fig.1).

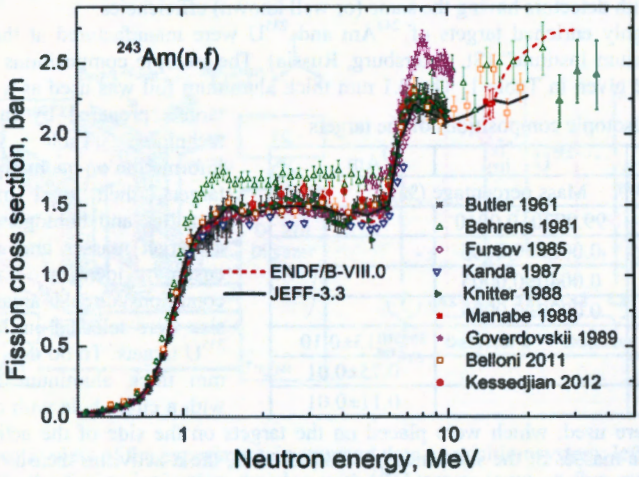

Fig. 1. The fission cross sections of ^{243}Am.

The maximum deviation from the array of experimental data and estimated data from the ENDF/B-VIII.0 and JEFF-3.3 libraries are the experimental data of Behrens et al. [5] and Goverdovskii et al. [9]. These data on the ^{243}Am fission cross sections were measured by the standard method relative to the ^{235}U fission cross section, but absolute normalization was carried out using the threshold cross section method (Behrens et al.) and similar method of elemental impurities (Goverdovskii et al.) instead of accurately measuring the number of target nuclei ^{243}Am and ^{235}U. This circumstance, apparently, was the reason for the significant deviation of the data (Behrens et al. and Goverdovskii et al.) in absolute magnitude, while maintaining the shape of the cross-section curve in the above-threshold region of neutron energies. There are practically no experimental data for neutron energies above 20 MeV. Therefore, new measurements with absolute normalization of the fission cross section of ^{243}Am should be made in a wide neutron energy range on neutron beams with a continuous spectrum using the time-of-flight method.

General description of the experiment

The measurements were carried out at the 36 m flight path of the neutron TOF-spectrometer GNEIS based on the spallation neutron source at 1 GeV proton synchrocyclotron SC-1000 of the NRC KI – PNPI (Gatchina, Russia) [12, 13]. The short pulse width 10 ns of the neutron source enables to carry out TOF-measurements with the energy resolution from 0.8% (at 1 MeV) to 13% (at 200 MeV). A detailed description of the set-up can be found in our previous publications [14–22]. The main features of the present measurements are described below.

The fission cross section of the nucleus under study was measured relative to the cross section of a reaction that is known with high accuracy (standard cross section), in present measurements, that is the neutron induced fission of ^{235}U. To do this, it was necessary to prepare the target of ^{243}Am and reference target of ^{235}U with exactly known ratio of number of nuclei (N_{Am3}/N_{U5}), to place these targets in the same neutron flux and to register fission fragments with detectors having the same (or well known) efficiencies.

The highly enriched targets of ^{243}Am and ^{235}U were manufactured at the JSC "V.G. Khlopin Radium Institute" (St. Petersburg, Russia). The isotopic compositions of the target materials are given in Table 1. The 0.1 mm thick aluminum foil was used as a substrate for targets prepared by the "painting" technique. Table 2 provides information on geometry sizes of the targets, their total masses, areal densities and homogeneity, as well as target masses and activities. To ensure identical measurement conditions, circular areas of the same size were selected on the ^{243}Am and ^{235}U targets. To do this, identical 0.1 mm thick aluminum foil "masks" with a circle hole with a diameter of 48.0 mm were used, which were placed on the targets on the side of the active layer. To determine the masses of the substance in selected areas, the α-activities measurements of the masked targets were carried out using semiconductor detector. The measured ratio of number of nuclei (N_{Am3}/N_{U5}) was found with relative statistical uncertainty 1.7 %.

Table 1. Isotopic compositions of the targets

	^{235}U	^{243}Am
Isotope	Mass percentage (%)	
^{235}U	99.9920±0.0010	
^{234}U	0.0020±0.0005	
^{236}U	0.0040±0.0005	
^{238}U	0.0020±0.0005	
^{243}Am		99.13±0.10
^{241}Am		0.75±0.01
^{244}Cm		0.11±0.01

Table 2. Parameters of the targets

Main isotope	^{235}U	^{243}Am
Thickness of active layer (μg/cm2)	203(11)	142(7)
Homogeneity of active layer	10%	10%
Sizes of active layer (mm)	50×100	Ø 82
Total target mass (mg)	10.15(51)	7.5(4)
Main isotope mass inside mask Ø48 mm (mg)	3.480(48)	2.484(25)
Target activity inside the mask Ø48 mm (Bq)	295	2.92×10^7
Scaling factor (N_{Am3}/N_{U5})	0.690(12)	

A general view of the experimental setup and data acquisition system is shown in Fig. 2. The setup for measuring fission cross sections and angular distributions of fission fragments (FF) consists of two low pressure gaseous coordinate-sensitive multiwire proportional counters (MWPC) D1 and D2. The counters D1 and D2 were placed close to the target in the beam, one after the other. The neutron beam axis came through the geometrical centers of the target and the MWPC's electrodes being perpendicular to them. Data acquisition system was based on two waveform digitizers Acqiris DC-270 with sampling rate of 500 MSamples/s. This system as well as the methods of digital processing of signals from FF detector used enabled to perform measurements in a wide interval of neutron energy with a zero dead time. Herewith, almost perfect separation between fission events and products of other reactions was achieved at a practically zero FF registration threshold. To demonstrate the quality of this separation, for nuclei under study the amplitude spectra of fission fragments are shown in Fig. 3 for all events and for "useful" fission events selected by means of the procedure described in [15].

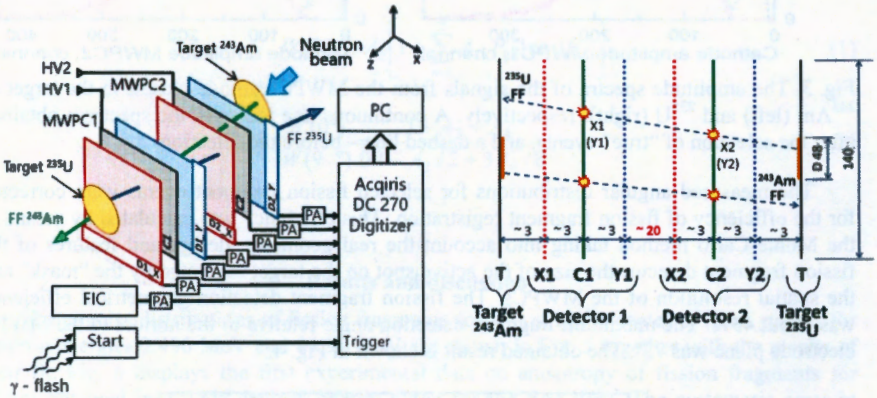

Fig. 2. Schematic view of the experimental setup and data acquisition system: left -Start - start detector; FIC - the fission ionization chamber with ^{238}U targets (neutron flux monitor); PA – preamplifier; HV1, HV2 – high-voltage power sources; C1, C2 are the cathodes of MWPC1 and MWPC2, respectively; D1_X, D2_X – detectors 1,2 (X axis); anodes D1_Y, D2_Y – detectors 1,2 (Y axis); right – the internal structure of the MWPCs, the distances between electrodes and diameters are given in mm.

A small admixture of ^{244}Cm in the ^{243}Am target (0.11%) creates a background of spontaneous fission fragments. The background induced by spontaneous fissions of ^{244}Cm was evaluated as 305±9 min^{-1}. It was calculated based on the efficiency of detection of fission fragments, the spontaneous fission half-life for ^{244}Cm, and the mass of ^{244}Cm in the "masked" target part, which was precisely determined in this work. Thus, at neutron energies about 200 keV the share of spontaneous fission in the total fission fragment counts rate was about 70%, and at energies above 1 MeV it does not exceed 0.2%. The spontaneous fission background was subtracted from the time-of-flight spectra and from the measured angular distributions of fission fragments.

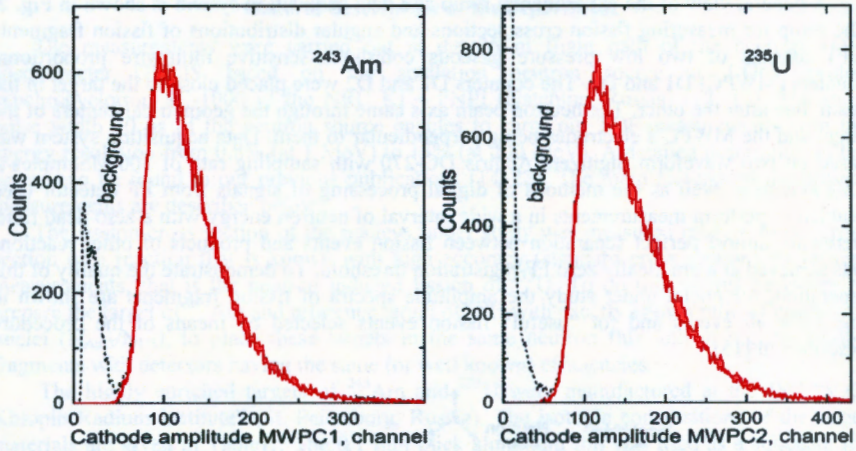

Fig. 3. The amplitude spectra of the signals from the MWPC cathode closest to the target of ^{243}Am (left) and ^{235}U (right), respectively. A continuous line indicates the spectrum obtained after the selection of "true" events, and a dashed line – before the selection.

The measured angular distributions for selected fission fragment events were corrected for the efficiency of fission fragment registration. This efficiency was calculated by means of the Monte-Carlo method taking into account the real geometry, design and features of the fission fragment detector the size of the active spot on the target separated by the "mask" and the spatial resolution of the MWPCs. The fission fragment detection geometrical efficiency was about 43%. The maximum fragment detection angle relative to the normal to the MWPC electrode plane was 72°. The obtained result is shown in Fig. 4.

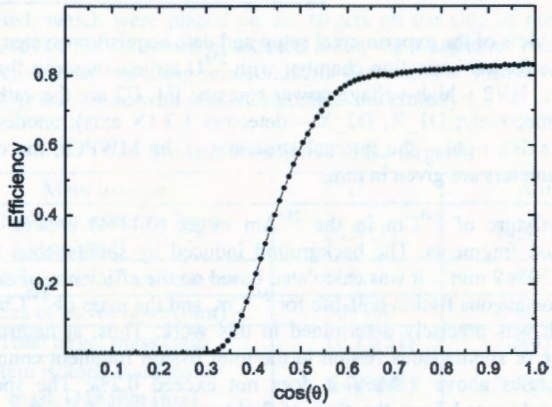

Fig. 4. The dependence of the efficiency of registration of fission fragments, ε, on the cosine of departure angle θ relative to the normal to the target plane.

Note that the effect of momentum transfer from the incident neutron to the fissioning system on the angular distributions in the laboratory system should be taken into account. To determine this effect, angular distributions of fission fragments in the laboratory system were measured for two setup orientations relative to the beam direction (downstream and upstream). In the first, downstream, position, the beam direction coincides with the longitudinal momentum component of the detected fission fragment. In the second, upstream, position, the beam direction is opposite to the longitudinal momentum component of the detected fission fragment.

The angular distributions of fission fragments in the center-of-mass system were deduced from the corrected $\cos(\theta)$ angular distributions in the laboratory system for two set-up orientations relative to the neutron beam direction ($\cos(\theta)$ bins were equal to 0.01). Then, these distributions were fitted in the range $0.35 < \cos(\theta) < 1.0$ by the sum of even Legendre polynomials up to the 4-th order and their anisotropy $W(0°)/W(90°)$ was calculated using the coefficients A_2 and A_4 (A_0=1) for the corresponding Legendre polynomials:

$$W(0°) = A_0\left[1 + \sum_{n=1}^{2} A_{2n} P_{2n}[\cos(\theta)]\right]. \quad (1)$$

$$\frac{W(0°)}{W(90°)} = \frac{1 + A_2 + A_4}{1 - A_2/2 + 3A_4/8}. \quad (2)$$

Results and discussion

The angular distributions of fission fragments for ^{243}Am in the center of mass system for neutron energies 2.496 MeV and 14.95 MeV are shown in Fig. 5 together with the results of their fit. Fig. 6 displays the first experimental data on anisotropy of fission fragments for ^{243}Am obtained in a wide neutron energy range for the first time. The systematic error in determining anisotropy in this experiment, which is related to the finite angular resolution of the arrays with MWPC and the uncertainty in the geometry of the experiment, is about 0.5%. The systematic error associated with the approximation used for fitting is 1–1.5%.

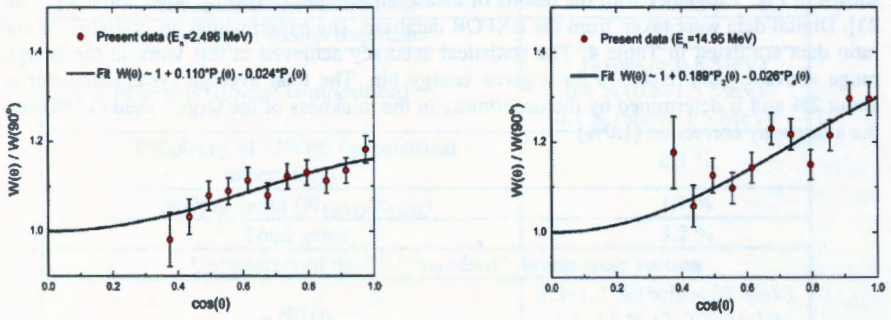

Fig. 5. Angular distributions of fission fragments for ^{243}Am.

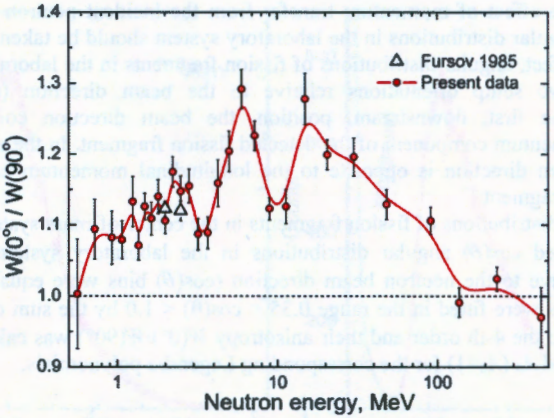

Fig. 6. Anisotropy of ^{243}Am fission fragments in comparison with the data of Fursov et al. [1]. The error bars of present data represent total uncertainties. The solid curve is shown only for visualization of experimental data.

A new stage in experimental studies of the angular distribution of fission fragments began when the GNEIS team at NRC KI - PNPI, the n_TOF collaboration at CERN and the NIFFTE collaboration at Los Alamos launched new experiments devoted to this problem almost simultaneously. The pulsed high-intensity sources of "spallation" neutrons of these facilities allow TOF-measurements of neutron-induced fission cross sections and angular distributions of fission fragments in the intermediate neutron energy range of 1–500 MeV. Two other important features of the experimental methods used by these research groups are the use of multichannel position-sensitive fission fragment detectors of varying degrees of complexity (MWPCs, PPACs, TPC) and the use of waveform digitizers for processing detector pulses. The results of these studies are presented in Table 3. Unfortunately, the results of measurements of the anisotropy of the ^{235}U and ^{238}U fission fragments obtained by the n_TOF collaboration and published in the materials of the ND-2016 conference have not yet been presented in the EXFOR database.

The measured ratio of the neutron-induced fission cross sections of ^{243}Am and ^{235}U is shown in Fig. 7 together with the results of measurements performed by other authors [5–10, 23]. Digital data were taken from the EXFOR database. The experimental uncertainties of our ratio data are listed in Table 4. The statistical accuracy achieved in this work in the energy range above 1 MeV is 2–3% for a given energy bin. The total average systematic error is about 2% and is determined by the uncertainty in the thickness of the targets used (1.7%) and the anisotropy correction (1.0%).

Table 3. Status of experiments on angular distributions of fission fragment study

Nucleus	GNEIS, KI-PNPI	n-TOF, CERN	NIFFTE, WNR, LANL
^{232}Th	JETP Lett.,102, 203(2015) EXFOR #41608002	Nucl. Data Sheets,119, 35 (2014) EXFOR #23209006	
^{233}U	JETP Lett.,104, 365(2016) EXFOR #41616006		
^{235}U	JETP Lett.,102, 203(2015) EXFOR #41608003 Phys. Rev. C 108, (2023) 014621, EXFOR #41757004	EPJ Web of Conf., 111 10002 (2016)	Phys. Rev. C 102, (2020) 014605, EXFOR #14660002 Phys. Rev. C 99, (2019) 064619, EXFOR #14606002
^{236}U	Phys. Rev. C 108, (2023) 014621, EXFOR #41757001		
^{238}U	JETP Lett.,102, 203(2015) EXFOR #41608004 JETP Lett.,117, 557(2023) EXFOR #41756002	EPJ Web of Conf., 111 10002 (2016)	Phys. Rev. C 102, (2020) 014605, EXFOR#14660003
^{237}Np	JETP Lett.,110, 242(2019) EXFOR #416886002		
^{239}Pu	JETP Lett.,107, 521(2018) EXFOR #41658003		
^{240}Pu	JETP Lett.,112, 323(2020) EXFOR #41737002		
^{242}Pu	Measurements completed		
^{243}Am	Measurements completed		
^{nat}Pb	JETP Lett.,107, 521(2018) EXFOR #41658004		
^{209}Bi	JETP Lett.,104, 365(2016) EXFOR #41616007		

Table 4. Relative uncertainties for fission cross section ratio

Statistical uncertainties	
Counting statistic	60–3 % (0.2–1.0 MeV) 2–3 % (above 1.0 MeV)
Attenuation of the neutron flux	< 0.3 %
Anisotropy of fission fragments	1 %
Purity of targets (isotope composition)	1 % (below 0.8 MeV) 0.4 % (0.8–1.5 MeV) 0.1 % (above 1.5 MeV)
Efficiency of MWPC (geometrical uncertainty)	0.3 %
Scaling factor (N_{Am243}/N_{U235})	1.7 %
Total error	3.2 %
Uncertainty of thr ^{235}U "standard" fission cross section	
$\sigma_f(^{235}U)$	1.3–1.5 % (below 20 MeV) 1.5–4.8 % (2–200 MeV) 5–7 % (above 200 MeV)

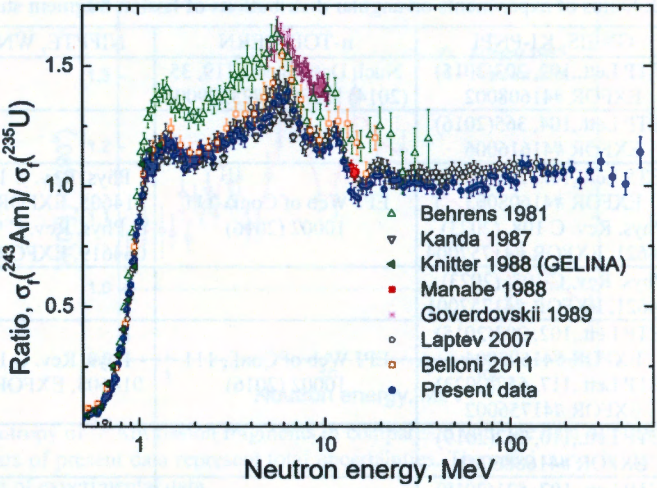

Fig. 7. Ratio of the fission cross sections of ^{243}Am and ^{235}U.

For neutron energies above 30 MeV, the ratio data obtained in this work can be compared only with the results of Laptev et al. [23]. It should be noted that the work of Laptev et al. was also performed at the GNEIS TOF-spectrometer using a multi-plate fission ionization chamber as a fission fragment detector. Unfortunately, in this work the measured ratio was not normalized to the number of nuclei in the targets. Instead, the authors normalized the ratio they obtained to the ratio of fission cross sections of ^{243}Am and ^{235}U taken from the ENDF/B-VII library for some neutron energy ranges. Nevertheless, it can be seen that, in general, there is good agreement between these and our present data over the entire neutron energy range studied.

It can be seen also that the ^{243}Am fission cross section obtained in this work mostly agrees with the results of Kanda et al. [6], Manabe et al. [8], Belloni et al. [10] and Knitter et al. [7], obtained at the GELINA Linac using the TOF-method, while the data of Behrens et al. [5] and Goverdovskii et al. [9] are more than 15 % higher. Taking into account that the uncertainty of the scaling of the ratio stated in these works is only 2–3 %, one can talk about the presence of unknown systematic errors.

Conclusion

In this work, new measurements of fission cross section and angular distributions of fission fragments for ^{243}Am were carried out on the neutron TOF-spectrometer GNEIS at Petersburg Nuclear Physics Institute of National Research Centre "Kurchatov Institute" in the neutron energy range 0.3–500 MeV. The neutron induced fission cross section of ^{243}Am was obtained in a wide energy range with the experimental uncertainty 3–4%. The data obtained on the fission cross section are mostly consistent with the results of earlier experimental works in the energy range up to 20 MeV, and above 20 MeV – the shape of the fission cross section agrees with the only existing old GNEIS data (Laptev et al. [23]). The differences between the existing experimental data seem to be mostly related to uncertainties in the detection efficiency of the fission fragment detectors used, the neutron flux and the target

masses (number of nuclei). The anisotropy of the angular distributions of ^{243}Am fission fragments are measured in the energy range 0.7–400 MeV for the first time.

Acknowledgments

The authors would like to thank the staff of the Accelerator Department of the NRC KI - PNPI for their permanent friendly assistance and smooth operation on the SC-1000 synchrocyclotron during the experiment, as well as L.S. Falev for help in creating the experimental setup.

References

1. B.I. Fursov, E.Yu. Baranov, M.P. Klemyshev, B.F. Samylin, G.N. Smirenkin, Yu.M. Turchin, Sov. At. En. **59**, 899 (1985). EXFOR 40837003. EXFOR 40837006.
2. Nuclear Science/WPEC-26, Report NEA No. 6410, OECD-NEA, 2008.
3. D.K. Butler, R.K. Sjoblom, Phys. Rev. **124**, 1129 (1961). EXFOR 12543003.
4. P.A. Seeger, Los Alamos Sci. Lab. Rep. LA-4420, p.138 (1970). EXFOR 10063004.
5. J.W. Behrens, J.C. Browne, Nucl. Sci. Eng. **77**, 444 (1981). EXFOR 10652003.
6. K. Kanda, H. Imaruoka, H. Terayama, Y. Karino, N. Hirakawa, Jour. of Nuclear Science and Technology **24**, 423 (1987). EXFOR 22044002.
7. H. Knitter, C. Budtz-Jorgensen, Nucl. Sci. Eng. **99**, 1 (1988). EXFOR 22032002.
8. F. Manabe, K. Kanda, T. Iwasaki, H. Terayama, Y. Karino, M. Baba, N. Hirakawa, Fac. of Engineering, Tohoku Univ. Tech. Report, Vol. 52, Issue. 2, p. 97 (1988). EXFOR 22282009.
9. A.A. Goverdovskii, A.K. Gordyushin, B.D. Kuz'minov, V.F. Mitrofanov, A.I. Sergachev, S.M. Solov'ev, T.E. Kuz'mina, Sov. At. En. **67**, 524 (1989). EXFOR 41058002.
10. F. Belloni, M. Calviani, N. Colonna, P. Mastinu, P.M. Milazzo, U. Abbondanno, G. Aerts, H. Álvarez, F. Alvarez-Velarde, S. Andriamonje, Eur. Phys. J. A **47**, 160 (2011). EXFOR 23148002.
11. G. Kessedjian, G. Barreau, M. Aïche, B. Jurado, A. Bidaud, S. Czajkowski, D. Dassié, B. Haas, L. Mathieu, L. Tassan-Got, J.N. Wilson, F.-J. Hambsch, S. Oberstedt, I. AlMahamid, J. Floyd, W. Lukens, D. Shuh, Phys. Rev. C **85**, 044613 (2012). EXFOR 22993003, 22993004, 22993005.
12. N.K. Abrosimov, G.Z. Borukhovich, A.B. Laptev, V.V. Marchenkov, G.A. Petrov, O.A. Shcherbakov, Yu.V. Tuboltsev, V.I. Yurchenko. Nucl. Instrum. Methods Phys. Res. A **242**, 121 (1985).
13. O.A. Shcherbakov, A.S. Vorobyev, E.M. Ivanov. Phys. Part. Nucl. **49**, 81 (2018).
14. A.S. Vorobyev, A.M. Gagarski, O.A. Shcherbakov, L.A. Vaishnene, A.L. Barabanov. JETP Letters **102(4)**, 203 (2015).
15. A.S. Vorobyev, A.M. Gagarski, O.A. Shcherbakov, L.A. Vaishnene, A.L. Barabanov. JETP Letters **104(6)**, 365 (2016).
16. A.S. Vorobyev, A.M. Gagarski, O.A. Shcherbakov, L.A. Vaishnene, A.L. Barabanov. JETP Letters **107**(9), 521 (2018).
17. A.M. Gagarski, A.S. Vorobyev, O.A. Shcherbakov, L.A. Vaishnene. In: "XXIII International Seminar on Interaction of Neutrons with Nuclei", Dubna, May 25–29, 2015. JINR, E3-2016-12, 2016, p.73.

18. A.M. Gagarski, A.S. Vorobyev, O.A. Shcherbakov, L.A. Vaishnene. In: "XXIV International Seminar on Interaction of Neutrons with Nuclei", Dubna, May 24–27, 2016. JINR, E3-2017-8, 2017, p.343.
19. A.S. Vorobyev, A.M. Gagarski, O.A. Shcherbakov, L.A. Vaishnene, A.L. Barabanov. In: "XXIV International Seminar on Interaction of Neutrons with Nuclei", Dubna, May 24–27, 2016. JINR, E3-2017-8, 2017, p.413.
20. A.M. Gagarski, A.S. Vorobyev, O.A. Shcherbakov, L.A. Vaishnene, A.L. Barabanov. In: "XXV International Seminar on Interaction of Neutrons with Nuclei", Dubna, May 22–26, 2017. JINR, E3-2018-12, 2018, p.342.
21. A.S. Vorobyev, A.M. Gagarski, O.A. Shcherbakov, L.A. Vaishnene, A.L. Barabanov. Proc. of the Int. Conf. "Nuclear data for Science and Technology ND-2016", September 11–16, 2016, Bruges, Belgium. EPJ Web of Conferences **146**, 04011 (2017).
22. A.S. Vorobyev, A.M. Gagarski, O.A. Shcherbakov, L.A. Vaishnene, A.L. Barabanov. JETP Letters **110**(**4**), 242 (2019).
23. A.B. Laptev, O.A. Shcherbakov, A.S. Vorobyev, R.C. Haight, A.D. Carlson, in Proceedings of the Conference on Fission and Properties of Neutron-Rich Nuclei, Sanibel Island (2007), edited by J.H. Hamilton, A.V. Ramayya, H.K. Carter (World Scientific, 2008) p. 462. EXFOR 41487015.

The Virtual Character of Spontaneous and Induced (with the Participation of Thermal Neutrons) Ternary Fission of Nuclei with the Emission of Prescission Nucleons and Light Nuclei

S.G. Kadmensky, Ya.O. Otvodenko

Voronezh State University, Voronezh, Russia E-mail: kadmensky@phys.vsu.ru

1. Introduction

In the field theory virtual reactions and decays, connected with the appearance in their amplitudes of states of intermediate elementary particles, whose momenta and energies are not related by Einstein's relativistic formula and therefore lie outside the mass surfaces of analyzed processes, are well known. Such reactions include, for example, the Compton scattering of γ-quanta by free electrons [1].

The question arises whether there are in nuclear physics the class of virtual decays and reactions associated with the appearance in their amplitudes of virtual intermediate states not only various elementary particles, but also composite atomic nuclei lie outside the mass surfaces of analyzed processes. A positive answer to this question was given on the basis of the generalized approach to the description of multistage decays and reactions in chains of genetically linked nuclei [2–4] using the Feynman diagram technique involving Green's functions of intermediate nuclei. The formation of this class at the first stage was started with two-proton decays of neutron-deficient nuclei, predicted by Goldansky [5], whose characteristics were successfully described using the concept of their virtuality [2–4]. This class was later extended [6–9] to include double β-decays of nuclei whose characteristics are calculated using the weak interaction Hamiltonian in second-order perturbation theory, which leads to the appearance of virtual states of intermediate nuclei. In recent years the characteristics of spontaneous and induced (with the participation of thermal neutrons) ternary and quaternary nuclear fission with the emission of prescission α-particles have been described [10] using the concept of virtuality of these types of fission.

The purpose of this work is to demonstrate the possibility of describing the experimental characteristics spontaneous and induced ternary fission of nuclei with the emission of prescission nucleons and light nuclei ^{2}H, ^{3}H and ^{6}He on the basis of the virtual presentation of these processes.

2. The mechanisms of spontaneous and induced (with the participation of thermal neutrons) binary fission of nuclei

The binary fission of fissile nucleus (FN) (A, Z) is connected with its scission into light (A_L, Z_L) and heavy (A_H, Z_H) fission fragments with close values of charges and masses. The process of this fission can be described on the base of the generalized model of nuclei [11], which simultaneously takes into account the nucleonic and collective modes of nuclear motion taking into account the evolution of shape of FN, described by its collective deformation parameters β_λ, from close to spherical through a prolonged spheroid to a dumbbell-like shape (see Fig. 1.).

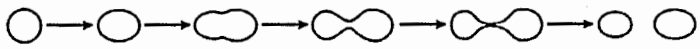

Fig. 1. Sequential stages of binary fission of nuclei.

For description of this evolution it can introduced the potential energy of deformation $E(\beta_\lambda)$ of FN by formula:

$$E(\beta_\lambda) = \tilde{E}(\beta_\lambda) + E_{sh}(\beta_\lambda), \tag{1}$$

where $\tilde{E}(\beta_\lambda)$ is the binding energy calculated in the liquid-drop model of the nucleus [12] and $E_{sh}(\beta_\lambda)$ is Strutinsky shell correction [13, 14]. Then the FN deformation potential $V(\beta_\lambda) = E(\beta_\lambda) - E(\beta_{20})$, where β_{20} is quadrupole deformation parameter of ground state of FN, can be represented [11] by Fig. 2.

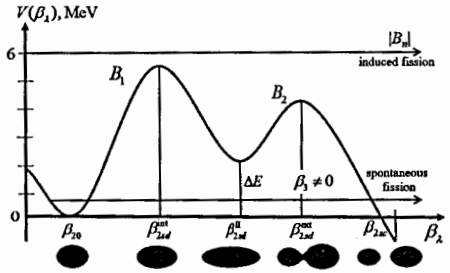

Fig. 2. Deformation potential $V(\beta_\lambda)$ for actinide nuclei

The spontaneous binary fission occurs if FN is in the ground state with the wave function $\psi_{K0}^{JM}(\beta_\lambda)$, where J is FN total spin with its projections M, K, taking into account the zero collective deformation vibration of this nucleus, at which FN passes into the prescission configuration through overcoming the potential deformation barriers shown in Fig. 2. This FN state with wave function $\psi_{K0}^{JM}(\beta_\lambda)$ corresponds to the transition fission state [11] of this nucleus. The binary fission is induced if the compound fissile nucleus (CFN) (A, Z) is formed when capturing of thermal neutron with a very low kinetic energy $T_n \approx 0.025$ eV by target nucleus (A-1, Z) in its ground state with the formation of excited state CFN with the excitation energy $|B_n| \approx 6$ MeV, where B_n is binding energy of captured neutron. For nuclear times $T_0 \approx 10^{-22}$ s this excited state transits into the neutron resonance state of CFN, whose wave function ψ_K^{JM} is represented when using the Wigner random matrix method [15–18] as:

$$\psi_K^{JM} = \sum_{i \neq 0} b_i \psi_{iK}^{JM} + b_0 \psi_{0K}^{JM}(\beta_\lambda). \tag{2}$$

In this formula the wave function ψ_{iK}^{JM} corresponds to the i-quasi-particle excited state of CFN and the wave function $\psi_{0K}^{JM}(\beta_\lambda)$ describes the collective deformation state of the CFN with the excitation energy $|B_n|$ and corresponds to the transition fission state of the CFN [11]. The squares of coefficients b_i and b_0 in (2) have average values of $\overline{(b_i)^2} = 1/N$, where N is the

total number of quasi-particle states participating in formation of wave function (2). The induced fission of CFN occurs with a noticeable probability if the energy $|B_n|$ exceeds heights of the internal and external fission deformation barriers of Fig. 2.

3. The mechanisms of spontaneous and induced (with the participation of thermal neutrons) ternary nuclear fission with the emission of light prescission particles

The spontaneous and induced ternary fission of FN (A, Z) with the emission of third light prescission particle p (A_p, Z_p) is similar to the binary fission of FN beginning with the transition of FN to its prescission configuration shown in Fig. 1. Then particle p flies out of this configuration with the appearance of the state of intermediate nucleus (A-A_p, Z-Z_p), which is further divided into light (A_{LF}, Z_{LF}) and heavy (A_{HF}, Z_{HF}) fission fragments. The angular distribution of particle p for spontaneous and induced ternary fission has anisotropic character with the maximum at emission angles θ_p in the equatorial direction to the direction of light fission fragment emission [19–20], that allows to conclude that the emitted p-particles are formed in the neck of FN prescission configuration. The experimental energy distribution $W(T_p)$ of particle p with kinetic energy T_p have maximum value at energies $T_{p\max}$, which noticeably exceeds the heat Q_p^A of the p-decay of the ground state of FN (A, Z) having the form:

$$Q_p^A = E(A,Z) - E(A - A_p, Z - Z_p) - E(A_p, Z_p), \tag{3}$$

where $E(A,Z)$ is binding energy of FN in liquid-drop model [12]. The indicated fact is serious argument for the justification of the virtual mechanism of the appearance of third light prescission particles p in ternary nuclear fission.

Using the results of works on the theory of virtual decays of atomic nuclei [2–4], can obtain a formula for the width Γ_{pf}^A of the virtual spontaneous ternary fission with the emission of third light particles p:

$$\Gamma_{pf}^{A} = \frac{1}{2\pi} \int_0^{Q_f^{A-A_p}} \frac{\Gamma_p^{A}(T_p)\Gamma_f^{(A-A_p)}(Q_f^{A-A_p} - T_p + Q_p^A)}{(Q_p^A - T_p)^2} dT_p \ , \tag{4}$$

where $\Gamma_p^A(T_p)$ is p-decay width of FN (A, Z) with the emission of ternary particle p (A_p,Z_p) in its ground state and the formation of daughter nucleus (A-A_p, Z-Z_p), $\Gamma_f^{(A-A_p)}(Q_f^{A-A_p} - T_p + Q_p^A)$ is full width of binary fission of nucleus (A-A_p, Z-Z_p) with the heat of this fission $Q_f^{A-A_p}$:

$$Q_f^{A-A_p} = E(A - A_p, Z - Z_p) - E(A_{LF}, Z_{LF}) - E(A_{HF}, Z_{HF}). \tag{5}$$

Note that the width of the induced ternary fission of CFN (A, Z) nucleus formed during the capture of a thermal neutron into the ground state of the target nucleus (A-1, Z) is also determined by formula (4), since the CFN excitation energy, equal to $|B_n|$, is conserved in the corresponding prescission configuration of this nucleus and does not participate in the formation of kinetic energy T_p of the p-particle. Now it is possible to introduce the yield of p-particles in ternary nuclear fission to the number of binary fission fragments, defined as $\delta_{pf} = \Gamma_{pf}^{A} / \Gamma_f^A(Q_f^{A-A_p})$:

$$\delta_{pf} = \frac{1}{2\pi} \int_0^{Q_f^{A-A_p}} \frac{\Gamma_p^{A}(T_p)\Gamma_f^{(A-A_p)}(Q_f^{A-A_p} - T_p + Q_p^{A})}{(Q_p^{A} - T_p)^2 \Gamma_f^{A}(Q_f^{A})} dT_p \ . \quad (6)$$

From here it is possible to obtain the energy distribution of the emission p-particles, normalized on the yield of p-particles:

$$W_{pf}(T_p) = \frac{1}{2\pi} \frac{\Gamma_p^{A}(T_p)\Gamma_f^{(A-A_p)}(Q_f^{A-A_p} - T_p + Q_p^{A})}{(Q_p^{A} - T_p)^2 \Gamma_f^{A}(Q_f^{A})}, \quad (7)$$

normalized to the yield of p-particles δ_{pf}. Taking into account that the energy Q_f^{A-4} for actinide nuclei reaches 170 MeV, which is much higher than the energies $T_p - Q_p^{A}$ and the proximity of the widths $\Gamma_f^{(A-A_p)}(Q_f^{A-A_p})$ and $\Gamma_f^{A}(Q_f^{A})$, formula (7) can be transformed into the form:

$$W_{pf}(T_p) = W_p(T_p) = \frac{1}{2\pi} \frac{\Gamma_p^{A}(T_p)}{(Q_p^{A} - T_p)^2}. \quad (8)$$

Hence the value of width $\Gamma_p^{A}(T_p)$ can be calculated through values $W_{pf}(T_p)$ (8):

$$\Gamma_p^{A}(T_p) = 2\pi W_p(T_p)(Q_p^{A} - T_p)^2. \quad (9)$$

The value $\Gamma_p^{A}(T_p)$ can be represented by Gamow formula:

$$\Gamma_p^{A}(T_p) = \omega_p \frac{\hbar\sqrt{2T_p}}{2r_{neck}\sqrt{m_p}} P(T_p), \quad (10)$$

where $P(T_p)$ is the penetrability factor of the Coulomb barrier, close to one for $T_p = T_{p\max}$, m_p is p-particle mass and ω_p is the probability of the formation of p-particle in the neck of parent nucleus with radius r_{neck}. Using the experimental values of the widths $\Gamma_p^{A}(T_{p\max})$ and the averaged values of the radii r_{neck} [21], it is possible to calculate by formula (10) the values of ω_p for such third prescission particles p as α-particles, protons, neutrons, and also light nuclei ^{2}H, ^{3}H, and ^{6}He, and compare their values with similar values calculated in the framework of the cluster model of the nucleus [22].

4. Spontaneous and induced ternary nuclear fission with the emission of prescission α-particles

When using experimental data for spontaneous (sf) ternary fission with the emission of α-particles from nuclei ^{244}Cm, ^{246}Cm, ^{248}Cm [23] and ^{250}Cf, ^{252}Cf [24] and for analogous induced (n,f) ternary fission of nuclei-targets ^{233}U, ^{235}U [20] and ^{239}Pu, ^{241}Pu [25] the characteristics of these processes were calculated.

As can be seen from Table 1 for all considered CFN the yields of α-particles $\delta_{\alpha f}$ as for spontaneous as well induced fission are close to each other: $1.7\times10^{-3} \le \delta_{\alpha f} \le 3.2\times10^{-3}$. The analogous situation is realized for the probabilities of α-particle formation ω_α: $2.0\times10^{-2} \le \omega_\alpha \le 3.1\times10^{-2}$. The noticeable positive values of differences $(T_{\alpha\max} - Q_\alpha^{A})$ show that the analyzed process of ternary fission has the virtual character.

Table 1. Characteristics of spontaneous (sf) and induced (n,f) ternary fission of CFN with the emission of α-particles

Compound nucleus	$\delta_{\alpha f}$ $\times 10^{-3}$		$T_{\alpha\max}$ (MeV)		Q_α^A (MeV)	r_{neck} (fm)	ω_α $\times 10^{-2}$	
	(sf)	(n,f)	(sf)	(n,f)			(sf)	(n,f)
^{244}Cm	3.2	2.4	16.0	16.1	5.9	2.5	3.1	2.6
^{246}Cm	2.5	2.2	16.4	16.4	5.5	2.5	2.8	2.4
^{248}Cm	2.3	1.9	16.0	16.0	5.2	2.5	2.6	2.0
^{250}Cf	2.9	2.8	16.0	16.1	6.1	2.5	2.4	2.6
^{252}Cf	2.6	2.4	16.0	15.9	6.2	2.5	2.4	2.2
^{234}U	-	2.2	-	15.7	4.9	2.5	-	2.9
^{236}U	-	1.7	-	15.5	4.6	2.5	-	2.1
^{240}Pu	-	2.2	-	15.9	5.3	2.5	-	2.4
^{242}Pu	-	1.9	-	15.9	5.0	2.5	-	2.1

As can be seen from Fig. 3 the energy distributions $W_{\alpha f}^A(T_\alpha)$ of α-particles for the spontaneous and induced ternary fission of the CFN ^{252}Cf are close.

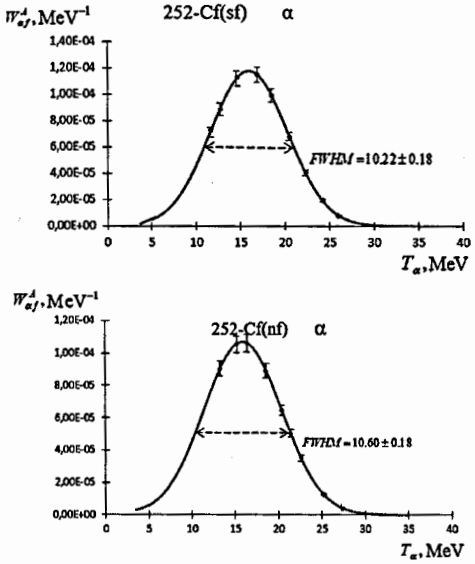

Fig. 3. The energy distributions $W_{\alpha f}^A(T_\alpha)$ for the spontaneous and induced ternary fission of ^{252}Cf with emission α-particle.

From Fig. 3 it can be seen that for both spontaneous and induced fission of CFN with emission α-particle such characteristics as width at half maximum *FWHM* and forms of energy distribution are close.

Similar dependences $W_{\alpha f}^A(T_\alpha)$ are also observed for all CFN of Table 1.

The experimental angular distributions of fragments of ternary fission of FN with emission of α-particles are close to the analogous angular distributions of binary fission fragments due to weak influence of the emitted third α-particle on the angular distributions of ternary fission fragments [18].

The experimental angular distributions of α-particle for all CFN [19–20] have the equatorial character with the maximum close to $\theta = 90°$, what could be related with the emission of α-particle from the neck of the prescission configuration of CFN. Confirmation of this fact can be found in [26] for the spontaneous fission of the ^{252}Cf nucleus.

5. Spontaneous and induced ternary nuclear fission with the emission of prescission ^{1}H

When using experimental data for spontaneous (sf) and induced (n,f) ternary fission with the emission of p-particle as ^{1}H from CFN nuclei ^{252}Cf [27] and ^{236}U [28] the characteristics of these processes were calculated.

Table 2. Characteristics of spontaneous (sf) and induced (n,f) ternary fission of CFN with the emission of ^{1}H

Compound nucleus	δ_{pf} ×10^{-5}		$T_{p\max}$ (MeV)		Q_p^A (MeV)	r_{neck} (fm)	ω_p ×10^{-4}	
	(sf)	(n,f)	(sf)	(n,f)			(sf)	(n,f)
^{252}Cf	4.6	-	7.8	-	–6.48	2.5	8.1	-
^{236}U	-	4.0	-	8.6	–6.71	2.5	-	7.6

As can be seen from Table 2 for all considered CFN the yields δ_{pf} of ^{1}H are close to each other as for spontaneous as well induced fission: $4.0\times10^{-5} \le \delta_{pf} \le 4.6\times10^{-5}$. The analogous situation is realized for the probabilities of ^{1}H formation ω_p: $7.6\times10^{-4} \le \omega_p \le 8.1\times10^{-4}$. The noticeable positive values of differences $(T_{p\max} - Q_p^A)$ show that the analyzed process of ternary fission has the virtual character.

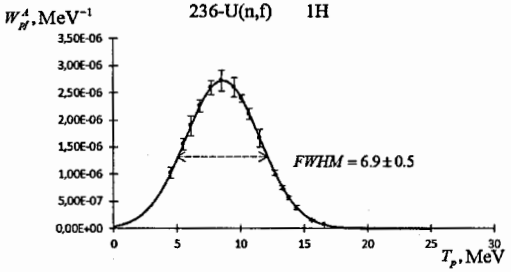

Fig. 4. The dependence $W_{pf}^A(T_p)$ for the induced fission of the compound nucleus ^{236}U with emission ^{1}H.

As can be seen from Figs. 4–5 the dependences $W_{pf}^A(T_p)$ from T_p for the spontaneous and induced ternary fission of the compound nuclei ^{236}U and ^{252}Cf with emission ^{1}H turn out to be close for all CFN considered.

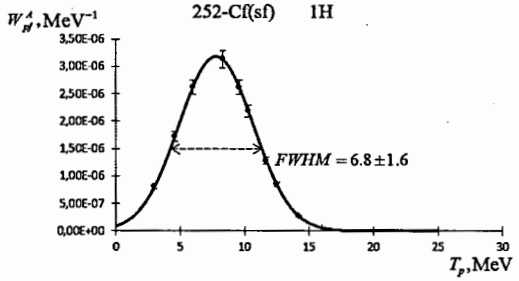

Fig. 5. The dependence $W_{pf}^{A}(T_p)$ for the spontaneous fission of the compound nucleus ^{252}Cf with emission ^{1}H.

As can be seen from Figs. 4–5 the dependences $W_{pf}^{A}(T_p)$ from T_p for the spontaneous and induced ternary fission of the compound nuclei ^{236}U and ^{252}Cf with emission ^{1}H turn out to be close for all CFN considered.

From Figs. 4–5 it can be seen that for both spontaneous and induced fission of CFN with emission ^{1}H such characteristics as width at half maximum *FWHM* and forms of energy distribution are close.

The experimental angular distributions of ^{1}H for all CFN [19–20] have the equatorial character with the maximum close to $\theta = 90°$, what could be related with the emission of ^{1}H from the neck of the prescission configuration of CFN. Confirmation of this fact can be found in [27] for the spontaneous fission of the ^{252}Cf nucleus.

6. Spontaneous and induced ternary nuclear fission with the emission of prescission ^{2}H

When using experimental data for spontaneous (sf) and induced (n,f) ternary fission with the emission of *p*-particle as ^{2}H from CFN nuclei ^{252}Cf [27] and ^{236}U [28] the characteristics of these processes were calculated.

Table 3. Characteristics of spontaneous (sf) and induced (n,f) ternary fission of CFN with the emission of ^{2}H

Compound nucleus	δ_{pf} ×10^{-5}		$T_{p\max}$ (MeV)		Q_p^A (MeV)	r_{neck} (fm)	ω_p ×10^{-4}	
	(sf)	(n,f)	(sf)	(n,f)			(sf)	(n,f)
^{252}Cf	1.5	-	8.0	-	–9.3	2.5	5.0	-
^{236}U	-	1.2	-	7.9	–10.1	2.5	-	4.5

As can be seen from Table 3 for all considered CFN the yields δ_{pf} of ^{2}H are close to each other as for spontaneous as well induced fission: $1.2\times10^{-5} \le \delta_{pf} \le 1.5\times10^{-5}$. The analogous situation is realized for the probabilities of ^{2}H formation ω_p: $4.5\times10^{-4} \le \omega_p \le 5.0\times10^{-4}$. The noticeable positive values of differences $(T_{p\max} - Q_p^A)$ show that the analyzed process of ternary fission has the virtual character.

As can be seen from Figs. 6–7 the dependences $W_{pf}^{A}(T_p)$ from T_p for the spontaneous and induced ternary fission of the compound nuclei ^{236}U and ^{252}Cf with emission ^{2}H turn out to be close for all CFN considered.

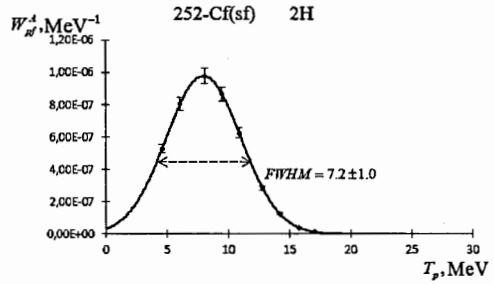

Fig. 6. The dependence $W_{pf}^{A}(T_p)$ for the spontaneous fission of the compound nucleus ^{252}Cf with emission ^{2}H.

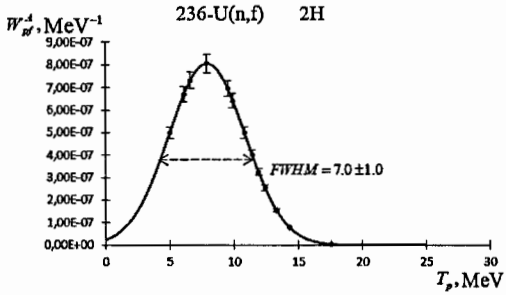

Fig. 7. The dependence $W_{pf}^{A}(T_p)$ for the induced fission of the compound nucleus ^{236}U with emission ^{2}H.

From Figs. 6–7 it can be seen that for both spontaneous and induced fission of CFN with emission ^{2}H such characteristics as width at half maximum *FWHM* and forms of energy distribution are close.

The experimental angular distributions of ^{2}H for all CFN [19–20] have the equatorial character with the maximum close to $\theta = 90°$, what could be related with the emission of ^{2}H from the neck of the prescission configuration of CFN. Confirmation of this fact can be found in [27] for the spontaneous fission of the ^{252}Cf nucleus.

7. Spontaneous and induced ternary nuclear fission with the emission of prescission ^{3}H

When using experimental data for spontaneous (sf) and induced (n,f) ternary fission with the emission of *p*-particle as ^{3}H from CFN nuclei ^{244}Cm, ^{246}Cm [23], and ^{250}Cf, ^{252}Cf [24] the characteristics of these processes were calculated.

Table 4. Characteristics of spontaneous (sf) and induced (n,f) ternary fission of CFN with the emission of ^{3}H

Compound nucleus	δ_{pf} $\times 10^{-4}$		$T_{p\max}$ (MeV)		Q_p^A (MeV)	r_{neck} (fm)	ω_p $\times 10^{-4}$	
	(sf)	(n,f)	(sf)	(n,f)			(sf)	(n,f)
^{244}Cm	2.0	2.0	8.1	8.2	–11.1	2.5	0.9	0.9
^{246}Cm	1.7	1.9	8.1	8.4	–12.3	2.5	0.9	1.0
^{250}Cf	2.1	2.1	8.3	8.5	–9.8	2.5	0.7	0.8
^{252}Cf	1.9	2.2	8.6	8.5	–9.3	2.5	0.8	0.8

As can be seen from Table 4 for all considered CFN the yields δ_{pf} of ^{3}H are close to each other as for spontaneous as well induced fission: $1.7\times10^{-4} \le \delta_{pf} \le 2.2\times10^{-4}$. The analogous situation is realized for the probabilities of ^{3}H formation ω_p: $0.7\times10^{-4} \le \omega_p \le 1.0\times10^{-4}$. The noticeable positive values of differences $(T_{p\max} - Q_p^A)$ show that the analyzed process of ternary fission has the virtual character.

As can be seen from Figs. 8–10 the dependences $W_{pf}^A(T_p)$ from T_p for the spontaneous and induced ternary fission of the compound nuclei ^{250}Cf, ^{244}Cm and ^{246}Cm with emission ^{3}H turn out to be close for all CFN considered.

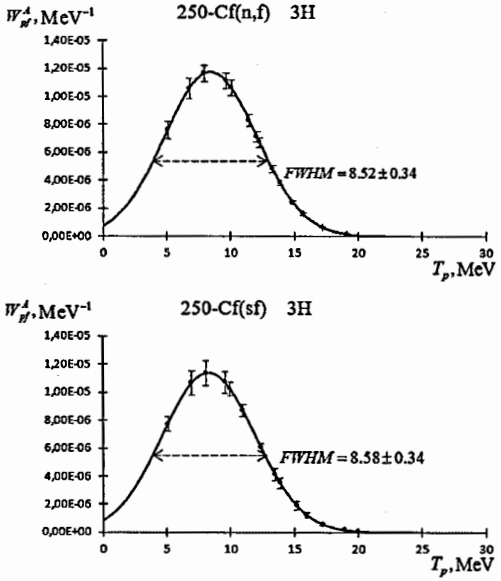

Fig. 8. The dependences $W_{pf}^A(T_p)$ for the induced and spontaneous fission of the compound nucleus ^{250}Cf with emission ^{3}H.

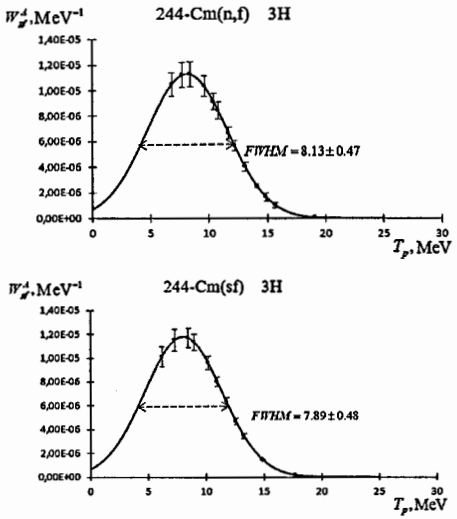

Fig. 9. The dependences $W_{pf}^{A}(T_p)$ for the induced and spontaneous fission of the compound nucleus ^{244}Cm with emission ^{3}H.

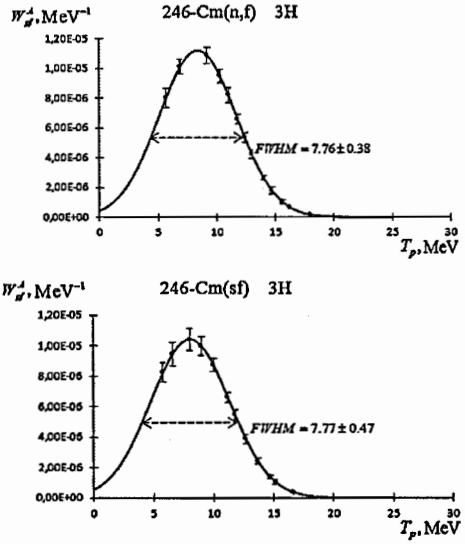

Fig. 10. The dependences $W_{pf}^{A}(T_p)$ for the induced and spontaneous fission of the compound nucleus ^{246}Cm with emission ^{3}H.

From Figs. 8–10 it can be seen that for both spontaneous and induced fission of CFN with emission ^{3}H such characteristics as width at half maximum *FWHM* and forms of energy distribution are close.

The experimental angular distributions of ^{3}H for all CFN [19–20] have the equatorial character with the maximum close to $\theta = 90°$, what could be related with the emission of ^{3}H from the neck of the prescission configuration of CFN. Confirmation of this fact can be found in [26] for the spontaneous fission of the ^{252}Cf nucleus.

8. Spontaneous and induced ternary nuclear fission with the emission of prescission ^{6}He

When using experimental data for spontaneous (sf) and induced (n,f) ternary fission with the emission of *p*-particle as ^{6}He from CFN nuclei ^{250}Cf and ^{252}Cf [24] the characteristics of these processes were calculated.

Table 5. Characteristics of spontaneous (sf) and induced (n,f) ternary fission of CFN with the emission of ^{6}He

Compound nucleus	δ_{pf} ×10^{-5}		$T_{p\max}$ (MeV)		Q_p^A (MeV)	r_{neck} (fm)	ω_p ×10^{-3}	
	(sf)	(n,f)	(sf)	(n,f)			(sf)	(n,f)
^{250}Cf	8.0	7.0	10.6	11.0	–5.91	2.5	2.6	2.4
^{252}Cf	7.7	7.6	11.2	10.9	–4.18	2.5	2.5	2.2

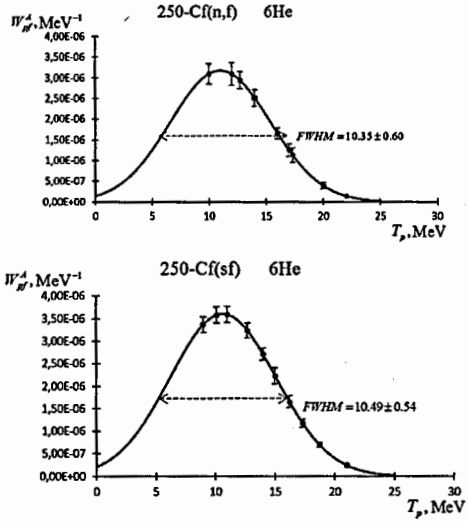

Fig. 11. The dependences $W_{pf}^{A}(T_p)$ for the induced and spontaneous fission of the compound nucleus ^{250}Cf with emission ^{6}H.

As can be seen from Table 5 for all considered CFN the yields δ_{pf} of ^{6}He are close to each other as for spontaneous as well induced fission: $7.0\times10^{-5} \le \delta_{pf} \le 8.0\times10^{-5}$. The analogous

situation is realized for the probabilities of ^{6}He formation ω_p: $2.2\times10^{-3} \le \omega_p \le 2.6\times10^{-3}$. The noticeable positive values of differences $(T_{p\max} - Q_p^A)$ show that the analyzed process of ternary fission has the virtual character.

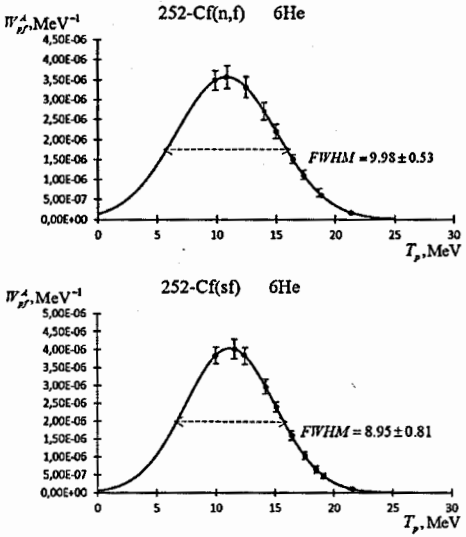

Fig. 12. The dependences $W_{pf}^A(T_p)$ for the spontaneous and induced fission of the compound nucleus ^{252}Cf with emission ^{6}He.

As can be seen from Figs. 11–12 the dependences $W_{pf}^A(T_p)$ from T_p for the spontaneous and induced ternary fission of the compound nuclei ^{250}Cf and ^{252}Cf with emission ^{6}He turn out to be close for all CFN considered.

From Figs. 11–12 it can be seen that for both spontaneous and induced fission of CFN with emission ^{6}He such characteristics as width at half maximum *FWHM* and forms of energy distribution are close.

The experimental angular distributions of ^{6}He for all CFN [19–20] have the equatorial character with the maximum close to $\theta = 90^\circ$, what could be related with the emission of ^{6}He from the neck of the prescission configuration of CFN. Confirmation of this fact can be found in [26] for the spontaneous fission of the ^{252}Cf nucleus.

9. Spontaneous and induced ternary nuclear fission with the emission of prescission neutrons

It is well known [11] that in the spontaneous and low-energy induced (by thermal neutrons) binary fission of actinide-nuclei the neutrons n with short characteristic escape times $\tau \le 10^{-4}$ s appear. The number of these neutron, normalized by their yield δ_{nf}, are determined by the normalized sum evaporated neutrons n_{ev} emitted from fission fragments, fully accelerated by their mutual Coulomb field, and prescission neutrons n_{pr}, emitted from prescission config-

urations of FN at times close to the moment of its scission into fission fragments. The angular and energy spectrum $n(T_n, \theta_n)$ of indicated neutrons n, where T_n and θ_n are the asymptotic kinetic energies of the emitted neutron and the angle between the directions of neutron emission and light fission fragment, can be presented as

$$n(T_n, \theta_n) = n_{pr}(T_n, \theta_n) + n_{ev}(T_n, \theta_n). \quad (11)$$

Experimental spectrum $n(T_n, \theta_n)$ are found for the spontaneous binary fission of the ^{252}Cf in [28, 29] and for neutron-induced binary fission of ^{233}U and ^{235}U in [29, 30]. Theoretical spectrum $n_{ev}(T_n, \theta_n)$ of evaporation neutrons can be calculated using the presentation [28]. The spectrum of prescission neutrons $n_{pr}(T_n, \theta_n)$ can be calculated using formula (11) with experimental values $n(T_n, \theta_n)$ and theoretical values $n_{ev}(T_n, \theta_n)$. The typical angular dependence of $n_{pr}(\theta_n)$ for the induced fission of the nucleus-target ^{233}U by thermal neutron with formation of CFN ^{234}U [29,30] shown on Fig. 13.

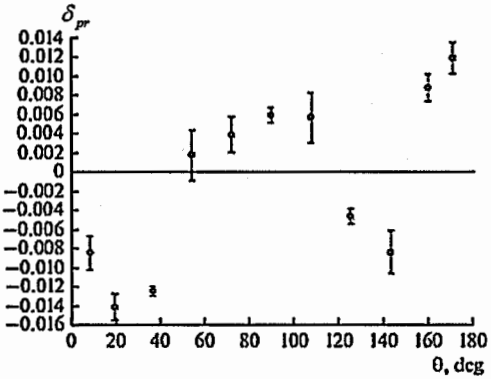

Fig. 13. Integral angular distribution prescission neutrons for CFN ^{234}U.

As can be seen from Fig. 13, the values of $n_{pr}(\theta_n)$ for certain angles θ turned out to be negative, which is physically impossible. This testifies to the inaccuracy of the formulas [28–31] used to calculate the evaporation spectra of neutrons. Therefore, the angular distributions of prescission neutrons calculated using formula (11) were corrected by throwing away the negative values of $n_{pr}(\theta_n)$ obtained in the calculations [28–31] and by conservation $n_{pr}(\theta_n)$ only for the angular range close to $\theta = 90°$.

Table 6. Characteristics of ternary fission of CFN with the emission of n_{pr}

Compound nucleus	δ_{pr} ×10^{-2}	Angular range	$T_{p\max}$ (MeV)	Q_p^4 (MeV)
^{233}U (n,f)	1.5	$54.5° \le \theta \le 107.8°$	0.5	-6.8
^{235}U (n,f)	1.8	$54.5° \le \theta \le 107.8°$	0.5	-6.5
^{252}Cf (sf)	2.0	$72.2° \le \theta \le 107.8°$	0.6	-6.2

As it can be seen from Table 6, where characteristics of spontaneous (sf) and induced (n,f) ternary fission with the emission of prescission neutrons n_{pr} from CFN nuclei ^{234}U [29, 30], ^{236}U [29, 30] and ^{252}Cf [28, 29] are presented, for all considered CFN the yields δ_{pr} for prescission neutrons are close for spontaneous and induced fission $1.5\times10^{-2} \le \delta_{pr} \le 2.0\times10^{-2}$. The noticeable positive values of differences $(T_{p\max} - Q_p^4)$ show that the analyzed process of ternary fission has the virtual character [4].

Figs. 14–15 demonstrate the corrected energy distributions of prescission neutrons n_{pr} for spontaneous fission of the ^{252}Cf nucleus [29] and induced fission of ^{235}U [30], respectively.

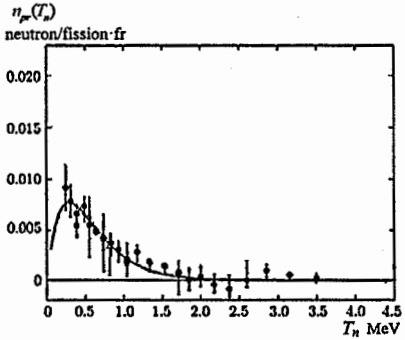

Fig. 14. Experimental energy distribution $n_{pr}(T_n)$ for spontaneous fission of the ^{252}Cf.

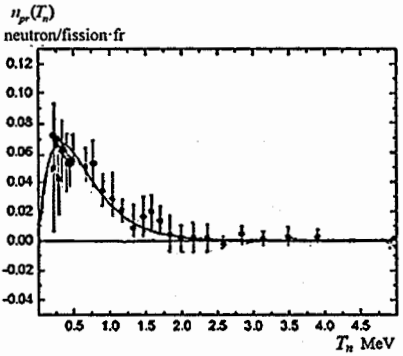

Fig. 15. Experimental energy distribution $n_{pr}(T_n)$ for induced fission of the ^{235}U.

From Figs. 14–15 it can be seen that for both spontaneous and induced fission of CFN with emission n_{pr} the energy distributions are close.

9. Conclusion

Based on the results obtained in this paper it can be concluded that for spontaneous and induced ternary fission the emission processes for prescission particles ^{1}H, ^{2}H, ^{3}H, ^{6}He and n_{pr} are similar to the analogous process for prescission α-particles.

Table 7. Characteristics of spontaneous (sf) and induced (n,f) ternary fission of CFN with the emission of prescission particles

Emitted particle p	δ_{pf}		$T_{p\max}$ (MeV)	Q_p^A (MeV)	ω_p	
	(sf)	(n,f)			(sf)	(n,f)
α	2.6×10^{-3}	2.2×10^{-3}	16	+6	2.6×10^{-2}	2.4×10^{-2}
^{1}H	4.6×10^{-5}	4.0×10^{-5}	8	–7	8.0×10^{-4}	6.0×10^{-4}
^{2}H	1.5×10^{-5}	1.2×10^{-5}	8	–9	5.0×10^{-4}	4.5×10^{-4}
^{3}H	1.9×10^{-4}	2.05×10^{-4}	8	–10	0.8×10^{-4}	0.9×10^{-4}
^{6}He	7.9×10^{-5}	7.3×10^{-5}	10	–6	2.6×10^{-3}	2.3×10^{-3}
n_{pr}	1.7×10^{-2}	2.0×10^{-2}	0,5	–6	-	-

From the Table 7, where the averaged values of yields δ_{pf}, of probabilities of formation ω_p, of maximal kinetic energies T_{pmax} of third particles p and of p-decay heats Q_p^A of CFN (A) for spontaneous and induced ternary fission with emission of all analyzed previously prescission particles p are presented, it can be obtained the following conclusions.

1. Birth processes for all prescission particles have virtual character, because differences $(T_{p\max} - Q_p^A)$ have noticeable positive values: 10 MeV for α-particles, (15–18) MeV for ^{1}H, ^{2}H, ^{3}H, ^{6}He and 6.5 MeV for prescission neutron. These differences are subtracted from the kinetic energy of fragments the binary fission of intermediate nuclei.

2. The values of energies T_{pmax}, yields δ_{pf} and probabilities of formation ω_p are close for each group of prescission particles in spontaneous and induced ternary fission of nuclei, since the excitation energy $|B_n|$ of CFN for the absorption of thermal neutron by the target-nucleus does not participate in the formation of the kinetic energy of prescission particles, but transforms to the excitation energy of binary fission fragments.

3. The yields δ_{pf} of prescission particles p have maximum values for prescission neutrons 1.85×10^{-2}, and then decrease to 2.4×10^{-3} for α-particles, to 2.0×10^{-4} for ^{3}H and then become less than 1.2×10^{-5} for ^{1}H, ^{2}H and ^{6}He. Similar changes occur for the formation probabilities ω_p calculated for all prescission particles, except for prescission neutrons.

Bibliography

1. A.I. Akhieser and V.B. Berestetsky, Quantum electrodynamics (Fizmatgiz, Moscow, 1959).
2. S.G. Kadmensky, U.V. Ivankov, Phys. Atom. Nucl. **77**. 1019 (2014); **77**. 1532 (2014).
3. S.G. Kadmensky, A.O. Bulychev, Bull. Russ. Acad. Sci., Phys. **79**. 872 (2015); **80**. 1009 (2016).
4. S.G. Kadmensky, L.V. Titova, D.E. Lyubashevsky, Phys. Atom. Nucl. **83**. 581 (2020).
5. V.I. Goldansky, JETP. **39**. 497 (1960); UFN 87. 255 (1965).
6. L.A. Sliv, JETP, **20**. 1035 (1950).
7. J.Suhoen, O.Civitareze, Phys. Rep. 300, 123 (1998).

8. V.I. Tretyak, Double beta decay: history and current status, Institute for Nuclear Research. (2014).
9. D. E. Lyubashevsky, Bull. Russ. Acad. Sci., Phys. **84**. 1406 (2020).
10. S.G. Kadmensky, L.V. Titova, Bull. Russ. Acad. Sci., Phys. **85**. 732 (2021).
11. A. Bohr, B. Mottelson Nuclear Structure (Benjamin, New York, 1974), V.1, V2.
12. C.F. Weizssacker, Zs. f. Phys. **96**. 431 (1935).
13. V.M. Strutinsky, JETP. **37**. 613 (1960).
14. V.M. Strutinsky, Nucl. Phys. **3**. 614 (1965).
15. E.P. Wigner, Ann. Math. **62**. 548 (1955); **65**. 203 (1958); **67**. 325 (1958).
16. S.G. Kadmensky, V.P. Markushev, V.I. Furman, Nucl. Phys. **35**. 300 (1982).
17. S.G. Kadmensky, Nucl. Phys. **65**. 1833 (2002).
18. S.G. Kadmensky, L.V. Titova, P.V. Kostryukov, Bull. Ras. Phys. **82**. 1299 (2015).
19. M. Mutterer, J.P. Theobald, Dinuclear Decay Modes. Bristol: IOP Publ., Chap. 1. 12. (1996).
20. M. Mutterer, Yu.N. Kopatch, P. Jesinger et al., Nucl. Phys. A. **738**. 122 (2004).
21. O. Serot, N. Carjan, C. Wagemans, Eur. Phys. J. A. **8**. 187 (2000).
22. S.G. Kadmensky, V.I. Furman, Alpha decay and related nuclear reactions, M.: Energoatomizdat, 1985.
23. S. Vermote, C. Wagemans, O. Serot, Nucl. Phys. A. **806**. 1 (2008).
24. S. Vermote, C. Wagemans, O. Serot, Nucl. Phys. A. **837**. 176 (2010).
25. O. Serot, C. Wagemans, J. Heyse AIP Conf. Proc. **769**. 857 (2005).
26. Yu.N.Kopatch, M.Mutterer Phys. Rev. C. **65**. P. 044614-1, (2002).
27. G. M. Raisbeck, T.D. Thomas, Phys. Rev. **172**. 1272 (1968).
28. J. Chwaszczewska, Phys. Lett. **24B**. 87 (1967).
29. A.S. Vorobyev et al., JETF. **152**. 730 (2017).
30. A.S. Vorobyev et al., Bull. Russ. Acad. Sci., Phys. **82**. 1373 (2018).
31. A.S. Vorobyev et al., EPJ Web of Conferences. **239**. 05008 (2020).
32. R. Capote et al., Nucl. Data Sheets. **131**. 1 (2016).

Status and Prospect of Studies of (γ, f) Reaction at MT-25 Microtron

D.V. Kamanin[1], Yu.V. Pyatkov[1,2], A.N. Solodov[1], V.E. Zhuchko[1], Z.I. Goryainova[1], E.A. Kuznetsova[1], O.V. Strekalovsky[1], A.O. Zhukova[1]

[1]*Joint Institute for Nuclear Research, Dubna, Russia*

[2]*National Nuclear Research University "MEPhI" (Moscow Engineering Physics Institute), Moscow, Russia*

INTRODUCTION

Before to attack the main topic, namely, (γ, f) reactions, it is necessary to recall some our previous results. The black plot in figure 1(a) is the fragments mass correlation distribution measured at the two-armed time-of-flight COMETA spectrometer. The projection onto the vertical axis (figure 1(b)) shows the peaks that are centered on the masses 68, 69 ,72 associated with the magic isotopes of Ni. The last peak at the mass 74 is likely corresponds to the semi-magic Cupper nucleus with the charge 29. These peaks were observed earlier in our experiments at the 4π -FOBOS spectrometer and the corresponding pictures are shown in figures 1(c, d). It is clearly seen that only in one spectrometer arm, facing the backing of the Cf source there is a broad peak - which was called Ni-bump.

Another structure so called "rhombic meander" is marked in figure 1(a) by the thick arrow. It consists of the lines were $M_1 + M_2 = \text{const}$ and $M_1 - M_2 = \text{const}$. Figure 1(e) shows schematically the prescission configuration for one specific partition in the Ni-bump. Ni & Sn FFs were really detected in the *opposite arms* due to the break-up of the light FF in the source backing.

The second result also needs to be cited to understand what is observed in the (γ, f) reactions. The experiment was performed using a two-armed LIS spectrometer presented in figure 2(a).

The essence of the experiment was that the mass of the fragment was measured ("balanced") twice namely before and after it passes the degrader-foil in the timing detector TD1. Event by event the "initial" mass M_{tt} was measured using the TOF–TOF (time-of-flight–time-of-flight) method (see figure 2(a)) while the TOF–E (time-of-flight–energy) method was applied to measure the "resultant" mass M_{te}. The results are presented in figures 2(b, c).

The obvious expectation was that we would see just the usual line M_{tt}, accurate to evaporated neutrons, equal to M_{te}. However, it turned out that a much more complex and physically interesting structure is observed. For instance, the mass M_{tt} of the initial fragment was 140, but due to the break-up in the foil, its mass became predominantly 128. A projection of the two-dimensional distribution onto the Y axis is shown in figure 2(b). For comparison, the spectrum from binary fission is presented in grey. The difference is obvious mainly due to the intense peaks of masses 128 u and 134 u associated with the magic isotopes of ^{128}Sn and ^{134}Te.

Bearing in mind that the fusion-fission reaction is out ruled a break-up of the fragment due to inelastic Coulomb scattering in the foil is decisive for the effect observed. In its turn it is possible if the fragment was in the shape isomer state before passing the foil. A mean flight

time between the Cf source and the foil let us to obtain the lower estimate of the shape isomer state life time to be more than 15 ns. This is a mean flight-time for the FF at the base between Cf source and TD1 detector with the Cupper degrader inside.

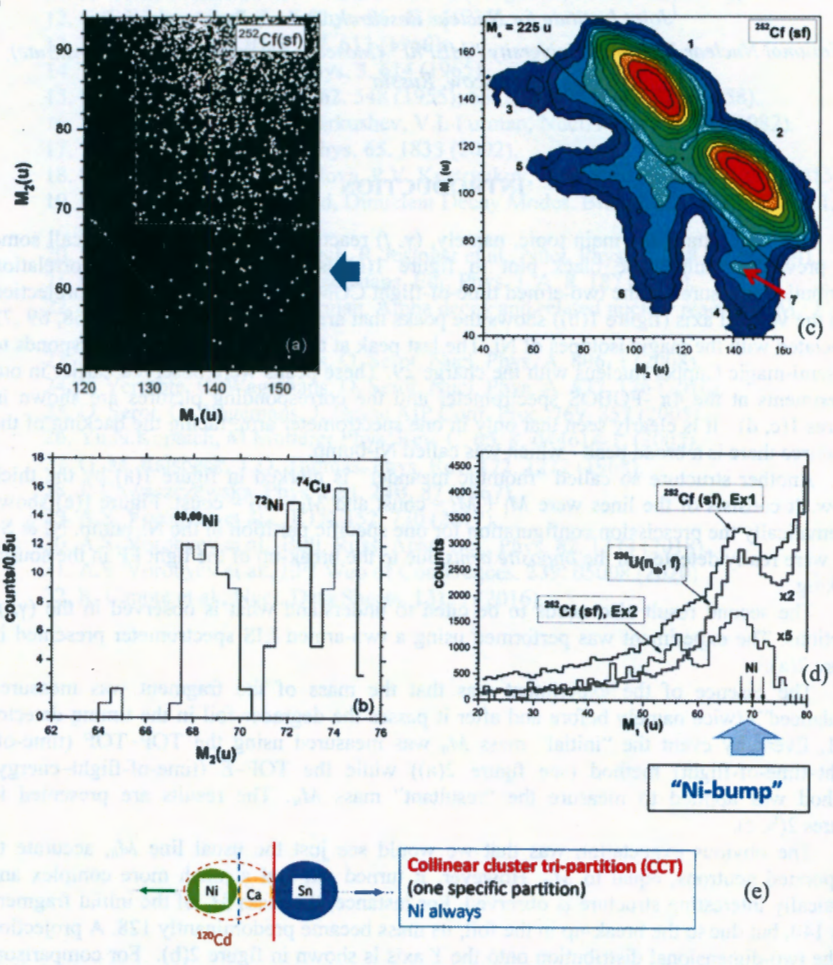

FIGURE 1. FFs mass correlation distribution from ^{252}Cf (sf) (a). Projection of the distribution onto M_1 axis under condition that M_2 = (65 – 76) u – (b). These figures were published in Ref. [1]. Contour map in logarithmic scale of the mass-mass distribution of the collinear fragments of ^{252}Cf (sf), detected in coincidence in the two opposite arms of the FOBOS spectrometer. The arrow marks a specific bump in arm1. (c) Projection of the Ni bump onto M_1 axis obtained in three different experiments performed at the FOBOS spectrometer modules (d). The figures were published in Refs. [2, 3]. Prescission configuration for one specific partition in the Ni-bump (e).

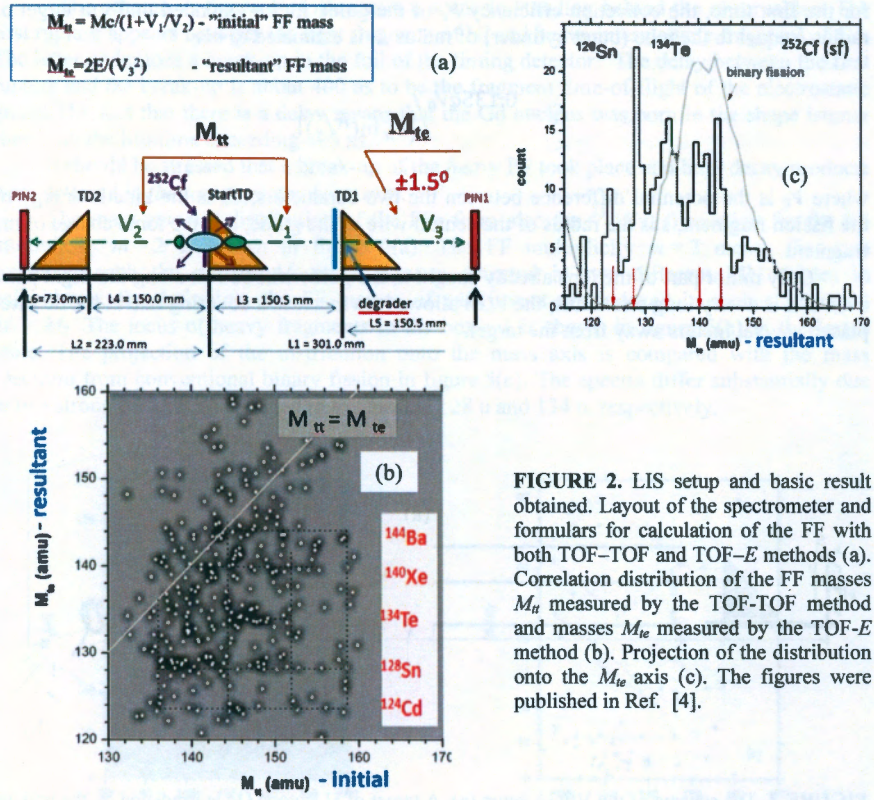

FIGURE 2. LIS setup and basic result obtained. Layout of the spectrometer and formulars for calculation of the FF with both TOF–TOF and TOF–E methods (a). Correlation distribution of the FF masses M_{tt} measured by the TOF-TOF method and masses M_{te} measured by the TOF-E method (b). Projection of the distribution onto the M_{te} axis (c). The figures were published in Ref. [4].

EXPERIMENTS AT THE BEAM OF THE MT-25 IN FLNR (JINR)

The experiments dedicated to study of the (γ, f) reactions were performed at the beam of the MT-25 microtron in the Flerov Lab, using VEGA (V-E Guide based Array) setup. The scheme of the spectrometer is shown in figure 3(a).

Fission fragments (FFs) from the (γ, f) reaction in the target (1) is captured by the electrostatic guide system (EGS) consisted of the tube (2) and the central wire (3). The FF energy E and velocity V required for calculation of the FF mass are measured in the time-of-flight spectrometer consisted of the microchannel-plates based timing detector (4) and the mosaic of four PIN diodes (5).

Typical trajectories of the ions in the guide are shown in figure 3(b).

The EGS constitutes a cylindrical capacitor with a thin wire as a central electrode. Some fraction of the ions emitted from the target at one end of the guide can be involved in the spiral-like movement along the guide axis, thanks to the radial electric field, which suppresses the radial component of the ion velocity. According to [5], in which the EGS was proposed

for the first time, the collection efficiency F_c of the guide for an extended uniform target of radius b equal to the tube (outer cylinder) of radius R, is estimated to be:

$$F_c = {}^{0.135qV_0}/_{\{E_n \ln({}^{R}/_{s})\}},$$

where V_0 is the potential difference between the two conductors, E_n is the kinetic energy of the fission fragment, s is the radius of the central wire of the guide, q is the ionic charge of the fragment.

Only minor part of the ions already caught in the guide will be lost along the flight pass, even if it is a very long one. Thus, the EGS allows it to increase a counting rate at the detector placed several meters away from the target.

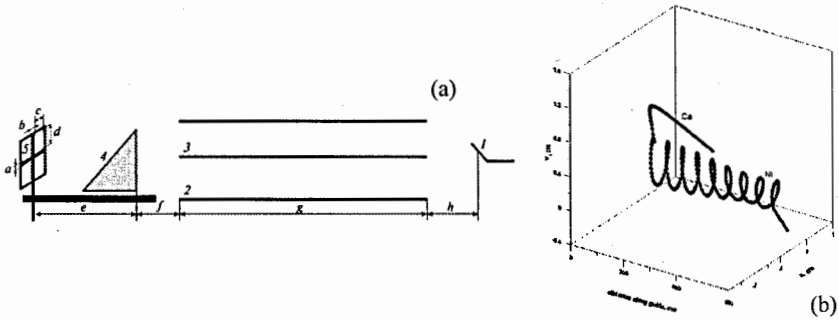

FIGURE 3. The scheme of the VEGA setup (a). A target of U isotope (1) is irradiated by the braking gamma quanta of the electron beam of the MT-25 microtron. Some fraction of the fission fragments is captured by the electrostatic guide system (EGS) consisting of a tube (2) at zero potential and the central wire (3) at a potential –10 kV. At the exit of the EGS, the FF energy E and velocity V for calculation of the FF mass are measured in the time-of-flight spectrometer consisting of the timing detector (4) and a mosaic of PIN diodes (5). The main dimensions of the setup: (*a*) vertical gap between the PIN diodes, 0.5 cm; (*b*) horizontal gap between the PIN diodes, 0.6 cm; (*c*) PIN diode's width, 1.8 cm; (*d*) PIN diode's length, 1.8 cm; (*e*) distance between the timing detector and the PIN diodes, 17.9 cm; (*f*) distance between the EGS and the timing detector, 3 cm; (*g*) EGS length, 400 cm; (*h*) distance between the target and the EGS, 3 cm. Typical trajectories of the ions in the guide (b).

The mass correlation distribution for the FFs from ^{235}U(γ, *f*) reaction detected in coincidence in two different PIN diodes of the mosaic is presented in figure 4(a).

Some linear structures inside the box w1 attract attention. This region is shown on a larger scale in figure 4(b). Solid lines 1–4 running at 45^0 to the M_1 axis match the expression $M_1 + M_2 = \text{const}$. Bottom two lines in figure 4(b) correspond to the missing masses 72 u and 68 u, respectively. These masses are associated with magic isotopes of ^{72}Ni and ^{68}Ni. As was shown in figure 1(b) just these really detected fragments manifested themselves as "Ni-bump".

The scheme in figure 4(c) illustrates a scenario standing behind the observables. The first rupture appears between the light fragment of Ni and heavy intermediate fragment of Gd. The letter undergoes a break-up in the foil of the timing detector. The delay between the first rupture and the break-up is about 400 ns to be the fragment time-of-flight of the electrostatic guide. The fact that there is a delay means that the Gd nucleus was born in the shape isomer state with the life-time exceeding 400 ns.

It should be stressed that a break-up of the *heavy* FF took place and both decay products were detected in *the same spectrometer arm.*

The mass-velocity distribution of the FFs from also the $^{235}U(\gamma, f)$ reaction for the FF multiplicity $m = 2$ is shown in figure 5(a). The FF multiplicity $m = 2$ means that two fragments with the masses M_1 and M_2 were detected in two different PIN diodes in coincidence. By definition, the FF masses of each event are indexed in such a way that $M_1 > M_2$. The locus of heavy fragments in the box *w*1 is shown in figure 5(b) in the larger scale. The projection of the distribution onto the mass axis is compared with the mass spectrum from conventional binary fission in figure 5(c). The spectra differ substantially due to two strong peaks corresponded to the masses 128 u and 134 u, respectively.

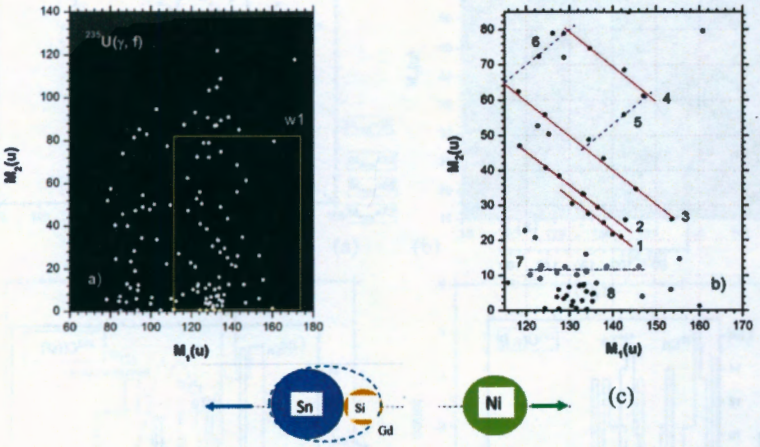

FIGURE 4. Mass correlation distribution for the FFs detected in coincidence in two different PIN diodes (a) and its part from box *w*1 (b). See text for details. The figures (a), (b) were published in Ref. [6].

And the last but not list – the spectrum in figure 5(c) agrees perfectly with the spectrum in figure 5(d) obtained at the LIS setup (see figure 2 (c)).

Thus, we observe similar result of the break-up of heavy FFs of two different mother systems in two different foils. Magic nuclei of ^{128}Sn and ^{134}Te demonstrate themselves as the cores of the deformed heavy fission fragments being in the shape isomer states.

The next figure 6 is dedicated to the $^{238}U(\gamma, f)$ reaction. The mass correlation distribution in figure 6(a) looks more complicated than in the previous reaction. Indeed, it includes not only the lines $M_1 + M_2 = \text{const}$ but also additional linear structures marked by the

arrows and vertical line at the mass 132 u in figure 6(b). The spectrum of the missing mass is shown in figure 6(c). Even the harshest referee could not deny the presence of at least a wide peak in the mass range (48–72) u. The same spectrum with 1 mass per channel is shown in figure 6(d).

The last one in the series of the targets studied so far was ^{232}Th (figure 7). We referred to the rhombic meander (figure 1(a)) in the introduction. As was shown by machine learning methods [8], the probability of a random realization of such a structure (rhombic meander) is negligible. Here, again, the lines $M_1 + M_2 = \text{const}$ and the lines $M_1 - M_2 = \text{const}$ are seen (figure 7). They perfectly describe the set of points that were obtained in this experiment. It should be noted that the ^{26}Ne fragment is seen both as detected and missing one. The points corresponded to the missing magic $^{46}Ar_{28}$ fragment is marked by the arrow.

The possible nature of the lines along which the sum of the masses is a constant, was discussed in our publication [9]. As for the structure $M_1 - M_2 = \text{const}$, its analysis is still in progress.

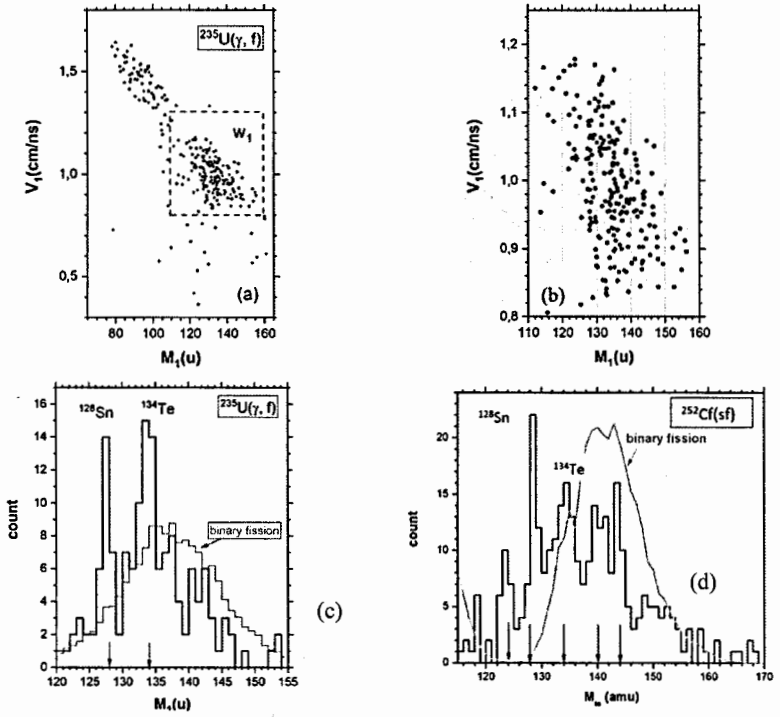

FIGURE 5. (a) – mass-velocity distribution of the heavy FFs from the ^{235}U(γ, *f*) reaction for the FF multiplicity $m = 2$; (b) – the distribution points from box *w*1 in figure 5(a); (c) – FFs mass spectra: the black one is a projection of the distribution in figure 5(b) on the axis M_1, the grey one is a mass spectrum for the FF's multiplicity $m = 1$. Positions of the magic FFs are marked by the arrows; (d) – a spectrum from figure 2(c) presented here for comparison with figure 5(c). The figures (a), (b), (c) were published in Ref. [7].

The experiments that are presented became possible after difficult and lengthy methodical work. For all the signals in the spectrometer we record their digital copy. For this purpose, a fast multichannel flash ADC is used. The current value of the signal is fixed each 200 ps for a gate duration of 200 ns. The data processing is performed offline. Our approach to the data processing is presented in Ref. [10] and references therein.

The main problem that we encountered, which is common for experiments on MT, is the background noise from the accelerator. In order to select only "suitable" events the base-line is inspected during 20 ns before the signal and both mean value and variance of the base-line are calculated. If actual fluctuations of the base-line exceed the level $C+3\sigma$ the signal is rejected. Unfortunately, only 20% of full statistics remains after such a selection.

Summing up, it should be stressed that exclusively thanks to the special impulse shaping unusual for the "classical" amplitude spectrometry and off-line processing of the digital images of all the signals we succeeded in the experiments at the gamma-beam.

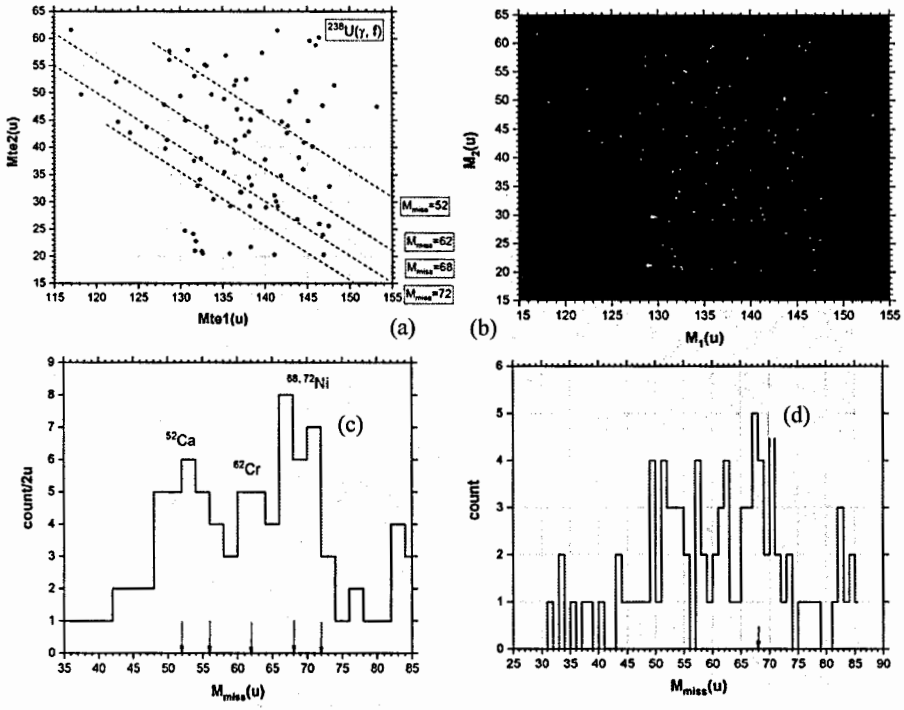

FIGURE 6. Mass correlation distribution for the FFs from the $^{238}U(\gamma, f)$ reaction detected in coincidence in two different PIN diodes (a), (b) and the spectrum of the missing mass $M_{miss}= 238 - (M_1+M_2)$ for the same distribution (c), (d). The figures (a), (c) were published in Ref. [1].

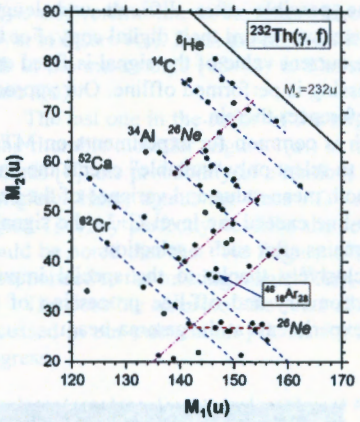

FIGURE 7. Mass correlation distribution for the FFs from the $^{232}Th(\gamma, f)$ reaction detected in coincidence in two different PIN diodes.

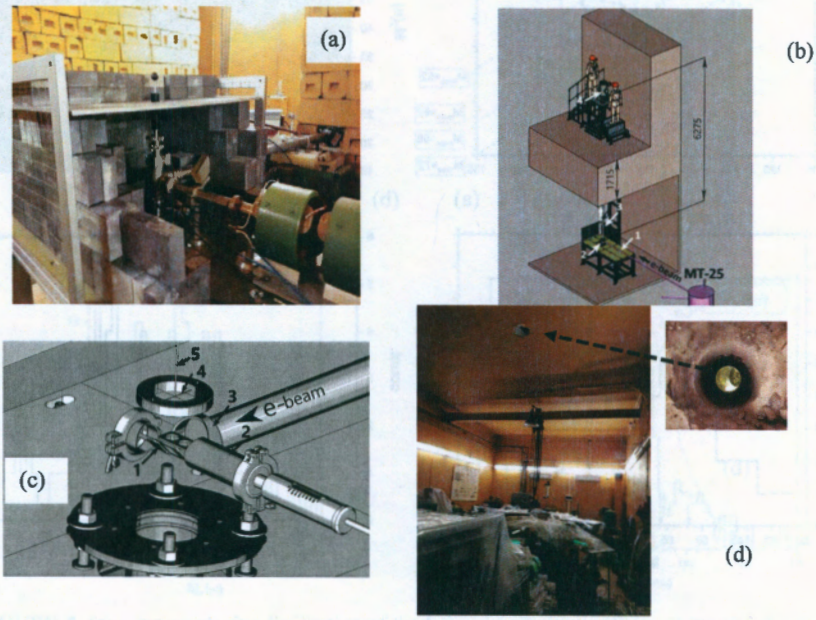

FIGURE 8. VEGA and VEGA-m setups. Target block of the VEGA setup in the lead shield (a). Schematical view of the VEGA-m setup (b): beam-line of the MT-25 microtrone (1), target block (2), EGS (3), detector chamber (4). Target holders and the bottom end of the EGS (c). Microtrone hall at the stage of drilling the concrete slab under the hall (d).

VEGA-M PROJECT

The main problem that was encountered, which is common for experiments on MT, is the background noise from the accelerator. Trivial but really ponderous way to protect the setup was already realized - significant time was spent to build a lead shield weighing several tons (figure 8(a)) what improved the experimental conditions but only partially.

To improve the situation radically, a new VEGA-m project is underway. The guide of about 6 meters long will now be positioned vertically and therefore enters the second floor of the microtron hall, passing about 2 *m* of concrete, which protects from radiation (figure 8(b)). Figure 8(c) shows the target holders and the bottom end of the EGS. Fortunately, one critical moment of the project is in the past: the stage of drilling the concrete slab has already been successfully completed (figure 8(d)) and a hole with a diameter of 220 mm for the new EGS is ready.

CONCLUSION

The following scenario could be proposed. Binary fission of the excited heavy nucleus occurs in the prescission configuration with the light magic fragment, for instance, Ni nucleus. The fragment is lost in the target backing, while the heavy fragment which is flying in the opposite direction is caught into EGS. After approximately *400 ns* ($<V_1> \approx 1$ cm/ns and the EGS length is about 400 cm) the heavy fragment reaches the start detector where its binary brake-up in very thin foil (50 μg/cm^2 of Al_2O_3) occurs. *The main conclusion which can be drawn from the result under discussion is that the heavy fragment of photo-fission of* ^{235}*U and* ^{232}*Th nuclei are born in the shape isomer states and the life time of these states exceeds 400 ns.* The result was obtained for the first time.

ACKNOWLEDGMENTS

The authors are grateful to V.I. Furman, Yu.M. Tchuvil'sky, G.G. Adamian, N.V. Antonenko, A.K. Nasirov for numerous fruitful discussions and stimulated criticism.

REFERENCES

1. D.V. Kamanina et al., Bull. Russ. Acad. Sci.: Phys. 87 (2023) 1238.
2. Yu.V. Pyatkov et al., Eur. Phys. J. A 45 (2010) 29.
3. Yu.V. Pyatkov et al., Eur. Phys. J. A 48, (2012) 94.
4. Yu.V. Pyatkov et al., Proceedings of the 23th International Seminar on Interaction of Neutrons with Nuclei, Dubna, Russia, 25-29 May 2015. Dubna 2016, p. 97–101.
5. N.C. Oakey, P.D. McFarlane, NIM 49 (1967) 220.
6. Yu.V. Pyatkov et al., Proceedings of the 27th International Seminar on Interaction of Neutrons with Nuclei, Dubna, Russia, 10-14 June 2019. Dubna 2020, p. 249–252.
7. Yu.V. Pyatkov et al., Physics of Atomic Nuclei 85 (2022) 292.
8. G. A. Ososkov et al., Phys. Part. Nucl. Lett. 18 (2021) 559.
9. Yu.V. Pyatkov et al., Eur. J. Phys. Funct. Mat. 4 (2020) 13.
10. Yu.V. Pyatkov et al., Bull. Russ. Acad. Sci.: Phys. 82 (2018) 804.

Revision of Analytical Properties of Reaction Amplitude near Thresholds Using the Example of Muon-Induced Prompt Fission

F.F. Karpeshin

D.I. Mendeleev All-Russian Research Institute for Metrology, 190005, Saint-Petersburg, Russia

E-mail: fkarpeshin@gmail.com

Experimental data on the muon-induced prompt fission are analyzed and compared to theory. Good agreement is observed for the $2p$–$1s$ and $3d$–$1s$ transitions. Anomalously big nonradiative width in the case of $3d$–$1s$ transition is surprised. Ways of resolving this puzzle are discussed.

1. Introduction

I start with an example which clearly demonstrates bounds of our knowledge. Consider fission of ^{238}U on the final stage of saddle-to-scission descend. Two scenarios are possible. Neck may rupture at small distance between the fragments. Strong Coulomb repulsion accelerates the fragments to some asymptotic value of TKE. Otherwise, the neck may rupture later. The distance between the fragments is larger, Coulomb repulsion is weaker. But if the fragments already have an initial velocity, they can accelerate to the same TKE. So, in the first case, the distance is small, repulsion – great. In the second case, the distance is larger, repulsion is weaker, but the TKE are the same, however. The first scenario implies strong dissipation, the second – weak dissipation. Therefore, one can say nothing about dissipation basing on experiment.

However, there is a tool which can help. This is prompt fission in muonic atoms, induced by nonradiative muon transitions. And the muons play the role of Maxwell's demons, or spectators, who watch the fission spectacle directly from the inside, and transfer the information to us. The process is as follows.

Muons "slow down" in matter then they start to be captured into atoms, to the muonic orbits with n about 14. Then they cascade down by means of Auger- or radiative transitions. In the final transition, for example $2p$ to $1s$, they have a chance to transfer the energy to the nucleus. The nucleus gets excited, and then it can undergo fission, which is called prompt. Otherwise, the muon will be captured by the nucleus due to weak interactions, and the nucleus also can undergo fission. This is called delayed fission.

It was Wheeler who proposed such a process [1]. He supposed tat nuclear excitation can occur in the $2s$–$1s$ transition. These transitions compete with the radiative $2s$–$2p$ transitions. Other possible nonradiative transitions, like $2p$–$1s$, $3p$–$1s$ compete with the same radiative transitions. And $3p$ to $1s$ transition also competes with the radiative $3p$–$2s$ transition. However, Zaretsky showed [2] that the probability of nuclear excitation in these transitions is also high, of the order of 1. Furthermore, Teller and Weiss showed [3] that in the $E2$ transition $3d$–$1s$ the nonradiative probability is about the same. Those results were confirmed by Nesterenko and me [4]. Moreover, they showed that the nonradiative probability in the $E3$

transition, $3d$–$2p$, is also high. It achieves 15% in spite of it competes with the $E1$ radiative transition. In this transition, excitation of the low-lying electric octupole resonance (LEOR) takes place. The energy 3.5 MeV is too small in order to induce fission, but LEOR can be studied in this way as excited by monochromatic photons.

Experimental discovery was induced due to Zaretsky's calculations. It took place in Dubna in 1960, with the paper by Pontekorvo et al. [5, 6]. For this purpose, muonic spectra of two atoms were compared to one another: ^{238}U and ^{208}Pb. They might be similar as uranium and lead have close atomic numbers. But the lead nucleus has a very low level density, which makes nonradiative excitation unlikely. Opposite, the level density is high in the U case, hence nonradiative excitation was expected.

When the spectra had been obtained, they both showed distinctive peaks corresponding to the 2 to 1 transition for both nuclei. In the case of U, the peak was by about 20% lower. Therefore, a missing intensity was established, which evidenced an appreciable probability of the nonradiative transition in uranium nuclei. This discovery was included in the register of scientific discoveries of the USSR.

Numeric data on the nonradiative probabilities were obtained in the group of Prof. David at the University of Bonn. They studied balance of incoming and outgoing radiative intensities for each atomic level. As a result, they obtained the nonradiative probabilities presented in Table 1. The data are compared with theoretical calculations. In particular, the data are shown for various components of the $2p$–$1s$ transition. The mechanism of radiationless transitions is considered to be as follows. Let muon make a transition e.g. from the $2p$ to $1s$ state. The energy of the transition is transferred to the nucleus by means of a virtual photon. This is actually a reverse internal conversion (IC) process. Theory of IC teaches that its probability factorizes into the nuclear radiation probability and ICC (Internal conversion coefficient), which is practically independent of the nuclear model.

In a number of theoretical papers calculations of the probabilities of the dipole $2p$, $3p \rightarrow 1s$ as well as the quadrupole $3d \rightarrow 1s$ radiationless transitions were carried out. Along with those transitions, herein we also consider the $3d \rightarrow 2p$ radiationless transitions of $E3$ type accompanied by the excitation of the low-lying electric octupole giant resonance (LEOR). We shall show that they are expected to be of the same order of magnitude as the dipole and quadrupole transitions. For present purposes we have used the quasi-particle-phonon nuclear model (QPNM) [8], which is known to work well in the description of low-lying nuclear states as well as giant resonances both in spherical and deformed nuclei.

These results are listed in Table 1. They show a rather large variability of the radiative widths for various fine-structure components. Data for the $2p$–$1s$ transition are in agreement with theoretical calculations. The authors did not search for the $3d$–$2p$ transitions, as they did not know about Ref. [4] at the time of experiment. Surprisingly, a radical disagreement with theory was found for the $3p$–$1s$ transitions. It is not merely 20%. This difference shows that the ratio of nonradiative-to-radiative probabilities achieves an order of magnitude.

In order to better understand the nature of this divergence, I undertook model-independent calculation using the experimental cross-sections of photoexcitation and photofission of the uranium nuclei. This paper provides a detailed information concerning the cross-sections. Before turning to these results let us remind the physical principles which underlie the microscopic calculation in Ref. [4].

Outline of the model

Description of the radiationless transitions first of all requires knowledge of the nuclear electromagnetic strength functions which contain information about the nuclear structure. The strength functions from QPNM are quite appropriate for this purpose. Next important moment is the muonic conversion coefficients (MCC). Involving MCC makes the calculations considerably easier, reducing the problem to independent calculations of the nuclear strength functions and MCC due to factorization of the amplitude. Moreover, factorization justifies use of experimental cross-sections for calculation of the radiationless transition probabilities.

The expression for the radiationless transition width is obtained by using the principle of detailed balance. In accordance with the definition of the MCC the width of the inverse process is the product of the radiative nuclear width and the MCC only. Turning to the radiationless nuclear excitation one immediately obtains an expression for its width ($\hbar = c = 1$):

$$\Gamma_{rl} = \alpha_{\mu}^{(d)}(i \to f) \cdot \frac{8\pi(L+1)}{[(2L+1)!!]^2} \omega^{2L+1} b(EL; 0 \to \omega). \qquad (1)$$

Here L is the multipole order, ω is the transition energy, with $b(EL; 0 \to \omega)$ being the strength function for the nuclear excitation [8]. Then, $\alpha_{\mu}^{(d)}(i \to f)$ is the MCC for the muonic transition from level i to f. Superscript d underlines the fact that both muonic states belong to the discrete spectrum as distinct to the traditional internal conversion, when an electron (or a muon) transfers into the continuum. As a consequence, the discrete MCC become energy dimensional due to the other normalization of the wavefunction of the corresponding muonic state. Discrete MCC were earlier used by Zaretsky and Karpeshin. They predicted the previously mentioned effect of emission of muonic X-rays from the heavy fragment as a result of muonic promotion to the $2p$ state via internal conversion. To calculate $\alpha_{\mu}^{(d)}(i \to f)$ a number of programs was used from the RAINE set [9] intended for relativistic calculations of atomic structure, and modified for calculation of MCC. Finite nuclear extent, vacuum polarization and electronic screening are included along with relativistic effects. The nuclear electromagnetic strength functions have been calculated by means of the formula

$$b(EL; 0 \to \omega) = \sum_g B(EL; 0 \to \omega) \cdot \frac{\Delta/2\pi}{(\omega-\omega_g)^2+(\Delta/2)^2}, \qquad (2)$$

where ω_g the energy of a phonon state g, Δ being the averaging parameter. The procedure for calculating the strength functions is described in detail by Soloviev et al. [8]. We have used in the calculations the value of Δ = 300 – 500 keV. At the excitation energy of 6 – 10 MeV the density of the one-phonon states with given L is about 100 per MeV. The values of Δ used are fairly large to smooth away fluctuations in $b(EL; 0 \to \omega)$ produced by particular highly excited states ω_g. On the other hand, such values of Δ are fairly small so as not to distort the average value of $b(EL; 0 \to \omega)$ at the given excitation energy.

The radiationless transition probability per muonic atom is given by the branching ratio

$$W_{rl} = \Gamma_{rl}/(\Gamma_{rl} + \Gamma_{\gamma}^{(i)}), \qquad (3)$$

where $\Gamma_\gamma^{(i)}$ is the radiative width of the muonic state *i*. These widths were calculated allowing for the relativistic effects, analogously to $\alpha_\mu^{(d)}$, by using the Dirac wave functions.

Table1. Calculated radiationless transition probabilities in comparison with the experimental data. $\langle 2p-1s\rangle$ is averaging over the fine-structure components. Designations SC, VC show application of the surface or volume nuclear current models, respectively, for the sake of calculation of MCC

	$\langle 2p-1s\rangle$	$2p_{1/2}-1s$	$2p_{3/2}-1s$	$3p-1s$	$3d-1s$
Experiment [7]	26.2±2.6	21.6±3.2(1.6)	31.1±2.8(1.3)	88.9±4.3	12.8±1.4
Zaretsky & Novikov with σ from [10]	22.4	21.1	24.2	64.7	
Zaretsky & Novikov with σ from [11]	29.8	28.4	32.0	68.5	
Teller & Wess [3]	20.7	20.0	21.7	59	9.6
Karpeshin & Nesterenko [4]	$11-15^{SC}$ $19-26^{VC}$			$55-65^{SC}$ $57-69^{VC}$	$19-24^{SC}$ $25-32^{VC}$

2. Results and discussion

Note that a statement can be noted saying that the radiative widths of *np* muonic levels for $n > 2$ are mainly determined from the transition to the 1*s* state. However, the probabilities of the transitions to the 2*s* state turned out to be approximately equal. It is the finite nuclear extent which produces such an effect. For these transitions the strength function is mainly determined from the giant electric dipole resonance (GDR). However, their energies are smaller than the energy of the top of the GDR. This refers especially to the $2p\rightarrow 1s$ transitions but to a lesser degree also applies to the $3p$–$1s$ transitions in which the energy falls on a slope of the GDR. Under these circumstances, the collective mode of nuclear motion is not manifested so clearly. As a result, the strength function might not be calculated as reliable.

For this talk, I revised the calculations for the *E*1 nonradiative transitions in ^{238}U by making use of experimental photoexcitation cross-sections from the paper by Caldwell et al. [11]. Experimental data are perfectly fitted by two-humpered GDR. The formula for Γ_{rl} is factorized into MCC, the cross-section and geometric factor. The formula is very simple and universal for each kind and order of multipolarity. Indeed, cross-section can be expressed in terms of the strength function as follows:

$$\sigma_L = 8\alpha\pi^3 \cdot \frac{(L+1)\omega^{2L-1}}{L[(2L+1)!!]^2} b(EL; 0 \rightarrow \omega). \quad (4)$$

Making use of (4) in (1), one arrives at the following expression:

$$\Gamma_{rl} = \alpha_\mu^{(d)}(0 \rightarrow \omega) \cdot \frac{\omega^2}{\pi^2}\sigma_L. \quad (5)$$

The results of calculation are presented in Table 2. As above, there is a good agreement for the $2p$–$1s$ transition. However, there remains drastic contradiction between the theoretical and experimental probabilities in the case of the $3p$–$1s$ transition. A particular attention was paid to the ratio of the $3p$–$1s$ nonradiative-to-radiative probabilities. It can be clearly seen from Table 2 that in the case of the $3p$–$1s$ transitions, the experimental nonradiative probability is by an order of magnitude as high as the theoretical one. In the case of the $2p$–$1s$ transition, the agreement with experiment is good.

Table 2. Comparison of theory, based on using experimental cross-sections [11], with experiment [7] with respect to the radiationless transition probabilities W_{rl} as well as the ratios of the nonradiative-to-radiative transition widths

Transition	Energy, MeV	W_{rl}		$\Gamma_{rl}/\Gamma_{\gamma}^{(i)}$	
		theory	experiment	theory	experiment
$2p_{3/2}$–$1s$	6.5	31.6	31.1±2.8	0.46	0.45
$3p_{3/2}$–$1s$	9.5	66	88.9±4.3	1.92	15

3. Conclusion

Prompt fission provides multilateral information about fission dynamics. We understand a lot of data concerning the $2p$–$1s$ nonradiative transitions. Argumentation of fission barrier and suppression of the fission mode is of great interest, as well as properties of the fragments.

At the same time, the most intriguing seems the contradiction between theory and experiment for the $3p$–$1s$ transition. The experimental non-radiative width is 7 times higher than the theoretical one. It seems highly heuristic to involve the processes of throwing the muon back. Otherwise, it can be the fine structure of the GDR. In this case, the muon turns out to be a unique tool for investigating GDR structure with high resolution by 100% definite multipolarity monochromatic photons. Note that fission channel is suppressed by about an order of magnitude in the case of the $2p$–$1s$ radiationless transition. But experimental cross-section which is used in the calculations involves the photofission cross-section fully. How does this affect probability? And in the case of the $3p$–$1s$ transition, the suppression is not confirmed experimentally.

The simplest conjecture concerning the $3p$–$1s$ line broadening is based on the experimental non-radiative transition probability. As that is 15 times greater than the radiative one (see Table 2), therefore, broadening achieves as much as a factor of 15. That means that it increases from about 0.2 to 3 keV. At the same time, however, many details and questions remain unclear. There is also level doubling due to the non-radiative interaction, with the related broadening of the second radiative component within MeV scale. Moreover, the nucleus gets excited, properly speaking, not in the $3p$–$1s$ transition, but rather in the preceding cascade transition to this state, like $4d$–$3p$, even $3d$–$3p$ (virtually) or similar. Correspondingly, some missing intensities should manifest themselves in these transitions. The basis for such consideration is laid in Ref. [12] using an example of electronic atoms of ^{229}Th.

Regarding the fine structure of the giant resonances, all what is said above concerning their fine structure especially refers to the $3d$–$2p$ nonradiative transition accompanied with

excitation of LEOR. It is very appropriate to perform independent measurements on the ^{235}U isotope and other actinides. Undoubtedly, continuation of this research will yield in new unexpected discoveries.

References

1. Wheeler J.A. // Phys. Rev. 1948. Vol. 73. P. 1252.
2. Zaretski D.F., Novikov V.M. Nucl. Phys. 1959. Vol. 14. P. 540; 1961. Vol. 28. P. 177.
3. Teller E., Weiss M.S. UCRL report N 83616. 1979; Trans. NY Acad. Sci. 1980. Vol. 40. P. 222.
4. Karpeshin F.F. and Nesterenko V.O. J. Phys. G: Nucl. Part. Phys. 1991. Vol. 17. P. 705.
5. Balatz M.Y., Kondratiev L.N., Lansberg L.G. et al. Zh. Exp. Teor. Fiz. **38**, 1715 (1960); **39**, 1168 (1961).
6. State register of discoveries of the USSR. Non-radiative transitions in mesoatoms. B.M. Pontecorvo, D.F. Zaretsky, M.Ya. Balats, P.I. Lebedev, L.N. Kondratyev, Yu.V. Obukhov. No. 100 with priority dated June 17, 1959.
7. Ch. Roesel, P. David et al. Z. Phys. A **340**, 199 (1991).
8. V.G. Soloviev. Teoria slozhnyh yader. Moscow: Energoatomizdat, 1979.
9. I.M. Band, M.B. Trzhaskovskaya, C.W. Nestor Jr., P.O. Tikkanen, and S. Raman, At. Data Nucl. Data Tables **81**, 1 (2002); I.M. Band and M.B. Trzhaskovskaya, At. Data Nucl. Data Tables **55**, 43 (1993); **35**, 1 (1986).
10. V.E. Zhuchko et al. Sov. J. Nucl. Phys. **28**, 602 (1987).
11. J.T. Caldwell et al. Phys. Rev. C **21**, 1215 (1980).
12. F.F. Karpeshin, I.M. Band, M.B.Trzhaskovskaya and M.A. Listengarten, Phys. Lett. **B 372**, 1 (1996).

Anisotropy in pre-fission neutron spectra of ^{235}U(n, F)

V. M. Maslov[1]

220025 Minsk, Byelorussia

Angular anisotropy of secondary neutrons evidenced in neutron emission spectra (NES), and prompt fission neutron spectra (PFNS). In case of NES it is due to pre-equilibrium/semi-direct mechanism of emission of first neutron in $(n,nX)^1$ reaction, while in case of PFNS it is due to exclusive spectra of pre-fission neutrons of $(n,xnf)^1$. In ^{239}Pu(n,xnf) and ^{235}U(n,xnf) reactions observed PFNS demonstrate differing response to the emission of first pre-fission neutron in forward and backward semi-spheres with respect to the incident neutrons. Average energies of $(n,nf)^1$ neutrons depend on angle of emission θ with respect to the incident neutron beam. The average prompt fission neutron number, fission cross section, TKE are quite dependent on θ as well. Exclusive spectra of $(n,xnf)^{1,..x}$ neutrons at θ~90° are consistent with ^{235}U(n,F)(^{235}U(n,xn)) observed cross sections and neutron emission data at E_n~0.01–20 MeV. The correlations of the angular anisotropy of PFNS with the relative contribution of the (n,nf) fission chance to the observed fission cross section and angular anisotropy of neutron emission spectra are ascertained. The exclusive spectra of ^{235}U$(n,xnf)^{1,..x}$, ^{235}U$(n,n\gamma)$ and ^{235}U$(n,xn)^{1,..x}$ reactions are calculated simultaneously with ^{235}U(n,F) and ^{235}U(n,xn) cross sections within Hauser-Feshbach formalism with angular anisotropy of $(n,nX)^1$ neutrons. The ratios of mean PFNS energies $\langle E \rangle$ for forward and backward emission of ^{235}U$(n,xnf)^{1,..x}$ pre-fission neutrons are consistent with measured data.

Fission energy of ^{235}U(n,F) reaction is distributed between fission fragments kinetic energy, their excitation energy and kinetic energy of pre-fission neutrons. Pre-fission neutrons influence the PFNS shape in the energy range of E_n~E_{nnf} – 20 MeV, E_{nnf} being the threshold energy of ^{235}U(n,nf) pre-fission neutrons. They influence also the shape of TKE of fission fragments and products, prompt neutron number, mass distributions and produce the step-like structures in observed fission cross section. Pre-fission neutrons define PFNS shape of ^{235}U(n,F) [1–5] at E_n~E_{nnf} – 20 MeV. The variation of observed average energies $\langle E \rangle$ in the vicinity of ^{235}U(n,xnf) reaction thresholds, as shown in [6–11], are defined by the exclusive spectra of $(n,xnf)^{1,..x}$ neutrons. Henceforth, the upper indices $(1...x)$ notify the emitted pre-fission neutrons. The amplitude of variations of $\langle E \rangle$ in case of ^{235}U(n,F) [7, 9, 10, 12] were confirmed by PFNS measured data ^{235}U(n,F) [4, 5] in E_n~1 – 20 MeV energy range.

Pre-fission neutrons in [1–5] counted in coincidence with fission fragments, without separation with respect to the fragment masses. The evaporation neutrons emitted in a spherically symmetric way with respect to the neutron beam direction. The angular anisotropy of PFNS observed in [1] for ^{239}Pu(n,F), is generally due to pre-equilibrium emission of $(n,nX)^1$ neutrons. Henceforth, the direction of emission of $(n,nX)^1$ neutrons, as well as that of $(n,n\gamma)^1$, $(n,2n)^1$, $(n,3n)^1$ and $(n,nf)^1$, $(n,2nf)^1$ and $(n,3nf)^1$ neutrons, is correlated with the momentum of the incident neutrons. The direction of the neutrons emitted from the fission fragments correlates with the fission axis direction mostly. Both kinds of neutrons counted in coincidence with fission fragments. In [1–5] PFNS detected with ~50 counters mounted around beam direction.

[1]mvm2386@yandex.ru

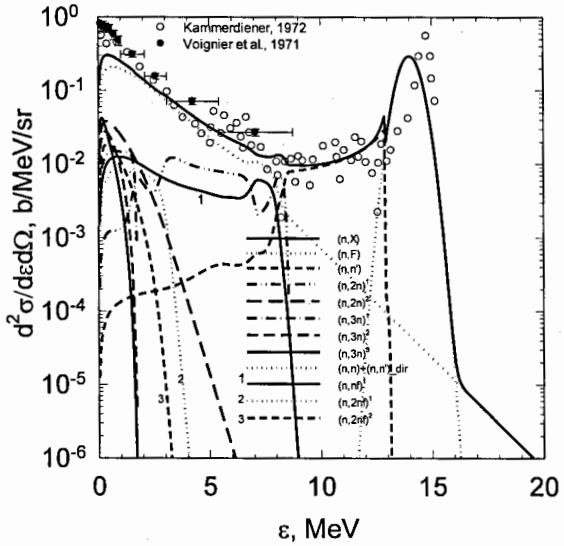

Fig. 1. Double differential neutron emission spectra for ^{235}U(n,F) at E_n =14 MeV, $\theta \approx 30°$ and its partial contributions; full line – (n,nX); dotted line – (n,F); dashed line – $(n,n\gamma)^1$; dash double dotted line –$(n,2n)^1$; dashed line–$(n,2n)^2$; dash–dotted line – $(n,3n)^1$; dashed line – $(n,3n)^2$; full line – $(n,3n)^3$; dashed line – (n,n) + ($n,n\gamma$) for discrete levels; ○ – [13]; ● – [14].

Angular anisotropy of NES of ^{235}U+n interaction observed long ago [13]. The anisotropic contribution of double differential spectra of first neutron, relevant for the excitations of first residual nuclide of 1~6 MeV, is evidenced in double differential NES and mostly in the component of ^{235}U$(n,n\gamma)^1$ reaction. The most investigated to define first neutron spectrum of $(n,nX)^1$ reaction is target nuclide ^{238}U [15]. Emissive neutron spectra of ^{238}U+n interaction are strongly anisotropic. The experimental quasi-differential emissive neutron spectra for ^{235}U+n, ^{238}U+n and ^{239}Pu+n interactions [16, 17] revealed the inadequacy of NES modelling [18, 19] and stimulated further efforts of NES modelling [20].

In the analysis of data on ^{235}U+n interaction the experience obtained in case of ^{238}U+n interaction was employed. Direct excitation of ^{238}U ground state band levels $J^\pi = 0^+, 2^+, 4^+, 6^+, 8^+$ was accomplished within rigid rotator model, while that of β–bands of $K^\pi = 0^+$ and γ–bands of $K^\pi = 2^+$, octupole band of $K^\pi = 0^-$ was accomplished within soft deformable rotator [15, 21, 22] (excitation energies for ^{238}U U=0~1.16 MeV). The net effect of these procedures is the adequate approximation of angular distributions of ^{238}U $(n,nX)^1$ first neutron inelastic scattering in continuum which corresponds to U=1.16~6 MeV excitations for E_n =1.16 MeV~20 MeV. The fictitious levels [19] are avoided, then the approach is applied for the ^{235}U+n interactions to estimate first neutron inelastic scattering in the continuum. The anisotropic part of double differential spectra of first neutron relevant for the excitations of the order of fission barrier value of ^{235}U, will be pronounced in exclusive spectra of $(n,nf)^1$, $(n,2nf)^1$ и $(n,2n)^1$ at E_n >12 MeV [12] which correspond to the various neutron emission angles. Angular distribution of pre-fission

neutrons in [1] was extracted from the observed PFNS of ^{239}Pu(n,F) by subtracting the post-fission neutron spectrum, which was estimated in an approximate manner.

Prompt fission neutron spectra $S(\varepsilon,E_n,\theta)$ at angle θ relative to the incident neutron beam, is a superposition of exclusive spectra of pre-fission neutrons, $(n,nf)^1$, $(n,2nf)^{1,2}$, $(n,3nf)^{1,2,3}$ $-\dfrac{d^2\sigma^k_{nxn}(\varepsilon,E_n,\theta)}{d\varepsilon d\theta}$ (x=1, 2, 3; k=1, ..., x), and spectra of prompt fission neutrons, emitted by fission fragments, $S_{A+1-x}(\varepsilon,E_n,\theta)$:

$$S(\varepsilon,E_n,\theta)=\widetilde{S}_{A+1}(\varepsilon,E_n,\theta)+\widetilde{S}_{A}(\varepsilon,E_n,\theta)+\widetilde{S}_{A-1}(\varepsilon,E_n,\theta)+\widetilde{S}_{A-2}(\varepsilon,E_n,\theta)=$$
$$\nu_p^{-1}(E_n,\theta)\cdot\{\ \nu_{p1}(E_n)\cdot\beta_1(E_n,\theta)S_{A+1}(\varepsilon,E_n,\theta)+\nu_{p2}(E_n-\langle E_{nnf}(\theta)\rangle)\beta_2(E_n,\theta)S_{A}(\varepsilon,E_n,\theta)+$$
$$+\beta_2(E_n,\theta)\frac{d^2\sigma^1_{nnf}(\varepsilon,E_n,\theta)}{d\varepsilon d\varepsilon}+\nu_{p3}(E_n-B_n^A-\langle E^1_{n2nf}(\theta)\rangle-\langle E^2_{n2nf}(\theta)\rangle)\beta_3(E_n,\theta)S_{A-1}(\varepsilon,E_n,\theta)+\beta_3(E_n,\theta)\times$$
$$\left[\frac{d^2\sigma^1_{n2nf}(\varepsilon,E_n,\theta)}{d\varepsilon d\theta}+\frac{d^2\sigma^2_{n2nf}(\varepsilon,E_n,\theta)}{d\varepsilon d\theta}\right]+\nu_{p4}(E_n-B_n^A-B_n^{A-1}-\langle E^1_{n3nf}(\theta)\rangle-\langle E^2_{n3nf}(\theta)\rangle-\langle E^3_{n3nf}(\theta)\rangle)\times$$
$$\beta_4(E_n,\theta)S_{A-2}(\varepsilon,E_n,\theta)+\beta_4(E_n,\theta)\left[\frac{d^2\sigma^1_{n3nf}(\varepsilon,E_n,\theta)}{d\varepsilon d\theta}+\frac{d^2\sigma^2_{n3nf}(\varepsilon,E_n,\theta)}{d\varepsilon d\theta}+\frac{d^2\sigma^3_{n2nf}(\varepsilon,E_n,\theta)}{d\varepsilon d\theta}\right]\}. \quad (1)$$

In equation (1) $\widetilde{S}_{A+1-x}(\varepsilon,E_n,\theta)$ is the contribution of x-chance fission to the observed PFNS $S(\varepsilon,E_n,\theta)$, $\langle E^k_{nxnf}(\theta)\rangle$ – average energy of k–th neutron of (n,xnf) reaction with spectrum $\dfrac{d^2\sigma^k_{nxn}(\varepsilon,E_n,\theta)}{d\varepsilon d\theta}$, $k\le x$. Spectra $S(\varepsilon,E_n,\theta)$, $S_{A+1-x}(\varepsilon,E_n,\theta)$ and $\dfrac{d^2\sigma^k_{nxn}(\varepsilon,E_n,\theta)}{d\varepsilon d\theta}$ are normalized to unity. Index x denotes the fission chance of $^{236-x}$U after emission of x pre-fission neutrons, $\beta_x(E_n,\theta)=\sigma_{n,xnf}(E_n,\theta)/\sigma_{n,F}(E_n,\theta)$ – contribution of x–th fission chance to the observed fission cross section, $\nu_p(E_n,\theta)$ is the observed average number of prompt fission neutrons, $\nu_{px}(E_{nx})$ – average number of prompt fission neutrons, emitted by $^{236-x}$U nuclides. Spectra of prompt fission neutrons, emitted from fragments, $S_{A+2-x}(\varepsilon,E_n,\theta)$, as proposed in [23], were approximated by the sum of two Watt [24] distributions with different temperatures, the temperature of light fragment being higher.

Modelling the angular distribution for the exclusive spectra of pre-fission neutrons ^{239}Pu(n,xnf)$^{1,\dots,x}$ we reproduced [25] measured data of [1], namely, the ratios of $\langle S(\varepsilon,E_n,\Delta\theta)\rangle_{\Delta E_n}/\langle S(\varepsilon,E_n,\Delta\theta^1)\rangle_{\Delta E_n}$ at $\Delta\theta$~35°–40°, $\Delta\theta^1\approx 130^o-140^o$ and wide energy range of ΔE_n ~15–17.5 MeV. The ratios of mean energies of PFNS $\langle E(\theta\approx 37.5^o)\rangle/\langle E(\theta^1\approx 135^o)\rangle$, i.e. of energies $\langle E\rangle$ for neutrons counted at angular intervals $\Delta\theta$~35°–40° and $\Delta\theta^1$~130°–150° in E_n~1–20 MeV range. Angular and spin correlations during prompt fission neutron emission are rather tedious, meanwhile the main factor for the observed features of PFNS like ratios for intervals $\langle S(\varepsilon,E_n,\Delta\theta)\rangle_{\Delta E_n}/\langle S(\varepsilon,E_n,\Delta\theta^1)\rangle_{\Delta E_n}$ and $\langle E(\theta\approx 37.5^o)\rangle/\langle E(\theta^1\approx 135^o)\rangle$, is the excitation energy of fissioning nuclides emerging after x pre-fission neutron emission.

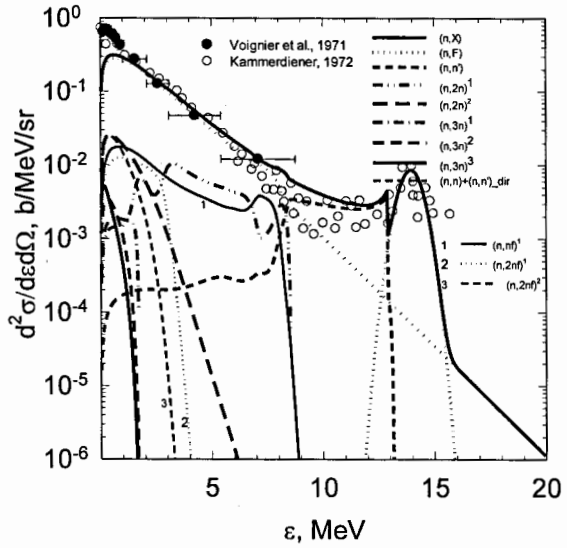

Fig. 2. Double differential neutron emission spectra at E_n =14 MeV, $\theta \approx 30°$ for ^{235}U(n,F) and its partial contributions: full line – (n,nX); dotted line – (n,F); dashed line – $(n,n\gamma)^1$; dash-double-dotted line – $(n,2n)^1$; dashed line – $(n,2n)^2$; dash-dotted line–$(n,3n)^1$; dashed line – $(n,3n)^2$; full line – $(n,3n)^3$; dashed line – sum of (n,n) and ($n,n\gamma$) for discrete levels;○ – [13]; • – [14].

Double differential NES could be defined as

$$\frac{d^2\sigma(\varepsilon,E_n,\theta)}{d\varepsilon d\theta}=\frac{1}{2\pi}\Big[\nu_p(E_n,\theta)\sigma_{nF}(E_n,\theta)S(\varepsilon,E_n,\theta)+\sigma_{nn\gamma}(\varepsilon,E_n,\theta)\frac{d^2\sigma^1_{nn\gamma}(\varepsilon,E_n,\theta)}{d\varepsilon d\theta}+$$
$$\sigma_{n2n}(\varepsilon,E_n,\theta)\left(\frac{d^2\sigma^1_{n2n}(\varepsilon,E_n,\theta)}{d\varepsilon d\theta}+\frac{d^2\sigma^2_{n2n}(\varepsilon,E_n,\theta)}{d\varepsilon d\theta}\right)+$$
$$\sigma_{n3n}(\varepsilon,E_n,\theta)\left(\frac{d^2\sigma^1_{n3n}(\varepsilon,E_n,\theta)}{d\varepsilon d\theta}+\frac{d^2\sigma^2_{n3n}(\varepsilon,E_n,\theta)}{d\varepsilon d\theta}+\frac{d^2\sigma^3_{n3n}(\varepsilon,E_n,\theta)}{d\varepsilon d\theta}\right)+ \quad (2)$$
$$\sum_q \frac{d\sigma_{nn\gamma}(\varepsilon,E_q,E_n,\theta)}{d\theta}G(\varepsilon,E_q,E_n,\Delta_\theta)\Big],$$

$$G(\varepsilon,E_q,E_n,\Delta_\theta)=\frac{2}{\Delta_\theta\sqrt{\pi}}\exp\left\{-\left[\frac{\varepsilon-(E_n-E_q)}{\Delta_\theta}\right]^2\right\}. \quad (3)$$

NES in Eq. (2) is a superposition of prompt fission neutron spectra $S(\varepsilon,E_n,\theta)$, exclusive spectra of $(n,n\gamma)^1$, $(n,2n)^{1,2}$ и $(n,3n)^{1,2,3}$, $\frac{d^2\sigma^k_{nxn}(\varepsilon,E_n,\theta)}{d\varepsilon d\theta}$, normalized to unity, and spectra of elastic

and inelastic scattered neutrons, followed by excitation of collective levels of ^{235}U, $\frac{d^2\sigma_{nny}(\varepsilon,E_q,E_n,\theta)}{d\varepsilon d\theta}$. $G(\varepsilon,E_q,E_n,\Delta_\theta)$–resolution function, which depends on E_n and weakly depends on θ. The NES are normalized with average prompt fission neutron number and (n,xn) and (n,F) cross sections.

The excitation energy of residual nuclides, after emission of (n,xnf) neutrons, is decreased by the binding energy of emitted neutron B_{nx} and its average kinetic energy:

$$U_x = E_n + B_n - \sum_{x,1\le k\le x}(< E^k_{nxnf}(\theta) > + B_{nx}). \qquad (4)$$

The excitation energy of fission fragments is

$$E_{nx} = E_r - E^{pre}_{fx} + E_n + B_n - \sum_{x,1\le k\le x}\left(\left\langle E^k_{nxnf}(\theta)\right\rangle + B_{nx}\right). \qquad (5)$$

Value of TKE, kinetic energy of fission fragments prior prompt neutron emission, E_F^{pre}, is approximate by a superposition of partial TKE of $^{240-x}$Pu($^{236-x}$U) nuclides as

$$E_F^{pre}(E_n) = \sum_{x=0}^{X} E^{pre}_{fx}(E_{nx})\cdot\sigma_{n,xnf}/\sigma_{n,F}\ . \qquad (6)$$

Kinetic energy of fission fragments, i.e. post-fission fragments after neutron emission, E_F^{post}, are defined as

$$E_F^{post} \approx E_F^{pre}\left(1-\nu_{post}/\left(A+1-\nu_{pre}\right)\right). \qquad (7)$$

Similar relation was used for E_f^{post} in [26] at $E_n<E_{nnf}$. Observed average number of prompt fission neutrons $\nu_p(E_n)$ maybe defined as

$$\nu_p(E_n) = \nu_{post} + \nu_{pre} = \sum_{x=1}^{X}\nu_{px}(E_{nx}) + \sum_{x=1}^{X}(x-1)\cdot\beta_x(E_n). \qquad (8)$$

The post-fission, $\nu_{post}(E_n)$, and pre-fission $\nu_{pre}(E_n)$ partials of $\nu_p(E_n)$ were obtained via consistent description of $\nu_p(E_n)$ and observed fission cross sections at E_n <20 MeV.

Contribution of x–th fission chance (n,xnf) to the observed fission cross section (n,F) is defined as

$$\sigma_{nF}(E_n) = \sigma_{nf}(E_n) + \sum_{x=1}^{X}\sigma_{n,xnf}(E_n)\ . \qquad (9)$$

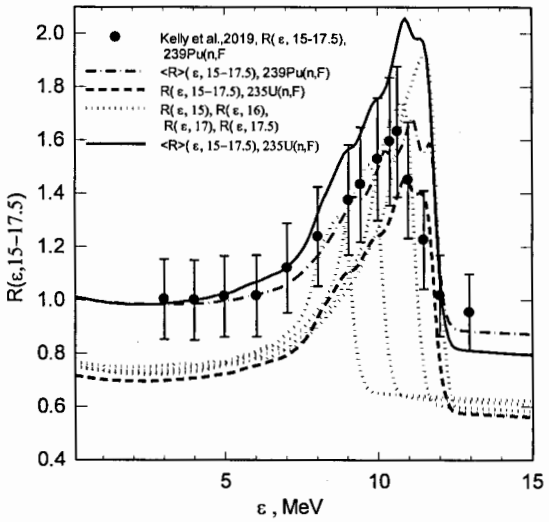

Fig. 3 Measured ratio $R^{exp} = S(\varepsilon, E_n \approx 15-17.5, \Delta\theta)/S(\varepsilon, E_n \approx 15-17.5, \Delta\theta^1)$ of ^{235}U(n,F) PFNS and calculated $R(\varepsilon,15\div17.5)$ for "forward", $\Delta\theta$~35°–40°, and "backward" emission, $\Delta\theta^1$=130°–140°; •–^{239}Pu(n,F) [1]; full line – ^{235}U(n,F) PFNS normalized to unity; dashed line – ^{235}U(n,F) PFNS equated at ε~3–5 MeV; dash-dotted line – ^{239}Pu(n,F) PFNS equated at ε~3–5 MeV; dotted line – partials of ^{235}U(n,F) $R(\varepsilon,15\div17.5)$ at E_n ~ 15 MeV, E_n ~ 16 MeV, E_n ~ 17 MeV and E_n ~ 17.5 MeV.

That means the (n,xnf) contributions are defined by the fission probability $P^{J\pi}_{f(A+1-x)}(E)$ of $^{236-x}$U nuclides:

$$\sigma_{n,xnf}(E_n) = \sum_{J\pi} \int_0^{U_x} W^{J\pi}_{A+1-x}(U) P^{J\pi}_{f(A+1-x)}(U) dU , \qquad (10)$$

here $W^{J\pi}_{A+1-x}(U)$ is the population of excited states of $(A+1-x)$ nuclides with excitation energy U after emission of x post-fission neutrons.

The QRPA methods are the most advanced, however they are still incapable to describe NES of ^{238}U+n [18]. Emission spectrum of $(n,nX)^1$ reaction, $\frac{d^2\sigma^1_{nnx}(\varepsilon,E_n,\theta)}{d\varepsilon d\theta}$, could be represented by the sum of compound and weakly dependent on emission angle pre-equilibrium components, and phenomenological function, modelling energy and angle dependence of NES [13] with first neutron inelastic scattering in continuum [1, 12, 27, 28]:

$$\frac{d^2\sigma^1_{nnx}(\varepsilon,E_n,\theta)}{d\varepsilon d\theta} \approx \frac{d^2\tilde{\sigma}^1_{nnx}(\varepsilon,E_n,\theta)}{d\varepsilon d\theta} + \sqrt{\frac{\varepsilon}{E_n}}\frac{\omega(\theta)}{E_n-\varepsilon} \qquad (11)$$

$$\omega(\theta) = 0.4\cos^3(\theta) + 0.16 \qquad (12)$$

Angle-averaged function $\omega(\theta)$ [28], $\langle\omega(\theta)\rangle_\theta$ for angles $\theta_2-\theta_1=135^\circ-30^\circ$ [1], is approximated as $\langle\omega(\theta)\rangle_\theta \approx \omega(90^\circ)$, then angle-integrated spectrum equals

$$\frac{d\sigma^1_{nnx}(\varepsilon,E_n)}{d\varepsilon} \approx \frac{d\tilde{\sigma}^1_{nnx}(\varepsilon,E_n)}{d\varepsilon} + \sqrt{\frac{\varepsilon}{E_n}}\frac{\langle\omega(\theta)\rangle_\theta}{E_n-\varepsilon}. \quad (13)$$

To retain the flux conservation in cross section and spectra calculations the compound reaction cross sections in [28] renormalized to account for extra semidirect neutron emission:

$$\sigma_c(E_n)=\sigma_a(E_n)(1-q-\tilde{q}), \quad (14)$$

Emission spectrum of $(n,nX)^1$, q–ratio of pre-equilibrium neutrons in a standard pre-equilibrium model [29],

$$\frac{d\tilde{\sigma}^1_{nnx}(\varepsilon,E_n)}{d\varepsilon}=\sum_{J,\pi}W_A^{J\pi}(E_n-\varepsilon,\theta), \quad (15)$$

depends on fission probability of $(A+1)$ nuclide. It defines the exclusive spectra of each partial reaction in STAPRE [29] framework, $W_A^{J\pi}(E_n-\varepsilon,\theta)$ is the population of residual nuclide A states with spin/parity J^π and excitation energy $U=E_n-\varepsilon$, after first neutron emission at angle θ. Henceforth the indexes J^π in fission, Γ_f, neutron Γ_n and total Γ widths described in [30], as well as relevant summations, omitted. The angular dependence of partial width, calculated with spin and parity conservation, is due to dependence of excitation energy of residual nuclides on the emission angle of first neutron. The exclusive spectra of pre-fission $(n,nf)^1$ neutron is

$$\frac{d^2\sigma^1_{nnf}(\varepsilon,E_n,\theta)}{d\varepsilon d\theta}=\frac{d^2\sigma^1_{nnx}(\varepsilon,E_n,\theta)}{d\varepsilon d\theta}\frac{\Gamma_f^A(E_n-\varepsilon,\theta)}{\Gamma^A(E_n-\varepsilon,\theta)}. \quad (16)$$

First neutron spectra of $(n,2nf)^1$ for reaction $(n,2nf)$, is defined as:

$$\frac{d^2\sigma^1_{n2nf}(\varepsilon,E_n,\theta)}{d\varepsilon d\theta}=\int_0^{E-B_n^A}\frac{d^2\sigma^1_{n2nx}(\varepsilon,E_n,\theta)}{d\varepsilon d\theta}\frac{\Gamma_f^{A-1}(E_n-B_n^A-\varepsilon-\varepsilon_1)}{\Gamma^{A-1}(E_n-B_n^A-\varepsilon-\varepsilon_1)}d\varepsilon_1, \quad (17)$$

here first neutron spectra of $(n,2nx)$ reaction, i.e. $(n,2nx)^1$, is defined by the neutron spectrum of $(n,nX)^1$ and neutron emission probability of nuclide A as:

$$\frac{d^2\sigma^1_{n2nx}(\varepsilon,E_n,\theta)}{d\varepsilon d\theta}=\frac{d^2\sigma^1_{nnx}(\varepsilon,E_n,\theta)}{d\varepsilon d\theta}\frac{\Gamma_n^A(E_n-\varepsilon,\theta)}{\Gamma^A(E_n-\varepsilon,\theta)}. \quad (18)$$

Spectra of first and next neutrons of ^{238}U($n,3nf$) reaction are covered in [6], in case of ^{235}U($n,3nf$) reactions they are defined in a similar fashion, but their contribution is quite low, actually less than ~10-20 mb.

Phenomenological approach enables to reproduce NES in case of ^{235}U+n interactions. Fig. 1 and Fig. 2 show comparisons of calculated double differential NES of ^{235}U +n, at E_n~14 MeV, θ~30° and θ~135° with measured data [13, 14]. Exclusive pre-fission neutron spectra of ^{235}U(n,xnf)^{1,2} are shown on Fig. 1 and Fig. 2 as $\frac{\sigma_{n,xnf}(E_n,\theta)}{4\pi}\frac{d\sigma^{1,2}_{nnf}(\varepsilon,E_n,\theta)}{d\varepsilon}$ at angles θ~30° and θ~135°. They comprise small part of $(n,nX)^1$ spectrum, nonetheless they reproduce angular dependence of PFNS with respect to the incident neutron beam.

Angular distributions of ^{239}Pu(n,xnf) pre-fission neutrons at E_n~14–18 MeV, measured in [1], may be quite well described as $0.25\,\omega(\theta)$, if θ>135°, then $0.25\,\omega(\theta=135°)$. Estimate of pre-fission neutrons contribution in [1] at any E_n or θ, was obtained as difference of observed PFNS and some simple estimate of post-fission neutrons evaporated from fission fragments. Though the procedure adopted in [1] is susceptible to systematic uncertainties, since post-fission neutrons may emerge from (x+1) fissioning nuclides [6–12], it seems hidden normalizations were used in [1]. It seems the normalization in [1] was accomplished in the energy range $\varepsilon>E_{nnf1}$, here E_{nnf1} is the upper energy of exclusive neutron spectra of $(n,nf)^1$ neutrons.

Angular anisotropy of PFNS relative to incident neutron beam was detected in ^{239}Pu(n,F) [1] at E_n~15–17.5 MeV range and at $\Delta\theta$~35°–40° (forward direction) and $\Delta\theta^1$=130°–140° (backward direction). The data normalization obtained by equating PFNS at ε~3–5 MeV energy range. Alternative representation of PFNS, against that shown on Fig.3 in [1], as a ratio $R^{exp}=S(\varepsilon,E_n\approx15-17.5,\Delta\theta)/S(\varepsilon,E_n\approx15-17.5,\Delta\theta^1)$ for $\Delta\theta$~35°–40° (forward direction) and $\Delta\theta^1$=130°–140° (backward direction) is virtually independent upon the normalizations adopted in [1].

Fig. 3 shows R^{exp} of ^{239}Pu(n,F) ratio R^{exp} of PFNS and calculated ratio of ^{235}U(n,F) at E_n~15–17.5 MeV $\Delta\theta$~35°–40° (forward direction) and $\Delta\theta^1$=130°–140° (backward direction) are compared with calculated ratio

$$R(\varepsilon,15\div17.5)\approx\frac{\int_{15}^{17.5}\nu_p(E_n,\approx30^o)\sigma_{nF}(E_n,\approx30^o)S(\varepsilon,E_n,\theta\approx30^o)\varphi(E_n)dE_n}{\int_{15}^{17.5}\nu_p(E_n,\theta\approx135^o)\sigma_{nF}(E_n,\theta\approx135^o)S(\varepsilon,E_n,\theta\approx135^o)\varphi(E_n)dE_n},\qquad(19)$$

here $\varphi(E_n)$ is the incident neutron spectrum, which is unknown. Spectra $S(\varepsilon,E_n,\theta)$ normalized to unity. As a first order approximation $R(\varepsilon,15\div17.5)$ might be calculated as a ratio of $\nu_p(E_n,\theta)\sigma_{nF}(E_n,\theta)S(\varepsilon,E_n\approx15-17.5,\Delta\theta)/\nu_p(E_n,\theta)\sigma_{nF}(E_n,\theta)S(\varepsilon,E_n\approx15-17.5,\Delta\theta^1)$ for E_n ~ 15 MeV, E_n ~ 16 MeV, E_n ~ 17 MeV and E_n ~ 17.5 MeV. Values of $\nu_p(E_n,\theta)$ and $\sigma_{nF}(E_n,\theta)$ were calculated at the same energies E_n, as those in $S(\varepsilon,E_n\approx15-17.5,\Delta\theta)$. In case of angular dependent observables for ^{235}U(n,F) hidden structures in lumped $R(\varepsilon,15\div17.5)$ constituents (for monochromatic beams) are smoothed, then R^{exp} and $R(\varepsilon,15-17.5)$ seem to have similar shapes,

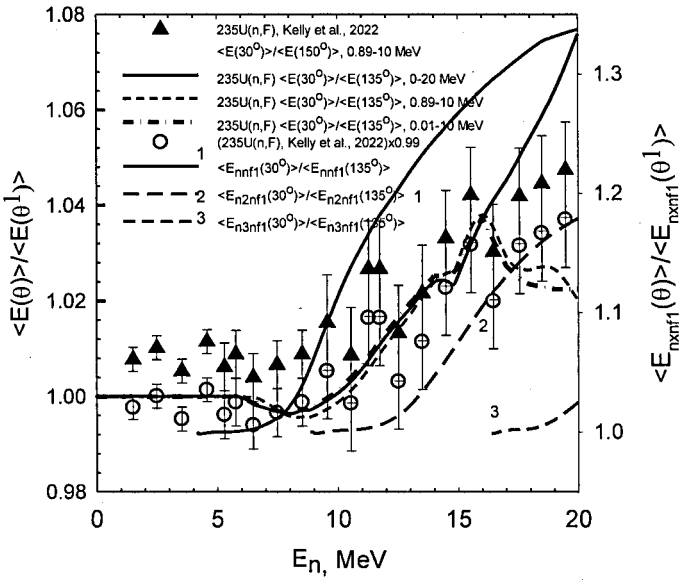

Fig. 4. Ratio $\langle E(\theta)\rangle/\langle E(\theta^1)\rangle$ for ^{235}U(n,F) PFNS: ▲– $\langle E(\theta\approx 30^o)\rangle/\langle E(\theta^1\approx 135^o)\rangle$, ε~1–12 MeV [4]; o–$\langle E(\theta\approx 30^o)\rangle/\langle E(\theta^1\approx 135^o)\rangle\times 0.99$, [4]; full line–$\langle E(\theta\approx 30^o)\rangle/\langle E(\theta^1\approx 135^o)\rangle$, ε~1–20 MeV; dashed line–$\langle E(\theta\approx 30^o)\rangle/\langle E(\theta^1\approx 135^o)\rangle$, ε~0.89–10 MeV; dash–dotted line – $\langle E(\theta\approx 30^o)\rangle/\langle E(\theta^1\approx 135^o)\rangle$, ε~0.01–10 MeV; dash–dotted line –$\langle E(60^o)/E(90^o)\rangle$, ε~0–20 MeV; lines 1, 2, 3 –$\langle E_{n,xnf}(\theta\approx 30^o)\rangle/\langle E_{n,xnf}(\theta^1\approx 135^o)\rangle$, x=1, 2, 3.

but the latter is shifted downwards. Smooth line of $R(\varepsilon,15-17.5)$ at Fig. 3 obtained by assuming in equation (20) equality of numerator and denominator values at ε~3–5 MeV energy range, as adopted in [1]. In case of ^{235}U(n,F) and ^{239}Pu(n,F) at $\varepsilon>E_{nnf1}$, both R^{exp} and $R(\varepsilon,15-17.5)$ are less then unity, that might be due to influence of angular dependence of (n,xnf) neutron emission on the fission chances distribution. The renormalized $R(\varepsilon,15-17.5)$ seems to be consistent with R^{exp} data.

The calculated anisotropy of pre-fission neutrons of ^{235}U(n,xnf) reaction is a bit higher than in case of ^{239}Pu(n,F). That might be due to correlation of anisotropy of pre-fission neutrons with contribution of emissive fission (n,nf) to the observed fission cross section, PFNS and angular anisotropy of NES. In case of ^{235}U(n,F) and ^{239}Pu(n,F) at $\varepsilon>E_{nnf1}$, both R^{exp} and $R(\varepsilon,15-17.5)$ are less then unity, that also might be due to influence of angular dependence of (n,xnf) neutron emission on the fission chances distribution.

Angular dependence of the first pre-fission neutron in reactions $(n,nf)^1$ and $(n,2nf)^1$ [25] allows to interpret the experimental data trend in case of ratio of average energies for "forward"

and "backward" emission of pre-fission neutrons in ^{239}Pu(n,xnf)^{1,2,3} [1] and ^{235}U(n,xnf)^{1,2,3} [4] reactions. The ratio of $\langle E(\theta)\rangle/\langle E(\theta^1)\rangle$ [1] in case of ^{239}Pu(n,F) for "forward", $\Delta\theta$~35°–40°, and "backward", $\Delta\theta^1$=130°–140°, emission of pre-fission neutrons steeply increases starting from E_n~10–12 MeV. Pre-fission (n,nf)^1 neutrons are responsible for that. The angular anisotropy of (n,xnf)^1 neutrons emission is due to pre-equilibrium/semidirect emission of first neutron in (n,nX)^1. When average energies are calculated at energy range of ε~1–3 MeV, ratios $\langle E(\theta)\rangle/\langle E(\theta^1)\rangle$ are virtually independent on E_n, while the dependence of ratio $\langle E(60^\circ)\rangle/\langle E(90^\circ)\rangle$ upon E_n, when averaging is for ε~1–12 MeV, is rather weak [25].

The ratio of average energies of exclusive neutron spectra of ^{235}U(n,nf)^1, $\frac{d^2\sigma^1_{nnf}(\varepsilon,E_n,\theta\approx 30^\circ)}{d\varepsilon d\theta}$ and $\frac{d^2\sigma^1_{nnf}(\varepsilon,E_n,\theta\approx 135^\circ)}{d\varepsilon d\theta}$, $\langle E_{n,xnf}(\theta\approx 30^\circ)\rangle/\langle E_{n,xnf}(\theta^1\approx 135^\circ)\rangle$, is much higher than that of $\langle E(\theta)\rangle/\langle E(\theta^1)\rangle$, however it follows the shape of experimental ratio $\langle E(\theta\approx 30^\circ)\rangle/\langle E(\theta^1\approx 135^\circ)\rangle$ [1, 4]. Angular dependence of the ratio of average energies of exclusive neutron spectra of ^{235}U($n,2nf$)^1 $\frac{d^2\sigma^1_{n2nf}(\varepsilon,E_n,\theta\approx 30^\circ)}{d\varepsilon d\theta}$ and $\frac{d^2\sigma^1_{n2nf}(\varepsilon,E_n,\theta\approx 150^\circ)}{d\varepsilon d\theta}$ is much weaker. In the ratio of average energies of exclusive neutron spectra of ^{235}U($n,3nf$)^1, $\frac{d^2\sigma^1_{n3nf}(\varepsilon,E_n,\theta\approx 30^\circ)}{d\varepsilon d\theta}$ and $\frac{d^2\sigma^1_{n3nf}(\varepsilon,E_n,\theta\approx 150^\circ)}{d\varepsilon d\theta}$, the angular dependence is quite weak. Ratios $\langle E(\theta\approx 30^\circ)\rangle/\langle E(\theta^1\approx 135^\circ)\rangle$ are virtually independent upon the lower threshold of neutron detection, while the dependence upon angular range and value of higher neutron detection threshold (ε~12 or ε~20 MeV) is crucial. That is illustrated on Fig. 4 for ratios of $\langle E(\theta\approx 30^\circ)\rangle/\langle E(\theta^1\approx 135^\circ)\rangle$ and $\langle E(\theta\approx 60^\circ)\rangle/\langle E(\theta^1\approx 90^\circ)\rangle$.

Calculated ratio $\langle E(\theta\approx 30^\circ)\rangle/\langle E(\theta^1\approx 135^\circ)\rangle$ for ^{235}U(n,F) PFNS is also somewhat higher than in case of ^{239}Pu(n,F) PFNS [25, 28], which seems to be compatible with higher contribution of ^{235}U(n,nf) reaction to the observed fission cross section ^{235}U(n,F). For emitted neutrons energy range of ε~1–12 MeV or ε~0–20 MeV, as evidenced on Fig. 4, $\langle E(\theta\approx 30^\circ)\rangle/\langle E(\theta^1\approx 135^\circ)\rangle$ is quite consistent with measured data for ^{235}U(n,F) up to E_n~16 MeV. Calculated ratios $\langle E(\theta\approx 30^\circ)\rangle/\langle E(\theta^1\approx 135^\circ)\rangle$ for ε~0–20 MeV are much higher than measured data for ε~1–12 MeV. Data of [4] for ^{235}U(n,F) were multiplied by 0.99 factor to attain visible consistency of measured and calculated data $\langle E(\theta\approx 30^\circ)\rangle/\langle E(\theta^1\approx 135^\circ)\rangle$. For exclusive neutron spectra of ^{235}U(n,nf)^1 the ratios of $\frac{d^2\sigma^1_{nnf}(\varepsilon,E_n,\theta\approx 30^\circ)}{d\varepsilon d\theta}$ and $\frac{d^2\sigma^1_{nnf}(\varepsilon,E_n,\theta\approx 135^\circ)}{d\varepsilon d\theta}$ average energies are also much higher than those of $\langle E(\theta)\rangle/\langle E(\theta^1)\rangle$, but their shape is virtually consistent with that of $\langle E(\theta\approx 30^\circ)\rangle/\langle E(\theta^1\approx 135^\circ)\rangle$ [4] (see Fig. 4).

Average energy $\langle E\rangle$ is a rough integral estimate of PFNS, however the angular anisotropy of pre-fission neutron emission exerts quite an influence on it. Dependence of $\langle E\rangle(E_n)$ in case of ^{235}U(n,F) is compared with measured data for energy range ε~0.01 – 10 MeV [2, 3] on Fig. 5.

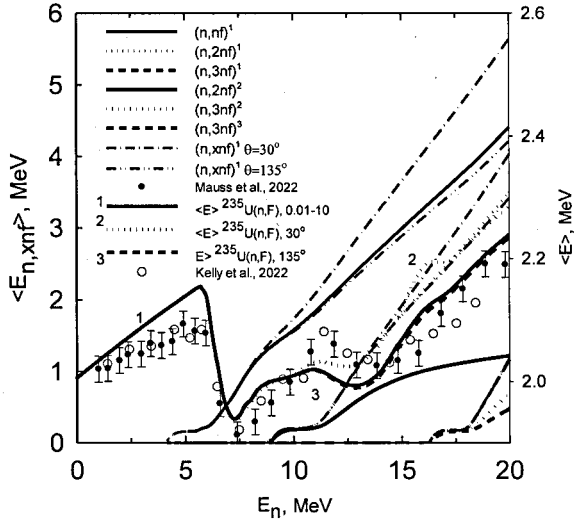

Fig. 5 PFNS $\langle E \rangle$ for ^{235}U(*n, F*): o–[4]; • –[5]; full line, 1 –$\langle E(90^o) \rangle$; dotted line, 2 – $\langle E(30^o) \rangle$; dashed line, 3–$\langle E(135^o) \rangle$; full line – $\langle E_{n,xnf}(\theta \approx 90^o) \rangle$; dash-dotted line–$\langle E_{n,xnf}(\theta \approx 30^o) \rangle$; dash–double dotted line–$\langle E_{n,xnf}(\theta \approx 135^o) \rangle$.

The estimates of $\langle E \rangle$ for PFNS of ^{235}U(*n,F*) are strongly correlated with PFNS influence of exclusive neutron spectra of $(n,nf)^1$ and $(n,2nf)^{1,2}$ which they exert on $\langle E \rangle$ in case of ^{235}U(*n,F*) are much stronger than in case of ^{239}Pu(*n,F*). There still are some minor discrepancies between measured and calculated $\langle E \rangle$, that might be due to arbitrary normalizations when two neutron detectors are used in [1, 3, 4] at ε<1.5 MeV and ε>0.8 MeV. Mutual normalization in these two overlapping energy ranges is susceptible uncertainty of detector efficiency and data scatter.

Analysis of prompt fission neutron spectra of ^{235}U(*n,F*) evidenced correlations of a number observed data structures with $(n,xnf)^{1\cdots x}$ pre-fission neutrons. Pre-fission neutron spectra turned out to be quite soft as compared with neutrons emitted by excited fission fragments. The net outcome of that is the decrease of $\langle E \rangle$ in the vicinity of the (*n,xnf*) thresholds of ^{235}U(*n,F*). The amplitude of the $\langle E \rangle$ variation is much higher in case of ^{235}U(*n,F*) as compared with ^{239}Pu(*n,F*). The correlation of PFNS shape with different angles of emission of $(n,xnf)^1$ neutrons and emissive fission contributions for ^{235}U(*n,F*) is established. The angular anisotropy of exclusive pre-fission neutron spectra strongly influences the PFNS shapes and $\langle E \rangle$. These peculiarities are due to differing emissive fission contributions in ^{239}Pu(*n,F*) and ^{235}U(*n,F*) [31, 32]. Calculated ratio of $\langle E \rangle$ for "forward" and "backward" emission of pre-fission neutrons steeply increases with the increase of average energies of exclusive pre-fission neutron spectra.

References

1. K. J. Kelly, T. Kawano, J.M. O'Donnel et al., Phys. Rev. Lett., 122, 072503 (2019).
2. P. Marini, J. Taieb, B. Laurent et al., Phys. Rev. C, 101, 044614 (2020).
3. K. J. Kelly, M. Devlin, O'Donnel J.M. et al., Phys. Rev. C, 102, 034615 (2020).
4. K. J. Kelly, J.A. Gomez, M. Devlin et al., Phys. Rev. C, 105, 044615 (2022).
5. B. Mauss, J. Taieb, B. Laurent et al., https://oecd-nea.org/dbdata/nds_jefdoc/jefdoc-2200.pdf, Nuclear Data Week, November, 2022, JEFDOC-2200.
6. V.M. Maslov, Yu. V. Porodzinskij, M. Baba, A. Hasegawa, N.V. Kornilov, A.B. Kagalenko and N.A. Tetereva, Phys. Rev. C, 69, 034607 (2004).
7. V.M. Maslov, N.V. Kornilov, A.B. Kagalenko and N.A. Tetereva, Nucl. Phys. A, 760, 274 (2005), https://www–nds.iaea.org/ minskact/ data/ 92235f18.txt.
8. V.M. Maslov, At. Energy, 103, 119 (2007).
9. V.M. Maslov, V.G. Pronyaev, N.A. Tetereva et al., At. Energy, 108, 352 (2010).
10. V.M. Maslov,V.G. Pronyaev, N.A. Tetereva et al., J. Kor. Phys. Soc. 59, 1337 (2011).
11. V.M. Maslov, Yad. Fiz., 71, 11 (2008)
12. V.M. Maslov In: Proc. LXXII Intern. Conf. Nucleus 2022, Fundamental problems and applications, Moscow, 11–16 July, 2022, Book of abstracts, p. 111, https:// events . sinp.msu.ru/event/8/attachments/181/875 nucleus–2022–book–of–abstracts–www.pdf.
13. J.L. Kammerdiener, UCRL–51232, 1972.
14. J. Voignier, R.G. Clayeux, F. Bertrand, CEA-R-3936, 1970.
15. V.M. Maslov, M. Baba, A. Hasegawa, A. B Kagalenko., N.V. Kornilov, N.A. Tetereva, INDC (BLR)-14, Vienna: IAEA, 2003; https://www-nds.iaea.org/publications/ indc/indc -blr-0014/.
16. A.M. Daskalakis, R.M.Bahran, E.J. Blain et al., Ann. Nucl. Energy, 73, 455 (2014).
17. K. S. Mohindroo, Y. Danon, E.J. Blain et al., Ann. Nucl. Energy, 165, 108647 (2022).
18. M. Dupuis, S. Hilaire, S. Peru, EPJ Web of Conferences, 146, 12002 (2017).
19. P. Young, M. Chadwick, R. MacFarlane et al., Nucl. Data Sheets, 108, 2589 (2007).
20. M. R. Mumpower, D. Neudecker, H. Sasaki, et al., Phys. Rev. C, 107, 034606 (2023).
21. V.M. Maslov, Yu.V. Porodzinskij, M. Baba, A. Hasegawa, Bull. RAS, Ser. Fyz. 67, 1597 (2003).
22. V.M. Maslov, Yu.V. Porodzinskij, N.A. Tetereva et al., Nucl. Phys. A, 2006, 764, 212.
23. N.V. Kornilov, A.B. Kagalenko, F.-J. Hambsch, Yad. Fiz. 62, 209 (1999).
24. B.E. Watt, Phys. Rev., 87, 1037, (1952)
25. V.M. Maslov, Proc. 28th International Seminar on Interactions of Neutrons with Nuclei, 2021, May, 24-28, Dubna, Russia, Book of Abstracts, p. 113, http://isinn.jinr.ru/past-isinns/isinn 28/ISINN 28 %20 Abstract%20 Book.pdf.
26. D.G. Madland, A.C. Kahler, Nucl. Phys. A 957, 289 (2017).
27. V.M. Maslov, in: Proc. LXXII Intern. Conf. Nucleus 2022, Fundamental problems and applications, Moscow, 11–16 July, 2022, p. 168. https://events.sinp.msu.ru/event/ 8/contributions/ 586/attachments/568/881/mvmNucl 2022%2 B.pdf
28. V.M. Maslov, Physics of Particles and Nuclei Letters, 20, 1401 (2023).
29. M. Uhl and B. Strohmaier, IRK-76/01, IRK, Vienna, 1976.
30. V.M. Maslov, Phys. Rev. C, 72, 044607 (2005).
31. V.M. Maslov, Physics of Particles and Nuclei Letters, 20, 565 (2023).
32. V.M. Maslov, Yad. Fyz., 86, 562 (2023).

Angular anisotropy of secondary neutron spectra in ^{232}Th + n

V. M. Maslov[1]

220025 Minsk, Byelorussia

Neutron emission spectra (NES) of ^{232}Th+n interaction provide strong evidence of angular anisotropy of secondary neutron emission, another evidence might be predicted in ^{232}Th(n,F) prompt fission neutron spectra (PFNS). In case of NES observed angular anisotropy is presumably due to angular dependence of elastic scattering, direct excitation of collective levels and pre-equilibrium emission of (n,nX)^1 neutrons. In ^{232}Th+n direct excitation data analysis, ground state band levels $J^\pi = 0^+, 2^+, 4^+, 6^+, 8^+$ are coupled within rigid rotator model, while those of β–bands with $K^\pi=0^+$, γ–bands with $K^\pi=2^+$ and octupole band $K^\pi=0^-$ are coupled within soft deformable rotator model. NES of ^{232}Th+n at E_n~6, ~12, ~14, ~18 MeV exhaustively described. The net effect of these procedures for E_n up to ~20 MeV is the adequate approximation of angular distributions of ^{232}Th(n,nX)^1 first neutron inelastic scattering in continuum, which corresponds to U= 1.2~6 MeV excitations of ^{232}Th.

The contribution of ^{232}Th(n,F) PFNS to the NES is exceptionally low. PFNS anisotropy occurs because some portion of (n,nX)^1 neutrons might be involved in exclusive pre-fission neutron spectra. In ^{232}Th(n,xnf) reactions PFNS demonstrate different response to forward and backward (n,xnf)^1 neutron emission relative to the incident neutron momentum, when compared with ^{235}U(n,xnf) or ^{239}Pu(n,xnf) reactions. Average energy of (n,xnf)^1 neutrons depends on the neutron emission angle θ, i.e. fission cross section, prompt neutron number and total kinetic energy are shown to vary with the angle θ as well. Exclusive neutron spectra (n,xnf)^{1,x} at θ~90° are consistent with observed ^{232}Th(n,F) and ^{232}Th(n,xn) reaction cross sections within E_n~1–20 MeV energy range. Exclusive neutron spectra of (n,xnf)^{1,x}, ($n,n\gamma$) and (n,xn)^{1,x} reactions are calculated with Hauser-Feshbach formalism simultaneously with (n,F) and (n,xn) reaction cross sections, angular dependence of first neutron (n,nX)^1 emission $\omega(\theta)$ being included.

Neutron emission spectra (NES) of ^{232}Th+n interaction provide strong evidence of angular anisotropy of secondary neutron spectra [1], as observed in [2, 3]. Another evidence might be predicted in ^{232}Th(n,F) prompt fission neutron spectra (PFNS) anisotropy in a similar fashion as for ^{238}U(n,F) [4]. In case of NES observed angular anisotropy of neutron emission is mostly due to angular dependence of elastic scattering, direct excitation of collective levels and pre-equilibrium emission of (n,nX)^1 neutrons [5, 6]. In ^{232}Th+n direct excitation data analysis, ground state band levels $J^\pi = 0^+, 2^+, 4^+, 6^+, 8^+$ are coupled within rigid rotator model, while those of β–bands with $K^\pi = 0^+$ and γ–bands with $K^\pi = 2^+$ and octupole band $K^\pi = 0^-$ are coupled within soft deformable rotator model [7, 8]. Levels of second $K^\pi = 0^+$ band (0.73035 MeV) classified as quadrupole longitudinal β-vibrations, while levels of third $K^\pi = 0^+$ band (1.0787 MeV) - as quadrupole transversal γ-vibrations. Both defined by softness parameters to respective vibrations μ_β and μ_γ [1, 7–9]. Anomalous rotational γ-band $K^\pi=2^+$ levels characterized by the non-axiality parameter γ_o. That latter band lies much lower (~0.3 MeV) than respective band in case of ^{238}U, at the other hand this band lowering is accompanied by shift of $K^\pi = 0^+$ band (1.0787 MeV) -that of quadrupole transversal γ-vibrations, to higher excitation (by ~0.250 MeV), than in case of ^{238}U nuclide. Quadrupole longitudinal β-vibration

[1]mvmmvm1955@mail.ru

band levels also lowered as compared with relevant band of ^{238}U nuclide (by ~0.250 MeV). That means ^{232}Th nuclide, within soft rotator model, is much softer with respect to quadrupole longitudinal β-vibrations, which pronounces as higher μ_β parameter values [7, 8]. As regards quadrupole transversal γ-vibrations, static non-axiality parameter γ_o for ^{232}Th is higher than in case of ^{238}U. Its value was extracted by fitting position of band-head of anomalous γ–band $K^\pi = 2^+$, which is appreciably lower than in case of ^{238}U. This mask possible difference of softness to transversal γ-vibrations of ^{232}Th and ^{238}U, i.e. μ_γ parameter values differ only slightly [1, 7–9]. In ^{232}Th+n direct level excitation data analysis [1, 7–9] ground state band levels $J^\pi = 0^+, 2^+, 4^+, 6^+, 8^+$ are coupled within rigid rotator model, while those of β-bands with $K^\pi = 0^+$, γ–bands with $K^\pi = 2^+$ and octupole band $K^\pi = 0^-$ are modelled within soft deformable rotator model (^{232}Th levels excitation energies U=0~1.2 MeV). Actually, the calculation of direct inelastic scattering [1, 7–9] was made adding each of 17 levels of $K^\pi = 0^+, 2^+, 0^-$ bands, one by one, to the 0^+–2^+–4^+–6^+–8^+ coupling basis, replacing the last 8^+ member of ground state rotational band. That is justified, since the coupling with ground state band levels is the strongest for any band level. This procedure only slightly changes total and reaction cross sections, the same response is to the increase of coupling basis, i.e. from 3 to 5 levels within a rigid rotator model. At $E_n < E_{nnf}$, E_{nnf} being the threshold of ^{232}Th(n,nf) reaction, ^{232}Th+n NES in the vicinity of the elastic peak are analyzed in [1], the same procedure [7–9] as in case of ^{238}U+n was applied.

In the energy range $E_{nnf} < E_n < 20$ MeV double differential NES are a superposition of prompt fission neutron spectra $S(\varepsilon, E_n, \theta)$, normalized to unity exclusive spectra of $(n,n\gamma)^1$, $(n,2n)^{1,2}$ и $(n,3n)^{1,2,3}$, $\frac{d^2\sigma^k_{nxn}(\varepsilon,E_n,\theta)}{d\varepsilon d\theta}$ and spectra of elastic and inelastic scattered neutrons, followed by excitation of collective levels $(n, n')_d$ of ^{232}Th, $\frac{d^2\sigma_{nn\gamma}(\varepsilon,E_q,E_n,\theta)}{d\varepsilon d\theta}$:

$$\frac{d^2\sigma(\varepsilon,E_n,\theta)}{d\varepsilon d\theta} = \frac{1}{2\pi}\Big[\nu_p(E_n,\theta)\sigma_{nF}(E_n,\theta)S(\varepsilon,E_n,\theta) + \sigma_{nn\gamma}(\varepsilon,E_n,\theta)\frac{d^2\sigma^1_{nn\gamma}(\varepsilon,E_n,\theta)}{d\varepsilon d\theta} +$$
$$\sigma_{n2n}(\varepsilon,E_n,\theta)\left(\frac{d^2\sigma^1_{n2n}(\varepsilon,E_n,\theta)}{d\varepsilon d\theta} + \frac{d^2\sigma^2_{n2n}(\varepsilon,E_n,\theta)}{d\varepsilon d\theta}\right) +$$
$$\sigma_{n3n}(\varepsilon,E_n,\theta)\left(\frac{d^2\sigma^1_{n3n}(\varepsilon,E_n,\theta)}{d\varepsilon d\theta} + \frac{d^2\sigma^2_{n3n}(\varepsilon,E_n,\theta)}{d\varepsilon d\theta} + \frac{d^2\sigma^3_{n3n}(\varepsilon,E_n,\theta)}{d\varepsilon d\theta}\right) + \quad (1)$$
$$\sum_q \frac{d\sigma_{nn\gamma}(\varepsilon,E_q,E_n,\theta)}{d\theta} G(\varepsilon,E_q,E_n,\Delta_\theta)\Big],$$

$$G(\varepsilon,E_q,E_n,\Delta_\theta) = \frac{2}{\Delta_\theta\sqrt{\pi}}\exp\left\{-\left[\frac{\varepsilon-(E_n-E_q)}{\Delta_\theta}\right]^2\right\}. \quad (2)$$

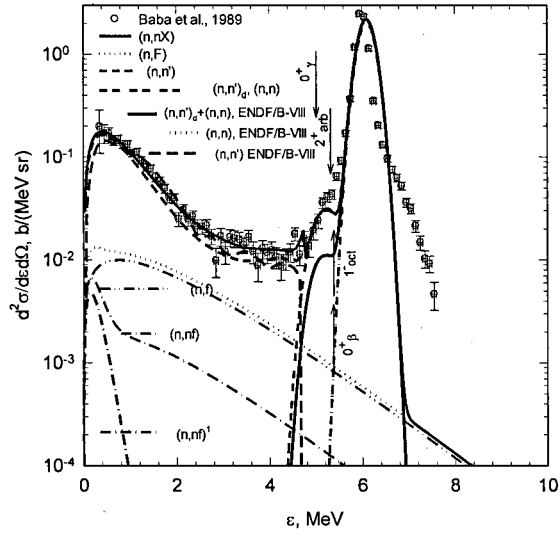

Fig. 1 Double differential NES of ^{232}Th+n for E_n = 6.1 MeV, $\theta \approx 30^o$ and its partial constituents; full line – (n,nX); dotted line – (n,F); dashed line – $(n,n\gamma)^1$; dash double dotted line – $n,2n)^1$; dashed line – $(n,2n)^2$; dash–dotted line – $(n,3n)^1$; dashed line – $(n,3n)^2$; full line – $(n,3n)^3$; dashed line – $(n,n)_d$ + $(n,n\gamma)$ for discrete levels; o – [2, 3].

In equation (2) $G(\varepsilon, E_q, E_n, \Delta_\theta)$–resolution function, which depends on E_n and only weakly depends on angle θ. The NES are normalized with average prompt fission neutron number, (n,xn) and (n,F) cross section values.

The QRPA [10] methods are the most advanced in the field, however they still incapable to describe NES of heavy nuclides like ^{238}U or ^{232}Th, when inelastic scattering in continuum corresponds to the excitations of residual nuclei U= 1.2~6 MeV. Emission spectrum of $(n,nX)^1$ reaction, $\dfrac{d^2\sigma^1_{nnx}(\varepsilon, E_n, \theta)}{d\varepsilon d\theta}$, could be represented by the sum of compound and pre-equilibrium components, both weakly dependent on emission angle, and phenomenological function, modelling energy and angle dependence of NES [2, 3]. Double differential spectra of first neutron inelastic scattering in continuum is approximated as

$$\frac{d^2\sigma^1_{nnx}(\varepsilon, E_n, \theta)}{d\varepsilon d\theta} \approx \frac{d^2\tilde{\sigma}^1_{nnx}(\varepsilon, E_n, \theta)}{d\varepsilon d\theta} + \sqrt{\frac{\varepsilon}{E_n}}\frac{\omega(\theta)}{E_n - \varepsilon} \qquad (3)$$

$$\omega(\theta) = 0.4\cos^3(\theta) + 0.16 \qquad (4)$$

The value of the second term at right hand side of equation (3) depends on the lumped contribution of the direct excitation of the collective levels of β–bands with $K^\pi = 0^+$, γ–bands

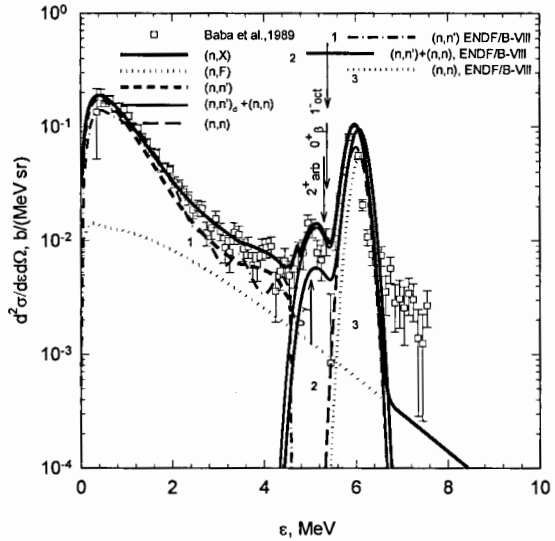

Fig. 2. Double differential neutron emission spectra for ^{232}Th+n at E_n =6.1 MeV, $\theta \approx 120^o$ and its partial constituents; full line – (n,nX); dotted line – (n,F); dashed line – $(n,n\gamma)^1$; dash-double-dotted line – $(n,2n)^1$; dashed line – $(n,2n)^2$; dash-dotted line–$(n,3n)^1$; dashed line – $(n,3n)^2$; full line – $(n,3n)^3$; dashed line – sum of $(n,n)_d$ and $(n,n\gamma)$ for discrete levels;○ – [2, 3].

K^π =0$^+$, γ –bands with K^π =2$^+$ and octupole band K^π = 0$^-$. Angle-averaged function $\omega(\theta)$, $\langle\omega(\theta)\rangle_\theta$ for scattering angles $\theta_2 - \theta_1 = 135^o - 30^o$, approximated as $\langle\omega(\theta)\rangle_\theta \approx \omega(90^o)$, gives angle-integrated spectrum as

$$\frac{d\sigma^1_{nnx}(\varepsilon,E_n)}{d\varepsilon} \approx \frac{d\tilde{\sigma}^1_{nnx}(\varepsilon,E_n)}{d\varepsilon} + \sqrt{\frac{\varepsilon}{E_n}}\frac{\langle\omega(\theta)\rangle_\theta}{E_n-\varepsilon}. \qquad (5)$$

To retain the flux conservation in cross section and spectra calculations the compound reaction cross sections normalized to account for extra neutron emission:

$$\sigma_c(E_n) = \sigma_a(E_n)(1-q-\tilde{q}), \qquad (6)$$

here, q–ratio of pre-equilibrium neutrons in a standard pre-equilibrium model [11], $\tilde{q}$ –value easily obtained using equation (5). The compound contribution to the emission spectrum of $(n,nX)^1$ reaction is

$$\frac{d\tilde{\sigma}^1_{nnx}(\varepsilon,E_n)}{d\varepsilon} = \sum_{J,\pi} W^{J\pi}_A(E_n-\varepsilon,\theta)\cdot \qquad (7)$$

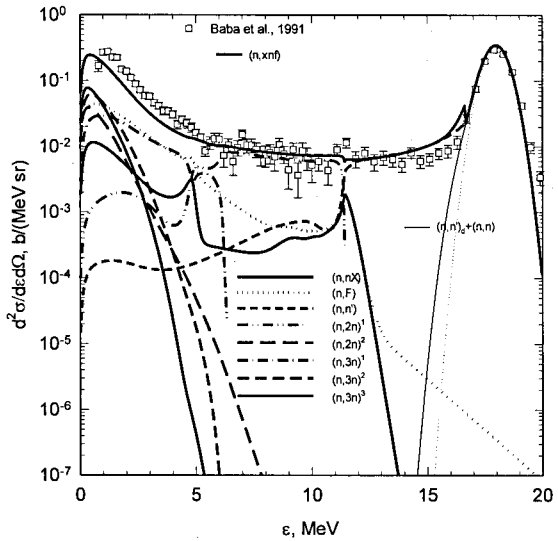

Fig. 3. Double differential neutron emission spectra for ^{232}Th+n at E_n =141 MeV, $\theta \approx 30°$ and its partials; full line – (n,nX); dotted line – (n,F); dashed line – $(n,n\gamma)^1$; dash double dotted line –$(n,2n)^1$; dashed line–$(n,2n)^2$; dash–dotted line – $(n,3n)^1$; dashed line – $(n,3n)^2$; full line – $(n,3n)^3$; dashed line – $(n,n) + (n,n\gamma)$ for discrete levels; ○ – [2, 3].

Population of states with spin/parity J^π and excitation energy $U=E_n-\varepsilon$, after first neutron emission at angle θ depends on fission probability of $(A+1)$ nuclide. It defines the exclusive spectra of each partial reaction in STAPRE [11] framework, $W_A^{J\pi}(E_n-\varepsilon,\theta)$ is the population of excited states of residual nuclide A. The net effect of these procedures is the adequate approximation of double differential NES and angular distributions of ^{232}Th$(n,nX)^1$ first neutron inelastic scattering in continuum, which corresponds to U= 1.2~6 MeV excitations for E_n =1.16 MeV~20 MeV.

Angular anisotropy of NES of ^{232}Th+n interaction as observed in [2, 3] allows to extract the anisotropic contribution to double differential spectra of the first neutron, relevant for the excitations of first residual nuclide of 1.2~6 MeV and attribute observed NES anisotropy mostly to the component of ^{232}Th$(n,n\gamma)^1$ reaction. The experimental quasi-differential emissive neutron spectra for ^{238}U+n interactions [14] revealed the inadequacy of NES modelling in [12, 13] and stimulated further efforts of NES modelling [15] aimed to abandon fictitious levels.

Figures 1 and 2 show NES at E_n ~6.1 MeV for forward and backward scattering of first $(n,nX)^1$ neutron. The contribution of prompt fission neutrons to NES is exceptionally low. The inelastic scattering when residual nuclide excitation energy is larger than ~1.2 MeV and elastic scattering are the major contributors to the NES. The step-like structure to the left of elastic peak

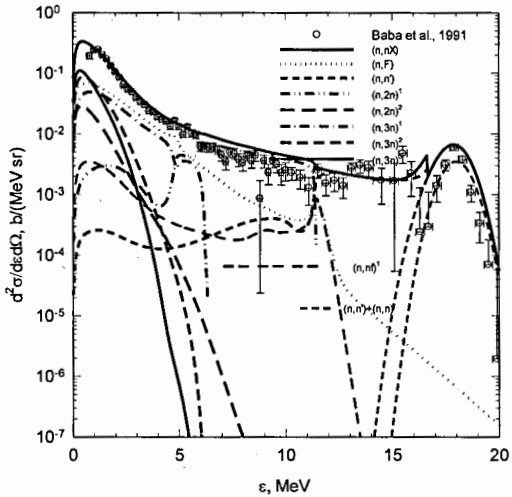

Fig. 4. Double differential neutron emission spectra for ^{232}Th+n at E_n =14 MeV, $\theta \approx 120°$ and its partial contributions: full line – (n,nX); dotted line – (n,F); dashed line – $(n,n\gamma)^1$; dash-double-dotted line – $(n,2n)^1$; dashed line – $(n,2n)^2$; dash-dotted line–$(n,3n)^1$; dashed line – $(n,3n)^2$; full line – $(n,3n)^3$; dashed line – sum of (n,n) and $(n,n\gamma)$ for discrete levels;○ – [2, 3].

is due to direct excitation of collective levels of β–bands with K^π =0$^+$, γ–bands with K^π =2$^+$ and octupole band K^π = 0$^-$. Both elastic and inelastic scattering contributors to the NES are much dependent on angle θ. The elastic and inelastic scattering contributors to the NES of ENDF/B-VIII [12, 13], though they roughly approximate the NES around elastic peak and inelastic scattering contribution when residual nuclide excitation energy is larger than ~1.2 MeV, waive off the direct excitation of β–bands with K^π =0$^+$, γ–bands with K^π =2$^+$ and octupole band K^π =0$^-$. The fictitious levels with J^π = 2$^+$, 3$^-$ as in [12, 13] we avoid.

PFNS anisotropy occurs because some portion of $(n,nX)^1$ neutrons might be involved in exclusive pre-fission neutron spectra. It was observed and interpreted in ^{238}U(n,xnf) [4], ^{235}U(n,xnf) [5, 6, 16, 17] and ^{239}Pu(n,xnf) [6, 16, 18–20] reactions. Since the contribution of PFNS to the NES of ^{232}Th+n interaction is relatively low, the major evidence of NES angular anisotropy would occur in $(n,n\gamma)$ reaction. However, in ^{232}Th(n,xnf) reactions PFNS would demonstrate different response to forward and backward $(n,xnf)^1$ neutron emission relative to the incident neutron momentum, much stronger than in case of ^{238}U(n,xnf) reaction [4]. The partial PFNS components of ^{232}Th(n,F), shown on Fig. 1, were calculated as follows.

Prompt fission neutron spectra $S(\varepsilon, E_n, \theta)$ at angle θ relative to the incident neutron beam is a superposition of exclusive spectra of pre-fission neutrons, $(n,nf)^1$, $(n,2nf)^{1,2}$, $(n,3nf)^{1,2,3}$ –

$\frac{d^2\sigma^k_{nxn}(\varepsilon,E_n,\theta)}{d\varepsilon d\theta}$ (x=1, 2, 3; k=1,...,x), and spectra of neutrons, emitted by fission fragments, $S_{A+1-x}(\varepsilon,E_n,\theta)$:

$$S(\varepsilon,E_n,\theta)=\widetilde{S}_{A+1}(\varepsilon,E_n,\theta)+\widetilde{S}_{A}(\varepsilon,E_n,\theta)+\widetilde{S}_{A-1}(\varepsilon,E_n,\theta)+\widetilde{S}_{A-2}(\varepsilon,E_n,\theta)=$$
$$\nu_p^{-1}(E_n,\theta)\cdot\{\ \nu_{p1}(E_n)\cdot\beta_1(E_n,\theta)S_{A+1}(\varepsilon,E_n,\theta)+\nu_{p2}(E_n-\langle E_{nnf}(\theta)\rangle)\beta_2(E_n,\theta)S_A(\varepsilon,E_n,\theta)+$$
$$+\beta_2(E_n,\theta)\frac{d^2\sigma^1_{nnf}(\varepsilon,E_n,\theta)}{d\varepsilon d\varepsilon}+\nu_{p3}(E_n-B_n^A-\langle E^1_{n2nf}(\theta)\rangle-\langle E^2_{n2nf}(\theta)\rangle)\beta_3(E_n,\theta)S_{A-1}(\varepsilon,E_n,\theta)+\beta_3(E_n,\theta)\times$$
$$\left[\frac{d^2\sigma^1_{n2nf}(\varepsilon,E_n,\theta)}{d\varepsilon d\theta}+\frac{d^2\sigma^2_{n2nf}(\varepsilon,E_n,\theta)}{d\varepsilon d\theta}\right]+\nu_{p4}(E_n-B_n^A-B_n^{A-1}-\langle E^1_{n3nf}(\theta)\rangle-\langle E^2_{n3nf}(\theta)\rangle-\langle E^3_{n3nf}(\theta)\rangle)\times$$
$$\beta_4(E_n,\theta)S_{A-2}(\varepsilon,E_n,\theta)+\beta_4(E_n,\theta)\left[\frac{d^2\sigma^1_{n3nf}(\varepsilon,E_n,\theta)}{d\varepsilon d\theta}+\frac{d^2\sigma^2_{n3nf}(\varepsilon,E_n,\theta)}{d\varepsilon d\theta}+\frac{d^2\sigma^3_{n2nf}(\varepsilon,E_n,\theta)}{d\varepsilon d\theta}\right]\}. \quad (8)$$

In equation (8) $\widetilde{S}_{A+1-x}(\varepsilon,E_n,\theta)$ is the contribution of x-chance fission to the observed PFNS $S(\varepsilon,E_n,\theta)$, $\langle E^k_{nxnf}(\theta)\rangle$ – average energy of k–th neutron of (n,xnf) reaction with spectra $\frac{d^2\sigma^k_{nxn}(\varepsilon,E_n,\theta)}{d\varepsilon d\theta}$, $k\le x$. Spectra $S(\varepsilon,E_n,\theta)$, $S_{A+1-x}(\varepsilon,E_n,\theta)$ and $\frac{d^2\sigma^k_{nxn}(\varepsilon,E_n,\theta)}{d\varepsilon d\theta}$ are normalized to unity. Index x denotes the fission chances ^{232}Th($n,nxnf$) of ^{232}Th(n,F) after emission of x pre-fission neutrons, $\beta_x(E_n,\theta)=\sigma_{n,xnf}(E_n,\theta)/\sigma_{n,F}(E_n,\theta)$ – contribution of x–th fission chance to the observed fission cross section, $\nu_p(E_n,\theta)$ is the observed average number of prompt fission neutrons, $\nu_{px}(E_{nx})$ – average number of prompt fission neutrons, emitted by fission fragments of $^{233-x}$Th nuclides. Spectra of prompt fission neutrons, emitted from fragments, $S_{A+2-x}(\varepsilon,E_n,\theta)$, as proposed in [21], were approximated by the sum of two Watt [22] distributions with different temperatures, the temperature of the light fragment being higher.

The Fig. 1 shows also partial contributions of ^{232}Th(n,f), ^{232}Th(n,nf) and ^{232}Th(n,nf)^1 to NES at E_n~6.1 MeV for forward scattering of first (n,nX)^1 neutron. The contribution of exclusive ^{232}Th(n,nf)^1 pre-fission neutrons to the NES is exceptionally low. With increase of the incident neutron energy E_n up to ~20 MeV exclusive spectra of pre-fission neutrons, (n,nf)^1, ($n,2nf$)^{1,2}, ($n,3nf$)^{1,2,3}, when accounted for properly, will strongly influence the shapes of NES and PFNS [23].

Figures 3 and 4 show NES at E_n~18 MeV for forward and backward scattering, respectively. The contribution of prompt fission neutrons to the NES is still rather low, however the contribution of exclusive prefission neutron spectra is of peculiar shape. In an approach pursued in [12, 13] the direct excitation of levels other than those of ground state band is waived off and coupling strength erroneously transferred to fictitious levels with $J^\pi = 2^+, 3^-$. The inelastic scattering, when residual nuclide excitation energy is 1.2~6 MeV as well as elastic scattering are the major contributors to the NES at $\varepsilon > E_{nnf1}$, the latter being the cutoff energy of the prefission (n,nf)^1 neutron. The direct excitation of collective levels of β–bands with $K^\pi = 0^+$, γ–bands with $K^\pi = 2^+$ and octupole band $K^\pi = 0^-$ is no longer pronounced as a step-like structure to the left side of elastic peak. It leads just to broadening of quasi-elastic peak. In case

of backward scattering the direct excitation is even more important contributor to NES because backward elastic scattering is suppressed. The anisotropic part of double differential spectra of first neutron of $(n,nX)^1$ reaction relevant for the excitation energy amounting fission barrier value of ^{232}Th, will be strongly pronounced in exclusive spectra of $(n,nf)^1$, $(n,2nf)^1$ и $(n,2n)^1$ at E_n >12 MeV at various emission angles of first pre-fission neutron.

Modelling the angular distribution for the exclusive spectra of pre-fission neutrons of ^{235}U$(n,xnf)^{1,\ldots,x}$ and ^{239}Pu$(n,xnf)^{1,\ldots,x}$ we reproduced [5, 6] measured data of [17–20], namely, the ratios of $\langle S(\varepsilon,E_n,\Delta\theta)\rangle_{\Delta E_n} / \langle S(\varepsilon,E_n,\Delta\theta^1)\rangle_{\Delta E_n}$ at $\Delta\theta \approx 35^\circ - 40^\circ$, $\Delta\theta^1 \approx 130^\circ - 140^\circ$ and rather wide energy range of incident neutrons ΔE_n ~15–17.5 MeV (see Fig. 5). Angular and spin correlations during prompt fission neutron emission are rather tedious, if possible at all, meanwhile the main factor for observed features of PFNS like $\langle S(\varepsilon,E_n,\Delta\theta)\rangle_{\Delta E_n} / \langle S(\varepsilon,E_n,\Delta\theta^1)\rangle_{\Delta E_n}$ and $\langle E(\theta \approx 37.5^\circ)\rangle / \langle E(\theta^1 \approx 135^\circ)\rangle$, is the excitation energy of fissioning nuclides emerging after emission of x neutrons. The same approach might be pursued in case of ^{232}Th$(n,xnf)^{1,\ldots,x}$ reactions.

The excitation energy of residual nuclides, after emission of (n,xnf) neutrons, is decreased by the binding energy of emitted neutron B_{nx} and its average kinetic energy:

$$U_x = E_n + B_n - \sum_{x,1\le k\le x} \left(\left\langle E^k_{nxnf}(\theta)\right\rangle + B_{nx}\right). \qquad (4)$$

Fission energy of ^{232}Th(n,F) reaction is distributed between fission fragments kinetic energy, their excitation energy and kinetic energy of pre-fission neutrons. The excitation energy of fission fragments is

$$E_{nx} = E_r - E^{pre}_{fx} + E_n + B_n - \sum_{x,1\le k\le x}\left(\left\langle E^k_{nxnf}(\theta)\right\rangle + B_{nx}\right). \qquad (5)$$

Value of TKE, kinetic energy of fission fragments prior prompt neutron emission, E^{pre}_F, is approximated as a superposition of partial TKE of $^{233-x}$Th nuclides as

$$E^{pre}_F(E_n) = \sum_{x=0}^{X} E^{pre}_{fx}(E_{nx}) \cdot \sigma_{n,xnf} / \sigma_{n,F} \ . \qquad (6)$$

Kinetic energy of fission fragments, i.e. post-fission fragments after neutron emission, E^{post}_F, are defined as

$$E^{post}_F \approx E^{pre}_F\left(1 - \nu_{post} / \left(A + 1 - \nu_{pre}\right)\right). \qquad (7)$$

Similar relation was used for E^{post}_f in [24] at E_n<E_{nnf}. Observed average number of prompt fission neutrons $\nu_p(E_n)$ is defined as

$$\nu_p(E_n) = \nu_{post} + \nu_{pre} = \sum_{x=1}^{X} \nu_{px}(E_{nx}) + \sum_{x=1}^{X} (x-1)\cdot\beta_x(E_n). \qquad (8)$$

The post-fission, $\nu_{post}(E_n)$, and pre-fission $\nu_{pre}(E_n)$ partials of $\nu_p(E_n)$ were obtained via

consistent description of $\nu_p(E_n)$ and observed fission cross sections at E_n <20 MeV.

Contribution of x–th fission chance (n,xnf) to the observed fission cross section (n,F) is

$$\sigma_{nF}(E_n)=\sigma_{nf}(E_n)+\sum_{x=1}^{X}\sigma_{n,xnf}(E_n)\ . \qquad (9)$$

That means the (n,xnf) contributions are defined by fission probability $P^{J\pi}_{f(A+1-x)}(E)$ of $^{232-x}$Th nuclides:

$$\sigma_{n,xnf}(E_n)=\sum_{J\pi}^{J}\int_0^{U_x}W^{J\pi}_{A+1-x}(U)P^{J\pi}_{f(A+1-x)}(U)dU\,, \qquad (10)$$

here $W^{J\pi}_{A+1-x}(U)$–is the population of excited states of $(A+1-x)$ nuclides with excitation energy U after emission of x post-fission neutrons [25].

The direction of emission of $(n,nX)^1$ neutrons, as well as that of $(n,n\gamma)^1$, $(n,2n)^1$, $(n,3n)^1$ and $(n,nf)^1$, $(n,2nf)^1$ and $(n,3nf)^1$ neutrons, is correlated with the momentum of the incident neutrons. The direction of the neutrons emitted from the fission fragments correlates with the fission axis direction mostly. Pre-fission neutrons influence the PFNS shape of ^{232}Th(n,F) in the energy range of E_n~E_{nnf1} –20 MeV. They influence also the shape of TKE of fission fragments and products [26], prompt neutron number, mass distributions and produce the step-like structures in observed fission cross section of rather peculiar shape. The variation of observed average energies $\langle E\rangle$ in the vicinity of ^{238}U(n,xnf) reaction thresholds, as shown in [23, 27, 28], is defined by the exclusive spectra of $(n,xnf)^{1,\cdots x}$ neutrons. The amplitude of variations of $\langle E\rangle$ in case of ^{238}U(n,F) [23, 27–29] was confirmed by PFNS measured data ^{238}U(n,F) [30] in E_n~1–20 MeV energy range.

Henceforth omitted are the indexes J^π in fission, Γ_f, neutron Γ_n and total Γ widths described in [31], as well as relevant summations. The angular dependence of partial width, calculated with spin and parity conservation, is due to dependence of excitation energy of residual nuclides on emission angle of first $(n,nX)^1$ neutron. The exclusive spectra of pre-fission $(n,nf)^1$ neutron is

$$\frac{d^2\sigma^1_{nnf}(\varepsilon,E_n,\theta)}{d\varepsilon d\theta}=\frac{d^2\sigma^1_{nnx}(\varepsilon,E_n,\theta)}{d\varepsilon d\theta}\frac{\Gamma^A_f(E_n-\varepsilon,\theta)}{\Gamma^A(E_n-\varepsilon,\theta)}. \qquad (11)$$

First neutron spectra of $(n,2nf)^1$ for reaction $(n,2nf)$, is defined as:

$$\frac{d^2\sigma^1_{n2nf}(\varepsilon,E_n,\theta)}{d\varepsilon d\theta}=\int_0^{E-B^A_n}\frac{d^2\sigma^1_{n2nx}(\varepsilon,E_n,\theta)}{d\varepsilon d\theta}\frac{\Gamma^{A-1}_f(E_n-B^A_n-\varepsilon-\varepsilon_1)}{\Gamma^{A-1}(E_n-B^A_n-\varepsilon-\varepsilon_1)}d\varepsilon_1 \qquad (12)$$

here first neutron spectra of $(n,2nx)$ reaction, i.e. $(n,2nx)^1$, is defined by the neutron spectrum of $(n,nX)^1$ and neutron emission probability of nuclide A as:

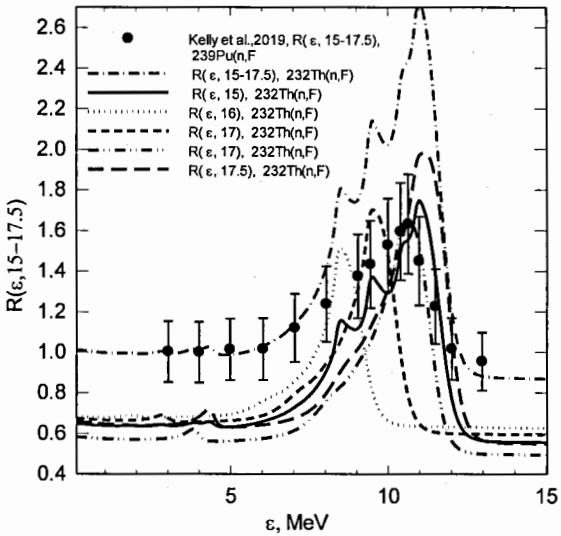

Fig. 5 Measured ratios $R^{exp} = S(\varepsilon, E_n \approx 15-17.5, \Delta\theta)/S(\varepsilon, E_n \approx 15-17.5, \Delta\theta^1)$ of ^{235}U(n,F) PFNS and calculated $R(\varepsilon,15\div17.5)$ for "forward", $\Delta\theta \sim 35°–40°$ and "backward" emission; $\Delta\theta^1$=130°–140°; •– ^{239}Pu(n,F) [1]; full line – ^{235}U(n,F) PFNS normalized to unity; dashed line – ^{235}U(n,F) PFNS equated at ε~3–5 MeV; dash-dotted line – ^{239}Pu(n,F) PFNS equated at ε~3–5 MeV; dotted line – partials of ^{235}U(n,F) $R(\varepsilon,15\div17.5)$ at $E_n \sim 15$ MeV, $E_n \sim 16$ MeV, $E_n \sim 17$ MeV and $E_n \sim 17.5$ MeV.

$$\frac{d^2\sigma^1_{n2nx}(\varepsilon,E_n,\theta)}{d\varepsilon d\theta} = \frac{d^2\sigma^1_{nnx}(\varepsilon,E_n,\theta)}{d\varepsilon d\theta}\frac{\Gamma^A_n(E_n-\varepsilon,\theta)}{\Gamma^A(E_n-\varepsilon,\theta)}. \quad (13)$$

Spectra of first and next neutrons of ^{232}Th($n,3nf$) reaction are covered in [23], but their contribution is quite low. Adopted phenomenological approach enables to reproduce NES in case of ^{232}Th+n interactions at E_n~1–18 MeV. Exclusive pre-fission neutron spectra of ^{232}Th(n,xnf)^{1,2} are shown on Figs. 3 and 4 as $\frac{\sigma_{n,xnf}(E_n,\theta)}{4\pi}\frac{d\sigma^{1,2}_{nnf}(\varepsilon,E_n,\theta)}{d\varepsilon}$ at angles θ~30° и θ~135°. They comprise small part of (n,nX)^1 spectrum, but relatively large part of the observed PFNS.

Angular distributions of ^{239}Pu(n,xnf) pre-fission neutrons at E_n~14–18 MeV, measured in [18], were quite well described as ~$0.25\,\omega(\theta)$, if $\theta > 135°$, then $0.25\,\omega(\theta = 135°)$. Estimate of pre- fission neutrons contribution in [18] they extracted as difference of observed PFNS and some approximated estimate of post-fission neutrons evaporated from fission fragments.

Angular anisotropy of PFNS relative to incident neutron beam was detected in ^{239}Pu(n,F) [1] at E_n~15–17.5 MeV range, $\Delta\theta$~35°–40° (forward direction) and $\Delta\theta^1$=130°–140° (backward direction) ranges. The data normalization obtained by equating observed PFNS at ε~3–5 MeV energy range. Alternative representation of PFNS, against that shown on Fig.3 in [18], as a ratio $R^{exp} = S(\varepsilon, E_n \approx 15-17.5, \Delta\theta)/S(\varepsilon, E_n \approx 15-17.5, \Delta\theta^1)$ for $\Delta\theta$~35°–40° (forward direction) and $\Delta\theta^1$=130°–140° (backward scattering) is virtually independent upon the normalizations adopted in [18].

On Fig. 5 R^{exp} of ^{239}Pu(n,F) at E_n~15—17.5 MeV $\Delta\theta$~35°–40° (forward direction) and $\Delta\theta^1$=130°–140° (backward direction) compared with of ^{232}Th(n,F) calculated ratio

$$R(\varepsilon,15\div17.5) \approx \frac{\int_{15}^{17.5} \nu_p(E_n,\approx 30^\circ)\sigma_{nF}(E_n,\approx 30^\circ)S(\varepsilon,E_n,\theta\approx 30^\circ)\varphi(E_n)dE_n}{\int_{15}^{17.5} \nu_p(E_n,\theta\approx 135^\circ)\sigma_{nF}(E_n,\theta\approx 135^\circ)S(\varepsilon,E_n,\theta\approx 135^\circ)\varphi(E_n)dE_n}, \qquad (14)$$

here $\varphi(E_n)$ is the incident neutron spectrum, which is not known. Spectra $S(\varepsilon,E_n,\theta)$ normalized to unity. As a first order approximation $R(\varepsilon,15\div17.5)$ (14) might be calculated as a ratio of lumped sums for E_n ~ 15 MeV, E_n ~ 16 MeV, E_n ~ 17 MeV and E_n ~ 17.5 MeV $\nu_p(E_n,\theta)\sigma_{nF}(E_n,\theta)S(\varepsilon,E_n\approx 15-17.5,\Delta\theta)$ and $\nu_p(E_n,\theta)\sigma_{nF}(E_n,\theta)S(\varepsilon,E_n 5-17.5,\Delta\theta^1)$. Values of $\nu_p(E_n,\theta)$ and $\sigma_{nF}(E_n,\theta)$ calculated at the same E_n and θ as those in $S(\varepsilon,E_n\approx 15-17.5,\Delta\theta)$. In case of angular dependent observables for ^{232}Th(n,F) hidden structures in lumped $R(\varepsilon,15\div17.5)$ constituents (evident for monochromatic beams) are smoothed, then R^{exp} and calculated $R(\varepsilon,15-17.5)$ seem to have similar shapes, but $R(\varepsilon,15-17.5)$ is shifted downwards. Smooth line of $R(\varepsilon,15-17.5)$ on Fig. 5 obtained by assuming in equation (14) that numerator and denominator values at ε~3–5 MeV energy range equal, as assumed in [18]. In case of ^{232}Th(n,F) and ^{239}Pu(n,F) both R^{exp} and $R(\varepsilon,15-17.5)$ are less then unity at $\varepsilon > E_{nnf1}$, that might be due to influence of angular dependence of (n,xnf) neutron emission on the fission chances distribution.

The calculated anisotropy of pre-fission neutrons of ^{232}Th(n,xnf) reaction is appreciably higher than in case of ^{239}Pu(n,F). That is due to correlation of anisotropy of pre-fission neutrons with contribution of emissive fissionreaction ^{232}Th (n,nf) to the observed fission cross section ^{232}Th (n,F), PFNS and angular anisotropy of NES. In case of ^{232}Th(n,F) and ^{239}Pu(n,F) at $\varepsilon > E_{nnf1}$, both R^{exp} and $R(\varepsilon,15-17.5)$ are less then unity, that also is due to influence of angular dependence of (n,xnf) neutron emission on the fission chances distribution.

Angular dependence of the first pre-fission neutron in reactions $(n,nf)^1$ and $(n,2nf)^1$ allows to interpret the experimental data trend observed in case of ratio of average energies for "forward" and "backward" emission of pre-fission neutrons in ^{235}U(n,xnf)^{1,2,3} [17] and ^{239}Pu(n,xnf)^{1,2,3} [18] reactions. The ratio of $\langle E(\theta)\rangle/\langle E(\theta^1)\rangle$ in case of ^{232}Th(n,F) for "forward", $\Delta\theta$~35°–40° and "backward", $\Delta\theta^1$=130°–140°, pre-fission neutron emission steeply increases

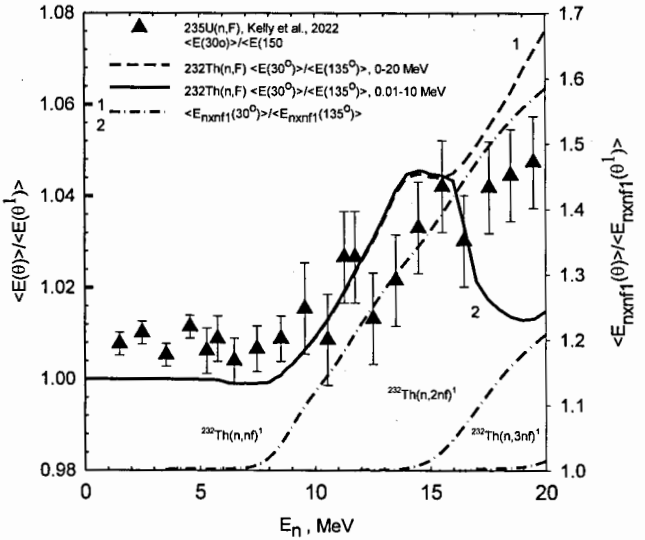

Fig. 6. Ratio of average energies of ^{235}U(n,F) PFNS $\langle E(\theta)\rangle/\langle E(\theta^1)\rangle$: ▲– $\langle E(\theta\approx 30^o)\rangle/\langle E(\theta^1\approx 135^o)\rangle$, ε~1–12 MeV [17]; full line –$\langle E(\theta\approx 30^o)\rangle/\langle E(\theta^1\approx 135^o)\rangle$, ε~1–20 MeV; dashed line –$\langle E(\theta\approx 30^o)\rangle/\langle E(\theta^1\approx 135^o)\rangle$, ε~0.89–10 MeV; dash–dotted line – $\langle E(\theta\approx 30^o)\rangle/\langle E(\theta^1\approx 135^o)\rangle$, ε~0.01–10 MeV; dash–dotted line — $\langle E(60^o)/E(90^o)\rangle$, ε~0–20 MeV; lines 1, 2, 3 –$\langle E_{n,xnf}(\theta\approx 30^o)\rangle/\langle E_{n,xnf}(\theta^1\approx 135^o)\rangle$, x=1, 2, 3.

starting from E_n~10–12 MeV. The angular anisotropy of $(n,xnf)^1$ neutrons emission is due to pre-equilibrium/semidirect emission of first neutron in $(n,nX)^1$ (see Fig. 6).

The ratio of average energies of exclusive neutron spectra of ^{232}Th(n,nf)^1, $\frac{d^2\sigma^1_{nnf}(\varepsilon,E_n,\theta\approx 30^o)}{d\varepsilon d\theta}$ and $\frac{d^2\sigma^1_{nnf}(\varepsilon,E_n,\theta\approx 135^o)}{d\varepsilon d\theta}$, $\langle E_{n,xnf}(\theta\approx 30^o)\rangle/\langle E_{n,xnf}(\theta^1\approx 135^o)\rangle$, is much higher than that of $\langle E(\theta)\rangle/\langle E(\theta^1)\rangle$, however it follows the shape of experimental ratio $\langle E(\theta\approx 30^o)\rangle/\langle E(\theta^1\approx 135^o)\rangle$ [17] of ^{235}U(n,F). Angular dependence of the ratio of average energies of exclusive neutron spectra ^{232}Th($n,2nf$)^1: $\frac{d^2\sigma^1_{n2nf}(\varepsilon,E_n,\theta\approx 30^o)}{d\varepsilon d\theta}$ and $\frac{d^2\sigma^1_{n2nf}(\varepsilon,E_n,\theta\approx 150^o)}{d\varepsilon d\theta}$ is much weaker. In the ratio of average energies of exclusive neutron spectra of ^{232}Th($n,3nf$)^1, $\frac{d^2\sigma^1_{n3nf}(\varepsilon,E_n,\theta\approx 30^o)}{d\varepsilon d\theta}$ and $\frac{d^2\sigma^1_{n3nf}(\varepsilon,E_n,\theta\approx 150^o)}{d\varepsilon d\theta}$, the angular dependence is quite weak.

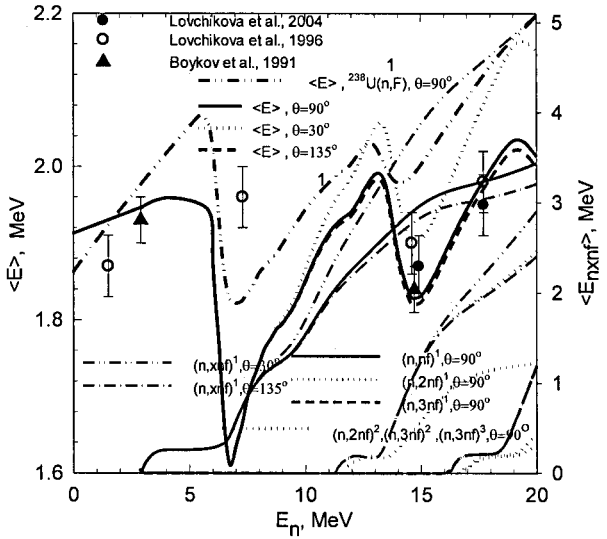

Fig. 7 Average energies of PFNS $\langle E \rangle$ of ^{235}U(n, F): • –[32]; ○–[33]; ▲ – [34]; full line, 1 – $\langle E_{n,xnf}(\theta \approx 90^o) \rangle$; dotted line, 2– $\langle E(30^o) \rangle$; dotted line, 3–$\langle E(135^o) \rangle$; dash–dotted line – $\langle E_{n,xnf}(\theta \approx 30^o) \rangle$; dash–double dotted line –$\langle E_{n,xnf}(\theta \approx 135^o) \rangle$.

Ratios $\langle E(\theta \approx 30^o) \rangle / \langle E(\theta^1 \approx 135^o) \rangle$ are virtually independent upon the lower threshold of neutron detection, while the dependence upon angular range and value of higher neutron detection threshold (ε~10, ε~12 or ε~20 MeV) is crucial. For emitted neutrons energy range of ε~1–12 MeV or ε~0–20 MeV, as evidenced on Fig. 6, shape of $\langle E(\theta \approx 30^o) \rangle / \langle E(\theta^1 \approx 135^o) \rangle$ of ^{232}Th(n,F) is roughly consistent with measured data for ^{235}U(n,F) up to E_n ~16 MeV. For exclusive neutron spectra of ^{232}Th(n,nf)^1 the ratios of $\frac{d^2\sigma^1_{nnf}(\varepsilon, E_n, \theta \approx 30^o)}{d\varepsilon d\theta}$ and $\frac{d^2\sigma^1_{nnf}(\varepsilon, E_n, \theta \approx 135^o)}{d\varepsilon d\theta}$ average energies are also much higher than those of $\langle E(\theta) \rangle / \langle E(\theta^1) \rangle$, but their shape is virtually consistent with that of $\langle E(\theta \approx 30^o) \rangle / \langle E(\theta^1 \approx 135^o) \rangle$ [17] (see Fig. 6). Average energy $\langle E \rangle$ is a rough integral signature of PFNS, however the angular anisotropy of pre-fission neutron emission exerts quite an influence on its values. Dependence of $\langle E \rangle (E_n)$ in case of ^{232}Th(n,F) is compared with measured data [32–34] on Fig. 7. The estimates of $\langle E \rangle$ for PFNS of ^{232}Th(n,F) are strongly correlated with PFNS shape. The influence of exclusive neutron

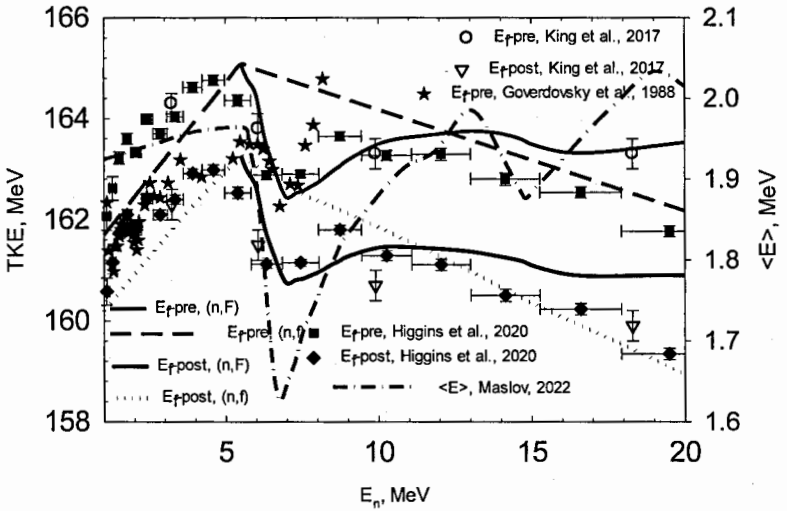

Fig. 8 Average total kinetic energies TKE of ^{232}Th(n, F): black stars–[35]; • –[36]; ■ – [36]; ♦ –[37]; ■ – [37]; dash–dotted line –$\langle E \rangle$ of PFNS.

spectra of $(n,nf)^1$ and $(n,2nf)^{1,2}$ which they exert on $\langle E \rangle$ in case of ^{232}Th(n,F) are much stronger than in case of ^{238}U(n,F) [23, 27–30]. Drop in $\langle E \rangle(E_n)$ in the vicinity of ^{232}Th($n,2nf$) reaction threshold is the deepest ever observed in measured PFNS data.

Another complication of observables in neutron-induced fission of ^{232}Th is the total kinetic energy TKE trend. Local minimum in TKE for the pre-neutron emission fission fragments in ^{232}Th(n,F) around ^{232}Th(n,nf) threshold first observed in [35]. That strong TKE variation is due to the pre-fission (n,xnf) neutrons. Contribution of the (n,xnf) reaction to the $\sigma_{n,F}$ of ^{232}Th(n,F) around E_n~7 MeV is exceptionally high [1], as well as provoked dip in TKE [26]. Partial contributions of (n,xnf), initially fixed in [23, 25], reproduce TKE variations. TKE values $E_f^{pre}(E_f^{post})$ before (after) prompt neutron emission from fission fragments were calculated with equations (6–9) provided above. Components ν_{post} and ν_{pre} of ν_p are defined via ν_p and PFNS analysis at E_n up to 20 MeV. Assuming $E_f^{pre}(E_n)$ for $^{233-x}$Th nuclides are similar to that of ^{233}Th, we obtained TKE both before and after prompt fission neutron emission, as shown on the Fig. 8. Neutrons emitted from the fission fragments ν_{post} and composite nuclide ^{233}Th, ν_{pre}, are predicted. Calculated TKE values shown on the Fig. 8 are consistent with the observed ^{232}Th+n data on neutron cross sections and PFNS. Straight lines approximate TKE values for the first chance fission of ^{233}Th nuclide. The (n,xnf)-neutrons influence TKE values E_f^{pre} and E_f^{post}, it is pronounced in case of ^{232}Th(n,F) reaction mostly as a sharp drop around

^{232}Th(n,nf) reaction threshold. That is due to the transition states structure of ^{232}Th fissioning nuclide and competition of ^{232}Th($n,n\gamma$) and ^{232}Th(n,nf) reactions at $E_n \leq 6.5$ MeV and ^{232}Th($n,2n$) at higher energies. In case of ^{238}U(n,F) TKE behaves in a mirror-like character [38], in [29] the observed local maxima were interpreted in similar fashion. The major difference in case of first chance fission of ^{233}Th ^{239}U is, respectively, the increasing and decreasing trend of TKE.

Analysis of neutron emission spectra ^{232}Th+n and prompt fission neutron spectra of ^{232}Th(n,F) evidence correlations of many observed data structures with $(n,xnf)^{1\cdots x}$ pre-fission neutrons. In case of NES observed angular anisotropy is due to angular dependence of elastic scattering, direct excitation of collective levels and pre-equilibrium emission of $(n,nX)^1$ neutrons. Proper description of ^{232}Th+n NES is attained when ground state band levels $J^\pi = 0^+, 2^+, 4^+, 6^+, 8^+$ are coupled within rigid rotator model, while those of β–bands with $K^\pi = 0^+$, γ–bands with $K^\pi = 2^+$ and octupole band $K^\pi = 0^-$ are coupled within soft deformable rotator model. NES of ^{232}Th+n at E_n~6, ~12, ~14, ~18 MeV are described. The net effect of these procedures for E_n up to ~20 MeV is the adequate approximation of angular distributions of ^{232}Th$(n,nX)^1$ first neutron inelastic scattering in continuum, which corresponds to U=1.2~6 MeV excitations of ^{232}Th.

Pre-fission neutron spectra turned out to be quite soft as compared with neutrons emitted by excited fission fragments. The net outcome of that is the decrease of $\langle E \rangle$ in the vicinity of the ^{232}Th(n,xnf) thresholds of ^{232}Th(n,F). The amplitude of the $\langle E \rangle$ variation is much higher in case of ^{232}Th(n,F) as compared with ^{238}U(n,F). The correlation of PFNS shape with different angles of emission of $(n,xnf)^1$ neutrons and emissive fission contributions for ^{232}Th(n,F) is established. The angular anisotropy of exclusive pre-fission neutron spectra strongly influences the PFNS shapes and $\langle E \rangle$. These peculiarities are due to strong emissive fission contributions in ^{232}Th(n,F). Predicted ratio of PFNS $\langle E \rangle$ for "forward" and "backward" emission of pre-fission neutrons seems to be the largest among stable actinide target nuclides. It steeply increases alongside with the increase of the average energies of the exclusive pre-fission neutron spectra [39].

References

1. V. M. Maslov, M. Baba, A. Hasegawa, A. B. Kagalenko, N.V. Kornilov, N.A. Tetereva, INDC(BLR)-16, IAEA, Vienna (2003), https://www-nds.iaea.org/publications/indc/indc-blr-0016/.
2. M. Baba, H. Wakabayashi, N. Ito et al., JAERI-M-89-143, 1989.
3. S. Matsuyama, M. Baba, N. Ito et al., JAERI-M-91-032, 219, 1991.
4. V.M., Maslov LXXII International Conference " NUCLEUS-2022, Fundamental problems and applications", Moscow, July, 11—16, 2022, Book of Abstracts, p.168, https://events.sinp.msu.ru /event/ 8/attachments/181/875 nucleus-2022-book-of-abstracts-www.pdf.
5. V.M. Maslov, Physics of Particles and Nuclei Letters, 20, 1401 (2023).
6. V.M. Maslov, Yad. Fyz., 86, 562 (2023).
7. V.M. Maslov, Yu.V. Porodzinskij, M. Baba, A. Hasegawa, Bull. RAS, Ser. Fyz., 67, 1597 (2003).
8. V.M. Maslov, Yu.V. Porodzinskij, N.A. Tetereva et al., Nucl. Phys. A, 764,212 (2006).
9. V. M. Maslov, M. Baba, A. Hasegawa, A. B. Kagalenko, N.V. Kornilov, N.A. Tetereva, INDC(BLR)-14, IAEA, Vienna (2003), https://www-nds.iaea.org/publications/indc/indc-blr-0014/.

10. M. Dupuis, S. Hilaire, S. Peru, EPJ Web of Conferences, 146, 12002 (2017).
11. M. Uhl and B. Strohmaier, IRK-76/01, IRK, Vienna, 1976.
12. P.G. Young, M. Chadwick, R. MacFarlane et al., Nucl. Data Sheets, 108, 2589 (2007).
13. D. A. Brown, M. B. Chadwick, R. Capote et al., Nucl. Data Sheets 148, 1 (2018).
14. A.M. Daskalakis, R.M.Bahran, E.J. Blain et al., Ann. of Nucl. Energy 73, 455 (2014).
15. M. R. Mumpower, D. Neudecker, H. Sasaki, et al., Phys. Rev. C, 107, 034606 (2023).
16. V.M. Maslov In: Proc. LXXII Intern. Conf. Nucleus 2022, Fundamental problems and applications, Moscow, 11—16 July, 2022, Book of abstracts, p. 111, https://events.sinp.msu.ru/event/8/attachments/181/875 nucleus–2022–book–of–abstracts–www.pdf.
17. K. J. Kelly, J.A. Gomez, M. Devlin et al, Phys. Rev. C 105, 044615 (2022).
18. K. J. Kelly, T. Kawano, J.M. O'Donnel et al., Phys. Rev. Lett., 122, 072503 (2019).
19. P. Marini, J. Taieb, B. Laurent et al., Phys. Rev. C, 101, 044614 (2020).
20. K. J. Kelly, M. Devlin, O'Donnel J.M. et al., Phys. Rev. C, 102, 034615 (2020).
21. N.V. Kornilov, A.B. Kagalenko, F.-J. Hambsch, Yad. Fiz., 62, 209 (1999).
22. B.E. Watt, Phys. Rev., 87, 1037, (1952).
23. V.M. Maslov, Yu. V. Porodzinskij, M. Baba, A. Hasegawa, N.V. Kornilov, A.B. Kagalenko and N.A. Tetereva, Phys. Rev. C, 69, 034607 (2004).
24. D. Madland, Nucl. Phys. A 772, 113 (2006).
25. V.M. Maslov. Nucl. Phys. A743, 236 (2004).
26. V.M. Maslov 27th International Seminar on Interactions of Neutrons with Nuclei, 2020, May, Dubna, Russia, http://isinn.jinr.ru/past-isinns/isinn-27/abstracts/Maslov.pdf/
27. V.M. Maslov, Yad. Fiz., 71, 11 (2008).
28. V. M. Maslov, EPJ Web Conf. 8, 02002 (2010); https://epjwoc.epj.org/articles/epjconf/abs/2010/07/epjconf_efnudat2010_02002/epjconf_efnudat2010_02002.html
29. V.M. Maslov, Physics of Particles and Nuclei Letters, 20, 565 (2023); https://www.pleiades.online/cgi-perl/search.pl?type=abstract&name=physpnlt&number=4&year=23&page=565.
30. K. J. Kelly, M. Devlin, J.M. O'Donnel et al., Phys. Rev. C, 108, 024603 (2023).
31. V.M. Maslov, Phys. Rev. C, 72, 044607 (2005).
32. G.N.Lovchikova,A.M.Trufanov,M.I.Svirin,V.A.Vinogradov Yad. Fyz. 67, 914 (2004); https://link.springer.com/article/10.1134/1.1777281
33. G.N. Lovchikova, A.M. Trufanov, VANT, Ser. Yadernye Konstanty, 1, 102, 1996; INDC(CCP)-409,115,1997.
34. G.S. Boykov, V.D. Dmitriev, G.A. Kydyaev, Ostapenko, M.I. Svirin, G.N. Smirernkin, Yad. Fyz., 53, 628 (1991).
35. A.A. Goverdovsky, B.D. Kuzminov, V.F. Mitrofanov, A.I. Sergachev, Proc. Conf. on Nucl. Data for Sci. and Technol., Mito. 1988 p. 695.
36. J. King, W. Loveland, J. S. Barrett et al., Eur. Phys. Journ. A, 53, 238 (2017).
37. D. Higgins, U. Greife, F. Tovesson et al., Phys. Rev. C, 101, 014601 (2020).
38. C. Zoller, Ph.D. thesis, Technische Hochschule Darmstadt, 1995, http://www-win.gsi.de/charms/data.htm.
39. V.M. Maslov, Proc. 28th International Seminar on Interactions of Neutrons with Nuclei, 2021, May, 24-28, Dubna, Russia, Book of Abstracts, p. 113, http://isinn.jinr.ru/past-isinns/isinn 28/ISINN 28 %20 Abstract%20 Book.pdf.

^{236s}Np isomer yields in ^{237}Np(n, 2n) and ^{238}U(p, 3n) reactions

Vladimir Maslov[1]

220025, Minsk, Byelorussia

Modeling $r(E_n)$, ratio of the yields of short-lived (1^-) and long-lived (6^-) of ^{237}Np(n,2n) reaction from threshold energy up to 20 MeV allowed to infer also the yield of the short-lived state ^{236s}Np in ^{238}U(p,3n) reaction. The different initial spin populations is probed in (p,3n) and (n,2n) reactions. The consistent description of the data base on cross sections ^{237}Np(n,F), ^{237}Np(n,2n)^{236s}Np and ^{238}U(p,F), ^{238}U(p,n) and ^{238}U(p,3n)^{236s}Np is achieved. The branching ratio $r(E_n)$ obtained by modeling the residual nuclide ^{236}Np levels. Excited levels of ^{236}Np are modeled using predicted Gallher-Moshkowski doublets. The branching ratios $r(E_n)$ and $r(E_p)$ are defined by the ratio of the populations of the two lowest states, isomer ^{236s}Np, with spin J= 1 and ground state ^{236l}Np with spin J= 6. The $r(E_n)$ and $r(E_p)$ have similar shapes in case of (n,2n) and (p,3n) reactions, which is due to some internal compensation of differing angular momentum and excitation energy distributions of ^{236}Np yields. The populations of ^{236s}Np and ^{236l}Np states defined by the γ-decay of the excited states of ^{236}Np in the continuum. The exclusive spectra of (n,xnf) and (n,2n)^{1,2} and (p,xnf) and (p,3n)^{1,2,3} influence $r(E_n)$ and $r(E_p)$ at higher energies and prompt fission neutron spectra.

Neptunium-237 is a major constituent of the spent nuclear fuel. Main chains for its production are neutron captures in ^{235}U and (n, 2n) reactions in ^{238}U, namely, ^{235}U(n, γ) ^{236}U(n, γ) ^{237}U(β$^-$)^{237}Np and ^{238}U(n,2n) ^{237}U(β$^-$)^{237}Np. The transmutation of the ^{237}Np in thermal power reactors is affected by the neutron capture cross sections of the reaction chain ^{237}Np(n,γ) ^{238}Np(β$^-$)^{238}Pu(n,γ) ^{239}Pu. The yield of the ^{236s}Np short-lived isomer happens via reaction chain ^{237}Np(n,2n) ^{236s}Np(β$^-$) [1–4].

The reaction chain ^{237}Np(n,2n)^{236s}Np(β$^-$)^{236}Pu(α)^{232}U is one of the major sources of the accumulation of ^{232}U in the irradiated reactor fuel. The half-life of ^{236s}Np $T^s_{1/2} = 22.5h$, the long-lived state, emerging in the reaction ^{237}Np(n,2n) ^{236l}Np ($T^l_{1/2} = 1.55\times10^5 y$) has a large thermal fission cross section, which may strongly influence the nuclear core reactivity [5]. Modeling $r(E_n)$, ratio of the yields of short-lived (1^-) and long-lived (6^-) of ^{237}Np(n,2n) reaction from threshold energy up to 20 MeV allowed to infer the yield of the short-lived state ^{236s}Np in ^{238}U(p,3n) reaction. The $r(E_n)$ and $r(E_p)$ are susceptible to the influence of differing initial spin populations probed in (p,3n) and (n,2n) reactions. The exclusive spectra of (n,xnf), (n,2n)^{1,2} and (p,xnf), (p,3n)^{1,2,3} influence $r(E_n)$ and $r(E_p)$ at higher energies and prompt fission neutron spectra [6–8]. They are used to define the exclusive spectra of (n,2n)^{1,2} reaction. These latter spectra define populations of ^{236}Np states.

The yield of short-lived 1^- state in ^{237}Np(n,2n) ^{236s}Np measured in the vicinity of the threshold [9] and around 14 MeV [10–15]. The ratio of yields of short- and long-lived states measured at ~14 MeV [16] allows to check the compatibility of measured data on ^{237}Np(n,2n)^{236s}Np reaction with the calculated cross sections of ^{237}Np(n,2n) and ^{237}Np(n,F).

[1]mvmmvm2386@yandex.ru

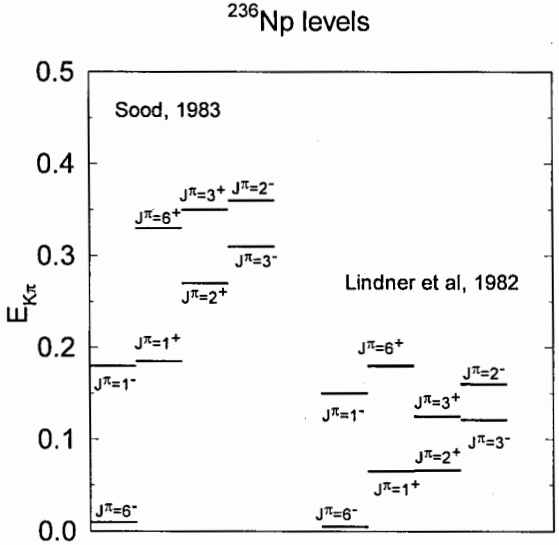

Fig. 1 Levels of ^{236}Np.

$$r(E_n) = \sigma^{I}_{n2n}(E_n)/\sigma^{s}_{n2n}(E_n), \qquad (1)$$

That means consistent description of the data base on fission and ^{237}Np(n,2n)^{236s}Np might be challenged at E_n~14 MeV, while at lower and higher values of E_n the $r(E_n)$ might be predicted. The branching ratio $r(E_n)$ is rather sensitive to the residual nuclide ^{236}Np levels. Excited levels of ^{236}Np are modeled using predicted Gallher-Moshkowski doublets by Sood [17] and Lindner et al. [18]. Modeling of the ratio of the yields of short-lived (1^-) and long-lived (6^-) from threshold energy of (n,2n) reaction up to 20 MeV, allows to infer the yield of the short-lived state ^{236s}Np as

$$\sigma^{s}_{n2n}(E_n) = \sigma_{n2n}(E_n)/(1 + r(E_n)). \qquad (2)$$

It provides a description of ^{237}Np(n,2n) ^{236s}Np data around E_n~14 MeV [10–15] and data from ^{237}Np (n,2n) reaction threshold up to E_n ~10 MeV [9].

Cross sections of (n,2n) and (n,3n) reactions are obtained with the statistical model calculations with account of pre-equilibrium neutron emission. Pre-equilibrium neutron emission contribution fixed according to consistent description of (n, F) and (n,xn) reaction data [3]. Myers et al. [16] measured the isomer branching ratio $r(E_n) = \sigma^{I}_{n2n}(E_n)/\sigma^{s}_{n2n}(E_n)$ with neutrons of the thermonuclear bomb-shot for the average beam energy of ~14 MeV. In the report [11] the isomer ratio $r(E_\gamma) = \sigma^{I}_{\gamma n}(E_n)/\sigma^{s}_{\gamma n}(E_n)$ of ~0.41 for ^{237}Np(γ,n) reaction was mentioned

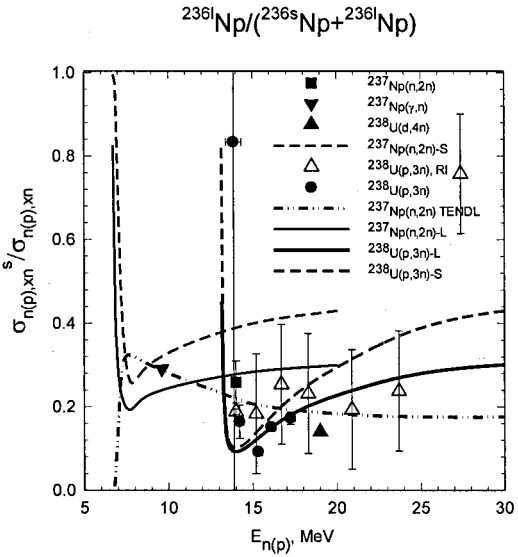

Fig. 2 Relative yield of long-lived (6^-) ^{236l}Np state in ^{237}Np(n,2n) and ^{238}U(p,3n) reactions; ■– [9]; ▼– [11]; ▲– [19]; ●– [49]; Δ– [48].

for the excitation energy of ~9.6 MeV. That presents the evidence of the decrease of $r(E_n)$ with the increase of the incident neutron energy E_n, if not the possible influence of the entrance channel on the initial spin population of ^{236}Np residual/excited nuclide. That conclusion is supported also by the data on the isomer branching ratio for the reaction ^{238}U(d,4n) for E_d~21 MeV [19]. In [19] it was found that the states of the residual nuclide ^{236s}Np with J= 1 are ~7 times more populated than the states ^{236l}Np with spin J=6. The modeling of the $r(E_n)$ for the ^{237}Np(n,2n) gives complex behavior, than just fitting [20], the trend of $r(E_{n,\gamma,d})$ measured values.

The branching ratio $r(E_n)$ is defined by the ratio of the populations of the two lowest states of ^{236s}Np, with spin J= 1 and ^{236l}Np, with spin J= 6. These populations defined by the γ-decay of the continuum excited states of ^{236}Np. For (n,γ) reaction the γ-decay was modeled in [21]. That approach could be applied in case of ^{237}Np(n,2n) or ^{238}U(p,3n) reactions probing the different initial spin populations for neutron capture, (n,2n) and (p,3n) reactions.

The γ-decay of the excited nucleus described by the following kinetic equation [21]

$$\frac{\partial \omega_k(U,J^\pi,t)}{\partial t} = \sum_{J'\pi'} \int_0^{U_g} \omega_{k-1}(U',J^{\pi'},t) \frac{\Gamma_\gamma(U',J^{\pi'},U,J^\pi)}{\Gamma(U',J^{\pi'})} dt - \omega_k(U,J^\pi,t) \frac{\Gamma_\gamma(U,J^\pi)}{\Gamma(U,J^\pi)}, \quad (3)$$

here $\omega_k(U,J^\pi,t)$ is the population of the state J^π at excitation U at time t, after emission of k γ-quanta; $\Gamma_\gamma(U',J^{\pi'},U,J^\pi)$ is the partial width of γ-decay from the $(U',J^{\pi'})$ to the state (U,J^π),

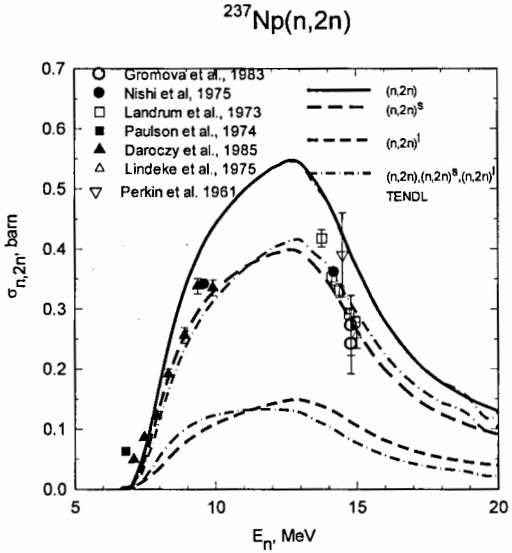

Fig. 3 Cross sections of ^{237}Np(n,2n), ^{237}Np(n,2n)^{236g}Np and ^{237}Np(n,2n)^{236l}Np reaction.

while $\Gamma(U,J^{\pi})$ is the total decay width of the state (U,J^{π}). For any state (U,J^{π}) with the excitation energy $0 \le U \le U_g$, the initial population is

$$\omega_k(U,J^{\pi},t=0) = \delta_{ko}\omega_0(U,J^{\pi}). \qquad (4)$$

The equation (4) means that in the initial state of (n,2n) or (p,3n) reactions we deal with the ensemble of states (U,J^{π}). Integrating the Eq. (3) over t, one gets the population $W(U,J^{\pi})$ of the state (U,J^{π}) after emission of k γ-quanta:

$$\omega_k(U,J^{\pi},\infty) - \omega_k(U,J^{\pi},0) = \sum_{J'\pi'} \int_U^{U_g} \frac{\Gamma_\gamma(U',J^{\pi'},U,J^{\pi})}{\Gamma(U',J^{\pi'})} \int_0^{\infty} \omega_{k-1}(U',J^{\pi'},t)dtdU' -$$

$$\frac{\Gamma_\gamma(U,J^{\pi})}{\Gamma(U,J^{\pi})} \int_0^{\infty} \omega_k(U,J^{\pi},t)dt. \qquad (5)$$

Denoting the population of the state (U,J^{π}) after emission of k γ-quanta as

$$W_k(U,J^{\pi}) = \frac{\Gamma_\gamma(U,J^{\pi})}{\Gamma(U,J^{\pi})} \int_0^{\infty} \omega_k(U,J^{\pi},t)dt, \qquad (6)$$

and taking into account the condition that $\omega_k(U,J^\pi,\infty)=0$ for any state, belonging to ensemble (U,J^π), Eq. (5) could be rewritten [21, 22] as

$$W_k(U,J^\pi)=\sum_{J'\pi'}\int_U^{U_g}\frac{\Gamma_\gamma(U',J^{\pi'},U,J^\pi)}{\Gamma(U',J^{\pi'})}W_{k-1}(U',J^{\pi'})dU'+\omega_k(U,J^\pi,0). \quad (7)$$

The population of any state (U,J^π) after emission of any number of γ-quanta defined as

$$W(U,J^\pi)=\sum_k W_k(U,J^\pi), \quad (8)$$

then from Eq. (6) one easily gets [21, 22]

$$W(U,J^\pi)=\sum_{J'\pi'}\int_U^{U_g}\frac{\Gamma_\gamma(U',J^{\pi'},U,J^\pi)}{\Gamma(U',J^{\pi'})}W(U',J^{\pi'})dU'+W_0(U,J^\pi). \quad (9)$$

The integral equation (9) in the code STAPRE [23] solved as a system of linear equations, the integration range (U,U_g) binned, in the assumption that there are no γ-transitions inside the narrow energy bins.

The isomer branching ratio depends mostly on the low-lying levels scheme and relevant γ-transitions probabilities. The latter data are missing for the ^{236}Np nuclide. As regards the low-lying levels of odd-odd nuclides like ^{236}Np, extensive experimental data are available only for ^{238}Np, ^{242}Am, ^{244}Am and ^{250}Bk [24]. It was established for the ^{236l}Np [19, 24] that the decay of ^{236l}Np(β$^-$) ^{236}Pu yields $J^\pi=6^+$ states, while in e-capture the yield of $J^\pi=6^+$ state of ^{236}U is observed. That is a strong argument that the long-lived state might be $J^\pi=6^-$. It was established for the ^{236s}Np [18, 25–28], that the decay ^{236s}Np(β$^-$)^{236}Pu yields $J^\pi=0^+, 2^+$ states, while in e-capture the yield of $J^\pi=0^+, 2^+, 2^-$ states of ^{236}U is observed. That is a strong argument, that for the short-lived state $J^\pi=1$, while the parity of the low-spin short-lived state is still uncertain. With these arguments one may stay assured that the spins of the two low-lying states of ^{236}Np are fixed. What are the energies of the ^{236s}Np and ^{236l}Np states is uncertain also. There is no experimental data about the other low-lying levels of ^{236}Np, with the exception of $J^\pi=3^-$, which was observed in [28] when investigating the enhanced α-decay of ^{240}Am.

Modeling of low-lying levels of in [17, 18] is accomplished based on the assumption that ground and first few excited states are of two-quasi-particle nature. For actinides with quadrupole deformations the superposition principle is usually adopted, the band-head energies of the doubly-odd nucleus are generated by adding to the each unpaired configuration (Ω_p,Ω_n), as observed in the isotopic/isotonic nucleus, the rotational energy contribution and residual n–p interaction energy contribution. The angular momenta of neutron and proton quasi-particles could be parallel or anti-parallel. In the independent quasi-particle model the two-quasi-particle states, $K^+=|K_n+K_p|$ and $K^-=|K_n-K_p|$, are degenerate. Gallaher-Moshkowski doublets [17, 18] appear because of n–p residual interaction. Figure 1 (left) shows the predicted in [17] band-head energies for the two-quasi-particle states expected up to ~400 keV in the odd-odd nuclide

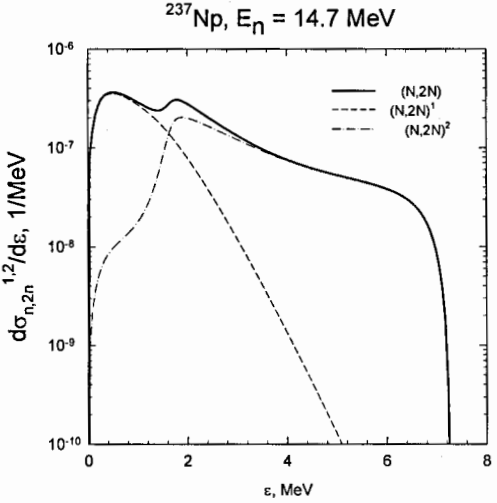

Fig. 4 Exclusive (n, $2n$) neutron spectra of ^{237}Np+n for incident neutron energy 14.7 MeV.

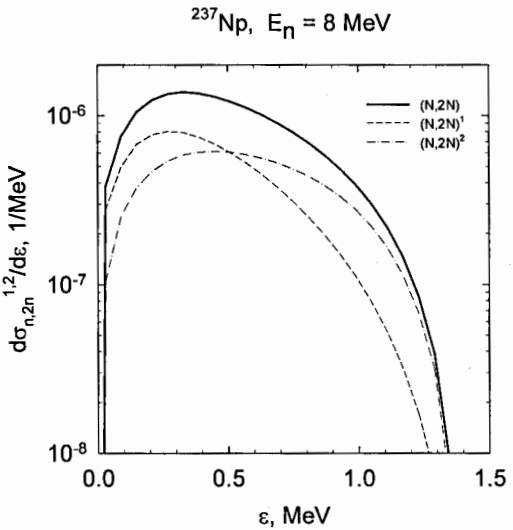

Fig. 5 Exclusive (n, $2n$) neutron spectra of ^{237}Np+n for incident neutron energy 8 MeV.

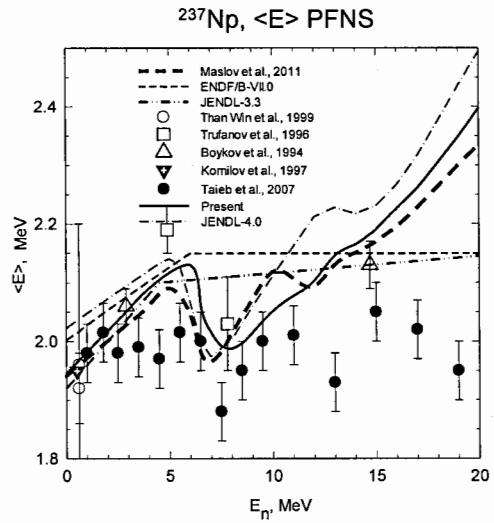

Fig. 6 Dependence of average energy of ^{237}Np(n,F) prompt fission neutrons on the E_n.

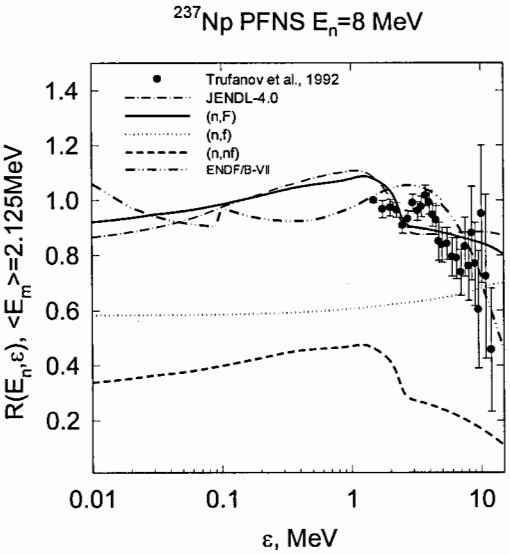

Fig. 7 Multiple-chance fission contributions to the prompt fission neutron spectrum for ^{237}Np (n, F) reaction, incident neutron energy ~8 MeV plotted as a ratio to Maxwellian with of <E>=2.125 MeV.

^{236}Np. The spectroscopic properties of two pairs of proton and neutron single particle states were derived from those experimentally observed in the isotopic (Z=93) and isotonic (N=143) odd-mass nuclei with mass (A-1). Figure 1 (right) shows levels expected up to ~250 keV of [18]. Obviously, the relative placement of LSI (low spin isomer), as well as its parity are different, though the underlying proton and neutron single particle states are similar. In short, in [17] LSI $J^{\pi}=1^{-}$ is just below $J^{\pi}=1^{+}$ counterpart, while in [18] the predicted LSI $J^{\pi}=1^{+}$ is lying much lower than the $J^{\pi}=1^{-}$ counter-part. However, the splits of LSI and HSI of [17] and [18] are quite different. For the band-heads, shown on Figure 1, the rotational bands generated as

$$E_{JK\pi}=E_{JK}+5.5\left[J(J+1)-K(K+1)\right]. \qquad (10)$$

Obviously, neither of the schema presented on Fig. 1 represents a complete set to allow the calculation of absolute yields of ^{237}Np(n,2n)^{236s}Np and ^{237}Np(n,2n)^{236l}Np reactions. However, in both cases attributed rotational bands were constructed up to ~700 keV, modeling levels with spins $J^{\pi}\le 10$, in total up to ~70 levels. It was shown in [29], that simple estimate of the number of levels in odd-odd nuclei as

$$N(U)=e^{2\Delta_0/T}(e^{U/T}-1), \qquad (11)$$

predicts up to 280 level at U~700 keV, T=0.388 MeV, Δ=12/$A^{1/2}$, MeV. We assume that the modeled angular momentum distribution would not be much different from a real one. Since the data on the γ-transitions are missing, we assumed the simple decay scheme, i.e. only E1, E2 and M1 transitions allowed in continuum energy range. Inter-band transitions forbidden, i.e., only γ-transitions within the rotational bands are assumed to occur. This methodology pursued, the populations of the lowest doublets calculated. Then we assumed that the transition to the high-spin, long-lived ground state $J^{\pi}=6^{-}$ or low-spin, short-lived isomer state $J^{\pi}=1^{-}$ [17] or $J^{\pi}=1^{+}$ [18] defined by "minimum multi-polarity" rule. That means states with spins $J>3$ should populate the ground state $J^{\pi}=6$, while those with $J\le 3$ should feed the isomer state $J^{\pi}=1$.

Then the branching ratio obtained as the ratio of the level populations, derived from Eq. (9):

$$r(E_n)=\frac{\sum_{J>(J_i+J_t)/2}W(U,J^{\pi})}{\sum_{J\le(J_i+J_t)/2}W(U,J^{\pi})} \qquad (12)$$

Figure 2 shows the branching ratios, calculated for the level schema of [17] and [18], presented at left and right parts of Fig. 1. The level scheme of [18] appears to be compatible with the measured data for $r(E_n)=\sigma^{l}_{n2n}(E_n)/\sigma^{s}_{n2n}(E_n)$ at 14 MeV [16], it is adopted in [3, 32], while the branching ratio for the level scheme of [17] has a similar shape of $r(E_n)$, but higher absolute value. The measured data of [11] and [19] for ^{237}Np(γ,n) and ^{238}U(d,4n) reactions, respectively, are much different from the predicted trend. The $r(E_n)$ in JENDL-4 [30] is independent on the energy of incident neutron, which strongly contradicts present predicted shape. The branching

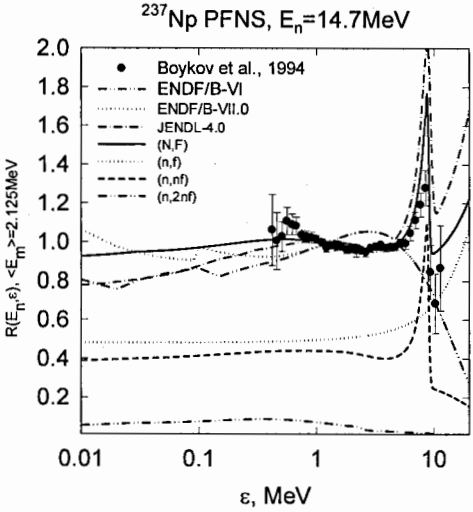

Fig. 8 Multiple-chance fission contributions to the prompt fission neutron spectrum for ^{237}Np (n,F) reaction, incident neutron energy 14.7 MeV plotted as a ratio to Maxwellian with average energy of $\langle E \rangle$=2.125 MeV.

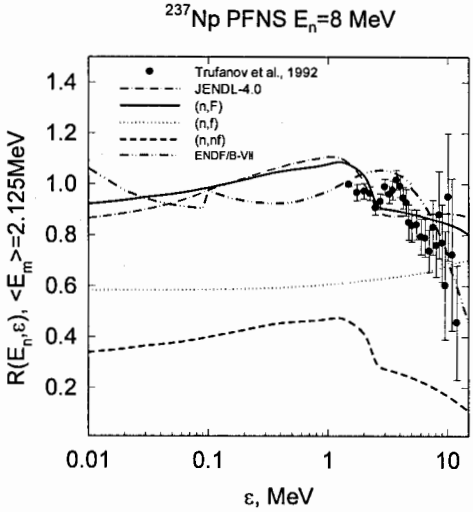

Fig. 9 Multiple-chance fission contributions to the prompt fission neutron spectrum for ^{237}Np (n,F) reaction, incident neutron energy 8 MeV plotted as a ratio to Maxwellian with average energy of $\langle E \rangle$= 2.125 MeV.

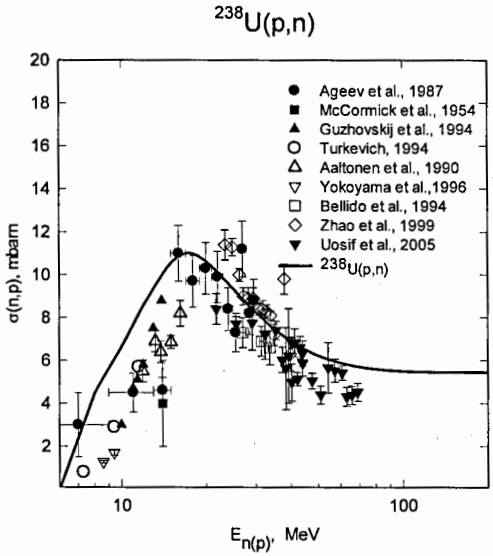

Fig. 10 Cross sections of $^{238}U(p, n)$.

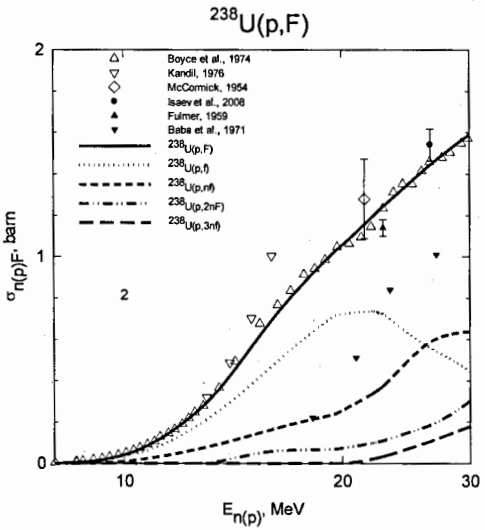

Fig, 11 Multiple-chance fission contributions to $^{238}U(p,F)$ reaction.

ratio $r(E_n)$ of ENDF/B-VIII [31] is adopted from [3, 32]. The branching ratio $r(E_n)$ used to estimate ^{237}Np(n,2n) ^{236s}Np and ^{237}Np(n,2n)^{236l}Np reaction cross sections using ^{237}Np(n,2n) reaction cross section compatible with ^{237}Np(n,F) cross section [2, 33].

Figure 3 shows ^{237}Np(n,2n), ^{237}Np(n,2n)^{236s}Np and ^{237}Np(n,2n)^{236l}Np reaction cross sections. Measured data base on ^{237}Np(n,2n)^{236s}Np [9-15] was corrected in [3] using the modern decay and cross section data standards. The decay data for the ^{236m}Np were those from [33]. Recent evaluation by E.Browne and J.K.Tuli [34], which is in Decay Radiation Data Base [35], is consistent with the former data of [33]. The half-life, estimated in [33, 34] is $T_{1/2}$= (22.5±0.04) hours. The electron-capture and β$^-$-decay branching ratios of [34] equal: I_{ec} =0.52±0.01 and I_{β^-} =0.48±0.01, respectively. In [35] $I_{ec} = I_{\beta^-}$ = 0.50±0.03. The neutron flux monitor reaction were those of ^{27}Al(n,α)^{24}Na, ^{238}U(n,2n)^{238}U and ^{238}U(n,f), evaluated in [36], [37] and [38], respectively. It was possible to update measured database, except data [15]. ^{237}Np(n,2n), ^{237}Np(n,2n)^{236s}Np and ^{237}Np(n,2n)^{236l}Np reaction cross sections [3, 32] shown on Fig. 2 are adopted in [31], in [20] they adopted ^{237}Np(n,2n) cross section only. Though ^{237}Np(n,2n)^{236s}Np and ^{237}Np(n,2n)^{236l}Np reaction cross section of [20] seem to be close to those of [3, 32], the branching ratios $r(E_n)$ are very much different, since in [20] the $r(E_{n,\gamma,d})$ just reproduces trend measured values of (γ,n), (n,2n) and (d,4n) reactions.

Exclusive spectra of first neutrons, $\frac{d\sigma^1_{n2n}}{d\varepsilon}$, and $\frac{d\sigma^2_{n2n}}{d\varepsilon}$ second neutrons of (n,2n) reaction, calculated as in [39–41] are shown on Fig. 4 and Fig. 5. They define the populations of ^{236}Np nuclide states. The spectra presented normalized to 10^{-6}, since in data files [3, 32] the emitted neutron energies given in eV. The major competing reaction to ^{237}Np(n,2n) is ^{237}Np(n,xnf). Actually, x pre-fission neutrons define the shape of exclusive spectra of first neutrons, $\frac{d\sigma^1_{n2n}}{d\varepsilon}$, and $\frac{d\sigma^2_{n2n}}{d\varepsilon}$ second neutrons. They influence also the average energy of prompt fission neutrons measured in [42–46] as shown on Fig. 6, and shapes of prompt fission neutron spectra (PFNS). Figures 7 and 8 demonstrate the PFNS at E_n~14.7 MeV and E_n~8 MeV. The partial contributions of observed PFNS are sensitive to ^{237}Np(n,xnf) contributions to the observed fission cross section ^{237}Np(n,F) [3] and exclusive pre-fission neutron spectra.

Modeling the ratio $r(E_n)$ of the yields of short-lived (1$^-$) and long-lived (6$^-$) of ^{237}Np(n,2n) reaction from threshold energy up to 20 MeV allows to infer the yields of the short-lived state ^{236s}Np and long-lived state ^{236l}Np in ^{238}U(p,3n) reaction. Since entrance channel J^π populations in case of ^{238}U+p and ^{237}Np are quite different [47] as well as spin populations of (p,3n) and (n,2n) reactions, $r(E_n)$ and $r(E_p)$ would demonstrate various behavior. The consistent description of the data base on fission reaction ^{238}U(p,F) and ^{238}U(p,n) and ^{238}U(p,3n)^{236s}Np was achieved within STAPRE environment [23]. The contribution of the yield ^{238}U(p,3n)^{236s}Np to the ^{238}U(p,3n) reaction cross section is compatible with measured data on $r(E_p)$ [48] and [49]. The contribution of the yield ^{238}U(d,4n)^{236s}Np to the ^{238}U(d,4n) would have similar shape, but shifted to higher energies.

The absolute values of ^{238}U(p,3n)^{236s}Np contribution to the ^{238}U(p,3n) are obtained simultaneously with ^{238}U(p,F) and ^{238}U(p,n) cross sections. Fig. 10 shows description of ^{238}U(p,n) data [49–57] up to E_p~70 MeV with the direct neutron emission as described in [39, 40], with the exception that the (p,nX)^1 spectra are much softer than in case of ^{237}Np+n interaction.

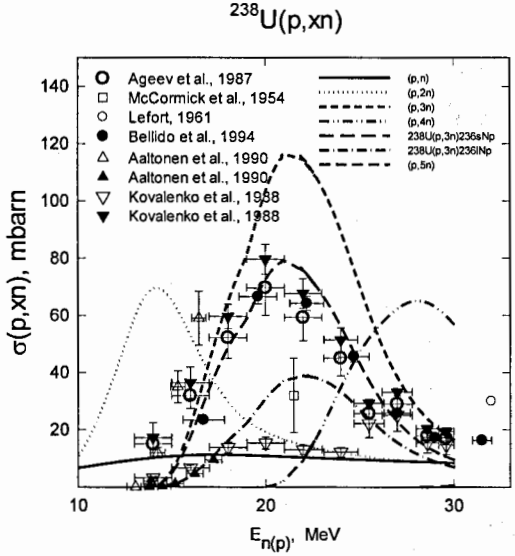

Fig. 12 Cross sections of ^{238}U(p,2n), ^{238}U (p,3n), ^{238}U (p,3n)^{236s}Np and ^{238}U (p,3n)^{236l}Np reaction. neutron spectra [39–41].

Fission reaction cross section ^{238}U(p, F) comprise the major part of proton absorption cross section which is defined in [47]. Modelling the (p,nX)^1 spectra in a way described in [39, 40] the ^{238}U(p,F) data could be reproduced up to 200 MeV. Figure 11 shows the fission cross section data [58–62] up to E_p~30 MeV and partial contributions of ^{238}U($pxnf$) chances to the observed cross section of ^{238}U(p,F). Figure 11 shows the calculated symmetric ^{238}U(p,xnf)^{sym}, asymmetric ^{238}U(p,xnf)^{asym} and ^{238}U(p,F) fission cross sections. In case of the proton-induced fission reaction ^{238}U(p,F) the observed fission reaction cross section is calculated using the fission-barrier and level-density parameters of Np nuclei, obtained by fitting the ^{237}Np(n,F) fission cross section [32]. It might be anticipated that ^{238}U(p,xnf) reactions give the dominant contribution to the observed fission cross section [63].

Absolute values of ^{238}U (p,3n)^{236s}Np and ^{238}U (p,3n)^{236l}Np contributions to the ^{238}U(p,3n) cross section measured data are compared on Fig. 12. Data [49] are quite compatible with calculated cross sections of ^{238}U (p,3n)^{236s}Np and ^{238}U (p,3n)^{236l}Np reactions. In case of data [48] there is some discrepancy around peak crass section values.

Modeling $r(E_{n(p)})$, ratio of the yields of short-lived (1$^-$) ^{236s}Np and long-lived (6$^-$) ^{236l}Np in ^{237}Np(n,2n) reaction from threshold energy up to 20 MeV and ^{238}U(p,3n) reaction from threshold energy up to 30 MeV allowed to describe the measured yield of the short-lived state ^{236s}Np. The different initial spin populations are probed in (p,3n) and (n,2n) reactions. The consistent description of the data base on cross sections of fission ^{237}Np(n,F), ^{237}Np(n,2n)^{236s}Np and ^{238}U(p,F), ^{238}U(p,n) and ^{238}U(p,3n)^{236s}Np is achieved. The branching ratio $r(E_n)$ obtained by modeling the residual nuclide ^{236}Np levels using predicted Gallher-Moshkowski doublets.

The branching ratio $r(E_n)$ is defined by the ratio of the populations of the two lowest states, isomer ^{236s}Np, with spin J= 1 and ground state ^{236l}Np with spin J= 6. The $r(E_n)$ and $r(E_p)$ have similar shapes in case of $(n,2n)$ and $(p,3n)$ reactions, which is due to internal compensation of differing angular momentum and excitation energy distributions of ^{236}Np yields. The populations of ^{236s}Np and ^{236l}Np states defined by the γ-decay of the excited states of ^{236}Np in the continuum. The exclusive spectra of (n,xnf) and $(n,2n)$[1,2] and (p,xnf) and $(p,3n)$[1,2,3] influence $r(E_n)$ at higher energies and prompt fission neutron spectra [64].

References

1. Ignatyuk A.V., Kornilov N.V., Maslov V.M., Atomnaya Energiya 63, 110 (1987).
2. Maslov V.M. VANT, Ser. Yad, Konst., 4, 1987, INDC(CCP)-366, p. 27, 1994 .
3. Maslov V.M., Pronyaev V.G., N.A. Tetereva, Kolesov A.M., Zolotarev K.I., Granier T., Hambsch F.-J., INDC (BLR)-21, Vienna: IAEA, 2003; https://www-nds.iaea.org/publications/ indc/indc-blr- 0021/
4. Fort E., Derrien H., Doat J.P. In: Proc. Int. Conf. Nuclear Data for Science and Technology, Antwerpen, Belgium, September 6-10, 1982, p. 673, 1983.
5. Belyaev B.N., Gromova E.A., Kovalenko S.S. et al., Atomnaya Energiya, 60, 141 (1986).
6. Maslov V.M. In: Proc. 5th Workshop on Neutron Measurements, Evaluations and applications. Nuclear Data for sustainable nuclear energy, JRC-IRMM-EU (Geel, Belgium), 27-29 October, 2008, Ljubljana, Slovenia, p. 73, 2008.
7. Maslov V.M., in: Proc. Intern. 2nd Intern. Conf. Frontiers in Nuclear Structure, Astro-physics and Reactions. FINUSTAR 2. Crete, Greece, 10-14 September 2007, AIP, CP-1012, 2008, p. 398.
8. Maslov V.M. Atomic Energy, 104, 4, 330 (2008).
9. Daroczy S., Raics P., Csikai J., Kornilov N.V. et al., Atomnaya Energiya, 58, 117 (1985).
10. Gromova E.A., Kovalenko S.S., Nemilov Yu.A. et al., Atomnaya Energiya, 54, 198 (1983).
11. Nishi T., Fujiwara I., Imanishi N., NEANDC(J_-42L, 20, 1975.
12. Landrum J.H., Nagel R.J., Lindner M., Phys. Rev. C 8, 1938 (1973).
13. Paulson C.K., Hennelly E.J., Nucl. Sci. Eng. 5, 24 (1974).
14. Lindeke K., Specht S., Born H.J., Phys. Rev. C 12, 1507 (1975).
15. Perkin J.L., Coleman R.F., Ann. Nucl. Energy, 14, 69 (1961).
16. Myers W.A., Lindner M., Newburry R.S., Journ. Inorg. Nucl. Chem. 37, 637 (1975).
17. Sood P.C. Z. Phys. A-Atomic Nuclei, 348, 111 (1984).
18. Lindner M., Dupzyk R.J., Hoff R.W. and Nagle R.J., J. Inorg. Nucl. Chem., 43, 3071 (1981).
19. Huizenga J.R., Vandenbosh R. Nuclear Fission, 1964, vol. 2, p. 51, Atomizdat.
20. Koning A.J., Rochman D., Sublet J. et al., Nuclear Data Sheets 155, 1 (2019); https://tendl. web.psi.ch/tendl_2021/tendl2021.html
21. Strutinsky V.M., Groshev L.V., Akimova M.K., Atomnaya Energiya, 38, 598 (1960).
22. Dovbenko A.G., Zakharova S.M., Kolesov V.E., Malyshev A.V., Atomnaya Energiya, 18, 114 (1964).
23. Uhl M., Strohmaier B., IRK-76/01, IRK, Vienna (1976).
24. Ahmad J. Hines J. and Cindler J.E., Phys. Rev. C27, 2239 (1983).

25. Gray P.H. Phys. Rev. 101, 306 (1956).
26. Cindler J. and Sjoblom R. J. Inorg. Nucl. Chem. 12, 8 (1959).
27. Lederer C.M., Jaklevic J.M. and Prussin S.G., Nucl. Phys., A135, (1969).
28. Gorman D.J., Asaro F., Phys. Rev. C, 2, 2406 (1970).
29. Maslov V.M., Porodzinskij Yu.V., JAERI Research, 98-038, 1998.
30. Shibata K., Iwamoto O., Nakagawa T. et al. J. Nucl. Sci. Technol., 48, 1 (2011).
31. Brown D., Chadwick M., Capote R. et al. Nuclear Data Sheets, 148, 1 (2018).
32. Maslov V. M., Porodzinskij Yu. V., Baba M. et al. IAEA-NDS-164. Vienna: IAEA, 2003, https://www-nds.iaea.org/minskact.
33. Firestone R.B., Table of Isotopes CD-ROM, Eighth Edition, Version 1.0, March 1996, S.Y. Frank Chu, CD-ROM Ed., V.S.Shirley, Ed., Wiley-Interscience, 1996
34. Browne E., Tuli J.K., Nuclear Data Sheets, 107, 2649 (2006).
35. Decay Radiation Data Base, version 12/11/2009, www.nndc.bnl.gov/ nudat2/index dec.jcp
36. Zolotarev K.I., INDC(NDS)-0546, IAEA, Vienna, April 2009.
37. Zolotarev K.I., Evaluation of cross-section data for the U-238(n,2n)U-237 reaction from threshold to 30 MeV. Private communication, Obninsk, FEI, May 2009.
38. Pronyaev V.G. et al., In: Proc. of Int. Conf. on Nuclear Data for Science and Technology, Santa Fe, New Mexico, USA, September 26 - October 1, 2004.
39. Maslov V.M., Physics of Particles and Nuclei Letters, 20, 565 (2023).
40. Maslov V.M., Physics of Particles and Nuclei Letters, 20, 1401 (2023).
41. Maslov V.M., Porodzinskij Yu. V., Baba M., Hasegawa A., Kornilov N. V., Kagalenko A. B., Tetereva N.A., Phys. Rev. C, 69, 034607 (2004).
42. Boykov G.S., Dmitriev V.D., Svirin M.I., Smirenkin G.N., Physics of Atomic Nucleus, 57, 2047 (1994).
43. Kornilov N.V., Kagalenko A.B., Baryba V.Ya. et al. In: Proc. of Intern. Conference on Nuclear Data for Science and Technology, May 19-24, Trieste, Italy, p.577.
44. Taieb J., Granier T., Ethvignot T. et al. In Proc. of the Inter. Conf. on Nuclear Data for Science and Technology (O. Bersillon, F. Gunsing, E. Bauge, R. Jacqmin and S. Leray, eds.), p. 429, Nice, France, April 22-27, 2007, EDP Sciences.
45. Trufanov A.M., Lovchikova G.N., Sukhih S.E. et al., Phys.Atom. Nucl., 55, 289(1992).
46. Than Win, Baba M., Ibaraki M. et al., J. Nucl. Sci. Techn. 36, 486 (1999).
47. Maslov V.M., Porodzinskij Yu. V., Tetereva N.A, Baba M., Hasegawa A. Nucl. Phys. A 736, 77 (2004).
48. Kovalenko S.S., Selitsky Yu.A., Funshtein V.B., Khlebnikov S.V., Yakovlev V.A., Proc. Int. Conf. Nuclear Data for Science and Technology, Mito, USA, September 6-10, 1988, p. 995, 1988.
49. Aaltonen J., Brenner M., Egorov S.A., et al., Phys. Rev. C, 41,513 (1990).
50. Turkevich A., Radiochimica Acta, 64, 145 (1994).
51. Guzhovskii B.Ya., Abramovich S.N., Zvenigorodskii A.G. et al., Proc. Int. Conf. Nuclear Data for Science and Technology, Gattlinburg, USA, May, 1994, p. 390,1994.
52. Bellido L.F., Robinson V.J., Sims H.E., Radiochimica Acta, 64, 11 (1994).
53. Uosif M.A.M., Michel R., Herpers U., et al. In: Proc. Int. Conf. Nuclear Data for Science and Technology, Santa Fe, USA, October, 2004, p. 1547, 2005.
54. Ageev A., Golovnya V.Ya., E.A.Gromova et al., Yad. Fyz., 46, 700 (1987).
55. McCormick G.H., Cohen B.L., Phys. Rev. 96, 722, (1954).
56. Yokoyama A., Takahashi N., Nitani N. et al., Zeit. Phyz./A, 356, 55 (1996).

57. Zhao Y.L., Tanikawa M., Sueki K., et al., Radiochimica Acta, 86, 79 (1999).
58. Boyce J.R., Hayward T.D., Bass R. et al., Phys. Rev. C 10, 231(1974).
59. Kandil A.T., Journ. Inorg. Chemistry 38, 37 (1976).
60. Fulmer C.B., Phys. Rev. 116, 418 (1959).
61. Isaev S., Prieels R., Keutgen Th. et al. Nucl. Phys. A 809, 1 (2008).
62. Baba S., Umezawa H., Baba H., Nucl. Phys. A 175, 177 (1971).
63. Maslov V.M., Phys. Lett. B, 649, 863 (2007).
64. Maslov V.M., Yad. Fyz., 86, 562 (2023).

Научное издание

FUNDAMENTAL INTERACTIONS & NEUTRONS, NUCLEAR STRUCTURE, ULTRACOLD NEUTRONS, RELATED TOPICS

XXIX International Seminar on Interaction of Neutrons with Nuclei

Proceedings of the Seminar

ФУНДАМЕНТАЛЬНЫЕ ВЗАИМОДЕЙСТВИЯ И НЕЙТРОНЫ, СТРУКТУРА ЯДРА, УЛЬТРАХОЛОДНЫЕ НЕЙТРОНЫ, СВЯЗАННЫЕ ТЕМЫ

XXIX Международный семинар по взаимодействию нейтронов с ядрами

Труды семинара

Ответственная за подготовку сборника к печати *Л. В. Мицына.*

Сборник отпечатан методом прямого репродуцирования с оригиналов, предоставленных оргкомитетом.

Е3-2023-58

Подписано в печать 21.11.2023
Формат 60×90/16. Бумага офсетная. Печать цифровая
Усл. печ. л. 20,12. Уч.-изд. л. 33,09. Тираж 82 экз. Заказ № 60753

Издательский отдел Объединенного института ядерных исследований
141980, г. Дубна, Московская обл., ул. Жолио-Кюри, 6.
E-mail: publish@jinr.ru
www.jinr.ru/publish/